Technische Universität München
TUM School of Natural Sciences

# Rational Design and Stimuli-Responsiveness of Metal-Organic Frameworks and Molecular Perovskites

**Silva Maria Kronawitter**

Vollständiger Abdruck der von der TUM School of Natural Sciences der Technischen Universität München zur Erlangung des akademischen Grades einer

**Doktorin der Naturwissenschaften (Dr. rer. nat.)**

genehmigten Dissertation.

Vorsitz: Prof. Dr. Lukas Hintermann

Prüfende der Dissertation:

1. Priv.-Doz. Dr. Gregor Kieslich
2. Prof. Dr. Torben Gädt

Die Dissertation wurde am 08.07.2024 bei der Technischen Universität München eingereicht und durch die TUM School of Natural Sciences am 24.07.2024 angenommen.

# RATIONAL DESIGN AND STIMULI-RESPONSIVENESS OF METAL-ORGANIC FRAMEWORKS AND MOLECULAR PEROVSKITES

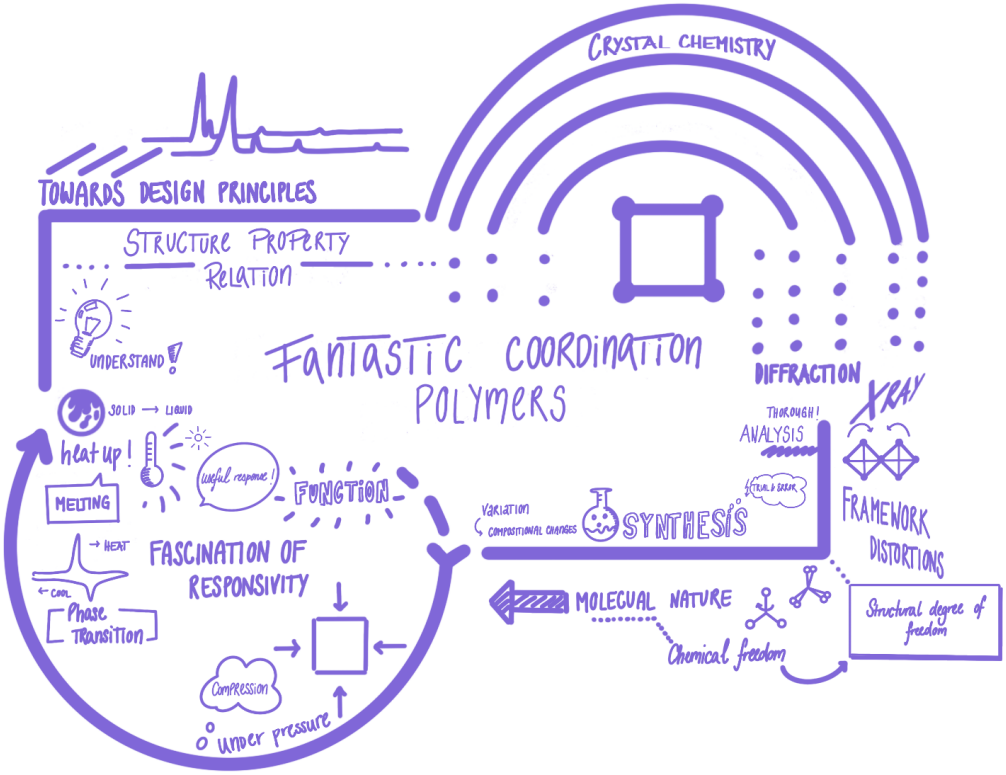


## Dissertation

Silva Maria Kronawitter

Die vorliegende Arbeit wurde im Zeitraum von Januar 2021 bis Juli 2024 in der Nachwuchsgruppe „Structural Chemistry of Functional Materials“ im Fachgebiet Anorganische und Metallorganische Chemie der Technischen Universität München angefertigt.

# DANKSAGUNG

Zunächst möchte ich Priv.- Doz. Dr. Gregor Kieslich danken. Lieber Gregor, es war mir ein Fest! Danke dir, für dein Vertrauen und die Möglichkeit, nach meiner Masterarbeit bei dir zu promovieren. Du hast mich gefördert, geprägt, mir zugehört und mich immer wieder gefordert –eine sehr gute Mischung und Arbeitsatmosphäre. Für mich war es eine ganz besondere Zeit und Erfahrung, für die ich dir immer dankbar sein werde. Viele denken, die Promotion sei ein Einzelkampf und manchmal eine Qual, aber das war sie für mich überhaupt nicht. Es war eine tolle Zeit, dank dir! Deine Faszination für die fundamentale Strukturchemie und Kreativität hat auf mich abgefärbt und gleichzeitig hast du mir Perspektiven darüber hinaus gezeigt, auf die ich immer zurückgreifen werde. Ich drücke dir die Daumen für deinen weiteren akademischen Weg. Abschließend ist es wohl an der Zeit zu sagen – End(t)e gut, alles gut, wir sehen uns wieder!

Herzlichen Dank an die finanzielle Unterstützung über die letzten Jahre, insbesondere an die Deutsche Forschungsgemeinschaft (DFG), TUM Graduate School und die Gesellschaft Deutscher Chemiker (GDCh), die meine Teilnahmen an nationalen und internationalen Konferenzen ermöglicht haben.

Ganz lieben Dank an alle Studenten: Sylvia Dörschmidt, Sebastian Hallweger, Zoe Lambert, Jan Meyer, Carmen Pedri, Melvin Resch, Alexander Spears und Anna Tratter, für euer Vertrauen und Engagement. Die Zusammenarbeit mit euch hat mir große Freude bereitet, und ihr habt maßgeblich zu dieser Arbeit beigetragen. Besonders freue ich mich, dass du lieber Sebastian am Lehrstuhl geblieben ist. Du bist ein toller Kollege und Freund geworden! Danke für den wissenschaftlichen Austausch und die witzigen Momente, besonders die Lachflashs am Synchrotron. Ich wünsche dir nur das Beste!

Ein herzliches Dankeschön an unseren Mittelbau: Dr. Mirza Cokoja, Dr. Romy Ettlinger, Dr. Christian Gemel, Dr. Dominik Halter und Dr. Julien Warnan. Ihr habt maßgeblich zur großartigen Atmosphäre am Lehrstuhl beigetragen! Besonders danke ich Dr. Markus Drees für deine schnelle und unkomplizierte organisatorische Hilfe, die DFT Rechnungen und deine Humor. Danke an Dr. Gabriele Raudaschl-Sieber für die Wandertipps und Gespräche. Eure Hilfsbereitschaft war super. Besonderer Dank an Dr. Alexander Pöthig für deinen Support bei der Einkristalldiffraktometrie. Ein großes Dankeschön auch an Dr. Dana Weiß und Martin Schellerer für eure organisatorischen Support. Besten Dank an den gesamten AMC-Lehrstuhl für die unvergessliche Zeit und die großartigen gemeinsamen Momente der letzten Jahre! Besonders hervorheben möchte ich Alexandra H., Anna Lisa S., Fabian S., Kathrin K., Margit A., Maximilian M., Patricia W., Raphael B., Sebastian W.und Stefan B.. Danke an Dr. Christian Jandl für deinen Support bei der Einkristallstrukturanalyse zu Beginn. Ein großes Dankeschön

an die tolle ACS-Gang – es war ein Fest. Vielen Dank an Johanna H., ich habe deine ruhige Art als Kollegin und deine OC-Tipps sehr geschätzt. Herzlichen Dank an dich liebe Pia V. für die superleckeren Kuchensnacks auch nach deiner Zeit am Lehrstuhl und dein offenes Ohr. Wir haben in euch beiden zwei neue Freunde gefunden und freuen uns auf weitere Momente mit euch und Benedikt. Ganz herzlichen Dank an Lena S. und Simon D.. Lena, ich werde unsere Zeit jeden Donnerstag nie vergessen. Du warst die erste, die ich kennengelernt habe, und wir hatten sofort eine Verbindung. Danke für deine ehrliche Art! Dann kam der liebe Simon dazu. Danke, lieber Simon, dein Humor hat meine Promotionszeit bereichert und ich schätze unsere Freundschaft sehr. Wir waren sofort auf einer Wellenlänge – 97-er Baujahr passt eben gut zusammen. Ein riesiges Dankeschön an Karina H. bzw. jetzt S. für unsere gemeinsame Zeit am Lehrstuhl und unsere Freundschaft. Dein strahlendes Lachen, charmanter Dialekt und unvergleichliche Herzlichkeit sind ansteckend. Auf dich kann man sich immer verlassen und die schönen Dinge im Leben genießen. Danke dir! Vielen vielen Dank an dich lieber Philip S., dass du die letzten Jahren maßgeblich zur schönen Atmosphäre innerhalb und außerhalb der Promotion beigetragen hast. Unser gemeinsamer USA-Trip war großartig – more to come! Auf dich kann ich mich immer verlassen, dafür an dieser Stelle nochmals ausdrücklich Danke! Wie sollte es auch anders sein, warst du die einzige Person, die auch diese Arbeit zur Korrektur gelesen hat. Von Herzen tausend Dank! Herzlichen Dank an Stefanie P., wir sind zusammen in Regenburg in den Bachelor gestartet. Es war nicht Liebe auf den ersten Blick, aber dafür eine Größere auf den Zweiten. Ab dem Ionenlotto haben wir uns lieben gelernt und diese Zeit mit Anne und dir werde ich nie vergessen. Das Chemiestudium hat mir eine Freundin fürs Leben geschenkt und umso schöner war es, als du nach München kamst.

Ein großes Dankeschön an meine Freunde und Familie außerhalb der Chemie-Bubble. Ihr alle helft mir die Chemie auch mal beiseite zu lassen. Besonderen Dank an Adrian, Beni, Carlo, Celina, Chrise, Dominik, Fabian, Flo, Hendrik, Lena, Nina, Silvia, Staze und all die anderen. Ein riesengroßes Dankeschön geht an dich liebe Ami. Du bist Familie für mich und mit dir bin ich durch alle Hochs und Tiefs durchgeangen. Wir haben uns gegenseitig geprägt und trotz Distanz nie verloren. Du hast mir immer das Gefühl gegeben, dass ich viel erreichen kann und stets bestärkt. Ich schätze dich sehr und freue mich auf weitere gemeinsame Erfolge beruflich sowie vor allem privat in den kommenden Jahren.

Zuletzt danke ich meiner Familie. Zunächst euch beiden, liebe Ninette und lieber Lars, ihr seid für mich zu meiner zweiten Familie geworden und ich kann euch nicht genug danken für eure Liebe und Unterstützung über die letzten 10 Jahre. Das ist nicht selbstverändlich. Ihr als Unterstützung im Hintergrund gebt uns stets Rückenwind. Ein riesiges Dankeschön an meine eigene ganz verrückte, aber tolle Familie. Liebe Mama, lieber Papa, als Einzelkind bin ich bis heute eure Nummer 1 und das spüre ich bis heute. Ihr habt mir alle Türen geöffnet und mir die

Freiheit gelassen, meinen eigenen Weg zu gehen, den ihr immer unterstützt habt, ohne zu hinterfragen. Besonders dir, liebe Mama, verdanke ich meinen Ehrgeiz und Stärke. Wir haben wundervolle, aber auch schwere Zeiten durchgestanden. Rückblickend war jede Erfahrung wichtig, um mein Ziel nie aus den Augen zu verlieren und weiterzukämpfen. Papa, du warst immer mein größter Fan und kannst heute noch stolzer auf deine Tochter sein. Danke für eure Liebe und Hingabe. Ganz besonderer Dank geht an die tollste Oma, du bist der Knaller und hast so lange durchgehalten bis ich nun endlich diesen Hut bekomme, der in echt doch größer ist als in den Filmen – wir haben es geschafft!

Zu guter Letzt danke ich von ganzem Herzen dir lieber Torben. Du bist und warst immer da, als ich Höhen und Tiefen, vor allem zu Beginn des Studiums, erlebt habe. Du bist und warst mein größter Unterstützer, mein bester Freund, die Liebe meines Lebens und dieser Erfolg ist ebenso deiner wie meiner! Du gibst mir die nötige Ruhe und Leichtigkeit und glaubst an mich, wenn ich es selbst kann. Deine Lebensfreude ist ansteckend und hat zum Glück allmählich auch auf mich abgefärbt und so waren der Großteil dieser Reise vor allem seit München doch wirklich eine tolle Zeit. Es gibt nichts Schöneres, als diese „once in a lifetime“ Momente gemeinsam zu erleben und gebührend zu feiern. Das machen wir – cheers to us! Auf uns, auf dich, auf unsere Gesundheit, auf unsere Liebe und unseren weiteren gemeinsamen Weg, denn mit dir kann es nur gut werden.

*“Maybe the best any of us can do is not to quit, play the hand we’ve been given, and accessorize the outfit we got”, Sex and the City.*

# TABLE OF CONTENTS

Table of Contents ..... 1
Kurzzusammenfassung ..... 3
Abstract ..... 4
List of Abbreviations ..... 5
1. Introduction ..... 6
1.1. Scientific Context ..... 6
1.1.1. The Evolution of the Perovskite Structure ..... 6
1.1.2. Historical Remarks ..... 8
1.2. Structure Chemical Properties of Molecular Perovskites ..... 10
1.2.1. Tolerance Factor as a Synthetic Compass ..... 10
1.2.2. Framework Distortions: Octahedral Tilts and Shifts ..... 12
1.2.3. Tilt and Shift Polymorphism in Molecular Perovskites ..... 14
1.2.4. Structure Analytical Concept: Complexity of (Molecular) Perovskites ..... 16
1.2.5. Molecular Perovskites and Beyond: $AB_2X_6$ Materials ..... 17
1.3. Research Highlights and Advances ..... 19
1.3.1. Melting of Molecular Perovskites ..... 19
1.3.2. Molecular Perovskites as Barocalorics ..... 21
1.3.3. Ferroelectric and Ferroelastic Ordering in Molecular Perovskites ..... 23
1.4. Concluding Remarks ..... 26
1.5. Methodology of Synthesis and Characterisation of Molecular Perovskites ..... 27
2. Results and Discussion ..... 35
2.1. Study I: $Li(C_2N_3)$ as Eutectic Forming Modifier in the Melting Process of the Molecular Perovskite $[(C_3H_7)_3N(C_4H_9)]Mn(C_2N_3)_3$ ..... 35
2.2. Study II: Understanding and Controlling Molecular Compositions and Properties in Mixed-Linker Porphyrin Metal-Organic Frameworks ..... 43
2.3. Study III: Spin-State Dependent Pressure Responsiveness of Fe(II)-based Triazolate Metal-Organic Frameworks ..... 53
2.4. Study IV: Tuning the Mechanical Properties of Molecular Perovskites by Controlling Framework Distortions *via* A-site Substitution ..... 62
3. Conclusion and Outlook ..... 70
4. Supporting Information ..... 74
4.1. Supporting Information for Study I ..... 74
4.2. Supporting Information for Study II ..... 113
4.3. Supporting Information for Study III ..... 143
4.4. Supporting Information for Study IV ..... 185
4.5. Source Data for Literature Survey of Molecular Perovskites ..... 261
5. References ..... 267

6. Appendix ..... 278
6.1. Complete List of Publications ..... 278
6.1.1. First Author Publications ..... 278
6.1.2. Contributions to Other Publications ..... 280
6.2. Reprint Permissions ..... 281

# KURZZUSAMMENFASSUNG

Die Entdeckung neuer struktureller und funktioneller Materialien treibt das Materialdesign in der Material- und Festkörperchemie voran. Ziel ist es, den „trial-and-error“-Ansatz durch Prinzipien zu ersetzen, die Struktur-Eigenschaftsbeziehungen rationalisieren, um Synthesewege zu einer gewünschten Eigenschaft zu ermöglichen. Fortschritte in künstlicher Intelligenz und maschinellem Lernen sind vielversprechend für ein datengestütztes Materialdesign; der Designraum erfordert jedoch weiterhin definierte Designregeln. Die Herausforderung bleibt daher bestehen, die häufig zufällig entdeckte Funktion eines Materials zu verstehen, um seine Leistung zu optimieren oder es durch nachhaltigere, weniger toxische oder stabilere Alternativen zu ersetzen. Konzeptionelle und experimentelle Ansätze sind erforderlich, die eine Materialfunktion als nützliches, oft ungewöhnliches Antwortverhalten auf einen externen Stimulus betrachten. Koordinationspolymere wie molekulare Perowskite und metallorganische Gerüstverbindungen (MOFs) dienen aufgrund ihrer Modularität und chemischen Vielfalt als wichtige Modellplattformen, da sie Variationen der chemischen Zusammensetzung, Struktur und Eigenschaften ermöglichen.

Diese Arbeit präsentiert vier Studien über Koordinationspolymere, die zum fundamentalen Verständnis der Struktur-Zusammensetzung-Eigenschaftsbeziehungen beitragen. Alle Studien diskutieren die Auswirkungen von Veränderungen der chemischen Zusammensetzung von Koordinationspolymere auf ihre makroskopischen Eigenschaften, um konzeptionelle Einblicke für die Entwiclkung von Designprinzipien zu liefern. Dies wird durch die Zugabe eines Modifizierungsalzes zum molekularen Perowskiten, gemischte Porphyrin-basierte Linker in MOFs, sowie durch Änderung der Form und Größe von molekularen Bausteinen in Fe(II)-basierten MOFs oder in molekularen Perowskiten erforscht. Dabei charakterisieren strukturanalytische Methoden das jeweilige Antwortverhalten auf äußere Reize. Die Temperatur steht dabei im Fokus der ersten Studien, wobei der Einfluss eines Modifizierers auf das Schmelzverhalten des molekularen Perowskiten bzw. die thermische Expansion als Funktion der gemischten Linker erprobt wird. Die letzten Studien diskutieren das Verhalten bei hohen Drücken, wie die inverse Kompressibilität von MOFs und molekularen Perowskiten, die durch chemische Modifikation der Bausteine gesteuert werden kann. Zudem wird ein Zusammenhang zwischen der Chemie der organischen Baueinheiten und dem Spin-Zustand der Fe(II)-basierten MOFs bzw. der Verzerrung des Perowskitnetzwerks hergestellt.

*Die wundersame Welt der molekularen Perowskite** ist das Leitthema dieser Dissertation, das in einer Einleitung mit einem umfassenden Literaturüberblick hervorgehoben wird. Darauf folgt ein methodischer Teil, der konzeptionelle und synthetische Einblicke in das Design neuer molekularer Perowskite gibt, die in dieser Arbeit synthetisiert wurden.

*adaptiert aus “The Wondrous World of Perovskites” von Glazer im Jahr 2017 bei der Bragg Lecture der Royal Institution

# ABSTRACT

The discovery of new structural and functional materials is driving *material design* in the field of material and solid-state chemistry. It aims to replace the trial-and-error approach with principles that rationalise fundamental structure-property relationships, enabling targeted synthetic methods towards a desired functionality. Recent advances in artificial intelligence and machine learning offer great promise for data-driven material design and discovery; however, the design space still requires well-defined design rules. Hence, the key challenge in material design remains: understanding a certain material's function – often initially discovered by chance – to optimise its performance or to replace it with sustainable, less toxic or more stable and durable alternatives. To conceptually and experimentally address this challenging task, approaches are required that consider the material's functionality as a useful (often unusual) response of a material to an external stimulus. Coordination polymers, such as Molecular Perovskites and Metal-Organic Frameworks (MOFs), serve as powerful material platforms due to their modular building principle and both broad and deep chemical parameter space that allow to tune the chemical composition, structure and material's function.

This thesis demonstrates four studies on coordination polymers that contribute to the fundamental understanding of structure-composition-property relationships in Molecular Perovskites and MOFs. All studies discuss the impact of changing the chemical composition of coordination polymers on their macroscopic properties, providing conceptual insights for the development of design rules. This is explored, for instance, by adding a modifier salt to a Molecular Perovskite, by using mixed-linker porphyrin-based MOF systems, and by changing the size and shape of the triazolate-linker in Fe(II)-based MOFs or of piperidinium-based organic cations in Molecular Perovskites. Advanced structure analytical methods are applied to characterise the stimuli-responsive behaviour. The first studies focus on temperature as an external stimulus, with emphasis on the melting behaviour in the presence of a modifier salt and the thermal expansion behaviour as a function of mixed-linker systems. The latter studies highlight pressure responsiveness, in particular the bulk moduli of MOFs and Molecular Perovskites, which can be tuned by the choice of the molecular component. Additionally, the chemical modification of the molecular building units is linked to the spin-state in Fe(II)-based MOFs and to unit cell distortions in Molecular Perovskites.

*The Wondrous World of Molecular Perovskites** is the key theme of this thesis, which is highlighted in a review-style introduction complemented by a comprehensive literature survey. This is followed by a methodological section that provides conceptual and synthetical insights into the design of new Molecular Perovskites discovered in this thesis.

*adapted from "The Wondrous World of Perovskites" by Glazer in 2017 at the Bragg Lecture of the Royal Institution

# LIST OF ABBREVIATIONS

| | |
|---|---|
| **α** | **Tolerance factor** |
| **$A_p$** | Parent-cell normalised distortion mode amplitude |
| **B** | Bulk modulus |
| **B-M** | Birch-Murnaghan |
| **CCDC** | Cambridge Crystallographic Data Centre |
| **DSC** | Differential scanning calorimetry |
| **ED** | Electron diffraction |
| **HOIPs** | Hybrid organic inorganic perovskites |
| **HPPXRD** | High-pressure powder X-ray diffraction |
| **$I_G$** | Information content of a crystal structure |
| **IL** | Ionic liquid |
| **irrep** | Irreducible representation |
| **irrev.** | irreversible |
| **k** | Crystallographic orbit |
| **LFSE** | Ligand field stabilisation energy |
| **m** | Multiplicity |
| **MOF** | Metal-Organic framework |
| **NLC** | Negative linear compressibility |
| **NMR** | Nuclear magnetic resonance |
| **NTE** | Negative thermal expansion |
| **p** | Pressure |
| **PCN** | Porous coordination network |
| **PL** | Photoluminescence |
| **PTM** | Pressure transmitting medium |
| **PXRD** | Powder X-ray diffraction |
| **r** | Radius |
| **rev.** | reversible |
| **RT** | Room temperature |
| **RUM** | Rigid-unit modes |
| **ΔS** | Entropy change |
| **SCO** | Spin-crossover |
| **SCXRD** | Single crystal X-ray diffraction |
| **SHG** | Second-harmonic generation |
| **T** | Temperature |
| **TGA-DSC** | Thermogravimetric analysis-differential scanning calorimetry |
| **v** | Number of atoms in the reduced unit cell |
| **VTPXRD** | Variable-temperature powder X-ray diffraction |
| **ZIF** | Zeolitic imidazolate framework |

# 1. INTRODUCTION

## 1.1. Scientific Context

### 1.1.1. The Evolution of the Perovskite Structure

In material chemistry, understanding *how* – on a fundamental level – a material's macroscopic responsiveness to external stimuli such as temperature, pressure, a magnetic/electric field, or chemical triggers can be controlled is key for the targeted design of functional materials. In this context, the simple act of substituting atoms in all-inorganic structure motifs – making the material a *hybrid* – has opened up many exciting research directions.[1–5] Some fascinating examples are Metal-Organic Frameworks (MOFs) and Hybrid organic inorganic perovskites (HOIPs), referred to as the broad class of coordination polymers, that are composed of metal-based nodes linked by organic ligands to form extended network structures.[4,6] These framework materials provide a modular building principle, whilst the use of molecular building units unlocks a large, virtually unlimited chemical scope. In practice, this offers many possibilities for synthesising and developing new materials with optimised or even currently unknown functional responsiveness, *e.g.* chemically engineered HOIPs with tailored optoelectronic properties and photovoltaic performance.[7] In addition to this, many framework materials are structurally related to their dense inorganic counterparts enabling the application of solid-state principles to rationalise structure-property relationships. Some typical examples are zeolitic imidazolate frameworks (ZIFs),[8] diamondoids MOFs[5], HOIPs[4] and Ruddlesden Popper-type layered HOIPs.[9,10] Given the large chemical parameter space available to these hybrid materials, there is clearly a need for developing principles that can serve as a compass for material development, avoiding time-consuming trial-and-error experiments.

In this context, framework materials with the iconic $ABX_3$ perovskite architecture[11–13] have emerged as an important platform. From a historical perspective,[14] inorganic perovskites have played a unique role in solid-state and materials chemistry. This dates back to the early discovery of the ferroelectric and piezoelectric properties in $BaTiO_3$,[15] $PbZr_{1-x}Ti_xO_3$[16] and $PbMg_{1-x}Nb_xO_3$.[17] Over time, the compositional variability of the $ABX_3$ perovskite structure has been explored, resulting in a broad material class of inorganic perovskites with diverse properties, *e.g.* ferromagnetic $SrRuO_3$,[18] non-linear optical $KNbO_3$,[19] antiferromagnetic $KNiF_3$,[20,21] multiferroic $BiMnO_3$[22] and superconductive $YBa_2Cu_3O_7$.[23,24] Going one step further in the structural and chemical evolution of the $ABX_3$ structure motif, the use of molecules (*e.g.* $A^+$ cations = $[CH_3NH_3]^+$ or $[(NH_2)_2CH]^+$) on the A-site has paved the way for the discovery of HOIPs or metal halide perovskites (MHPs).[25–27] Their purely inorganic $[BX_3]^-$ network structures are formed by corner-sharing $BX_6$ octahedra, typically with halides on the X-site and divalent metals (*e.g.* Pb and Sn) on the B-site, in which small organic A-site cations are located

in the network cavities. Here, the discovery of $[CH_3NH_3]PbI_3$[28] and $[(NH_2)_2CH]PbI_3$[29,30] semiconducting materials, with extraordinary optoelectronic properties for solar energy conversion and optoelectronic applications in general, marks a milestone that has inspired research on perovskite-based solar cells to date.

The chemical substitution of single atoms with molecular components on the X-site has opened up another dimension to the $ABX_3$ structure, expanding the $ReO_3$-type network structure to *Molecular Perovskites* (Figure 1).[4,27,31–33] This, in principle, marks a clear distinction from HOIPs, as molecular components are used on both the A- and X-site. Some typical examples are $[(CH_3)_2NH_2]Mn(HCOO)_3$,[34] $[(CH_3)_4N]Cd(N_3)_3$[35] and $[(C_3H_7)_4N]Ni(C_2N_3)_3$.[36] In such materials, the divalent B-site metal ($B^{2+}$) is octahedrally coordinated to six coordinating atoms of the monovalent molecular X-site anion ($X^-$) to form $BX_6$ octahedra. These $BX_6$ octahedra are corner-connected *via* $\mu$-1,5-$X^-$ bridges to build a negatively charged 3D $[BX_3]^-$ framework with **pcu** (α-Po type) topology. The molecular A-site cations ($A^+$) are located in the framework

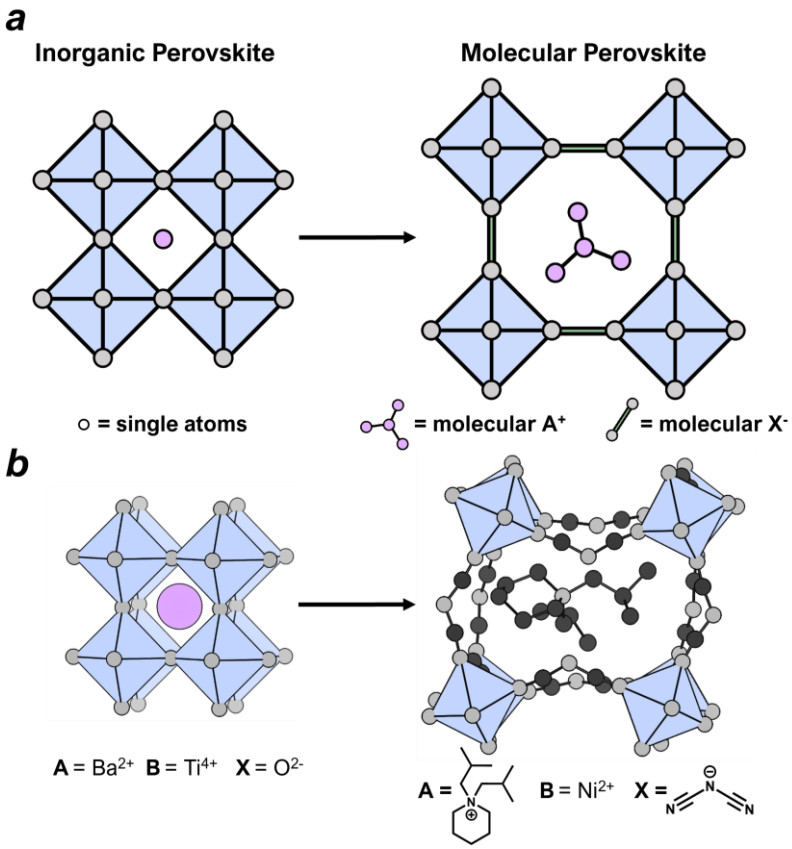


Figure 1: Illustration of the schematic building principle of Molecular Perovskites, originating from the inorganic $ABX_3$ perovskite structure (**a**). The incorporation of molecular components on the cationic A-site and the anionic X-site opens up the $ReO_3$-type network structure (right side of (**a**) and (**b**)). (**b**) shows the structural development of the perovskite structure with schematic crystal structures exemplified with $BaTiO_3$ (CCDC number: 1032384; left side of (**b**); Colour code: Ba – pink, Ti – light purple and O – light grey) and $[(C_5H_{10})N\text{-}(iso\text{-}C_4H_9)_2]Ni(C_2N_3)_3$ (studied within this thesis; right side of (**b**); Colour code: Ni – light purple, N – light grey and C – dark grey, with H atoms excluded for better visualisation).

cavities to enable charge balance and to adopt the perovskite architecture, plus they can interact with the $[BX_3]^-$ network *via* hydrogen bonding and dispersion interactions. In principle, this makes Molecular Perovskites less promising for applications in optoelectronics such as HOIPs, as the bonding situation within the $[BX_3]^-$ network is different compared to the electronic characteristics present in a purely inorganic $[BX_3]^-$ network of HOIPs. However conceptually, the presence of molecules on the A- and X-site gives rise to new unconventional chemical and structural degrees of freedom[31] – purely absent in $ABX_3$ inorganics – that are directly linked to the functional response. This unlocks phase transition phenomena linked to the motion of the organic A-site[37,38] or unconventional octahedral tilts and shifts related to the molecular nature of the X-site linker,[39,40] making Molecular Perovskites promising candidates for exploring application-oriented research areas such as barocalorics[41] or hybrid improper ferroelectrics.[42]

### 1.1.2. Historical Remarks

To give a very broad scientific context of the historical development of Molecular Perovskites over time, this thesis provides an up-to-date (June 2024) literature survey encompassing all reported Molecular Perovskite structures, which excludes metal-free organic halide perovskites and HOIPs. A detailed overview of all structures categorised by the used X-site anion is given in the supporting information of this thesis, see *Chapter 4.5*.

Historically, first reports of Molecular Perovskites date back to 1973 (Figure 2),[43] which was five years before the intial structure analysis of $[CH_3NH_3]PbI_3$.[25] However, the conceptual relationships to their inorganic analogues have not been discussed in literature before 2005.[44,45] In the early stages, between 1973–2000, structures with smaller X-site molecules, *i.e.* $X^-$ = $[HCOO]^-$ and $[N_3]^-$, have been reported with emphasis on the preparation details and crystal structure determination of these newly discovered materials (Figure 2). Inspired by these early reports, the diffusion method under ambient conditions was established as a suitable crystallisation strategy in many follow-up studies to grow single crystals of new Molecular Perovskites. In subsequent years (from about 2003), the research direction turned to larger X-site anions, such as $X^-$ = $[C_2N_3]^-$ and $[M(CN)_2]^-$, providing new chemical freedom for synthetically exploring the A-site towards larger or chemically more complex A-site cations as the $[BX_3]^-$ cage size increases.[46–48]

Hence, over the past two decades, this material class has become a rich field for exploring material properties, in particular *via* molecular substitution on the A-site, with approximately 50 different A-site molecules incorporated in Molecular Perovskites to date. An overview of A-site cations used in different X-site families is given in *Chapter 4.5*. In total, over 160 Molecular Perovskites have been reported to date, which can be categorised into seven different X-site families: $[A]_2BB'(CN)_6$, $[A]B(N_3)_3$, $[A]B(M(CN)_2)_3$, $[A]B(BX_4)_3$, $[A]_2BB'(SCN)_6$, $[A]B(ClO_4)_3$ and

$[A]B(H_2POO)_3$ (Figure 2). Among these subclasses, formate- and dicyanamide-based Molecular Perovskites represent the most widely studied systems, as visualised in the pie-chart of Figure 2. Both families occupy an important position within Molecular Perovskites, as some prominent examples of multiferroic $[A]B(HCOO)_3$[44,49] and barocaloric $[A]B(C_2N_3)_3$[41] materials have mainly paved the way for functional Molecular Perovskites. In parallel, the structural analogy to their inorganic perovskites has been developed over the past decades,[42,50] which has sharpened our understanding of material design to conceptually rationalise the stimuli-responsive behaviour of Molecular Perovskites. Since then, research interest, particularly in structure-property relationships, has been stimulated tremendously, resulting in a chemically diverse material class.

Directly apparent from the pie-chart (Figure 2), it is very obvious that the other remaining X-site families such as $[A]_2BB'(CN)_6$, $[A]B(N_3)_3$, $[A]B(M(CN)_2)_3$, $[A]B(BX_4)_3$, $[A]_2BB'(SCN)_6$, $[A]B(ClO_4)_3$ and $[A]B(H_2POO)_3$ still offer many opportunities to discover new Molecular Perovskites. In particular through synthetically exploring the A-site chemistry as mainly commercially available A-site cations have been used so far. However, it is unclear to what extent the molecular substitution approach will be further developed as design ideas for suitable molecular components (*e.g.* for the X-site building unit) and their synthetic realisation are currently scarce. Future research studies require systematic approaches that allow to identify *structure chemical* factors – which are crucial for the design of synthetic guidelines. In the context of this thesis, some key structure chemical phenomena that have been found in Molecular Perovskites will be discussed in the following chapters. Additionally, a selection of some topical research highlights, such as melting, barocaloric, ferroelectric and ferroelastic properties, with emphasis on the underlying structure-property relations, will be outlined.

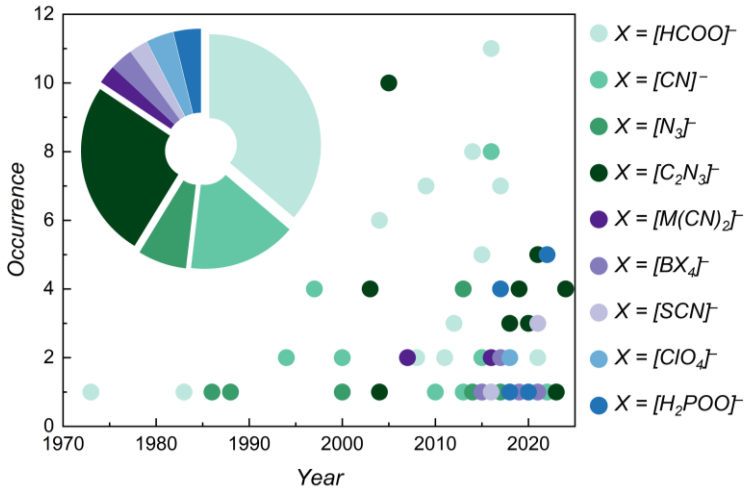


Figure 2: The chronological evolution of $ABX_3$ Molecular Perovskite structures over recent decades, categorised by the X-site linker, shown with the number of published structures per year. A pie chart visualises the cross-category comparison of all X-site families. The corresponding source data for the literature survey can be found in *Chapter 4.5*.

## 1.2. Structure Chemical Properties of Molecular Perovskites

This chapter focuses on the ramifications of using molecules in Molecular Perovskites, with particular emphasis on their structure chemical properties. As we will see, Molecular Perovskites are closely linked to their inorganic counterparts, which allows us to describe their structural chemistry and, hence, to understand how structure and composition dictate their properties. Yet, it is important to note that those fundamental insights set the basis for rational design concepts. From an experimental chemist's point of view, it can guide and motivate research with a focus on unlocking the synthetic goal, which enables the targeted design of Molecular Perovskites with a specific materials function.

### 1.2.1. Tolerance Factor as a Synthetic Compass

In the original geometrical approach, Goldschmidt described the dense ionic packing of conventional oxide $ABX_3$ perovskite structures based on the relative relationship of the ionic sizes of cations and anions that a typical inorganic perovskite structure can tolerate.[51,52] Therefore, a geometrical parameter ($\alpha$) – the tolerance factor – can be calculated following the equation:

$$\alpha = \frac{r_A + r_X}{\sqrt{2}\,(r_B + r_X)}, \qquad (1)$$

with $r_i$ = effective radii of ions on the A-, B- and X-site. It has been further developed for decades as a key synthetic guideline in solid-state chemistry. This semiempirical relation (eqn (1)) has sparked enormous attention for exploring the $ABX_3$ composition *via* A-, B- and X-site substitution, making the $ABX_3$ perovskite structure an iconic structure motif to date.

In 2014,[53] this solid-state principle was extended to HOIPs and Molecular Perovskites by estimating the sizes of both molecular ions. Here, the A-site cation and X-site anion were approximated as rigid bodies based on a semiempirical method using crystallographic data. A rigid sphere model was used to describe the A-site cation with an effective ionic radius ($r_{A,eff} = r_{mass} + r_{ion}$, with $r_{mass}$ obtained from crystallographic data, displaying the distance between the centre of mass of the $A^+$ cation and the atom with the largest distance to this centre and $r_{ion}$ being the associated ionic radii of this atom). The $X^-$ anions were modelled by rigid cylinders with an effective height ($h_{X,eff}$) and effective radii ($r_{X,eff}$). The ionic radii from Shannon[54] were used for the effective radii of the B-site metals. Accordingly, eqn (1) has since been modified to eqn (2).

$$\alpha = \frac{r_{A,eff} + r_{X,eff}}{\sqrt{2}\,(r_B + 0.5 \cdot h_{X,eff})}, \qquad (2)$$

Applying this rather simple relation as a synthetic compass[50,55] for HOIPs and Molecular Perovskites yields many $ABX_3$ permutations with $\alpha$ in the range between 0.8 and 1, which were predicted to form the $ABX_3$ structure motif. In other words, it demonstrates the chemically rich playground within HOIPs and Molecular Perovskite as eqn (2) qualitatively captures the modular $ABX_3$ building principle. Hence, the conceptual understanding of the extended tolerance factor as a stability criterion and guideline for the design of HOIPs[55–58] and Molecular Perovskites[41,46,59–62] has stimulated great research efforts. And for good reason: the beauty of this geometric concept lies in its simplicity. But this rather simple description of molecules by spheres also entails inaccuracies, in particular when larger X-site and A-site ions are involved. For instance, it has been shown that $\alpha$s of $[A]B(C_2N_3)_3$[63,64] and $[A]B(M(CN)_2)_3$[65] structures were slightly above the range proposed by Kieslich *et al.* with $\alpha > 1$. Therefore, the calculated $\alpha$s should be treated with care and only used for qualitative considerations.

As already indicated above, the use of longer X-site anions and chemically more complex A-site cation, makes in principle an accurate calculation of $r_{X,eff}$ and $r_{A,eff}$ even more challenging, as the sizes of the ions are often overestimated and the centre of mass is difficult to estimate. Hence, other methods are required, that are easy to use and enable a more precise description of the large molecule sizes. Recently, a very promising method to calculate the effective volume and radii of A-site molecules was proposed.[66] This approach allows to estimate the size of the A-site molecular species using the freely available software CrystalExplorer based on crystallographic data.[67] Here, the isosurface of the A-site molecule's electron density is calculated which gives a value of the A-site cation's volume. Compared to the approach using the distance between the centre of mass and the most distant atom, this alternative procedure also considers the shape of the A-site cation, which minimises overestimation. Similar to the original approach, the volume is approximated by a sphere, which allows to calculate $r_{A,eff}$. By following this approach, it was shown that $\alpha$s of $[A]B(C_2N_3)_3$ structures lie between 0.85 and 0.925, which is within the initially proposed range. It further motivates to apply this alternative method to the other remaining X-site families, which would provide a comprehensive data set of $\alpha$s that are in comparison to $\alpha$s determined by Kieslich *et al.*. Until today, a simple but accurate ionic size estimation is still challenging and, hence, requires continuous validations and improvements, *e.g.* developing new methods to describe larger X-site anions, that minimise deviations from experimental observations.[68] Nonetheless, the tolerance factor for Molecular Perovskites has sharpened the interpretation of their crystal chemistry and our chemical intuition guiding their synthesis – and the simplicity should be kept for synthetic chemists.

### 1.2.2. Framework Distortions: Octahedral Tilts and Shifts

For small changes in the $ABX_3$ composition, the overall symmetry of a perovskite can decrease, and structural unit cell distortions such as cation displacement, octahedral tilts and distortions of the octahedra can occur. In 1972, an important solid-state principle was established for inorganic perovskites that describes how corner-shared $BX_6$ octahedra can rotate or tilt cooperatively. In the original concept, the octahedral tilt distortions from an ideal undistorted perovskite structure have been categorised by Glazer's notation using the rigid-unit modes (RUMs).[69–71] The essence behind this concept is a rather simple idea based on geometrical considerations. For $\alpha < 1$, it was shown that inorganic perovskites have a lower symmetry, *i.e.* they are distorted or tilted structures that can be derived from a cubic aristotype structure by simply tilting the rigid octahedra around different axes or angles. Here, group theoretical symmetry analysis has been established to identify the active octahedral tilt distortions with 3D irreducible representations (irreps) of the high symmetry parent structure in *Pm*-3*m* symmetry.[71,72]

For Molecular Perovskites, the structural analysis of such framework distortions becomes more complex, as restrictions for the tilting of the corner-shared $BX_6$ octahedra are unlocked when using molecular X-site ions to link the neighbouring rigid $BX_6$ units (Figure 3). In this regard, it is crucial to consider the additional structural degrees of freedom and, hence, the available framework distortions unique to Molecular Perovskites to fully characterise all possible structural distortion modes of the octahedra. Consequently, new unconventional or 'forbidden' types of structural distortions are present in Molecular Perovskites – "forbidden", as these are absent and intrinsically not accessible in conventional inorganic perovskites.[39,65] This leads to a wide range of possible arrangement sets of framework distortions as rigid octahedra can rotate in the same direction and layers and columns of octahedra can translate, *i.e.* new types of octahedral tilt systems and shifts emerge, which can couple to break inversion symmetry.[42] Framework distortions in Molecular Perovskites encompass conventional ($M_2^+$ and $R_5^-$), unconventional tilting ($M_5^+$, $X_5^-$, $X_1^-$ and $\Gamma_4^+$) and columnar shifts ($\Gamma_5^+$, $X_5^+$ and $M_2^-$). These can be described by using irreps with respect to a hypothetical high symmetry structure, analogous to Glazer's notation.[40] In total, nine RUMs are available to Molecular Perovskites, which can also couple to other distortion modes such as multipolar A-site ordering (*e.g. via* reorientation of polar $A^+$)[42] or Jahn-Teller distortions effects (*e.g.* by using $B^{2+}$ = $Cu^{2+}$ in $[C(NH_2)_3]Cu(HCOO)_3$).[73]

In 2018, the powerful concept of tilt engineering *via* group theoretical analysis, known from inorganic perovskites,[74] was applied to Molecular Perovskites by M. S. Senn and A. L. Goodwin.[42] They proposed design rules for Molecular Perovskites, *i.e.* several coupling sets of structural distortions that lead to bulk polarisation and potentially to ferroelectricity *via* a

hybrid improper ferroelectric coupling mechanism. One topical example is $[NH_4]Cd(HCOO)_3$,[75] which exhibits a polar symmetry, resulting from a combination of a columnar shift ($X_5^+$) and an unconventional tilt ($X_5^-$), that results in *Cmc*$2_1$ symmetry, and couples with $M_2^+$ to *Pna*$2_1$. Yet, the concept of tilt engineering, which helps to understand and identify combinations of structural framework distortions as design criteria, which are crucial for a specific material function, is only just developing.

In 2020, the group theoretical method was applied to a large set of Molecular Perovskites with X-site anions such as $[HCOO]^-$, $[H_2POO]^-$, $[N_3]^-$, $[C_2N_3]^-$ and $[M(CN)_2]^-$, highlighting favoured tilt and shift modes, most notably in dependence on the used multiatomic X-site linker.[40] Here, the linker geometry was identified as an important criterion, with bent X-site anions showing a tendency for conventional tilting, while linear X-site molecules such as $[N_3]^-$ drive unconventional tilting. Columnar shifts are typically found in large $[BX_3]^-$ network sizes. In such a typical tilt and shift analysis, the freely available web-based software ISODISTORT is used,[76,77] which identifies and describes all active framework distortion modes of the Molecular Perovskite structure by their irreps and distortion mode amplitudes. Therefore, a simplified crystal structure of the distorted Molecular Perovskite is analysed compared to an ideal undistorted structure.

Since not only the use of molecules on the X-site leads to new structural degrees of freedom within the $[BX_3]^-$ network, it can be expected that chemically more complex A-site molecules, with their own *e.g.* point symmetry or accessible degrees of rotation, also impact such symmetry breaking phenomena. In other words, it can be assumed that the A-site molecule's size and shape themselves have a templating effect on the surrounding $[BX_3]^-$ network structure and its degree of distortion. Therefore, symmetry breaking design principles must

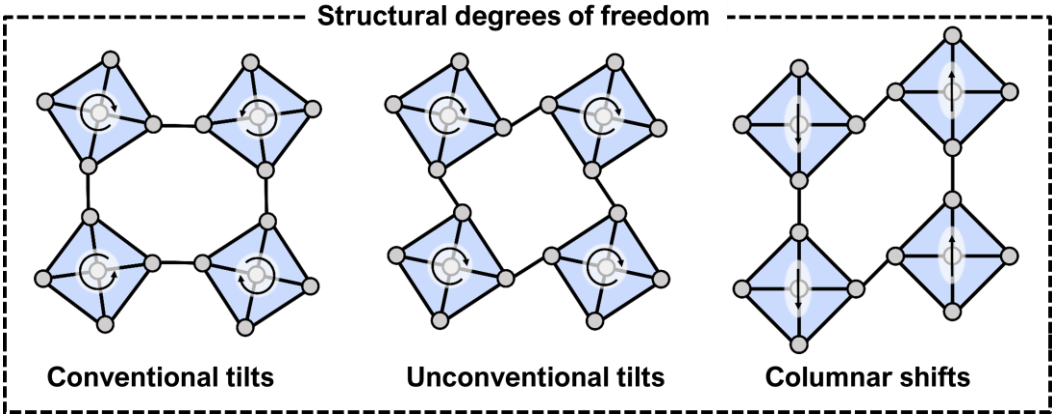


Figure 3: Schematic 2D illustration of tilts and shifts of rigid $BX_6$ octahedra, showing the structural degrees of freedom available to Molecular Perovskites. X-site linkers are simplified as black lines and the A-site cations were neglected to highlight the $[BX_3]^-$ framework distortions.

consider both molecular components to understand and potentially control the framework distortions in Molecular Perovskites. This will be the focus of study IV, discussed in *Chapter 2.4*. From the author's perspective, the group-theoretical analysis will provide important fundamental insights and become a more widely established method for structurally characterising newly synthesised Molecular Perovskites – and, beyond that, for engineering functional $ABX_3$ materials by synthetically tailoring and combining distinct framework distortion types.

### 1.2.3. Tilt and Shift Polymorphism in Molecular Perovskites

Inorganic materials are famous for their rich polymorphic nature in dependence on temperature and pressure, with prominent examples such as $CaCO_3$ and carbon, covering different physicochemical properties depending on their polymorphic phase.[78,79] This phenomenon describes the ability of a crystalline material to exhibit different polymorphs without changing the overall chemical composition.[80] Inorganic perovskites adopt a large number of perovskite polymorphs when changing the crystal symmetry in response to temperature or pressure, which is directly linked to framework distortions when tilting octahedra compared to the high symmetry cubic structure.[81–83]

In 2019, $ReO_3$-type polymorphs have been identified for A-site deficient hypophosphite-based $M(H_2POO)_3$ materials (with $M^{3+}$ = $V^{3+}$, $Al^{3+}$ and $Ga^{3+}$). These materials transform from the α-phase into a less distorted structure (β/γ-phase) upon temperature or pressure change.[84] Two years later, a so far unknown polymorphism type was found that is unique to Molecular

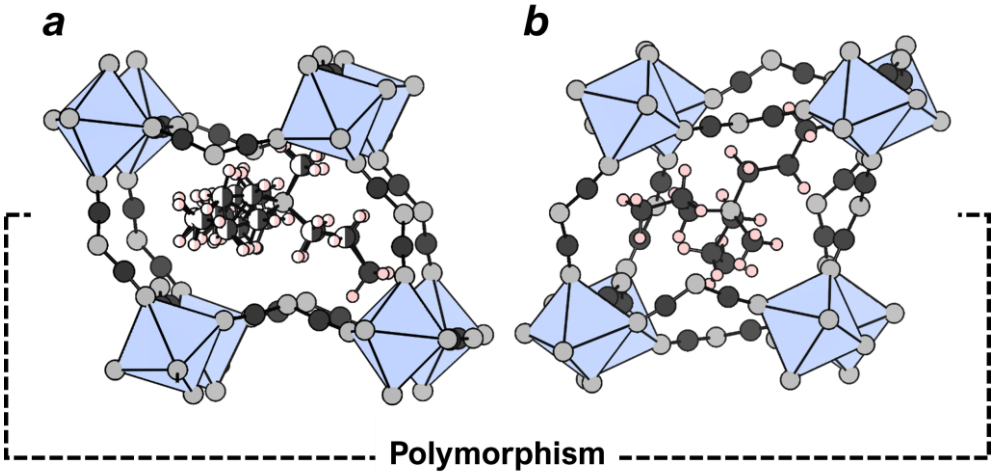


Figure 4: Representation of crystal structures of two polymorphic phases of $[(CH_3)N\text{-}(n\text{-}C_3H_7)_3]Ni(C_2N_3)_3$, with (a) available from CCDC number: 2068712 and (b) from CCDC number: 2068844. (a) represents the kinetically favoured polymorphic structure, while (b) is the thermodynamic stable polymorph. Particular emphasis is given to the different binding modes of $[C_2N_3]^-$ anions in both network structures. Colour code: Ni – light purple, C – dark grey, N – light grey and H – light pink.

Perovskites.[85] Using molecules on the X-site allows for different binding modes of the X-site linkers within the $[BX_3]^-$ network. This conformational isomerism of the X-site anions enables the formation of new Molecular Perovskite polymorphs, *i.e.* tilt and shift polymorphs, which are close in energy. Here, a new concept of tilt and shift polymorphism was introduced to Molecular Perovskites with a family of $[A]B(C_2N_3)_3$ materials (with $A^+$ = tripropylmethylammonium and $B^{2+}$ = $Mn^{2+}$, $Co^{2+}$ and $Ni^{2+}$), which adopt two polymorphs with the same composition but different framework distortions, which can be irreversibly transformed into each other with increasing temperature (Figure 4). In addition, both polymorphs are synthetically accessible when changing the synthetic conditions. To understand the structural origin of both polymorphs, the underlying framework distortions of the low- and high-temperature polymorphic structure were described *via* Glazer notation,[40,69] showing different tilting periodicities. The observed irreversible symmetry breaking from the kinetically favoured *Pnma* to the thermodynamic stable *R*-3*c* polymorph is related to changes in the activated conventional tilt modes. This can be rationalised by observed changes in the binding modes of the $X^-$ linkers, *i.e.* conformational isomerism from *anti-anti* to *syn-anti* connectivity of the $[C_2N_3]^-$ anions, which is closely related to conformational polymorphism found in molecular crystals.[86] This polymorphism concept can be extended for unconventional tilts and columnar shifts as demonstrated by the irreversible phase transition of $[A]Cd(C_2N_3)_3$ (with $A^+$ = azaspiroundecanium).[46]

Since irreversible perovskite to perovskite phase transitions are so far only observed in Molecular Perovskites with X-site anions such as $[H_2POO]^-$ and $[C_2N_3]^-$,[87–90] it can be assumed that an interplay of several factors leads to the formation of one metastable polymorph, which is close in energy to the thermodynamic stable polymorphic structure. This includes X-site anions with conformational degrees of freedom that allow variations of binding arrangements, torsion angles and distortions of the molecules within the $[BX_3]^-$ network. Likewise, relatively large A-site cations, such as tripropylmethyl-,[85] benzyltriethyl-,[89] tributylmethyl-ammonium[87] and tetraethyl-,[90] tributylmethyl-phosphonium,[90] that are capable of forming hydrogen bonding interactions (*e.g.* guanidinium), are favoured.[88] Tilt and shift polymorphism is another blueprint for conceptualising the role of structural degrees of freedom that are not present in inorganic perovskites. So far, this phenomenon has rarely been described in Molecular Perovskites due to challenges in identifying both polymorphs, as it is difficult to access both polymorphs synthetically. However, from the author's perspective, the structural and chemical factors driving tilt and shift polymorphism are expected to be further explored alongside developments in the field of tilt engineering.

### 1.2.4. Structure Analytical Concept: Complexity of (Molecular) Perovskites

It is already apparent from the previous chapters that the chemical scope of Molecular Perovskites exceeds that of inorganic perovskites. Therefore, it becomes more important to achieve the goal of overarching design principles for Molecular Perovskites. This requires the development of further concepts that help to understand the crystal chemistry of their new structural degrees of freedom and how they can be further used to formulate more thermodynamic rules. In this pursuit, considering the crystal structure as an information source has paved the way for such a structure analytical concept. In 2012, a seminal approach was introduced that describes a structural *complexity* measure using the information content of the crystal structure based on Shannon's formula – the more complex a structure is, the more information is required to describe its crystal structure.[91,92] Here, S. V. Krivovichev has applied the Shannon entropy to quantify the complexity of a structure based on the derived structural information content from the reduced unit cell of the crystal in bits per atom, which is defined as follows:

$$I_G \left[\frac{bit}{atom}\right] = -\sum_k \frac{m_k}{v} \cdot log_2 \frac{m_k}{v}, \qquad (3)$$

, with $I_G$ = information content of a crystal structure and its complexity, $k$ = crystallographic orbits, $m_k$ = the multiplicity of the crystallographic orbits and $v$ = the number of atoms in the reduced unit cell. Further, S. V. Krivovichev presented an inverse relation between the complexity of a crystal structure and the configurational entropy of a crystalline material, meaning more complex structures exhibit lower entropies than simple ones.[93] In 2020, the established correlation of eqn (3) has been further improved from $I_G$ to the combinatiorial complexity ($I_{G,comb}$) and coordinational complexity ($I_{G,coor}$) to distinguish the structural complexity of structures that have the same number of atoms in their reduced cell but differ in their intrinsic degrees of freedom (*e.g.* different site occupancies). In addition, the configurational complexity ($I_{G,conf}$) was proposed as sum of combinatorial and coordinational complexity.[94] One year later, our group implemented this updated concept using eqn (3) into a Python-based program crystIT.[95] This structure analytical program offers an easy-to-use calculator of the complexity ($I_G$) and configurational entropy ($S_{cfg}$) of a crystal structure based on a reliable crystallographic information file (*i.e.* *.cif file) defined by crystallographic orbits.

More recently, our group has demonstrated a comprehensive complexity analysis using crystIT for a broad dataset (178 *.cif files) of perovskite materials,[96] including inorganic perovskites, HOIPs and Molecular Perovskites. Here, a complexity trend has been observed among all perovskite subclasses categorised by their X-site ion, showing a logarithmic

relationship between their calculated configurational complexities ($I_{G,conf}$) and the B–B distances that serve as a relative approximation to capture the $ReO_3$-type network size. The structural evolution of the $ABX_3$ perovskite structure from inorganics to HOIPs and further to Molecular Perovskites is captured by their complexity, which significantly increases when a larger number of crystallographic orbits is used to describe the structure, which is entirely consistent with chemical intuition.

Future perspectives were showcased that couple the underlying structural complexity of an $ABX_3$ structure to their structural distortions from the ideal, undistorted perovskite structure, *e.g.* higher $I_{G,conf}$ for systems with activated octahedral shifts. This highlights the potential for applying a structural complexity analysis combined with tilt and shift analysis to understand symmetry breaking phenomena in Molecular Perovskites, such as the phase transition thermodynamics related to barocaloric Molecular Perovskites. We believe that thermodynamic guidelines based on the crystal structure complexity method may potentially emerge, following further advances in the information theory for calculating $S_{cfg}$ and $I_{G,conf}$ . Additionally, links between configurational entropies and complexities and the experimentally obtained phase transition thermodynamics could be identified by studying all parameters in a carefully selected model series of functional materials (*e.g.* barocaloric Molecular Perovskites).

### 1.2.5. Molecular Perovskites and Beyond: $AB_2X_6$ Materials

In the search for new design concepts for functional Molecular Perovskites, we have started to interpret the material's structure from the perspective of its structural and chemical degrees of freedom and the function of the material as an interplay of these *structure chemical elements*.[31] Looking for new degrees of freedom and making them accessible to external stimuli, $ReO_3$-type network structures have proven to be an extraordinary platform for their structural evolution from inorganic to Molecular Perovskites.[4] A typical example of a new type is the A-site order pattern in $[A]Mn_2(H_2POO)_6$ (with a divalent A-site cation ($A^{2+}$) such as 1,4-diazabicyclo[2.2.2.]octane-1,4-dabconium),[88] showing an ordering of vacancies and divalent A-site cations ($A^{2+}$) in a perovskite-type structure.

In 2022, another A-site order pattern was introduced as a new type of structural degree of freedom – of geometrical nature – with the discovery of a new material class, referred to as $AB_2X_6$ coordination networks.[97] Their extended $ReO_3$-type network materials are closely related to Molecular Perovskites; composed of metal nodes (*i.e.* $Mn^{2+}$), which are octahedrally linked by $[C_2N_3]^-$ anions to build the host network structure $[Mn(C_2N_3)_3]^-$ (Figure 5). Compared to the typical $ABX_3$ perovskite structure motif, a divalent A-site cation ($A^{2+}$) with two spatially separated charges is located between two neighbouring pseudocubic $[Mn(C_2N_3)_3]^-$ cages for charge balancing. Here, the incorporation of $[(C_3H_7)_3N(CH_2)_nN(C_3H_7)_3]^{2+}$ (with $n$ = 4 and 5)

generates spatial orientation of $A^{2+}$ in the $ReO_3$-type network, *i.e.* a new geometrical degree of freedom in addition to the structural degrees of freedom available to Molecular Perovskites, see Figure 4. Hence, depending on the choice of $A^{2+}$ cation, different order patterns were found to be synthetically accessible: the herringbone (for $n$ = 4) and head-to-tail (for $n$ = 5) motif. Further, their ramifications on the stimuli-responsive properties have been investigated in response to temperature and pressure. As expected from related materials with a herringbone motif in their framework topology,[98–100] $AB_2X_6$ with $A^{2+}$ = $[(C_3H_7)_3N(CH_2)_4N(C_3H_7)_3]^{2+}$ exhibits counterintuitive large uniaxial negative thermal expansion (NTE) and negative linear compressibility (NLC) which can be rationalised by a "hinging" mechanism of $A^{2+}$ molecules in combination with $[Mn(C_2N_3)_3]^-$ framework distortions. When changing the $A^{2+}$ cation ordering to a head-to-tail arrangement, the responsive behaviour of $AB_2X_6$ is different as only moderate NTE and zero linear compressibility are observed for $A^{2+}$ = $[(C_3H_7)_3N(CH_2)_5N(C_3H_7)_3]^{2+}$. Hence, the herringbone ordering provides a larger margin for pressure- and temperature-induced structural distortion pathways. This work showcases that the famous $ReO_3$-type network structure still provides chemical scope for exploring new as well as known types of *structure chemical elements* when molecular substitution is extended to a new dimension – *e.g.* by using trivalent A-site molecules (*i.e.* $A^{3+}$).

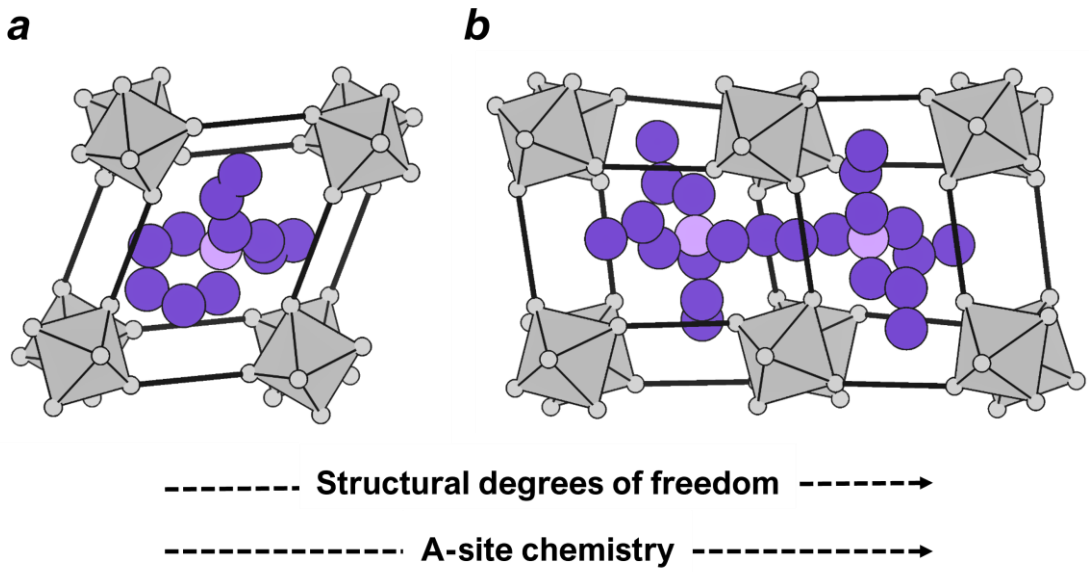


Figure 5: Structural development of the $ReO_3$-type network structure, starting from the Molecular Perovskites (a) and extending to $AB_2X_6$ materials (b), with emphasis on the molecular A-site cations. For a better visualisation of the A-site molecules, the crystal structures were simplified by removing all H atoms and using grey lines as X-site anions ($X^-$ = $[C_2N_3]^-$). In addition, the size of all C and N atoms on the A-site was increased (Colour code: $BX_6$ octahedra – grey, C – dark purple and N – light purple). A prototypical Molecular Perovskite with the general formula $[(C_5H_{10})N\text{-}(n\text{-}C_3H_7)_2]Ni(C_2N_3)_3$ (new and discussed within this thesis) and $[(C_3H_7)_3N(CH_2)_4N(C_3H_7)_3]Mn_2(C_2N_3)_6$ (available from CCDC number: 2059110) were used to illustrate the crystal structures.

## 1.3. Research Highlights and Advances

While the outlined introductory points demonstrate fundamental aspects, this chapter will highlight some key functional properties of Molecular Perovskites that have attracted the most attention in the past decade. In principle, these properties have fascinated material scientists to date, with emphasis on their origin, which can be understood and potentially controlled using structure chemical factors that are directly linked to a specific property, as outlined above.

### 1.3.1. Melting of Molecular Perovskites

With the recent discovery of meltable Molecular Perovskites in 2021, research interest has turned to a new research dimension: the non-crystalline Molecular Perovskites and their liquid and glassy states.[101] Molecular Perovskite-based glasses, *e.g.* $[Pr_4N]B(C_2N_3)_3$ ($[Pr_4N]^+$ = tetrapropylammonium and $B^{2+}$ = $Mn^{2+}$, $Co^{2+}$ and $Fe^{2+}$),[101] $[Bu_3NMe]B(C_2N_3)_3$ ($[Bu_3NMe]^+$ = tributylmethylammonium and $B^{2+}$ = $Mn^{2+}$, $Fe^{2+}$, $Co^{2+}$ and $Ni^{2+}$)[87] and $[Pr_3NBu]Mn(C_2N_3)_3$ ($[Pr_3NBu]^+$ = tripropylbutylammonium)[102] are referred to as the emerging material class of glass-forming coordination polymers, which are accessible by rapid quenching of coordination polymer liquids (Figure 6). These cover all dimensions available for coordination polymer structures, including other 3D network materials (*e.g.* carboxylate-based MOFs[103,104] and predominantly ZIFs)[105,106] as well as structures connected in 1 or 2 dimensions (*e.g.* gold thiolate-based[107] and Zn-phosphate-based[108,109] coordination polymers) that form liquids and glasses.[110,111]

In principle, the liquid state of coordination polymers is accessible when heating results in the melting of the material (with the melting temperature $T_m$) before thermal decomposition (with the temperature of decomposition $T_d$) processes occur, *i.e.* $T_m < T_d$, which is a rather atypical behaviour for most MOFs and Molecular Perovskites.[112–114] Upon quenching the liquid

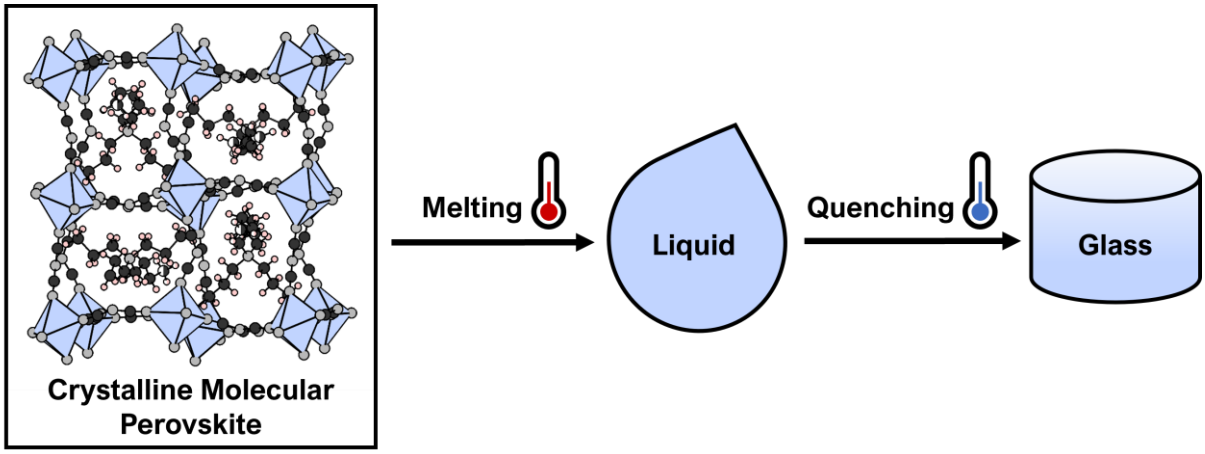


Figure 6: Schematic presentation of the formation of Molecular Perovskite-based glasses, starting from the crystalline state *via* the liquid towards the glassy state of Molecular Perovskite.

coordination polymer, the glassy state can be obtained, characterisied by the absence of bragg peaks (*i.e.* amorphous phase) and a glass transition temperature ($T_g$). So far, only a few combinations of organic and inorganic building units were discovered to melt with such a high ionicity character, stabilising the liquid state when accessing $T_m < T_d$.[115] One prototypical example is demonstrated in study I, which achieved a widening of the $\Delta T$ between $T_m$ and $T_d$ in a Molecular Perovskite. Here, similarities to ionic liquids (ILs) are recognised,[64,116,117] considering the melting process of coordination polymers as the partial dissociation of coordination bonds forming an IL-like fragmented coordination network.[113]

For the design of Molecular Perovskite-based glasses, the choice of the organic X-site anion (*e.g.* $X^- = [C_2N_3]^-$) seems to be key together with suitable divalent metals (*e.g.* $B^{2+} = Mn^{2+}$, $Fe^{2+}$, $Co^{2+}$ or $Ni^{2+}$) to lower the metal-ligand (*e.g.* B-N) coordination bond strength, and hence, the energy pathway for the bond breaking required for melting. So far, the melting has only been observed for a few members of the $[A]B(C_2N_3)_3$ family,[118] highlighting the unique role of the $[C_2N_3]^-$ ligand in coexistence with quaternary ammonium species such as $A^+ = [Pr_3NBu]^+$, $[Pr_4N]^+$ and $[Bu_3NMe]^+$, which are known from ILs composed of the same organic moieties.[119] This indicates that meltable $[A]B(C_2N_3)_3$ can be designed by a rational choice of a suitable $ABX_3$ combination for controlling $T_m$, which has been investigated in a recent study by Shaw *et al.*.[64] Here, the size effect of the A-site cation on $T_m$ was systematically investigated through A-site substitution in a $[A]B(C_2N_3)_3$ series, where an increase of the A-site cation, *i.e.* by an increase of the alkyl chains from $[Pr_4N]^+ < [Bu_4N]^+ < [Pe_4N]^+$ (with $[Bu_4N]^+$ = tetrabutylammonium and $[Pe_4N]^+$ = tetrapentylammonium), decreases $T_m$ while lowering the symmetry – forming different structure types compared to the $ABX_3$ structure for the smallest A-site cation ($A^+ = [Pr_4N]^+$).[64] In addition, the impact of the divalent metal was tested, showing a decrease of $T_m$ when changing the size of the B-site metal (*e.g.* along $Mn^{2+} > Fe^{2+} > Co^{2+}$);[64] explained by the "hard and soft acids and bases" concept suggesting strong interactions between the soft $Mn^{2+}$ and the soft $[C_2N_3]^-$ ligand.[101] However, we would like to note here that this trend is not found for the meltable B-site series of $[Bu_3NMe]B(C_2N_3)_3$ with $B^{2+} = Mn^{2+}$, $Fe^{2+}$, $Co^{2+}$ and $Ni^{2+}$.[87] Here, the highest $T_m$ is observed for $[Bu_3NMe]Ni(C_2N_3)_3$, which could be rationalised by the large ligand field stabilisation energy (LFSE) with the smallest B-site metal, which increases the metal-ligand bond strength compared to the analogue structure with $B^{2+} = Mn^{2+}$.[120] The conclusion based on the LFSE of the B-site metal and the B-N bond strength has been widely used to describe differences in the mechanical properties[120–122] and phase transition temperatures[85] as a function of the B-site metal choice. At this point, we can conclude that further studies are required to understand the role of the B-site metal, but so far, the close link to ILs is an ideal starting point for the A-site choice, suggesting suitable candidates with long alkyl chains, and hence, larger entropic contributions for the design of meltable Molecular Perovskites.

More recently, the approach for engineering glassy Molecular Perovskites was extended, *i.e.* for controlling $T_m$, from the intrinsically available $ABX_3$ compositional range towards using modifier salts – see more details of this concept in study I presented in *Chapter 2.1*.[102] This study was inspired by work on inorganic glasses where modifiers have been added to tune the glass properties.[123] In our work, we showcased how a suitable modifier, *e.g.* $Li(C_2N_3)$, can be identified for lowering $T_m$ of $[Pr_3NBu]Mn(C_2N_3)_3$ while an eutectic mixture of both components is formed. This has widened the window ($\Delta T$) between $T_m$ and $T_d$, which hinders partial decomposition when melting is too close to the decomposition onset. In addition, slow cooling of the mixture enables a scalable glass formation instead of established melt quenching methods, *e.g.* thermogravimetric analysis-differential scanning calorimetry (TGA-DSC) based routines of only small amounts in aluminium oxide crucibles.

Moving forward, the next development step will potentially be the targeted introduction of functionality, possibly by the use of functional modifiers or functional Molecular Perovskites *per sé*. As already demonstrated for MOF-based glasses, other perspectives are received when considering Molecular Perovskite-based glasses as a new glass matrix to form crystal-glass composite materials. At the same time, overarching principles for tailoring $T_m$ and/or $T_d$ are needed. In particular, the control of $T_d$ is challenging but crucial to understand why $[A]B(C_2N_3)_3$ materials melt and other X-site families do not. Here, the stability of $[C_2N_3]^-$ in the liquid state seems to be key, and hence, its decomposition, *i.e.* through a trimerisation mechanism forming triazine, must be linked across meltable compounds to access the open window for melts. Yet, the entire accessible range of Molecular Perovskite-based glasses is largely unknown, providing a great playground for future studies that can address the challenging task of developing functional Molecular Perovskite-based glasses.

### 1.3.2. Molecular Perovskites as Barocalorics

In 2017, the responsive nature of Molecular Perovskites, which typically undergo single or multiple phase transitions with large temperature changes in response to external stimuli, has been recognised as a useful stimuli-responsive behaviour for the design of caloric materials.[41] In principle, solid-state caloric materials, including magneto-, electric-, mechano- (*i.e.* elasto- and barocalorics) calorics, make use of the strong changes in entropy and temperature across the phase transition induced by external stimulation. When those caloric effects are very large (*i.e.* $\Delta S > 10\ J\ K^{-1}\ kg^{-1}$), they offer potential as an alternative cooling system to replace environmentally harmful refrigerants used today in common vapour compression technologies.[124] The cooling process of caloric materials works very similar to compressor-based cooling, *i.e.* when the working material is exposed to an external field, it heats up and cools down again when the field is removed.[125,126]

Some Molecular Perovskites are striking examples of barocalorics, *e.g.* $[Pr_4N]B(C_2N_3)_3$ (with $B^{2+}$ = $Mn^{2+}$ and $Cd^{2+}$)[41,59] and $[Me_4N]B(N_3)_3$ (with $[Me_4N]^+$ = tetramethylammonium and $B^{2+}$ = $Mn^{2+}$ and $Cd^{2+}$),[35,127,128] which undergo structural phase transitions when hydrostatic pressure is applied. Akin to other state-of-the-art barocalorics such as plastic crystals of neopentylglycol ($(CH_3)_2C(CH_2OH)_2$)[129] or molecular Fe(II) spin-crossover compounds ($[FeL_2][BF_4]_2$ with L = 2,6-di(pyrazol-1-yl)pyridine),[130] which require high driving pressures ($p$ > 1000 bar),[131] Molecular Perovskites generate extremely high isothermal entropy changes ($\Delta S > 10\ J\ K^{-1}\ kg^{-1}$) at relatively small working pressures ($p$ < 70 bar) and low temperatures (*i.e.* near room temperature).[41] Notably here, $[(CH_3)_2NH_2]Mg(HCOO)_3$ presents one example which shows a giant barocaloric effect ($\Delta S \sim 39\ J\ K^{-1}\ kg^{-1}$) at a relatively large driving pressure ($p$ < 2000 bar).[132] However, when considering now barocalorics and their operating pressures and temperatures by using the barocaloric strength (*i.e.* $\Delta S/\Delta p$), $[Pr_4N]Mn(C_2N_3)_3$ outperforms the other competing barocalorics.[66]

From a broader perspective, there are many potential barocaloric materials – but what they all have in common is that individual challenges still remain work-in-progress.[131] For instance, plastic crystals show colossal reversible isothermal entropy changes ($\Delta S > 250 \sim 500\ J\ K^{-1}\ kg^{-1}$)[129,133,134] across the solid to solid phase transition, but many practical concerns such as large thermal hysteresis, moderate sensitivity to low pressures and low thermal conductivity for heat transfer predominantly prevent further development towards commercialisation as the cooling efficiency is limited.[135–137] More recently, the solid to liquid transition in *n*-alkanes (*e.g.* $C_{16}H_{34}$, $C_{18}H_{38}$ and $C_{20}H_{42}$)[138,139] has turned out to be extremely promising for barocalorics, as extremely large barocaloric effects ($\Delta S > 700\ J\ K^{-1}\ kg^{-1}$) were found upon changing the phase, similar to the well-known gas to liquid transition used in vapour compression cooling systems; yet, their low thermal conductivity remains a major drawback. Compared to plastic crystals and long-chain *n*-alkanes, Molecular Perovskites show much smaller reversible entropy changes ($\Delta S > 10 \sim 80\ J\ K^{-1}\ kg^{-1}$) but under practically more feasible conditions, in particular under lower working pressures. Here, we can conclude that all potential barocalorics require targeted material optimisation, and hence, there is still large space for improvement to finally discover the ideal material fitting all requirements. Therefore, design concepts are required that go beyond a specific material class, inspiring the discovery and/or improvement of materials ideally suited for barocaloric cooling. Here, a distinct design feature, *e.g.* structural disorder of long-chain alkanes, has been adapted to metal-halide perovskites, where long alkylammonium cations (*i.e.* $A^+$ = $[C_{10}H_{21}NH_3]^+$ and $[C_9H_{19}NH_3]^+$) have been incorporated into a 2D layered metal-halide perovskite network leading to a colossal barocaloric effect ($\Delta S > 200\ J\ K^{-1}\ kg^{-1}$ at $p$ < 300 bar).[140] This example showcases that formulated design features are key, and thus, the combination of them across several material classes is a powerful concept. Further, it motivates optimising barocaloric Molecular

Perovskites by exploiting their compositional range accessible to the molecular building units, *e.g.* by incorporating alkylammonium or alkylphosphonium species with long alkyl chains on the A-site. Additionally, we consider Molecular Perovskites as a suitable playground to systematically study barocaloric performance parameters as a function of chemical changes. For instance, the phase transition temperature ($T_{trs.}$) has been found to be sensitive to the choice of the B-site metal with $T_{trs}$ increasing along the metal series ($B^{2+} = Mn^{2+} > Co^{2+} > Ni^{2+}$).[85] A similar tunability has been reported for the compressibility, which improves the barocaloric performance when being large (*i.e.* small bulk modulus) – the softer materials are the better barocalorics.[134] Here, two substitution approaches have been introduced to increase the compressibility of Molecular Perovskites, either by increasing the $B^{2+}$ radius[141] or *via* changing the A-site shape, and hence, reducing the overall $[BX_3]^-$ framework distortion.[142] The latter has been explored in depth in study IV, presented in *Chapter 2.4*. These are blueprints on how to identify first design rules, which at the same time unlock the potential of many more to come – *e.g.* studies with particular emphasis on the Δ*S*, which are currently scarce.

### 1.3.3. Ferroelectric and Ferroelastic Ordering in Molecular Perovskites

Typical ferroic materials encompass ferroelectrics (exhibting spontaneous polarisation), ferroelastics (exhibting a spontaneous strain) and ferromagnetics (exhibting spontaneous magentisation).[143] These are characterised by spontaneously forming domains that can be reversibly reoriented (switched) under an external field, such as an electric, stress or magnetic field, which is observed in a hysteresis loop. This switching behaviour between different domains makes ferroics fascinating materials for many diverse applications such as sensors, capacitors, piezoelectric and memory devices.[144]

The phenomenon of ferroelectricity describes materials that exhibit intrinsic lattice polarisation, which can be reversed by an electric field. This switching of ferroelectric polarisation is closely related to the iconic $ABX_3$ perovskite structure.[145] With the discovery of ferroelectricity in $BaTiO_3$, research on structurally related ferroelectrics has experienced a boom as demonstrated by the extensive history of ferroelectric perovskites such as $SrTiO_3$[146] and $LiTaO_3$.[147] This also involves the well-known piezoelectric $PbZr_{1-x}Ti_xO_3$ (PZT) material,[145,148] that converts mechanical energy into electrical energy, important for many applications from ultrasound devices, energy harvesting systems to sensors.[144] Upon cooling, those materials undergo a symmetry lowering phase transition across the ferroelectric Curie Temperature ($T_c$) from a paraelectric (*i.e.* non-ferroelectric) into the ferroelectric state with non-centrosymmetric crystal symmetry.[149] In principle, the ferroelectric nature arises from the crystal structure *per sé*, *i.e.* spontaneous dipole moments must exist (*e.g.* charge displacement induces $TiO_6$ dipoles in $BaTiO_3$)[150] within the crystal structure, which can be reoriented by an

external electric field. Among all 32 crystallographic point groups, 21 point groups have no centre of symmetry. Out of these non-centrosymmetric point groups, 20 are piezoelectric, with 10 being polar. These polar point groups (with a unique polar axis) can be ferroelectric if the polarisation is switchable upon application and removal of an external electric field.[149]

Since ferroelectricity exists in many $ABX_3$, it is not surprising that this phenomenon has been found in HOIPs[151–153] and Molecular Perovskites. Both can serve as a playground for discovering new promising $ABX_3$ ferroelectrics[42,153–155] or even for optimising the ferroelectric properties compared with their purely inorganic counterparts.[156] In this pursuit, the molecular design strategies of "molecular ferroelectrics"[157] have proven to be a powerful approach for tuning ferroelectric HOIPs,[156,158] which can be adapted to the field of Molecular Perovskite ferroelectrics. Here, design criteria for the molecular component on the A-site have been identified as the origin of polarisation, such as order-disorder and displacive characteristics of the A-site cation, inducing dipole moments.[158] Additionally, subtle but tailored modifications of the A-site molecules can also contribute to the spontaneous polarisation, *e.g. via* lowering molecular symmetry of $[Me_4N]^+$ to $[Me_3NCH_2Cl]^+$[159] or $[Me_3NCH_2Br]^+$[160] in HOIP systems, that induce additional dipole moments within the A-site cation. Similar advances are expected when applying these design features, *e.g.* by a suitable choice or tailored chemical modification of the molecular A-site ion, to some prototypical examples such as $[A]Mn(C_2N_3)_3$ (A-site cations such as $[Et_4P]^+$ = tetraethylphosphonium and $[TriBuMeP]^+$ = tributylmethylphosphonium),[90] $[Me_2N]Mn(N_3)_3$,[161] $[Me_2N]Mn(HCOO)_3$[162] ($[Me_2N]^+$ = dimethylammonium) and $[Me_3NOH]_2KFe(CN)_6$ ($[Me_3NOH]^+$ = trimethylhydroxylammonium).[163] Additionally, Molecular Perovskites have been explored as a platform for identifying some main ferroelectric coupling schemes of individual distortion modes of the $[BX_3]^-$ network.[42] By understanding how these structural degrees of freedom can be synthetically controlled through tailored chemical modifications of the molecular components, we can formulate design strategies towards polar coupling schemes and, hence, ferroelectric Molecular Perovskites. In this context, the molecular solid solution approach offers great opportunities for engineering the framework distortions and consequently ferroelectricity. It potentially unlocks the systematic on/off switching of a particular irrep, inducing a polar coupling combination, and secondly, the control of the amplitudes of individual framework distortions, allowing fine-tuning the macroscopic polarisation. Moreover, a carefully selected solid solution series of Molecular Perovskite ferroelectrics shows great promise for understanding and manipulating key ferroelectric features as a function of the molecular component, as demonstrated by tuning $T_c$ in a series of mixed chiral cations in metal halide perovskites.[164]

Closely related to ferroelectrics are ferroelastics, where a spontaneous strain generates ferroelastic domains in a material below $T_c$ when mechanical stress is applied.[165] Upon heating,

those materials typically undergo a structural phase transition into the paraelastic state where no ferroelastic domains exist. Symmetry lowering into the ferroelastic state is observed in many $ABX_3$ structures[166,167] as captured by Aizu's notation[168,169] encompassing 94 structural lattice distortions from the paraelastic phase, potentially generating ferroelasticity. Compared to some prototypical examples of purely inorganic ferroelastic materials, *e.g.* $BaTiO_3$,[170] $BiVO_4$[171] and $Gd_2(MoO_4)_3$,[172] HOIPs and Molecular Perovskites show great promise for discovering new types of ferroelastic materials with one-, two- or multi-step ferroelastic phase transitions.[35,173,174] In particular, Molecular Perovskites offer a large chemical and structural parameter space for studying and tailoring ferroelastic characteristics, as ferroelastic behaviour has been reported across many Molecular Perovskite families (with X-site anions such as $[HCOO]^-$,[175] $[BF_4]^-$,[176,177] $[C_2N_3]^-$,[178] $[SCN]^-$[179] and $[N_3]^-$[35]). This allows to develop design strategies towards ferroelastics with an emphasis on the role of the molecular components either on the A- or X-site, as ferroelastic phase transitions mainly originate from molecular dynamics rather than from the $BO_6$ tilting mechanism in conventional perovskites.[175] In particular, the A-site chemistry has been explored as a powerful design tool for tuning the ferroelastic transition as demonstrated by the choice of a suitable polar and flat A-site cation in $[H_2hpz]K(BF_4)_3$ ($[H_2hpz]^+$ = homopiperazine-1,4-diium),[176] or by targeted modifications of phosphonium and ammonium species in $[A]B(C_2N_3)_3$ (*e.g.* $A^+ = [Et_3P(CH_2)_2Cl]^+$, $[Et_3P(CH_2)_2F]^+$, $[Pr_3(CH_2CHOHCH_3)N]^+$ and $[Pr_3(CH_3CHCH_2OH)N]^+$)[178,180,181] and $[A]B(SCN)_3$ (*e.g.* $A^+ = [(CH_3)_3PCH_2F]^+$).[179] Beyond the widely explored A-site substitution approach, even in a first ferroelastic solid solution series with $[Et_3P(CH_2)_2F]_x[Et_3P(CH_2)_2Cl]_{1-x}Mn(C_2N_3)_3$,[182] the ordering effect of the X-site linker has only been studied in $[Me_4N]Cd(N_3)_3$.[35] This leaves many more possibilities to systematically study the overall interplay of order-disorder behaviour of the A- and the X-site, the chemical interactions within the network, as well as octahedral distortions, which in combination contribute to the ferroelastic phenomenon.

Molecular Perovskites have proven to exhibit both ferroic properties; however, the potential for advanced material design has not been fully exploited – still leaving open questions that are currently being investigated to unlock the ferroelectric and ferroelastic origin in Molecular Perovskites.

## 1.4. Concluding Remarks

When we reconsider the introductory points about material design, there is a very clear objective for coordination polymers, *i.e.* to design materials with a tailored functional response. Among this very broad material class, Molecular Perovskites, with their molecular substitution principle and resulting chemical and structural diversity, have emerged as a unique platform for identifying fundamental structure chemical principles to date. Moreover, they show great promise in different application-oriented research branches, often related to their propensity for phase transitions.

Current research on Molecular Perovskites has already yielded considerable progress in emerging new structure chemical paradigms, but to move to the next stage of development we need to focus on how to control the macroscopic behaviour. To better understand the interplay between crystal structure, composition and the overall macroscopic response, systematic approaches are necessary to study how and to what (potential) extent the functional response can be chemically controlled. Here, two scenarios are possible, in which selective compositional $ABX_3$ variations or targeted chemical modifications of the molecular species are tested as a function of the responsive properties. In particular, the latter, the systematic approach will be investigated within this thesis, as outlined in more detail in the following *Chapter 1.5*, introducing the general methodology of studying new Molecular Perovskites with emphasis on small chemical changes on a molecular level.

## 1.5. Methodology of Synthesis and Characterisation of Molecular Perovskites

In addition to the studies outlined in *Chapter 2*, further results have been obtained in the course of this thesis that both experimentally and conceptually contribute to the development of designing new Molecular Perovskites. Therefore, this chapter provides a comprehensive overview of all discovered and characterised Molecular Perovskite structures. The underlying methodology, including conceptual design ideas, subsequent material synthesis routines and experimental standard and advanced characterisation techniques, will be presented in the following.

As a first step, a model system was defined that allows to study the impact of molecular substitution in Molecular Perovskites, *i.e.* small targeted chemical changes of the molecular component. In this pursuit, the $[C_2N_3]^-$ organic linker was chosen as a suitable and robust X-site anion in combination with divalent B-site metals ($B^{2+}$ = $Mn^{2+}$, $Co^{2+}$ and $Ni^{2+}$) for hosting different ammonium species on the A-site. The A-site cation was selected as the key tool for synthetically exploring molecular substitution within this thesis (Figure 7). Motivated by the incorporation of azaspiroundecanium into the $[B(C_2N_3)_3]^-$ network,[46] several tailormade piperidinium derivatives were designed and consequently synthesised by simple organic chemistry as they are commercially not available (Figure 7).[183] Various alkyl chain modifications of the piperidinium nitrogen were obtained by adapted synthetic procedures, all based on nucleophilic substitution reactions (*i.e.* one- or two-step $S_N2$-type reactions) of nucleophilic secondary or ternary amines with alkyl bromides. Typical reaction schemes and

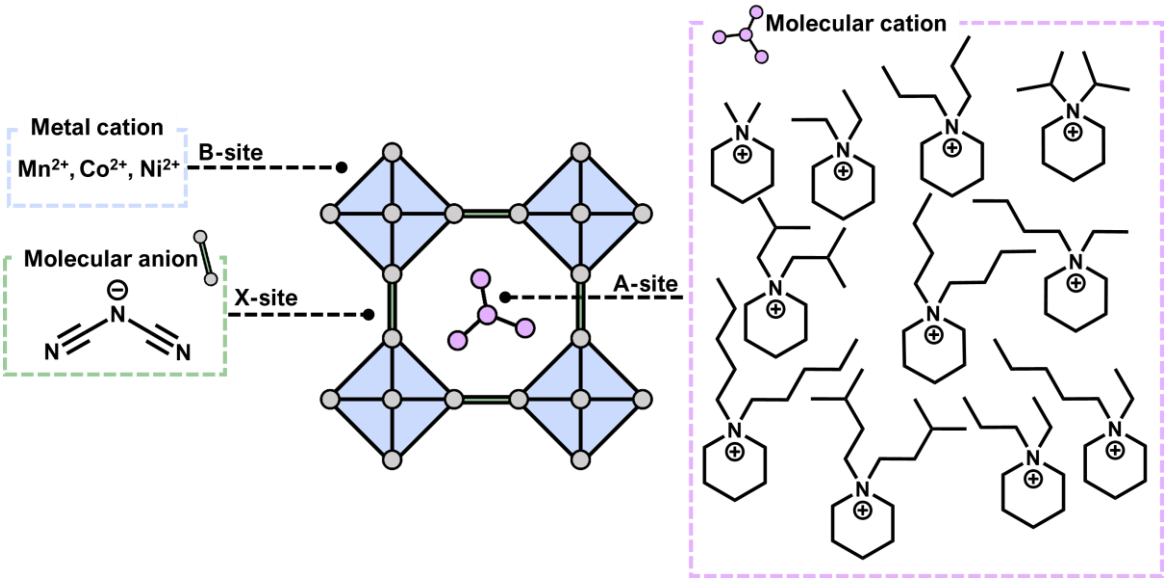


Figure 7: Representation of conceptual design ideas developed in this thesis for the synthesis of new Molecular Perovskites that allow for systematic investigation of molecular substitution on the A-site. The wide range of substituted piperidinium cations chosen for the A-site is highlighted in the pink box.

preparation details are given in the supporting information of study I and IV. After work-up procedures (*e.g.* recrystallisation), ten different tailor-made organic precursor salts were yielded in high purity, as confirmed *via* $^{1}$H NMR and $^{13}$C NMR spectroscopy (see Figure 7 for organic A-site cation structures).

In a subsequent step, crystallisation experiments were performed to incorporate the potential A-site cations into the $[B(C_2N_3)_3]^-$ network. Therefore, the well-established mild solution crystallisation routine[46,85,102] was applied in multiple batch experiments with varying ratios and concentrations of all aqueous precursor salt solutions (using commercially available sodium dicyanamide, various metal salts and the respective synthesised A-site precursor salts) in glass vials at ambient conditions or in the refrigerator. For each batch, observations such as crystal formation, precipitation of polycrystalline powder, or no precipitation at all were carefully documented to screen and subsequently optimise the crystallisation conditions. Diffraction techniques such as powder X-ray diffraction (PXRD) and single crystal X-ray diffraction (SCXRD) were used to control and analyse the crystalline materials and, in the best cases, confirm the formation of crystalline Molecular Perovskites. Among the entire potential range of different A-site candidates, crystallisation attempts with dimethylpiperdinium, diisopentylpiperidinium and dipentylpiperidnium failed (Figure 8). This indicates that they are either too small or too large to be incorporated into the $[B(C_2N_3)_3]^-$ network, underlining that the size criteria (of the A- and B-site cation selection) are key in the formation step of crystalline $[A]B(C_2N_3)_3$ materials (Figure 8). In total, eight suitable A-site cations were identified (Figure 9), resulting in 23 new $[A]B(C_2N_3)_3$ materials (Table 1). Therefore, suitable crystals were taken from the bottom of the glass vial and mounted on a microsample loop with perfluorinated ether to determine the crystal structure by performing SCXRD experiments at 100 K (or 300 K).

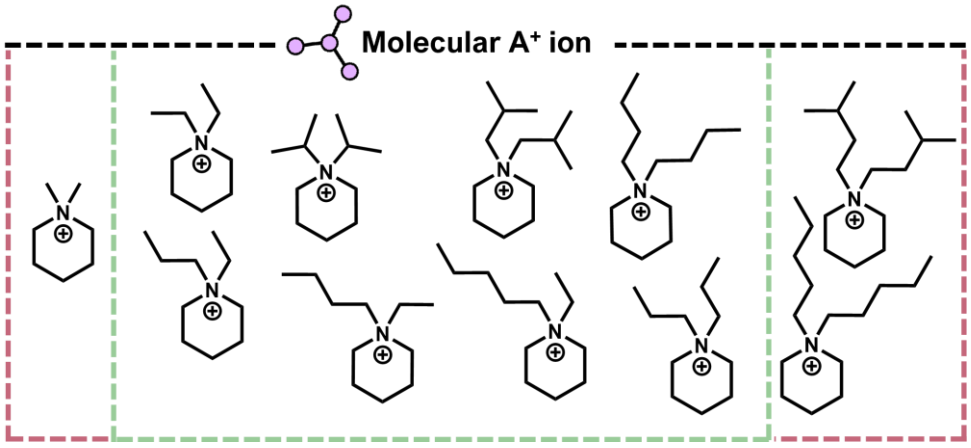


Figure 8: Illustration of different A-site cations, which have been used in the synthesis of dicyanamide-based Molecular Perovskites. All A-site cations highlighted in the green area were successfully incorporated, while molecular A-site cations shown in the red area were found to be unsuitable for the synthesis of Molecular Perovskites.

After working up the crystalline Molecular Perovskites in several washing steps with ultrapure water, drying *in vacuo*, crushing and finely grounding the crystals, a subsequent characterisation of the bulk material was performed. In the first step, the phase purity of the bulk material was checked by PXRD and confirmed by Pawley[184] (and/or Rietveld)[185] refinements of the collected PXRD data using space groups as determined from SCXRD. In addition, elemental analysis quantifications were carried out by the technical staff of the Catalysis Research Centre of TU Munich to check for impurities. Several samples of each newly synthesised material (approx. 20 – 30 batch vials, depending on the amount of crystals obtained per experiment) were combined into one polycrystalline sample of approximately 100 mg, which is required for subsequent analysis. Next, thermal analysis was performed using a TGA-DSC to measure the mass loss (TGA curve) and heat flow (DSC) in one experiment from room temperature to 1073.15 K using a heat rate of 10 K $min^{-1}$. This allows for simultaneously screening changes of the sample mass upon heating (in the TGA curve), which identifies thermal stability and endothermic and exothermic events (in the DSC curve) when no mass loss is observed, that can indicate melting, crystallisation or phase transition phenomena. From this experiment, the thermal decomposition temperatures ($T_d$) of all Molecular Perovskites were determined (Table 1). Further, reversible DSC measurements with subsequent heating and cooling runs were performed using controlled heating rates of 10 or 20 K $min^{-1}$, well below $T_d$, to better characterise the heat flow signals associated with the thermal transitions within a material. The analysed characteristics of the heat signals, such as peak shape, area and direction, provide important information for material properties such as exothermic (crystallisation and cold crystallisation) and endothermic processes (solid to solid phase transition, melting and glass transition). To provide a comprehensible thermal analysis data set, it is important to give information about the heating rate and the temperature determination of a respective heat signal when using different methods such as peak onset, offset, or maximum. Therefore, $T_d$ of all $[A]B(C_2N_3)_3$ materials were determined as the onset of significant decomposition in the TGA curve. The endothermic events observed in cyclic DSC runs across all $[A]B(C_2N_3)_3$ compounds were assigned to irreversible or reversible solid to solid phase transitions with the respective phase transition temperatures ($T_{ss}$), determined as peak onset (Table 1). Especially in study I, the DSC technique was further explored to follow the impact of a modifier salt on thermal events of a Molecular Perovskite, *i.e.* melting ($T_m$) during heating and crystallisation ($T_c$) during cooling. Further, the DSC data was applied to create a temperature-composition phase diagram of the binary system (*i.e.* modifier salt and Molecular Perovskite).

Table 1: Overview of all synthesised [A]B($C_2N_3$)$_3$ materials with the respective space group (from SCXRD data), decomposition temperature (obtained as onset of weight loss from weight TGA-DSC experiment) and phase transition temperature (obtained as peak onset of the 1st heating cycle in the DSC runs).

| **[A]B($C_2N_3$)$_3$ Materials** | **Molecular A-site ion $A^+$** | **Space group** | **Decomposition $T_d$ / K** | **Phase Transition $T_{ss}$ / K** |
|---|---|---|---|---|
| [DEP]Co($C_2N_3$)$_3$ | diethylpiperidinium | *C*2/*c* | 546.3 | rev. 352 |
| [DEP]Ni($C_2N_3$)$_3$ | diethylpiperidinium | *P*2$_1$/*c* | 595.15 | rev. 312, 338 |
| [DIP]Mn($C_2N_3$)$_3$ | diisopropylpiperidinium | *P*2$_1$/*c* | 558.65 | rev. 300, 332, 445 |
| [DIP]Co($C_2N_3$)$_3$ | diisopropylpiperidinium | *P*2$_1$/*c* | 546.25 | rev. 393 |
| [DIP]Ni($C_2N_3$)$_3$ | diisopropylpiperidinium | *P*2$_1$/*c* | 568.95 | rev. 415 |
| [DPP]Mn($C_2N_3$)$_3$ | dipropylpiperidinium | *C*2/*c* | 561.15 | rev. 365 |
| [DPP]Co($C_2N_3$)$_3$ | dipropylpiperidinium | *C*2/*c* | 552.25 | rev. 412 |
| [DPP]Ni($C_2N_3$)$_3$ | dipropylpiperidinium | *C*2/*c* | 598.05 | rev. 433 |
| [PEP]Mn($C_2N_3$)$_3$ | ethylpropylpiperidinium | *P*2$_1$/*c* | 560.65 | rev. 225, 331, 370 |
| [PEP]Co($C_2N_3$)$_3$ | ethylpropylpiperidinium | *P*2$_1$/*c* | 549.65 | rev. 236, 355, 391 |
| [PEP]Ni($C_2N_3$)$_3$ | ethylpropylpiperidinium | *P*2$_1$/*c* | 598.35 | rev. 236, 360, 397 |
| [BEP]Mn($C_2N_3$)$_3$ | butylethylpiperidinium | *P*2$_1$/*c* | 555.65 | rev. 368, 382, 443 |
| [BEP]Co($C_2N_3$)$_3$ | butylethylpiperidinium | *P*2$_1$/*c* | 548.65 | rev. 347, 378, 450 |
| [BEP]Ni($C_2N_3$)$_3$ | butylethylpiperidinium | *P*2$_1$/*c* | 575.95 | rev. 329, 386, 438 |
| [DBP]Mn($C_2N_3$)$_3$ | dibutylpiperidinium | *C*2/*c* | 569.95 | irrev. 368 rev. 382, 450 |
| [DBP]Co($C_2N_3$)$_3$ | dibutylpiperidinium | *C*2/*c* | 555.25 | rev. 346, 378, 450 |
| [DBP]Ni($C_2N_3$)$_3$ | dibutylpiperidinium | *C*2/*c* | 576.45 | irrev. 329 rev. 386, 438 |
| [EPP]Mn($C_2N_3$)$_3$ | ethylpentylpiperidinium | *P*2$_1$/*n* | 570.05 | rev. 405 |
| [EPP]Co($C_2N_3$)$_3$ | ethylpentylpiperidinium | *P*2$_1$/*n* | 551.85 | rev. 476 |
| [EPP]Ni($C_2N_3$)$_3$ | ethylpentylpiperidinium | *P*2$_1$/*n* | 576.25 | rev. 499 |
| [DIB]Mn($C_2N_3$)$_3$ | diisobutylpiperidinium | *P*2$_1$/*c* | 549.15 | rev. 419, 448 |
| [DIB]Co($C_2N_3$)$_3$ | diisobutylpiperidinium | *P*2$_1$/*c* | 533.75 | rev. 399, irrev. 424 |
| [DIB]Ni($C_2N_3$)$_3$ | diisobutylpiperidinium | *P*2$_1$/*c* | 581.85 | rev. 402, 458 |

In a further characterisation step, we used X-ray diffraction methods to monitor the structural response of these flexible materials upon temperature or pressure influence *in situ*, thus characterising their stimuli-responsive properties.[186,187] Variable-temperature powder X-ray diffraction (VTPXRD) experiments were conducted in the laboratory or at synchrotrons to follow the behaviour in response to temperature changes (typically in the temperature range between 100 – 400 K at laboratory experiments and 290 – 485 K at synchrotron facilities with small defined temperature step sizes of 5 – 20 K). This provides diffraction information about thermally induced solid to solid phase transitions, melting events, or decomposition processes

that support observations from the DSC data. For instance, in study I, we observed a crystalline to crystalline phase transition and, for higher temperatures, a thermal amorphisation, which we assigned to a crystalline to liquid phase transition, *i.e.* the melting process of the Molecular Perovskite. Notably here, high-resolution pair distribution function (PDF) measurements by X-ray total scattering at synchrotrons would provide further diffraction information about the local structure, *i.e.* the interatomic distances and coordination environment within a structure, of the crystalline (*e.g.* with long-range order > 20 Å) and the glassy (*e.g.* with short-range order up to 8 Å) state of a Molecular Perovskite.[188] In addition, the thermal response of a Molecular Perovskite can be further described by using thermal expansion coefficients. Therefore, the web-based software tool PASCal,[189] *i.e.* a principal axis strain calculator, can be applied using lattice parameters extracted from Pawley fits of the VTPXRD data as input. This identifies the direction of the three principal axes relative to the crystallographic axes (*a*, *b* and *c*), and hence, the linear coefficients of thermal expansion with projections of the principal axes on the unit cell axes. High-pressure experiments (HPPXRD) were performed at synchrotron facilities using a custom-built "high-pressure jump cell"[190] to probe the response of the Molecular Perovskites to the application of mechanical pressure under hydrostatic conditions (typically in the range between ambient pressure and 0.4 GPa with a small defined pressure step size of 0.02 GPa). Therefore, silicon oil (AP100, polyphenyl-methylsiloxane) was used as a non-penetrating pressure transmitting medium (PTM) with a hydrostatic limit of up to 0.9 GPa.[191,192] HPPXRD data allows to characterise the material's pressure response (*e.g.* described with the bulk modulus (*B*) as the inverse of the material's compressibility) and follow pressure-induced phase transitions or pressure-induced amorphisation processes.[193] For instance, the mechanical response of a new family of dicyanamide-based Molecular Perovskites (study IV) and Fe(II)-based MOFs (study III) was tested within this thesis. These studies offer fundamental insights into factors that dictate the mechanical properties, *i.e.* the impact of A-site chemistry in Molecular Perovskites or the spin-state in Fe(II)-containing MOFs. The mechanical resistance of a material can be described with *B* determined by fitting a Birch-Murnaghan (B-M) equation of state to the HPPXRD data derived from Pawley profile fitting. Therefore, two different methods can be applied, *i.e.* PASCal[189] and EOSFit7-Gui,[194] that both in combination provide a comprehensive data set of 2$^{nd}$ and 3$^{rd}$ order B-M equation of state fits. In addition, it is important to include the obtained standard errors ($\sigma B$) in relation to the $\sigma B$ of the measured standard material (*e.g.* $Ni(dmgH)_2$ with $dmgH^-$ = anionic form of dimethylglyoxime).

Seeking for relationships to rationalise the different stimuli-responsive properties found in various Molecular Perovskites (study IV), we analysed structural differences of the ambient $[B(C_2N_3)_3]^-$ network in more detail *via* group theoretical analysis[76,195] using the web-based software ISODISTORT.[40] For a complete mode decomposition analysis of the distorted

$[B(C_2N_3)_3]^-$ structures, a low-symmetry structure (*.cif file generated from SCXRD of 100 or 300 K of the corresponding Molecular Perovskite), simplified by removing the A-site cation, was applied compared to a hypothetical cubic perovskite structure with selected and fixed lattice parameters ($a$ = 8 Å and $\alpha$ = 90°). An overview of distortion modes associated with a

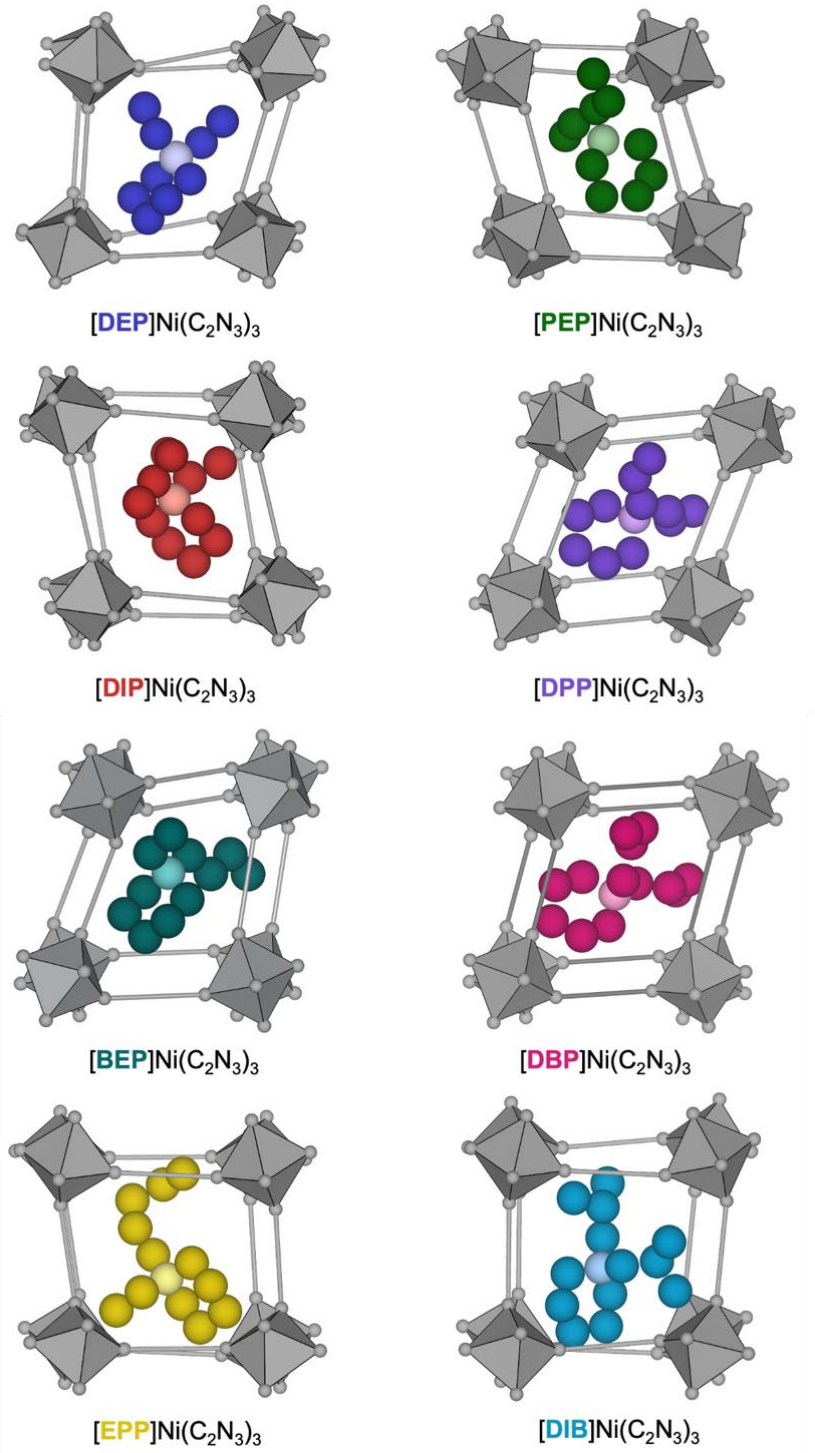


Figure 9: Illustration of all synthesised $[A]Ni(C_2N_3)_3$ materials exhibiting a $ABX_3$ perovskite structure motif, emphasising the use of various A-site cations explored within this thesis. Colour code: $NiN_6$ octahedra are shown in grey, A-site cations are highlighted with N atoms in the corresponding lighter colour and C atoms in the darker colour, H atoms were omitted for visualisation purposes.

combination of irreps of the space group symmetry of the cubic parent structure (*e.g.* conventional ($M_2^+$and $R_5^-$), unconventional tilting ($M_5^+$, $X_5^-$ and $\Gamma_4^+$) and columnar shifts ($\Gamma_5^+$)) active in the distorted Molecular Perovskite structures (from SCXRD data of 100 K) is given in Table 2. This involves the displacive mode amplitudes for each irrep and the overall distortion amplitude ($A_p$) displaying an amplitude for the entire framework distortion that is normalised to the parent structure given in the Angström unit.

Among all structures, a trend is apparent when exchanging the B-site metal from B = $Mn^{2+}$ to $Ni^{2+}$ towards decreasing $A_p$, which can be rationalised by a decrease in the network size and an increase in chemical bond strength within the $[B(C_2N_3)_3]^-$ network. In addition, these materials allow to study the impact of the A-site chemistry, as no hydrogen bonding interactions are formed between the A-site cations and the surrounding $[B(C_2N_3)_3]^-$ network. This systematic approach is demonstrated in study IV with four A-site cations ($A^+$ = $[DEP]^+$, $[PEP]^+$, $[DIP]^+$ and $[DPP]^+$) to seminally link the overall distortion amplitude to the mechanical response of Molecular Perovskites. Looking at the role of the A-site cations across the range of all structures studied in this thesis (Table 2), an overall higher $A_p$ was observed for structures with

Table 2: Distortion mode decomposition analysis details (determined from group theoretical analysis of SCXRD data of 100 K) of the distorted $[A]B(C_2N_3)_3$ structures compared to the cubic parent cell.

| **Compounds** | $R_5^-$ | $M_2^+$ | $\Gamma_4^+$ | $X_5^-$ | $M_5^+$ | $\Gamma_5^+$ | $A_p$ / Å |
|---|---|---|---|---|---|---|---|
| $[DEP]Co(C_2N_3)_3$ | 2.72057 | | 2.66098 | | | 2.10449 | 4.44101 |
| $[DEP]Ni(C_2N_3)_3$ | 1.17738 | 1.64960 | 0.19103 | 0.56322 | 0.44891 | 0.60846 | 2.27946 |
| $[DIP]Co(C_2N_3)_3$ | 1.75947 | 0.75824 | 0.25789 | 0.37910 | 0.74124 | 0.46496 | 2.18627 |
| $[DIP]Ni(C_2N_3)_3$ | 1.67136 | 0.74040 | 0.23561 | 0.37122 | 0.69707 | 0.42617 | 2.08543 |
| $[DPP]Mn(C_2N_3)_3$ | 2.71438 | | 2.94609 | | | 2.06009 | 4.64034 |
| $[DPP]Co(C_2N_3)_3$ | 2.45929 | | 2.88500 | | | 2.04785 | 4.43172 |
| $[DPP]Ni(C_2N_3)_3$ | 2.39294 | | 2.86078 | | | 2.09049 | 4.39524 |
| $[PEP]Mn(C_2N_3)_3$ | 2.19862 | 0.36080 | 0.15364 | 0.24872 | 0.54656 | 0.99173 | 2.53338 |
| $[PEP]Co(C_2N_3)_3$ | 1.97319 | 0.33600 | 0.12671 | 0.28525 | 0.46274 | 0.85763 | 2.26516 |
| $[PEP]Ni(C_2N_3)_3$ | 1.91172 | 0.33760 | 0.12105 | 0.25950 | 0.45264 | 0.83306 | 2.19858 |
| $[BEP]Mn(C_2N_3)_3$ | 1.63275 | | 0.56897 | | | 0.85014 | 3.59065 |
| $[BEP]Co(C_2N_3)_3$ | 1.73766 | | 0.05922 | | | 0.78830 | 3.33381 |
| $[BEP]Ni(C_2N_3)_3$ | 1.66915 | | 0.07020 | | | 0.75743 | 3.25922 |
| $[DBP]Mn(C_2N_3)_3$ | 2.19137 | | 3.02642 | | | 2.09179 | 4.36724 |
| $[DBP]Co(C_2N_3)_3$ | 1.89228 | | 2.97777 | | | 2.12375 | 4.20041 |
| $[DBP]Ni(C_2N_3)_3$ | 1.79236 | | 2.93138 | | | 2.11207 | 4.11649 |
| $[EPP]Mn(C_2N_3)_3$ | 1.21124 | 1.69792 | 0.23386 | 0.67870 | 0.22471 | 0.63569 | 2.32713 |
| $[EPP]Co(C_2N_3)_3$ | 0.78342 | 1.79676 | 0.15449 | 0.64727 | 0.28505 | 0.37693 | 2.15039 |
| $[EPP]Ni(C_2N_3)_3$ | 0.74223 | 1.72080 | 0.13899 | 0.60864 | 0.28978 | 0.34933 | 2.05837 |
| $[DIB]Mn(C_2N_3)_3$ | 1.48893 | 1.25168 | 0.06081 | 0.69917 | 0.59837 | 0.33807 | 2.20021 |
| $[DIB]Co(C_2N_3)_3$ | 1.25360 | 1.17232 | 0.07733 | 0.60772 | 0.48270 | 0.27477 | 1.93254 |
| $[DIB]Ni(C_2N_3)_3$ | 1.16664 | 1.06960 | 0.04695 | 0.55048 | 0.43568 | 0.24295 | 1.78037 |

symmetric cations ($A^+$ = $[DEP]^+$, $[DPP]^+$ and $[DBP]^+$) compared to the Molecular Perovskites with asymmetric ($A^+$ = $[PEP]^+$, $[BEP]^+$ and $[EPP]^+$) and more branched ($A^+$ = $[DIP]^+$ and $[DIB]^+$) substituted piperidinium cations. In addition, more predominant distortion modes are active when $A_p$ is reduced, while structures with higher $A_p$ exhibit less but individually stronger distortion modes. These observations underline the templating role effect of the A-site cations for octahedral distortions of the overall network discovered in study IV. Moreover, the analysis of distortion modes, as showcased in study IV, provides a future perspective to understand the impact of molecular substitution on the material's properties by linking active framework distortion modes to the stimuli-responsive behaviour.

Among all the studies presented in the following chapters, the heart of this thesis lies in study IV (*Chapter 2.4*), which provides a systematic study of how the modular Molecular Perovskite structure allows studying how small changes on an atomic level impact the macroscopic response. From the author's perspective, this study captures the beauty of Molecular Perovskites by combining both the purely inorganic and the molecular characteristics, *i.e.* with particular emphasis on the chemically rich playground for the molecular components and the applicability of solid-state principles. As we will see in the following chapters, study I (*Chapter 2.1*, tuning the melting behaviour of Molecular Perovskites by adding a modifier salt), study II (*Chapter 2.2*, characterising and understanding mixed-linker porphyrin-based MOF systems) and study III (*Chapter 2.3*, studying the impact of different triazolate-based linkers on the spin-state and overall mechanical response) contribute experimentally and conceptually to the understanding of composition-structure-property relations in coordination polymers in general.

# 2. Results and Discussion

## 2.1. Study I: $Li(C_2N_3)$ as Eutectic Forming Modifier in the Melting Process of the Molecular Perovskite $[(C_3H_7)_3N(C_4H_9)]Mn(C_2N_3)_3$

While the crystalline state of Molecular Perovskites has attracted much attention in the past, there are only a few, however very promising, studies on their melted and glassy state. Molecular Perovskites, which melt before thermal decomposition and thus enable the formation of Molecular Perovskite-based glasses, offer great potential as they combine both the liquid and solid state. Yet, the impact of glass modifiers on the thermal and functional properties of glass-forming Molecular Perovskites has not been explored.

In this work, we draw inspiration from inorganic glasses where modifiers have been established to tune the thermal and physicochemical properties of the resulting glasses. Herein, we report the synthesis of a new Molecular Perovskite $[(C_3H_7)_3N(C_4H_9)]Mn(C_2N_3)_3$ and investigate its solid-liquid and liquid-glass transition. We systematically study the impact of $Na(C_2N_3)$ and $Li(C_2N_3)$ as potential modifiers on its melting and glass-forming properties. We showed how a modifier, *i.e.* $Li(C_2N_3)$, can be used to lower the melting temperature while forming a eutectic mixture that allows for a straightforward synthesis of a Molecular Perovskite-based glass by slow cooling. This work showcases the applicability of an established concept that can be used to tune the thermal properties of melting Molecular Perovskites and other coordination networks. The manuscript further describes the following unprecedented findings:

While $Na(C_2N_3)$ shows no potential as a modifier in the first TGA-DSC screening runs, $Li(C_2N_3)$ influences the melting behaviour significantly. Systematically varying the Molecular Perovskite-modifier ratio by increasing the amount of $Li(C_2N_3)$ – studied by comprehensive DSC experiments – shows that the melting temperature monotonically decreases towards the eutectic mixture is reached. This widens the window between the melting and decomposition temperature, avoiding any potential decomposition processes. Upon slowly cooling down the eutectic mixture melt, no recrystallisation is observed in the DSC and PXRD, enabling an easy scale-up synthesis of Molecular Perovskite-based glasses. This seminal study of a modified Molecular Perovskite-based glass unlocks the potential to tailor the macroscopic glass properties by carefully selecting an additive that can act as a modifier and incorporate promising physicochemical properties.

S. M. Kronawitter performed the experiments, including project design and optimisation, data analysis and interpretation, with contributions to the DSC experiments and data discussion by A. Alhadid. S. Burger, S. A. Hallweger, J. Meyer; while C. Pedri contributed to the material

synthesis. S. Henke provided input for the discussion of the results and data validation, with G. Kieslich providing overarching scientific guidance and project design ideas. The manuscript was written by S. M. Kronawitter and G. Kieslich and subsequently critically reviewed and edited by all co-authors.



S. M. Kronawitter, S. A. Hallweger, J. Meyer, C. Pedri, S. Burger, A. Alhadid, S. Henke and G. Kieslich: $Li(C_2N_3)$ as Eutectic Forming Modifier in the Melting Process of the Molecular Perovskite $[(C_3H_7)_3N(C_4H_9)]Mn(C_2N_3)_3$, *APL Mater* **2023**, 11, 31119

APL Materials

RESEARCH ARTICLE | MARCH 27 2023

# $Li(C_2N_3)$ as eutectic forming modifier in the melting process of the molecular perovskite $[(C_3H_7)_3N(C_4H_9)]Mn(C_2N_3)_3$

**Special Collection:** Challenges and Perspectives in Materials Chemistry—A Celebration of Prof. Sir Anthony K. Cheetham's 75th Birthday

Silva M. Kronawitter ; Sebastian A. Hallweger ; Jan Meyer ; Carmen Pedri ; Stefan Burger ; Ahmad Alhadid ; Sebastian Henke ; Gregor Kieslich



*APL Mater.* 11, 031119 (2023)
https://doi.org/10.1063/5.0143404



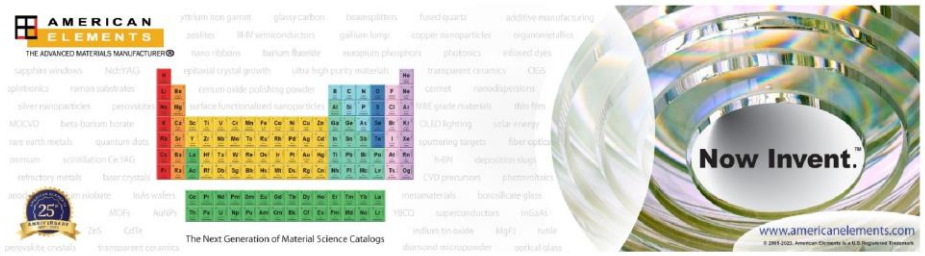

APL Materials ARTICLE scitation.org/journal/apm

# $Li(C_2N_3)$ as eutectic forming modifier in the melting process of the molecular perovskite $[(C_3H_7)_3N(C_4H_9)]Mn(C_2N_3)_3$ ±

Cite as: APL Mater. 11, 031119 (2023); doi: 10.1063/5.0143404
Submitted: 23 January 2023 • Accepted: 6 March 2023 •
Published Online: 27 March 2023



Silva M. Kronawitter,[1] Sebastian A. Hallweger,[1] Jan Meyer,[1] Carmen Pedri,[1] Stefan Burger,[1] Ahmad Alhadid,[2] Sebastian Henke,[3] and Gregor Kieslich[1,a)]

## AFFILIATIONS

[1] Department of Chemistry, TUM School of Natural Sciences, Technical University of Munich, Lichtenbergstraße 4, 85748 Garching, Germany
[2] Biothermodynamics, TUM School of Life Sciences, Technical University of Munich, Maximus-von-Imhof Forum 2, 85354 Freising, Germany
[3] Department of Chemistry and Biological Chemistry, Technical University of Dortmund, Otto-Hahn-Straße 6, 44227 Dortmund, Germany

**Note:** This paper is part of the Special Topic on Challenges and Perspectives in Materials Chemistry - A Celebration of Professor Sir Anthony K. Cheetham's 75th Birthday.

[a)] **Author to whom correspondence should be addressed:** gregor.kieslich@tum.de



## ABSTRACT

Coordination polymer (CP) glasses have recently emerged as a new glass state. Given the young state of the field, the discovery of concepts that guide the synthesis of CP glasses with targeted thermal and macroscopic properties is at the center of ongoing research. In our work, we draw inspiration from research on inorganic glasses, investigating the impact of $Li(C_2N_3)$ as a modifier on the thermal properties of the new molecular perovskite $[(C_3H_7)_3N(C_4H_9)]Mn(C_2N_3)_3$ (with $[C_2N_3]^-$ = dicyanamide, DCA). We derive the phase diagram and show that $Li(C_2N_3)$ and $[(C_3H_7)_3N(C_4H_9)]Mn(C_2N_3)_3$ form a eutectic mixture, in which the melting temperature is decreased by 30 K. Additionally, for the eutectic mixture at $x_{LiDCA} \approx 0.4$, a CP glass forms under slow cooling, opening interesting pathways for scalable synthesis routes of CP glasses. Given the virtually unlimited parameter space of hybrid modifiers, they will play a major role in the future to alter the glass' properties where the availability of rigorously derived phase diagrams will be important to identify material class overarching trends.



## INTRODUCTION

Coordination polymers (CPs) are composed of inorganic and organic building units, offering a large chemical space to address various applications, such as water harvesting,[1] ferroelectrics,[2] fine chemical catalysis,[3] and sensing[4] among many more. The discovery of glass-forming CPs is one of the latest milestones in the field,[5,6] conceptually closing the gap between inorganic and polymer-based glasses. Examples of glass-forming CPs are zeolitic imidazolate frameworks, such as ZIF-4 ($[Zn(Im)_2]$, $Im^-$ = imidazolate),[7] ZIF-62 ($[Zn(Im)_{1.75}(bIm)_{0.25}]$, $bIm^-$ = benzimidazolate),[8] and ZIF-62(M)-$bIm_x$[9] (M = $Co^{2+}$, $Zn^{2+}$), thiocyanate and nitrile-based CPs, such as $[Cu_2(SCN)_3(C_2bpy)]$[10] ($C_2bpy^+$ = 1-ethyl-[4,4-bipyridin]-1-ium) and $[Ag(mL1)(CF_3SO_3)]\cdot 2C_6H_6$ (*m*L1 = 1,3,5-tris(3-cyanophenylethynyl)benzene),[11] and low-dimensional CPs, such as $[Zn(HPO_4)(H_2PO_4)_2]\cdot 2H_2Im$[12] and $[Au(SPh)]_n$[13] ($SPh^-$ = thiophenolate). In addition to the fundamental interest in this new glass-state, CP-based glasses show potential in various applied areas, such as gas separation[14] and solid electrolytes.[15,16] CP glasses are typically synthesized by rapid cooling of a melt that is obtained by heating a crystalline CP. Therefore, the melt, as a key intermediate state toward CP glasses, deserves close attention, where conceptual progress for tailoring the melting temperature ($T_m$) through chemical and compositional

changes to suppress parasitic decomposition processes is of great importance.[9,17,18]

More recently, a series of $ABX_3$ molecular perovskites $[Pr_4N]B(C_2N_3)_3$ ($[Pr_4N]^+$ = tetrapropylammonium, B = $Mn^{2+}$, $Fe^{2+}$, and $Co^{2+}$) was reported to melt before thermal decomposition ($T_m < T_d$) and to form a stable coordination polymer glass upon rapid cooling.[19,20] Subsequently, the manipulation of $T_m$ by A- and B-site substitution was investigated for $AB[C_2N_3]_3$ CPs; $T_m$ decreases with increasing alkyl chain length of the A-site cation ($[Pe_4N]^+ > [Bu_4N]^+ > [Pr_4N]^+$ with Pe = pentyl, Bu = butyl, and Pr = propyl) or decreasing Shannon ionic radius of the B-site metal ($Mn^{2+} > Fe^{2+} > Co^{2+}$).[21] A similar impact of A-site cation substitution on $T_m$ and the glass transition temperature ($T_g$) was observed for 2D perovskite-related $A_2BX_4$ materials, such as $[A]_2PbI_4$ with six alkylammonium A-site cations (*n*-bua, *sec*-bua, 1-me-bua, *n*-hexa, 1-me-hexa, and 2-et-hexa with me = methyl, et = ethyl, bu = butyl, hex = hexyl, and a = ammonium),[22,23] despite the chemically different bonding situation within the inorganic 2D layers. These studies show that melting properties are heavily impacted by the A-site cations' entropic contributions and that B-site substitution allows for fine-tuning the materials' thermal properties. Therefore, $ABX_3$ perovskite-type CPs have proved as a powerful model platform for studying composition–structure–thermal property relationships by systematic compositional changes on the A-, B-, and X-site. An open opportunity that has yet not been explored for glass-forming perovskite-type materials is tailoring of glass formation properties, i.e., $T_g$ and $T_m$, by the use of glass modifiers.

Our work is inspired by decades of work on inorganic glasses, where the addition of modifiers is established as a tool for tailoring glass properties,[24] i.e., their structural,[25] optical,[26] and electronic[27] properties. Recent studies on the impact of various glass-network modifiers, i.e., inorganic metal oxides ($Li_2O$, $Na_2O$, CaO, MgO, BaO, and ZnO) on the thermal properties and glass forming ability of phosphate and aluminate glasses, emphasize the suitability of this approach toward CP glass chemistry.[28,29] Additionally, it was recently shown that the superprotonic properties of $CsHSO_4$ are preserved through the formation of a binary $CsHSO_4$-CP system that shows eutectic behavior.[30] Here, we report a new molecular perovskite $[Pr_3NBu]Mn(C_2N_3)_3$, investigate its melting behavior and glass-forming ability, and explore the impact of $Na(C_2N_3)$ and $Li(C_2N_3)$ on these processes. We identify $Li(C_2N_3)$ as a suitable compound for the formation of a eutectic mixture, which stabilizes the formation of a CP glass at high amounts. Our study emphasizes that the established principles from inorganic glasses are an important research compass to unlock the potential of CP glasses, which we expect to be key in deriving CP glasses with targeted thermal properties in the future.

## RESULTS AND DISCUSSION

### Synthesis and thermal properties of $[Pr_3NBu]Mn(C_2N_3)_3$

In the first step, the A-site cation butyltri-*n*-propylammonium ($[Pr_3NBu]^+$) was synthesized from tri-*n*-propylamine and 1-bromobutane in a one-step nucleophilic substitution reaction, see the supplementary material (S-2) for details and Fig. S1. Single crystals of the molecular perovskite $[Pr_3NBu]Mn(C_2N_3)_3$ were obtained by following an established mild solution synthesis route by starting from $[Pr_3NBu]Br$, $MnCl_2{\cdot}6H_2O$, and $Na(C_2N_3)$ in $H_2O$, see Fig. S2 and the supplementary material (S-3). The structure of $[Pr_3NBu]Mn(C_2N_3)_3$ was determined via single crystal x-ray diffraction, see Fig. 1(a), Table S1, and Fig. S5 for crystallographic data. At room temperature, $[Pr_3NBu]Mn(C_2N_3)_3$ crystallizes in the space group *Pbcn* with the cell parameters $a$ = 16.5315(17) Å, $b$ = 17.5441(17) Å, and $c$ = 32.348(3) Å, $V$ = 9382.0(17) Å$^3$. Thermogravimetric analysis–differential scanning calorimetry (TGA–DSC) was carried out on the as-synthesized $[Pr_3NBu]Mn(C_2N_3)_3$ material, showing thermal decomposition at $T_d$ = 570 K. Two endothermic events were observed at 371 and 474 K in the DSC signal before thermal decomposition, see Fig. S11. Variable temperature powder x-ray diffraction (VTPXRD) and cyclic DSC (Differential scanning calorimetry) measurements show that the heat event at $T_{ss}$ = 368 K belongs to an irreversible crystalline-to-crystalline (solid-to-solid, $T_{ss}$) phase transition, see Fig. 1(d) and the supplementary material (Figs. S15, S16, and S26). Comparing the PXRD pattern of the high-temperature phase with the PXRD of the molecular perovskite $[Pr_3NBu]Ni(C_2N_3)_3$ suggests that both materials are isostructural. In turn, both crystalline phases of $[Pr_3NBu]Mn(C_2N_3)_3$ exhibit a perovskite-type structure motif, making $[Pr_3NBu]Mn(C_2N_3)_3$ to another molecular perovskite that shows tilt and shift polymorphism,[31] see the supplementary material (Figs. S14, S17, and S18) for details on the structure discussion. Furthermore, VTPXRD shows that the second heat event at $T_m$ = 469.4 K, which occurs significantly before $T_d$, corresponds to a crystalline-to-amorphous phase transition, see Figs. 1(d) and Fig. S25. Following on from previous reports on the melting behavior of related dicyanamide-based materials,

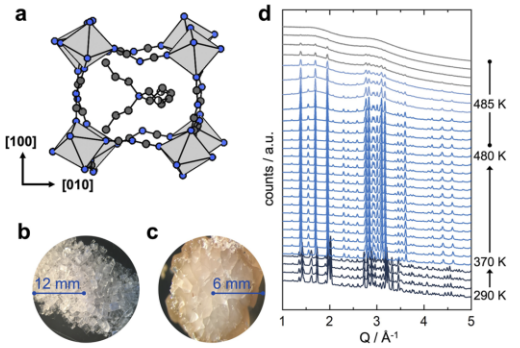


**FIG. 1.** (a) Structure visualization of the molecular perovskite $[Pr_3NBu]Mn(C_2N_3)_3$, where $[Mn(C_2N_3)_3]^-$ forms a 3D $ReO_3$-type network and the A-site molecule sits in its void for charge balance, forming the perovskite structure motif (color code: Mn polyhedral—light gray, N—dark blue, C—dark gray, and H atoms were deleted for better visualization). Optical images of the as-synthesized crystals (b) and the melt-quenched $[Pr_3NBu]Mn(C_2N_3)_3$ (c). (d) PXRD patterns ($\lambda$ = 0.206 79 Å) during heating from 290 to 485 K, showing a crystalline-to-crystalline phase transition at approximately $T_{ss}$ = 371 K (dark to light blue), followed by amorphization (gray) on holding at 485 K.

such as $[Pr_4N]Mn(C_2N_3)_3$ and $[Bu_4N]Mn(C_2N_3)_3$,[20,21,32] the second heat event is assigned to a solid-to-liquid phase transition, i.e., melting of $[Pr_3NBu]Mn(C_2N_3)_3$. This is further supported by the glass-like appearance of the melt-quenched material, see Fig. 1(c).

### Melted and glassy state of $[Pr_3NBu]Mn(C_2N_3)_3$

Compared to other $ABX_3$ molecular perovskites, $T_m$ = 474 K for $[Pr_3NBu]Mn(C_2N_3)_3$ is the lowest reported melting temperature to date, and the difference of $\Delta T$ = 96 K between $T_d$ and $T_m$ stands out being 61 K higher than for $[Pr_4N]Mn(C_2N_3)_3$ ($\Delta T$ = 35 K), see Fig. S11. However, it is important to mention that related $ABX_3$ non-perovskite $[C_2N_3]^-$-based CPs, such as $[Bu_4N]Mn(C_2N_3)_3$ and $[Pe_4N]Mn(C_2N_3)_3$, have been reported to melt at around 423 K.[21,32] Therefore, by drawing comparisons to ionic liquids, these results suggest describing $AB(C_2N_3)_3$ materials as $AX{\cdot}BX_2$ compounds, a perspective that highlights the inorganic–organic–ionic nature of CP melts and helps in rationalizing their thermal properties.[33] Following this train of thought, the $T_m$ of $[Pr_3NBu]C_2N_3{\cdot}Mn(C_2N_3)_2$ agrees with previous reports: with increasing the alkyl chain length of the quaternary ammonium A-site cation, an increased entropy of melting is observed, resulting in a monotonic decrease of $T_m$ along the series $[Pr_4N]C_2N_3{\cdot}Mn(C_2N_3)_2$ (535 K)[19,20,32] > $[Pr_3NBu]C_2N_3{\cdot}Mn(C_2N_3)_2$ (474 K) > $[Bu_4N]C_2N_3{\cdot}Mn(C_2N_3)_2$ (458 K)[21,32] > $[Pe_4N]C_2N_3{\cdot}Mn(C_2N_3)_2$ (422 K).[21,32]

Taking a closer look at the melting process of $[Pr_3NBu]Mn(C_2N_3)_3$ via cyclic DSC measurements, reversible melting is observed with a small decrease of $T_m$ of ~4.5 K from the first cycle $T_m$ = 469.4 K to the second cycle $T_m$ = 464.9 K, see Fig. S26. The thermogravimetric analysis combined with mass spectrometry was used to search for potential decomposition processes during melting, see Fig. S38. No evidence for material decomposition was found up to 493.15 K, and the first fragmentation products of the A-site alkyl chain were observed at $T$ = 513.15 K. Furthermore, $^1$H NMR spectroscopy of the acid-digested solid after melting shows no additional signals, see Fig. S9. Therefore, decomposition processes during the melting process are expected to play a minor role if any. Slowly cooling the melt to room temperature at a rate of 5 K min$^{-1}$ leads to recrystallization, which is observed in the DSC as a sharp exothermic event at $T_c$ = 452.7 K, see Figs. S24 and S26. Interestingly, recrystallization after melting, which might open opportunities for new synthesis routes of functional, crystalline thin film CPs, can still be considered as an unusual behavior for CPs and has only been reported for a few examples, such as Co-bis(acetamide)[34] and Cu(isopropylimidazolate).[35] Applying a rapid cooling procedure by quenching the $[Pr_3NBu]Mn(C_2N_3)_3$ melt in liquid $N_2$ suppresses recrystallization and leads to x-ray amorphous, glass-like fragments, see Fig. 1(c) and Fig. S19. Elemental analysis of the melt-quenched $[Pr_3NBu]Mn(C_2N_3)_3$ agrees with the $ABX_3$ stoichiometry of the starting compound, see details in the supplementary material (S-5). DSC measurements of the melt-quenched $[Pr_3NBu]Mn(C_2N_3)_3$ show a glass transition at around $T_g$ = 253.28 K, see Fig. S37. Therefore, the molecular perovskite $[Pr_3NBu]Mn(C_2N_3)_3$ forms a stable liquid upon heating and a coordination polymer glass upon rapid cooling akin to previous reports on $[Pr_4N]B(C_2N_3)_3$ ($B = Mn^{2+}$, $Co^{2+}$, and $Ni^{2+}$).

### $Li(C_2N_3)$ as eutectic forming modifier

Drawing inspiration from research works on inorganic glasses, we investigated the impact of $M(C_2N_3)$(with $M = Li^+$ and $Na^+$) as a modifier on the melting behavior and glass formation of $[Pr_3NBu]Mn(C_2N_3)_3$. $Na(C_2N_3)$ is commercially available and was used as purchased, while $Li(C_2N_3)$ was synthesized in a modified literature procedure starting from $Na(C_2N_3)$, see preparation details in the supplementary material (S-4). The phase purity of $Li(C_2N_3)$ was confirmed by TGA–DSC analysis and IR spectroscopy, see Figs. S10 and S39–S41. Both $Li(C_2N_3)$ and $Na(C_2N_3)$ undergo a trimerization reaction upon heating while no melting is observed, see the supplementary material (S-13). Before preparation of modifier–$[Pr_3NBu]Mn(C_2N_3)_3$ mixtures of various mole ratios, both $M(C_2N_3)_3$ salts and $[Pr_3NBu]Mn(C_2N_3)_3$ were dried, see preparation details in the supplementary material (S-12). In the first step, we screened the impact of the modifier on $T_m$ via TGA–DSC experiments of different mole fractions, see Figs. S12 and S13. From this screening series, it can be observed that the melting point of $[Pr_3NBu]Mn(C_2N_3)_3$ decreases when mixing with increasing mole fractions $x_{LiDCA}$ of $Li(C_2N_3)$, while $Na(C_2N_3)$ as modifier has no evident impact. Applying established equations that describe the solid–liquid thermodynamics in the studied system, our experimental results suggest a large difference in theoretical melting temperatures of $Li(C_2N_3)$ and $Na(C_2N_3)$, which can be expected based on their different crystal structures; for a more elaborate discussion, see the supplementary material (S-37).

Subsequently, we explored the impact of $Li(C_2N_3)$ on $T_m$ as a function of increasing mole fractions $x_{LiDCA}$ ($x_{LiDCA}$ = 0, 0.15, 0.25, 0.32, 0.38, 0.41, 0.45, 0.49, 0.58, and 0.66) via DSC in more detail, see Fig. 2 and Figs. S27–S35. From the DSC traces, it is evident that an increase in $x_{LiDCA}$ has no significant impact on $T_{ss}$ of

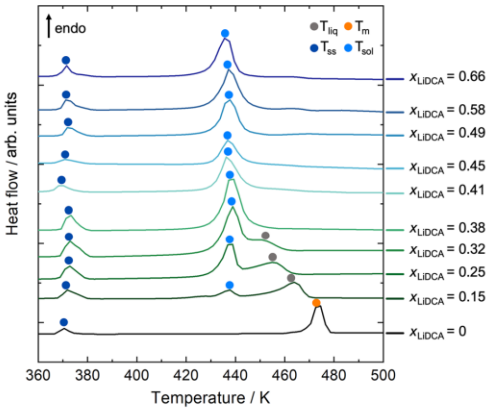


**FIG. 2.** DSC curves of $Li(C_2N_3)$–$[Pr_3NBu]Mn(C_2N_3)_3$ mixtures with varying the amount of modifier salt, $x_{LiDCA}$. The DSC data of various mole fractions obtained on heating were used to build a phase diagram. For better visualization, the curves are offset by a random shift.

$[Pr_3NBu]Mn(C_2N_3)_3$. This is expected as there is no obvious pathway of how $Li(C_2N_3)$ as a modifier impacts the internal structural reorganization of $[Pr_3NBu]Mn(C_2N_3)_3$ prior to melting. In contrast, already at $x_{LiDCA}$ = 0.15, two distinct endothermic signals become visible in the DSC traces, which belong to the liquidus ($T_{liq}$) and the solidus temperature ($T_{sol}$), see Fig. S27. Further increasing $x_{LiDCA}$ leads to a monotonic decrease of $T_{liq}$ until approximately $x_{LiDCA}$ ≈ 0.4, where the eutectic mixture ($T_{sol}$ = $T_{liq}$) is reached. Furthermore, in the second heating cycle of the mixtures $x_{LiDCA}$ = 0.15, 0.25, 0.32, and 0.38, an exothermic event is observed, see Figs. S27–S30. This exothermic event reflects a structural reorganization related to crystallization and is known as cold crystallization ($T_{cc}$). Overall, for $x_{LiDCA}$ = 0.38, a decrease of ~30 K in the melting of the homogeneous mixture ($T_{liq}$) is observed; for comparison purposes with literature data, the offset temperature of $T_m$ is used for the discussion, while Table S3 contains both $T_m$ as determined from peak onset and offset. Taken together, the data provide the basis to build a temperature–composition phase diagram up to $x_{LiDCA}$ = 0.41, see Fig. 3. To the best of our knowledge, this is the first report of a molecular perovskite-related eutectic mixture, showcasing the applicability of established concepts to tailor the thermal properties of melting coordination polymers.

The decreased $T_m$ of $[Pr_3NBu]Mn(C_2N_3)_3$ by the formation of a eutectic mixture with $Li(C_2N_3)$ as a modifier provides improved opportunities for glass formation compared to currently employed TGA–DSC-based processes. Additionally, opening the gap between $T_m$ and $T_d$ is expected to further suppress any potential decomposition processes. To demonstrate this, we performed simple model experiments by heating 20 mg of mixtures near the eutectic ($x_{LiDCA}$ = 0.38 and 0.41) to 443 or 441 K in a glass vial under Ar atmosphere, see method details in the supplementary material (S-5). Initial melting started after 10 min, and after 30 min, the melting process was completed. After cooling slowly to room temperature, the remaining solids were transparent and had a drop-like appearance, see Fig. S4. Comparing the PXRD pattern prior to and after melting of the mixture closest to the eutectic ($x_{LiDCA}$ = 0.41), all sharp reflections disappeared, see Fig. S23. For the mixture of $x_{LiDCA}$ = 0.38, however, evidence for crystalline domains remained, which is expected from the observed recrystallization event in the DSC traces of the $x_{LiDCA}$ = 0.38 mixture when cooled slowly, see Figs. S21, S22, and S30. Importantly, an excess of $Li(C_2N_3)$ ($x_{LiDCA}$ = 0.41 and higher) avoids any recrystallization even when cooled slowly. This suggests that the composition of the eutectic mixture is at a mole fraction of approximately $x_{LiDCA}$ ≈ 0.4. In parallel, for all mixtures with a mole fraction $x_{LiDCA}$ ≥ 0.41–0.66, a clear glass transition $T_g$ is visible, which decreases from $T_g$ = 312.3 K ($x_{LiDCA}$ = 0.41) to $T_g$ = 301.3 K ($x_{LiDCA}$ = 0.66), see Figs. S31–S35. Furthermore, miscibility of $[Pr_3NBu]Mn(C_2N_3)_3$ and $Li(C_2N_3)$ in the liquid state is assumed since only a single $T_g$ was obtained for mixtures between $x_{LiDCA}$ = 0.41 and 0.66, see Figs. S31–S35. Therefore, $Li(C_2N_3)$ is a suitable modifier for tailoring the melting behavior of the molecular perovskite $[Pr_3NBu]Mn(C_2N_3)_3$.

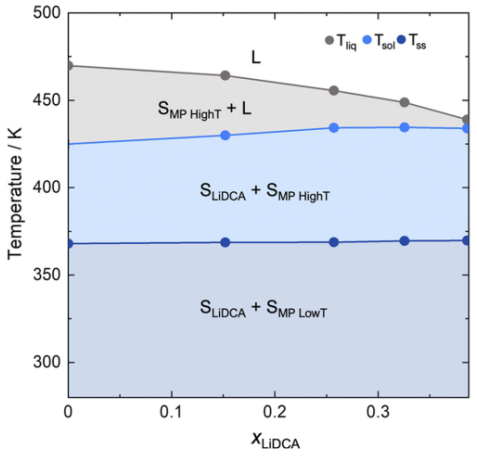


**FIG. 3.** Partial phase diagram of the binary$Li(C_2N_3)$–$[Pr_3NBu]Mn(C_2N_3)_3$ system at ambient pressure showing simple eutectic behavior, with S = solid phase, L = liquid phase, MP = molecular perovskite, and LiDCA = $Li(C_2N_3)$. We would like to note that the phase diagram was built from DSC data of the initial heating run up to $x_{LiDCA}$ = 0.41 since $T_{liq}$ of mixtures with higher mole fractions ($x_{LiDCA}$ = 0.41, 0.45, 0.49, 0.58, 0.66) are not possible to determine. For small mole fractions, we observed a very weak signal without a clear peak onset and offset, and for larger mole fractions, we assume that $T_{liq}$ raises quickly above the temperature where trimerization of $Li(C_2N_3)$ and/or decomposition of $[Pr_3NBu]Mn(C_2N_3)_3$ start.

## CONCLUSION

We report the synthesis of the new molecular perovskite $[Pr_3NBu]Mn(C_2N_3)_3$, investigate its melting behavior, and show that $Li(C_2N_3)$ is a suitable eutectic forming glass modifier. For the eutectic mixture at $x_{LiDCA}$ ≈ 0.4, we observe a decrease of $T_m$ of 30 K and show that a CP glass can be obtained even when cooled slowly. Our results underpin that established principles for inorganic glasses are a suitable compass for progressing the area of CP glasses, and specifically, the use of eutectic mixtures provides a myriad of opportunities to alter the glass' resulting macroscopic properties.

In going forward, the use of "non-innocent" glass modifiers, i.e., modifiers with an intrinsic physical property, such as optical activity or interesting photophysics, might offer a pathway to incorporate new properties in the resulting glass beyond its impact as a modifier *per se*. For instance, for an AX modifier, $A^+$ might be optical active while $X^-$ guarantees high miscibility with the parent material when chosen according to the chemistry of the glass forming CP. Additionally, we propose that established formulas that describe the underlying solid–liquid thermodynamics can guide the search for other potential eutectic formers for CP forming glasses such as purely organic $[C_2N_3]^-$-based modifier salts with suitable melting temperatures for $[C_2N_3]^-$-based molecular perovskites. Future research opportunities include the investigation of materials' mechanical properties, such as compressibility, bulk moduli, and thermal expansion behavior, as a function of mole fractions $x_{LiDCA}$. Therefore, we believe that the use of modifiers will become an increasingly important research branch in the field of CP glasses, for which our results provide an important fundamental groundwork.

## SUPPLEMENTARY MATERIAL

See the supplementary material for the complete material synthesis, characterization and thermal analysis of the studied perovskite, modifier salts, and perovskite–modifier mixtures.

## DEDICATION

Dedicated to the 75th Birthday of A. K. Cheetham.

## ACKNOWLEDGMENTS

We like to thank Alba S. J. Méndez and Martin Etter for their support during data collection at Beamline P02.1 at the Deutsche Elektronensynchrotron DESY (PETRA III, Hamburg, Germany). G.K. gratefully thanks the Fonds der Chemischen Industrie and the DFG (Project No. 450070835) for financial support.

## AUTHOR DECLARATIONS

### Conflict of Interest

The authors have no conflicts to disclose.

### Author Contributions

**Silva M. Kronawitter**: Data curation (equal); Formal analysis (equal); Investigation (equal); Methodology (equal); Validation (equal); Visualization (equal); Writing – original draft (equal). **Sebastian A. Hallweger**: Data curation (equal); Investigation (equal). **Jan Meyer**: Investigation (equal). **Carmen Pedri**: Investigation (equal). **Stefan Burger**: Investigation (equal); Writing – review & editing (equal). **Ahmad Alhadid**: Data curation (equal); Investigation (equal); Writing – review & editing (equal). **Sebastian Henke**: Validation (equal); Writing – review & editing (equal). **Gregor Kieslich**: Conceptualization (equal); Funding acquisition (equal); Project administration (equal); Resources (equal); Supervision (equal); Writing – review & editing (equal).

## DATA AVAILABILITY

The data that support the findings of this study are available within the supplementary material.

## REFERENCES

[1]H. Kim, S. Yang, S. R. Rao, S. Narayanan, E. A. Kapustin, H. Furukawa, A. S. Umans, O. M. Yaghi, and E. N. Wang, Science **356**, 430 (2017).
[2]Y.-M. Xie, J.-H. Liu, X.-Y. Wu, Z.-G. Zhao, Q.-S. Zhang, F. Wang, S.-C. Chen, and C.-Z. Lu, Cryst. Growth Des. **8**, 3914 (2008).
[3]L. Jiao, Y. Wang, H.-L. Jiang, and Q. Xu, Adv. Mater. **30**, 1703663 (2018).
[4]L. E. Kreno, K. Leong, O. K. Farha, M. Allendorf, R. P. van Duyne, and J. T. Hupp, Chem. Rev. **112**, 1105 (2012).
[5]T. D. Bennett and S. Horike, Nat. Rev. Mater. **3**, 431 (2018).
[6]S. Horike, S. S. Nagarkar, T. Ogawa, and S. Kitagawa, Angew. Chem., Int. Ed. **59**, 6652 (2020).
[7]T. D. Bennett, J.-C. Tan, Y. Yue, E. Baxter, C. Ducati, N. J. Terrill, H. H.-M. Yeung, Z. Zhou, W. Chen, S. Henke, A. K. Cheetham, and G. N. Greaves, Nat. Chem. **6**, 8079 (2015).
[8]T. D. Bennett, Y. Yue, P. Li, A. Qiao, H. Tao, N. G. Greaves, T. Richards, G. I. Lampronti, S. A. T. Redfern, F. Blanc, O. K. Farha, J. T. Hupp, A. K. Cheetham, and D. A. Keen, J. Am. Chem. Soc. **138**, 3484 (2016).
[9]L. Frentzel-Beyme, M. Kloß, P. Kolodzeiski, R. Pallach, and S. Henke, J. Am. Chem. Soc. **141**, 12362 (2019).
[10]S. S. Nagarkar, H. Kurasho, N. T. Duong, Y. Nishiyama, S. Kitagawa, and S. Horike, Chem. Commun. **55**, 5455 (2019).
[11]C. Das, T. Ogawa, and S. Horike, Chem. Commun. **56**, 8980 (2020).
[12]D. Umeyama, S. Horike, M. Inukai, T. Itakura, and S. Kitagawa, J. Am. Chem. Soc. **137**, 864 (2015).
[13]S. Vaidya, O. Veselska, A. Zhadan, M. Diaz-Lopez, Y. Joly, P. Bordet, N. Guillou, C. Dujardin, G. Ledoux, F. Toche, R. Chiriac, A. Fateeva, S. Horike, and A. Demessence, Chem. Sci. **11**, 6815 (2020).
[14]Y. Wang, H. Jin, Q. Ma, K. Mo, H. Mao, A. Feldhoff, X. Cao, Y. Li, F. Pan, and Z. Jiang, Angew. Chem., Int. Ed. **59**, 4365 (2020).
[15]T. Ogawa, K. Takahashi, S. S. Nagarkar, K. Ohara, Y.-L. Hong, Y. Nishiyama, and S. Horike, Chem. Sci. **11**, 5175 (2020).
[16]N. Ma, S. Kosasang, A. Yoshida, and S. Horike, Chem. Sci. **12**, 5818 (2021).
[17]H. Kimata and T. Mochida, Chem. - Eur. J. **25**, 10111 (2019).
[18]M. Lusi, Cryst. Growth Des. **18**, 3704 (2018).
[19]B. K. Shaw, A. R. Hughes, M. Ducamp, S. Moss, A. Debnath, A. F. Sapnik, M. F. Thorne, L. N. McHugh, A. Pugliese, D. S. Keeble, P. Chater, J. M. Bermudez-Garcia, X. Moya, S. K. Saha, D. A. Keen, F.-X. Coudert, F. Blanc, and T. D. Bennett, Nat. Chem. **13**, 778 (2021).
[20]J. M. Bermúdez-García, M. Sánchez-Andújar, S. Yáñez-Vilar, S. Castro-García, R. Artiaga, J. López-Beceiro, L. Botana, Á. Alegría, and M. A. Señarís-Rodríguez, Inorg. Chem. **54**, 11680 (2015).
[21]B. K. Shaw, C. Castillo-Blas, M. F. Thorne, M. L. Ríos Gómez, T. Forrest, M. D. Lopez, P. A. Chater, L. N. McHugh, D. A. Keen, and T. D. Bennett, Chem. Sci. **13**, 2033 (2022).
[22]A. Singh, M. K. Jana, and D. B. Mitzi, Adv. Mater. **33**, 2005868 (2021).
[23]T. Li, W. A. Dunlap-Shohl, E. W. Reinheimer, P. Le Magueres, and D. B. Mitzi, Chem. Sci. **10**, 1168 (2019).
[24]J. Lu, Z. Shan, J. Zhang, Y. Su, K. Yi, Y. Zhang, and Q. Zheng, J. Non-Cryst. Solids: X **16**, 100125 (2022).
[25]N. Ghribi, M. Dutreilh-Colas, J.-R. Duclère, T. Hayakawa, J. Carreaud, R. Karray, A. Kabadou, and P. Thomas, J. Alloys Compd. **622**, 333 (2015).
[26]A. Marzuki and D. E. Fausta, IOP Conf. Ser.: Mater. Sci. Eng. **858**, 012035 (2020).
[27]B. Roling and M. D. Ingram, J. Non-Cryst. Solids **265**, 113 (2000).
[28]Y. He, X. Shen, Y. Jiang, and A. Lu, Mater. Chem. Phys. **258**, 123865 (2021).
[29]K. Griebenow, C. B. Bragatto, E. I. Kamitsos, and L. Wondraczek, J. Non-Cryst. Solids **481**, 447 (2018).
[30]N. Ma, N. Horike, L. Lombardo, S. Kosasang, K. Kageyama, C. Thanaphatkosol, K. Kongpatpanich, K.-I. Otake, and S. Horike, J. Am. Chem. Soc. **144**, 18619 (2022).
[31]S. Burger, S. Grover, K. T. Butler, H. L. B. Boström, R. Grau-Crespo, and G. Kieslich, Mater. Horiz. **8**, 2444 (2021).
[32]J. A. Schlueter, J. L. Manson, and U. Geiser, Inorg. Chem. **44**, 3194 (2005).
[33]J. Dupont, Acc. Chem. Res. **44**, 1223 (2011).
[34]M. Liu, A. H. Slavney, S. Tao, R. D. McGillicuddy, C. C. Lee, M. B. Wenny, S. J. L. Billinge, and J. A. Mason, J. Am. Chem. Soc. **144**, 22262 (2022).
[35]T. Watcharatpong, T. Pila, T. Maihom, T. Ogawa, T. Kurihara, K. Ohara, T. Inoue, H. Tabe, Y.-S. Wei, K. Kongpatpanich, and S. Horike, Chem. Sci. **13**, 11422 (2022).

## 2.2. Study II: Understanding and Controlling Molecular Compositions and Properties in Mixed-Linker Porphyrin Metal-Organic Frameworks

Zr-based MOFs with porphyrins as linkers offer intrinsic properties such as high porosity for the incorporation of guest molecules and a porphyrin core for the integration of metals. Therefore, they have been established as model platform for studying and designing multifunctional systems for catalysis. However, the synthesis and characterisation of phase-pure Zr-based MOFs and, thus, of multifunctional systems still remain a challenge.

This work addresses the challenge of incorporating chemically modified porphyrins (*ß*-ethyl-functionalised porphyrin linkers) into the well-known PCN-222. By using the mixed-linker strategy, we presented a series of solid solution PCN-222 analogues with synthetic control over a broad range of varying ethyl-porphyrin content. Thus, these materials enabled a systematic study of the impact of the non-planar linkers on structure-property relations in PCN-222 systems. Therefore, we thoroughly analysed the structural and chemical properties, showing controllable features such as the BET surface area or linker fluorescence as a function of increasing amount of modified linker. Further, we show rather unexpected complexity, such as different crystallinity, defect concentration and thermal response, resulting from only minor chemical changes of the porphyrin linker. Our study highlights that the design of Zr-based MOF systems with controllable properties requires a combination of complementary techniques, which is often poorly explored in literature.

K. Hemmer performed the bulk of experiments, including material synthesis. Further experiments, data analysis, interpretation and conceptualisation were conducted by K. Hemmer and S. M. Kronawitter with the support of N. Grover and B. Twamley. M. Cokoja, R. A. Fischer, G. Kieslich and M. O. Senge gave overarching scientific guidance. R. A. Fischer and G. Kieslich provided financial support and resources. The manuscript was written equally by K. Hemmer and S. M. Kronawitter and subsequently edited with support from G. Kieslich and reviewed by all co-authors.



K. Hemmer,[†] S. M. Kronawitter,[†] N. Grover, B. Twamley, M. Cokoja, R. A. Fischer, G. Kieslich, M. O. Senge: Understanding and Controlling Molecular Compositions and Properties in Mixed-Linker Porphyrin Metal-Organic Frameworks, *Inorg. Chem.* **2024**, *63*, 4, 2122-2130

[†] Equal contribution

Inorganic Chemistry

pubs.acs.org/IC Article

# Understanding and Controlling Molecular Compositions and Properties in Mixed-Linker Porphyrin Metal–Organic Frameworks

Karina Hemmer,[⊥] Silva M. Kronawitter,[⊥] Nitika Grover, Brendan Twamley, Mirza Cokoja, Roland A. Fischer, Gregor Kieslich,* and Mathias O. Senge*

Cite This: *Inorg. Chem.* 2024, 63, 2122–2130 Read Online

ACCESS | Metrics & More | Article Recommendations | Supporting Information



**ABSTRACT:** Porphyrin-based metal–organic frameworks (MOFs) are attractive materials for photo- and thermally activated catalysis due to their unique structural features related to the porphyrin moiety, guest-accessible porosity, and high chemical tunability. In this study, we report the synthetic incorporation of nonplanar $\beta$-ethyl-functionalized porphyrin linkers into the framework structure of PCN-222, obtaining a solid-solution series of materials with different modified linker contents. Comprehensive analysis by a combination of characterization techniques, such as NMR, UV–vis and IR spectroscopy, powder X-ray diffraction, and $N_2$ sorption analysis, allows for the confirmation of linker incorporation. A detailed structural analysis of intrinsic material properties, such as the thermal response of the different materials, underlines the complexity of synthesizing and understanding such materials. This study presents a blueprint for synthesizing and analyzing porphyrin-based mixed-linker MOF systems and highlights the hurdles of characterizing such materials.

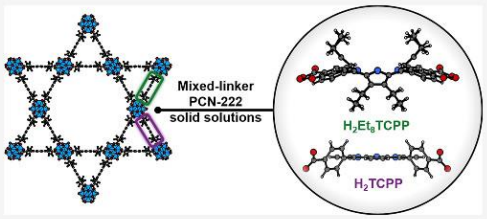


## INTRODUCTION

In catalysis, the concept of multifunctionality is prominent to exploit synergistic effects or for tandem catalysis where more than one catalytic transformation is performed within one system.[1−3] Due to their enormous design flexibility and tunability, metal–organic frameworks (MOFs) have emerged as a promising material platform for the realization of multifunctional synthetic systems.[4−7] MOFs are built from metal nodes and linkers, and either of these components can be varied to obtain a multifunctional porous system. Likewise, several functionalities can be integrated either in situ or postsynthetically, making MOFs into an exciting material platform.[8−10] This allows for the synthesis of different catalytically active MOFs, and the study of their specific properties via advanced/in situ characterization techniques, ideally revealing structure–property relations and catalysis insights. Exemplarily, molecular catalysts are frequently incorporated into established MOF scaffolds to introduce further reactivities.[11,12]

Porphyrin-based MOFs with porphyrins as linkers are predestined for the design of multifunctional catalysis due to (1) the capability of porphyrin core metalation with a large variety of transition metals allowing for several catalytic applications, and (2) the large pore volumes where even sterically demanding guests can be incorporated without significantly preventing molecule diffusion within the pores.[13−17] In parallel, significant synthetic challenges have to be faced when working with Zr-based frameworks since different framework topologies are accessible based on the combination of the same building units such as Zr-oxo-clusters and porphyrin linkers. Therefore, precise tuning of reaction conditions is important for phase-pure synthesis as was recently shown for PCN-222 and PCN-224 as model systems.[18−23] Changing any synthetic conditions or reaction parameters, which include subtle changes in the chemistry of linker molecules, might therefore result in altered outcomes.

One prominent strategy for the implementation of new functionalities based on a Zr-based framework is a mixed-linker approach.[24,25] This renders pore blockage unlikely since the functionality is part of the linker, leaving free pore space. Therefore, a rational choice is $\beta$-functionalized porphyrins, e.g., with halides or alkyl chains attached to the macrocycle, with a similar structure motif as conventionally used porphyrin linkers. Previous reports have shown that the chemical functionalization of the porphyrin with ethyl groups results in a conformational flexibility from planar to nonplanar[26,27] where the nitrogen atoms are located out-of-plane.[28,29] This results in a high basicity enabling metal-free catalysis and preferable kinetics for metal incorporation into the porphyrin

Received: November 8, 2023
Revised: December 18, 2023
Accepted: December 25, 2023
Published: January 11, 2024





https://doi.org/10.1021/acs.inorgchem.3c03943
*Inorg. Chem.* 2024, 63, 2122–2130

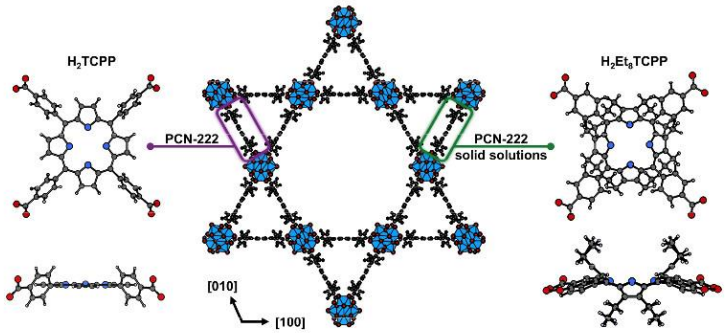


**Figure 1.** Structure of PCN-222 (middle, CCDC code BEDYEQ)[16] and schematics of porphyrin linkers **$H_2$TCPP** (left; top and side-view) and the functionalized bulkier linker **$H_2Et_8$TCPP** (right; top and side-view) that are used in this work in a mixed-linker solid-solution approach (color code: C, N, O, and H are shown in dark gray, blue, red, and light gray).

core, which usually has to change its conformation for metalation (especially for metals of larger size like Ru, Rh, etc.).[30] Therefore, adding nonplanar porphyrins such as 2,3,7,8,12,13,17,18-octaethyl-5,10,15,20-tetrakis(4-carboxyphenyl)porphyrin (**$H_2Et_8$TCPP**) as a linker in MOF synthesis may unlock further functionalities and/or material-property-relations compared to the parent porphyrin-based material, while keeping the underlying network topology.

By varying (and controlling) one crucial structural parameter, i.e., the porphyrin modification, we here provide a systematic study of the impact of linker modification and its framework amount on the MOF properties. In this pursuit, we used the mixed-linker strategy to incorporate the nonplanar porphyrin (**$H_2Et_8$TCPP**) in PCN-222, which is a porphyrin-based Zr-MOF with a 3D network architecture and an underlying Kagomé-like topology (Figure 1). We prepared a series of mixed-linker solid-solution PCN-222 analogues with different contents of nonplanar porphyrin and thoroughly analyzed the resulting materials by $^1$H NMR, infrared (IR) and UV−vis spectroscopy, powder X-ray diffraction (PXRD), $N_2$ sorption measurements, inductively coupled plasma mass spectrometry (ICP-MS), thermogravimetric analysis (TGA), and scanning electron microscopy (SEM). Moreover, we performed variable-temperature PXRD (VTPXRD) experiments to investigate the structural consequences of the integrated bulkier linker **$H_2Et_8$TCPP** in this series of functionalized PCN-222 derivatives as a function of temperature. Additionally, material properties, such as pH stability, fluorescence, and metalation capability, are examined. Thus, the detailed investigation of structural and chemical properties of functionalized MOFs accessible via a mixed-linker approach, realized by a combination of different characterization techniques, presents an important step toward understanding and controlling multifunctional MOF synthesis and highlights the synthetic and subsequent analytical challenges in obtaining such multifunctional materials.

## RESULTS AND DISCUSSION

**Synthesis and Characterization.** The porphyrin linker 5,10,15,20-tetrakis(4-carboxyphenyl)porphyrin (**$H_2$TCPP**) was prepared according to a literature procedure,[31] while 2,3,7,8,12,13,17,18-octaethyl-5,10,15,20-tetrakis(4-carboxyphenyl)porphyrin (**$H_2Et_8$TCPP**) (Figures S1 and S2) was prepared via saponification of the ester precursors.[32] Both were analyzed with $^1$H NMR and UV−vis spectroscopy (Figures S3 and S6). The **$H_2Et_8$TCPP** and its ester analogue could be crystallized as dication salts in the orthorhombic space-group *Pnma* (see Figures S4, S5 and Table S1 for details of crystal structure solution). PCN-222 was synthesized with **$H_2$TCPP** as the organic linker by following a published procedure.[17] The incorporation of **$H_2Et_8$TCPP** into the MOF framework, i.e., applying **$H_2Et_8$TCPP** as a linker, was achieved via a mixed-linker approach (Figure 2). Different molar ratios

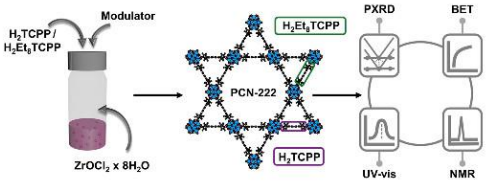


**Figure 2.** Schematic of the approach to synthesize and characterize a series of mixed-linker PCN-222 type MOFs. After MOF synthesis, a combination of analytical techniques [PXRD, $N_2$ sorption analysis (BET), solid-state UV−vis, and $^1$H NMR spectroscopy] was applied to determine the underlying structure and composition.

of **$H_2Et_8$TCPP** and **$H_2$TCPP** were used in the synthesis of PCN-222 where both linkers were added simultaneously (see the experimental and SI S2 for detailed synthesis protocols).

After solvothermal synthesis, the MOF powders were isolated by centrifugation, washed, and characterized by $^1$H NMR spectroscopy to determine the varying molar ratios of **$H_2$TCPP** and **$H_2Et_8$TCPP** (Figures 3b and S6, S7). For $^1$H NMR spectroscopy, the MOFs were digested in a DCl/DMSO-$d_6$ solution (0.1 mL/0.3 mL). The molar ratio of both linkers was calculated by comparison of the phenyl signal integrals of **$H_2$TCPP** (8.55, 8.62, and 8.75 ppm) and **$H_2Et_8$TCPP** (8.38 and 8.64 ppm), respectively (Table S2). Note that the signals in the $^1$H NMR spectrum of **$H_2$TCPP** and **$H_2Et_8$TCPP** were slightly shifted in the spectrum of the dissolved MOF (8.49, 8.55, and 8.69 ppm for **$H_2$TCPP** and 8.35 and 8.61 ppm for **$H_2Et_8$TCPP**) as a result of an acid-based concentration dependent proton shift. For an accurate determination of the **$H_2Et_8$TCPP** content in the MOFs, three


https://doi.org/10.1021/acs.inorgchem.3c03943
Inorg. Chem. 2024, 63, 2122−2130

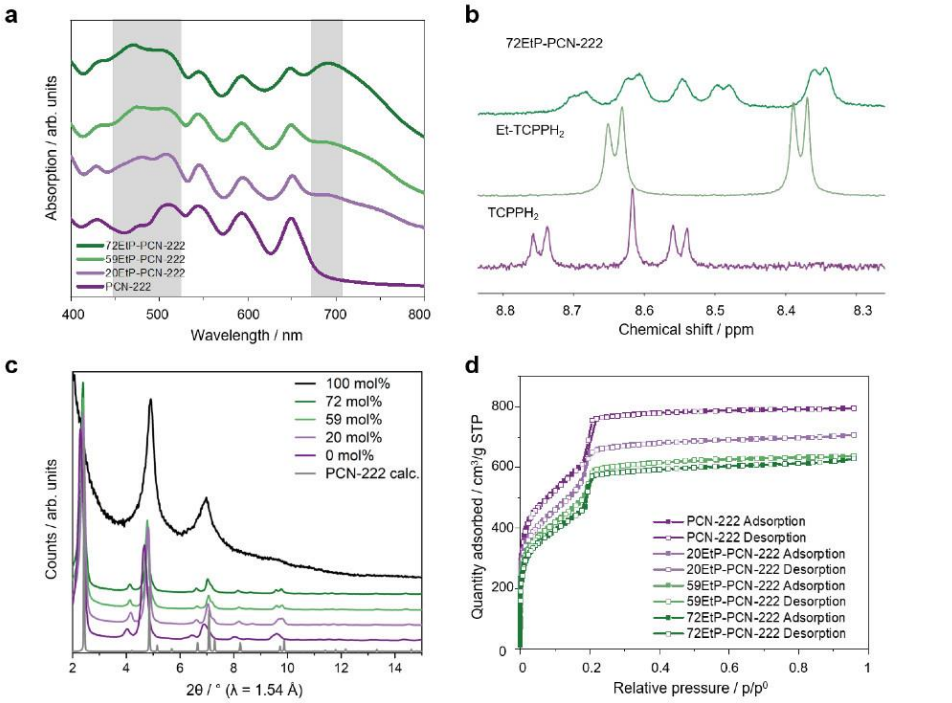


**Figure 3.** (a) Normalized solid-state UV−vis spectra of 72EtP-PCN-222, 59EtP-PCN-222, and 20EtP-PCN-222 were compared to PCN-222. (b) Solution-based $^1$H NMR spectra of digested 72EtP-PCN-222 compared to the linkers **$H_2Et_8TCPP$** and **$H_2TCPP$** in the range of the porphyrin signals (measured in DCl/DMSO-$d_6$). (c) PXRD data of PCN-222 with 0, 20, 59, 72, and 100 mol % **$H_2Et_8TCPP$** compared to the calculated pattern of PCN-222. (d) $N_2$ adsorption isotherms at 77 K were determined for as-synthesized PCN-222, 20EtP-PCN-222, 59EtP-PCN-222, and 72EtP-PCN-222.

different spectra of the same acid-digested MOF were recorded to obtain a weighted average and a standard deviation.

Three **$H_2Et_8TCPP$** modified PCN-222 materials with different **$H_2Et_8TCPP$** content were synthesized: 20EtP-PCN-222 (20 mol % **$H_2Et_8TCPP$**, 80 mol % **$H_2TCPP$** in PCN-222), 59EtP-PCN-222 (59 mol % **$H_2Et_8TCPP$**, 41 mol % **$H_2TCPP$** in PCN-222), and 72EtP-PCN-222 (72 mol % **$H_2Et_8TCPP$**, 28 mol % **$H_2TCPP$** in PCN-222). Importantly, we stress that both 20EtP-PCN-222 and 72EtP-PCN-222 were obtained by weighing in 20 mol % and 80 mol % **$H_2TCPP$** for the mixed-linker synthesis; the difference between both synthetic approaches was a different batch of **$H_2Et_8TCPP$** linker, which differed in size of single crystals, i.e., single crystals compared to a more powdered sample of **$H_2Et_8TCPP$**. In our experiments, we have observed that this has a rather large impact on the solubility of **$H_2Et_8TCPP$**, and overall, in the amount that is incorporated into the MOF. This finding agrees with the general view that even small changes in synthetic parameters can have a large impact on the composition and morphology of the product.[33,34] Thus, with the same amount of linker used for synthesis, the more powdered **$H_2Et_8TCPP$** batch—and therefore the more soluble batch—resulted in 72EtP-PCN-222 while, with the more crystal-like batch, 20EtP-PCN-222 was obtained. A similarly large impact of linker solubility on the synthetic outcomes has previously been reported.

The IR spectra of the four materials did not show significant variations (Figure S11), while changes of the porphyrin's Soret and Q bands were discernible in the solid-state UV−vis spectra (Figures 3a and S12). With increasing amount of **$H_2Et_8TCPP$** in the MOF, the development of **$H_2Et_8TCPP$** bands in the ranges 450−530 nm (Soret & Q bands) and 680−720 nm (Q bands) is observed, confirming the incorporation of **$H_2Et_8TCPP$** into the material network. Additionally, analysis of the different materials with confocal microscopy allowed for the evaluation of their optical properties. The fluorescence of the samples decreases upon nonplanar porphyrin incorporation (Figure S21), which agrees with the reported lower fluorescence properties of **$H_2Et_8TCPP$** compared to **$H_2TCPP$**.[35] It has to be noted that this method allows for only qualitative discussions of the fluorescence. Additionally, no general trend in fluorescence properties depending on the nonplanar porphyrin content was observable.

PXRD of the synthesized materials revealed phase purity and clear Bragg reflections for **$H_2Et_8TCPP$** modified PCN-222 derivatives with up to a stoichiometry of approximately 80 mol % **$H_2Et_8TCPP$**. The PXRD patterns of all materials were similar to that of PCN-222 (Figure S8). PCN-222 itself was reported to crystallize in a hexagonal crystal system (space-


https://doi.org/10.1021/acs.inorgchem.3c03943
Inorg. Chem. 2024, 63, 2122−2130

group *P6/mmm*) with a *csq* topology and the $Zr_6$ oxo cluster with an eightfold connectivity.[16,36] Based on the PXRD pattern, where no changes in peak number and peak intensities were observed, we conclude that the mixed-linker solid-solution series of EtP-PCN-222 forms isostructural single-phase solid solutions. Raising the **$H_2Et_8$TCPP** content in the MOF (above 72 mol %) resulted in a significant increase of the peak width of Bragg reflections, which we ascribe to a decreasing size of diffraction domains (Figure S8). For instance, the PXRD pattern of synthesized PCN-222 with 100 mol % **$H_2Et_8$TCPP** still features the main Bragg reflections of PCN-222; however, with significantly increased full width at half-maximum. In turn, this material was not used for further studies. Therefore, based on PXRD analysis, the isostructural series of PCN-222, 20EtP-PCN-222, 59EtP-PCN-222, and 72EtP-PCN-222 is suitable for studying properties as a function of compositional changes.

SEM images of the powdered samples are in good agreement with published shapes and morphologies of PCN-222 from the literature.[17,37,38] The images show that the rod shape and morphology of the crystals were maintained upon porphyrin modification—excluding a change in topology (Figures S17−S20). Simultaneously, no particle agglomeration of the rods—which show a flat surface—was observable. The size of the crystals was of the same order of magnitude independent of the degree of functionalization.

After establishing the composition and structure of the mixed-linker series, we would like to note that other approaches were demonstrated in the literature to incorporate (linker) molecules into MOFs postsynthetically, such as solvent-assisted ligand incorporation (SALI) or solvent-assisted linker exchange (SALE).[39−41] The latter could be applied in our case to further increase the content of **$H_2Et_8$TCPP** in the synthesized MOFs since the content of **$H_2Et_8$TCPP** in PCN-222 accessible via the mixed-linker approach presented here is limited to a certain amount (here up to 72%). The reaction conditions for SALI and SALE are rather similar, soaking the synthesized MOF in a linker solution at elevated temperatures. Therefore, the coordination of the linker cannot be controlled, i.e., linker exchange and coordination to the unsaturated Zr-node into the pores are possible−comparable to the MOF synthesis itself. Thus, due to the entailing characterization challenges (and likely no benefits toward understanding resulting material properties), this approach was not further followed.

$N_2$ sorption properties of PCN-222 and its **$H_2Et_8$TCPP** modified analogues were investigated, encompassing the evaluation of $N_2$ adsorption quantities and Brunauer−Emmett−Teller (BET) surface areas. The isotherms observed in sorption analysis suggest the presence of both micro- and mesopores, which is comparable to $N_2$ sorption properties reported for PCN-222 materials (type IV isotherms).[16,37,38] With increasing amount of **$H_2Et_8$TCPP**, a decrease in the adsorbed $N_2$ quantity and BET surface area was observed (Figure S9). For instance, for PCN-222 we obtained a BET surface area of 2079 ± 6.9 $m^2\ g^{-1}$, while the surface area decreased to 1744 ± 15 $m^2\ g^{-1}$ for 20EtP-PCN-222, 1594 ± 12 $m^2\ g^{-1}$ for 59EtP-PCN-222 and 1512 ± 10 $m^2\ g^{-1}$ for 72EtP-PCN-222, i.e., a monotonic decrease of BET surface area with increasing amount of **$H_2Et_8$TCPP** (Figure S10). This is ascribed to reduced pore space due to the incorporation of the bulkier porphyrin linker with ethyl groups and is in a similar range to porphyrin metalation.[16,37,42,43] We note, however, that the remaining porphyrin linkers in the pore space after washing cannot be fully excluded. Using the related Fe(III)Cl complex of **$H_2Et_8$TCPP** in PCN-224 (which crystallizes in the Im3*m* space group with a *she* topology) showed that the decrease of surface area upon ethyl porphyrin incorporation is smaller;[32] however, this phenomenon is also observed upon metal incorporation.[37,44]

The thermal stability of the materials was analyzed by TGA, where all four materials showed similar thermal stabilities up to approximately 405−415 °C (Figures S13−S16). These decomposition temperatures are comparable to previously published temperatures of PCN-222.[16,44,45] Furthermore, the amount of point defects, i.e., linker defects and/or missing node defects, was determined based on the TGA traces since Zr-MOFs are prone to defect formation.[17−19,44,46,47] In general, the amount of **$H_2$TCPP** linkers derived from the ideal sum formula is two. Based on our analysis which follows an established protocol from the literature,[48] the real linker quantity was calculated to 2.53 for PCN-222, 2.08 for 20EtP-PCN-222, 2.20 for 59EtP-PCN-222, and 2.27 for 72EtP-PCN-222, which is in the typical range for PCN-222 materials (Table S3).[44,47]

In summary, the presented characterizations show that a combination of different analytical techniques is necessary to evaluate the incorporation of modified linkers into the desired MOF. While PXRD gives insights into the average MOF structure, phase purity, and crystallinity, the degree of modification can be followed by $^1$H NMR and solid-state UV−vis spectroscopy, supported by $N_2$ sorption measurements and TGA.

**Material Properties.** In addition to the detailed characterization of the materials, their thermal, chemical, and catalytical properties, and metalation capability (compared to PCN-222) were studied.

Given the conformational change from planar to nonplanar linkers (Figure 1), the framework flexibility is anticipated to alter across the series of chemically modified PCN-222 derivatives. To assess this flexibility, we investigated the thermal expansion as a proxy[49,50] through VTPXRD experiments in the range of 150 ≤ T ≤ 400 K. Accordingly, Pawley profile fits were performed using *P6/mmm* symmetry for extracting PCN-222's lattice parameters (*a*,*c*) and volume (*V*) as a function of increasing **$H_2Et_8$TCPP** content (Tables S4−S7 and Figures S23−S26). We observe changes in the hexagonal lattice parameters when varying the **$H_2$TCPP/$H_2Et_8$TCPP** composition (Figure S31). Looking at the VTPXRD data along the PCN-222 series (Figures S27−S30), no clear trends were visible in the individual data sets (Figures S32−S34), making a reliable calculation of thermal expansion coefficients impossible. From a qualitative inspection, we observe only a stronger sensitivity of the defect-poor 20EtP-PCN-222 (Table S3), showing the largest volume reduction (Figure S34) related to the decrease of *a* (Figure S33a). For PCN-222 and 72EtP-PCN-222, more linkers are integrated which probably limits the framework flexibility—in accordance with the hypothesis of a decreased thermal responsiveness with increasing guest content.[51] This is supported by a study on UiO-66(Hf) series where negative thermal expansion is reduced for higher defect concentration in the framework.[52] This is rather counter-intuitive since the framework flexibility and hence the thermomechanical response is expected to be greater in a defect-rich framework, i.e., in a less rigid network. We would like to note here that the interplay between the modulator in


https://doi.org/10.1021/acs.inorgchem.3c03943
Inorg. Chem. 2024, 63, 2122−2130

the pores, defects, and the integrated nonplanar **$H_2Et_8$TCPP** represents a more complex case that remains only rarely described in the literature. Furthermore, we cannot exclude surface area/particle size effects stemming from different particle sizes of the samples (Figures S17−S20), although we expect this to be a minor contribution. Due to this complexity, extensive experimental work to selectively remove the modulator fully was not performed due to potential adverse effects on linker ratios, crystallinity, etc.

In addition to the thermal stability and their thermal response, the chemical stability of PCN-222 and its **$H_2Et_8$TCPP** functionalized analogues were evaluated with 59EtP-PCN-222 as a representative example for the series with >50 mol % modified linker. The stability of **$H_2$TCPP**-based Zr-MOFs has previously been confirmed in aqueous media within a broad pH range (0−11).[53] Testing the stability of the materials synthesized here in basic solutions was necessary to avoid protonation of the porphyrin core of **$H_2Et_8$TCPP** for potential applications, such as metal-free catalysis. Both MOFs were soaked in different aqueous sodium hydroxide solutions at room temperature for 24 h with specific pH values: 8.0, 8.5, 10.3, 11.0, and 12.3. In the NaOH/$H_2O$ solution with pH = 12.3, both MOF samples rapidly decomposed. For all other solutions, no change compared with pure $H_2O$ was apparent. After washing the MOF with water and subsequent drying, the powder was analyzed by PXRD. The patterns of each sample showed the typical Bragg reflections for PCN-222 and crystallinity was maintained up to pH = 11 for both base-treated PCN-222 and 59EtP-PCN-222 (Figures S35 and S36). The increased background for the latter soaked in pH = 11 solution results from sample preparation and the decreased amount of solid material (a certain loss of very fine powdered MOF upon washing and centrifugation needs to be taken into account).

One promising feature of porphyrin-based MOFs is the capability of introducing several transition metals in the porphyrin core, which allows for various applications, especially in catalysis. Therefore, the metalation ability of **$H_2Et_8$TCPP** functionalized PCN-222 via a postsynthetic approach was explored. Rhodium was selected since its integration is in general more challenging due to the metal's size compared to the space in the porphyrin core. The saddle conformation of **$H_2Et_8$TCPP** is beneficial since the four N atoms are already located out of plane, facilitating metal incorporation (Figure 1). In a typical reaction setup, the MOF was suspended in DMF with the addition of the metal precursor ($RhCl_3 \bullet H_2O$), and different setups were tested such as heating to reflux versus heating in an oven without stirring (see SI Table S8 for details). After being washed and dried, the MOF was analyzed by PXRD and ICP-MS to determine the metal content. The results were compared with unmodified PCN-222. Confirmed by the PXRD pattern, the structure and crystallinity of EtP-PCN-222 were retained upon Rh incorporation with both methods, while the crystallinity of PCN-222 decreased after Rh metalation under reflux conditions (indicated by the decreased signal-to-noise ratio and broadening of Bragg's reflections, Figures S37 and S38). ICP-MS analysis revealed comparable Zr:Rh ratios for both MOFs with significantly higher ratios (i.e., lower absolute metalation) for the metalation method using an oven instead of refluxing (Table S8). For complete metalation (100% of porphyrins in the MOF metalated with Rh), a Zr:Rh ratio of 3 is expected (note that this is calculated from the ideal sum formula and does not take defects into account). Thus, less than approximately 30% of the porphyrins are metalated in both MOFs (Table S7). The results show that the metalation capability of PCN-222 is not changed upon **$H_2Et_8$TCPP** modification and allows for the application of EtP-PCN-222, e.g., in metal catalysis. A potential explanation includes that while the nonplanarity of **$H_2Et_8$TCPP** yields preferential metalation kinetics at the porphyrin core itself, the protonation of **$H_2Et_8$TCPP** to $[H_4Et_8TCPP]^{2+}$ is favored in the nonplanar case under the applied conditions. Since deprotonation of **$H_2Et_8$TCPP** is required for metalation, the latter is limited for the nonplanar porphyrin, thus leading to comparable total metalation in both cases.

## ■ CONCLUSIONS

In summary, we report the preparation of a series of mixed-linker solid-solution PCN-222 analogues with $\beta$-ethyl-functionalized porphyrin linkers via a mixed-linker approach, showing synthetic control over ethyl-porphyrin content over a large range of 0−72 mol %. The successful incorporation of this nonplanar linker into the framework was confirmed by a combination of analytical techniques, such as $^1$H NMR, solid-state UV−vis and IR spectroscopy, PXRD, SEM, $N_2$ sorption measurements, and TGA. We find that the material properties, e.g., the BET surface area or the linker's fluorescence, change as the amount of modified linker increases. Thus, our work presents an appealing strategy for the design of, in principle, multifunctional systems with controllable modified material properties and their detailed characterization. Additionally, this PCN-222 case study highlights the need to thoroughly characterize such mixed-component materials with several complementary analytical techniques—currently often a caveat in the MOF literature. It further showcases how rigidifying a flexible/nonplanar molecule (here **$H_2Et_8$TCPP**) in a MOF backbone gives rise to altered and complex intertwined material properties.

In theory, a straightforward characterization was expected since only one parameter was altered in the synthesis, i.e., the linker modification. However, our results highlight the complexity arising from subtle linker variations, such as different crystallinity, defect concentration changes, and altered thermal and optical properties. Likewise, the showcased increasing complexity upon subtle changes reinforces the importance of fundamental studies with model systems and their precise/detailed characterization. While the complexity of porphyrinic MOF systems—starting with their synthetic challenges—is already reported in the literature,[18,19,23] further investigations are required to understand these MOF structures. This is particularly desirable, as their showcased multifunctionality makes them interesting candidates to mimic certain enzyme properties, i.e., the arrangement of different functionalities in a confined environment. This would allow for tailored molecular-level structure−property relationship control and will be the subject of future studies.

## ■ EXPERIMENTAL SECTION

**Material Synthesis.** The linker synthesis of **$H_2$TCPP** was adapted from a literature known procedure.[31] First, 5,10,15,20-tetrakis(4-methoxycarbonylphenyl)porphyrin (TPPCOOMe) was synthesized by adding pyrrole (3.09 mL, 44.9 mmol, 1.1 equiv) and methyl-*p*-formylbenzoate (6.93 g, 42.3 mmol, 1.0 equiv) to refluxing propionic acid (100 mL). After refluxing under continuous stirring for 22 h, the precipitate was filtrated and washed with methanol (MeOH, 30 mL),


https://doi.org/10.1021/acs.inorgchem.3c03943
Inorg. Chem. 2024, 63, 2122−2130

ethyl acetate (EtOAc, 10 mL), and tetrahydrofuran (THF, 10 mL) to yield the purple-colored product (5.45 g, 6.44 mmol, 15% yield) (see SI S2 for analytical data). Next, TPPCOOMe (1.00 g, 1.19 mmol, 1.0 equiv) was dissolved in a 1:1 mixture of THF/MeOH (70 mL) and a solution of KOH (3.5 g, 62.4 mmol, 52 equiv) in $H_2O$ (30 mL) was added. The resulting mixture was refluxed for 15 h. After removal of the organic solvents in vacuo, the solid was redissolved in $H_2O$ (150 mL) at 90 °C for 15 min. The solution was filtered and acidified with 1 M HCl (100 mL). The resulting green precipitate was filtered and dried to obtain the product (864 mg, 1.09 mmol, 92% yield) (see SI S2 for analytics). For the synthesis of **$H_2Et_8$TCPP**, 3,4-diethyl pyrrole was synthesized following a reported procedure[54] and the linker synthesis was adapted according to a literature known procedure.[32] A solution of methyl 4-formyl benzoate (3.28 g, 20 mmol) and 3,4-diethypyrrole in dry $CH_2Cl_2$ (1 L) was purged with argon for 20 min. 0.30 mL of $BF_3$•$OEt_2$ was added to the above solution, and the reaction mixture was stirred at room temperature overnight. After that, 3,4-dicholoro-5,6-dicyano-1,4-benzoquinone (DDQ, 2 g, 8.8 mmol) was added and the reaction mixture was stirred at room temperature for 15 min. The solvent was evaporated, and the crude compound was subjected to silica gel column chromatography. The title compound was eluted using 1% EtOAc in $CH_2Cl_2$ (30% yield) (see SI for the analytical data of Et-TPPCOOMe). Et-TPPCOOMe (0.490 g, 0.457 mmol) was dissolved in 30 mL of THF/MeOH (1:1 v/v) mixture. To this, 0.513 mg of KOH in 3 mL of $H_2O$ was added, and the resulting mixture was heated to reflux overnight. The reaction mixture was cooled to room temperature; the solvent was evaporated under reduced pressure, and the crude compound was redissolved in 3−4 mL of $H_2O$. 20% HCl was added dropwise to the aqueous solution of porphyrin, and the green precipitate was filtered and dried in vacuo to obtain the product (85% yield). The synthesis of PCN-222 was adapted from a literature known procedure.[17,45] In a 20 mL screw cap vial, **$H_2$TCPP** (and **$H_2Et_8$TCPP** for the solid solutions, see quantities below) and $ZrOCl_2$•$8H_2O$ (117.5 mg, 0.35 mmol, 4.6 equiv) were dissolved in *N*,*N*-diethylformamide (DEF, 15 mL). After the addition of 4-*tert*-butylbenzoic acid (13.5 g, 37.9 mmol, 473 equiv), the mixture was ultrasonicated for 10 min. Seed crystals were added to increase the yield. The mixture was heated at 120 °C for 12 h in an oven. The solid was separated by centrifugation and soaked in *N*,*N*-dimethylformamide (DMF, 3 × 35 mL) and acetone (3 × 35 mL), and dried in vacuo to yield the product. For dehydration (=activation), the product was heated at 120 °C in vacuo ($10^{-3}$ mbar) overnight. Analytical data matched literature reports of PCN-222. For the synthesis of PCN-222 solid solutions (EtP-PCN-222-20), the general synthetic procedure for EtP-PCN-222 was followed; however, the reaction was upscaled (×2) to increase the amount of product and ensure homogeneity in the final **$H_2Et_8$TCPP** content. To achieve 20 mol % of **$H_2Et_8$TCPP** in PCN-222 100 mg of **$H_2$TCPP** (0.127 mmol) and 32.0 mg of **$H_2Et_8$TCPP** (0.032 mmol) were used. Note that the batch of **$H_2Et_8$TCPP** used for this synthesis showed a crystalline nature comparable to **$H_2$TCPP**, which seems to be crucial for the solubility of the starting materials and thus the final amount of **$H_2Et_8$TCPP** in PCN-222. In the synthesis of EtP-PCN-222-59 (59 mol %) of **$H_2Et_8$TCPP** in PCN-222 56.3 mg of **$H_2$TCPP** (0.071 mmol) and 8.1 mg of **$H_2Et_8$TCPP** (0.008 mmol) were used. In the synthesis of EtP-PCN-222-72 (72 mol %) of **$H_2Et_8$TCPP** in PCN-222 50.8 mg of **$H_2$TCPP** (0.064 mmol) and 15.8 mg of **$H_2Et_8$TCPP** (0.016 mmol) were used.

**Single Crystal X-ray Diffraction.** SCXRD data were collected on a Bruker Kappa Apex Duo instrument using $CuK_\alpha$ ($\lambda$ = 1.54178 Å) and $MoK_\alpha$ ($\lambda$ = 0.71073 Å) radiation. Suitable crystals were selected, mounted on a MiTeGen microsample loop, and cooled to 100(2) K using an Oxford Instruments Cryostream (Bruker ECO) and Cobra (Bruker Kappa Apex Duo) low-temperature device for cooling control. Bruker APEX[55−57] software package was used for data collection and reduction, and space-group determination. Structures were solved using intrinsic phasing with the SHELXT structure solution program and refined with the SHELXL refinement package using least-squares minimization with Olex2.[58,59] Crystal data and details of data collection and refinement are given in the SI (Table S1). Crystals of the dication salts **$H_2Et_8$TCPP** and its ester analogue were grown following the protocol developed by Hope, by dissolving the compounds in $CHCl_3$-MeOH/$H_2SO_4$ or $CHCl_3$-DMSO and allowing for slow evaporation over time.[60]

**Solid-State UV−Vis.** All spectra were recorded on a Shimadzu UV-3600 Plus UV−vis-NIR spectrophotometer. Powder samples were fixed between two quartz glass slides for measurement. For the measurement, the following parameters were used: medium scan speed, slit width (20) with external (3Detector) unit, enabled stair correction, baseline correction ($BaSO_4$ background), *S*/*R* exchange normal, and slit and detector lock normal.

**Adsorption Measurements.** Adsorption measurements with $N_2$ (99.999 vol %) at 77 K were carried out on a 3Flex Physisorption from Micromeritics Instrument Corp., which uses a volumetric method to determine the amount adsorbed under an equilibrated gas pressure. Adsorption data were processed using the 3Flex Software Version 5.01 by Micromeritics Instrument Corp. and plotted in OriginPro 2019b by OriginLab Corp. Samples were transferred into preweighed sample tubes and capped with Micromeritics CheckSeals. Samples were subsequently activated at 393 K for 12 h under a dynamic vacuum ($10^{-3}$ mbar) using a SmartVac Prep by Micromeritics Instrument Corp. to ensure the absence of unwanted adsorbates and identical premeasurement states of all samples. In particular, these unusually low activation temperature and time were chosen for all samples to ensure structural integrity of the immobilized molecular complexes, which are known to sublime and decompose comparatively readily. The mass of the adsorbents was then recorded (25−40 mg). The free space of the sample tube was determined prior to measuring each adsorption isotherm using He (99.999 vol %). The apparent surface area was derived using the BET model, given as the 'BET area' and based on $N_2$ isotherms measured at 77 K. To determine this value for microporous materials, care was taken to adhere to the Rouquerol criteria.[61,62] The pore size distribution (PSD) was derived by fitting $N_2$ isotherms (at 77 K) with sets of theoretical isotherms (kernel) derived from two-dimensional nonlocal-density functional theory-based methods for specific pore sizes and geometry. As an approximation, cylindrical pores on an oxide surface were assumed for all materials to allow for comparability within this series. Fitting was done using the respective kernel available via the 3Flex Software Version 5.01 by Micromeritics Instrument Corp.[63]

**Thermal Analysis.** TGA was performed to compare the thermal stabilities of the samples. All measurements were carried out using a TGA/STA 409 PC apparatus from Mettler-Toledo Intl. Inc. under flowing synthetic air from room temperature to 1000 °C. The onset of significant decomposition temperature was determined by extrapolation of the linear range of the relative mass loss observed with a continuous heating rate of 5 K $min^{-1}$. Linker defects of the samples were calculated from TGA curves according to a literature known method.[47]

**Variable-Temperature Powder X-ray Diffraction.** VTPXRD measurements were performed in Debye−Scherrer geometry on a STOE Stadi P diffractometer (STOE & Cie, Germany) equipped with a DECTRIS MYTHEN2R 1K (Dectris, Switzerland) strip detector using ge-monochromated Mo K$\alpha$ radiation ($\lambda$ = 0.70926 Å). The samples were prepared by fine grinding and sealing in borosilicate glass capillaries with a diameter of 0.8 mm (Hilgenberg, Germany). VTPXRD data were collected between 150 and 400 K using a Cryostream 800 cooler (OXFORD Cryosystems, U.K.) for temperature control with 20 K step size (and 10 K steps from 390 to 400 K). In order to analyze VTPXRD data, we carried out Pawley profile fit analysis using TOPAS v6 software.[64,65] Details of the Pawley refinement are given in the SI.

**Inductively Coupled Mass Spectrometry.** To obtain an accurate quantification of the Zr and Rh amount immobilized in MOF samples, ICP-MS for Zr and Rh, respectively, was conducted on a PerkinElmer NexIon 350D ICP-MS instrument. The respective samples were immersed in concentrated 7.5 mL of nitric acid and 2.5 mL of $H_2O_2$ 30% (v/v) and treated in the microwave at 150 °C for 10 min. Subsequently, the microwave-digested samples were diluted 1/


https://doi.org/10.1021/acs.inorgchem.3c03943
Inorg. Chem. 2024, 63, 2122−2130

100 with Millipore Milli-Q water. Each solvent was extra pure and checked for possible analyte contaminations before measurement. $^{103}$Rh and $^{94}$Zr were used as target masses for the analytes and $^{115}$In as an internal standard. Analyte quantification was carried out in standard mode with a correction equation to avoid polyatomic interferences. The detection limit for Zr was 0.13 and 0.29 $\mu g\ L^{-1}$ for Rh. The external calibration was performed in the range of 0−100 $\mu g\ L^{-1}$. Each sample was measured with five measurement replicates, a dwell time per 50 ms, and an integration time of 750 ms. The Zr and Rh concentrations were blank corrected via measurement of the blank samples.

## ■ ASSOCIATED CONTENT

### Supporting Information

The Supporting Information is available free of charge at https://pubs.acs.org/doi/10.1021/acs.inorgchem.3c03943.

Further experimental and analytical details, structures of the organic linkers, crystallographic information and refinement notes of the linkers, NMR spectra, IR spectra, PXRD data, $N_2$ adsorption isotherms, UV−vis spectra, TGA curves, SEM images, confocal microscopy, VTPXRD data and results of Pawley profile fit analysis, pH stability tests, and catalytic tests (PDF)

### Accession Codes

CCDC 2302383−2302384 contains the supplementary crystallographic data for this paper. These data can be obtained free of charge via www.ccdc.cam.ac.uk/data_request/cif, or by emailing data_request@ccdc.cam.ac.uk, or by contacting The Cambridge Crystallographic Data Centre, 12 Union Road, Cambridge CB2 1EZ, U.K.; fax: +44 1223 336033.

## ■ AUTHOR INFORMATION


### Corresponding Authors

**Gregor Kieslich** − *TUM School of Natural Sciences, Technical University of Munich, 85748 Garching, Germany;* orcid.org/0000-0003-2038-186X; Email: gregor.kieslich@tum.de

**Mathias O. Senge** − *School of Chemistry, Chair of Organic Chemistry, Trinity Biomedical Sciences Institute, 152-160 Pearse Street, Trinity College Dublin, The University of Dublin, Dublin D02R590, Ireland; Institute for Advanced Study (TUM-IAS), Focus Group − Molecular and Interfacial Engineering of Organic Nanosystems, Technical University of Munich, 85748 Garching, Germany;* orcid.org/0000-0002-7467-1654; Email: sengem@tcd.ie

### Authors

**Karina Hemmer** − *TUM School of Natural Sciences, Technical University of Munich, 85748 Garching, Germany*

**Silva M. Kronawitter** − *TUM School of Natural Sciences, Technical University of Munich, 85748 Garching, Germany;* orcid.org/0000-0001-7421-6152

**Nitika Grover** − *School of Chemistry, Chair of Organic Chemistry, Trinity Biomedical Sciences Institute, 152-160 Pearse Street, Trinity College Dublin, The University of Dublin, Dublin D02R590, Ireland*

**Brendan Twamley** − *School of Chemistry, Trinity College Dublin, The University of Dublin, Dublin 2, Ireland*

**Mirza Cokoja** − *TUM School of Natural Sciences, Technical University of Munich, 85748 Garching, Germany;* orcid.org/0000-0003-3144-4678

**Roland A. Fischer** − *TUM School of Natural Sciences, Technical University of Munich, 85748 Garching, Germany;* orcid.org/0000-0002-7532-5286

Complete contact information is available at: https://pubs.acs.org/10.1021/acs.inorgchem.3c03943

### Author Contributions

$^{\perp}$K.H. and S.M.K. equally contributed to this work.


### Notes

The authors declare no competing financial interest.

## ■ ACKNOWLEDGMENTS

K.H. would like to thank the Chemical Industry Fonds (FCI) for a PhD fellowship. S.M.K. and G.K. acknowledge support from the DFG through a research grant (450070835) and Heisenberg program (524525093). Thanks to Sarah Dummert for SEM and confocal microscopy images, as well as Martin Elsner and Christine Benning for ICP-MS measurements. This work was prepared with the support of the Technical University of Munich—Institute for Advanced Study through a Hans Fischer Senior Fellowship (M.O.S.) and Science Foundation Ireland (award 21/FFP-A/9469). The authors are thankful for the help from the Central Analytics Facility of the TUM Catalysis Research Center, especially from Jürgen Kudermann.

## ■ REFERENCES


(1) Park, J.; Hong, S. Cooperative bimetallic catalysis in asymmetric transformations. *Chem. Soc. Rev.* **2012**, *41* (21), 6931−6943.

(2) Felpin, F.-X.; Fouquet, E. Heterogeneous multifunctional catalysts for tandem processes: an approach toward sustainability. *ChemSusChem* **2008**, *1* (8−9), 718−724.

(3) Jagadeesan, D. Multifunctional nanocatalysts for tandem reactions: A leap toward sustainability. *Appl. Catal., A* **2016**, *511*, 59−77.

(4) Zhou, H.-C. J.; Kitagawa, S. Metal-organic frameworks (MOFs). *Chem. Soc. Rev.* **2014**, *43* (16), 5415−5418.

(5) Freund, R.; Zaremba, O.; Arnauts, G.; Ameloot, R.; Skorupskii, G.; Dincă, M.; Bavykina, A.; Gascon, J.; Ejsmont, A.; Goscianska, J.; Kalmutzki, M.; Lächelt, U.; Ploetz, E.; Diercks, C. S.; Wuttke, S. The Current Status of MOF and COF Applications. *Angew. Chem., Int. Ed.* **2021**, *60* (45), 23975−24001.

(6) Cohen, S. M.; Zhang, Z.; Boissonnault, J. A. Toward "metalloMOFzymes": Metal-Organic Frameworks with Single-Site Metal Catalysts for Small-Molecule Transformations. *Inorg. Chem.* **2016**, *55* (15), 7281−7290.

(7) Stanley, P. M.; Haimerl, J.; Shustova, N. B.; Fischer, R. A.; Warnan, J. Merging molecular catalysts and metal-organic frameworks for photocatalytic fuel production. *Nat. Chem.* **2022**, *14* (12), 1342−1356.

(8) Xu, C.; Fang, R.; Luque, R.; Chen, L.; Li, Y. Functional metal−organic frameworks for catalytic applications. *Coord. Chem. Rev.* **2011**, *2019* (388), 268−292.

(9) Bavykina, A.; Kolobov, N.; Khan, I. S.; Bau, J. A.; Ramirez, A.; Gascon, J. Metal-Organic Frameworks in Heterogeneous Catalysis: Recent Progress, New Trends, and Future Perspectives. *Chem. Rev.* **2020**, *120* (16), 8468−8535.

(10) Jeoung, S.; Kim, S.; Kim, M.; Moon, H. R. Pore engineering of metal-organic frameworks with coordinating functionalities. *Coord. Chem. Rev.* **2020**, *420*, No. 213377.

(11) Chughtai, A. H.; Ahmad, N.; Younus, H. A.; Laypkov, A.; Verpoort, F. Metal-organic frameworks: versatile heterogeneous catalysts for efficient catalytic organic transformations. *Chem. Soc. Rev.* **2015**, *44* (19), 6804−6849.

(12) Yang, Q.; Xu, Q.; Jiang, H.-L. Metal-organic frameworks meet metal nanoparticles: synergistic effect for enhanced catalysis. *Chem. Soc. Rev.* **2017**, *46* (15), 4774−4808.
(13) Nakagaki, S.; Ferreira, G. K. B.; Ucoski, G. M.; de Freitas, Dias; Castro, K. A. Chemical reactions catalyzed by metalloporphyrin-based metal-organic frameworks. *Molecules* **2013**, *18* (6), 7279−7308.
(14) Carrasco, S.; Sanz-Marco, A.; Martín-Matute, B. Fast and robust synthesis of metalated PCN-222 and their catalytic performance in cycloaddition reactions with CO2. *Organometallics* **2019**, *38* (18), 3429−3435.
(15) Hemmer, K.; Cokoja, M.; Fischer, R. A. Exploitation of intrinsic confinement effects of MOFs in catalysis. *ChemCatChem.* **2021**, *13* (7), 1683−1691.
(16) Feng, D.; Gu, Z.-Y.; Li, J.-R.; Jiang, H.-L.; Wei, Z.; Zhou, H.-C. Zirconium-metalloporphyrin PCN-222: mesoporous metal-organic frameworks with ultrahigh stability as biomimetic catalysts. *Angew. Chem., Int. Ed.* **2012**, *51* (41), 10307−10310.
(17) Gong, X.; Shu, Y.; Jiang, Z.; Lu, L.; Xu, X.; Wang, C.; Deng, H. Metal-organic frameworks for the exploitation of distance between active sites in efficient photocatalysis. *Angew. Chem., Int. Ed.* **2020**, *59* (13), 5326−5331.
(18) Koschnick, C.; Stäglich, R.; Scholz, T.; Terban, M. W.; Mankowski, A. V.; Savasci, G.; Binder, F.; Schökel, A.; Etter, M.; Nuss, J.; Siegel, R.; Germann, L. S.; Ochsenfeld, C.; Dinnebier, R. E.; Senker, J.; Lotsch, B. V. Understanding disorder and linker deficiency in porphyrinic zirconium-based metal-organic frameworks by resolving the $Zr_8O_6$ cluster conundrum in PCN-221. *Nat. Commun.* **2021**, *12* (1), 3099.
(19) Shaikh, S. M.; Usov, P. M.; Zhu, J.; Cai, M.; Alatis, J.; Morris, A. J. Synthesis and defect characterization of phase-pure Zr-MOFs based on meso-tetracarboxyphenylporphyrin. *Inorg. Chem.* **2019**, *58* (8), 5145−5153.
(20) Gong, X.; Noh, H.; Gianneschi, N. C.; Farha, O. K. Interrogating kinetic versus thermodynamic topologies of metal-organic frameworks via combined transmission electron microscopy and X-ray diffraction analysis. *J. Am. Chem. Soc.* **2019**, *141* (15), 6146−6151.
(21) Hong, S. W.; Paik, J. W.; Seo, D.; Oh, J.-M.; Jeong, Y. K.; Park, J. K. Substrate templated synthesis of single-phase and uniform Zr-porphyrin-based metal−organic frameworks. *Inorg. Chem. Front.* **2020**, *7* (1), 221−231.
(22) Koschnick, C.; Terban, M. W.; Frison, R.; Etter, M.; Böhm, F. A.; Proserpio, D. M.; Krause, S.; Dinnebier, R. E.; Canossa, S.; Lotsch, B. V. Unlocking new topologies in Zr-based metal-organic frameworks by combining linker flexibility and building block disorder. *J. Am. Chem. Soc.* **2023**, *145* (18), 10051−10060.
(23) Boström, H. L. B.; Emmerling, S.; Heck, F.; Koschnick, C.; Jones, A. J.; Cliffe, M. J.; Al Natour, R.; Bonneau, M.; Guillerm, V.; Shekhah, O.; Eddaoudi, M.; Lopez-Cabrelles, J.; Furukawa, S.; Romero-Angel, M.; Martí-Gastaldo, C.; Yan, M.; Morris, A. J.; Romero-Muñiz, I.; Xiong, Y.; Platero-Prats, A. E.; Roth, J.; Queen, W. L.; Mertin, K. S.; Schier, D. E.; Champness, N. R.; Yeung, H. H.-M.; Lotsch, B. V. How reproducible is the synthesis of Zr-porphyrin metal-organic frameworks? An interlaboratory study. *Adv. Mater.* **2023**, No. e2304832.
(24) Kleist, W.; Maciejewski, M.; Baiker, A. MOF-5 based mixed-linker metal−organic frameworks: Synthesis, thermal stability and catalytic application. *Thermochim. Acta* **2010**, *499* (1−2), 71−78.
(25) Qin, J.-S.; Yuan, S.; Wang, Q.; Alsalme, A.; Zhou, H.-C. Mixed-linker strategy for the construction of multifunctional metal−organic frameworks. *J. Mater. Chem. A* **2017**, *5* (9), 4280−4291.
(26) Kalisch, W. W.; Senge, M. O. Synthesis and structural characterization of nonplanar tetraphenylporphyrins with graded degree of $\beta$-ethyl substitution. *Tetrahedron Lett.* **1996**, *37* (8), 1183.
(27) Kalisch, W. W.; Senge, M. O. Synthesis and structural characterization of nonplanar tetraphenylporphyrins and their metal complexes with graded degrees of $\beta$-ethyl substitution. *Inorg. Chem.* **1997**, *36* (26), 6103.
(28) Kielmann, M.; Senge, M. O. Molecular engineering of free-base porphyrins as ligands—The N−H···X binding motif in tetrapyrroles. *Angew. Chem., Int. Ed.* **2019**, *58* (2), 418.
(29) Roucan, M.; Kielmann, M.; Connon, S. J.; Bernhard, S. S. R.; Senge, M. O. Conformational control of nonplanar free base porphyrins: towards bifunctional catalysts of tunable basicity. *Chem. Commun.* **2018**, *54* (1), 26−29.
(30) Kingsbury, C. J.; Senge, M. O. The shape of porphyrins. *Coord. Chem. Rev.* **2021**, *431* (15), No. 213760.
(31) Datta-Gupta, N.; Bardos, T. J. Synthetic porphyrins. I: Synthesis and spectra of some para-substituted meso - Tetraphenylporphines. *J. Heterocycl. Chem.* **1966**, *3* (4), 495−502.
(32) Huang, N.; Yuan, S.; Drake, H.; Yang, X.; Pang, J.; Qin, J.; Li, J.; Zhang, Y.; Wang, Q.; Jiang, D.; Zhou, H.-C. Systematic engineering of single substitution in zirconium metal-organic frameworks toward high-performance catalysis. *J. Am. Chem. Soc.* **2017**, *139* (51), 18590−18597.
(33) Huelsenbeck, L.; Luo, H.; Verma, P.; Dane, J.; Ho, R.; Beyer, E.; Hall, H.; Geise, G. M.; Giri, G. Generalized Approach for Rapid Aqueous MOF Synthesis by Controlling Solution pH. *Cryst. Growth Des.* **2020**, *20* (10), 6787−6795.
(34) Abdelkareem, M. A.; Abbas, Q.; Mouselly, M.; Alawadhi, H.; Olabi, A. G. High-performance effective metal−organic frameworks for electrochemical applications. *J. Sci. Adv. Mater. Dev.* **2022**, *7* (3), No. 100465.
(35) Röder, B.; Büchner, M.; Rückmann, I.; Senge, M. O. Correlation of photophysical parameters with macrocycle distortion in porphyrins with graded degree of saddle distortion. *Photochem. Photobiol. Sci.* **2010**, *9*, 1152.
(36) Morris, W.; Volosskiy, B.; Demir, S.; Gándara, F.; McGrier, P. L.; Furukawa, H.; Cascio, D.; Stoddart, J. F.; Yaghi, O. M. Synthesis, structure, and metalation of two new highly porous zirconium metal-organic frameworks. *Inorg. Chem.* **2012**, *51* (12), 6443−6445.
(37) Stanley, P. M.; Hemmer, K.; Hegelmann, M.; Schulz, A.; Park, M.; Elsner, M.; Cokoja, M.; Warnan, J. Topology- and wavelength-governed CO2 reduction photocatalysis in molecular catalyst-metal-organic framework assemblies. *Chem. Sci.* **2022**, *13* (41), 12164−12174.
(38) Zhang, G.-Y.; Zhuang, Y.-H.; Shan, D.; Su, G.-F.; Cosnier, S.; Zhang, X.-J. Zirconium-based porphyrinic metal-organic framework (PCN-222): Enhanced photoelectrochemical response and its application for label-free phosphoprotein detection. *Anal. Chem.* **2016**, *88* (22), 11207−11212.
(39) Islamoglu, T.; Goswami, S.; Li, Z.; Howarth, A. J.; Farha, O. K.; Hupp, J. T. Postsynthetic tuning of metal-organic frameworks for targeted applications. *Acc. Chem. Res.* **2017**, *50* (4), 805−813.
(40) Deria, P.; Mondloch, J. E.; Karagiaridi, O.; Bury, W.; Hupp, J. T.; Farha, O. K. Beyond post-synthesis modification: evolution of metal-organic frameworks via building block replacement. *Chem. Soc. Rev.* **2014**, *43* (16), 5896−5912.
(41) Karagiaridi, O.; Bury, W.; Mondloch, J. E.; Hupp, J. T.; Farha, O. K. Solvent-assisted linker exchange: an alternative to the de novo synthesis of unattainable metal-organic frameworks. *Angew. Chem., Int. Ed.* **2014**, *53* (18), 4530−4540.
(42) Epp, K.; Bueken, B.; Hofmann, B. J.; Cokoja, M.; Hemmer, K.; de Vos, D.; Fischer, R. A. Network topology and cavity confinement-controlled diastereoselectivity in cyclopropanation reactions catalyzed by porphyrin-based MOFs. *Catal. Sci. Technol.* **2019**, *9* (22), 6452−6459.
(43) Zhang, H.; Wei, J.; Dong, J.; Liu, G.; Shi, L.; An, P.; Zhao, G.; Kong, J.; Wang, X.; Meng, X.; Zhang, J.; Ye, J. Efficient visible-light-driven carbon dioxide reduction by a single-atom implanted metal-organic framework. *Angew. Chem., Int. Ed.* **2016**, *55* (46), 14310−14314.
(44) Hemmer, K.; Bühler, R.; Elsner, M.; Cokoja, M.; Fischer, R. A. Stereo-controlled cyclopropanation catalysis within the confined pores of porphyrin MOFs. *Catal. Sci. Technol.* **2023**, *13*, 3304−3312.
(45) Epp, K.; Semrau, A. L.; Cokoja, M.; Fischer, R. A. Dual site lewis-acid metal-organic framework catalysts for CO2 fixation:


https://doi.org/10.1021/acs.inorgchem.3c03943
*Inorg. Chem.* 2024, 63, 2122−2130

Counteracting effects of node connectivity, defects and linker metalation. *ChemCatChem.* **2018**, *10* (16), 3506−3512.
(46) Valenzano, L.; Civalleri, B.; Chavan, S.; Bordiga, S.; Nilsen, M. H.; Jakobsen, S.; Lillerud, K. P.; Lamberti, C. Disclosing the complex structure of UiO-66 metal organic framework: A synergic combination of experiment and theory. *Chem. Mater.* **2011**, *23* (7), 1700−1718.
(47) Shearer, G. C.; Chavan, S.; Ethiraj, J.; Vitillo, J. G.; Svelle, S.; Olsbye, U.; Lamberti, C.; Bordiga, S.; Lillerud, K. P. Tuned to perfection: Ironing out the defects in metal−organic framework UiO-66. *Chem. Mater.* **2014**, *26* (14), 4068−4071.
(48) Shearer, G. C.; Vitillo, J. G.; Bordiga, S.; Svelle, S.; Olsbye, U.; Lillerud, K. P. Functionalizing the defects: Postsynthetic ligand exchange in the metal organic framework UiO-66. *Chem. Mater.* **2016**, *28* (20), 7190−7193.
(49) Balestra, S. R. G.; Bueno-Perez, R.; Hamad, S.; Dubbeldam, D.; Ruiz-Salvador, A. R.; Calero, S. Controlling thermal expansion: A metal-organic frameworks route. *Chem. Mater.* **2016**, *28* (22), 8296−8304.
(50) Coudert, F.-X. Responsive metal−organic frameworks and framework materials: Under pressure, taking the heat, in the spotlight, with friends. *Chem. Mater.* **2015**, *27* (6), 1905−1916.
(51) Boström, H. L. B.; Bette, S.; Emmerling, S. T.; Terban, M. W.; Lotsch, B. V. Guest-responsive thermal expansion in the Zr−porphyrin metal−organic framework PCN-222. *APL Mater.* **2022**, *10* (7), 71106.
(52) Cliffe, M. J.; Hill, J. A.; Murray, C. A.; Coudert, F.-X.; Goodwin, A. L. Defect-dependent colossal negative thermal expansion in UiO-66(Hf) metal-organic framework. *Phys. Chem. Chem. Phys.* **2015**, *17* (17), 11586−11592.
(53) Feng, D.; Chung, W.-C.; Wei, Z.; Gu, Z.-Y.; Jiang, H.-L.; Chen, Y.-P.; Darensbourg, D. J.; Zhou, H.-C. Construction of ultrastable porphyrin Zr metal-organic frameworks through linker elimination. *J. Am. Chem. Soc.* **2013**, *135* (45), 17105−17110.
(54) Sessler, J. L.; Mozaffari, A.; Johnson, M. R. 3,4-Diethylpyrrole and 2,3,7,8,12,13,17,18- Octaethylporphyrin. *Org. Synth.* **1992**, *70*, 68.
(55) *Saint; Version 8.37a.*; Bruker AXS; Inc.: Madison; WI, 2013.
(56) *SADABS; Version 2016/2*; Bruker AXS; Inc.: Madison, WI, 2014.
(57) *APEX3; Version 2016.9-0*; Bruker AXS; Inc.: Madison, WI, 2016.
(58) Dolomanov, O. V.; Bourhis, L. J.; Gildea, R. J.; Howard, J. A. K.; Puschmann, H. OLEX2: a complete structure solution, refinement and analysis program. *J. Appl. Crystallogr.* **2009**, *42* (2), 339−341.
(59) Sheldrick, G. M. SHELXT - integrated space-group and crystal-structure determination. *Acta Crystallogr., Sect. A* **2015**, *71* (Pt 1), 3−8.
(60) Hope, H. X-ray crystallography: A fast, first-resort analytical tool. *Prog. Inorg. Chem.* **1994**, *41*, 1−19.
(61) Rouquerol, J.; Llewellyn, P.; Rouquerol, F.; Rouquerol, J.; Llewellyn, P.; Rouquerol, F. *Is the bet equation applicable to microporous adsorbents?*. In Characterization of Porous Solids VII - Proceedings of the 7th International Symposium on the Characterization of Porous Solids (COPS-VII), Aix-en-Provence, France, 26−28 May 2005; Studies in Surface Science and Catalysis; Elsevier, 2007; pp 49−56.
(62) Thommes, M.; Kaneko, K.; Neimark, A. V.; Olivier, J. P.; Rodriguez-Reinoso, F.; Rouquerol, J.; Sing, K. S.W. Physisorption of gases, with special reference to the evaluation of surface area and pore size distribution (IUPAC Technical Report). *Pure Appl. Chem.* **2015**, *87* (9−10), 1051−1069.
(63) *3Flex; Version 5.01*; Micromeritics Instrument Corporation, 2018.
(64) Coelho, A. A. TOPAS and TOPAS-Academic: an optimization program integrating computer algebra and crystallographic objects written in C++. *J. Appl. Crystallogr.* **2018**, *51* (1), 210−218.
(65) Pawley, G. S. Unit-cell refinement from powder diffraction scans. *J. Appl. Crystallogr.* **1981**, *14* (6), 357−361.


https://doi.org/10.1021/acs.inorgchem.3c03943
*Inorg. Chem.* 2024, 63, 2122−2130

## 2.3. Study III: Spin-State Dependent Pressure Responsiveness of Fe(II)-based Triazolate Metal-Organic Frameworks

Switching response in Fe(II)-containing MOFs, *i.e.* thermally induced spin-crossover phenomena, shows great potential for technological development of microsensors, memory, or data storage devices. The understanding of how MOF`s crystal chemistry determines the mechanical behaviour relevant for application-oriented purposes, such as the material`s processability and longevity, is only just developing.

In this work, we focus on the impact of the metal centre spin-state and investigate its impact on the mechanical response under hydrostatic conditions. In this pursuit, we designed two new Fe(II)-based MOFs, *i.e.* $Fe(cta)_2$ ($(cta)^-$ = 1,4,5,6-tetrahydrocyclopenta[d][1,2,3]triazolate) and $Fe(mta)_2$ ($(mta)^-$ = methyltriazolate), that are in high-spin at ambient conditions compared to the isostructural $Fe(ta)_2$ ($(ta)^-$ = 1,2,3-triazolate), which is in its low-spin state. Here, we were able to synthetically control the Fe(II) spin-state *via* chemical modification of the triazolate linker. HPPXRD allowed the determination of the bulk moduli, showing surprisingly similar *B* values despite significantly different void fractions of $Fe(ta)_2$ and $Fe(cta)_2$. Hence, we emphasise the role of the spin-state as a design criterion for the pressure response over other determining factors such as steric effects, the coordination bond strength, and void fraction.

S. M. Kronawitter conducted experiments and data analysis, with R. Röß-Ohlenroth contributing to material synthesis, supported by M Hirrle and H. Krug von Nidda for magnetic measurements. S. A. Hallweger, E. Myatt, J. Pitcairn and D. Daisenberger assisted during HPPXRD beamtime at the beamline I15 (Diamond Light Source, UK). J. Wojciechowski performed 3D ED experiments. S. M. Kronawitter, R. Röß-Ohlenroth, D. Volkmer and G. Kieslich designed the project and discussed the results. D. Volkmer and G. Kieslich gave overarching academic guidance and financial support. M. J. Cliffe provided input for data interpretation. The manuscript was written by S. M. Kronawitter and G. Kieslich and subsequently edited by all co-authors.



S. M. Kronawitter,† R. Röß-Ohlenroth,† S. A. Hallweger, M. Hirrle, H. Krug von Nidda, T. Luxenhofer, E. Myatt, J. Pitcairn, M. J. Cliffe, D. Daisenberger, J. Wojciechowski, D. Volkmer, G. Kieslich: Spin-state dependent pressure responsiveness of Fe(II)-based triazolate metal-organic frameworks, *J. Mater. Chem. C* **2024**, 12, 4954-4960

† Equal contribution

Volume 12
Number 14
14 April 2024
Pages 4907–5258

# Journal of Materials Chemistry C

Materials for optical, magnetic and electronic devices

rsc.li/materials-c

ISSN 2050-7526

ROYAL SOCIETY OF CHEMISTRY

**PAPER**
Dirk Volkmer, Gregor Kieslich *et al.*
Spin-state dependent pressure responsiveness of Fe(II)-based triazolate metal–organic frameworks

Journal of Materials Chemistry C

ROYAL SOCIETY OF CHEMISTRY

PAPER

View Article Online
View Journal | View Issue



Cite this: J. Mater. Chem. C, 2024, 12, 4954

# Spin-state dependent pressure responsiveness of Fe(II)-based triazolate metal–organic frameworks†

Silva M. Kronawitter, ‡[a] Richard Röß-Ohlenroth, ‡[b] Sebastian A. Hallweger, [a] Marcel Hirrle,[b] Hans-Albrecht Krug von Nidda,[c] Tobias Luxenhofer,[b] Emily Myatt, [d] Jem Pitcairn, [d] Matthew J. Cliffe, [d] Dominik Daisenberger, [e] Jakub Wojciechowski,[f] Dirk Volkmer *[b] and Gregor Kieslich *[a]

Received 29th January 2024,
Accepted 20th February 2024

DOI: 10.1039/d4tc00360h

rsc.li/materials-c

Fe(II)-containing Metal–Organic Frameworks (MOFs) that exhibit temperature-induced spin-crossover (SCO) are candidate materials in the field of sensing, barocalorics, and data storage. Their responsiveness towards pressure is therefore of practical importance and is related to their longevity and processibility. The impact of Fe(II) spin-state on the pressure responsiveness of MOFs is yet unexplored. Here we report the synthesis of two new Fe(II)-based MOFs, *i.e.* $Fe(cta)_2$ ($(cta)^-$ = 1,4,5,6-tetra hydrocyclopenta[*d*][1,2,3]triazolate) and $Fe(mta)_2$ ($(mta)^-$ = methyl[1,2,3]triazolate), which are both in high-spin at room temperature. Together with the isostructural MOF $Fe(ta)_2$ ($(ta)^-$ = [1,2,3]triazolate), which is in its low-spin state at room temperature, we apply these as model systems to show how spin-state controls their mechanical properties. As a proxy, we use their bulk modulus, which was obtained *via* high-pressure powder X-ray diffraction experiments. We find that an interplay of spin-state, steric effects, void fraction, and absence of available distortion modes dictates their pressure-induced structural distortions. Our results show for the first time the role of spin-state on the pressure-induced structural deformations in MOFs and bring us a step closer to estimating the effect of pressure as a stimulus on MOFs *a priori*.



## Introduction

Metal–organic frameworks (MOFs) are built from inorganic metal nodes and multitopic organic linkers, providing a large chemical parameter space for synthesising materials with targeted functionalities. On the most fundamental level, designing material functionality means control over the materials' responsiveness to stimuli such as pressure, temperature, electric and magnetic fields, and chemical triggers *via* composition and structure.[1,2]

In this work, we focus on hydrostatic pressure as a stimulus. In 2008, it was proposed that "[The MOFs'] well documented structural complexities can be expected to yield unprecedented pressure-induced phenomena".[3] High-pressure research on MOFs over the past 15 years has fulfilled these expectations, revealing a variety of fascinating phenomena. Examples include pressure-induced structural flexibility with large volume changes as interesting for damping, shock absorbers, and mechanical energy storage;[4–6] large negative linear compressibility as a potential starting point for new actuating technologies,[7,8] pressure-induced postsynthetic modification reactions of the metal node,[9] and defect-dependent material stabilities[10] with implications for material processing parameters.

As MOFs move closer to practical use, their mechanical properties such as bulk modulus ($B$), or their compressibility as the inverse, hardness, Young's modulus, and stress stability are attracting increasing attention.[11–14] Learning about the relationships between chemical composition, structure, and macroscopic mechanical properties, will allow these properties to be targeted synthetically. In this context, $B$, and its linear components, as a measure of the resistance of a MOF to hydrostatic pressure are important parameters. These parameters are tied to interatomic potentials and the inner energy of a crystal structure.[15] Therefore, they are important measures of how the MOF's crystal chemistry as a whole, *i.e.* chemical

[a] Technical University of Munich, TUM Natural School of Sciences, Lichtenbergstr. 4, Garching 85748, Germany. E-mail: gregor.kieslich@tum.de
[b] Chair of Solid State and Materials Chemistry, Institute of Physics, University of Augsburg, Universitätsstr. 1, Augsburg 86159, Germany. E-mail: dirk.volkmer@physik.uni-augsburg.de
[c] Experimental Physics V, Center for Electronic Correlations and Magnetism, Institute of Physics, University of Augsburg, Universitätsstr. 1, Augsburg 86159, Germany
[d] School of Chemistry, University of Nottingham, Nottingham NG7 2RD, UK
[e] Diamond Light Source Ltd., Diamond House, Harwell Campus, Didcot OX11 ODE, UK
[f] Rigaku Europe SE, Hugenottenallee 167, Neu-Isenburg, Germany

† Electronic supplementary information (ESI) available. CCDC 2311804–2311811. For ESI and crystallographic data in CIF or other electronic format see DOI: https://doi.org/10.1039/d4tc00360h

‡ Shared contribution.

bond strength, nature of chemical bonds, connectivity, available pore space, and defect chemistry together determine its pressure responsiveness.

Over the past years, a few important principles between a MOF's crystal chemistry and $B$ have been discovered.[12,16,17] For instance, in a comprehensive study by K. Chapman and O. Farha on isoreticular MOF series with **fcu** and **scu** topology, a relation between void fraction, linker length, and $B$ has been established.[18] It has been found that within an isoreticular MOF series, a larger void space (longer linkers) correlates to a reduction of $B$. Moreover, it has been pointed out that MOFs with rotated and out-of-plane bended linker molecules such as DUT-52 ($B$ = 17(2) GPa) and PCN-57 ($B$ = 4.6(1) GPa) show a significantly smaller $B$ when compared to their isoreticular counterparts with linear linkers ($B$ between 21.1(6) and 37.9(6) GPa). This finding suggests that pre-distorted linkers introduce preferred low-energy pathways for structural distortion as a response to hydrostatic pressure. Furthermore, it has been shown for NU-901 that post-synthetic incorporation of a linker between two open metal-sites, a process known as retrofitting,[19] increases $B$.[20] This result agrees with intuition and with recent results from computation where a positive correlation between metal-node connectivity and $B$ has been found.[21] Additionally, it has been discovered that the coordination bond strength between the linker and the metal-node[22] and the concentration of point defects influences $B$.[10] Importantly, both factors also influence the critical pressure where pressure-induced amorphisation occurs.[23] There has been interest in the pressure-dependent spin-state of MOF-related Hoffman-type clathrates[24–26] and the elastic properties of molecular Fe(II) SCO complexes,[27,28] highlighting that changing the spin-state significantly impacts $B$. The impact of the spin-state of metal centres within the metal-node on the mechanical properties of MOFs has not been explored to our knowledge. Knowing about the role of coordinative bond strength in determining $B$, it can be anticipated that the metal-centre spin-state, which comes with a change in coordination bond length and strength, will significantly impact the material response to hydrostatic pressure.

$Fe(ta)_2$ is a MOF with thermal SCO, $(ta)^-$ = 1,2,3-triazolate.[29] $Fe(ta)_2$ belongs to a larger family of isostructural MOFs, $M(ta)_2$ (with $M^{2+}$ = $Cu^{2+}$, $Cd^{2+}$, $Cr^{2+/3+}$, $Mn^{2+}$, $Co^{2+}$, $Zn^{2+}$, and $Mg^{2+}$),[30–34] where the divalent metal centres are octahedrally coordinated by $\mu_3$-bridging 1,2,3-triazolate ligands to form a 3D network with two crystallographically independent Fe(II) sites, see Fig. 1. Notably, the underlying topology is of type **dia**, or when treating both Fe(II) sites independently, parallels to the structure of β-cristobalite can be drawn. Initially, $Fe(ta)_2$ has high intrinsic electrical conductivity of $7.7 \times 10^{-5}$ S cm$^{-1}$,[30] which is sensitive towards gas pressure[35] and can be further increased upon partial oxidation of metal centres *via* $I_2$ or thianthrenium tetrafluorborate.[36] More recently, $Fe(ta)_2$ has been shown to exhibit a large hysteresis SCO in a bistable region between 320 °C (heating) and 185 °C (cooling), associated with a change of unit cell volume of approximately 22%, while retaining its structural connectivity and cubic symmetry.[37] Notably, the SCO

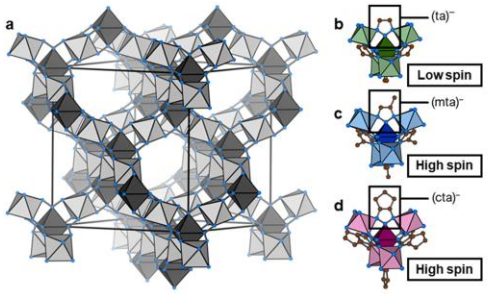


Fig. 1 (a) Schematic of the isostructural **dia**-type network of Fe(II)-containing MOFs investigated in this work. The modification in $Fe(mta)_2$ and $Fe(cta)_2$ has a significant impact on the void fraction which is reduced in $Fe(mta)_2$ and $Fe(cta)_2$ when compared to $Fe(ta)_2$. In (b–d) a visualisation of metal nodes of $Fe(ta)_2$ (b), $Fe(mta)_2$ (c), and (d) $Fe(cta)_2$ is shown, where the colour-code highlights the different coordinating triazolate ligands used in this work. For visualisation purposes, disorder of the $-CH_3$ group of $(mta)^-$ is not shown in (c). Likewise, H atoms were deleted for clarity. Colour-code: brown spheres – carbon, blue spheres – nitrogen; different colour saturations of polyhedrons indicate the two crystallographically independent Fe(II) sites.

comes with a significant change in Fe–N bond lengths ($\Delta d$ = 0.18–0.21 Å), which accounts for the changes in unit cell volume. Long-range cooperativity was recently found to be responsible for the large hysteresis of the SCO in $Fe(ta)_2$.[38]

Drawing inspiration from the extensive work on Fe(II)-containing SCO compounds such as Hofmann-type clathrates and molecular complexes,[39] we expect that chemical modification of the $(ta)^-$ backbone impacts the critical temperature of the SCO transition. For our purpose, *i.e.* the study of Fe(II) spin-state on the pressure response, we seek to decrease the SCO temperature below room temperature while maintaining the overall connectivity and cubic symmetry of the material. Together with $Fe(ta)_2$, such a compound would provide a model system for studying the impact of Fe(II) spin-state on the compressibility.

Here we report the synthesis of $Fe(cta)_2$ ($(cta)^-$ = 1,4,5,6-tetra hydrocyclopenta[*d*][1,2,3]triazolate) and $Fe(mta)_2$ ($(mta)^-$ = methyl [1,2,3]triazolate), two new Fe(II)-based MOFs that are in their high-spin state at room temperature. We apply $Fe(cta)_2$ as model system for exploring the impact of spin-state on the pressure response of Fe(II) containing MOFs *via* high-pressure powder X-ray diffraction (HPPXRD). It is shown that $Fe(ta)_2$ and $Fe(cta)_2$ exhibit similar $B$ which is ascribed to the difference in void fraction and Fe–N bond strengths as counteracting effects. The results advance our understanding of the crystal chemical factors that contribute to the mechanical properties of MOFs, knowledge that is of increasing importance when considering their potential as working media in barocalorics[40] and mechanical energy storage.[41]

## Results and discussion

### Material synthesis and characterisation

$Fe(ta)_2$ was synthesised by following a previously established route,[29,35] and similar procedures were used for the synthesis of

$Fe(cta)_2$ and $Fe(mta)_2$, see ESI† for synthetic details (S-2). We would like to mention that H-ta (1*H*-1,2,3-triazole) is commercially available, while H-cta (1,4,5,6-tetrahydrocyclopenta-1*H*-1,2,3-triazole) and H-mta (4-methyl-1*H*-1,2,3-triazole) were synthesised by following adapted synthetic procedures from the literature, see ESI† for details (S-2).[42,43] After synthesis of the MOFs, IR spectroscopy was performed, where signals from stretch vibrations of cyclopentyl and methyl hydrogen atoms between 2800–3000 $cm^{-1}$ confirm the presence of (chemically modified)-triazolate linkers in the obtained powders (Fig. S2, ESI†). To remove potential residual *N*,*N*-dimethylformamide (DMF), $Fe(cta)_2$ and $Fe(mta)_2$ were washed with methanol (MeOH) and dried *in vacuo* at room temperature (for $Fe(cta)_2$) or at 280 °C (for $Fe(mta)_2$). Thermogravimetrical analysis (TGA) and differential scanning calorimetry (DSC) of $Fe(cta)_2$ and $Fe(mta)_2$ show that both compounds exhibit a relatively high thermal stability with a decomposition onset at approximately 670 K (Fig. S4 and S5, ESI†). This is slightly higher than previously observed for $Fe(ta)_2$, where decomposition processes start at approximately 613 K.[29] Similarly to $Fe(ta)_2$, no evidence for the release of solvent molecules from potential void space was observed for both compounds (Fig. S3–S5, ESI†).

Since the applied synthetic route led to crystalline powders of $Fe(ta)_2$, $Fe(cta)_2$, and $Fe(mta)_2$, powder X-ray diffraction (PXRD) was used for structure analysis, see ESI† for details (Fig. S13, S16, and Table S3). In an initial step, the synthesis of phase pure $Fe(ta)_2$ was confirmed *via* a Pawley profile fit analysis, and subsequently, atomic positions were obtained by Rietveld refinements (Fig. 2(a) and Fig. S22, ESI†). $Fe(ta)_2$ was refined in the previously reported cubic structure, space-group $Fd\bar{3}m$ ($a$ = 16.5969 Å). The obtained Fe–N bond lengths (Fe1–N1 = 1.9736 Å and Fe2–N2 = 1.99082 Å) are indicative for Fe(II) centres in their low-spin state, which agree with the literature.[29] Visual comparison of all PXRD pattern suggests that $Fe(ta)_2$, $Fe(cta)_2$, and $Fe(mta)_2$ are isostructural MOFs, which was confirmed *via* Rietveld-based structure refinement, see ESI† for refinement details (Fig. 2 and Fig. S16, S-19–S-21).

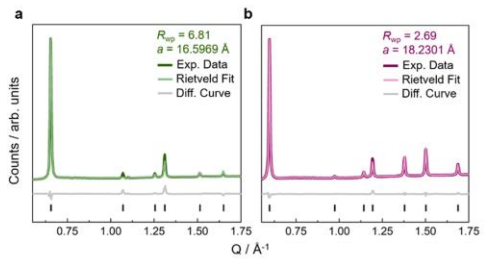


Fig. 2 Rietveld refinements against high-resolution PXRD pattern at ambient pressure of $Fe(ta)_2$ (a) in green and $Fe(cta)_2$ (b) in purple. Experimental data is shown as dark line, the calculated data from Rietveld refinement as light line, and the difference curve (fit – data) as grey line. Reflection positions are shown as black vertical tick marks. Rietveld fit of $Fe(mta)_2$ is given in the ESI† (Fig. S20).

The structures of $Fe(cta)_2$ and $Fe(mta)_2$ were refined in the cubic space-group $Fd\bar{3}m$ with lattice parameters of $a$ = 18.2301 Å ($Fe(cta)_2$) and $a$ = 17.3175 Å ($Fe(mta)_2$) (Fig. 2). Compared to $Fe(ta)_2$ (Fig. S20, ESI†), where Fe(II) centres are in their low-spin state at room temperature, the observed Fe–N bond lengths of $Fe(cta)_2$ and $Fe(mta)_2$ (*i.e.* Fe(II)–N > 2.0 Å) indicate that both compounds are in their high-spin state. This was confirmed by variable temperature magnetic susceptibility measurements in the temperature range between 2 and 700 K of all compounds, see ESI† for detailed data interpretation (Fig. S9 and S-12). To further verify structure refinement from PXRD data, 3D electron diffraction (3DED) at variable temperatures between 173 and 373 K was applied for structure solution from small crystallites, for experimental details and crystallographic outcomes see ESI† (Tables S8, S9 and Fig. S35–S38). The 3DED structures at room temperature, including bond distances and lattice parameters of the high-spin MOFs $Fe(cta)_2$ (Fe1–N1 = 2.223(18) Å, Fe2–N2 = 2.231(15) Å, and $a$ = 18.19(10) Å) and $Fe(mta)_2$ (Fe1–N1 = 2.198(15) Å, Fe2–N2 = 2.117(14) Å, and $a$ = 17.26(9) Å), are in close agreement to the results from the Rietveld analysis.

Therefore, the backbone modification of the triazolate linker impacts the critical temperature of the SCO effect and its nature. With increasing bulkiness of the chemical modification, *i.e.* $(ta)^-$ < $(mta)^-$ < $(cta)^-$, the SCO temperature decreases and suppresses hysteretic behaviour. By drawing parallels to molecular SCO complexes,[44] this is rationalised by steric effects which provide an energy penalty for compression of the frameworks into the low-spin state. Especially in the high-spin $Fe(cta)_2$ framework, opposing hydrogen atoms of the $(cta)^-$ ligands are already in a repulsive range, with distances of H7A–H7A 2.1008(82) Å and H6A–H6A 2.1763(85) Å when looking at the 3DED data. In $Fe(mta)_2$, the larger distances between the methyl groups allow for more flexibility, although their steric demand still results in a significant shift of the phase transition to lower temperatures, as well as a two-step transition behaviour. Moreover, residual DMF trapped in the voids of the as-synthesised $Fe(mta)_2$-as seems to contribute to the steric crowding, causing a smeared-out transition at lower temperatures (Fig. S6, S7 and S9, ESI†). In addition, we calculated the void fraction of all three materials *via* Platon[45] (SOLV option), see Table 1. As expected, chemical modification of the $(ta)^-$ backbone in $Fe(cta)_2$ significantly decreases the existing void fraction compared to $Fe(ta)_2$, which can be expected to significantly influence the materials' pressure responsiveness.

Overall, a series of isostructural triazole-based Fe(II) MOFs is obtained where Fe(II) centres are in different spin-states at ambient conditions. These represent a good model series to study the impact of spin-state on their pressure response. An overview of structural and magnetic data of $Fe(ta)_2$ and $Fe(cta)_2$ is given in Table 1 and full crystallographic data, including details of structure refinement is given in the ESI.†

### High-pressure structural response

With the isostructural series of $Fe(ta)_2$, $Fe(cta)_2$, and $Fe(mta)_2$ on hand, we used HPPXRD to investigate the impact of varying spin-state of Fe(II) on the MOF's response to hydrostatic

 

Table 1 Overview of structural and magnetic data for $Fe(ta)_2$ and $Fe(cta)_2$. *B*s were calculated by using the 2nd B–M equation of states fits *via* EOSFit. Because of the pressure-induced phase transition in $Fe(mta)_2$, no *B* was calculated. Void fractions were calculated in PLATON (using SOLV option) based on the Rietveld refined structures in this work. The Fe(II)–N bond distances were derived from Rietveld refinement. The calculated void fraction of $Fe(ta)_2$ including bond distances is in good agreement with previous structural reports (*26.2% – CCDC 837468 and 27.6% – CCDC 1963573)

| MOF | $Fe(ta)_2$ | $Fe(cta)_2$ |
|---|---|---|
| Spin-state | Low-spin | High-spin |
| Void fraction/%* | 25.8 | 5.9 |
| Fe(II)–N/Å | 1.9736(Fe1–N1)<br>1.99082(Fe2–N2) | 2.15631(Fe1–N1)<br>2.09172(Fe2–N2) |
| *B*/GPa | 28.2 ± 0.2 | 29.5 ± 0.5 |

pressure as a stimulus. HPPXRD was performed at beamline I15 at the Diamond Light Source (DLS, UK). For obtaining an excellent pressure resolution of our $V(p)$ datasets, which is critical for obtaining accurate *B*s, we have applied the "high-pressure jump cell".[46] This is a custom-made high-pressure cell that enables HPPXRD measurements up to $p_{max}$ = 0.4 GPa with defined pressure increments of $\Delta p$ = 0.02 GPa (Fig. 3), see ESI† for the measurement of a standard material (S-32). Silicone oil AP-100 was used as a pressure transmitting medium (PTM), which has previously been applied for HPPXRD experiments of Zr-based MOFs[47] and molecular perovskites.[48] To the best of our knowledge, silicone oil AP-100 acts as hydrostatic, non-penetrating PTM, enabling to study the mechanical response of the MOFs without any additional effects such as penetration of the PTM into the pores of the MOF.[3,49]

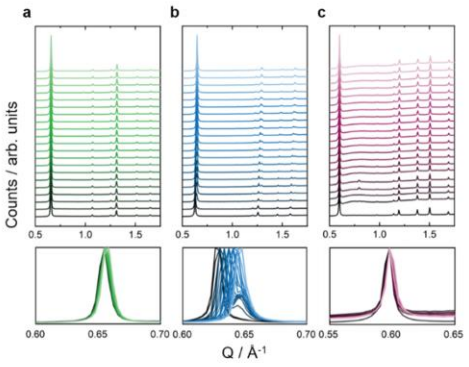


Fig. 3 Stacked HPPXRD pattern ($\lambda$ = 0.4246 Å) of (a) $Fe(ta)_2$ in green, (b) $Fe(mta)_2$ in blue, and (c) $Fe(cta)_2$ in purple. The HPPXRD pattern were collected between ambient pressure (bottom) and 0.4 GPa (top) with the step size of $\Delta p$ = 0.02 GPa. For visualisation purposes, the data was normalised to the (111) reflection. The bottom panel focus on the peak of the reflection of the (111) plane, showing a gradual shift for $Fe(ta)_2$ and $Fe(cta)_2$. For $Fe(mta)_2$ an additional peak is observed starting from approximately $p_{crit}$ = 0.04 GPa which is ascribe to a pressure-induced phase transition that is incomplete at $p_{max}$.

From visual inspection of HPPXRD data (Fig. 3), none of the studied MOFs exhibits pressure-induced amorphisation up to 0.4 GPa.[50] The analysis of the full-width at half maximum (fwhm) of the applied peak profile function of $Fe(ta)_2$ and $Fe(cta)_2$ confirms this observation (Fig. S26, ESI†). For $Fe(mta)_2$, a pressure-induced phase transition complicates such an analysis, see below. This is expected since only a few MOFs, such as UiO-66 with a large concentration of point defects,[10] and DMOF-1 with non-functionalized benzendicarboxylate linkers,[51] have been reported to irreversibly amorphise at hydrostatic pressures below $p < 0.4$ GPa. Please note, that amorphisation under non-hydrostatic compression is known to occur significantly earlier, as reported for ZIF-8 and MOF-5.[50,52] Upon increasing pressure, a peak shift is observed for $Fe(ta)_2$, $Fe(cta)_2$, and $Fe(mta)_2$, showing structural compression (Fig. 3). For $Fe(ta)_2$ and $Fe(cta)_2$ no evidence for a phase transition is observed, while $Fe(mta)_2$ undergoes a pressure-driven phase transition at approximately $p_{crit}$ = 0.04 GPa. This can be expected due to the temperature dependent SCO just below room temperature. Therefore, $Fe(ta)_2$ and $Fe(cta)_2$ were selected as model systems to learn about the impact of spin-sate on the pressure responsiveness. $Fe(mta)_2$ with its pressure-induced phase transition and open questions related to its ambient crystal structure, see S-43 (ESI†), displays a more complex case and will be addressed independently in a follow-up study. HPPXRD data of $Fe(ta)_2$ and $Fe(cta)_2$ have been analysed *via* Pawley profile fits and Rietveld-based structural refinements for extracting lattice parameters (*a*), volumes (*V*) and atomic positions as well as Fe–N bond length as a function of pressure, providing complete $V(p)$ data sets up to $p_{max}$ for both samples, see ESI† for a full list of Pawley profile fit results, *i.e.* lattice parameters, $R_{wp}$ values, and fwhm (Tables S4, S5 and Fig. S21, S26).

For describing the mechanical resistance of $Fe(ta)_2$ and $Fe(cta)_2$ against pressure as a stimulus, we focus on *B* as the inverse of the material's compressibility. *B*s were calculated by fitting a Birch–Murnaghan (B–M) equation of state to the $V(p)$ data up to $p_{max}$ = 0.4 GPa by using both second and third order B–M equation of state fits *via* EoSFit7-Gui (Table 1), see ESI† for details (Fig. S27 and S28).[53] Similar results were obtained by using PASCal[54] (Table S8, ESI†). We would like to note that for both methods, *i.e.* EOSFit and PASCal, only 2nd order B–M fits show standard errors ($\sigma B$) in the range of the measured reference material (S-32, ESI†) and are used for further discussion.

For both MOFs, we obtain similar *B*s, $B(Fe(ta)_2)$ = 28.2 ± 0.2 GPa and $B(Fe(cta)_2)$ = 29.5 ± 0.5GPa. Compared to other prototypical MOFs such as UiO-66(Zr) ($B$ = 37.9(6) GPa),[18] HKUST-1 ($B$ = 30 GPa)[3], ZIF-4(Zn) ($B$ = 2–4.4 GPa),[55] and ZIF-8 ($B$ = 6.5 GPa),[50] $Fe(ta)_2$ and $Fe(cta)_2$ can be considered relatively rigid or rather 'hard MOFs'.[56] To rationalise these values, we anticipate that the absence of a clear pressure-induced low-energy distortion pathway in the structures of $Fe(ta)_2$ and $Fe(cta)_2$ is key. Example for such pathways are pressure-induced wine-rack type network motions as observed in MOFs such as MIL-53(Al) ($Al[O_2C–C_6H_4–CO_2]OH$)[57] and $Cu_2$(DB-bdc)$_2$ dabco (DB-bdc = 2,5-dibutoxy-1,4-benzendicarboxylate, dabco = 1,4-diazabicyclo[2.2.2]octane)[51] and MOFs with predistorted linkers such as DUT-52 and PCN-57.[18] The structures of $Fe(ta)_2$ and $Fe(cta)_2$ are

related to the structure of β-cristobalite, where temperature and pressure are known to activate tilts of polyhedra,[58,59] however, the $\mu_3$-connectivity of 1,2,3-triazolate ligands makes similar distortions in $Fe(ta)_2$ and $Fe(cta)_2$ energetically unfavourable. Therefore, any pressure-induced structural deformation is coupled to bond-length compression and linker bending, where the latter becomes energetically favoured by void space, which reduces steric hindrance. The same argumentation applies to UiO-66(Zr) and HKUST-1, where presumably the metal-node coordination number is the dominating structural feature in defining *B*. This train of thought agrees with the observation that increasing the length of the linker leads to a reduction of *B* as previously shown for UiO-66(Zr) ($B$ = 37.9(6) GPa) and UiO-67(Zr) ($B$ = 21.1(6) GPa).[18]

Looking more specifically at the comparison of $Fe(ta)_2$ and $Fe(cta)_2$, the difference in the void fraction of $Fe(ta)_2$ (0.26) and $Fe(cta)_2$ (0.06) should first be emphasised. Therefore, based on previous HPPXRD studies,[18] a significant smaller *B* for $Fe(ta)_2$ is expected. In contrast, the similar *B* of $Fe(ta)_2$ and $Fe(cta)_2$ imply that other factors contribute to the structural response. Looking at the evolution of Fe–N bond length in both compounds between $p$ = ambient − 0.4 GPa, very similar relative changes of approximately 0.008% for $Fe(ta)_2$ and 0.009% for $Fe(cta)_2$ are observed despite the difference in spin-state which makes bond-compression for $Fe(ta)_2$ energetically more demanding, see ESI† for a full list of Rietveld refinement results, *i.e.* bond lengths and $R_{wp}$ values (Tables S1 and S2). Therefore, we hypothesise that in $Fe(ta)_2$, the larger bond strength is the dominating factor, which limits the effect of the relatively low packing density. In $Fe(cta)_2$, the cyclopentyl backbone of the $(cta)^-$ linker is crowding the network, and instead of bond compression, the steric hindrance of the cyclopentyl molecules is sought to be the dominating structural feature. Notably, increased steric hindrance was recently found to lower *B*,[60] which we do not observe for $Fe(cta)_2$ in comparison to $Fe(ta)_2$. Therefore, we identify the spin-state as determining factor over steric hindrance and void fraction for the mechanical properties of Fe(II) MOFs with different Fe(II) spin-states.

## Conclusion

In conclusion, we report the synthesis of two new Fe(II)-containing MOFs based on modified triazolate linkers, *i.e.* $(cta)^-$ and $(mta)^-$, which are in their high-spin states at ambient conditions. We thus show that design principles for Fe(II)-based MOFs rely on backbone modification of the linker, very much akin to what is known for SCO complexes; however, cooperative effects make property-by-design such as critical temperature of SCO and hysteresis effects very challenging. We then apply $Fe(ta)_2$ and $Fe(cta)_2$ as model systems to investigate their structural response to hydrostatic pressure, obtaining similar *B*s despite a large difference in their void fraction which was previously identified as important factor in determining the high-pressure responsiveness of MOFs. Instead, we rationalise their similar behaviours based on the interplay of several counteracting factors such as spin-state and resulting differences in Fe–N bond-strength, steric effects due to linker-backbone modification and void fraction, overall demonstrating the complexity of comprehending MOFs' response to pressure as a stimulus.

In the bigger context, as MOFs move closer to application, the interest in learning about their responsiveness to pressure will further increase. High-pressure diffraction experiments return important application-oriented properties, such as mechanical stability related to processibility concerns and material longevity. Additionally, high-pressure diffraction experiments can reveal counterintuitive effects such as negative compressibility and pressure-induced phase transitions in flexible MOFs which might initiate new actuation, energy storage, and energy dissipation technologies in the future. In all these areas, material optimisation is coupled to an in-depth knowledge of factors that contribute to the pressure-responsive properties of MOFs, a gap that is in the process of being closed since a few years – with surely many exciting discoveries to follow.

## Data availability

3D electron diffraction data have been deposited in the CCDC (2311804–2311811).†

## Author contributions

S. M. K.: methodology, validation, formal analysis, investigation, data curation, writing – original draft, review and editing, visualisation. R. R.: validation, formal analysis, investigation, data curation, writing – review and editing, visualisation. S. A. H., M. H., H. K., T. L., E. M., J. P., M. J. C., D. D., J. W.: investigation such as material synthesis, HPPXRD, magnetic measurements and 3DED. D. V.: conceptualisation, writing – review and editing, resources. G. K.: visualisation, conceptualisation, writing – review and editing, supervision, resources, project administration.

## Conflicts of interest

There are no conflicts to declare.

## Acknowledgements

The authors would like to thank the DFG for financial support (project (450070835) and project SPP 1928 COORNETs Coordination Networks: Building Blocks for Functional Systems (107745057)) and the Diamond Light Source for granting HPPXRD beamtime (CY30815-2). G. K. acknowledges support from the Heisenberg program (524525093). The authors are grateful for help with DSC measurements from Dr Robert Horny. The authors would like to thank Dr Maciej Grzywa for assistance with 3DED measurements and Shinjoo Park for assistance with Rietveld analysis.

## Notes and references

1 C. L. Hobday and G. Kieslich, *Dalton Trans.*, 2021, **50**, 3759–3768.
2 A. P. Katsoulidis, D. Antypov, G. F. S. Whitehead, E. J. Carrington, D. J. Adams, N. G. Berry, G. R. Darling, M. S. Dyer and M. J. Rosseinsky, *Nature*, 2019, **565**, 213–217.
3 K. W. Chapman, G. J. Halder and P. J. Chupas, *J. Am. Chem. Soc.*, 2008, **130**, 10524–10526.
4 P. Iacomi, J. S. Lee, L. Vanduyfhuys, K. H. Cho, P. Fertey, J. Wieme, D. Granier, G. Maurin, V. van Speybroeck, J.-S. Chang and P. G. Yot, *Chem. Sci.*, 2021, **12**, 5682–5687.
5 X. Zhou, Y.-R. Miao, W. L. Shaw, K. S. Suslick and D. D. Dlott, *J. Am. Chem. Soc.*, 2019, **141**, 2220–2223.
6 G. F. Turner, S. C. McKellar, D. R. Allan, A. K. Cheetham, S. Henke and S. A. Moggach, *Chem. Sci.*, 2021, **12**, 13793–13801.
7 A. B. Cairns, J. Catafesta, C. Levelut, J. Rouquette, A. van der Lee, L. Peters, A. L. Thompson, V. Dmitriev, J. Haines and A. L. Goodwin, *Nat. Mater.*, 2013, **12**, 212–216.
8 W. Cai and A. Katrusiak, *Nat. Commun.*, 2014, **5**, 4337.
9 A. J. R. Thom, G. F. Turner, Z. H. Davis, M. R. Ward, I. Pakamorė, C. L. Hobday, D. R. Allan, M. R. Warren, W. L. W. Leung, I. D. H. Oswald, R. E. Morris, S. A. Moggach, S. E. Ashbrook and R. S. Forgan, *Chem. Sci.*, 2023, **14**, 7716–7724.
10 S. Dissegna, P. Vervoorts, C. L. Hobday, T. Düren, D. Daisenberger, A. J. Smith, R. A. Fischer and G. Kieslich, *J. Am. Chem. Soc.*, 2018, **140**, 11581–11584.
11 J. C. Tan and A. K. Cheetham, *Chem. Soc. Rev.*, 2011, **40**, 1059–1080.
12 L. R. Redfern and O. K. Farha, *Chem. Sci.*, 2019, **10**, 10666–10679.
13 S. A. Moggach and G. F. Turner, in *Mechanical Behaviour of Metal – Organic Framework Materials*, ed. J.-C. Tan, The Royal Society of Chemistry, 2023, pp. 205–266.
14 S. C. McKellar and S. A. Moggach, *Acta Crystallogr., Sect. B: Struct. Sci., Cryst. Eng. Mater.*, 2015, **71**, 587–607.
15 R. Gross and A. Marx, *Festkörperphysik*, De Gruyter Oldenbourg, 2014.
16 P. Vervoorts, J. Stebani, A. S. J. Méndez and G. Kieslich, *ACS Mater. Lett.*, 2021, **3**, 1635–1651.
17 J.-C. Tan, *Mechanical Behaviour of Metal – Organic Framework Materials*, The Royal Society of Chemistry, 2023.
18 L. R. Redfern, L. Robison, M. C. Wasson, S. Goswami, J. Lyu, T. Islamoglu, K. W. Chapman and O. K. Farha, *J. Am. Chem. Soc.*, 2019, **141**, 4365–4371.
19 C. Schneider, D. Bodesheim, J. Keupp, R. Schmid and G. Kieslich, *Nat. Commun.*, 2019, **10**, 4921.
20 L. Robison, R. J. Drout, L. R. Redfern, F. A. Son, M. C. Wasson, S. Goswami, Z. Chen, A. Olszewski, K. B. Idrees, T. Islamoglu and O. K. Farha, *Chem. Mater.*, 2020, **32**, 3545–3552.
21 P. Z. Moghadam, S. M. Rogge, A. Li, C.-M. Chow, J. Wieme, N. Moharrami, M. Aragones-Anglada, G. Conduit, D. A. Gomez-Gualdron, V. van Speybroeck and D. Fairen-Jimenez, *Matter*, 2019, **1**, 219–234.
22 L. R. Redfern, M. Ducamp, M. C. Wasson, L. Robison, F. A. Son, F.-X. Coudert and O. K. Farha, *Chem. Mater.*, 2020, **32**, 5864–5871.
23 S. M. J. Rogge, P. G. Yot, J. Jacobsen, F. Muniz-Miranda, S. Vandenbrande, J. Gosch, V. Ortiz, I. E. Collings, S. Devautour-Vinot, G. Maurin, N. Stock and V. van Speybroeck, *ACS Mater. Lett.*, 2020, **2**, 438–445.
24 R. Li, G. Levchenko, F. J. Valverde-Muñoz, A. B. Gaspar, V. V. Ivashko, Q. Li, B. Liu, M. Yuan, H. Fylymonov and J. A. Real, *Inorg. Chem.*, 2021, **60**, 16016–16028.
25 I. R. Reddy, P. M. Oppeneer and K. Tarafder, *J. Magn. Magn. Mater.*, 2021, **524**, 167637.
26 R. Li, V. M. Kalita, H. Fylymonov, W. Xu, Q. Li, J. A. Real, B. Liu and G. Levchenko, *Inorg. Chem.*, 2022, **61**, 14752–14760.
27 D. Paliwoda, L. Vendier, L. Getzner, F. Alabarse, D. Comboni, B. Martin, S. E. Alavi, M. P. Bello, L. Salmon, W. Nicolazzi, G. Molnár and A. Bousseksou, *Cryst. Growth Des.*, 2023, **23**, 1903–1914.
28 M. Mikolasek, M. D. Manrique-Juarez, H. J. Shepherd, K. Ridier, S. Rat, V. Shalabaeva, A.-C. Bas, I. E. Collings, F. Mathieu, J. Cacheux, T. Leichle, L. Nicu, W. Nicolazzi, L. Salmon, G. Molnár and A. Bousseksou, *J. Am. Chem. Soc.*, 2018, **140**, 8970–8979.
29 M. Grzywa, R. Röß-Ohlenroth, C. Muschielok, H. Oberhofer, A. Błachowski, J. Żukrowski, D. Vieweg, H.-A. K. von Nidda and D. Volkmer, *Inorg. Chem.*, 2020, **59**, 10501–10511.
30 F. Gándara, F. J. Uribe-Romo, D. K. Britt, H. Furukawa, L. Lei, R. Cheng, X. Duan, M. O'Keeffe and O. M. Yaghi, *Chem. – Eur. J.*, 2012, **18**, 10595–10601.
31 X.-H. Zhou, Y.-H. Peng, X.-D. Du, J.-L. Zuo and X.-Z. You, *CrystEngComm*, 2009, **11**, 1964.
32 M. Grzywa, D. Denysenko, J. Hanss, E.-W. Scheidt, W. Scherer, M. Weil and D. Volkmer, *Dalton Trans.*, 2012, **41**, 4239–4248.
33 J. G. Park, B. A. Collins, L. E. Darago, T. Runčevski, M. E. Ziebel, M. L. Aubrey, H. Z. H. Jiang, E. Velasquez, M. A. Green, J. D. Goodpaster and J. R. Long, *Nat. Chem.*, 2021, **13**, 594–598.
34 R. P. Nutakki, R. Röß-Ohlenroth, D. Volkmer, A. Jesche, H.-A. K. von Nidda, A. A. Tsirlin, P. Gegenwart, L. Pollet and L. D. C. Jaubert, *Phys. Rev. Res.*, 2023, **5**, L022018.
35 C. Muschielok, A. Reiner, R. Röß-Ohlenroth, A. Kalytta-Mewes, D. Volkmer, A. Wixforth and H. Oberhofer, *ACS Appl. Mater. Interfaces*, 2022, **14**, 33662–33674.
36 J. G. Park, M. L. Aubrey, J. Oktawiec, K. Chakarawet, L. E. Darago, F. Grandjean, G. J. Long and J. R. Long, *J. Am. Chem. Soc.*, 2018, **140**, 8526–8534.
37 A. B. Andreeva, K. N. Le, K. Kadota, S. Horike, C. H. Hendon and C. K. Brozek, *Chem. Mater.*, 2021, **33**, 8534–8545.
38 M. C. Demuth, K. N. Le, M. Sciprint and C. H. Hendon, *J. Phys. Chem. C*, 2023, **127**, 2735–2740.
39 Y. Garcia, V. Niel, M. C. Muñoz and J. A. Real, *Spin crossover in transition metal compounds*, Springer, Berlin, 2004, pp. 229–257.
40 D. Boldrin, *Appl. Phys. Lett.*, 2021, **118**, 170502.
41 J. Wieme, S. M. J. Rogge, P. G. Yot, L. Vanduyfhuys, S.-K. Lee, J.-S. Chang, M. Waroquier, G. Maurin and V. van Speybroeck, *J. Mater. Chem. A*, 2019, **7**, 22663–22674.

42 J. Thomas, S. Jana, S. Liekens and W. Dehaen, *Chem. Commun.*, 2016, **52**, 9236–9239.
43 P. R. Clark, G. D. Williams, J. F. Hayes and N. C. O. Tomkinson, *Angew. Chem., Int. Ed.*, 2020, **59**, 6740–6744.
44 M. A. Hoselton, L. J. Wilson and R. S. Drago, *J. Am. Chem. Soc.*, 1975, **97**, 1722–1729.
45 A. L. Spek, *J. Appl. Crystallogr.*, 2003, **36**, 7–13.
46 N. J. Brooks, B. L. L. E. Gauthe, N. J. Terrill, S. E. Rogers, R. H. Templer, O. Ces and J. M. Seddon, *Rev. Sci. Instrum.*, 2010, **81**, 64103.
47 G. P. Robertson, S. Mosca, C. Castillo-Blas, F. A. Son, O. K. Farha, D. A. Keen, S. Anzellini and T. D. Bennett, *Inorg. Chem.*, 2023, **62**, 10092–10099.
48 S. Grover, S. Burger, K. T. Butler, K. Hemmer, P. Vervoorts, G. Kieslich and R. Grau-Crespo, *CrystEngComm*, 2023, **25**, 3439–3444.
49 A. J. Graham, D. R. Allan, A. Muszkiewicz, C. A. Morrison and S. A. Moggach, *Angew. Chem., Int. Ed.*, 2011, **50**, 11138–11141.
50 K. W. Chapman, G. J. Halder and P. J. Chupas, *J. Am. Chem. Soc.*, 2009, **131**, 17546–17547.
51 P. Vervoorts, J. Keupp, A. Schneemann, C. L. Hobday, D. Daisenberger, R. A. Fischer, R. Schmid and G. Kieslich, *Angew. Chem., Int. Ed.*, 2021, **60**, 787–793.
52 Y. H. Hu and L. Zhang, *Phys. Rev. B: Condens. Matter Mater. Phys.*, 2010, **81**, 174103.
53 J. Gonzalez-Platas, M. Alvaro, F. Nestola and R. Angel, *J. Appl. Crystallogr.*, 2016, **49**, 1377–1382.
54 M. J. Cliffe and A. L. Goodwin, *J. Appl. Crystallogr.*, 2012, **45**, 1321–1329.
55 P. Vervoorts, C. L. Hobday, M. G. Ehrenreich, D. Daisenberger and G. Kieslich, *Z. Anorg. Allg. Chem.*, 2019, **645**, 970–974.
56 M. T. Wharmby, F. Niekiel, J. Benecke, S. Waitschat, H. Reinsch, D. Daisenberger, N. Stock and P. G. Yot, *Nanomaterials*, 2020, **10**, 1698.
57 A. U. Ortiz, A. Boutin, A. H. Fuchs and F.-X. Coudert, *J. Chem. Phys.*, 2013, **138**, 174703.
58 W. W. Schmahl, I. P. Swainson, T. Dove and A. Graeme-Barber, *Z. Kristallogr. – Cryst. Mater.*, 1992, **201**, 125–146.
59 K. D. Hammonds, M. T. Dove, A. P. Giddy, V. Heine and B. Winkler, *Am. Mineral.*, 1996, **81**, 1057–1079.
60 F. A. Son, K. M. Fahy, M. A. Gaidimas, C. S. Smoljan, M. C. Wasson and O. K. Farha, *Commun. Chem.*, 2023, **6**, 185.

## 2.4. Study IV: Tuning the Mechanical Properties of Molecular Perovskites by Controlling Framework Distortions *via* A-site Substitution

The substitution of atoms by organic molecules – realised in $ABX_3$ Molecular Perovskites on the A- and X-site – has opened up a new research dimension. In particular, the discovery of Molecular Perovskites with multifunctional responses to external stimuli, *e.g.* dicyanamide-based materials ($[A]B(C_2N_3)_3$), is now driving research that is both academically and technologically relevant for material design. Yet, the community is seeking to establish design principles and our understanding of how crystal chemistry factors and composition – *e.g.* network distortions and molecular substitution – dictate their macroscopic properties, such as the mechanical response, is only developing.

Herein, we showcase the design strategy of molecular substitution, *i.e.* A-site substitution, for tailoring material's functionalities. In this pursuit, we designed a new family of $[A]Ni(C_2N_3)_3$ materials with varying A-site cations, *i.e.* different alkylated piperidinium species ($A^+ = [C_9H_{20}N]^+$, $[C_{10}H_{22}N]^+$, $[C_{11}H_{24}N]^+$ and $[C_{11}H_{24}N]^+$). This series allowed us to study the templating role effect of $A^+$'s size and shape on the framework ($[Ni(C_2N_3)_3]^-$) distortions and its ramifications on the mechanical response while avoiding hydrogen bonding interactions. Therefore, we applied a combination of group theoretical considerations for framework distortion analysis of the ambient structures and HPPXRD experiments throughout hydrostatic conditions. Hence, we discovered a link between the distortion amplitude ($A_p$) of the $[Ni(C_2N_3)_3]^-$ network and the bulk modulus ($B$); where $B$ can be tuned with the choice of A-site cation. Further, the concept of molecular A-site solid solutions was applied to show the extent to which $A_p$ and $B$ can be fine-tuned. This study offers a blueprint of how framework distortion design *via* targeted chemical modifications of the molecular cation can be used to manipulate macroscopic properties for practical concerns such as mechanical behaviour and stability. We propose that the A-site shape – its asphericity character – is a directing factor for framework distortions and pressure responsiveness, which may inspire research on engineering-related coordination polymers.

S. M. Kronawitter conducted the bulk of experiments and data analysis with contributions to the PXRD analysis by S. Park and support on HPPXRD experiments at the beamline I15 (Diamond Light Source, UK) from S. A. Hallweger, E. Myatt, J. Pitcairn and D. Daisenberger. M. Drees performed DFT calculations. The project was conceived and designed by S. M. Kronawitter and G. Kieslich. G. Kieslich provided overarching academic guidance, project administration and financial support. M. J. Cliffe gave input for data validation. The manuscript

was written by S. M. Kronawitter and G. Kieslich and subsequently reviewed and edited by all co-authors.

Reprinted with permission from the Royal Society of Chemistry.

S. M. Kronawitter, S. Park, S. A. Hallweger, E. Myatt, J. Pitcairn, M. J. Cliffe, D. Daisenberger, M. Drees, G. Kieslich: Tuning the mechanical properties of molecular perovskites by controlling framework distortions *via* A-site substitution, *Mater. Adv.* **2024**, 10.1039/d4ma00587b

Materials Advances

ROYAL SOCIETY OF CHEMISTRY

PAPER

View Article Online
View Journal



Cite this: DOI: 10.1039/d4ma00587b

# Tuning the mechanical properties of molecular perovskites by controlling framework distortions *via* A-site substitution†

Silva M. Kronawitter,[a] Shinjoo Park,[a] Sebastian A. Hallweger,[a] Emily Myatt,[b] Jem Pitcairn,[b] Matthew J. Cliffe,[b] Dominik Daisenberger,[c] Markus Drees[a] and Gregor Kieslich *[a]

Received 6th June 2024,
Accepted 8th July 2024

DOI: 10.1039/d4ma00587b

rsc.li/materials-advances

Molecular perovskites are important materials in the area of barocalorics, improper ferroelectrics and ferroelastics, where the search for principles that link composition, structure and mechanical properties is a key challenge. Herein, we report the synthesis of a new series of dicyanamide-based molecular perovskites $[A]Ni(C_2N_3)_3$, where the A-site cation ($A^+$) is a range of alkylated piperidinium cations. We use this new family to explore how $A^+$ cations determine their mechanical response by measuring the bulk modulus (*B*) – using high-pressure powder X-ray diffraction. Within the series, we find a positive correlation between the network distortions of the pseudocubic $[Ni(C_2N_3)_3]^-$ network and *B*. Furthermore, we show that we can tune framework distortions, and therefore *B*, by synthesising A-site solid solutions. The applied methodology is a blueprint for linking framework distortions and mechanical properties in network materials and guides us toward principles for designing macroscopic properties *via* systematic compositional changes in molecular perovskites.



## Introduction

The substitution of atoms by molecules in the structure motifs of all-inorganic materials is a powerful approach for designing new materials. It opens up a large chemical design space for studying application-oriented[1] and fundamental[2] structure–property relationships, while still allowing the use of established principles[3] from inorganic solid-state chemistry to guide materials discovery. For instance, in coordination polymers that crystallise in an $AMX_3$ perovskite motif, such as $[CH_3NH_3]Mn(N_3)_3$[4] and $[C_{10}H_{20}N]Cd(C_2N_3)_3$,[5] here referred to as molecular perovskites, properties such as ferroelastic,[6] (improper) ferroelectric[1,7,8] and multiferroic[9,10] behaviour, their glass-forming abilities[11,12] and their application as barocalorics[13,14] are linked to the molecular nature of the A- and X-site. In molecular perovskites, a $ReO_3$-type $[MX_3]^-$ network is formed by the M-site cation ($M^{2+}$) and X-site anion ($X^-$) with the A-site cation ($A^+$) sitting in the void of the pseudocubic $[MX_3]^-$ network for charge balance (Fig. 1).

In molecular perovskites, the use of molecular ions as building units introduces new chemical and structural degrees

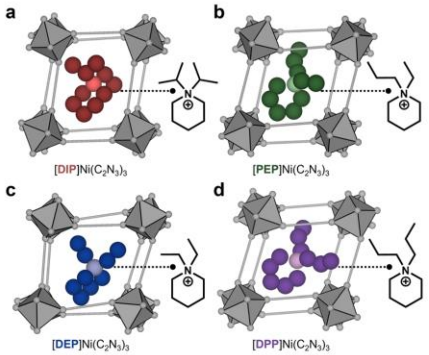


Fig. 1 Schematic of the perovskite structure of $[A]Ni(C_2N_3)_3$ materials studied in this work. Emphasis is given to the various $A^+$ cations $[DIP]^+$ (a), $[PEP]^+$ (b), $[DEP]^+$ (c) and $[DPP]^+$ (d), as incorporated in the distorted 3D $ReO_3$-type $[Ni(C_2N_3)_3]^-$ network. C atoms are shown in the darker colour, N atoms in the lighter colour, distorted $NiN_6$ octahedra in grey. The $X^- = [C_2N_3]^-$ are simplified as linear linker shown as grey bars and H atoms are not shown for clarity.

[a] Department of Chemistry, TUM School of Natural Sciences, Technical University of Munich, Lichtenbergstraße 4, 85748 Garching, Germany. E-mail: gregor.kieslich@tum.de
[b] School of Chemistry, University of Nottingham, Nottingham NG7 2RD, UK
[c] Diamond Light Source Ltd., Diamond House, Harwell Campus, Didcot OX11 ODE, UK

† Electronic supplementary information (ESI) available: Details to material synthesis and characterisation (SCXRD, PXRD, NMR, TGA, DSC, HPPXRD and DFT). CCDC 2309035, 2309036, 2309038, 2309039, 2309042, 2309043, 2309049 and 2309050. For ESI and crystallographic data in CIF or other electronic format see DOI: https://doi.org/10.1039/d4ma00587b

of freedom that can couple to external stimuli,[15,16] producing phenomena such as temperature and pressure-driven A-site order–disorder phase transitions,[17,18] unconventional octahedral tilts and shifts that can couple to break inversion symmetry,[1,19,20] melting processes as a response to heating[11] and a new type of polymorphism.[21] Given their role as model systems for understanding structure–property relationships,[1,22] investigating their mechanical properties, such as the bulk modulus (*B*), Young's modulus, hardness and material stability, becomes increasingly important. Since the material's crystal chemistry ultimately determines its properties, studies related to the mechanical properties address both our fundamental interest in the search for structure–property principles and operational concerns such as material processability and material longevity. Furthermore, a low *B* has recently been implicated to improve the barocaloric performance in molecular materials.[23] The compositional variability of molecular perovskites enables us,[24] therefore, to identify the underlying structure chemical principles that determine *B*, and therewith, to enhance a material's solid-state cooling performance.

A few principles of how composition determines the mechanical properties of molecular perovskites have already been established. For instance, nanoindentation and high-pressure diffraction studies on materials such as $[(CH_3)_2NH_2]M(HCOO)_3$ (with $M^{2+}$ = $Ni^{2+}$, $Co^{2+}$, $Zn^{2+}$ and $Mn^{2+}$),[25,26] $[C(NH_2)_3]M(HCOO)_3$ (with $M^{2+}$ = $Co^{2+}$ and $Mn^{2+}$)[27] and $[Pr_4N]M(C_2N_3)_3$ (with $[Pr_4N]^+$ = tetrapropylammonium, $M^{2+}$ = $Ni^{2+}$, $Co^{2+}$ and $Mn^{2+}$)[28] have demonstrated that a smaller size of $M^{2+}$ paired with a larger ligand field stabilisation energy (LFSE) leads to a larger Young's modulus and *B*. These findings agree with our recent results, where we observed a decreasing *B* as a function of increasing Shannon ionic radius of $M^{2+}$.[29]

Looking at the role of $A^+$, its capability to form hydrogen bonding interactions[20,30] (HBIs) to the $[MX_3]^-$ network has been found to be an important factor. For instance, the mechanical properties are tunable across the solid solution $[NH_3NH_2]_{1-x}[NH_3OH]_xZn(HCOO)_3$[31] *via* HBIs, *i.e.* the choice of $A^+$.[32,33] More recently, this strategy has been used to introduce ferroelasticity in $[Et_3P(CH_2)_2Cl]_{1-x}[Et_3P(CH_2)_2F]_xMn(C_2N_3)_3$.[34] Yet, our understanding of the interplay between the $A^+$ and active framework distortions of the $[MX_3]^-$ is only developing.[35–38]

In the pursuit to fill this gap, we have synthesised a new series of $[A]Ni(C_2N_3)_3$ molecular perovskites with $A^+$ = diisopropyl-piperidinium ($[DIP]^+$ = $[C_{11}H_{24}N]^+$), ethyl-propyl-piperidinium ($[PEP]^+$ = $[C_{10}H_{22}N]^+$), diethyl-piperidinium ($[DEP]^+$ = $[C_9H_{20}N]^+$) and dipropyl-piperidinium ($[DPP]^+$ = $[C_{11}H_{24}N]^+$) (Fig. 1). The absence of acidic hydrogen atoms in all $A^+$ excludes contributions from HBIs. Furthermore, by keeping $M^{2+}$ = $Ni^{2+}$ in the series, we have minimised the effect of $M^{2+}$ cation size and LFSE, and hence, the chemical bond strength in the $[Ni(C_2N_3)_3]^-$ network on the structure and properties of the molecular perovskites. Therefore, this series allows us to isolate the impact of the size and shape of the $A^+$ cation on the distortions of the 3D $[MX_3]^-$ network and their ramifications on the mechanical properties, which we measured *via* high-pressure powder X-ray diffraction (HPPXRD) by using *B* as a proxy. In addition – by employing a solid solution approach – we investigated to which extent *B* can be fine-tuned *via* $A^+$ substitution.

## Results and discussion

### Synthesis and characterisation

In the first step, we designed a range of $A^+$ to produce a series of molecular perovskites that can be used to determine how structural and pressure responsive properties are altered by small chemical changes. In this pursuit, we synthesised a series of piperidinium derivatives ($[DIP]^+$, $[PEP]^+$, $[DEP]^+$ and $[DPP]^+$), where different alkyl chain modifications of the piperidinium nitrogen enable studying the impact of small variations in size and/or shape (Fig. 1). All $A^+$ were synthesised *via* nucleophilic substitution of halides, see ESI† for details (Fig. S1–S5 and S11–S18). For instance, $[DEP]^+$ was obtained from the reaction of diethylamine and 1,5-dibromopentane in acetonitrile. Single crystals of the $[A]Ni(C_2N_3)_3$ series were obtained by a mild-solution crystallisation route that has previously been used for the synthesis of related materials,[5,21] see ESI† for details (S-5). In a typical reaction, the precursor materials [A]Br, $Na(C_2N_3)$ and $Ni(NO_3)_2{\cdot}6H_2O$ are dissolved in water, mixed and then left to crystallise overnight in a refrigerator. An overview of all synthesised compounds in this work is given in Table 1.

Single crystal X-ray diffraction (SCXRD) at 100 and 300 K was used to determine the structure of all perovskite materials. All compounds in the $[A]Ni(C_2N_3)_3$ series crystallise with the targeted $AMX_3$ perovskite structure (Fig. 1). $[DIP]Ni(C_2N_3)_3$, $[PEP]Ni(C_2N_3)_3$ and $[DEP]Ni(C_2N_3)_3$ crystallise in the monoclinic space group $P2_1/c$, see ESI† for details of data collection and crystal structure solution (S-7, Tables S1–S3 and Fig. S7–S9). In contrast, $[DPP]Ni(C_2N_3)_3$ crystallises in the space group $C2/c$ (Table S4 and Fig. S10, ESI†). To quantify the extent of network distortions across the series, we have applied an established group theoretical analysis[39–41] to SCXRD data of 300 K for all compounds. In this approach, the structures are first simplified to the underlying octahedral network and subsequently compared to an idealised cubic parent network. By using ISODISTORT,[40] the active distortions are then identified and described *via* their irreducible representation and amplitude. The latter enables the calculation

Table 1 $A^+$ size and shape as captured by the volume of $A^+$ ($V_{A^+}$) and the globularity factor (*G*); both were calculated *via* CrystalExplorer17 based on 300 K SCXRD data. $V_{cell}$ is the crystallographic volume of SCXRD data at 300 K. $A_p$ is the parent-cell normalised distortion amplitude as a measure for framework distortions. The bulk moduli (*B*) calculated *via* EOSFit and volumes ($V_0$, at zero pressure and temperature) obtained from experimental HPPXRD are also shown

| $[A]Ni(C_2N_3)_3$ | $A^+$ = $[DIP]^+$ | $[PEP]^+$ | $[DEP]^+$ | $[DPP]^+$ |
|---|---|---|---|---|
| $V_{A^+}$/Å$^3$ | 227.25 | 202.18 | 190.56 | 225.87 |
| *G* | 0.87 | 0.83 | 0.88 | 0.81 |
| Space group | $P2_1/c$ | $P2_1/c$ | $P2_1/c$ | $C2/c$ |
| $V_{cell}$/Å$^3$ | 2163.4(5) | 2028.08(14) | 2021.16(14) | 2079.38(10) |
| $A_p$/Å | 1.81 | 2.01 | 2.10 | 4.23 |
| $B(2^{nd})$/GPa | 8.2 ± 0.1 | 8.5 ± 0.1 | 8.8 ± 0.2 | 10.5 ± 0.2 |
| $V_0(2^{nd})$/Å$^3$ | 2157.1 ± 0.5 | 2030.3 ± 0.6 | 2025.9 ± 0.2 | 2073.8 ± 0.6 |

of the overall parent-cell normalised distortion amplitude of the network ($A_p$), providing a rigorous measure for network distortions across our series, see Table 1 for $A_p$ values of the different compounds at 300 K and ESI† for further tilt analysis details (S-69 and Table S22–S24).

To determine relationships between the size and shape of $A^+$ and the resulting network distortions (Fig. 1), atomic coordinates from SCXRD data at 300 K were used to extract the geometry of $A^+$. Following previous reports,[42] we use the globularity ($G$) as a measure for the asphericity of $A^+$, where $G = 1$ for a sphere. For this, we used DFT calculations to obtain the $A^+$ surface ($S_{m,A^+}$), the $A^+$ volume ($V_{A^+}$) as enclosed by $S_{m,A^+}$, and the surface of an idealised sphere ($S_{sp,A^+}$) with $V_{A^+}$ (Table S27, ESI†). Then, the $A^+$ globularity ($G = S_{sp,A^+}/S_{m,A^+}$) was calculated (Table 1). By using CrystalExplorer17,[43] we obtained $G > 0.8$ for all $A^+$, which agrees with previous results from the literature for $A^+$ of dicyanamide-based molecular perovskites.[42] A similar trend in $G$ with slightly smaller values is obtained when using Gaussian16[44] for calculating $S_{m,A^+}$, $S_{sp,A^+}$ and $V_{A^+}$, see ESI† for details (Tables S27 and S30). No correlation between $A_p$, $V_{A^+}$ and $G$ is observed (Table 1), while the importance of $G$ in dictating $A_p$ becomes apparent when considering $[DPP]^+$ and $[DIP]^+$. Both cations have a similar $V_{A^+}$ but are different in $G$. $[DPP]^+$ shows the significantly smaller $G$, and among the here investigated series of $[A]Ni(C_2N_3)_3$, the $A_p$ of $[DPP]Ni(C_2N_3)_3$ is by far the largest. Therefore, we hypothesise that the observed network distortions in $[DPP]Ni(C_2N_3)_3$ are a direct ramification of the interplay between $A^+$ and the 3D $[Ni(C_2N_3)_3]^-$ network, highlighting the templating role of $A^+$ and the possibility of tuning network distortions *via* chemical modifications on $A^+$. For instance, for symmetric functionalisation of the piperidine backbone, we find $A_p$ increasing with the length of the alkyl chains, *e.g.* from ethyl ($[DEP]^+$) to propyl ($[DPP]^+$). Hence, small alkyl chain modifications on the nitrogen atom of piperidinium, and thus its shape, evidently have an impact on $A_p$ of the 3D $[Ni(C_2N_3)_3]^-$ network (Fig. 1) and, as we will see in the following, on the resulting pressure responsiveness.

The phase purity of powder samples of $[A]Ni(C_2N_3)_3$ was verified using laboratory PXRD and Pawley analysis (Fig. S28–S31, ESI†). Furthermore, thermal analysis (TGA/DSC) showed decomposition temperatures ($T_d$) between 570 and 600 K (Fig. S20–S23, ESI†). These are at the upper end of previously reported $T_d$ of dicyanamide-based molecular perovskites.[21,45,46] In parts, we rationalise this by the stability of the here employed $A^+$, which has previously been suggested as an important factor determining $T_d$;[47] however, $T_d$ is a generally complex quantity, which depends upon many parameters, including crystal chemistry factors and analytic concerns.[45,48,49] In the DSC curves, several heat events related to 1st and 2nd order phase transitions were observed (Fig. S24–S27, ESI†), while no evidence of melting before $T_d$ was found;[11] however, the nature of these phase transitions is beyond the focus of this study. Here, we employ our new $[A]Ni(C_2N_3)_3$ family as model compounds to study the relation between $A^+$ and $B$.

### Molecular perovskites under high pressure

HPPXRD was used to obtain $B$ for all compounds (Table 1). Given the expected subtle differences in the materials' pressure response, we have used a custom-built HPPXRD setup[50] to collect HPPXRD data with finely spaced pressure points, step size of $\Delta p = 0.02$ GPa, up to a maximum pressure of $p_{max.} = 0.4$ GPa (Fig. 2 and Fig. S34–S37, ESI†). Visual inspection of the HPPXRD data (Fig. 2) reveals pressure-driven phase transitions at pressures of $p_{trs.} = 0.3$ GPa ($[DIP]Ni(C_2N_3)_3$), $p_{trs.} = 0.28$ GPa ($[PEP]Ni(C_2N_3)_3$) and $p_{trs.} = 0.3$ GPa ($[DEP]Ni(C_2N_3)_3$). Accordingly, Pawley profile fits[51] were performed up to $p_{trs.}$, or $p_{max.} = 0.4$ GPa for $[DPP]Ni(C_2N_3)_3$, for obtaining lattice parameters and $V(p)$ data, see ESI† for full details of the Pawley profile fits (Tables S11–S14 and Fig. S47–S50). $B$ was calculated for each $[A]Ni(C_2N_3)_3$ compound by fitting a Birch–Murnaghan (B–M) equation of state to the $V(p)$ data. For a better comparison with literature data, both 2nd and 3rd order B–M equation of state fits were performed using EOSFit,[52] see ESI† for the results and all fits of the $V(p)$ and $F(f)$ plots (Fig. S64–S67). Similar results were obtained by using PASCal (Table S28, ESI†).[53] Only fits using 2nd order B–M equation of state show standard errors in fitted $B$ comparable to those observed for the standard material $Ni(dmgH)_2$ ($dmgH^-$ = dimethylglyoximate), $\sigma B = \pm 0.09$ GPa. Much larger uncertainties for a 3rd order B–M fit suggest overparametrisation, see ESI† (S-66).

We observe a monotonically decreasing $B$ along the series $B$ ($A^+ = [DPP]^+$) = 10.5 ± 0.2 GPa, $B$ ($A^+ = [DEP]^+$) = 8.8 ± 0.2 GPa, $B$ ($A^+ = [PEP]^+$) = 8.5 ± 0.1 GPa and $B$ ($A^+ = [DIP]^+$) = 8.2 ± 0.1 GPa. We would like to note that deriving $B$ by using the same pressure range for each compound results in the same trend but with a slightly larger $\sigma$. Across the here investigated series of compounds, we find a correlation between $A_p$ and $B$ (Fig. 3). The more distorted the framework is at $p$ = ambient, the stiffer it is (Table 1). Since framework distortions summarised in $A_p$ are some of the lowest-energy pathways for pressure-induced structural changes, a smaller $A_p$ provides a larger margin for pressure-induced network distortions as a response to

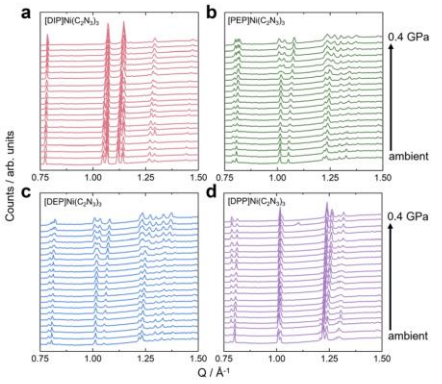


Fig. 2 HPPXRD data ($\lambda$ = 0.4246 Å) of $[A]Ni(C_2N_3)_3$ with $A^+ = [DIP]^+$ (a), $[PEP]^+$ (b), $[DEP]^+$ (c), and $[DPP]^+$ (d), collected in the pressure range between ambient pressure and 0.4 GPa. The data are shown as stacking plots, where intensities have been normalised.

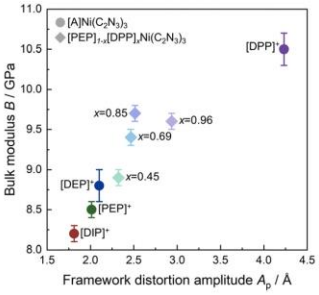


Fig. 3 Bulk modulus ($B$) including error bars as a function of the parent-cell normalised amplitude over all active framework distortion modes ($A_p$) for the $[A]Ni(C_2N_3)_3$ family with varying $A^+$ and molecular solid solutions $[PEP]_{1-x}[DPP]_xNi(C_2N_3)_3$.

hydrostatic pressure, and thus a larger compressibility, *i.e.* a smaller $B$. This interpretation links $A_p(\uparrow)$ and $B(\uparrow)$ along the $[A]Ni(C_2N_3)_3$ series, providing a heuristic understanding of the observed pressure response within this series (Fig. 3). Given that $A_p$ is very sensitive to chemical functionalisation of the piperidine backbone, we here show that chemical changes of $A^+$ are highly effective for manipulating $B$.

We note that using $A_p$ as a measure for available distortion pathways only accounts for distortion energies when treating the 3D framework isolated from $A^+$. Any directional interactions, such as HBIs between $A^+$ and the 3D network, give $A^+$ a more active role and thus produce larger variability in $B$, as found in $[(CH)_3NH_2]M(HCOO)_3$ ($M^{2+}$ = $Mn^{2+}$, $Fe^{2+}$ and $Cu^{2+}$)[54] and $[C(NH_2)_3]M(HCOO)_3$ ($M^{2+}$ = $Mn^{2+}$, $Co^{2+}$ and $Cd^{2+}$),[55,56] with $B$ varying between 21.3 and 27.2 GPa. HBIs thus strengthen the overall framework by making any network distortions energetically more demanding, resulting in an increase of $B$ overall.

Furthermore, considering the series $[(C_3H_7)_3CH_3N]M(C_2N_3)_3$ with varying framework cation $M^{2+}$ ($M^{2+}$ = $Mn^{2+}$, $Co^{2+}$ and $Ni^{2+}$) where $A_p$ decreases but $B$ increases,[29] *e.g.* $B$ ($M^{2+}$ = $Mn^{2+}$) = 7.1 ± 0.2 GPa and $A_p$ ($M^{2+}$ = $Mn^{2+}$) = 2.36, $B$ ($M^{2+}$ = $Co^{2+}$) = 9.9 ± 0.3 GPa and $A_p$ ($M^{2+}$ = $Co^{2+}$) = 2.17 and $B$ ($M^{2+}$ = $Ni^{2+}$) = 10.9 ± 0.2 GPa and $A_p$ ($M^{2+}$ = $Ni^{2+}$) = 2.09, it is evident that crystal chemistry factors other than $A_p$ can be decisive in determining $B$. For instance, when going from $Mn^{2+}$ to $Co^{2+}$ and $Ni^{2+}$, the 3D network is stiffened and overall, $B$ increases. Any network distortions increase in energy, and thus, $A_p$ is reduced, making the change in chemical bond strength the dominating factor in this comparison.

### Bulk moduli of A-site solid solutions

To further explore the tunability of $B$ *via* targeted changes of $A_p$, we have synthesised the solid solutions $[PEP]_{1-x}[DPP]_xNi(C_2N_3)_3$ with $x$ = 0, 0.45, 0.69, 0.85, 0.96 and 1. For their synthesis, the stoichiometry of precursor salts [PEP]Br and [DPP]Br has been varied and mixed with $Na(C_2N_3)$ and $Ni(NO_3)_2{\cdot}6H_2O$ in water as a solvent, see ESI† (S-6). Independent of the applied precursor stoichiometry, we only obtained members of the solid solution with $x \geq 0.45$. In previous studies, a full solid solution, *i.e.* $0 \leq x \leq 1$, has only been found in one example where chemically similar $A^+$ were used.[34] Therefore, we rationalise the here observed $x$ range by the difference in crystallisation kinetics due to the chemical difference of $A^+$. $^1$H NMR spectroscopy on acid-digested samples has been used to determine the chemical composition $x$ (Table S9 and Fig. S19, ESI†). We confirmed the formation of a solid solution using laboratory PXRD measurements of a mixture of the parent materials $[PEP]Ni(C_2N_3)_3$ and $[DPP]Ni(C_2N_3)_3$ (Fig. S32, ESI†). We determined the lattice parameters using Pawley refinements, using $P2_1/c$ for $x$ = 0 – 0.96 (Fig. S44 and S51–S54, ESI†) and $C2/c$ for $x$ = 1 (Fig. S46, ESI†). We observe a monotonic expansion of the volume from 2029.7(4) Å$^3$ ($x$ = 0) to 2076.9(4) Å$^3$ ($x$ = 1) with increasing $x$ at ambient pressure (Table S15, ESI†).

We then used HPPXRD, using the same methodology, to determine $B$ as a function of $x$ (Fig. S68–S71, ESI†). Within standard errors, we observe an increasing $B$ as a function of $x$ in $[PEP]_{1-x}[DPP]_xNi(C_2N_3)_3$ (Tables S20 and S29, ESI†). This points at a close to ideal solid solution behaviour[57] and suggests the absence of strong coupling effects,[58] *e.g.* behaviour that could arise from the ordering of $[PEP]^+$ and $[DPP]^+$.

Furthermore, we have performed Rietveld-based structural refinements for $x$ = 0.45, 0.69, 0.85 and 0.96 based on a simplified structural model for extracting the network geometry and framework distortion modes, see ESI† for the employed strategy of structure refinement (S-59) and for results (Table S26). Visual inspection of the PXRD pattern and differences curve of the Rietveld fits suggests that the results should be treated with care; however, for all compounds, $A_p$ lies between 2.013 ($x$ = 0) and 4.232 ($x$ = 1), suggesting tunability of $A_p$ *via* $A^+$ substitution (Fig. 3). Thus, by employing the solid solution approach, it is possible to fine-tune $B$ in a window as fine as $B$ = 8.5 ($x$ = 0) – 10.5 ($x$ = 1) GPa.

## Conclusion

In conclusion, we have synthesised a new series of $[A]Ni(C_2N_3)_3$ molecular perovskites, showing that framework distortions are sensitive towards small chemical changes of $A^+$. Subsequently, we applied this series to establish a link between the size and globularity of $A^+$, the active distortion modes in the $[Ni(C_2N_3)_3]^-$ framework and the pressure responsiveness of the molecular perovskites for the first time. In the absence of HBIs and changes in chemical bond strength within the network, we conclude that $A_p$ is the decisive parameter in defining the compressibility of a molecular perovskite. Additionally, we show tunability of $A_p$, and thus $B$, through the synthesis of A-site solid solutions. Such a tunability of $B$ *via* chemical modifications advances our understanding of underlying composition–structure–property relations and paves the way for the targeted design of molecular perovskites' mechanical properties for applications such as barocalorics.[13,23] Additionally, the here applied methodology to link network distortions and the pressure responsiveness is of general nature, with implications

for the analysis of the high-pressure responsiveness of closely related material families, including metal–organic frameworks, covalent organic frameworks and hydrogen-bonded frameworks.

Focusing on molecular perovskites, our results have important ramifications on how to think and approach the challenge of designing molecular perovskites with targeted mechanical properties and, more generally, targeted network distortions. Evidently, $A^+$ templates framework distortions, and when aiming for large distortions, $A^+$ should be chosen that largely diverges from a sphere. For $A^+$ based on alkylated ammonium or phosphonium, a chemical functionalisation that enables the formation of conformers with large anisotropies seems fruitful. This suggests the use of a more rigorous conformational analysis prior to the synthesis of $A^+$ cations.[59] In parallel, robust criteria for describing the asphericity of $A^+$ should be tested, where we consider $G$ as an important yet only qualitative measure since any templating effect can be expected to be related to asphericity and volume. Such developments have the potential to bring related fields to fruition, such as the targeted design of active distortion modes, with implications for the synthesis of improper ferroelectrics.[1]

## Author contributions

S. M. Kronawitter: methodology, validation, formal analysis, investigation, data curation, writing – original draft, review and editing, visualisation. S. Park: data curation, investigation. S. A. Hallweger, E. Myatt, J. Pitcairn, M. J. Cliffe, D. Daisenberger: investigation, review and editing. G. Kieslich: conceptualisation, writing – review and editing, supervision, resources, project administration.

## Data availability

The data supporting this article have been included as part of the ESI.† Furthermore, all crystallographic data have been deposited at the CCDC, see 2309035, 2309036, 2309038, 2309039, 2309042, 2309043, 2309049 and 2309050.

## Conflicts of interest

There are no conflicts to declare.

## Acknowledgements

We want to acknowledge beamtime at the Diamond Light Source (UK), Beamline I15 (CY30815-2). S. M. K., S. A. H. and G. K. acknowledge support from the DFG through research grants (450070835, 493871295) and the Heisenberg program (524525093). Thanks to Melvin Resch for his contributions to the synthesis of the solid solutions.

## Notes and references

1 H. L. B. Boström, M. S. Senn and A. L. Goodwin, *Nat. Commun.*, 2018, **9**, 2380.
2 S. Yuan, A. Stroppa and A. E. Phillips, *APL Mater.*, 2023, **11**, 061114.
3 G. Kieslich, S. Sun and A. K. Cheetham, *Chem. Sci.*, 2014, **5**, 4712–4715.
4 X.-H. Zhao, X.-C. Huang, S.-L. Zhang, D. Shao, H.-Y. Wei and X.-Y. Wang, *J. Am. Chem. Soc.*, 2013, **135**, 16006–16009.
5 S. Burger, S. Kronawitter, H. L. B. Boström, J. K. Zaręba and G. Kieslich, *Dalton Trans.*, 2020, **49**, 10740–10744.
6 Z.-B. Liu, L. He, P.-P. Shi, Q. Ye and D.-W. Fu, *J. Phys. Chem. Lett.*, 2020, **11**, 7960–7965.
7 K. Li, Z.-G. Li, J. Xu, Y. Qin, W. Li, A. Stroppa, K. T. Butler, C. J. Howard, M. T. Dove, A. K. Cheetham and X.-H. Bu, *J. Am. Chem. Soc.*, 2022, **144**, 816–823.
8 A. Sieradzki, M. Mączka, M. Simenas, J. K. Zaręba, A. Gągor, S. Balciunas, M. Kinka, A. Ciupa, M. Nyk, V. Samulionis, J. Banys, M. Paluch and S. Pawlus, *J. Mater. Chem. C*, 2018, **6**, 9420–9429.
9 P. Jain, V. Ramachandran, R. J. Clark, H. D. Zhou, B. H. Toby, N. S. Dalal, H. W. Kroto and A. K. Cheetham, *J. Am. Chem. Soc.*, 2009, **131**, 13625–13627.
10 A. Stroppa, P. Barone, P. Jain, J. M. Perez-Mato and S. Picozzi, *Adv. Mater.*, 2013, **25**, 2284–2290.
11 B. K. Shaw, A. R. Hughes, M. Ducamp, S. Moss, A. Debnath, A. F. Sapnik, M. F. Thorne, L. N. McHugh, A. Pugliese, D. S. Keeble, P. Chater, J. M. Bermudez-Garcia, X. Moya, S. K. Saha, D. A. Keen, F.-X. Coudert, F. Blanc and T. D. Bennett, *Nat. Chem.*, 2021, **13**, 778–785.
12 S. M. Kronawitter, S. A. Hallweger, J. Meyer, C. Pedri, S. Burger, A. Alhadid, S. Henke and G. Kieslich, *APL Mater.*, 2023, **11**, 31119.
13 J. M. Bermúdez-García, M. Sánchez-Andújar, S. Castro-García, J. López-Beceiro, R. Artiaga and M. A. Señarís-Rodríguez, *Nat. Commun.*, 2017, **8**, 15715.
14 J. Salgado-Beceiro, A. Nonato, R. X. Silva, A. García-Fernández, M. Sánchez-Andújar, S. Castro-García, E. Stern-Taulats, M. A. Señarís-Rodríguez, X. Moya and J. M. Bermúdez-García, *Mater. Adv.*, 2020, **1**, 3167–3170.
15 H. L. B. Boström and A. L. Goodwin, *Acc. Chem. Res.*, 2021, **54**, 1288–1297.
16 C. L. Hobday and G. Kieslich, *Dalton Trans.*, 2021, **50**, 3759–3768.
17 W. Wei, W. Li, K. T. Butler, G. Feng, C. J. Howard, M. A. Carpenter, P. Lu, A. Walsh and A. K. Cheetham, *Angew. Chem., Int. Ed.*, 2018, **57**, 8932–8936.
18 R. X. Silva, R. R. Hora, A. Nonato, A. García-Fernández, J. Salgado-Beceiro, M. A. Señarís-Rodríguez, M. S. Andújar, A. P. Ayala and C. W. A. Paschoal, *Spectrochim. Acta, Part A*, 2023, **289**, 122198.
19 S. G. Duyker, J. A. Hill, C. J. Howard and A. L. Goodwin, *J. Am. Chem. Soc.*, 2016, **138**, 11121–11123.
20 M. Mączka, M. Kryś, S. Sobczak, D. L. M. Vasconcelos, P. T. C. Freire and A. Katrusiak, *J. Phys. Chem. C*, 2021, **125**, 26958–26966.
21 S. Burger, S. Grover, K. T. Butler, H. L. B. Boström, R. Grau-Crespo and G. Kieslich, *Mater. Horiz.*, 2021, **8**, 2444–2450.
22 D. Boldrin, *Appl. Phys. Lett.*, 2021, **118**, 170502.

23 B. Li, Y. Kawakita, S. Ohira-Kawamura, T. Sugahara, H. Wang, J. Wang, Y. Chen, S. I. Kawaguchi, S. Kawaguchi, K. Ohara, K. Li, D. Yu, R. Mole, T. Hattori, T. Kikuchi, S.-I. Yano, Z. Zhang, Z. Zhang, W. Ren, S. Lin, O. Sakata, K. Nakajima and Z. Zhang, *Nature*, 2019, **567**, 506–510.
24 J. M. Bermúdez-García, M. Sánchez-Andújar and M. A. Señarís-Rodríguez, *J. Phys. Chem. Lett.*, 2017, **8**, 4419–4423.
25 J.-C. Tan, P. Jain and A. K. Cheetham, *Dalton Trans.*, 2012, **41**, 3949–3952.
26 S. Sobczak, A. Chitnis, M. Andrzejewski, M. Mączka, S. Gohil, N. Garg and A. Katrusiak, *CrystEngComm*, 2018, **20**, 5348–5355.
27 G. Feng, D. Gui and W. Li, *Cryst. Growth Des.*, 2018, **18**, 4890–4895.
28 L.-J. Ji, S.-J. Sun, Y. Qin, K. Li and W. Li, *Coord. Chem. Rev.*, 2019, **391**, 15–29.
29 S. Grover, S. Burger, K. T. Butler, K. Hemmer, P. Vervoorts, G. Kieslich and R. Grau-Crespo, *CrystEngComm*, 2023, **25**, 3439–3444.
30 K. L. Svane, A. C. Forse, C. P. Grey, G. Kieslich, A. K. Cheetham, A. Walsh and K. T. Butler, *J. Phys. Chem. Lett.*, 2017, **8**, 6154–6159.
31 G. Kieslich, S. Kumagai, A. C. Forse, S. Sun, S. Henke, M. Yamashita, C. P. Grey and A. K. Cheetham, *Chem. Sci.*, 2016, **7**, 5108–5112.
32 W. Li, A. Thirumurugan, P. T. Barton, Z. Lin, S. Henke, H. H.-M. Yeung, M. T. Wharmby, E. G. Bithell, C. J. Howard and A. K. Cheetham, *J. Am. Chem. Soc.*, 2014, **136**, 7801–7804.
33 G. Kieslich, A. C. Forse, S. Sun, K. T. Butler, S. Kumagai, Y. Wu, M. R. Warren, A. Walsh, C. P. Grey and A. K. Cheetham, *Chem. Mater.*, 2016, **28**, 312–317.
34 L. He, P.-P. Shi, M.-M. Zhao, C.-M. Liu, W. Zhang and Q. Ye, *Chem. Mater.*, 2021, **33**, 799–805.
35 I. E. Collings, J. A. Hill, A. B. Cairns, R. I. Cooper, A. L. Thompson, J. E. Parker, C. C. Tang and A. L. Goodwin, *Dalton Trans.*, 2016, **45**, 4169–4178.
36 M. Mączka, S. Sobczak, M. Kryś, F. F. Leite, W. Paraguassu and A. Katrusiak, *J. Phys. Chem. C*, 2021, **125**, 10121–10129.
37 A. Sieradzki, A. Nowok, S. Sobczak, K. Roszak, A. Szeremeta, M. Maczka, A. Katrusiak and S. Pawlus, *Research Square*, 2023, DOI: **10.21203/rs.3.rs-3657532/v1**.
38 J. Y. Lee, S. Ling, S. P. Argent, M. S. Senn, L. Cañadillas-Delgado and M. J. Cliffe, *Chem. Sci.*, 2021, **12**, 3516–3525.
39 H. T. Stokes, D. M. Hatch and B. J. Campbell, *ISODISTORT, ISOTROPY Software Suite*, **https://iso.byu.edu**.
40 B. J. Campbell, H. T. Stokes, D. E. Tanner and D. M. Hatch, *J. Appl. Crystallogr.*, 2006, **39**, 607–614.
41 H. L. B. Boström, *CrystEngComm*, 2020, **22**, 961–968.
42 J. García-Ben, A. García-Fernández, P. Dafonte-Rodríguez, I. Delgado-Ferreiro, U. B. Cappel, S. Castro-García, M. Sánchez-Andújar, J. M. Bermúdez-García and M. A. Señarís-Rodríguez, *J. Solid State Chem.*, 2022, **316**, 123635.
43 P. R. Spackman, M. J. Turner, J. J. McKinnon, S. K. Wolff, D. J. Grimwood, D. Jayatilaka and M. A. Spackman, *J. Appl. Crystallogr.*, 2021, **54**, 1006–1011.
44 M. J. Frisch, G. W. Trucks and H. B. Schlegel, *Gaussian 16 Rev. B.01*, Wallingford, CT, 2016.
45 J. García-Ben, L. N. McHugh, T. D. Bennett and J. M. Bermúdez-García, *Coord. Chem. Rev.*, 2022, **455**, 214337.
46 L. Zhou, X. Zheng, P.-P. Shi, Z. Zafar, H.-Y. Ye, D.-W. Fu and Q. Ye, *Inorg. Chem.*, 2017, **56**, 3238–3244.
47 C. Ye, L. N. McHugh, C. Chen, S. E. Dutton and T. D. Bennett, *Angew. Chem., Int. Ed.*, 2023, **62**, e202302406.
48 Y. Wang and W. J. Thomson, *Thermochim. Acta*, 1995, **255**, 383–390.
49 N. Khan, D. Dollimore, K. Alexander and F. Wilburn, *Thermochim. Acta*, 2001, **367–368**, 321–333.
50 N. J. Brooks, B. L. L. E. Gauthe, N. J. Terrill, S. E. Rogers, R. H. Templer, O. Ces and J. M. Seddon, *Rev. Sci. Instrum.*, 2010, **81**, 64103.
51 G. S. Pawley, *J. Appl. Crystallogr.*, 1981, **14**, 357–361.
52 J. Gonzalez-Platas, M. Alvaro, F. Nestola and R. Angel, *J. Appl. Crystallogr.*, 2016, **49**, 1377–1382.
53 M. J. Cliffe and A. L. Goodwin, *J. Appl. Crystallogr.*, 2012, **45**, 1321–1329.
54 I. E. Collings, M. Bykov, E. Bykova, M. Hanfland, S. van Smaalen, L. Dubrovinsky and N. Dubrovinskaia, *CrystEngComm*, 2018, **20**, 3512–3521.
55 Z. Yang, G. Cai, C. L. Bull, M. G. Tucker, M. T. Dove, A. Friedrich and A. E. Phillips, *Philos. Trans. R. Soc., A*, 2019, **377**, 20180227.
56 H. Gao, C. Li, L. Li, W. Wei, Y. Tan and Y. Tang, *Dalton Trans.*, 2020, **49**, 7228–7233.
57 K. T. Jacob, S. Raj and L. Rannesh, *Int. J. Mater. Res*, 2007, **98**, 776–779.
58 N. L. Evans, P. M. M. Thygesen, H. L. B. Boström, E. M. Reynolds, I. E. Collings, A. E. Phillips and A. L. Goodwin, *J. Am. Chem. Soc.*, 2016, **138**, 9393–9396.
59 A. M. Mroz, L. Turcani and K. E. Jelfs, *Electron. Struct.*, 2023, **5**, 45004.

# 3. CONCLUSION AND OUTLOOK

The research studies documented here focus on advancing our understanding of structure-composition-property relationships in coordination polymers (Figure 10). To achieve this, different conceptual and experimental approaches were applied to MOFs and Molecular Perovskites to follow changes in the chemical composition on the resulting structure and, hence, on the macroscopic properties. This again highlights the remarkable role of Molecular Perovskites and MOFs, which, due to their modular nature and chemical diversity, leave ample room for studying and identifying important structural chemistry factors. The four experimental studies and one literature review described in this thesis cover both of these multi-faceted material classes – with findings on MOFs summarised first below, followed by Molecular Perovskite insights as the core of this thesis.

In both studies on MOFs, small chemical changes of the organic linker were explored on a molecular scale to investigate their ramifications on the resulting structure and properties. In study II, the planar porphyrin linker was chemically modified with ethyl groups in the *ß*-position. The consequent change from a planar to a nonplanar porphyrin shape was explored in a PCN-222 solid solution series with varying linker ratios using the mixed-linker strategy. Since conformational freedom is introduced by incorporating the non-planar porphyrin linker, changes in the thermal expansion behaviour were expected to be in close relation to the amount of the nonplanar porphyrin linker. However, this study showcases a rather complex case where no linear trends along the series with an increasing amount of non-planar porphyrin linker were obtained. This is because other factors, such as defects and guest molecules in the pores, also influence the framework flexibility and, hence, thermal responsiveness, highlighting the breadth of parameters that control material properties and further rationalising such systematic bottom-up studies. In study III, the linker chemistry was investigated in less porous MOFs, in the absence of remaining guest molecules in the pores, by exploring the design space of a literature known Fe(II)-based MOF with triazolate as the coordinating linker. The linker was chemically tailored by using methyl groups and cyclopentyl on the triazolate backbone, which increases steric demand on the triazolate moiety. This linker engineering was directly correlated to the spin-state of the Fe(II) centres at ambient conditions, where both modified Fe(II)-based MOFs were found to be in their high-spin state compared to the typical low-spin $Fe(ta)_2$. Interestingly, the large difference in the void fraction between $Fe(ta)_2$ and $Fe(cta)_2$ was not apparent in the resulting mechanical response under pressure, with similar bulk moduli observed for both MOFs. Therefore, the spin-state was identified as a new design principle – which, in combination with other factors, determines the pressure responsiveness of MOFs, thereby broadening the physicochemical conceptual toolkit available for tailored material design.

The material class of Molecular Perovskites is discussed in a much broader context under the theme: *The Wondrous World of Molecular Perovskites*.* In this thesis, a historical review of the structural evolution of the perovskite structure is given, emphasising the unique ramifications of using molecules instead of single atoms while maintaining the $ABX_3$ motif. Besides a proprietary comprehensive overview of published Molecular Perovskite structures, some key structure chemical phenomena in close relation to their inorganic parents, as well as selected research highlights of Molecular Perovskites, are presented. In addition, synthetic advances, conceptual insights and systematic strategies for the design of new Molecular Perovskites using chemically tailored molecular A-site ions instead of commercially available cations are reported. The results documented here focus on studying the stimuli-responsive behaviour of Molecular Perovskites in dependence on the chemical composition. In study I, $Li(C_2N_3)$ was found to be a useful modifier salt for lowering the melting temperature compared

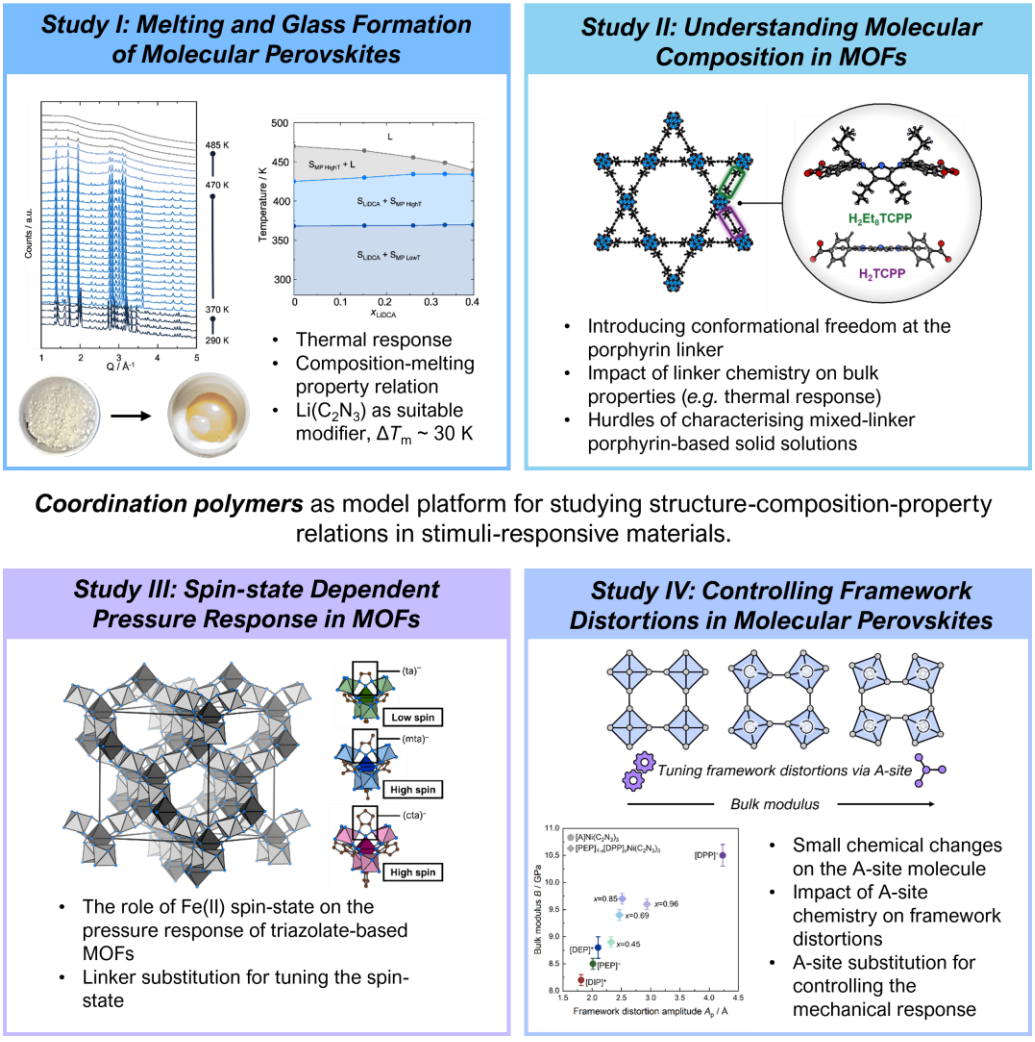


Figure 10: Graphical summary of the studies discussed in this thesis with emphasis on studying the composition-structure-property relationships in the broad field of coordination polymers.

*adapted from "The Wondrous World of Perovskites" by Glazer in 2017 at the Bragg Lecture of the Royal Institution

to the pure meltable Molecular Perovskites. This approach, inspired by inorganic glass chemistry, serves as a blueprint for the emerging class of coordination polymer glasses, which offers great opportunities for fine-tuning the melt and glass characteristics and, beyond that, for introducing functionality into the glass matrix. In study IV, a different concept was applied to investigate the stimuli-responsive behaviour as a function of subtle chemical changes at the molecular component, similar to the linker substitution described above. In principle, this is a representative report on how to design a systematic study to explore the molecular substitution approach on the A-site by using only four members of the large set of newly synthesised Molecular Perovskites in this thesis. In the absence of any interactions between the molecular cation and the surrounding $[BX_3]^-$ network, it was possible to focus on the impact of chemically tailored alkyl chains on the piperidinium moiety of the A-site cations. Accordingly, it was found that the choice of the A-site cation is decisive, with its shape templating the framework distortions of the $[BX_3]^-$ network, which is closely linked to the compressibility of the bulk Molecular Perovskites material. Moving forward and building on a large number of new Molecular Perovskites, similar fundamental studies can be conceptualised, which, in combination with the results outlined in this thesis, will provide important insights for the material design of coordination polymers.

This thesis clearly demonstrates that certain fundamental principles hold true for both worlds of MOFs and Molecular Perovskites despite their structural and chemical differences. These include i) unique responses to external stimuli, ii) complex structure-property relationships requiring systematic and analytics-driven investigations, as well as iii) access to a new set of functionalities by subtle molecular modifications - as evidenced in the respective studies above.

Finally, a few concluding remarks give a somewhat personal perspective by the author for future research on Molecular Perovskites. Looking at the iconic history of inorganic perovskites, the question arises where the class of Molecular Perovskites is heading.

The structural evolution and chemical diversity of the $ABX_3$ perovskite structure *per sé* (i): The extent to which molecular substitution will be further explored is yet unclear. Many scenarios are possible, from further expanding the $[BX_3]^-$ framework structure to introducing a new dimension to the $ReO_3$-type network structures, which could lead to yet unknown degrees of freedom. Here, organic chemistry offers a large design space that has not yet been fully exploited, *e.g.* for the introduction of larger X-site linkers or trivalent A-site cations, limited only by conceptual ideas or synthetic capabilities. Considering the large number of formate- and dicyanamide-based Molecular Perovskites, there is still a large playground for the discovery of new materials within other X-site families. Additionally, the rather poorly explored solid solution strategy holds great promise for future studies involving carefully selected Molecular

Perovskites – potentially moving beyond two components towards ternary systems. This provides a systematic concept that is currently favoured to advance this material class and aims to chemically control their physicochemical properties.

The potential of functional Molecular Perovskites (ii): With their diverse properties, this material class holds great promise for achieving a similar success story akin to that of HOIPs and inorganic perovskites. In particular, within the growing interest in coordination polymer glasses, Molecular Perovskites show great potential for introducing functionality by making use of their chemical diversity – which will be the next step in the development of these new glasses that lie between polymer and inorganic glasses. For instance, the incorporation of chiral molecules on the A-site or the addition of ion-conductive modifiers will potentially generate multifunctional Molecular Perovskite-based glasses.

Ending this thesis, it is certain that research on Molecular Perovskites will continue to progress in the context of material design, as they occupy a special position within coordination polymers due to their available structure and chemical principles.

# 4. SUPPORTING INFORMATION

## 4.1. Supporting Information for Study I

**Supporting Information**

**Li($C_2N_3$) as Eutectic Forming Modifier in the Melting Process of the Molecular Perovskite [($C_3H_7$)$_3$N($C_4H_9$)]Mn($C_2N_3$)$_3$**

Silva M. Kronawitter,[1] Sebastian A. Hallweger,[1] Jan Meyer,[1] Carmen Pedri,[1] Stefan Burger,[1] Ahmad Alhadid,[2] Sebastian Henke[3] and Gregor Kieslich[1,a]

[1] *Department of Chemistry, TUM School of Natural Sciences, Technical University of Munich, Lichtenbergstraße 4, 85748 Garching, Germany*
[2] *Biothermodynamics, TUM School of Life Sciences, Technical University of Munich, Maximus-von-Imhof Forum 2, 85354 Freising, Germany*
[3] *Department of Chemistry and Biological Chemistry, Technical University of Dortmund, Otto-Hahn-Straße 6, 44227 Dortmund, Germany*

**Table of contents:**

**Material synthesis** ..... **2**
Synthesis of the A-site precursor tri-(*n*-propyl)-N-butylammonium bromide – [$Pr_3$NBu]Br: ..... 2
Synthesis of the crystalline molecular perovskite [$Pr_3$NBu]Mn($C_2N_3$)$_3$: ..... 2
Synthesis of the modifier salt Li($C_2N_3$): ..... 4
Elemental analysis: ..... 5
Melting procedure of [$Pr_3$NBu]Mn($C_2N_3$)$_3$ mixed with Li($C_2N_3$): ..... 5
**Single crystal X-ray diffraction (SCXRD) data** ..... **6**
**NMR spectroscopy of the precursor A-site cation [$Pr_3$NBu]$^+$** ..... **10**
**Sample preparation of modifier-[$Pr_3$NBu]Mn($C_2N_3$)$_3$ mixtures** ..... **12**
**Thermogravimetric analysis and differential scanning calorimetry (TGA-DSC)** ..... **13**
**Powder X-ray diffraction (PXRD) data** ..... **17**
High temperature structure of [$Pr_3$NBu]Mn($C_2N_3$)$_3$: ..... 19
**Differential scanning calorimetry (DSC)** ..... **25**
..... **30**
..... **30**
..... **31**
**Thermogravimetric analysis and mass spectrometry (TGA-MS)** ..... **33**
**IR spectroscopy of the modifier salt Li($C_2N_3$)** ..... **34**
**Solid-liquid thermodynamics in the modifier-perovskite mixture** ..... **37**
**References** ..... **39**

[a] Corresponding author: gregor.kieslich@tum.de

## Material synthesis

**Synthesis of the A-site precursor tri-(*n*-propyl)-N-butylammonium bromide – [$Pr_3NBu$]Br:**

The A-site cation precursor was prepared from commercially available reagents purchased from Sigma Aldrich without further purification. In a three-necked flask, 10.70 mL (13.70 g, 0.10 mol) 1-bromobutane was added dropwise to a solution of 19.10 mL (14.33 g, 0.10 mol) tri-*n*-propylamine in 80 mL acetonitrile. The mixture was heated to reflux overnight and allowed to cool. The solvent was removed *in vacuo* and 70 mL ethyl acetate was added to the resulting off-white solid, forming a white precipitate. The suspension was filtered, yielding a white, crystalline solid which was recrystallized in ethyl acetate, yielding 16.43 g (58.62 mmol, 58.6 %) of pure product.

**$^1$H NMR:** (400 MHz, deuterium oxide): $\delta$ / ppm = 3.23-3.10 (*m*, 8 H), 1.76-1.58 (*m*, 8 H), 1.5 (*h, J* = 7.4 Hz, 2 H), 0.93 (*t*, *J* = 7.3 Hz, 12 H).

**$^{13}$C NMR:** (100 MHz, deuterium oxide): $\delta$ / ppm = 59.85 (3 C), 58.29 (1 C), 23.11 (1 C), 19.15 (1 C), 14.82 (3 C), 12.81 (1 C), 9.81 (1 C).

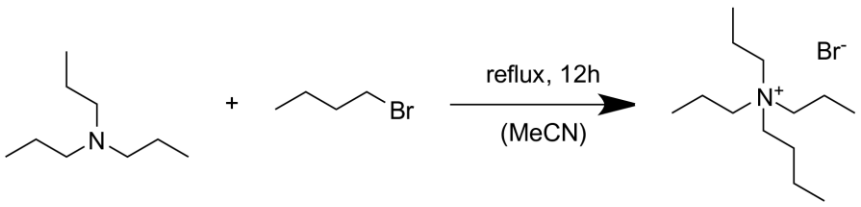


**Figure S1:** Nucleophilic substitution reaction scheme following the Menshutkin-type towards the synthesis of the A-site cation precursor salt [$Pr_3NBu$]Br.[1]

**Synthesis of the crystalline molecular perovskite [$Pr_3NBu$]Mn($C_2N_3$)$_3$:**

The synthesis of the crystalline compound [$Pr_3NBu$]Mn($C_2N_3$)$_3$ ($Pr_3NBu$ = tri-(*n*-propyl)-N-butylammonium) followed an established mild solution synthesis approach at ambient

temperature in aqueous solution from commercially available $Na(C_2N_3)$ (96 %, Sigma-Aldrich), $MnCl_2 \cdot 4H_2O$ (98 %, Sigma-Aldrich) and Millipore water. In a typical crystallization procedure, 0.3 mL Millipore water was added to a tube and the reagent solutions layered above in order of: 1.0 mL of the respective $[Pr_3NBu]Br$ solution (0.2 M), 1.0 mL of an aqueous $MnCl_2$ solution (0.2 M) and 0.3 mL of an aqueous sodium dicyanamide solution (2 M). After cooling for several hours, large well-defined block single crystals with sizes between 0.4 - 3 mm were collected at ambient temperature, washed with Millipore water and dried.

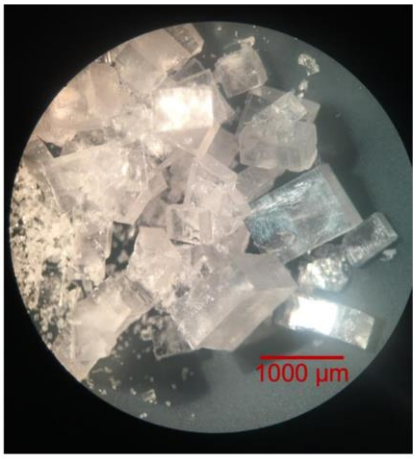


**Figure S1:** Microscopic image of the crystalline material $[Pr_3NBu]Mn(C_2N_3)_3$ showing block-shaped colorless crystals.

**Synthesis of the modifier salt Li($C_2N_3$):**

For the synthesis of the modifier precursor salt Li($C_2N_3$), a synthetic procedure known from literature[2,3] was adapted, which is based on the metathesis reaction between Na($C_2N_3$) (96 %, Sigma-Aldrich) and $Li_2SO_4 \cdot H_2O$ (99 %, Sigma-Aldrich) in aqueous solution. Both starting materials were dissolved separately in 10 mL deionized water, heated to 50 °C and then mixed at 50 °C for 45 min under stirring. After cooling down to room temperature, the $Na_2SO_4$ was separated and filtered off as a precipitate by using an excess amount of ethanol (40 mL) as washing solution. After solvent removal, the crude product contained Na($C_2N_3$) residue according to the IR spectra indicating insufficient separation. Therefore, a next purification approach of the crude product was used, *i.e.* recrystallization in methanol, followed by the formation of needle-shaped crystals of Na($C_2N_3$). After separation of the Na($C_2N_3$) crystals the IR spectrum still indicated residual amounts of Na($C_2N_3$) in the product. Therefore, the different solubility in tetrahydrofuran of both dicyanamide salts was used to dissolve Li($C_2N_3$), leaving Na($C_2N_3$) residue undissolved in the flask. The supernatant was separated, and the suspended particles of Na($C_2N_3$) were removed using a syringe filter for three times. After solvent removal, the purified product of Li($C_2N_3$) was characterized by elemental analysis (S-5), thermal analysis (Figure S10) and IR spectroscopy (Figure S39 and S40), indicating a product with a Na content of smaller than 0.5 wt% (below the lower measurement limit < 0.5 wt%), confirming the successful purification of the product.

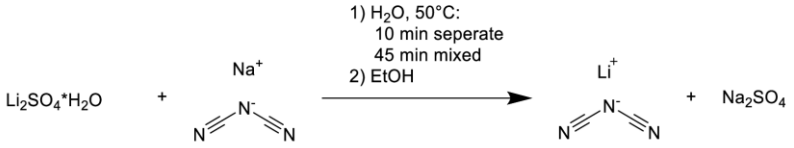


**Figure S3:** Reaction scheme of the synthesis of Li($C_2N_3$) by following the metathesis reaction of Na($C_2N_3$) and $Li_2SO_4 \cdot H_2O$.

**Elemental analysis:**

The elemental analysis including all measurements and quantifications were determined by the technical staff of the microanalytical laboratory at the Catalysis Research Center at the Technical University of Munich. The elemental composition of samples (sample weight around 20 mg) was analyzed using a *HEKAtech* Euro EA elemental analyzer with flash combustion at 1800 °C and subsequent chromatographical separation and quantification with a thermal conductivity detector (TCD).

**[$Pr_3NBu$]Br:** calc. C 55.66 H 10.81 N 4.99, found C 55.84 H 10.77 N 5.12

**[$Pr_3NBu$]Mn($C_2N_3$)$_3$:** calc. C 50.33 H 6.67 N 30.89 Mn 12.12, found C 50.15 H 6.52 N 30.59 Mn 12.06

**Melt-quenched [$Pr_3NBu$]Mn($C_2N_3$)$_3$:** calc. C 50.33 H 6.67 N 30.89 Mn 12.12, found C 50.16 H 6.56 N 30.96 Mn 12.03

**Synthesized Li($C_2N_3$):** calc. C 32.91 H - N 57.58 Li 9.51 Na -, found C 36.04 H 2.38 N 40.06 Li not determined Na < 0.5

**Melting procedure of [$Pr_3NBu$]Mn($C_2N_3$)$_3$ mixed with Li($C_2N_3$):**

Compared to the melting process of the pure [$Pr_3NBu$]Mn($C_2N_3$)$_3$ compound in a TGA-DSC experiment close to the melting temperature, we performed more simple melting experiments of the mixtures near the eutectic with a mole fraction of Li($C_2N_3$) ($x_{LiDCA}$ = 0.38 and 0.41, with DCA = $[C_2N_3]^-$). Therefore, we heated 20 mg of the powder in a heating block slightly above the determined solidus temperature ($T_{sol,Onset}$ = 433.9 K and 431.9 K) under constant argon flow. After a heating period of 30 min, the melting process was finished, and the glass vial was slowly cooled down to room temperature without a quenching method. The solid remains as transparent liquid drops, see Figure S4.

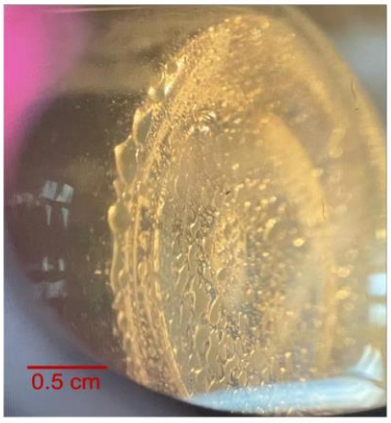


**Figure S4:** Microscopic image of the liquid drops after performing a model experiment of the [$Pr_3NBu$]Mn($C_2N_3$)$_3$ mixed with Li($C_2N_3$) ($x_{LiDCA}$ = 0.38).

## Single crystal X-ray diffraction (SCXRD) data

SCXRD data were collected on a *Bruker* APEX-II CCD diffractometer equipped with a fine-focus tube with a Mo $K_a$ radiation source ($\lambda$ = 0.71073 Å), a *Triumph* monochromator, a CMOS plate detector and an *Oxford Cryosystems* cooling device by using the APEX III software package, see Table S1 and S2.[4] The crystals were fixed on the top of a microsampler, transferred to the diffractometer and frozen under a stream of cold nitrogen. A matrix scan was used to determine the initial lattice parameters. Reflections were merged and corrected for Lorentz and polarization effects, scan speed, and background using SAINT.[5] Absorption corrections, including odd and even ordered spherical harmonics were performed using SADABS.[6] Space group assignments were based upon systematic absences, E-statistics, and successful refinement of the structures. Data reduction was performed with APEX3 and structure solution was performed by using SHELX[7,8] as integrated in Olex2.[9] Structures were solved by direct methods with the aid of successive difference Fourier maps, and were refined against all data. The VESTA software package 3.4.0 was used to visualize the crystal structure, see Figure S5 and S6.[10]

**Table S1:** Crystallographic data from SCXRD for the as-synthesized $[Pr_3NBu]Mn(C_2N_3)_3$ at 100 K.

| | |
|---|---|
| **Compound** | $[Pr_3NBu]Mn(C_2N_3)_3$ |
| **Chemical Formula** | $C_{38}H_{58}Mn_2N_{20}$ |
| **Formula weight (g/mol)** | 904.92 |
| **Temperature (K)** | 100(2) |
| **Crystal system** | orthorhombic |
| **Space group** | *Pbcn* |
| **a (Å)** | 16.5315(17) |
| **b (Å)** | 17.5441(17) |
| **c (Å)** | 32.348(3) |
| **α (°)** | 90 |
| **β (°)** | 90 |
| **γ (°)** | 90 |
| **Volume ($Å^3$)** | 9382.0(17) |
| **Z** | 8 |
| **$\rho_{calc}$ ($g/cm^3$)** | 1.281 |
| **μ ($mm^{-1}$)** | 0.589 |
| **F (000)** | 3808 |
| **Radiation** | $MoK_\alpha$ ($\lambda = 0.71073$) |
| **2θ range for data collection (°)** | 2.110 to 27.102 |
| **Index ranges** | $-21 \leq h \leq 21$ |
| | $-22 \leq k \leq 22$ |
| | $-41 \leq l \leq 41$ |
| **Reflections collected** | 471875 |
| **Independent reflections** | 10354 [$R_{int} = 0.0453$, $R_{sigma} = 0.0102$] |
| **Data/restraints/parameters** | 10354/0/568 |
| **Goodness of fit on $F^2$** | 1.149 |
| **Final R indexes [I > 2σ (I)]** | $R_1 = 0.0415$, $wR_2 = 0.1013$ |
| **Final R indexes [all data]** | $R_1 = 0.0445$, $wR_2 = 0.1032$ |
| **Largest diff. peak/hole/ ($Å^{-3}$)** | 0.853/-0.436 |
| **CSD number** | 2211193 |

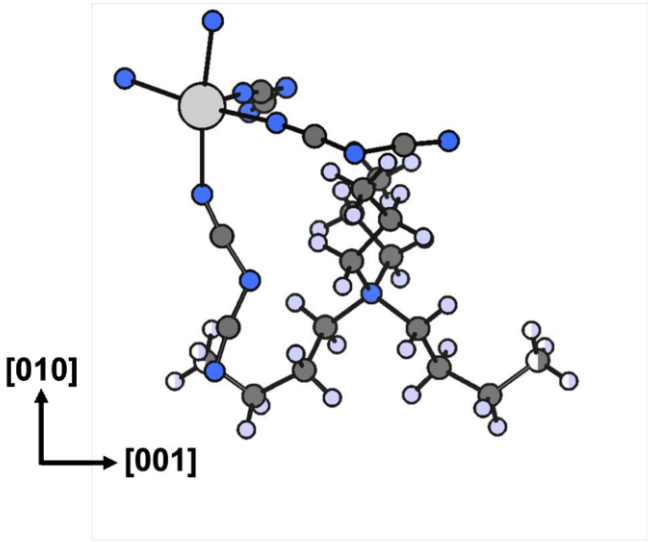


**Figure S5:** Structure of the asymmetric unit of $[Pr_3NBu]Mn(C_2N_3)_3$ when looking along the [100] axis with $(C_2N_3)^-$ ligands acting as bridges between the $Mn^{2+}$ cations while the $[Pr_3NBu]^+$ cations occupy the void of the pseudo-cubic $ReO_3$ cavities, with the longer butyl group slightly extending into the neighboring cavity. Color code: Mn – grey, N – blue, C – dark grey and H – light purple.

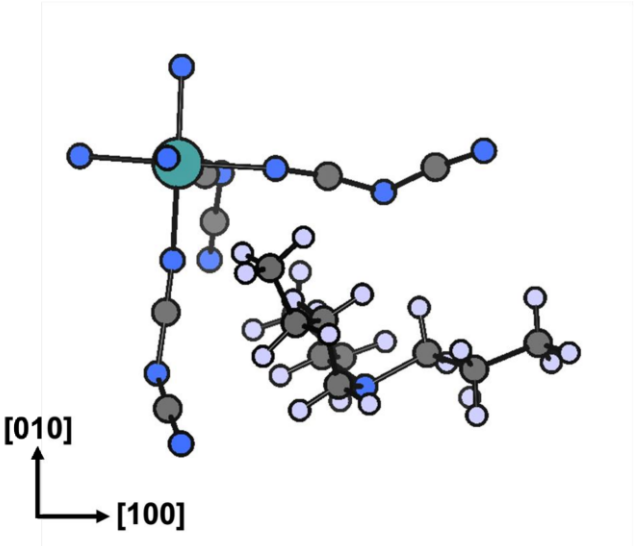


**Figure S6:** Structure of the asymmetric unit of $[Pr_3NBu]Ni(C_2N_3)_3$ when looking along the [001] axis with $(C_2N_3)^-$ ligands acting as bridges between the $Ni^{2+}$ cations while the $[Pr_3NBu]^+$ cations occupy the void of the pseudo-cubic $ReO_3$ cavities. Color code: Ni – green, N – blue, C – dark grey and H – light purple.

**Table S2:** Crystallographic data from SCXRD for the as-synthesized $[Pr_3NBu]Ni(C_2N_3)_3$ at 100 K.

| | |
|---|---|
| **Compound** | $[Pr_3NBu]Ni(C_2N_3)_3$ |
| **Chemical Formula** | $C_{19}H_{30}N_{10}Ni$ |
| **Formula weight (g/mol)** | 457.24 |
| **Temperature (K)** | 100(2) |
| **Crystal system** | orthorhombic |
| **Space group** | $Pna2_1$ |
| **a (Å)** | 17.2198(12) |
| **b (Å)** | 11.6501(8) |
| **c (Å)** | 11.5417(8) |
| **α (°)** | 90 |
| **β (°)** | 90 |
| **γ (°)** | 90 |
| **Volume (Å$^3$)** | 2315.4(3) |
| **Z** | 4 |
| **$\rho_{calc}$ (g/cm$^3$)** | 1.464 |
| **μ (mm$^{-1}$)** | 0.864 |
| **F (000)** | 968 |
| **Radiation** | $MoK_\alpha$ ($\lambda$ = 0.71073) |
| **2θ range for data collection (°)** | 2.111 to 26.370 |
| **Index ranges** | $-21 \leq h \leq 21$ |
| | $-14 \leq k \leq 14$ |
| | $-14 \leq l \leq 14$ |
| **Reflections collected** | 135250 |
| **Independent reflections** | 4726 [$R_{int}$ = 0.0420, $R_{sigma}$ = 0.0143] |
| **Data/restraints/parameters** | 4726/0/247 |
| **Goodness of fit on F$^2$** | 1.087 |
| **Final R indexes [I > 2σ (I)]** | $R_1$ = 0.0828, $wR_2$ = 0.2258 |
| **Final R indexes [all data]** | $R_1$ = 0.0839, $wR_2$ = 0.2264 |
| **Largest diff. peak/hole/ (Å$^{-3}$)** | 1.464/-0.754 |
| **CSD number** | 2236677 |

## NMR spectroscopy of the precursor A-site cation $[Pr_3NBu]^+$

$^1H$ and $^{13}C$ NMR spectra were recorded on a *Bruker* AVIII 400 US NMR spectrometer at ambient temperature (298 K). Chemical shifts are expressed in parts per million (ppm, δ) and are corrected for the strongest residual solvent shift as an internal standard for $^1H$ NMR spectra. The following abbreviations are used to describe signal multiplicity: *t* = triplet, *q* = quartet, *h* = sextet and *m* = multiplet. NMR data is reported in the order of chemical shifts (multiplicity, coupling constant, integral). All coupling constants are absolute values and are expressed in Hertz (Hz).[11]

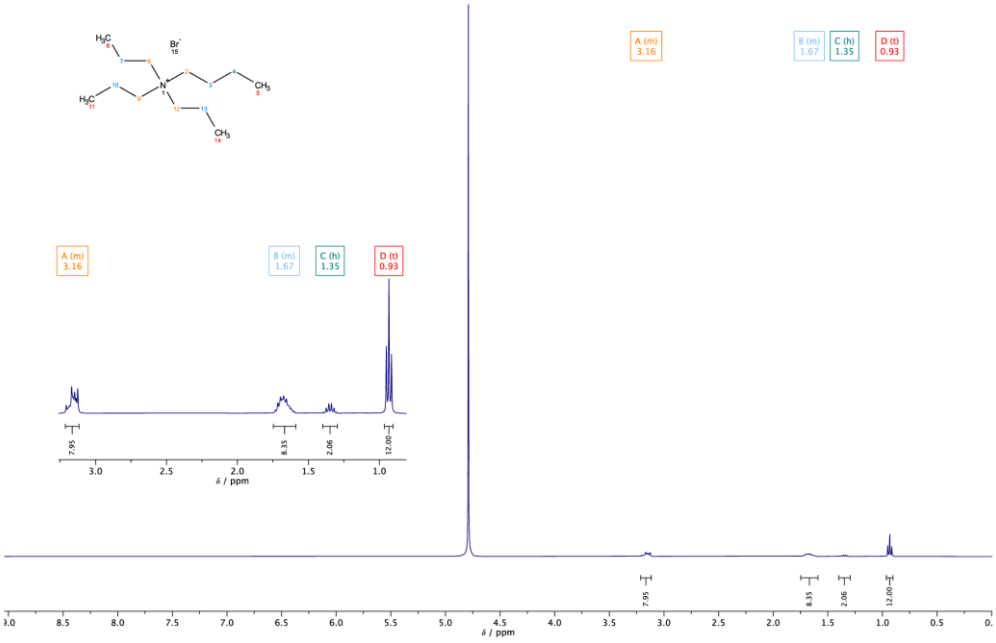


**Figure S7:** $^1H$ NMR spectrum of $[Pr_3NBu]Br$ in $D_2O$.

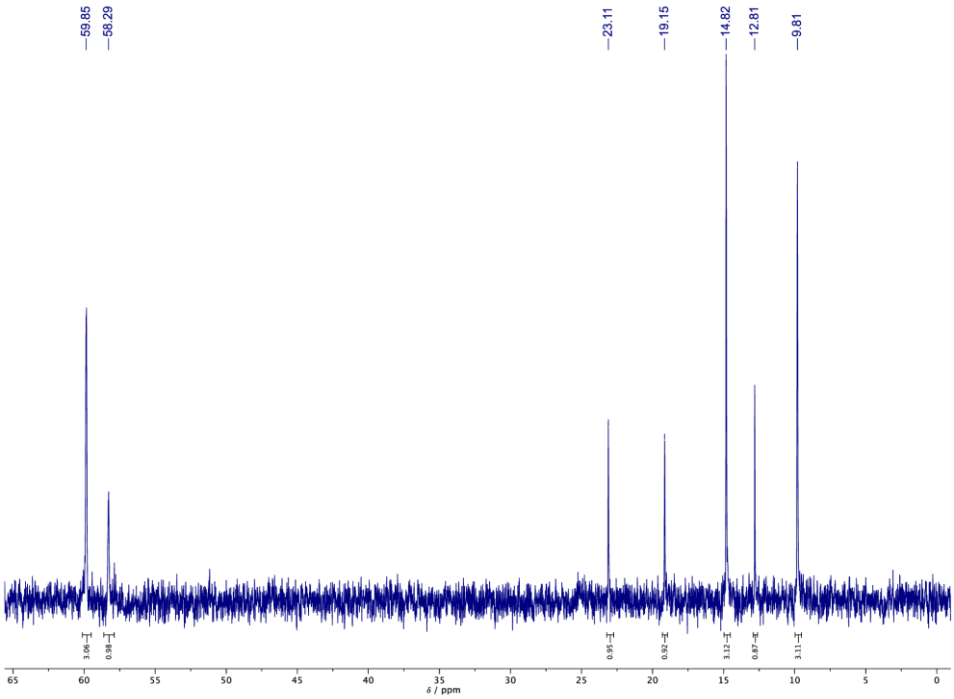


**Figure S8:** $^{13}$C-NMR spectrum of [$Pr_3$NBu]Br in $D_2O$, showing the expected number of signals with the correct integral ratios.

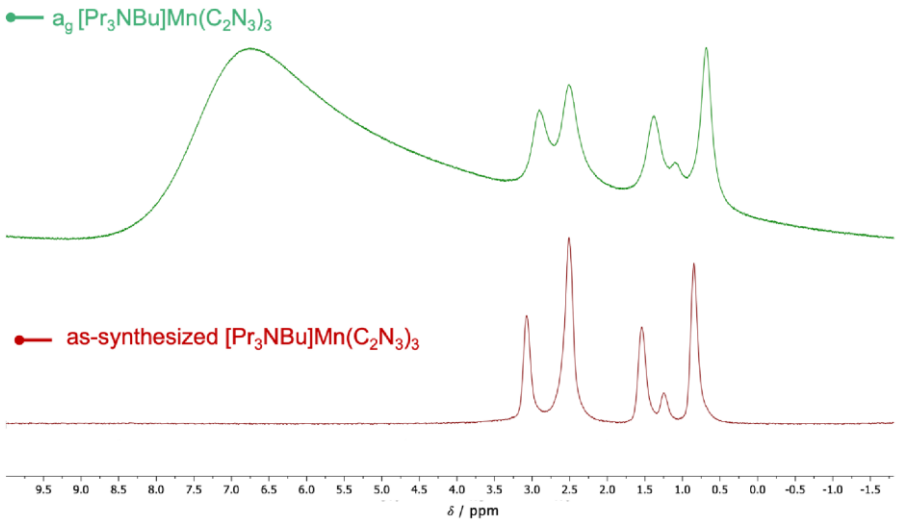


**Figure S9:** $^1$H-NMR spectra of the as-synthesized [$Pr_3$NBu]Mn($C_2N_3$)$_3$ (red) and the melt-quenched [$Pr_3$NBu]Mn($C_2N_3$)$_3$ (green) after acid digestion in DCl in $D_2O$, each solution was measured in DMSO-$d_6$.

## Sample preparation of modifier-$[Pr_3NBu]Mn(C_2N_3)_3$ mixtures

Before the respective modifier salt ($Na(C_2N_3)$ or $Li(C_2N_3)$) and the $[Pr_3NBu]Mn(C_2N_3)_3$ perovskite material were mixed to homogenous mixtures, the pure materials were dried at 343 K *in vacuo* for at least 24 h. After weighing the dry components in different mole ratios, various mixtures were prepared following a wet grinding procedure. Here, the solid mixtures were ground and pestled to a fine powder by adding a few drops of acetonitrile. For solvent residue removal, the mixtures were again dried *in vacuo* at 343 K, confirmed by DSC data showing hydrate-free $Li(C_2N_3)$ in the first heating cycle, see Figure S36.

## Thermogravimetric analysis and differential scanning calorimetry (TGA-DSC)

Thermal analysis of the potential modifier salts $Na(C_2N_3)$, $Li(C_2N_3)$ and the molecular perovskite was performed on a *Netzsch* STA449F5 Jupiter TGA-DSC device using aluminum oxide pans (70 µL) under constant argon atmosphere (20 mL $min^{-1}$). The temperature calibration of the oven cell was conducted based on the melting points of In, Sn, Bi, Zn, Al, Au and Ag. The baseline was corrected with an empty sample pan for the respective temperature program. The respective sample masses ($m_0$) are given below.

TGA-DSC experiments of both potential modifiers $Na(C_2N_3)$ and $Li(C_2N_3)$ were performed, providing complimentary data on a sufficient synthesis of $Li(C_2N_3)$ from $Na(C_2N_3)$ in a metathesis reaction. Upon heating $Li(C_2N_3)$, the dicyanamide anion forms triazine in a trimerization reaction appearing as a sharp exothermic event at approximately $T$ = 548.15 K in the DSC scan, shown as a light green line in Figure S10 (b), which is slightly lower than the literature reported trimerization temperature of 568.15 K.[2,3] The DSC data confirms a Na-free synthesized $Li(C_2N_3)$ since the trimerization temperature of phase pure $Na(C_2N_3)$ occurs at a significantly higher $T$ = 672.15 K approximately corresponding to the literature value, as shown in the DSC curve in Figure S10 (a).[2,3] Small deviations from the literature data can be related to different heating rates in the TGA-DSC experiments.

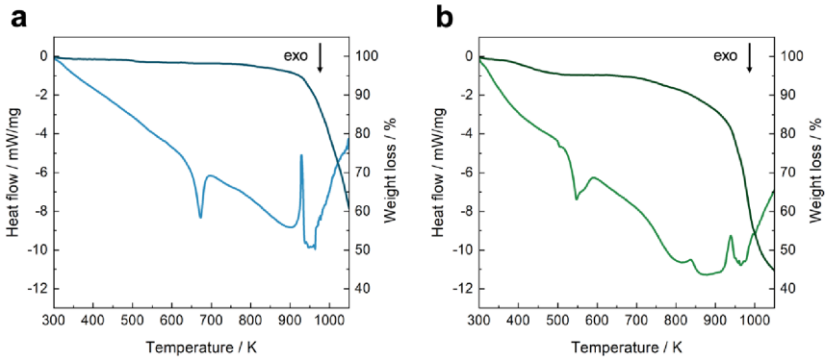


**Figure S10:** TGA-DSC of the materials $Na(C_2N_3)$ (a - blue) with a sample mass of 5.313 mg and $Li(C_2N_3)$ (b – green) with a sample mass of 4.230 mg from room temperature to 1073.15 K at a heating rate of 10 K $min^{-1}$. Sharp exothermic events correspond to the trimerization reaction of $Na(C_2N_3)$ at 672.15 K (a) and $Li(C_2N_3)$ at 548.15 K (b). The TGA curve is shown in the respective darker colour and the corresponding DSC curve in the respective lighter one.

In the thermal analysis of $[Pr_3NBu]Mn(C_2N_3)_3$, the first distinct endothermic signal corresponds to a solid-solid phase transition ($T_{ss}$ = 371K) and the second event at 474 K to the melting process ($T_m$), since no simultaneous weight loss can be observed, see Figure S11. In accordance with literature, both endothermic events ($T_{ss}$ and $T_m$) were determined as offset of the respective endothermal peak. The onset of significant decomposition $T_d$ = 570 K was determined by extrapolation of the linear range of the relative mass loss observed with a heating rate of 10 K $min^{-1}$.

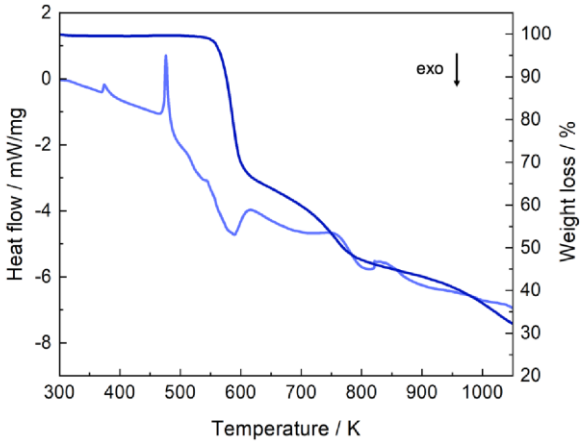


**Figure S11:** TGA-DSC of $[Pr_3NBu]Mn(C_2N_3)_3$ with a sample mass of 7.308 mg from room temperature to 1073.15 K at a heating rate of 10 K $min^{-1}$. TGA curve is shown in dark purple indicating the thermal stability under constant argon flow before decomposition and the corresponding DSC curve is highlighted in light purple.

When investigating one potential modifier such as $Na(C_2N_3)$, TGA-DSC experiments were performed as a first screening of the influence of such a modifier salt on the melting event. For this purpose, various powder samples of mixtures of $[Pr_3NBu]Mn(C_2N_3)_3$ perovskite with different mole fractions of $Na(C_2N_3)$ ($x_{NaDCA}$ = 0.05, 0.10, 0.30, 0.50, 0.70, 0.90) were measured in a simultaneous measurement routine. Analysis of the thermogravimetric and DSC data, as shown in Figure S12, reveals no significant changes in both endothermic signals corresponding to the phase transition and melting process. This indicates in principle no influencing character

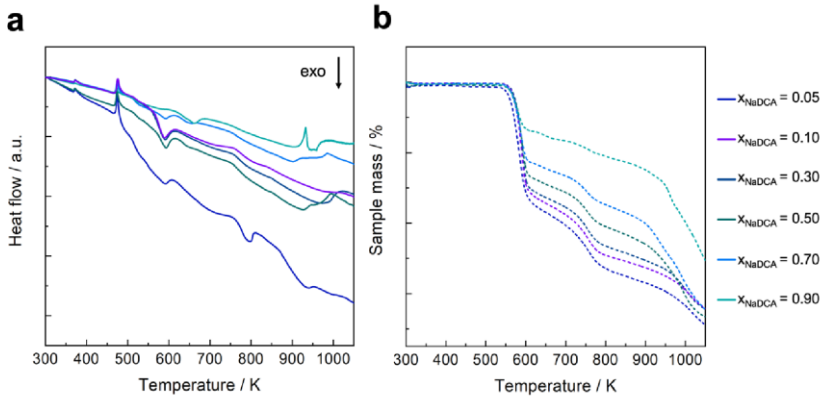


**Figure S12:** TGA-DSC screening of $[Pr_3NBu]Mn(C_2N_3)_3$ mixed with various mole fractions of $Na(C_2N_3)$ using sample masses between 5 – 6 mg, measured from room temperature to 800 °C at a heating rate of 10 K $min^{-1}$. DSC traces (a) are shown in continuous lines with the corresponding TGA curves (b) highlighted in dotted lines. For better comparison, the DSC curves were normalized and displayed in a stacking plot.

of the modifier $Na(C_2N_3)$, making it unsuitable for the $[Pr_3NBu]Mn(C_2N_3)_3$ perovskite material to form an eutectic mixture.

In the evaluation of another possible modifier salt such as $Li(C_2N_3)$, a simultaneous first screening of an influencing effect on the thermal response of the perovskite material was carried out by using TGA-DSC experiments, see Figure S13. Therefore, various powder samples of mixed $[Pr_3NBu]Mn(C_2N_3)_3$ perovskite with $Li(C_2N_3)$ ($x_{LiDCA}$ = 0.05, 0.10, 0.15, 0.22, 0.30, 0.35, 0.40, 0.50, 0.60) were measured using the same temperature program procedure. Similar as obtained for the $Na(C_2N_3)$ addition, no influence of the modifier salt on the phase transition temperature ($T_{ss}$), the first endothermic signal in the DSC curves, and no change of the decomposition temperature ($T_d$) in the TGA curves can be observed. However, when comparing the second endotherms in the DSC curves, a significant change in the melting temperature in contrast to the pure $[Pr_3NBu]Mn(C_2N_3)_3$ perovskite with $T_m$ = 474 K by adding altering amounts of $Li(C_2N_3)$ can be observed, see Figure S13 (a). With increasing mole fractions of up to 40 mol%, a decreasing trend in $T_m$ is observed, and with a further increase in the amount of $Li(C_2N_3)$, only a slight decrease in $T_m$ is observed. Therefore, the first TGA-DSC analysis of the $T_m$ as a function of the modifier amount mixed with $[Pr_3NBu]Mn(C_2N_3)_3$ shows the potential of $Li(C_2N_3)$ as a suitable modifier in the formation of a eutectic system, that is further investigated in a temperature-composition phase diagram by experimental DSC data.

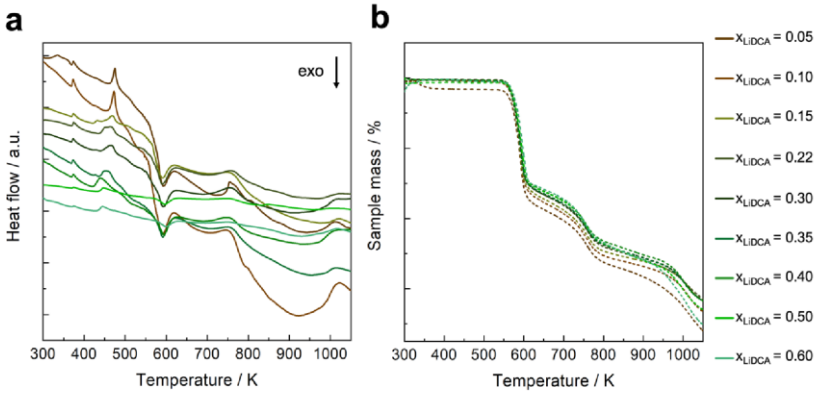


**Figure S13:** TGA-DSC screening of $[Pr_3NBu]Mn(C_2N_3)_3$ mixed with various mole fractions of $Li(C_2N_3)$ using sample masses between 5 – 7 mg, measured from room temperature to 1073.15 K at a heating rate of 10 K $min^{-1}$. DSC traces (a) are shown in continuous lines with the corresponding TGA curves (b) highlighted in dotted lines. For better visualization, the DSC curves were offset by an arbitrary shift.

## Powder X-ray diffraction (PXRD) data

The PXRD measurements were performed using *Debye-Scherrer* geometry with borosilicate glass capillaries (0.7 mm diameter) in a *STOE* Stadi P diffractometer with a *DECTRIS* MYTHEN 1K / *DECTRIS* Multi-MYTHEN detector, a curved Ge(111) monochromator and a Mo $K_{\alpha}$ radiation source ($\lambda = 0.70926$ Å). The measurement range was from 2° to 36.56° (2θ) with a step size of 0.015° (2θ). Variable temperature PXRD measurements were conducted in a *STOE* HT2 temperature control cell with quartz glass capillaries (1.0 mm diameter) in steps of 10 K with a heating rate of 10 K $min^{-1}$ from 303 K to 433 K, followed by subsequent cooling with a rate of 10 K $min^{-1}$ from 433 K to 303 K.

Pawley profile fit analysis was carried out for all patterns by using TOPAS v6.[12,13] Standard deviations of all parameters were calculated and the use of "randomize_on_errors" ensured that the minimum of refinement was achieved.

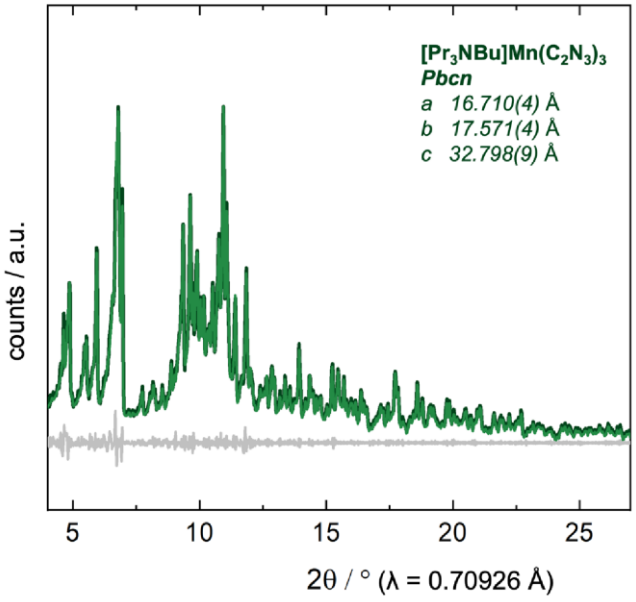


**Figure S14:** The PXRD pattern of the as-synthesized compound $[Pr_3NBu]Mn(C_2N_3)_3$ (dark green) compared to the calculated data from Pawley profile fit analysis (light green), with $R_{wp} = 2.927$, $R_{exp} = 1.032$ and GOF = 2.837. The difference curve of the Pawley profile fit (grey) and the experimental data indicates phase purity.

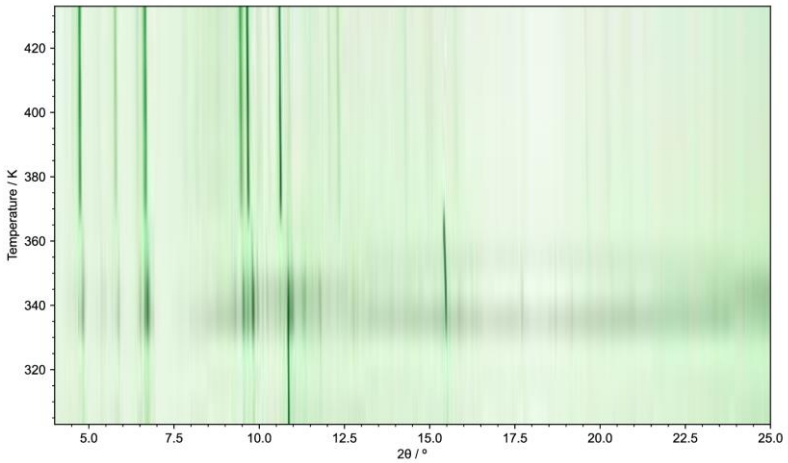


**Figure S15:** Variable temperature PXRD patterns of $[Pr_3NBu]Mn(C_2N_3)_3$ at temperature intervals of 10 K, heating from 303 K to 433 K. The temperature dependent PXRD data is illustrated as contour plot with darker regions corresponding to a higher intensity in the respective Bragg reflection.

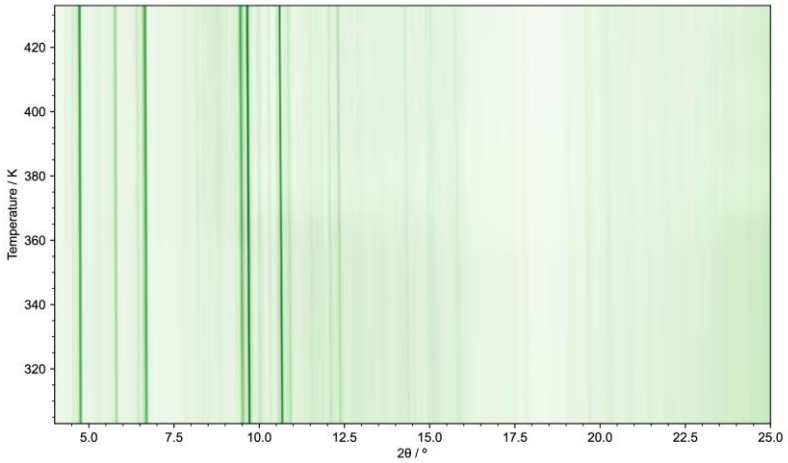


**Figure S16:** Variable temperature PXRD patterns of $[Pr_3NBu]Mn(C_2N_3)_3$ at temperature intervals of 10 K, cooling from 433 K to 303 K. The temperature dependent PXRD data is illustrated as contour plot with darker regions corresponding to a higher intensity in the respective Bragg reflection.

**High temperature structure of $[Pr_3NBu]Mn(C_2N_3)_3$:**

Since single crystals of $[Pr_3NBu]Mn(C_2N_3)_3$ break down to a powder over the irreversible solid-to-solid phase transition, structure solution of the high-temperature phase based on SCXRD was not possible. Based on the structure (Table S2 and Figure S6) and PXRD pattern of the closely related material $[Pr_3NBu]Ni(C_2N_3)_3$, which has no solid-to-solid phase transition, we assumed that both materials, *i.e.* the high-temperature phase of $[Pr_3NBu]Mn(C_2N_3)_3$ and as-synthesized $[Pr_3NBu]Ni(C_2N_3)_3$ are isostructural. To confirm this hypothesis, Pawley profile fits of $[Pr_3NBu]Mn(C_2N_3)_3$ with space-group ($Pna2_1$) and lattice parameters ($a$ = 17.111(1) Å, $b$ = 11.880(1) Å and $c$ = 11.667(1) Å) of $[Pr_3NBu]Ni(C_2N_3)_3$ were tested with a satisfactory result, *i.e.* $a$ = 17.049(9) Å, $b$ = 12.012(5) Å and $c$ = 12.244(6) Å, see Figure S17 and Figure S18. Comparing the resulting lattice parameters of both phases, we find a similar trend as previously found for $[Pr_3NMe]Ni(C_2N_3)_3$ (*Pnma*, $a$ = 10.0232(3) Å, $b$ = 16.1193(5) Å and $c$ = 12.6992(4) Å) and $[Pr_3NMe]Mn(C_2N_3)_3$ (*Pnma*, $a$ = 10.0193(5) Å, $b$ = 16.4215(10) Å and $c$ = 13.0125(7) Å) (with $[Pr_3NMe]^+$ = $[(C_3H_7)_3(CH_3)N]^+$).[14] A subsequent structure refinement based on a Rietveld refinement only lead to good results when using ADPs which showed a large dependency based on the starting parameters, *i.e.* no clear low-minimum structure, which are likely related to data quality and/or large disorder on the X-site position. In turn, there is evidence that the high-temperature structure of $[Pr_3NBu]Mn(C_2N_3)_3$ is best described with a perovskite-motif, but no atomic positions can be provided at this point.

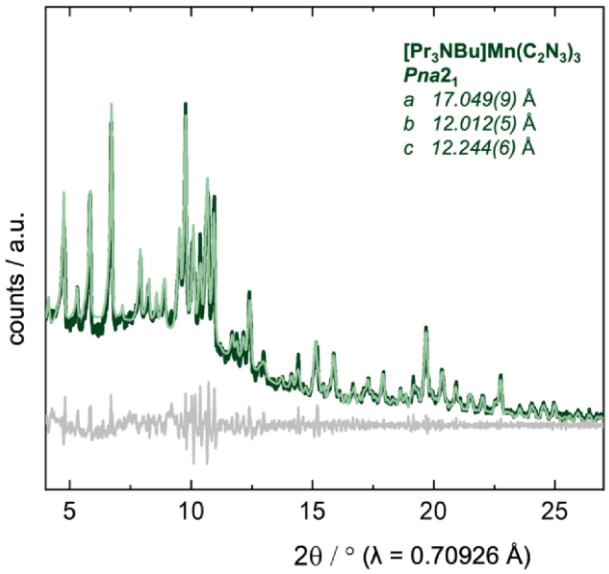


**Figure S17:** The PXRD pattern of the activated compound $[Pr_3NBu]Mn(C_2N_3)_3$ (dark green) in the high temperature phase compared to the calculated data from Pawley profile fit analysis (light green), with $R_{wp} = 5.562$, $R_{exp} = 2.845$ and GOF = 1.954. The difference curve of the Pawley profile fit (grey) and the experimental data indicates phase purity.

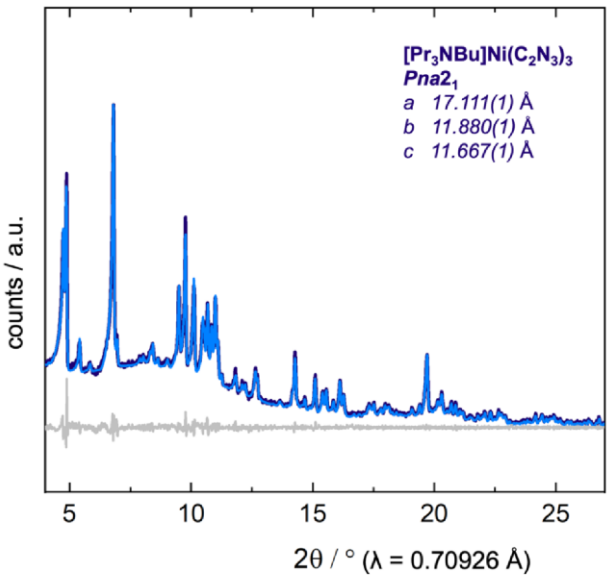


**Figure S18:** The PXRD pattern of the as-synthesized $[Pr_3NBu]Ni(C_2N_3)_3$ compared to the calculated data from Pawley profile fit analysis (light green), with $R_{wp} = 3.052$, $R_{exp} = 2.313$ and GOF = 1.319. The difference curve of the Pawley profile fit (grey) and the experimental data indicates the bulk phase purity of the $Ni^{2+}$ compound, that exhibits the isostructural phase to the high temperature phase of the $Mn^{2+}$ compound as shown above.

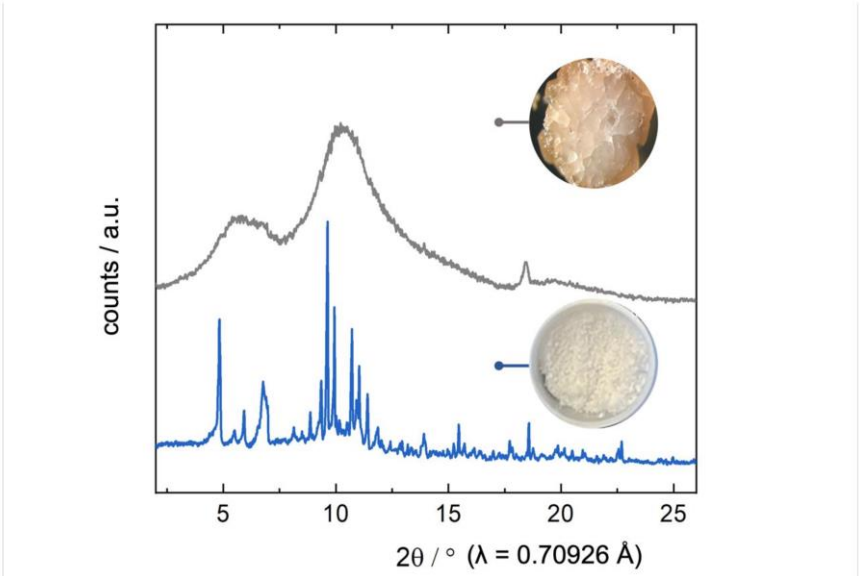


**Figure S19:** Ambient temperature PXRD patterns of the as-synthesized powder sample $[Pr_3NBu]Mn(C_2N_3)_3$ (blue) compared with the quenched $[Pr_3NBu]Mn(C_2N_3)_3$ sample (grey) after melting the sample in a TGA-DSC experiment slightly above $T_m$, confirming no crystallinity after rapid quenching procedure. The reflection around 18 ° is caused by the setup (collimator).

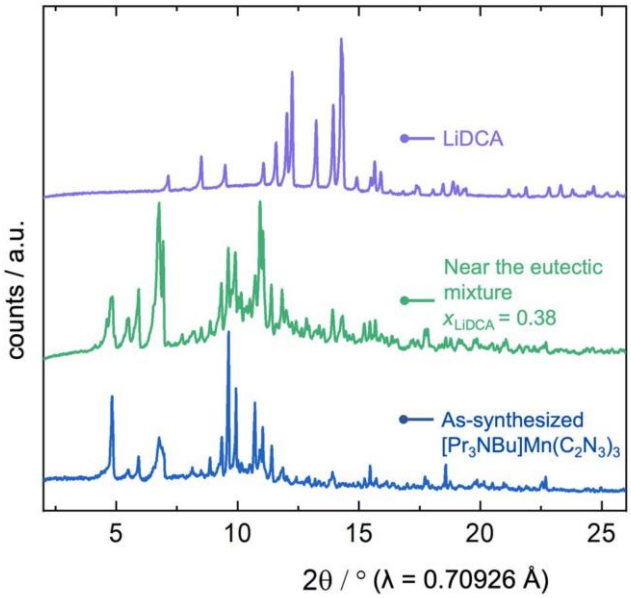


**Figure S20:** Ambient temperature PXRD patterns showing crystallinity of all compounds before melting procedures of the as-synthesized powder sample $[Pr_3NBu]Mn(C_2N_3)_3$ (blue) with $Li(C_2N_3)$ (purple) and the respective mixture of both compounds near the eutectic (green).

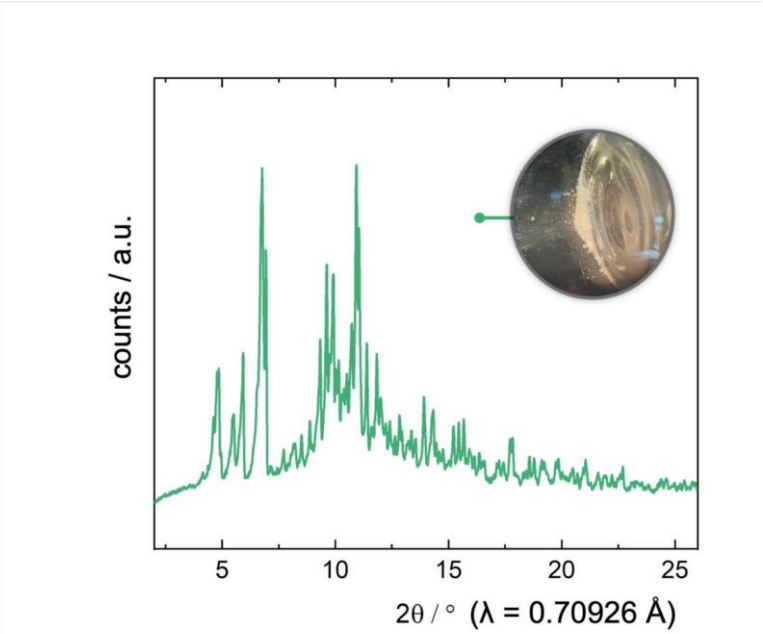


**Figure S21:** PXRD pattern of the mixture near the eutectic ($x_{LiDCA}$ = 0.38) measured at ambient conditions in a capillary as crystalline powder (green).

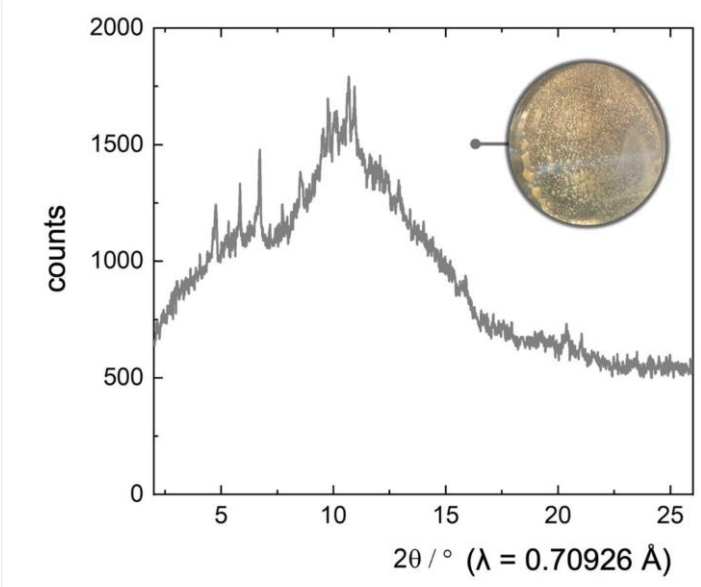


**Figure S22:** PXRD pattern of the mixture near the eutectic ($x_{LiDCA}$ = 0.38) measured at ambient conditions in a capillary after melting upon holding at 443 K, 10 K above the melting point of the mixture, revealing after slowly cooling down to room temperature an almost X-ray amorphous melt (grey).

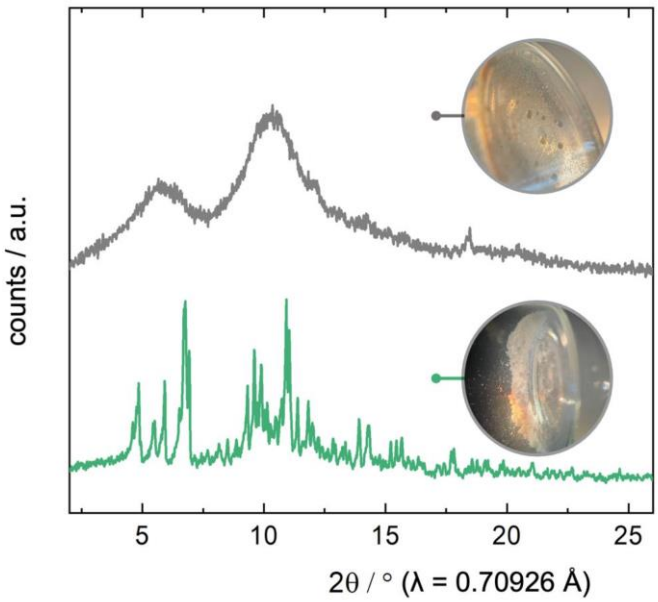


**Figure S23:** Ambient PXRD patterns of the mixture near the eutectic ($x_{LiDCA}$ = 0.41) measured at ambient conditions in a capillary as crystalline powder (green) and after melting upon holding at 441 K, 10 K above the melting point of the mixture, revealing after slowly cooling down to room temperature an X-ray amorphous melt (grey).

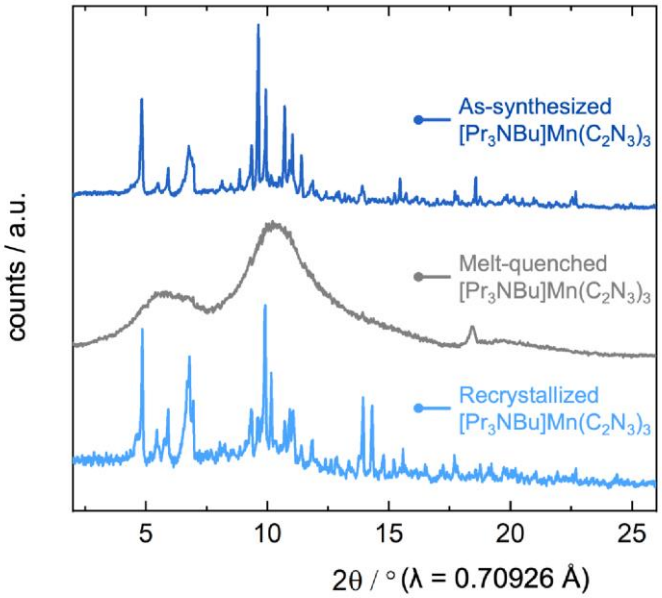


**Figure S24:** Ambient PXRD patterns of as-synthesized $[Pr_3NBu]Mn(C_2N_3)_3$ (dark blue), the X-ray amorphous melt-quenched $[Pr_3NBu]Mn(C_2N_3)_3$ (grey) and $[Pr_3NBu]Mn(C_2N_3)_3$ after complete recrystallization (light blue) under ambient conditions.

High-resolution temperature-dependent PXRD experiments were collected at beamline P02.1, PETRA III of the Deutsche-Elektronensynchrotron DESY (Hamburg, Germany) with a fixed operating photon energy of 60 keV ($\lambda$ = 0.20679 Å), equipped with a monochromator, a Perkin Elmer detector and a temperature control device from Oxford Cryosystems Plus (Habcryo-X). The experiments were carried out with borosilicate glass capillaries (0.8 mm diameter) in the temperature range between 290 K and 490 K, in 10 K steps from 430 K to 440 K and in 5 K intervals from 440 K to 485 K, see Figure S 25. In addition to the stacking plot as provided in Figure 1, Figure 25 shows a contour plot of the data, clearly showing a crystalline-to-crystalline phase transition and amorphisation (sample melting) before $T_d$ = 570 K.

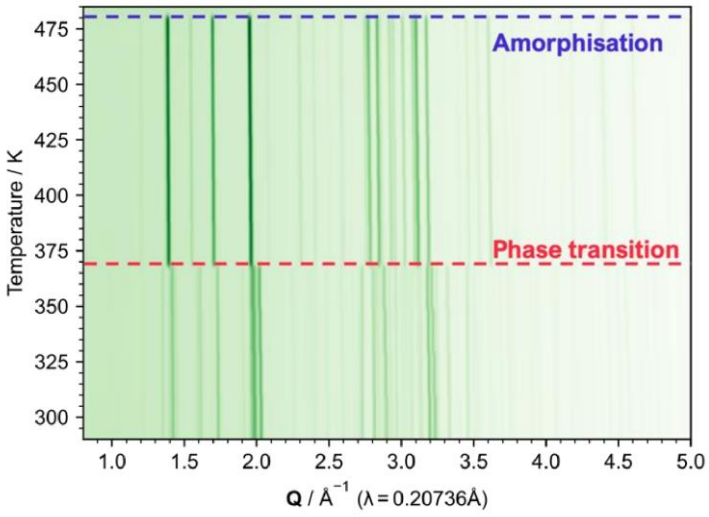


**Figure S25:** Synchrotron powder X-ray diffractograms of $[Pr_3NBu]Mn(C_2N_3)_3$ were measured in the temperature range from room temperature to 485 K shown as contour plot with darker colors corresponding to a higher intensity. The temperature induced crystalline to crystalline phase transition in $[Pr_3NBu]$ $Mn(C_2N_3)_3$ is highlighted with a dotted line in red. The second transition into an amorphous state before reaching $T_d$ is indicated with a dotted line in blue.

## Differential scanning calorimetry (DSC)

In the analysis of the eutectic system, DSC experiments of powder samples for the mixed perovskite $[Pr_3NBu]Mn(C_2N_3)_3$ with $Li(C_2N_3)$ ($x_{LiDCA}$ = 0, 0.15, 0.25, 0.32, 0.38, 0.41, 0.45, 0.49, 0.58, 0.66, 1) were performed using a DSC (NETZSCH DSC 200 F3, Germany). Temperature and sensitivity calibrations were performed using the transition enthalpy and temperature of standard materials (adamantane, bismuth, caesium chloride, indium, tin, and zinc) with a mass purity of 99.999 %. The standard uncertainty of the sensitivity and temperature measurements were 0.3 % and 0.1 K, respectively.

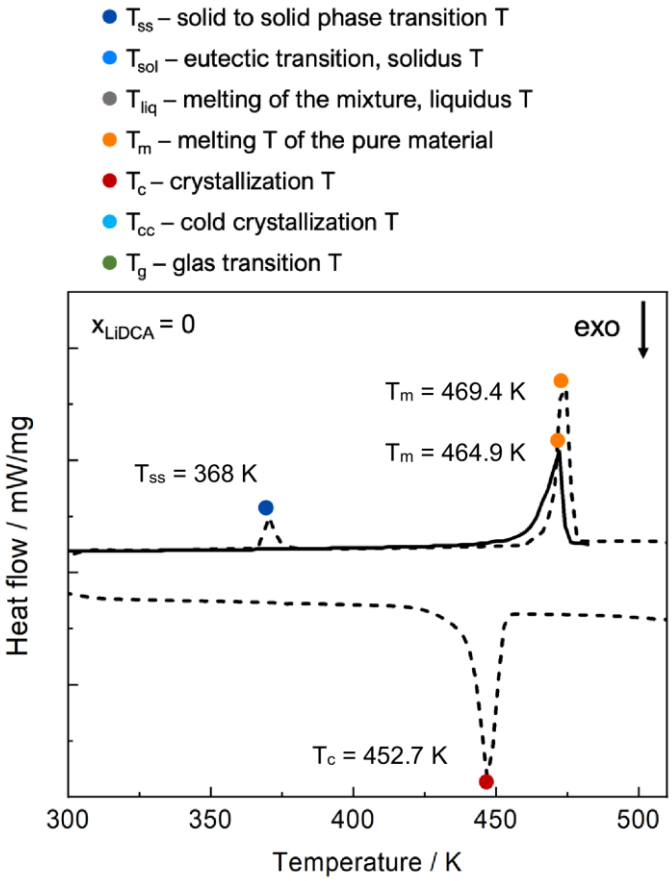


**Figure S26:** Reversible DSC measurement for $[Pr_3NBu]Mn(C_2N_3)_3$ without $Li(C_2N_3)$. After an initial heating treatment ($T_m$ = 469.9 K, dotted line) and the subsequent cooling run (($T_m$ = 464.9 K, dotted line), a re-heating run of the material is shown as continuous line. On subsequent analysis of the DSC scans, significant heat signals are assigned to specific events, with respective temperature points highlighted as colored points, as shown in the legend above.

The DSC scans were conducted under a constant nitrogen flow (150 mL $min^{-1}$), using a 5 K $min^{-1}$ heating rate to a final temperature of 493 K. The solid to solid transition temperature ($T_{ss}$), the melting temperature ($T_m$) of $[Pr_3NBu]Mn(C_2N_3)_3$ and the liquidus ($T_{liq}$) and solidus ($T_{sol}$) temperature of the mixtures were obtained from the peak maximum and onset temperature, respectively. In addition, all endothermal events ($T_{ss}$, $T_m$, $T_{liq}$ and $T_{sol}$) in the initial DSC heating run are given as the offset temperature of the endothermal peak in accordance with literature values, see Table S3. The glass transition temperature ($T_g$), as well as both crystallization temperatures ($T_c$ and $T_{cc}$) were determined as onset of the respective peak in the DSC curve. The basis for the convention of determining $T_{liq}$ and $T_{sol}$ of eutectic systems can be found in literature.[15,16]

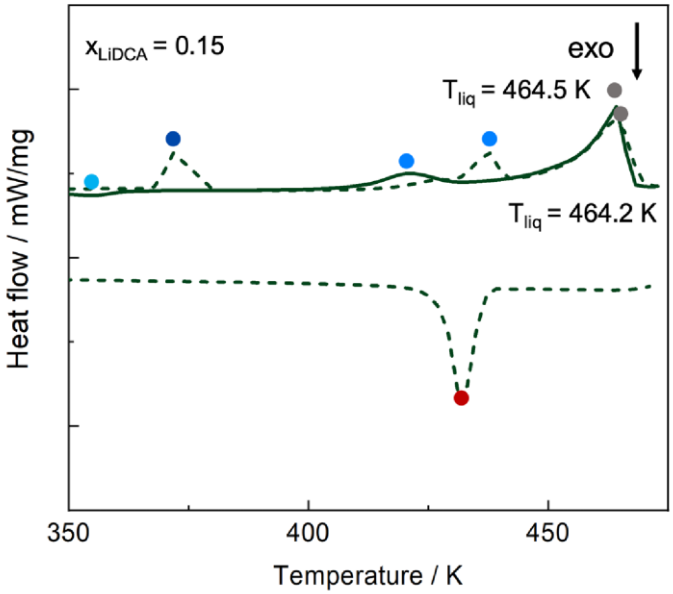


**Figure S27:** DSC curves of $[Pr_3NBu]Mn(C_2N_3)_3$ with a mole fraction of $x$ = 0.15 of $Li(C_2N_3)$. Initial heating ($T_{sol}$ = 430.4 K and $T_{liq}$ = 464.2 K) and the subsequent cooling run are shown as dotted line and the re-heating run ($T_{sol}$ = 410.3 K and $T_{liq}$ = 464.5 K) as continuous line.

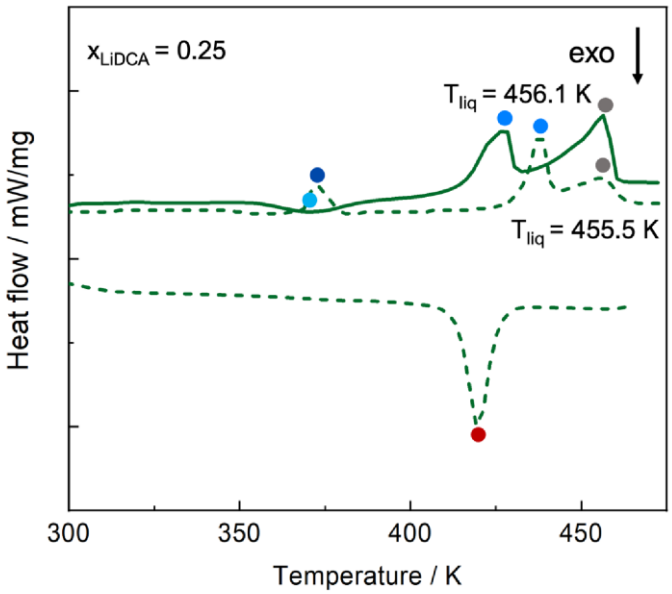


**Figure S28:** DSC curves of $[Pr_3NBu]Mn(C_2N_3)_3$ with a mole fraction of $x$ = 0.25 of $Li(C_2N_3)$. Initial heating ($T_{sol}$ = 434.3 K and $T_{liq}$ = 455.5 K) and the subsequent cooling run are shown as dotted line and the re-heating run ($T_{sol}$ = 418.6 K and $T_{liq}$ = 456.1 K) as continuous line.

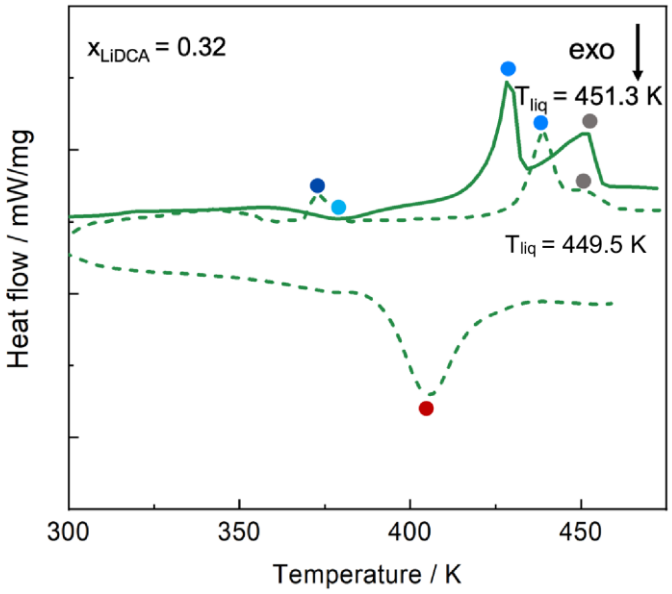


**Figure S29:** DSC curves of $[Pr_3NBu]Mn(C_2N_3)_3$ with a mole fraction of $x$ = 0.32 of $Li(C_2N_3)$. Initial heating ($T_{sol}$ = 434.5 K and $T_{liq}$ = 449.5 K) and the subsequent cooling run are shown as dotted line and the re-heating run ($T_{sol}$ = 422.7 K and $T_{liq}$ = 451.3 K) as continuous line.

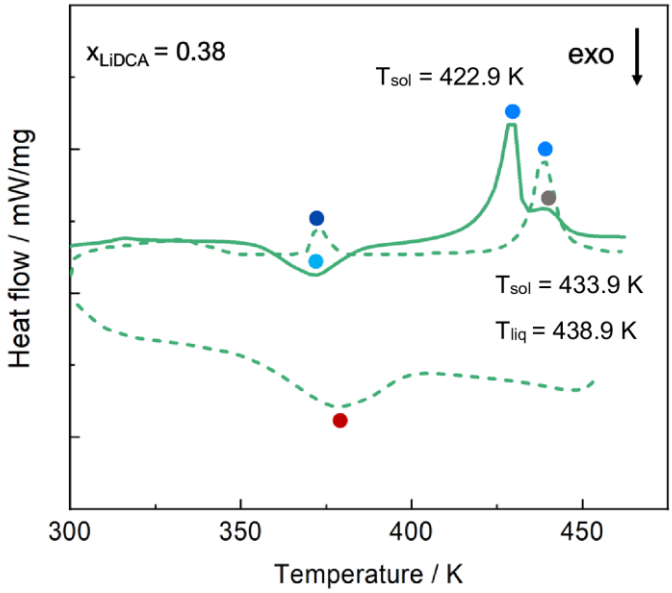


**Figure S30:** DSC curves of $[Pr_3NBu]Mn(C_2N_3)_3$ with a mole fraction of $x$ = 0.38 of $Li(C_2N_3)$. Initial heating ($T_{sol}$ = 433.9 K) and the subsequent cooling run are shown as dotted line and the re-heating run ($T_{sol}$ = 422.9 K and $T_{liq}$ = 438.9 K) as continuous line.

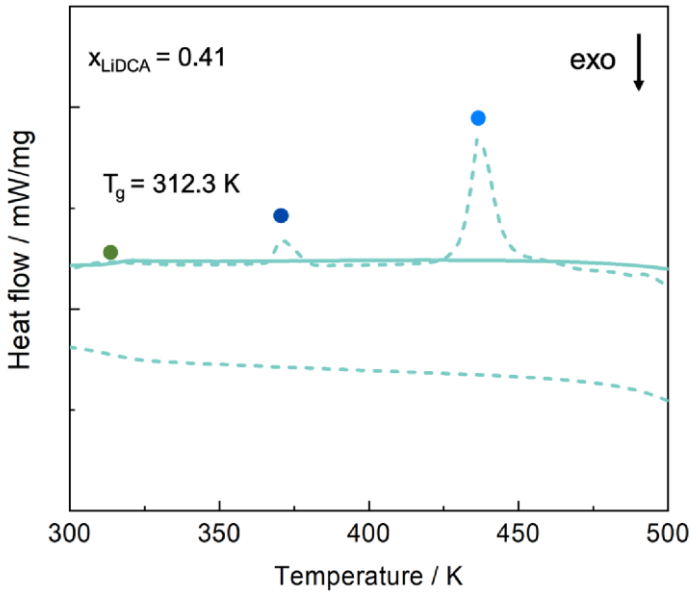


**Figure S31:** DSC curves of $[Pr_3NBu]Mn(C_2N_3)_3$ with a mole fraction of $x$ = 0.41 of $Li(C_2N_3)$. Initial heating ($T_{sol}$ = 431.9 K) and the subsequent cooling run are shown as dotted line and the re-heating run ($T_g$ = 312.3 K) as continuous line.

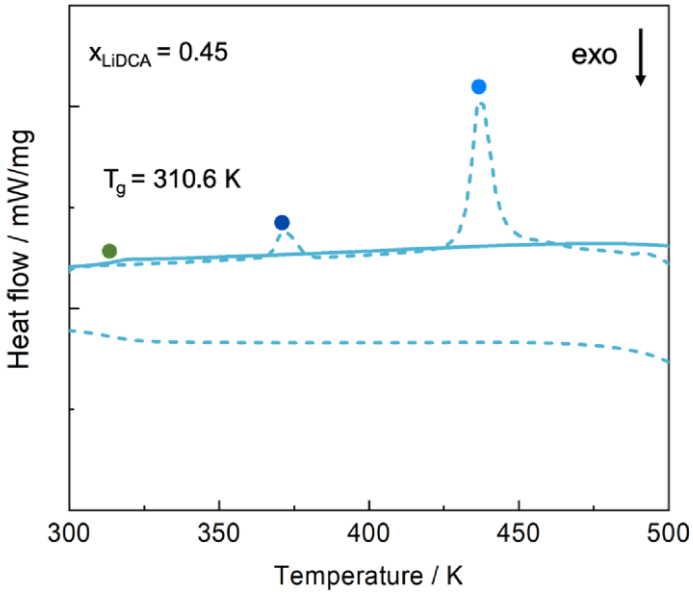


**Figure S32:** DSC curves of $[Pr_3NBu]Mn(C_2N_3)_3$ with a mole fraction of $x$ = 0.45 of $Li(C_2N_3)$. Initial heating ($T_{sol}$ = 430.8 K) and the subsequent cooling run are shown as dotted line and the re-heating run ($T_g$ = 310.6 K) as continuous line.

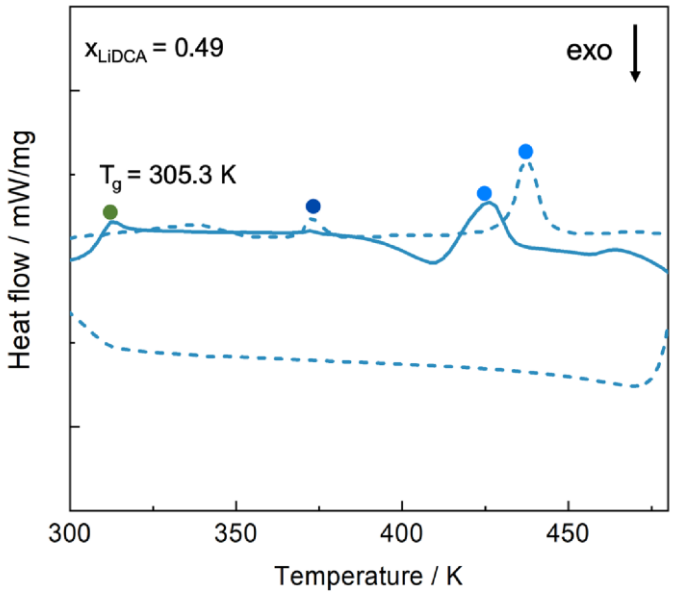


**Figure S33:** DSC curves of $[Pr_3NBu]Mn(C_2N_3)_3$ with a mole fraction of $x$ = 0.49 of $Li(C_2N_3)$. Initial heating ($T_{sol}$ = 433.2 K) and the subsequent cooling run are shown as dotted line and the re-heating run ($T_{sol}$ = 415.9 K and $T_g$ = 305.3 K) as continuous line.

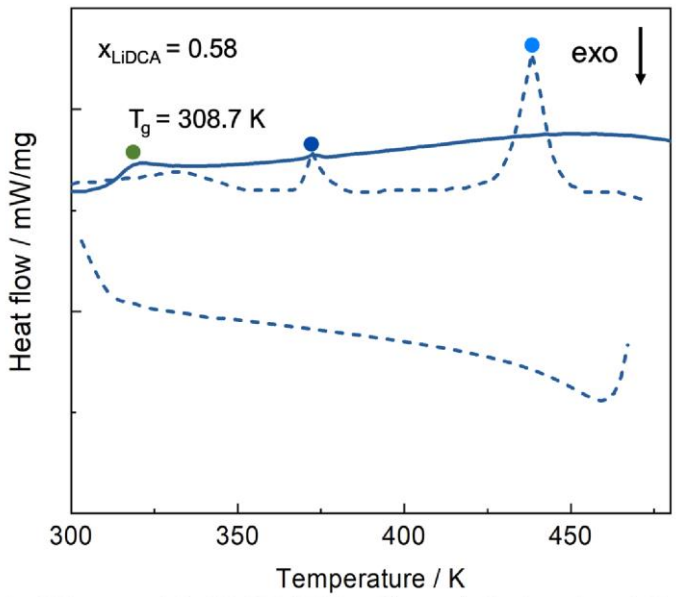


**Figure S34:** DSC curves of $[Pr_3NBu]Mn(C_2N_3)_3$ with a mole fraction of $x$ = 0.58 of $Li(C_2N_3)$. Initial heating ($T_{sol}$ = 433.9 K) and the subsequent cooling run are shown as dotted line and the re-heating run ($T_g$ = 308.7 K) as continuous line.

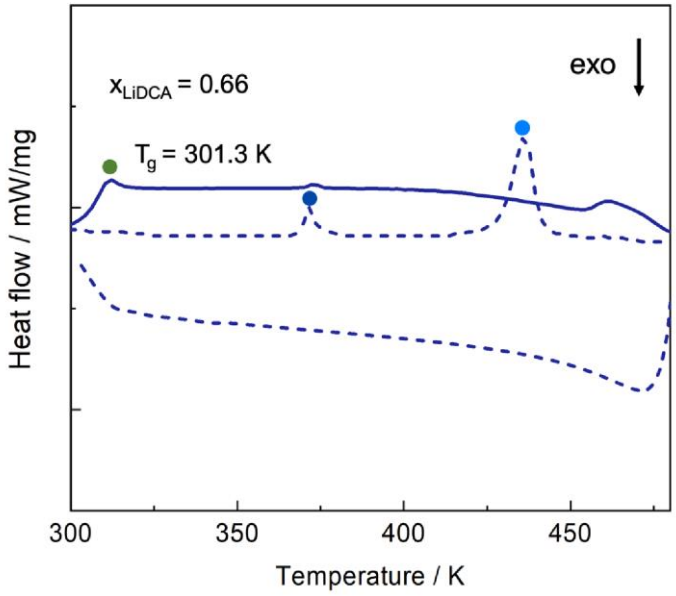


**Figure S35:** DSC curves of $[Pr_3NBu]Mn(C_2N_3)_3$ with a mole fraction of $x$ = 0.66 of $Li(C_2N_3)$. Initial heating ($T_{sol}$ = 430.4 K) and the subsequent cooling run are shown as dotted line and the re-heating run ($T_g$ = 301.3 K) as continuous line.

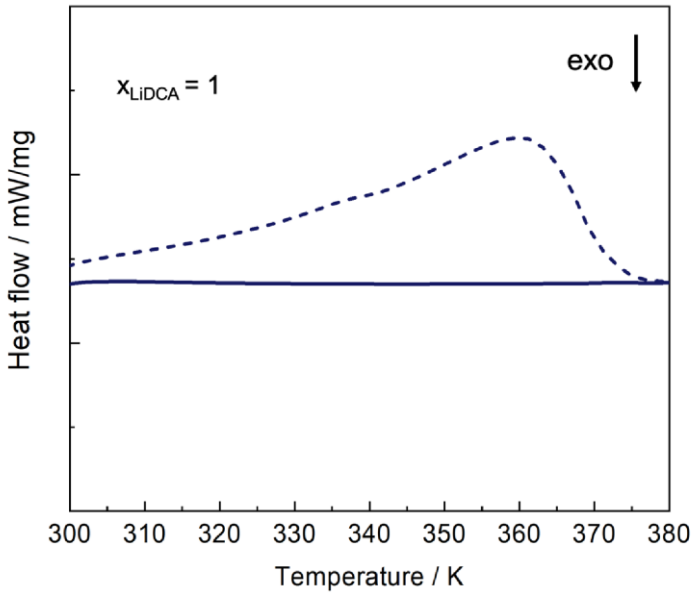


**Figure S36:** DSC curves of $Li(C_2N_3)_3$ showing a broad endotherm at 360 K in the initial heating run (dotted line) that is attributed to the thermal decomposition of the lithium hydrate. The re-heating run shown as continuous line confirms a hydrate-free $Li(C_2N_3)_3$ that is used as modifier salt.

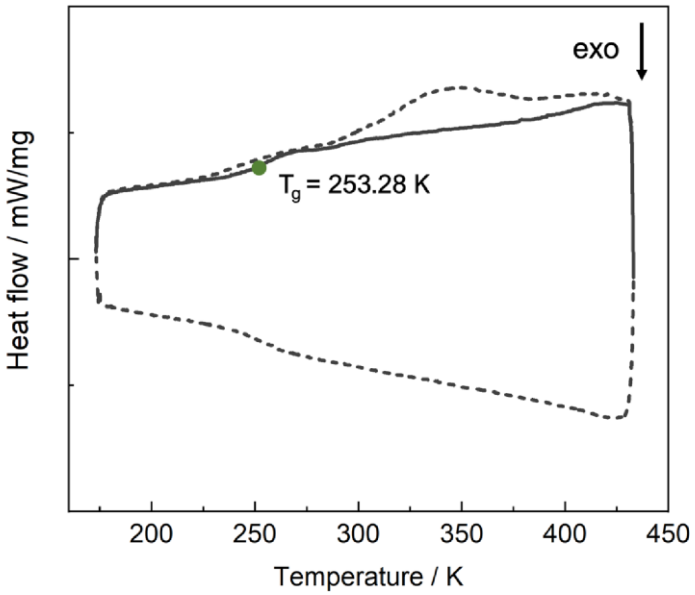


**Figure S37:** Subsequent heating and cooling DSC cycles of the melt-quenched $[Pr_3NBu]Mn(C_2N_3)_3$, showing a broad exotherm at 340 K in the initial heating run (dotted line) corresponding to removal of water. The re-heating run (continuous line) reveals a glass transition temperature of $T_{g,Onset}$ = 253.28 K, marked with a green dot.

The DSC scans of $[Pr_3NBu]Mn(C_2N_3)_3$ after melt quenching were carried out in a DSC (TA Instruments Q2000) under a constant helium purging gas flow (25 mL $min^{-1}$) with a heating rate of 20 K $min^{-1}$ in the temperature window from 173 K to 433 K by using liquid nitrogen for cooling control, see Figure S37.

**Table S3:** Depending on the field, the phase transition temperature from the DSC trace is determined differently (peak onset, peak offset, maximum). For better comparison to literature data, this table gives a comprehensive overview of the temperature determination including the onset, peak maximum and offset temperature in K for all observed endothermic events in the initial DSC heating run (*reheating run) of different mixtures of $[Pr_3NBu]Mn(C_2N_3)_3$ with various mole fraction of $x$ of $Li(C_2N_3)$. In some cases, the sensitivity was too low and peak areas too small for a valid determination (-) or the event is not observed ( ).

| $x_{LiDCA}$ | $T_{ss}$ Onset | $T_{ss}$ Peak | $T_{ss}$ Offset | $T_{sol}$ Onset | $T_{sol}$ Peak | $T_{sol}$ Offset | $T_{liq}$ Onset | $T_{liq}$ Peak | $T_{liq}$ Offset |
|---|---|---|---|---|---|---|---|---|---|
| 0 | 368 | 370.7 | 375.5 | | | | 469.4 ($T_m$) | 474 ($T_m$) | 477.3 ($T_m$) |
| 0.15 | 368.7 | 371.9 | 379.4 | 430.4 | 437.5 | 440.6 | - | 464.2 | 469.3 |
| 0.25 | 368.7 | 371.9 | 380 | 434.3 | 438.2 | 441.6 | - | 455.5 | 462.3 |
| 0.32 | 369.5 | 372.6 | 379.5 | 434.5 | 438.7 | 443.6 | - | 449.5 | 459.8 |
| 0.38 | 369.8 | 372.5 | 377.8 | 433.9 | 438.8 | 444.8 | - | 438.9* | 447.2* |
| 0.41 | 365.3 | 369.3 | 375.9 | 431.9 | 436 | 443.2 | - | - | - |
| 0.45 | 369.3 | 370 | 376.9 | 430.8 | 435.8 | 443.2 | - | - | - |
| 0.49 | 369.8 | 372.5 | 377.5 | 433.2 | 437.8 | 443.5 | - | - | - |
| 0.58 | 369.4 | 372.1 | 377.2 | 433.9 | 438 | 445.1 | - | - | - |
| 0.66 | 369.1 | 371.7 | 375.6 | 430.4 | 436.9 | 441.5 | - | - | - |

## Thermogravimetric analysis and mass spectrometry (TGA-MS)

To investigate the stability of the liquid $[Pr_3NBu]Mn(C_2N_3)_3$, a TGA/STA 409 PC apparatus (Mettler-Toledo Intl. Inc.) is used for thermogravimetric analysis under synthetic air with a continuous heating rate of 10 K $min^{-1}$ up to 300 °C in a three-step heating ramp. To follow the mass change and decomposed volatile fragments, the TGA setup is connected to a mass spectrometer (Thermostar GSD 320 T from Pfeiffer Vacuum GmbH). Looking at the mass change, the molten state of $[Pr_3NBu]Mn(C_2N_3)_3$ remains thermally stable up to 220 °C, see Figure S38. A first mass decrease of almost 1 wt% starts at 220 °C and a more significant mass loss of approximately 8 wt% appears at 240 °C. A further increase in the temperature to finally 300 °C reveals a mass loss of 25 wt%. The responsible species can be identified from the mass spectrometry data, showing the initial decomposition of the alkyl chains of the A-site cation $[Pr_3NBu]^+$ around 220 °C, followed by partial fragmentation of the dicyanamide-linker $[C_2N_3]^-$ at around 260 °C.

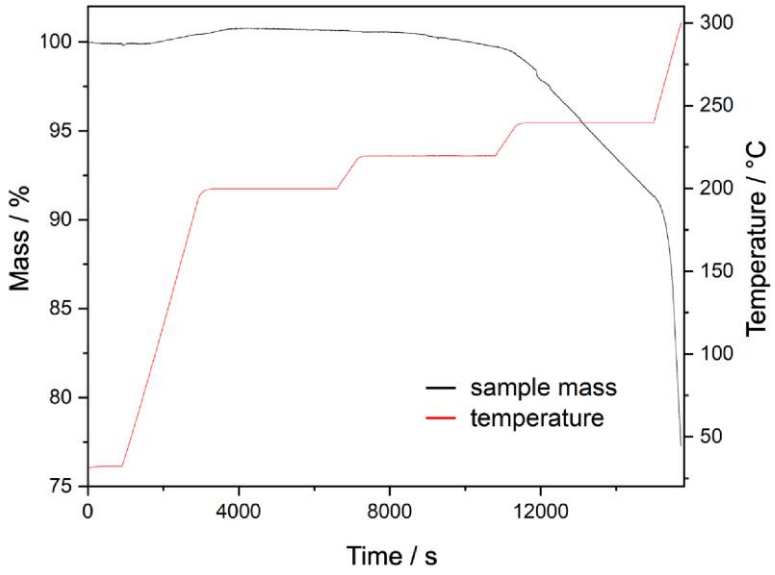


**Figure S38:** TGA-MS data as a function of time by heating $[Pr_3NBu]Mn(C_2N_3)_3$ up to 300 °C in a three-step heating rate (red, 1st step = 200 °C, 2nd step = 220 °C and 3rd step = 240 °C).

## IR spectroscopy of the modifier salt Li($C_2N_3$)

Fourier-transform infrared spectroscopy (FT-IR) was performed on a *PerkinElmer Frontier 102920* spectrometer using an ATR plate with a spectral range of 4000 $cm^{-1}$ to 650 $cm^{-1}$. FT-IR spectroscopy was used to screen the ion exchange in the metathesis reaction from Na($C_2N_3$) to Li($C_2N_3$). A FT-IR spectrum of the purchased Na($C_2N_3$) without further purification was recorded to compare with the synthesized Li($C_2N_3$) after all purification steps, see Figure S39-S41.

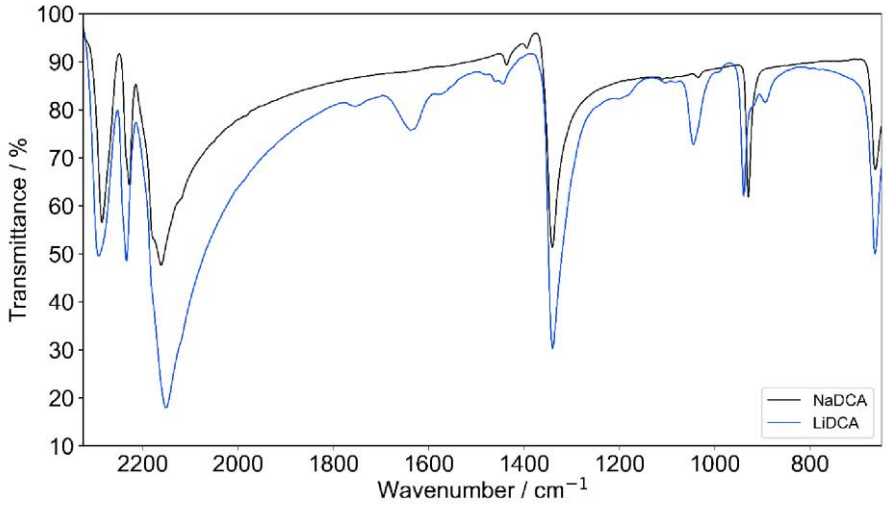


**Figure S39:** FT-IR spectra recorded at room temperature of the purified Li($C_2N_3$) (blue) in comparison with the purchased Na($C_2N_3$) (black) with DCA = $[C_2N_3]^-$.

**Table S4:** Overview of the vibrational modes of Na($C_2N_3$) and Li($C_2N_3$) with some selected modes highlighted in grey that are used for further analysis of the purification steps in the Li($C_2N_3$) synthesis, including the respective literature-known wavenumbers of Li($C_2N_3$).[2,3]

| Vibrational mode | Na($C_2N_3$) [$cm^{-1}$] | Li($C_2N_3$) [$cm^{-1}$] | Lit. Li($C_2N_3$) [$cm^{-1}$] |
|---|---|---|---|
| $\delta$(C-N-C) | | | |
| $\delta_{as}$(N-C≡N) | | | 506 |
| $\gamma_{as}$(N-C≡N) | | | 529 |
| $\gamma_s$(N-C≡N) | | | 548 |
| $\delta_s$(N-C≡N) | 663 | 664 | 666 |
| $\nu_s$(N-C) | 930 | 939.5 | 943 |

| | | | |
|---|---|---|---|
| $\nu_{as}$(N-C) | 1341 | 1340 | 1339 |
| $\nu_s$(N-C) + $\delta_{as}$(N-C≡N) | 1437 | 1445 | 1441 |
| $\nu_{as}$(C≡N) | 2161 | 2151 | 2154 |
| $\nu_{as}$(N-C) + $\nu_s$(N-C) | 2229 | 2234 | 2241 |
| $\nu_s$(C≡N) | 2285 | 2293 | 2295 |
| *Not assigned:* | | | |
| $\nu_{as}$(C≡N) + $\nu_s$(N-C) | 3062 | 3089 | 3089 |
| $\nu_s$(C≡N) + $\nu_s$(N-C) | 3211 | 3234 | 3243 |
| $\nu_s$(C≡N) + $\nu_{as}$(N-C) | 3575 | 3575 | 3575 |

Two distinct regions 850-1000 $cm^{-1}$ and 2100-2350 $cm^{-1}$ with significant differences in the respective signals and wavenumbers were selected for further analysis of the purified modifier salt, indicating a purely synthesized $Li(C_2N_3)$, as shown in Figure S40. A more detailed assignment of all vibration modes can be found in Table S4, confirming the successful ion exchange from Na to Li after several purification steps as previously described.

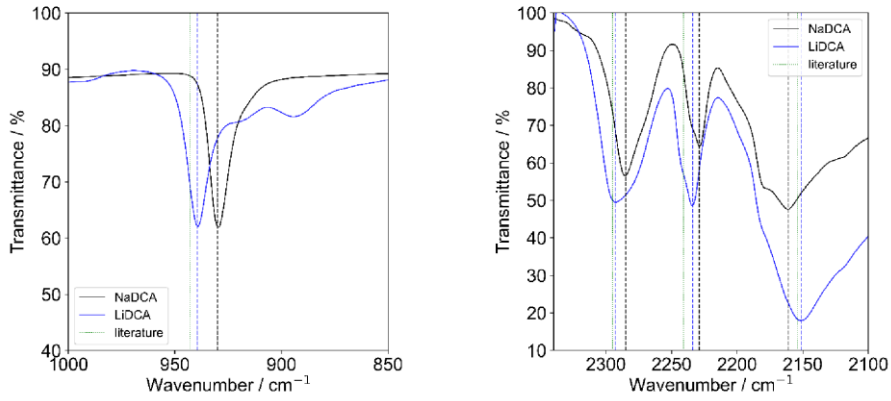


**Figure S40:** Sections of the FT-IR spectra showing $Na(C_2N_3)$ (black) and $Li(C_2N_3)$ (blue) used for the analysis of the purification process, with vertical dotted lines highlighting the signals of the purchased $Na(C_2N_3)$ (black) and synthesized $Li(C_2N_3)$ (blue) in comparison to the literature-known signals and wavenumbers of $Li(C_2N_3)$ (green).

Other observed signals in the FT-IR spectrum (Figure S39), not listed in Table S4, can be assigned to the remaining solvents (water and tetrahydrofuran (THF)), affecting the respective signals and wavenumbers, hence resulting in minor deviations from the literature-known IR modes for $Li(C_2N_3)$.[2,3]

To further investigate the modifier $Li(C_2N_3)$, THF residue was removed in a purification procedure as described in more detail in the sample preparation section (S-12). Both highlighted sections indicate significant regions of THF signals (700-1100 $cm^{-1}$ and 2700-3000 $cm^{-1}$) that can no longer be observed in the FT-IR spectrum of the dried $Li(C_2N_3)$, confirming a solvent-free $Li(C_2N_3)$ product, see Figure S41.

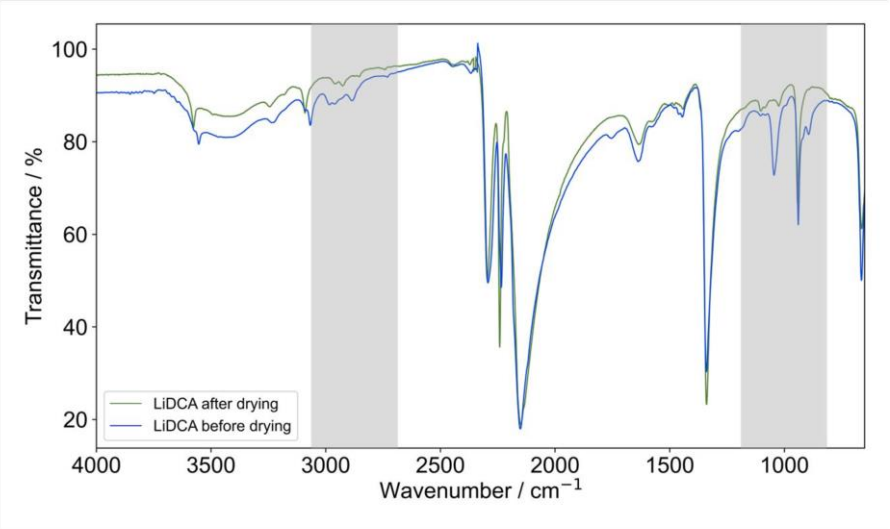


**Figure S41:** FT-IR spectra showing $Li(C_2N_3)$ before (blue) and after (green) the drying procedure as described below in the sample preparation section (S-11).

## Solid-liquid thermodynamics in the modifier-perovskite mixture

The underlying solid-liquid thermodynamics are discussed to understand the difference between the studied modifier-perovskite systems, *i.e.* $[Pr_3NBu]Mn(C_2N_3)_3$–$Li(C_2N_3)$ and $[Pr_3NBu]Mn(C_2N_3)_3$–$Na(C_2N_3)$ mixtures. The solid–liquid equilibrium (SLE) in the studied binary eutectic systems containing the modifier salt and perovskite is described using the following equation:[17]

$$\ln x_i\gamma_i = \frac{\Delta h_{m,i}}{R}\left(\frac{1}{T_{m,i}} - \frac{1}{T}\right) + \frac{1}{RT}\int_{T_{m,i}}^{T} \Delta c_{P,i}\, dT - \frac{1}{R}\int_{T_{m,i}}^{T} \frac{\Delta c_{P,i}}{T}\, dT \quad (1)$$

where $i \in [salt, perovskite]$; $x$ is the mole fraction of the component in the liquid phase; $\gamma$ is the activity coefficient of the component in the liquid phase; $\Delta h_m$ is the melting enthalpy of the pure component; $T_m$ is the melting temperature of the pure component; $T$ is the temperature; $R$ is the gas constant; $\Delta c_P$ is the difference between the heat capacity of the pure component in the liquid and solid states. The last two terms on the right-hand side have opposite signs and tend to cancel each other if $T$ is not far from $T_m$. Hence, these two terms can be neglected, and the equation can be reduced to:

$$\ln x_{salt} = \frac{\Delta h_{m,salt}}{R}\left(\frac{1}{T_{m,salt}} - \frac{1}{T}\right) - \ln \gamma_{salt} \quad (2)$$

$$\ln x_{per} = \frac{\Delta h_{m,per}}{R}\left(\frac{1}{T_{m,per}} - \frac{1}{T}\right) - \ln \gamma_{per} \quad (3)$$

At the eutectic point $x_{salt} + x_{perovskite} = 1$, and the following equation can be solved to determine the eutectic temperature ($T_e$) of the eutectic system:

$$\exp\left(\frac{\Delta h_{m,salt}}{R}\left(\frac{1}{T_{m,salt}} - \frac{1}{T_e}\right) - \ln \gamma_{salt}\right) + \exp\left(\frac{\Delta h_{m,per}}{R}\left(\frac{1}{T_{m,per}} - \frac{1}{T_e}\right) - \ln \gamma_{per}\right) = 1 \quad (4)$$

The eutectic temperature of the eutectic system depends on the melting properties of pure components and their activity coefficients in the liquid phase, as shown in Equation 4. Figure S42 shows the influence of the melting properties of the modifier salt on the eutectic point of the binary eutectic perovskite-modifier system, assuming an ideal solution model, *i.e.* $\gamma_{salt} = \gamma_{per} = 1$. In principle, increasing the melting temperature or enthalpy of the modifier salt results in a melting temperature similar to that of pure perovskite melting temperature, *i.e.* no

eutectic behaviour of the system, see Figure S42. Although $Na(C_2N_3)$ and $Li(C_2N_3)$ decompose before melting, our experimental results and the Equation 4 lead us to the conclusion that $Na(C_2N_3)$ cannot form an eutectic mixture with the perovskite $[Pr_3NBu]Mn(C_2N_3)_3$ due to higher theoretical melting temperature and enthalpy of $Na(C_2N_3)$ compared to $Li(C_2N_3)$. This in principle can be expected based on their different crystal structures, both crystallize in a monoclinic system, *i.e.* $Na(C_2N_3)$ in the space group $P2_1/c$ and $Li(C_2N_3)$ in $P2/c$, but the coordination geometry and bond strength are different. In $Na(C_2N_3)$ each $Na^+$ is octahedrally coordinated by six N-atoms, whilst $Li(C_2N_3)$ exhibits two inequivalent $Li^+$ sites, one tetrahedrally and the other octahedrally coordinated;[18,19] following on from Pauling rules of parsimony, a lower stability of $Li(C_2N_3)$ can be expected. This perspective agrees with their thermal behavior, where $Li(C_2N_3)$ exhibits a significantly lower temperature for trimerization, see Figure S10. Therefore, the SLE thermodynamics provide a reasonable understanding of the observed difference in the two studied systems and can be used as a valuable tool in the search and selection for other suitable modifiers in the future.

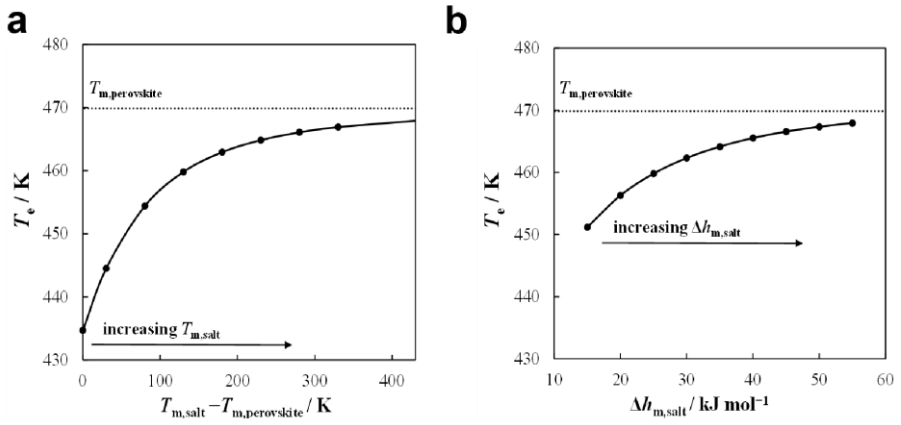


**Figure S42:** The eutectic temperature $T_e$ of a binary perovskite-modifier system as a function of increasing melting temperature of the modifier salt (a) and increasing melting enthalpy (b).

## References


1. N. Menschutkin, Z. Phys. Chem **5U**, 589 (1890).
2. O. Reckeweg, F. J. DiSalvo, A. Schulz, B. Blaschkowski, S. Jagiella, and T. Schleid, Z. Anorg. Allg. Chem. **640**, 851 (2014).
3. A. P. Purdy, E. Houser, and C. F. George, Polyhedron **16**, 3671 (1997).
4. APEX3 suite of crystallographic software, Bruker AXS Inc., Madison, Wisconsin, USA (2014).
5. SAINT, Bruker AXS Inc., Madison, Wisconsin, USA (2014).
6. SADBS, Bruker AXS Inc., Madison, Wisconsin, USA (2014).
7. G. M. Sheldrick, Acta Crystallogr. C Struct. Chem. **71**, 3 (2015).
8. G. M. Sheldrick, Acta Crystallogr., A, Found. Crystallogr. **71**, 3 (2015).
9. O. V. Dolomanov, L. J. Bourhis, R. J. Gildea, J. A. K. Howard, and H. Puschmann, J. Appl. Crystallogr. **42**, 339 (2009).
10. K. Momma and F. Izumi, J. Appl. Crystallogr. **44**, 1272 (2011).
11. G. R. Fulmer, A. J. M. Miller, N. H. Sherden, H. E. Gottlieb, A. Nudelman, B. M. Stoltz, J. E. Bercaw, and K. I. Goldberg, Organometallics **29**, 2176 (2010).
12. G. S. Pawley, J. Appl. Crystallogr. **14**, 357 (1981).
13. A. A. Coelho, J. Appl. Crystallogr. **51**, 210 (2018).
14. S. Burger, S. Grover, K. T. Butler, H. L. B. Boström, R. Grau-Crespo, and G. Kieslich, Mater. Horiz. **8**, 2444 (2021).
15. L. Rycerz, J. Therm. Anal. Calorim. **113**, 231 (2013).
16. A. van den Bruinhorst, L. J. B. M. Kollau, M. Vis, M. M. R. M. Hendrix, J. Meuldijk, R. Tuinier, and A. C. C. Esteves, J. Chem. Phys. **155**, 14502 (2021).
17. J. M. Prausnitz, R. N. Lichtenthaler, and E. G. de Azevedo, *Molecular thermodynamics of fluid-phase equilibria*, 3. ed. (Prentice-Hall PTR, Upper Saddle River, NJ, 1999).
18. The Materials Project, Materials Data on LiC2N3 by Materials Project (2020).
19. The Materials Project, Materials Data on NaC2N3 by Materials Project (2020).

## 4.2. Supporting Information for Study II

# Understanding and Controlling Molecular Compositions and Properties in Mixed-linker Porphyrin Metal-Organic Frameworks

Karina Hemmer,[a†] Silva M. Kronawitter,[a†] Nitika Grover,[b] Brendan Twamley,[c] Mirza Cokoja,[a]

Roland A. Fischer,[a] Gregor Kieslich*[a] and Mathias O. Senge*[b,d]

[a] Technical University of Munich, TUM Natural School of Sciences, Lichtenbergstr. 4, 85748, Garching, Germany.

[b] School of Chemistry, Chair of Organic Chemistry, Trinity Biomedical Sciences Institute, 152-160 Pearse Street, Trinity College Dublin, The University of Dublin, Dublin D02R590, Ireland.

[c] School of Chemistry, Trinity College Dublin, The University of Dublin, Dublin 2, Ireland.

[d] Institute for Advanced Study (TUM-IAS), Focus Group – Molecular and Interfacial Engineering of Organic Nanosystems, Technical University of Munich, Lichtenberg-Str. 2a, 85748 Garching, Germany.

[†] equal contribution

* corresponding authors

*gregor.kieslich@tum.de
*sengem@tcd.ie

## Supporting Information

**Contents**

1. Analytical Methods and Characterization Techniques ..... 2
2. Structures of the Organic Ligands ..... 4
3. Material Characterization ..... 6
4. Material Properties ..... 27
5. References ..... 30

# 1. Analytical Methods and Characterization Techniques

**Materials.**

Methanol (MeOH, HPLC grade), chloroform (HPLC grade), ethyl acetate (HPLC grade), tetrahydrofuran (THF, HPLC grade), *N,N*-dimethylformamide (DMF, HPLC grade), dichloromethane (DCM, HPLC grade), Celite® S, $ZrOCl_2$•8 $H_2O$, pyrrole, propionic acid, 4-tert-butylbenzoic acid, and potassium hydroxide were purchased from Sigma Aldrich. Methyl-*p*-formylbenzoate was purchased from ChemPUR. Diethylformamide was purchased from TCI Chemicals. $RhCl_3$•x$H_2O$ was purchased from Carbolution. 8-Dram vials for MOF synthesis (TraceClean®) were purchased from VWR. All purchased chemicals were used without further purification. All synthesis and catalysis runs were carried out under air, if not stated other.

**Analytical Data.**

The analysis of the synthesized 5,10,15,20-tetrakis(4-methoxycarbonylphenyl)porphyrin (TPPCOOMe) matched literature data with $^1$H NMR (400 MHz, $CDCl_3$): δ [ppm] = 8.82 (s, 8H, *β*-pyrrole), 8.45 (d, $^3J$ = 8.1 Hz, 8H, phenyl), 8.38 (d, $^3J$ = 8.2 Hz, 8H, phenyl), 4.12 (s, 12H, COOMe), -2.81 (s, 2H, N*H*) and elemental analysis with anal. calc. (%) for TPPCOOMe: C, 73.75; H, 4.52; N, 6.62. Found (%): C, 72.80; H, 4.66; N, 6.30. The subsequent synthesis of **$H_2$TCPP** was in line with literature reports with $^1$H NMR (400 MHz, DMSO-$d_6$): δ [ppm] = 13.29 (s, 4H, COO*H*), 8.87 (s, 8H, *β*-pyrrole), 8.40 (d, $^3J$ = 8.3 Hz, 8H, phenyl), 8.36 (d,$^3J$ = 8.4 Hz, 8H, phenyl), -2.94 (s, 2H, N*H*). Anal. calc. (%) for $H_2$TCPP: C, 72.91; H, 3.82; N, 7.09. Found (%): C, 67.85; H, 3.89; N, 6.37. Crystal water: 3 $H_2O$.

The porphyrin ester (Et-TPPCOOMe) obtained in the first step of the synthesis of **$H_2Et_8$TCPP** was confirmed *via* $^1$H NMR (400 MHz, $CDCl_3$): δ [ppm] = 8.33 (d, *J* = 8.1 Hz, 8H), 8.20 (d, *J* = 8.1 Hz, 8H), 4.10 (s, 12H), 2.38 (bs, 8H), 2.01 (bs, 8H), 0.52 (t, *J* = 7.3 Hz, 24H). $^{13}$C NMR (101 MHz, $CDCl_3$): δ [ppm] = 167.27, 145.55, 144.28, 134.30, 129.85, 128.28, 116.44, 52.39, 19.66, 16.90. The subsequent linker synthesis of **$H_2Et_8$TCPP** was confirmed *via* $^1$H NMR (600 MHz, DMSO-$d_6$): δ [ppm] = 8.80 (d, *J* = 8.0 Hz, 8H), 8.52 (d, *J* = 8.1 Hz, 8H), 2.44 (m, 8H), 2.05 (m, 8H), 0.21 (t, *J* = 7.4 Hz, 24H). $^{13}$C NMR (151 MHz, DMSO-$d_6$): δ [ppm] = 167.77, 143.71, 140.72, 137.81, 137.57, 132.38, 129.81, 117.86, 18.52, 15.93.

**NMR Spectroscopy.**

Liquid state NMR measurements were performed on a *Bruker* AVIII 400 US ($^1$H: 400.13 MHz) at ambient temperature (298 K) to confirm the chemical composition of the linking porphyrin ligands. The $^1$H NMR spectroscopic chemical shifts *δ* are reported in ppm relative to tetramethylsilane. $^1$H NMR spectra are calibrated against the residual proton and natural abundance carbon resonances of the respective deuterated solvent as an internal standard ($CDCl_3$: *δ* ($^1$H) = 7.26 ppm, DMSO-$d_6$: *δ* ($^1$H) = 2.50 ppm). The following abbreviations are used to describe signal multiplicities: s = singlet, d = doublet, t = triplet, m = multiplet.

**Elemental Analysis.**

Elemental analysis of the porphyrin linkers including all measurements and quantifications were carried out by the technical staff of the microanalytical laboratory at the Catalysis Research Center at the Technical University of Munich. The elemental composition of samples (sample weight around 3 mg) was analyzed using a *HEKAtech Euro EA* elemental analyzer through flash combustion at 1800 °C and subsequent chromatographical separation and quantification with a thermal conductivity detector (TCD).

**Attenuated Total Reflectance Infrared Spectroscopy.**

IR measurements were carried out on a *PerkinElmer* Frontier FT-IR spectrometer featuring an ATR plate with a diamond crystal with a 2 $cm^{-1}$ resolution and 16 accumulated scans.

**Laboratory Powder X-ray Diffraction.**

PXRD pattern were collected at ambient temperature on a silicon single-crystal wafer using *Bragg-Brentano* geometry in a *Rigaku* MiniFlex 600-C diffractometer. X-ray Cu $K_\alpha$ radiation ($\lambda_1$ - 1.5406 Å, $\lambda_2$ - 1.5444 Å, $I_2/I_1$ - 0.5) was used, and $K_\beta$ radiation was removed by a Ni-filter. The measurement range, unless stated otherwise, was from 2.0° to 50.0° (2θ) with a step size of 0.010 degrees and a scan rate of 5 degrees per minute.

**UV-Vis Spectroscopy.**

UV-vis spectra were recorded on an *Agilent Technologies* Cary 60 with a scan rate of 600 nm/min. Baseline correction was performed with the respective pure solvent. Each sample was measured in a QS Suprasil 10.00 mm quartz glass cuvette from *Heraeus Quarzglas GmbH.*

**Scanning Electron Microscopy.**

SEM images of the MOF samples were recorded on a *Carl Zeiss NVision40* field emission scanning electron microscope with an acceleration voltage of 5.0 kV and a working distance of 8 – 10 nm.

**Confocal Microscopy.**

Confocal microscopy was performed with with a STELLARIS 8 FALCON (*Leica Microsystems*, Germany) equipped with the HC PL APO CS2 63x/1.10 OIL objective (*Leica*). Solid samples were directly used without further preparation and placed in chambered coverslip wells. Excitation was performed at 405 nm (Diode 405 laser). Fluorescence images were obtained in the emission range of 700 – 760 nm. Merging of channels and localization of their fluorescence intensity was performed with the software *ImageJ*. [1]

## 2. Structures of the Organic Ligands

***5,10,15,20-Tetrakis*(4-carboxylphenyl)-porphyrin ($H_2$TCPP)**

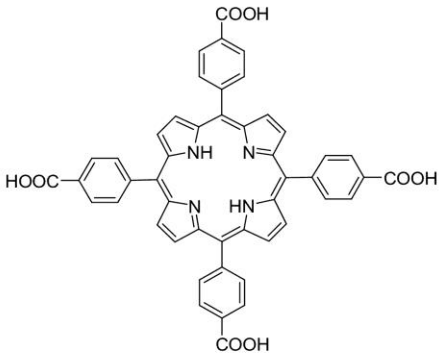


Figure S1: Structure of the synthesized organic ligand **$H_2$TCPP**.

**2,3,7,8,12,13,17,18-Octaethyl-5,10,15,20-tetrakis(4-carboxyphenyl)porphyrin ($H_2Et_8$TCPP)**

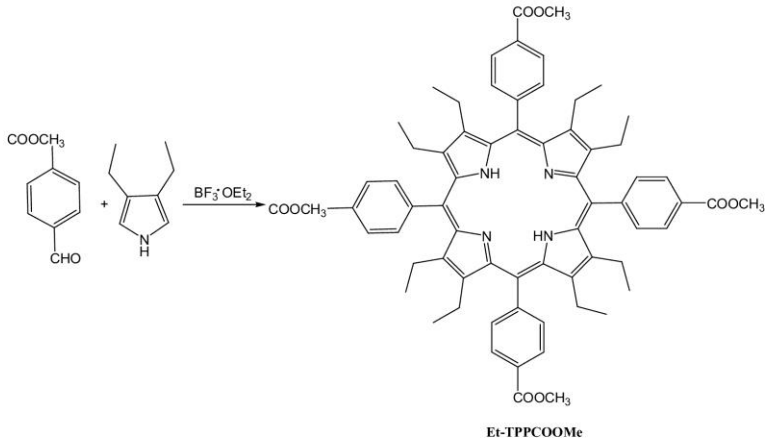


**Et-TPPCOOMe**

Scheme S1: Synthesis of 2,3,7,8,12,13,17,18-octaethyl-5,10,15,20-tetrakis(4-methoxy-carbonylphenyl)porphyrin (**Et-TPPCOOMe**).

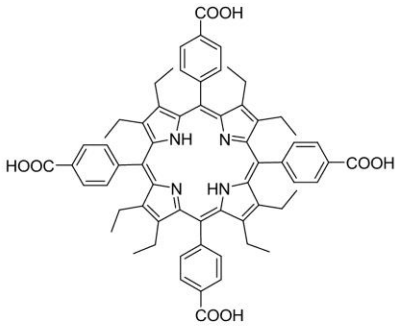


Figure S2: Structure of the synthesized organic ligand **$H_2Et_8TCPP$**.

## 3. Material Characterization

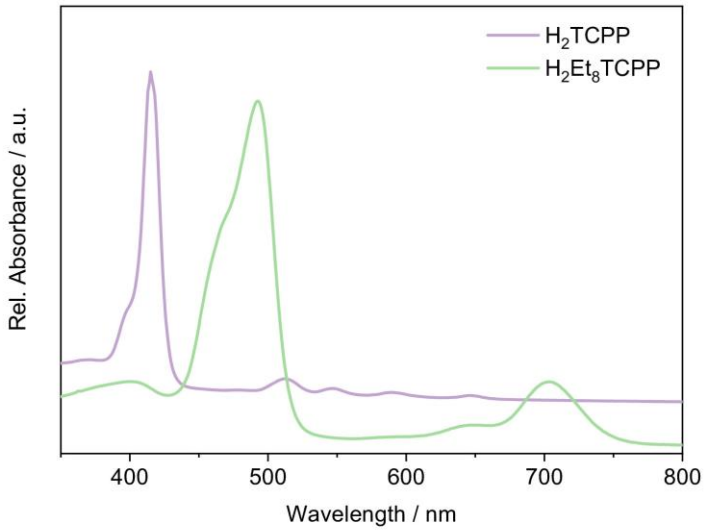


Figure S3: UV-vis spectra of **$H_2$TCPP** and **$H_2Et_8$TCPP** in ethanol. The spectrum of **$H_2Et_8$TCPP** indicates porphyrin core protonation (baselines adjusted arbitrarily).

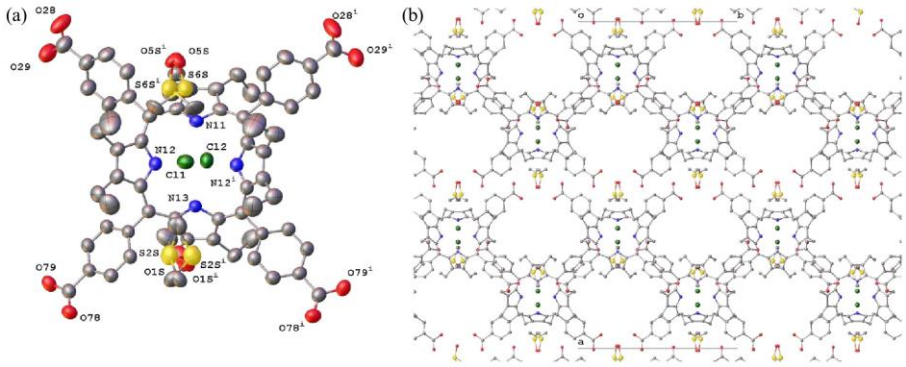


Figure S4: Molecular structure of TCD1743 with thermal displacement at 50% probability level; (b) Packing diagram for TCD 1743. TCD1743 refers to **$[H_4Et_8TCPP][Cl]_2$•DMSO**.

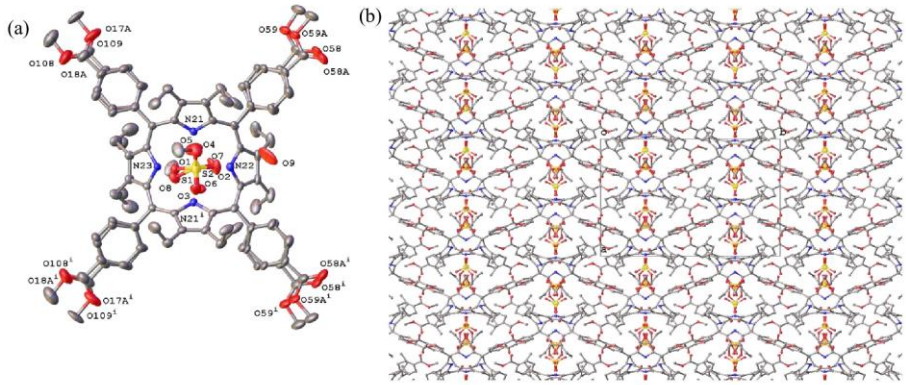


Figure S5: (a) Molecular structure of TCD1879 with thermal displacement at 50% probability level; (b) Packing diagram for TCD 1879. TCD1879 refers to **$[H_2Et_8$-TPPCOOMe][$MeSO_4H]_2$**.

Table S1: Crystallographic data for dication salts of the organic ligand **$H_2Et_8$TCPP** and its ester analogue.

| Table S1. Structural parameters for TCD1743 and TCD1879. | | |
|---|---|---|
| Compound | **$[H_4Et_8TCPP][Cl]_2$•DMSO** | **$[H_4$Et-TPPCOOMe][$MeSO_4H]_2$** |
| Internal Code | TCD1743_sq | TCD1879 |
| CCDC Code | 2302383 | 2302384 |
| Empirical Formula | $C_{68}H_{76}Cl_2N_4O_{10}S_2$ | $C_{70}H_{80}N_4O_{17}S_2$ |
| Formula weight (g/mol) | 1244.34 | 1313.50 |
| Temperature (K) | 100(2) | 100(2) |
| Crystal System | Orthorhombic | Orthorhombic |
| Space group | *Pnma* | *Pnma* |
| a (Å) | 41.133(2) | 16.9412(11) |
| b (Å) | 20.1027(10) | 25.9981(18) |
| c (Å) | 11.2225(6) | 14.5811(10) |
| α (°) | 90° | 90° |
| β (°) | 90° | 90° |
| γ (°) | 90° | 90° |
| Volume ($Å^3$) | 9279.8(8) | 6422.1(8) |
| Z | 4 | 4 |
| $\rho_{calc}$ ($g/cm^3$) | 0.891 | 1.359 |
| μ ($mm^{-1}$) | 0.629 | 0.159 |
| F(000) | 2632 | 2784 |
| Crystal size ($mm^3$) | 0.189 x 0.081 x 0.037 | 0.29 x 0.26 x 0.032 |

| Radiation | Cu Kα | Mo Kα |
|---|---|---|
| 2θ (°) | 2.148 to 54.396° | 2.419 to 25.507° |
| Reflections collected | 47160 | 78380 |
| Independent reflections | 5872 | 6109 |
| $R_{int}$ | 0.1214 | 0.1373 |
| $R_{sigma}$ | 0.0810 | 0.0494 |
| Restraints | 18 | 710 |
| Parameters | 428 | 630 |
| GooF (*S*) | 1.042 | 1.029 |
| $R_1$ [I> 2σ (I)] | 0.0599 | 0.0815 |
| $wR_2$ [I> 2σ (I)] | 0.1580 | 0.2013 |
| $R_1$ [all data] | 0.0933 | 0.1340 |
| $wR_2$ [all data] | 0.1775 | 0.2432 |
| Largest peak (e Å$^{-3}$) | 0.467 | 1.125 |
| Deepest hole (e Å$^{-3}$) | -0.268 | -0.560 |
| Flack parameter | - | - |

**Refinement note for TCD_1743** Poor diffraction at higher angles and the resolution was truncated to d=0.95 Å. Both DMSO solvent molecules were modelled half occupied with a rigid group. The diffuse diffraction components of the content of two voids in the asymmetric unit of 1796 Å$^3$ with approx. 542 electrons were removed from the data using the SQUEEZE subroutine in PLATON. This is approx. 13 $CH_2Cl_2$ molecules or 13 DMSO molecules or a combination. Attempts to model these solvents were unsuccessful.

**Refinement note for TCD1879** Half a molecule in the asymmetric unit. The porphyrin is disordered: each methyl benzoate group was modelled over two locations with C51:C51a 65:35% occupied, C101:C10A 69:31% occupied. Both moieties were modelled with restraints (SADI, SIMU) and a rigid ring model (AFIX). Two ethyl groups were also disordered (C31, 56:44%; C81, 51:49% occupied) and modelled with restraints (SADI, SIMU). The half-occupied methyl sulfonate groups were modelled as rigid groups. Pyrrole hydrogens were refined semi-free with restraints (DFIX). The water molecule is half occupied.

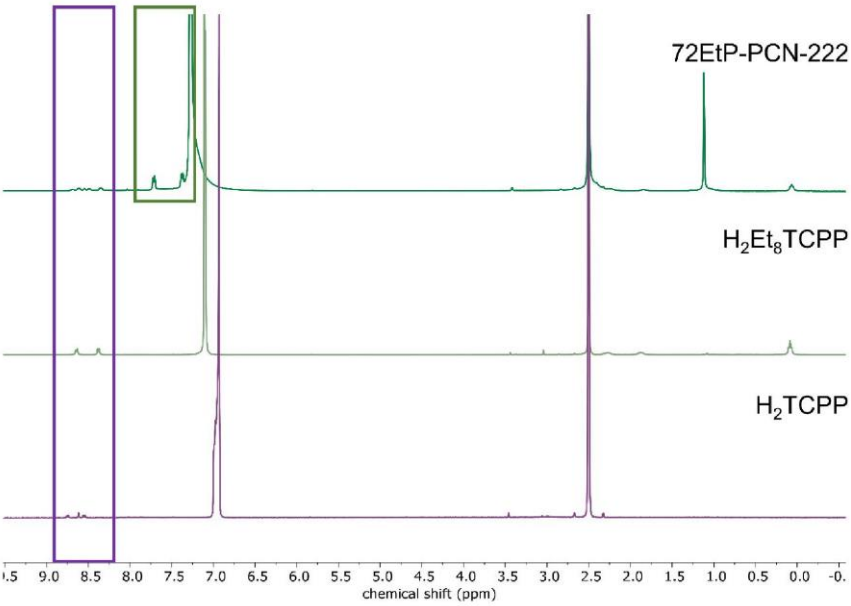


Figure S6: $^1$H NMR spectra of **$H_2$TCPP**, **$H_2Et_8$TCPP**, and **72EtP-PCN-222** which was dissolved in DCl/DMSO-$d_6$ (0.1 mL/0.3 mL). For comparison (since the shift of proton signals is pH dependent) 0.1 mL of DCl was added to a 0.3 mL solution of **$H_2Et_8$TCPP** and **$H_2$TCPP** dissolved in DMSO-$d_6$, respectively. The purple box represents the porphyrin signals while the green box shows the peaks of 4-*tert*-butylbenzoic acid which was applied as modulator in MOF synthesis and was not removed afterwards.

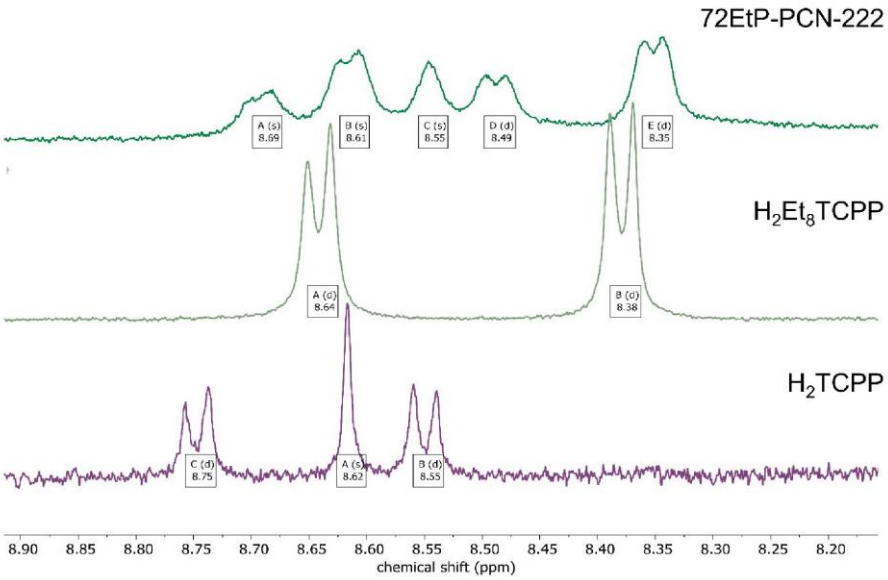


Figure S7: $^1$H NMR spectra of **$H_2$TCPP**, **$H_2Et_8$TCPP**, and **72EtP-PCN-222** samples dissolved in DCl/DMSO-$d_6$ (0.1 mL/0.3 mL). For comparison (since the shift of proton signals is pH dependent) 0.1 mL of DCl was added to a 0.3 mL solution of **$H_2Et_8$TCPP** and **$H_2$TCPP** dissolved in DMSO-$d_6$, respectively. For **$H_2$TCPP**, the $Ar_H$-porphyrin signals appear at 8.55 ppm, 8.62 ppm and 8.75 ppm, whereas the porphyrin signals of **$H_2Et_8$TCPP** are observable at 8.38 ppm and 8.64 ppm. Thus, the different signals in the porphyrin region in **72EtP-PCN-222** (chosen as example) were assigned as follows: 8.35 ppm and 8.61 ppm for **$H_2Et_8$TCPP**, 8.49 ppm, 8.55 ppm and 8.69 ppm for **$H_2$TCPP**. For determination of the **$H_2Et_8$TCPP** content in **72EtP-PCN-222**, the integrals of the resonances at 8.69 ppm (**$H_2$TCPP**) and 8.35 ppm (**$H_2Et_8$TCPP**) were compared since these signals are the most intense and signal overlap is less prominent than for the other porphyrin signals. For the calculation, the peak at 8.69 ppm was set to 1 and compared to the integral of 8.35 pm (which is 3.44) which resulted in an **$H_2Et_8$TCPP** content of 77% (=3.44/4.44).

Table S2: Mol% of **$H_2Et_8$TCPP** in PCN-222 determined by $^1$H NMR spectroscopy of acid digested MOF by comparison of the integrals of the phenyl peaks at 8.71 ppm (for **$H_2$TCPP**) and 8.36 ppm (for **$H_2Et_8$TCPP**).

| Sample | Weigh in **$H_2Et_8$TCPP** | Mol% **$H_2Et_8$TCPP** in PCN-222 (NMR) |
|---|---|---|
| 20EtP-PCN-222 | 20 | 20.3 ± 3.2 |
| 59EtP-PCN-222 | 10 | 59.3 ± 3.7 |
| 72EtP-PCN-222 | 20 | 72.1 ± 4.5 |

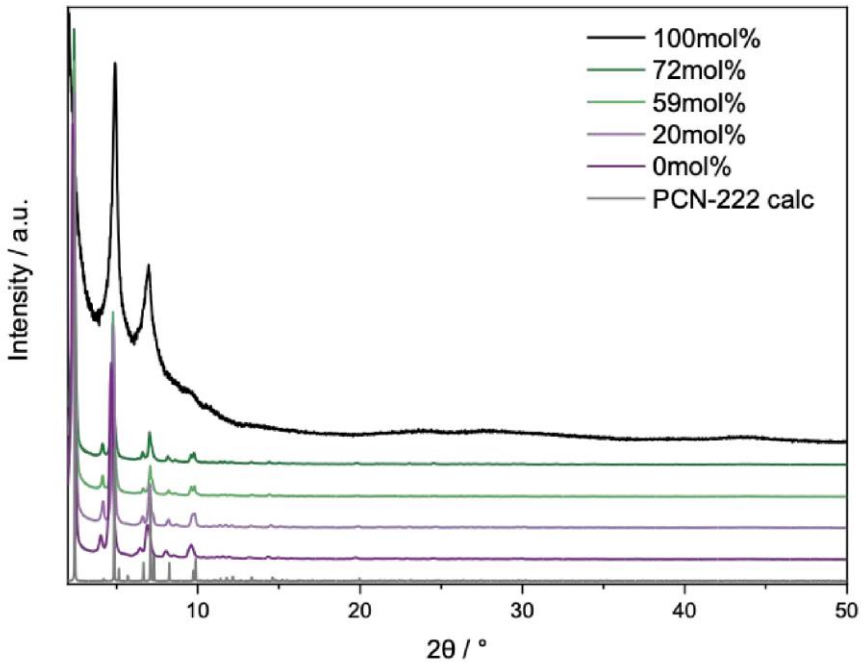


Figure S8: PXRD measurements (λ = 1.54 Å) of PCN-222 with 0 mol% **$H_2Et_8TCPP$** (100 mol% **$H_2TCPP$**), 20 mol% **$H_2Et_8TCPP$** (80 mol% **$H_2TCPP$**), 59 mol% **$H_2Et_8TCPP$** (41 mol% **$H_2TCPP$**), 72 mol% **$H_2Et_8TCPP$** (28 mol% **$H_2TCPP$**), and 100 mol% **$H_2Et_8TCPP$** (0 mol% **$H_2TCPP$**) compared to the pattern of PCN-222 calculated from single crystal structure data.

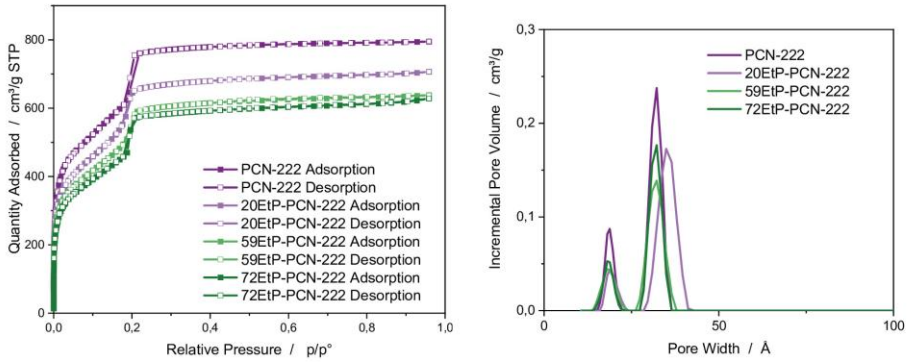


Figure S9: Left:$N_2$ adsorption isotherms at 77 K for as-synthesized PCN-222, 20EtP-PCN-222, 59EtP-PCN-222, and 72EtP-PCN-222 after activation at 120 °C *in vacuo* for 12 hours. The BET surface areas were calculated as 2079 ± 6.9 $m^2 \cdot g^{-1}$ (PCN-222), 1744 ± 15 $m^2 \cdot g^{-1}$ (20EtP-PCN-222), 1594 ± 12 $m^2 \cdot g^{-1}$ (59EtP-PCN-222), 1512 ± 10 $m^2 \cdot g^{-1}$ (72EtP-PCN-222). Right: Incremental pore volumes of PCN-222, 20EtP-PCN-222, 59EtP-PCN-222 and 72EtP-PCN-222.

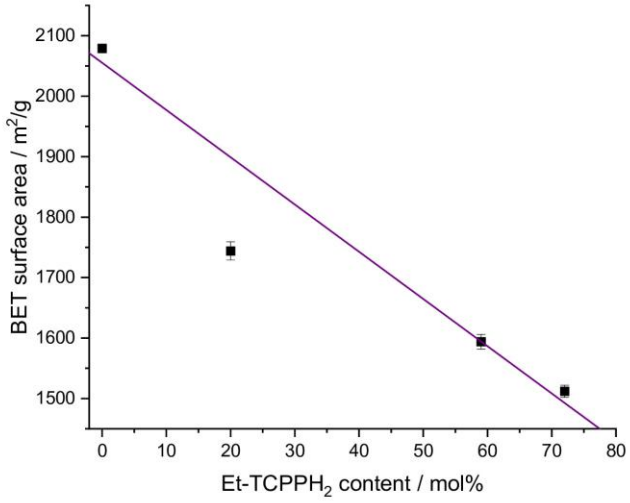


Figure S10: BET surface areas of PCN-222, 20EtP-PCN-222, 59EtP-PCN-222, and 72EtP-PCN-222 as a function of the **$H_2Et_8TCPP$** content. Purple line: Linear fit. y = -7.81x + 2055. $R^2$ = 0.93286.

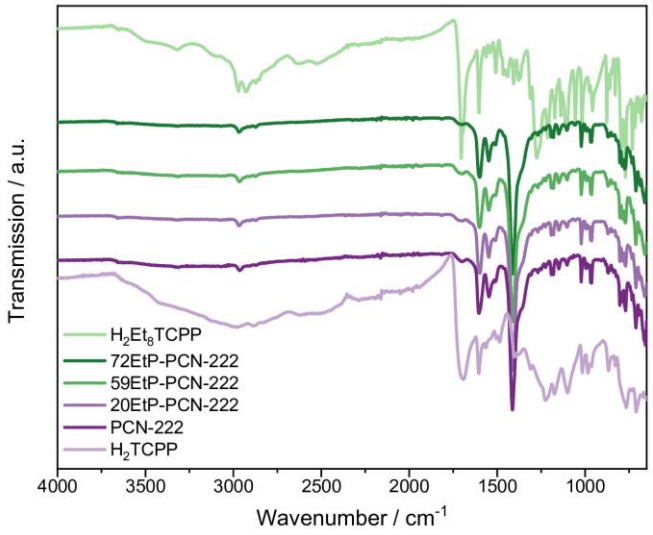


Figure S11: Normalized IR spectra of PCN-222, 20EtP-PCN-222, 59EtP-PCN-222, and 72EtP-PCN-222 in comparison to **$H_2TCPP$** and **$H_2Et_8TCPP$**.

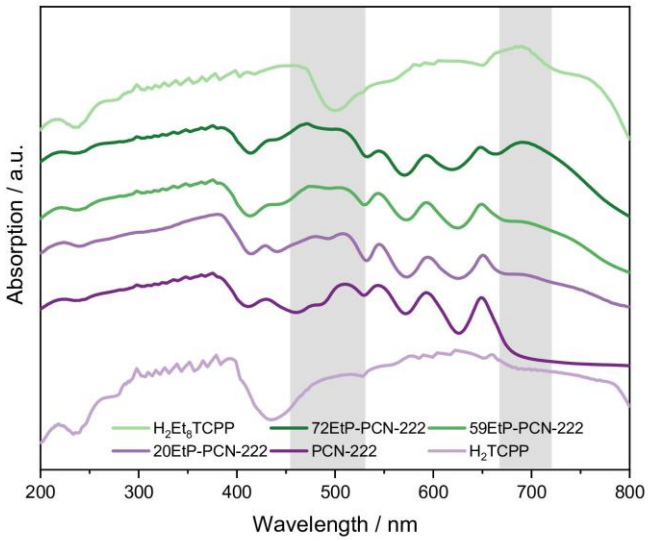


Figure S12: Normalized solid-state UV-vis spectra of PCN-222, 20EtP-PCN-222, 59EtP-PCN-222 and 72EtP-PCN-222 in comparison to **$H_2$TCPP** and **$H_2Et_8$TCPP**.

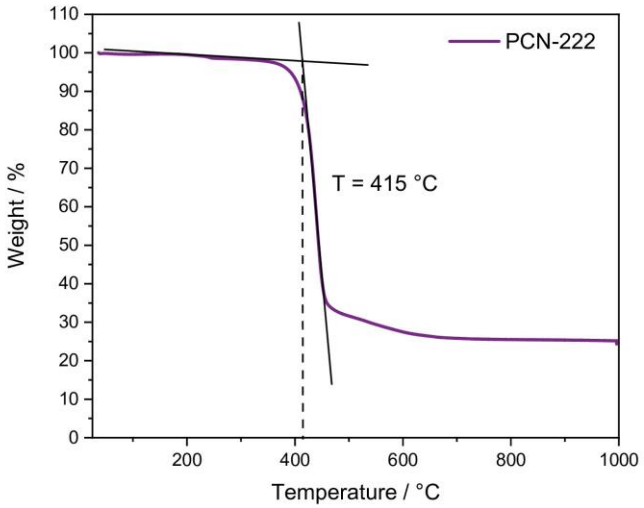


Figure S13: TGA curve of PCN-222.

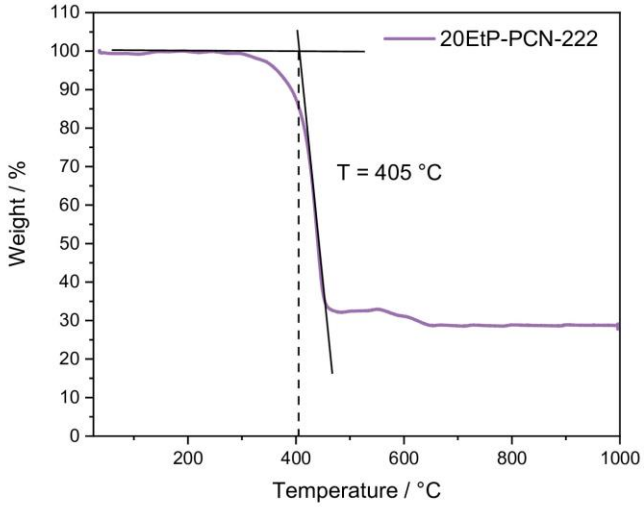


Figure S14: TGA curve of 20EtP-PCN-222.

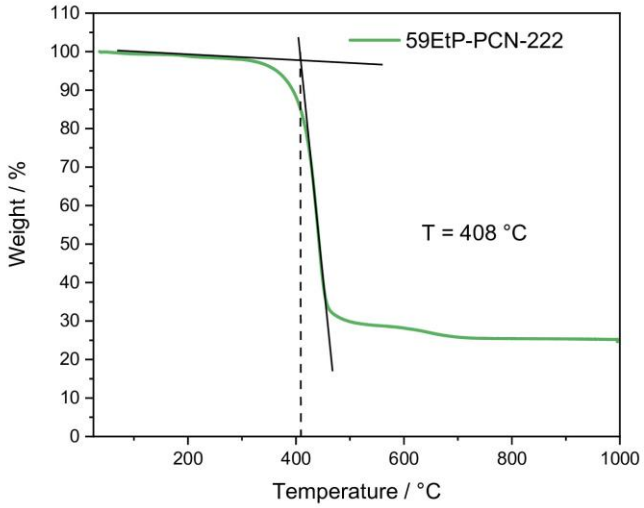


Figure S15: TGA curve of 59EtP-PCN-222.

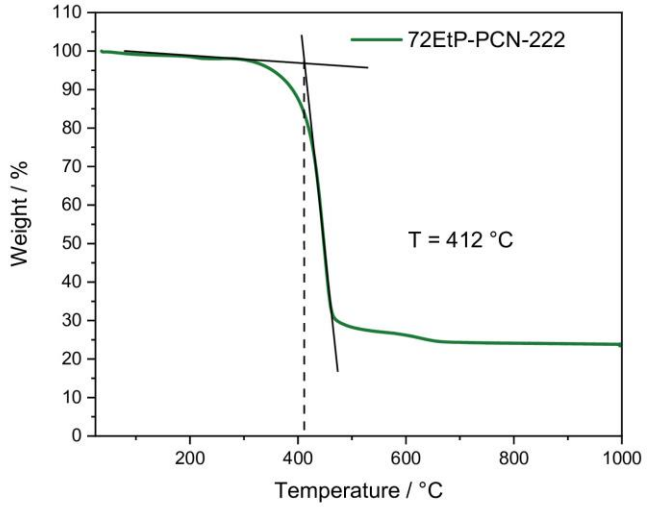


Figure S16: TGA curve of 72EtP-PCN-222.

Table S3: Linker defects of the different MOFs calculated from TGA curves according to the literature.[2] The ideal sum formula of PCN-222 is $Zr_6(OH)_{16}(TCPP\text{-}H_2)_2$.[a]

| | #$H_2$TCPP linkers$_{ideal}$ | #$H_2$TCPP linkers$_{real}$ |
|---|---|---|
| PCN-222 | 2 | 2.53 |
| 20EtP-PCN-222 | 2 | 2.08 |
| 59EtP-PCN-222 | 2 | 2.20 |
| 72EtP-PCN-222 | 2 | 2.27 |

[a] taken from [3,4].

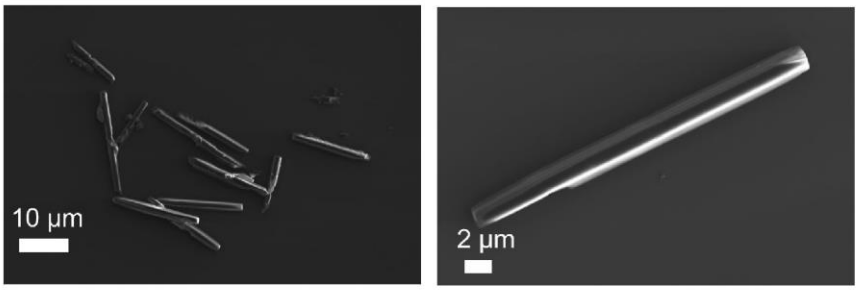


Figure S17: Scanning electron microscopy images of PCN-222 with different magnifications.

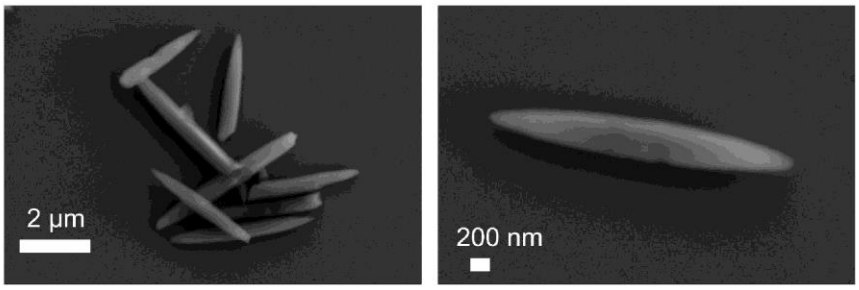


Figure S18: Scanning electron microscopy images of 20EtP-PCN-222 with different magnifications.

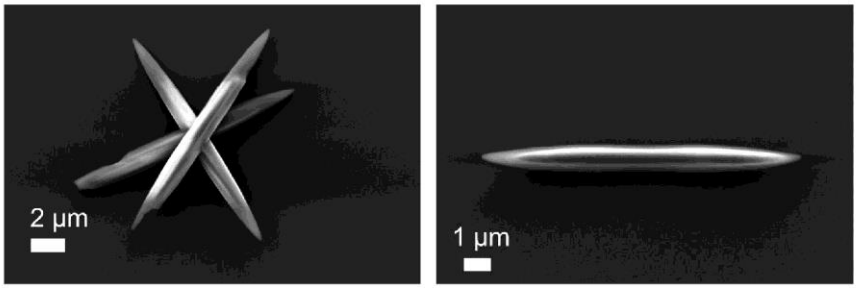


Figure S19: Scanning electron microscopy images of 59EtP-PCN-222 with different magnifications.

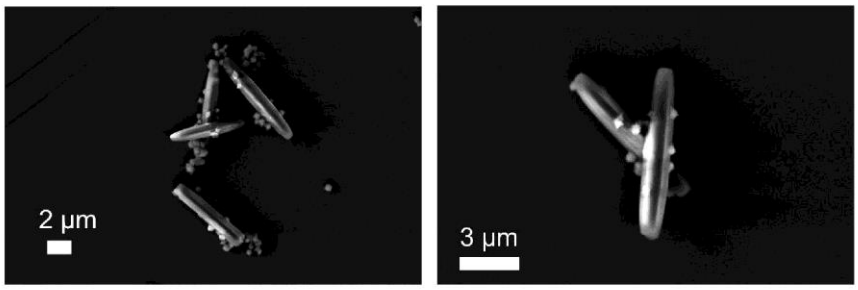


Figure S20: Scanning electron microscopy images of 72EtP-PCN-222 with different magnifications.

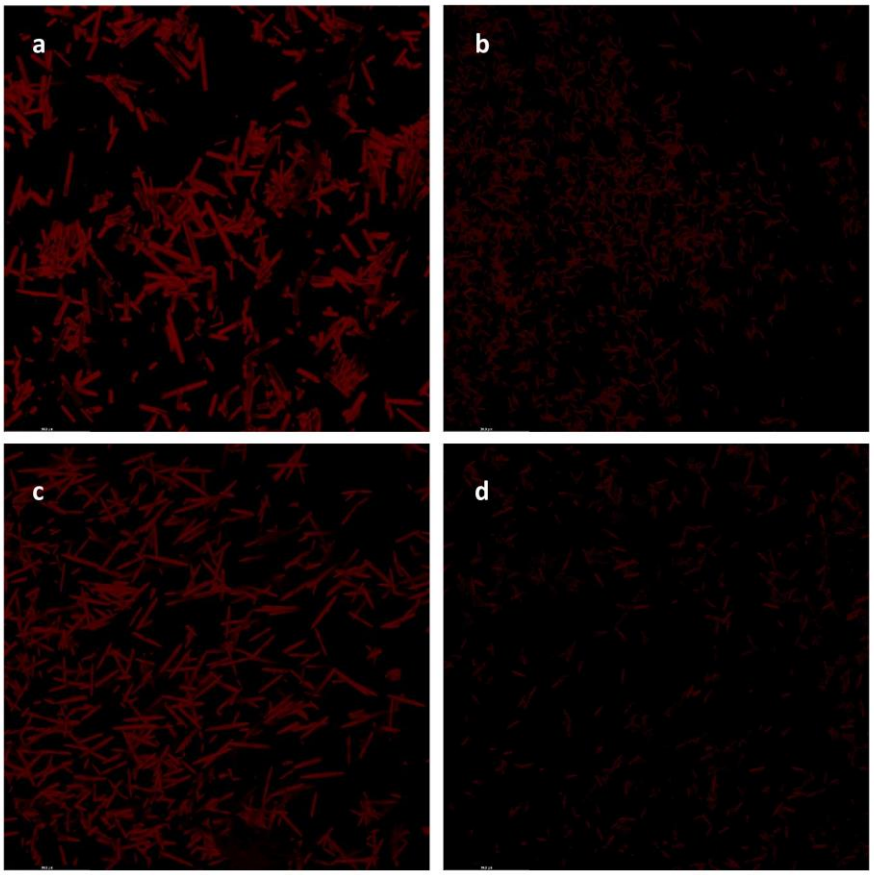


Figure S21: Confocal microscopy images of PCN-222 (a), 20EtP-PCN-222 (b), 59EtP-PCN-222 (c), and 72EtP-PCN-222 (d). Excitation at 405 nm with a diode 405 laser and imaged at 700 – 760 nm. For the recording of the images the same conditions were applied to allow for qualitative comparison of the different samples.

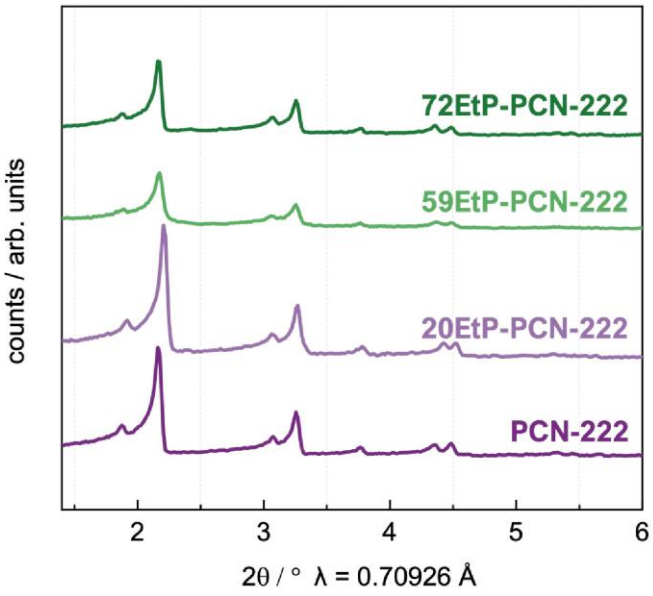


Figure S22: PXRD data recorded at 310 K of PCN-222 derivatives from bottom to top following an increasing **$H_2Et_8$TCPP** content (0 mol% **$H_2Et_8$TCPP** is shown in dark purple, 20 mol% **$H_2Et_8$TCPP** in light purple, 59 mol% **$H_2Et_8$TCPP** in light green and 72 mol% **$H_2Et_8$TCPP** in dark green).

**Note for Pawley profile fit analysis.** Pawley profile fit analysis was performed with TOPAS v6. Standard deviations of all extracted lattice parameters (*a*, *c,* and *V*) were calculated and by using "randomize_on_errors" it was ensured that the global minimum of refinement was achieved. We performed the zero point refinement to account for a zero shift due to misalignement by using "Zero_Error", and the "Simple_Axial_Model" macro was used to model the axial divergence. The zero error was refined for the first temperature point (100 K) and then kept constant for the subsequent temperature points. The profile was fitted using TCHZ_Peak_Type (the modified Thompson-Cox-Hastings pseudo-Voigt function with U, V, W, X, Y, Z as refined parameters).

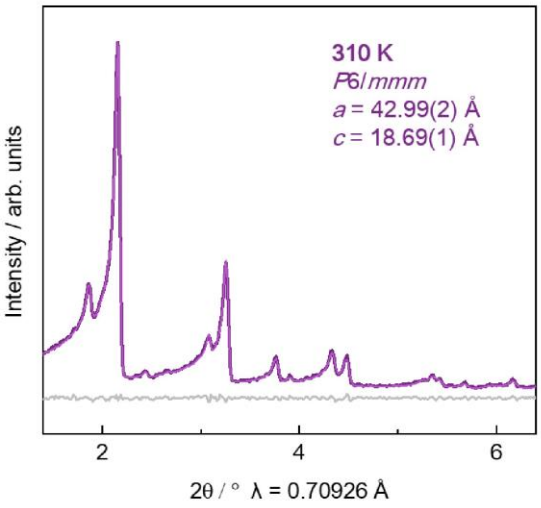


Figure S23: Pawley fit refinement (light purple line) of the PXRD pattern at 310 K of PCN-222 (dark purple line), with $R_{wp}$ = 3.98, $R_{exp}$ = 1.36 and GOF = 2.92. The difference curve of the profile fit (grey line) and the experimental PXRD data indicates phase purity.

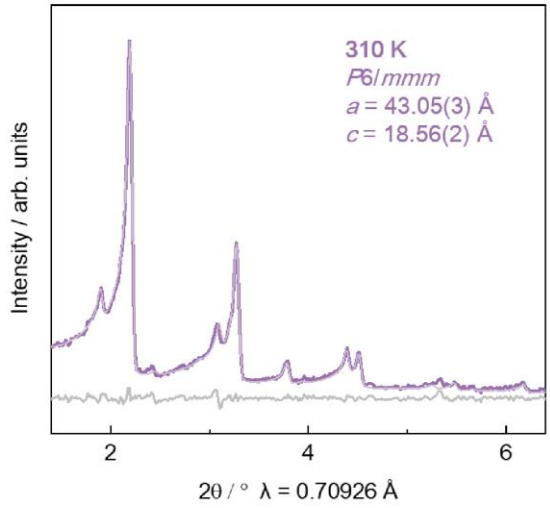


Figure S24: Pawley fit refinement (lighter purple line) of the PXRD pattern at 310 K of 20EtP-PCN-222 (darker purple line), with $R_{wp}$ = 3.10, $R_{exp}$ = 1.16 and GOF = 2.67. The difference curve of the profile fit (grey line) and the experimental PXRD data indicates phase purity.

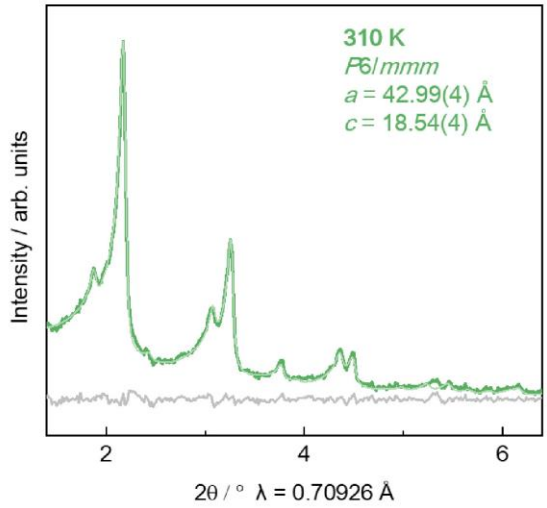


Figure S25: Pawley fit refinement (lighter green line) of the PXRD pattern at 310 K of 59EtP-PCN-222 (darker green line), with $R_{wp}$ = 3.24, $R_{exp}$ = 1.53 and GOF = 2.11. The difference curve of the profile fit (grey line) and the experimental PXRD data indicates phase purity.

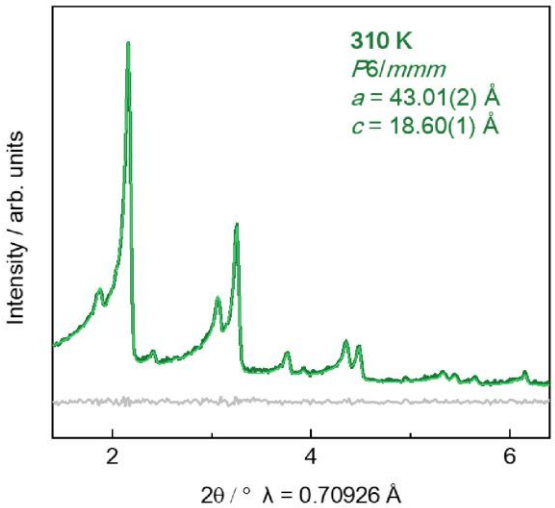


Figure S26: Pawley fit refinement (light green line) of the PXRD pattern at 310 K of 72EtP-PCN-222 (dark green line), with $R_{wp}$ = 2.73, $R_{exp}$ = 1.36 and GOF = 2.01. The difference curve of the profile fit (grey line) and the experimental PXRD data indicates phase purity.

Table S4: Results for PCN-222 as obtained by Pawley refinement against VTPXRD data.

| T / K | $R_{wp}$ | *a* / Å | *c* / Å | *V* / Å$^3$ |
|---|---|---|---|---|
| **150** | 3.1736 | 43.02(2) | 18.59(2) | 29793(43) |
| **170** | 3.1710 | 42.86(2) | 18.51(2) | 29448(38) |
| **190** | 3.4025 | 43.07(1) | 18.61(2) | 29903(38) |
| **210** | 3.2566 | 42.92(1) | 18.53(2) | 29563(36) |
| **230** | 3.4343 | 42.98(1) | 18.56(2) | 29708(33) |
| **250** | 3.4199 | 42.90(1) | 18.53(2) | 29534(37) |
| **270** | 3.6299 | 42.88(1) | 18.56(2) | 29557(35) |
| **290** | 3.3638 | 42.96(1) | 18.57(2) | 29679(40) |
| **310** | 3.9870 | 42.99(2) | 18.69(1) | 29780(37) |
| **330** | 4.3497 | 42.99(2) | 18.68(1) | 29902(42) |
| **350** | 4.3616 | 42.97(2) | 18.66(2) | 29839(43) |
| **370** | 4.1493 | 42.93(2) | 18.64(2) | 29754(40) |
| **390** | 4.4325 | 42.97(2) | 18.66(2) | 29833(45) |

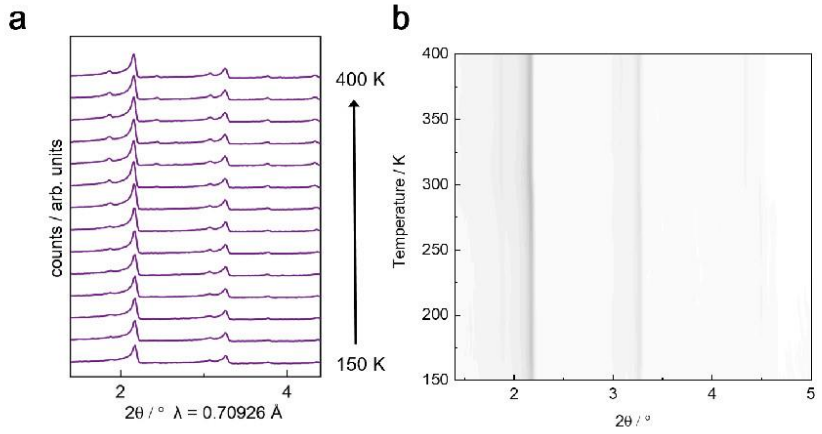


Figure S27: VT-PXRD data of PCN-222 (a) from 150 to 400 K shown as contour plot (b) with darker colors corresponding to a higher intensity.

Table S5: Results for 20EtP-PCN-222 as obtained by Pawley refinement against VTPXRD data.

| T / K | $R_{wp}$ | *a* / Å | *c* / Å | *V* / Å$^3$ |
|---|---|---|---|---|
| **150** | 3.5938 | 44.06(2) | 18.74(1) | 31511(40) |
| **170** | 3.5190 | 44.09(3) | 18.75(2) | 31569(61) |
| **190** | 3.5545 | 44.05(4) | 18.71(2) | 31442(73) |
| **210** | 3.6225 | 43.88(3) | 18.64(1) | 31092(60) |
| **230** | 3.6804 | 43.90(3) | 18.66(1) | 31153(54) |
| **250** | 3.6712 | 43.89(3) | 18.69(1) | 31187(53) |
| **270** | 3.9738 | 43.54(5) | 18.59(2) | 30532(98) |
| **290** | 3.9703 | 43.36(6) | 18.25(3) | 30241(87) |
| **310** | 3.1023 | 43.05(3) | 18.56(2) | 29786(46) |
| **330** | 3.3605 | 43.32(5) | 18.11(3) | 29769(50) |
| **350** | 3.2053 | 42.99(2) | 18.56(2) | 29714(43) |
| **370** | 3.1206 | 43.01(2) | 18.57(2) | 29741(40) |
| **390** | 3.0440 | 42.98(2) | 18.55(2) | 29688(39) |

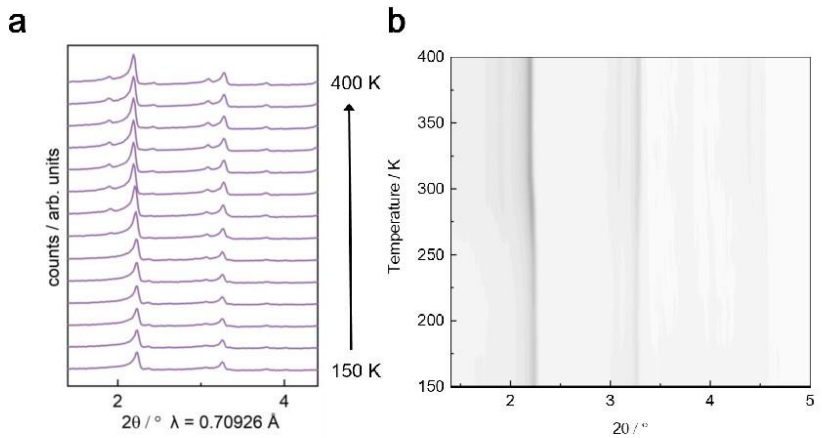


Figure S28: VT-PXRD data of 20EtP-PCN-222 (a) from 150 to 400 K shown as contour plot (b) with darker colors corresponding to a higher intensity.

Table S6: Results for 59EtP-PCN-222 as obtained by Pawley refinement against VTPXRD data.

| T / K | $R_{wp}$ | *a* / Å | *c* / Å | *V* / Å$^3$ |
|---|---|---|---|---|
| **150** | 3.1829 | 43.41(7) | 18.58(4) | 30326(122) |
| **170** | 3.3325 | 43.51(6) | 18.65(4) | 30587(112) |
| **190** | 3.3598 | 43.43(7) | 18.60(5) | 30392(130) |
| **210** | 3.3521 | 43.44(6) | 18.61(3) | 30416(104) |
| **230** | 3.1414 | 43.24(6) | 18.52(4) | 29988(108) |
| **250** | 3.6554 | 43.35(6) | 18.61(4) | 30736(114) |
| **270** | 3.6154 | 43.42(6) | 18.68(2) | 30510(90) |
| **290** | 3.3258 | 43.16(6) | 18.58(4) | 29969(98) |
| **310** | 3.2437 | 42.99(4) | 18.54(4) | 29688(88) |
| **330** | 3.3340 | 43.13 (4) | 18.83(3) | 30334(81) |
| **350** | 3.4108 | 43.08(5) | 18.62(3) | 29929(81) |
| **370** | 3.4666 | 43.07(4) | 18.77(3) | 30166(77) |
| **390** | 3.4923 | 43.12(4) | 18. 77(3) | 30228(77) |

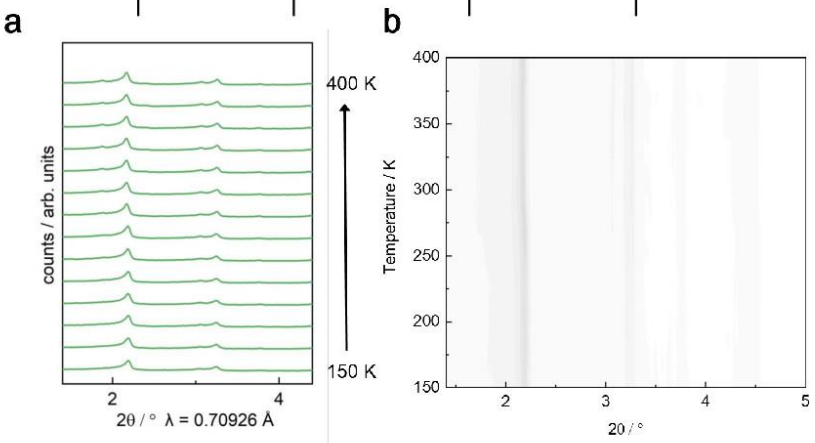


Figure S29: VT-PXRD data of 59EtP-PCN-222 (a) from 150 to 400 K shown as contour plot (b) with darker colors corresponding to a higher intensity.

Table S7: Results for 72EtP-PCN-222 as obtained by Pawley refinement against VTPXRD data.

| T / K | $R_{wp}$ | *a* / Å | *c* / Å | *V* / Å$^3$ |
|---|---|---|---|---|
| **150** | 2.5807 | 42.98(1) | 18.55 (2) | 29681(35) |
| **170** | 2.9254 | 43.04(2) | 18.58(1) | 29814(33) |
| **190** | 2.7682 | 43.09(1) | 18.62(1) | 29942(32) |
| **210** | 2.6598 | 43.06(1) | 18.59(1) | 29862(27) |
| **230** | 2.6602 | 42.99(1) | 18.56(2) | 29700(36) |
| **250** | 2.6996 | 43.09(2) | 18.63(2) | 29954(40) |
| **270** | 2.6300 | 42.95(2) | 18.56(1) | 29652(33) |
| **290** | 2.6242 | 42.97(2) | 18.57(1) | 29700(33) |
| **310** | 2.7344 | 43.01(2) | 18.60(1) | 29799(33) |
| **330** | 2.8042 | 43.02(2) | 18.61(1) | 29818(30) |
| **350** | 2.7071 | 42.96(1) | 18.59(1) | 29708(26) |
| **370** | 2.7038 | 42.98(1) | 18.59(1) | 29752(24) |
| **390** | 2.5958 | 42.94(1) | 18.62(1) | 29725(25) |

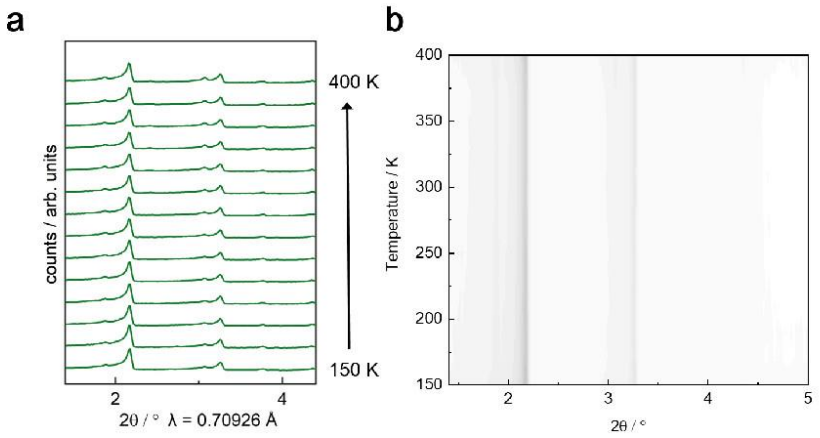


Figure S30: VT-PXRD data of 72EtP-PCN-222 (a) from 150 to 400 K shown as contour plot (b) with darker colors corresponding to a higher intensity.

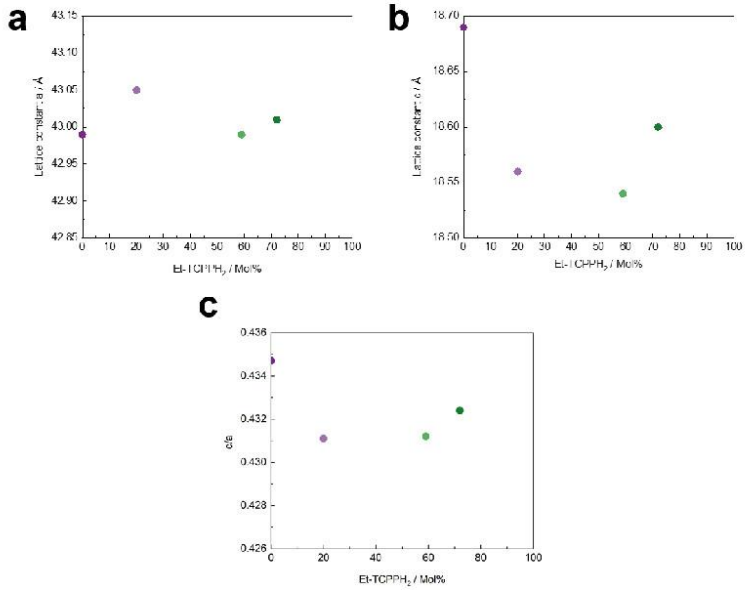


Figure S31: Structural details including lattice parameters *a* (a), *c* (b) and the ratio *c/a* (c) obtained by Pawley refinement against the PXRD data at 310 K as a function of increasing Mol% **Et-TCPPH$_2$**.

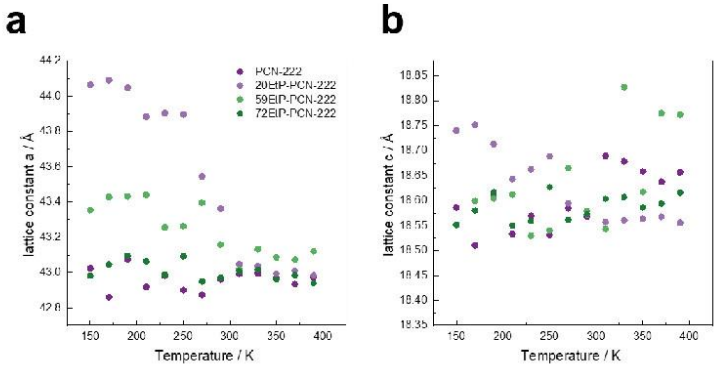


Figure S32: Lattice parameters *a* (a) and *c* (b) extracted by Pawley refinement against variable temperature PXRD data for the PCN-222 and its derivatives.

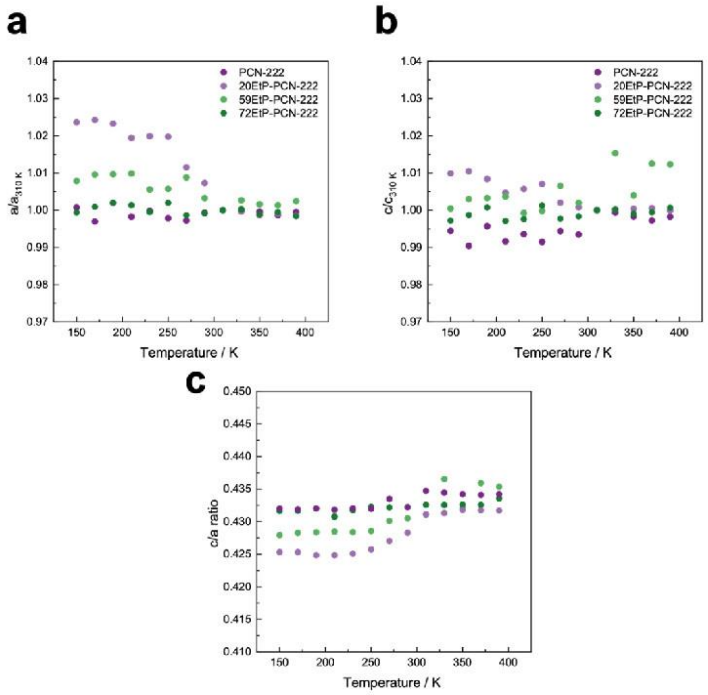


Figure S33: Normalized lattice constants $a/a_{310\,K}$ (a), $c/c_{310\,K}$ (b), and the c/a ratio (c) extracted by Pawley refinement against variable temperature PXRD data for the PCN-222 and its derivatives.

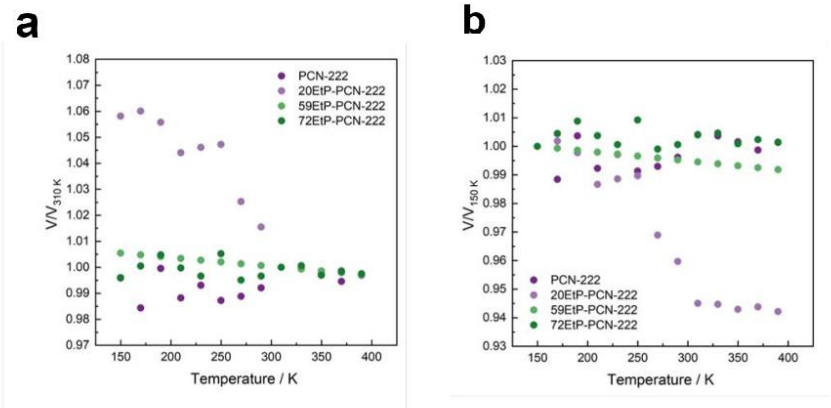


Figure S34: The evolution of the normalized volume $V/V_{310\,K}$ (a) and $V/V_{150\,K}$ (b) as determined by Pawley refinement against variable temperature PXRD data as a function of temperature along the series of PCN-222 solid solutions with increasing $H_2Et_8TCPP$ amount.

**pH stability**

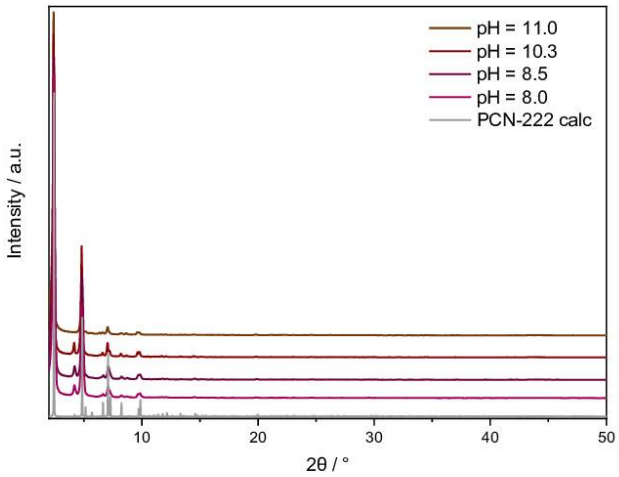


Figure S35: PXRD measurements (λ = 1.54 Å) of PCN-222 after 24 h of soaking in $NaOH/H_2O$ solutions with different pH values. After soaking, the MOF was washed with water and dried under vacuum before PXRD measurement.

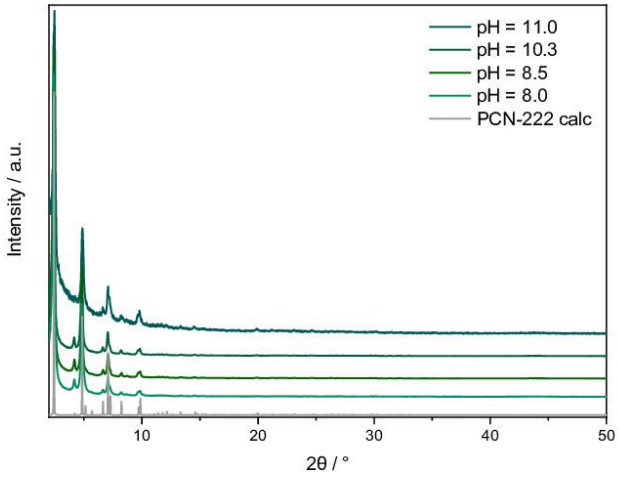


Figure S36: PXRD measurements (λ = 1.54 Å) of 59EtP-PCN-222 after 24 h of soaking in $NaOH/H_2O$ solutions with different pH values. After soaking, the MOF was washed with water and dried under vacuum before PXRD measurement.

**Catalytic Performance Testing – Thia-Michael Addition**

Excursus: PCN-222 was applied in the thia-Michael addition where organocatalytic activity was previously shown for an $H_2Et_8TCPP$ analogue in a homogeneous system.[5] Thus, the experiment aimed to investigate the performance of the non-planar porphyrin after MOF incorporation and simultaneously potential matrix integration effects. However, under the applied reaction conditions (see below, comparable to homogeneous conditions) no conversion was detected. Therefore, this approach was not further studied.

For the thia-Michael addition the EtP-PCN-222 catalyst (3 mol% **$H_2Et_8TCPP$**) was suspended in 2 mL dichloromethane (DCM, stored over $K_2CO_3$ for 2 days) in a 20 mL screw cap vial. The substrate phenyl vinyl sulfone (2.2 mg, 0.013 mmol, 1.0 equiv.) was added, the vial capped and flushed with argon. Afterwards, *tert*-butylbenzyl mercaptan (2.4 µL, 2.3 mg, 0.013 mmol, 1.0 equiv.) was added and an argon balloon placed on top of the vial. The reaction was performed in the dark at room temperature while stirring (350 rpm). After 24 h of reaction, the catalyst was separated via a syringe filter. The solution was analyzed via $^1$H NMR to evaluate selectivity and conversion; however, resulting in no conversion.
Additionally, the solvent was varied (acetonitrile and dimethyl sulfoxide) and the amount of sulfon increased (10 equiv.) which both did not result in any conversion. Although raising the temperature resulted in conversion of the substrates, blank experiments without catalyst indicated that this conversion enhancement is caused by the increased temperature instead of the catalyst.

**Porphyrin Metalation**

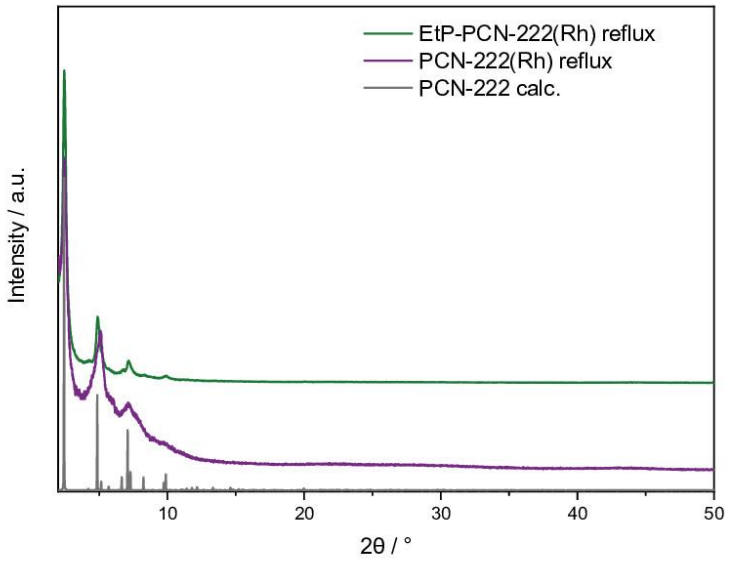


Figure S37: PXRD measurements (λ = 1.54 Å) of EtP-PCN-222(Rh) and PCN-222(Rh) compared to the calculated pattern of PCN-222 (calculation from crystal structure) after 22 h of refluxing while stirring the as-synthesized MOF with $RhCl_3 \bullet \times H_2O$ in DMF with subsequent washing and drying.

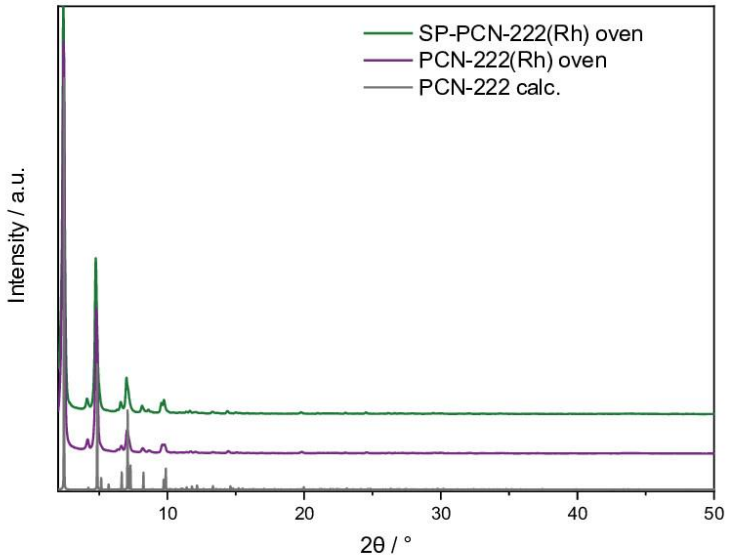


Figure S38: PXRD measurements (λ = 1.54 Å) of EtP-PCN-222(Rh) and PCN-222(Rh) compared to the calculated pattern of PCN-222 (calculation from crystal structure) after 12 h of reaction of the as-synthesized MOF with $RhCl_3 \bullet \times H_2O$ in DMF in an oven without stirring with subsequent washing and drying.

Table S8: wt% of Rh and Zr, approximated percentage of linker metalation (calculated from ideal sum formula of PCN-222 and therefore only for estimation) and Zr:Rh ratios for PCN-222(Rh) and EtP-PCN-222(Rh) prepared via different methods (reflux vs. oven) determined by ICP-MS analysis. The theoretical Zr:Rh ratio for complete linker metalation is 3 (calculated from the ideal sum formula and the ratio Zr:linker).

| | | wt% Zr | wt% Rh | Approximated % of linker metalation[a] | Zr:Rh |
|---|---|---|---|---|---|
| PCN-222(Rh) | Reflux | 17.57 | 2.32 | 28.43 | 8.55 |
| EtP-PCN-222(Rh) | Reflux | 17.04 | 1.96 | 23.96 | 9.80 |
| PCN-222(Rh) | Oven | 17.62 | 0.80 | 9.62 | 24.94 |
| EtP-PCN-222(Rh) | Oven | 16.72 | 0.84 | 10.18 | 22.37 |

[a]based on the ideal sum formula of PCN-222

## 5. References

(1) Schneider, C. A.; Rasband, W. S.; Eliceiri, K. W. NIH Image to ImageJ: 25 years of image analysis. *Nat. Methods* **2012**, *9* (7), 671–675. DOI: 10.1038/nmeth.2089.

(2) Shearer, G. C.; Chavan, S.; Ethiraj, J.; Vitillo, J. G.; Svelle, S.; Olsbye, U.; Lamberti, C.; Bordiga, S.; Lillerud, K. P. Tuned to perfection: Ironing out the defects in metal–organic framework UiO-66. *Chem. Mater.* **2014**, *26* (14), 4068–4071. DOI: 10.1021/cm501859p.

(3) Feng, D.; Gu, Z.-Y.; Li, J.-R.; Jiang, H.-L.; Wei, Z.; Zhou, H.-C. Zirconium-metalloporphyrin PCN-222: mesoporous metal-organic frameworks with ultrahigh stability as biomimetic catalysts. *Angew. Chem. Int. Ed.* **2012**, *51* (41), 10307–10310. DOI: 10.1002/anie.201204475.

(4) Bai, Y.; Dou, Y.; Xie, L.-H.; Rutledge, W.; Li, J.-R.; Zhou, H.-C. Zr-based metal-organic frameworks: design, synthesis, structure, and applications. *Chem. Soc. Rev.* **2016**, *45* (8), 2327–2367. DOI: 10.1039/c5cs00837a.

(5) Roucan, M.; Kielmann, M.; Connon, S. J.; Bernhard, S. S. R.; Senge, M. O. Conformational control of nonplanar free base porphyrins: towards bifunctional catalysts of tunable basicity. *Chem. Commun.* **2017**, *54* (1), 26–29. DOI: 10.1039/c7cc08099a.

## 4.3. Supporting Information for Study III



# Supporting Information

# Spin-State Dependent Pressure Responsiveness of Fe(II)-based Triazolate Metal-Organic Frameworks

Silva M. Kronawitter,[a†] Richard Röß-Ohlenroth,[b†] Sebastian A. Hallweger,[a] Marcel Hirrle,[b] Hans-Albrecht Krug von Nidda,[c] Tobias Luxenhofer,[b] Emily Myatt,[d] Jem Pitcairn,[d] Matthew J. Cliffe,[d] Dominik Daisenberger,[e] Jakub Wojciechowski,[f] Dirk Volkmer*[b] and Gregor Kieslich*[a]

[a]*Technical University of Munich, TUM Natural School of Sciences, Lichtenbergstr. 4, 85748, Garching (Germany).*

[b]*Chair of Solid State and Materials Chemistry, Institute of Physics, University of Augsburg, Universitätsstr. 1, 86159, Augsburg (Germany).*

[c]*Experimental Physics V, Center for Electronic Correlations and Magnetism, Institute of Physics, University of Augsburg, Universitätsstr. 1, 86159 Augsburg (Germany).*

[d]*School of Chemistry, University of Nottingham, Nottingham NG7 2RD (United Kingdom).*

[e]*Diamond Light Source Ltd., Diamond House, Harwell Campus, Didcot OX11 ODE (United Kingdom).*

[f]*Rigaku Europe SE, Hugenottenallee 167, Neu-Isenburg (Germany).*

† equal contribution

* corresponding authors

Dirk Volkmer: dirk.volkmer@physik.uni-augsburg.de

Gregor Kieslich: gregor.kieslich@tum.de

## Contents

**1. Material synthesis** ..... 2
**2. NMR spectroscopy** ..... 4
**3. Infrared spectroscopy** ..... 5
**4. Thermogravimetric analysis** ..... 7
**5. Differential scanning calorimetry** ..... 8
**6. Magnetic susceptibility measurements** ..... 10
**7. Laboratory powder X-ray diffraction** ..... 14
**8. High-pressure powder X-ray diffraction** ..... 16
**9. PXRD analysis** ..... 19
**10. Bulk moduli (EOSFit)** ..... 30
**11. Standard material for high-pressure PXRD analysis** ..... 32
**12. PASCal calculations** ..... 36
**13. Scanning electron microscopy and energy-dispersive X-ray spectroscopy** ..... 37
**14. 3D electron diffraction data** ..... 38
**15. Note to the structural chemistry of $Fe(mta)_2$** ..... 43
**16. References** ..... 44

## 1. Material synthesis

**Materials**

*N,N*-dimethylformamide (DMF, 99.8% analytical grade; VWR/ extra dry 99.8%; Acros), methanol (MeOH, 99.8% analytical grade; VWR), iron(II)chloride (99.999% Sigma Aldrich/ 98%; abcr), 4-methylbenzenesulfonohydrazide (97%; Alfa Aesar), ammonia (7M in methanol, Acros), and 1,1-dimethoxypropan-2-one (97%; Alfa Aesar) were used without further purification as obtained from the commercial supplier. 1*H*-1,2,3-triazole (**H-ta**, 98%, BLDpharm) was degassed and stored over molecular sieves under an argon atmosphere.

**Synthetic procedures – Linker synthesis**

The **1,4,5,6-tetrahydrocyclopenta-1*H*-1,2,3-triazole (H-cta)** ligand was prepared following a literature procedure[1] and purified further *via* sublimation, while **methyl-1*H*-1,2,3-triazole (H-mta)** was synthesised by a protocol adapted from literature[2] and purified *via* distillation.

**4-methyl-1*H*-1,2,3-triazole (H-mta)**

In the first step, 1,1-dimethoxypropan-2-one (20 g, 20.2 mL, 169 mmol) and 4-methylbenzenesulfonohydrazide (30.8 g, 165 mmol) were dissolved in 250 mL MeOH in an ACE round-bottomed pressure flask (400 mL inner volume, sealed with a silicone o-ring). After 5 min OF stirring the solution, ammonia (7M in methanol; 52 mL, 364 mmol) was added and the resulting mixture was heated to 110 °C. The solution was concentrated *under reduced pressure* and cooled to room temperature. The resulting oil was separated from the crystallised by-products *via* decantation, followed by two washing cycles with $CH_2Cl_2$ (10 mL). The solvent was evaporated, and the resulting mixture was distilled under reduced pressure to yield a fraction of the colourless product as an oil at approximately 130 °C (4.31 g, 1.61 mmol, 32% yield).

**$^1$H NMR** (400 MHz, $CDCl_3$) $\delta$ [ppm]: 11.9 (br. s, 1H, N-H) 7.45 (s, 1H), 2.3 (s, 3H);

**Synthetic procedures – MOF synthesis**

**Fe(ta)$_2$** was prepared according to a previously reported synthesis route, and the **Fe(cta)$_2$** and **Fe(mta)$_2$** coordination frameworks were synthesised in a similar fashion[3].

**Fe(cta)$_2$** was synthesised by combining $FeCl_2$ (64.5 mg, 0.509 mmol) and H-cta (164.1 mg, 1.504 mmol) in dry DMF (3 mL) under an argon atmosphere in a DURAN® culture tube and sealed with a teflon-lined screw cap. The vial was placed in a heating block and heated to 120 °C. After 3 d heating at this temperature, the resulting product was centrifuged and washed three times with DMF (3 mL) and

three times with MeOH (3 mL). After drying for 4 h *in vacuo* at room temperature, a phase pure product as a greyish powder (55 mg, 40%) was yielded.

**FT-IR** (ATR) 4000 – 400 $cm^{-1}$: 2974 (m), 2924 (w), 2859 (m), 1604 (w), 1533 (m), 1500 (w), 1441 (w), 1265 (w), 1212 (s), 1156 (s), 1126 (w), 1074 (s), 1028 (m), 900 (m), 727 (m), 677 (w), 574 (s); **EDX** Fe:Cl ratio: 1 : 0.066.

**Fe(mta)$_2$-as** (as-synthesised) was synthesised by combining $FeCl_2$ (316.9 mg, 2.5 mmol) and H-mta (623.3 mg, 7.5 mmol) in dry DMF (15 mL) under an argon atmosphere in an ACE pressure tube (38 mL inner volume, sealed with a silicone o-ring). After 3 d heating at 120 °C in a heating block, the resulting product was centrifuged and washed with DMF (5 mL) and three times with MeOH (5 mL). After drying *in vacuo* at room temperature, a phase pure product of **Fe(mta)$_2$-as** as a yellow powder (117 mg, 21%) was yielded. The as-synthesised $Fe(mta)_2$ was then activated *in vacuo* at 280 °C for 2 h to obtain **Fe(mta)$_2$**.

**FT-IR** (ATR) 4000 – 400 $cm^{-1}$: 2930 (w), 1620 (w), 1532 (m), 1455 (w), 1374 (m), 1306 (w), 1222 (m), 1178 (m), 1069 (m), 1013 (m), 825 (s), 718 (w), 677 (m); **EDX** Fe:Cl ratio: 1: 0.114.

## 2. NMR spectroscopy

To confirm the chemical composition of the triazole-based **H-mta** linker, we performed liquid state $^{1}H$ NMR measurements. The $^{1}H$ NMR spectrum (400 MHz) was recorded on a *Mercury plus 400 high-resolution (Fa. Varian Deutschland GmbH)* spectrometer at room temperature.

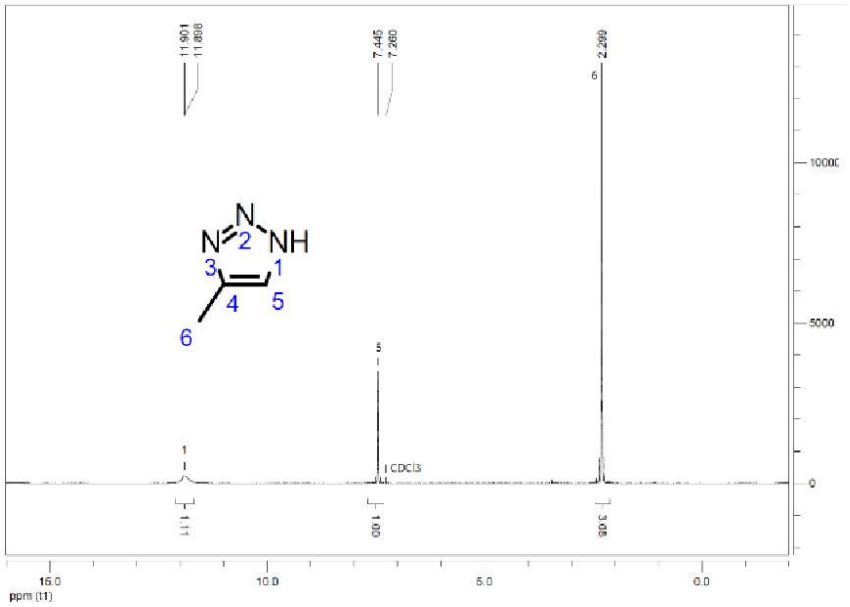


Figure S1: $^{1}H$ NMR of the 4-methyl-1*H*-1,2,3-triazole (H-mta) ligand in $CDCl_3$.

## 3. Infrared spectroscopy

We used Fourier transform infrared (FT-IR) spectroscopy to characterise the vibrational spectrum of $Fe(ta)_2$, $Fe(mta)_2$, and $Fe(cta)_2$ to compare all synthesised triazole-based MOFs. We measured in the range of 4000 – 400 $cm^{-1}$ on a *Bruker Equinox 55 FT-IR* spectrometer equipped with the *PLATINUM ATR* unit.

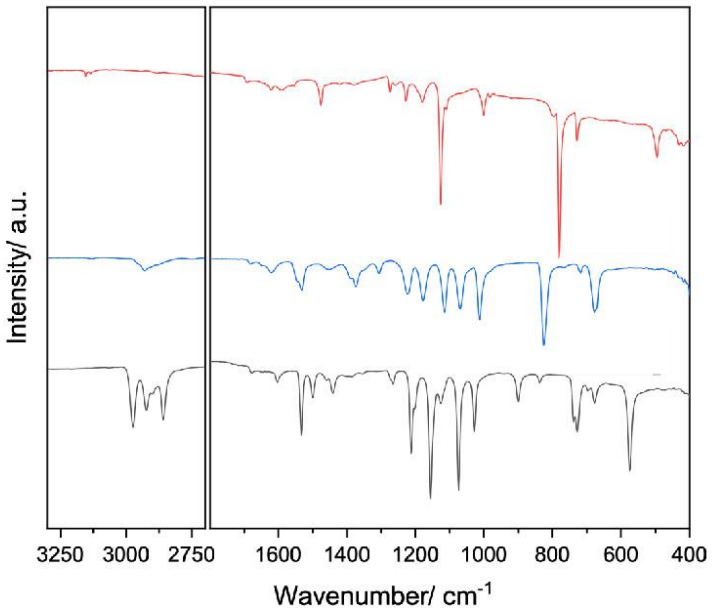


Figure S2: IR spectra comparison for $Fe(ta)_2$ (red), $Fe(mta)_2$ (blue), and $Fe(cta)_2$ (black). $Fe(ta)_2$ shows a small signal at 3150 $cm^{-1}$ for its hydrogen atoms at the triazole ring, which is barely visible for $Fe(mta)_2$, featuring only one of such hydrogen atoms.

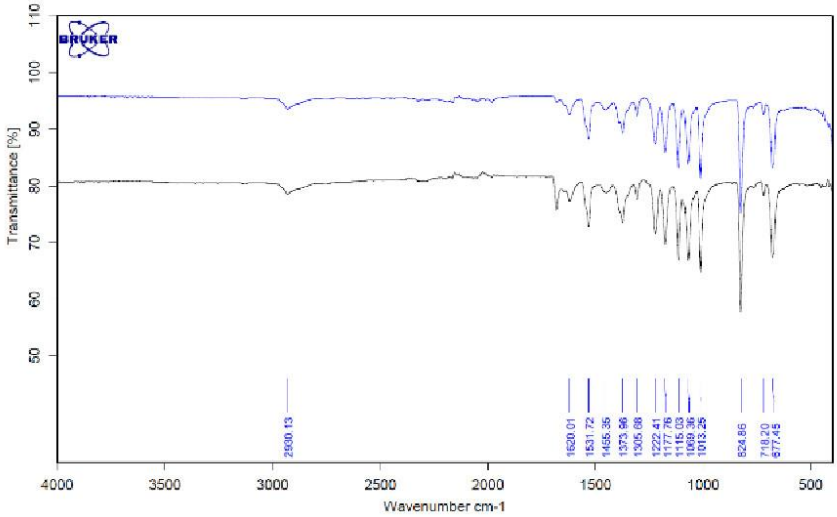


Figure S3: IR spectra recorded for as-synthesised (black) and activated (blue) $Fe(mta)_2$, showing the loss of the band around 1700 $cm^{-1}$ associated with residual solvent (DMF).

## 4. Thermogravimetric analysis

We performed thermogravimetric analysis (TGA) of the $Fe(ta)_2$, $Fe(mta)_2$, and $Fe(cta)_2$ samples with a *TA Instruments Q500* thermogravimetric analyser in a nitrogen atmosphere at a heating rate of 5 K $min^{-1}$ after a 5 min isothermal step in the temperature range of 25 – 800 °C.

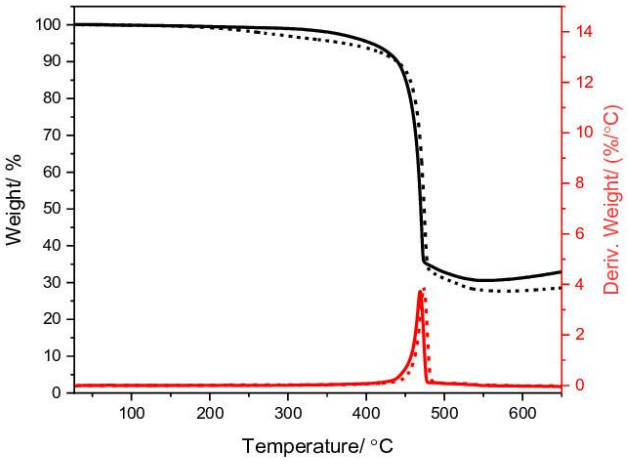


Figure S4: TGA curves of as-synthesised $Fe(mta)_2$-as (dotted) and activated (solid) $Fe(mta)_2$, showing the loss of approx. 2 wt% residual DMF from $Fe(mta)_2$-as as red traces, indicating the thermal derivative of the relative mass changes (red) shows the decomposition onset at 400 °C and the peak at approximately 470 °C.

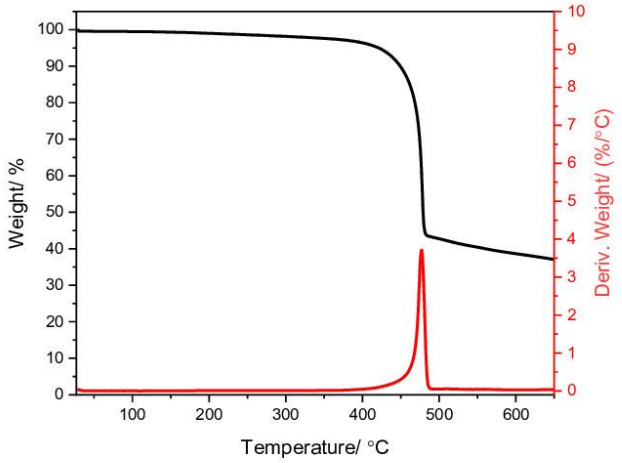


Figure S5: TGA curve of $Fe(cta)_2$ (black) and thermal derivative of the relative mass changes (red), showing the decomposition onset at 400 °C and the corresponding peak at approximately at 470 °C.

## 5. Differential scanning calorimetry

Differential scanning calorimetry (DSC) experiments of the powder $Fe(ta)_2$ and $Fe(mta)_2$ samples were performed in a DSC (*NETZSCH DSC 214*) under constant nitrogen purging flow (40 mL $min^{-1}$) and a heating rate of 10 K $min^{-1}$ in the temperature range between 193.15 – 383.15 K. The *NETZSCH-Proteus®* software was used to analyse the heat flow signals.

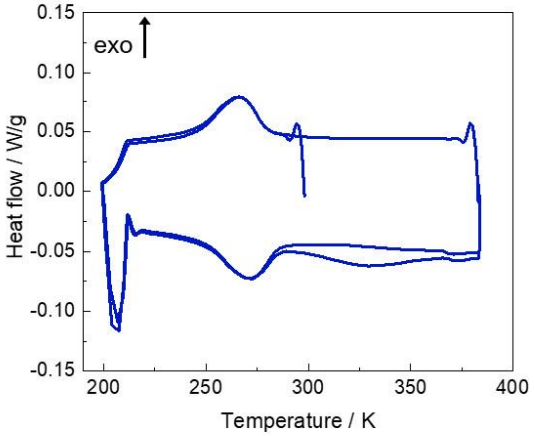


Figure S6: Cycling DSC measurement of the of activated $Fe(mta)_2$, showing a reversible phase transition. Note here that signals below 220 K are measurement artifacts. Running the DSC measurement with a heating rate of 20 K $min^{-1}$ splits the broad heat signal into two signals. This underlines the complexity about the temperature dependent behaviour and presumably the pressure-induced phase transition.

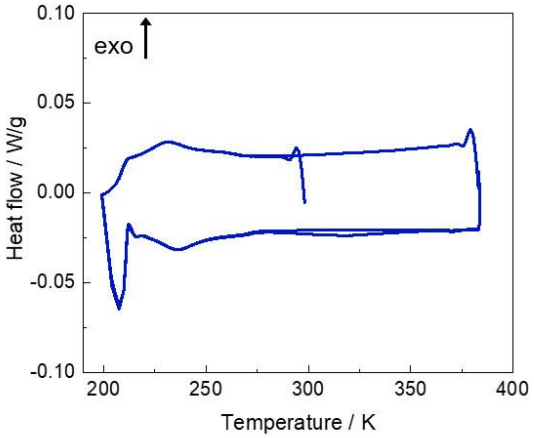


Figure S7: Cycling DSC measurement of the as-synthesised $Fe(mta)_2$-as, showing a phase transition shifted to lower temperatures. Note here that the phase transition goes down to the signals below 220 K, which are measurement artifacts.

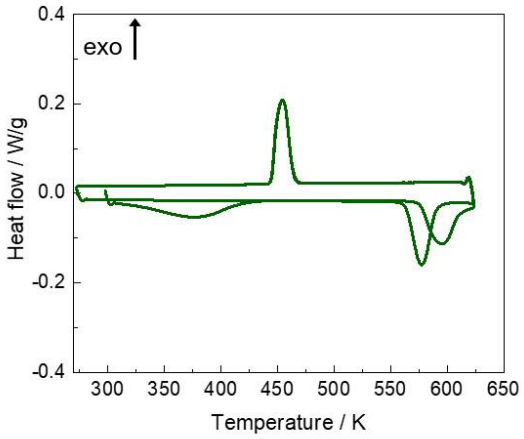


Figure S8: Cycling DSC measurement of $Fe(ta)_2$, showing a broad phase transition shifted to higher temperatures in the first heating curve, as well as the loss of some water residues in the initial heating run.

## 6. Magnetic susceptibility measurements

A superconducting quantum interference device (SQUID) magnetometer (*Quantum Design, MPMS5*), working in the temperature range of 2 K ≤ T ≤ 700 K and in magnetic fields −5 T ≤ μ0H ≤ 5 T, was used to measure the magnetization M of the powder MOF samples. A heating and cooling rate of 2 K $min^{-1}$ was applied, and the temperature dependence of the magnetic susceptibility at a given magnetic field was determined as $\chi = M/H$.

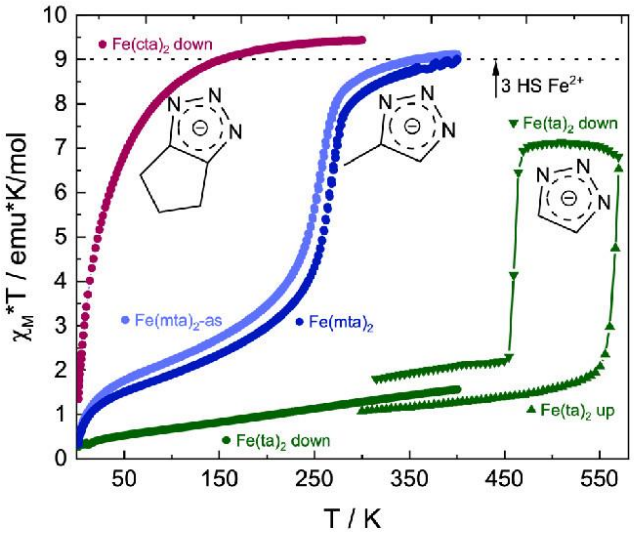


Figure S9: Thermal variation of the molar susceptibility, comparing the spin-crossover behaviour of $Fe(ta)_2$ (green), $Fe(mta)_2$-as (light blue), $Fe(mta)_2$ dry (blue), and $Fe(cta)_2$ (pink) in χMT representation taken on increasing and decreasing temperatures in the corresponding colour based on the respective sum formulas considering the different iron sites ($[FeFe_2(X)_6]$).

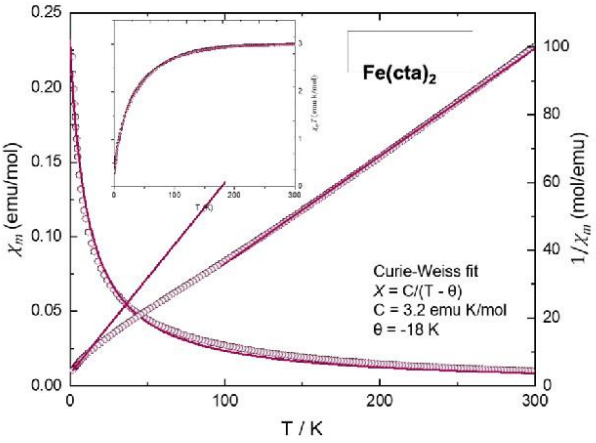


Figure S10: Temperature dependence of the magnetic susceptibility $\chi$ = M/H of Fe(cta)$_2$ based on the reduced form to one metal ion taken at an external field of H = 1000 Oe (left ordinate) and its inverse (right ordinate). Insert: temperature dependence of the product $\chi$T. The pink solid lines indicate the fit curves.

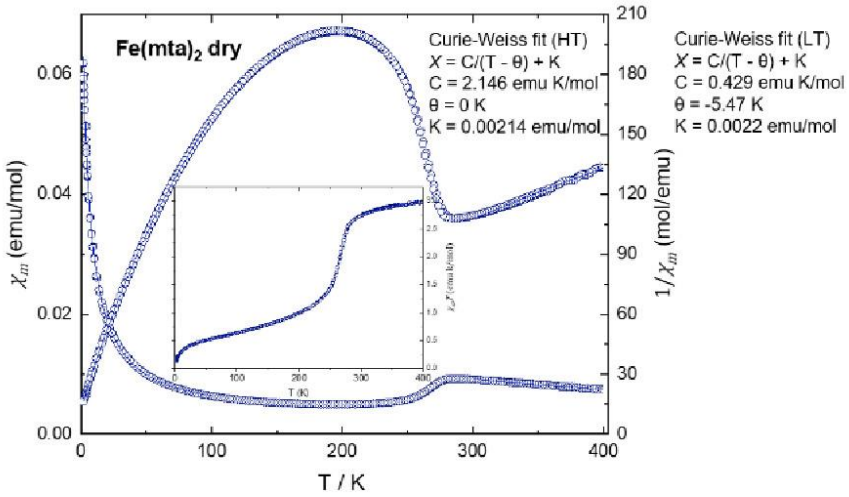


Figure S11: Temperature dependence of the magnetic susceptibility $\chi$ = M/H of Fe(mta)$_2$ based on the reduced form to one metal ion taken at an external field of H = 1000 Oe (left ordinate) and its inverse (right ordinate). Insert: temperature dependence of the product $\chi$T. The blue solid lines indicate the fit curves.

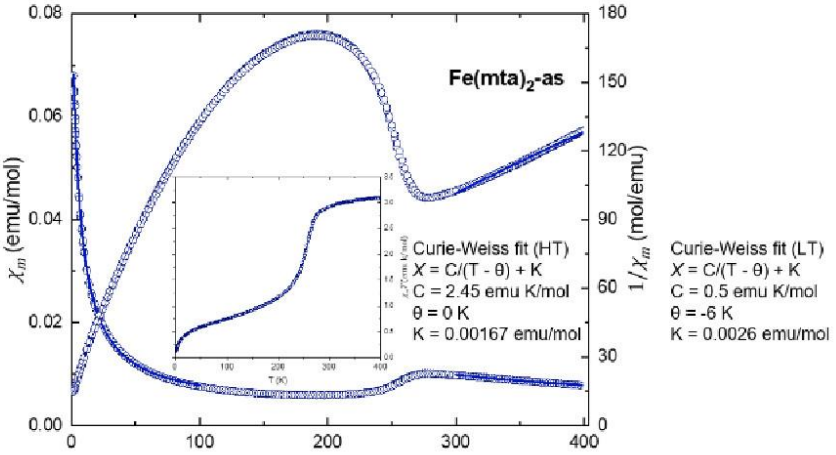


Figure S12: Temperature dependence of the magnetic susceptibility $\chi$ = M/H of Fe(mta)$_2$-as based on the reduced form to one metal ion taken at an external field of H = 1000 Oe (left ordinate) and its inverse (right ordinate). Insert: temperature dependence of the product $\chi$T. The blue solid lines indicate the fit curves.

Figure S9 shows the temperature dependence of the molar susceptibility of **Fe(ta)$_2$** already described in detail in the literature[3] in comparison to its new derivatives **Fe(cta)$_2$** and **Fe(mta)$_2$** in a $\chi$T plot. In general, the **Fe(ta)$_2$** showed the classical behaviour of a spin-crossover (SCO) transition at elevated temperatures, exhibiting the largest hysteresis observed for such a material so far.[4] In contrast, depending on the steric demand of the respective ligands resulting in larger unit cell constants (Table S3), the SCO takes place in a step-wise fashion and is shifted to lower temperatures for **Fe(mta)$_2$**, and only partially for **Fe(cta)$_2$** down to temperatures of 4 K.

The course of **Fe(mta)$_2$-as** starts with $\chi$T = 0.3 emu Kmol$^{-1}$, rises steeply up to 40 K, and then changes to a slightly rising plateau up to 240 K. The starting value, exceeding pure low-spin Fe(II), can be explained by an incomplete transition, or impurities, as already described in the literature.[5] The plateau starts at $\chi$T = 1.5 emu Kmol$^{-1}$ (0.5 HS Fe(II)) and goes up to $\chi$T = 3 emu Kmol$^{-1}$ (1 HS Fe(II)). It then goes into a steep transition to 280 K, ending at $\chi$T = 9 emu Kmol$^{-1}$, which corresponds well to 3 HS Fe(II). This course is in fair agreement with a stepwise transition of the different iron sites in the framework with a Fe1: Fe2 1:2 ratio, suggesting that with increasing temperature, first all "Fe1" (central Fe ion of the Kuratowski unit) iron atoms go into the high spin state in a relatively long temperature range before the "residual Fe2" (peripheral Fe ions of the Kuratowski unit) follow at higher temperatures with a cooperative phase transition. Removal of residual DMF occluded in the structure at 553 K does not change the general behaviour but shifts the spin transition of the Fe2 sites by approximately 15 K to higher temperatures. This indicates that not only steric strain from bulky ligands but also solvent molecules in the voids significantly influence the SCO transition behaviour in such frameworks, which

could be exploited to further influence the behaviour *via* the incorporation of sterically demanding molecules. Both **Fe(mta)$_2$** samples showed no signs of hysteresis in contrast to **Fe(ta)$_2$**.

Starting from $\chi T$ = 1.3 emu Kmol$^{-1}$, the susceptibility of **Fe(cta)$_2$** at 4 K is larger than expected for a pure Fe (II) low spin compound ($\chi T$ = 0 emu Kmol$^{-1}$) indicating that the material is already in a transition state and the $\chi^{-1}$ plot (Figure S10) suggests from its slope that approximately half of the Fe ions in **Fe(cta)$_2$** are already in the high-spin state at this temperature. The flat low-temperature range of **Fe(cta)$_2$** cannot be represented because it is below 0 K. Upon heating, the $\chi T$-curve increases until it flattens out at 150 K at $\chi T$ = 9 emu Kmol$^{-1}$ in a complete high spin state for all 3 Fe(II) ions. Here, the transition from low- to high-spin state seems to occur continuously, foreclosing a cooperative behaviour.

## 7. Laboratory powder X-ray diffraction

Powder X-ray diffraction (PXRD) data was collected at ambient temperature using the *Malvern Panalytical* Empyrean diffractometer equipped with a Bragg–Brentano$^{HD}$ mirror and a *PIXcel*$^{3D}$ 2×2 detector. For the variable temperature PXRD data, a CHC+ reaction chamber was used with $N_2$ gas flow for cooling control.

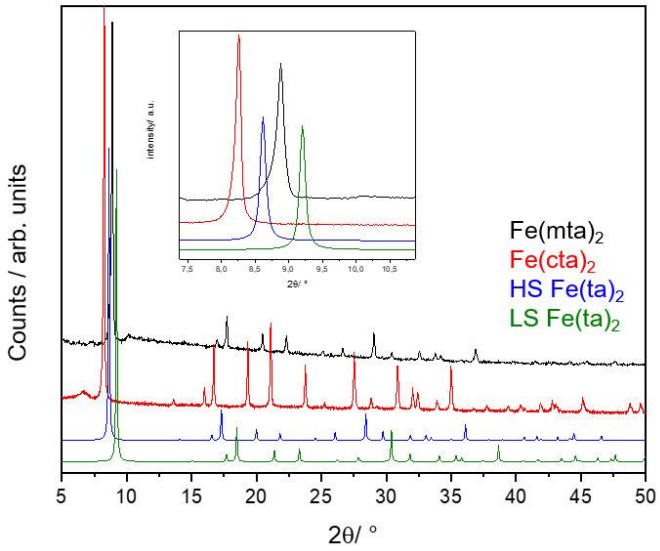


Figure S13: Collection of laboratory PXRD data (λ = 1.54 Å) of $Fe(mta)_2$, and $Fe(cta)_2$ compared to the calculated patterns of the high-spin and low-spin $Fe(ta)_2$.

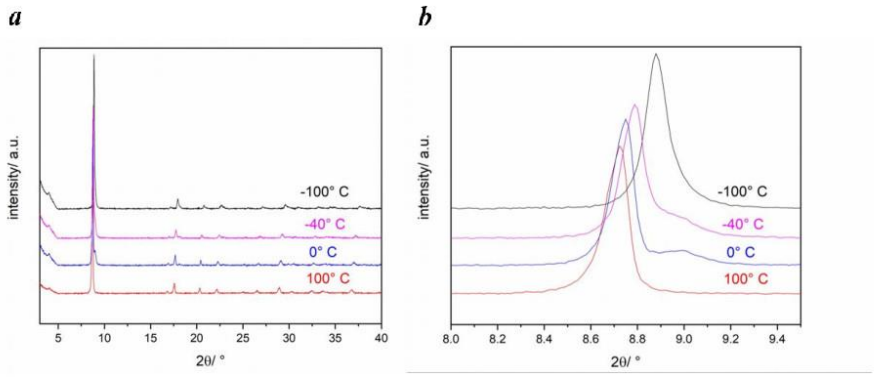


Figure S14: Variable Temperature PXRD data (λ = 1.54 Å) of $Fe(mta)_2$.

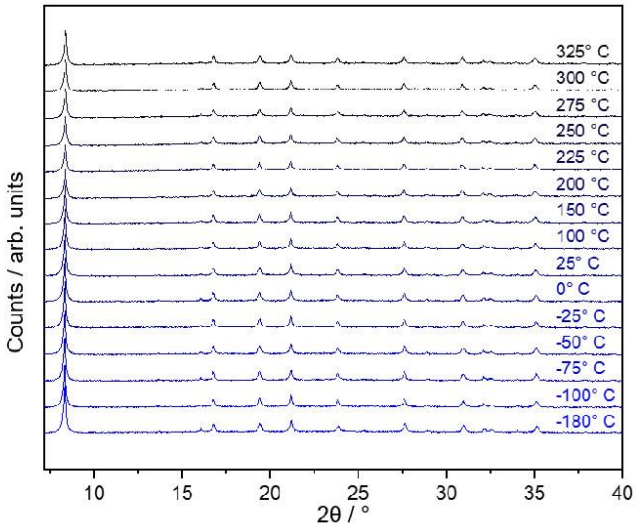


Figure S15: Variable Temperature PXRD data ($\lambda$ = 1.54 Å) of $Fe(cta)_2$. The measurement at -180°C was performed under vacuum instead of using $N_2$.

## 8. High-pressure powder X-ray diffraction

High-pressure powder X-ray diffraction (HPPXRD) data at variable pressure points was collected at the Diamond Light Source (UK), beamline (I15) within beamtime CY30815-2. We used a monochromatic X-ray beam $\lambda$ = 0.4246 Å (with a fixed operating beam energy 29.2 keV), equipped with a Pilatus3 X CdTe 2M area detector for HPPXRD data collection. The finely grounded MOF powders were handled in the glove box and filled into soft plastic capillaries (Makrolon, inside diameter 1.8 mm), together with Silicone oil AP100 (polyphenyl-methylsiloxane) as pressure transmitting medium to maintain hydrostatic conditions up to 0.4 GPa, and sealed with adhesive epoxy paste (Araldyte-2014-1) by heating up to 60 °C for 20 min. We used a hydraulic high-pressure cell as described in more detail in the literature.[6] Therefore, the samples were loaded into a chamber filled with water to transmit the hydrostatic pressure, and a hydraulic gauge pump was used to apply and release water pressure. HPPXRD measurements were performed through two diamond windows in the high-pressure chamber (metal block) along beam direction in the pressure range from ambient to 0.4 GPa in 0.02 GPa step size ($\Delta p$) with an estimated error of $\sigma p$ = ± 0.003 GPa.

**Stack plot of the ambient pressure data**

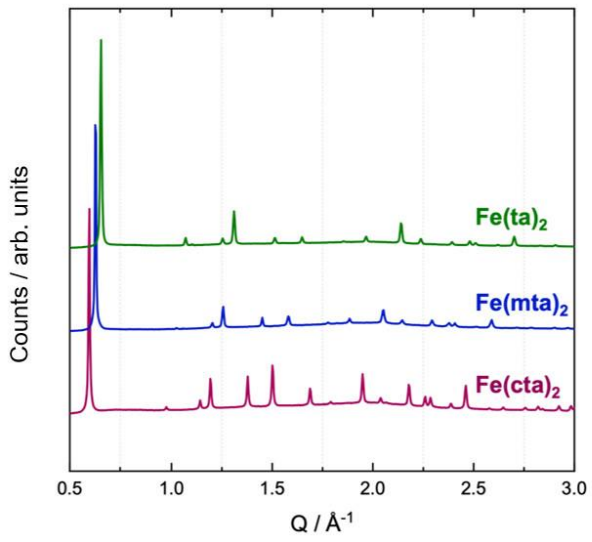


Figure S16: Collection of the normalised PXRD patterns of each MOF, *i.e.* $Fe(ta)_2$, $Fe(mta)_2$, and $Fe(cta)_2$ recorded at ambient pressure.

**Stack plots of the HPPXRD data**

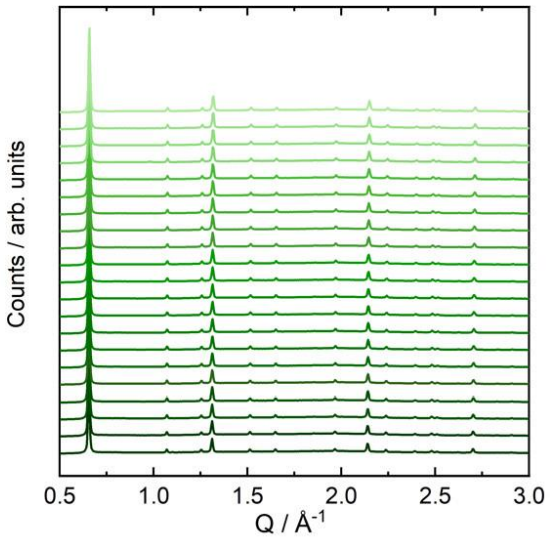


Figure S17: HPPXRD patterns for $Fe(ta)_2$ collected in the pressure range from ambient to 0.4 GPa.

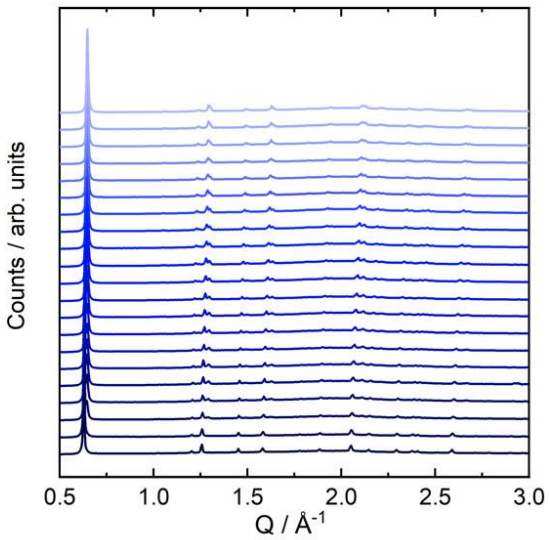


Figure S18: HPPXRD patterns for $Fe(mta)_2$ collected in the pressure range from ambient to 0.4 GPa.

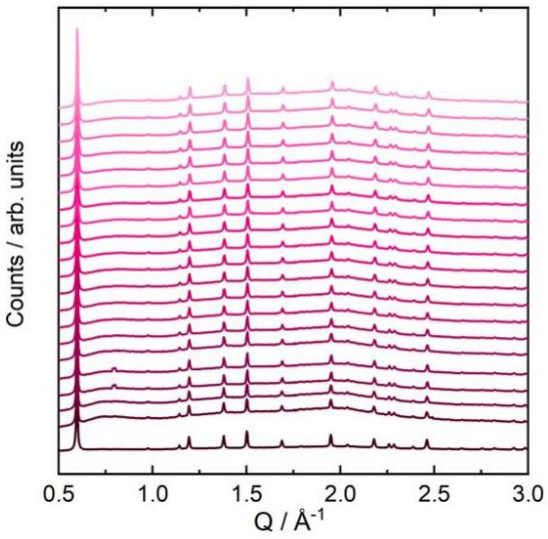


Figure S19: HPPXRD data for $Fe(cta)_2$ collected in the pressure range from ambient to 0.4 GPa.

## 9. PXRD analysis

The collected 2D detector images were integrated by DAWN software.[7] Profile fits (Pawley method)[8] of the collected pressure-dependent PXRD data sets were performed using routines implemented in TOPAS V6[9] to obtain unit cell parameters and cell volume (*a* and *V*) with standard deviations. The representative profile fits of the PXRD data collected at ambient pressure show a good fit using the published cubic crystal structure of $Fe(ta)_2$.[3,10] Additionally, Rietveld refinements[11] against high-resolution HPPXRD data were performed using TOPAS V6[9] to obtain bond lengths (Fe-N) as a function of increasing hydrostatic pressure. Therefore, the single crystal structure of the cubic $Fe(ta)_2$[3,10] and 3D electron diffraction data (Chapter 14) were used as the starting model, and Pawley fits provided unit cell and background parameters for the refinement. The peak shapes were refined using the macro "PVII_Peak_Type" (with *ha*, *hb*, *hc*, *lora*, *lorb*, *lorc* as refined parameters), and we performed zero point refinement to account for a zero shift due to misalignment using "Zero_Error". The zero error was refined for the first pressure point and then kept constant for subsequent pressure points. We described the structure models using atom coordinate sites and parameters as given below.

**Rietveld refinements**

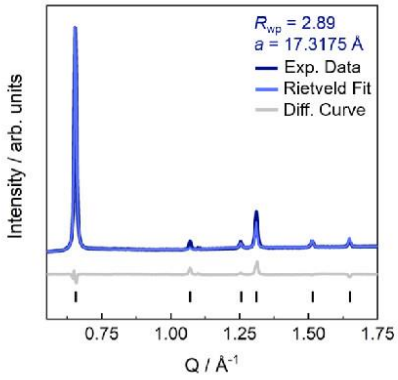


Figure S20: Rietveld refinement of $Fe(mta)_2$ at ambient pressure. Experimental data is shown as dark blue line and the calculated data from Rietveld refinement as light transparent blue line, and the difference curve (fit – data) as grey line. Reflection positions are shown as black vertical tick marks.

**Atom coordinates of $Fe(ta)_2$** used in the Rietveld refinement with fixed cell parameter ***a* = 16.5969 Å** extracted from Pawley refinement of the ambient PXRD data; Wyckoff position (site symmetry) for the crystallographic $Fe^{II}$: $Fe^{2+}$ (16c) and $Fe^{2+}$ (8a)

*site H1 x = H1x; y 0.817810 z 0.580600*

*site Fe1 x 0.00000 y 0.00000 z 0.00000*

*site Fe2 x 0.12500 y 0.12500 z 0.12500*

*site N1 x 0.67090 y 0.290360 z 0.579100*

*site C1 x 0.65421 y = C1y; z 0.595790*

*site N2 x 0.62500 y 0.244960 z 0.62500*

*prm H1x 0.93219`_0.01460 min 0.932190 max 0.932191*

*prm C1y 0.36780`_0.00291 min 0.3678 max 0.36781*

$R_{Bragg}$ *4.9143*

$R_{wp}$ *6.8140*

**Atom coordinates of $Fe(mta)_2$** used in the Rietveld refinement with fixed cell parameter ***a* = 17.3175 Å** extracted from Pawley refinement of the ambient PXRD data; Wyckoff position (site symmetry) for the crystallographic $Fe^{II}$: $Fe^{2+}$ (16d) and $Fe^{2+}$ (8b)

*site Fe1 x 0.375000 y 0.375000 z 0.375000*

*site Fe2 x 0.500000 y 0.250000 z 0.250000*

*site N1 x 0.375000 y 0.375000 z 0.24820*

*site N2 x = C1x +dc2x+dn2x; y = 0.75-C1x -dc2x-dn2x; z 0.20580*

*site C1 x = C1x; y = 0.75-C1x; z 0.13010*

*site C2 x = C1x+dc2x; y C2y 0.31967`_0.00868 z 0.05720 prm C1z 0.13025`_0.01022 min 0.1301 max 0.13025*

*prm C1x 0.40294`_0.00125 min 0.375*

*prm dc2x 0.01794`_0.00792 min 0 max 0.03*

*prm dn2x 0.00265`_0.00801 min 0 max 0.03*

*Flatten(N1 0 0 0 0 N2 0 0 0 0 N2 33 0 0 0 C1 0 0 0 0 C1 33 0 0 0, 0`, 0.2, 1000)*

*Distance_Restrain(N1 0 N2 0 0 0 0, 1.30656, 1.39690`_0.23615, 0.15, 1000)*

*Distance_Restrain(N2 0 C1 0 0 0 0, 1.37385, 1.40454`_0.09905, 0.15, 1000)*

*Distance_Restrain(C1 0 C1 33 0 0 0, 1.3692, 1.36837`_0.06146, 0.15, 1000)*

*Distance_Restrain(C1 0 C2 0 0 0 0, 1.43927, 1.38393`_0.05619, 0.15, 1000)*

*Angle_Restrain(N2 11 C1 11 C2 11,120, 135.02828`_13.70031, 5, 0.001)*

*Angle_Restrain(N2 11 C1 11 C2 88,120, 92.29834`_0.49327, 5, 0.001)*

$R_{Bragg}$ *1.1806*

$R_{wp}$ *2.8995*

**Atom coordinates of $Fe^{II}(cta)_2$** used in the Rietveld refinement with fixed cell parameter ***a* = 18.2301 Å** extracted from Pawley refinement of the ambient PXRD data; Wyckoff position (site symmetry) for the crystallographic $Fe^{II}$: $Fe^{2+}$ (16c) and $Fe^{2+}$ (8a)

*site Fe1 x 0.125000 y 0.625000 z 0.625000*

*site Fe2 x 0.250000 y 0.750000 z 0.750000*

*site N1 x 0.092750 y 0.705470 z 0.705470*

*site N2 x 0.135260 y 0.750000 z 0.750000*

*site C1 x 0.023380 y = C1y; z = C1y;*

*site C2 x -0.050130 y = C2y; z 1.200660*

*site C3 x 0.000000 y = C3y; z 1.000000*

*site H1 x = -1x; y 0.141570 z = H1z;*

*site H2a x = H2ax; y = H2ay; z = 1 + H2ax;*

*prm C1y 0.72430`_0.00188 min 0.724 max 0.7243*

*prm C2y 0.20100`_0.00355 min 0.200 max 0.201*

*prm C3y 0.65000`_0.00377 min 0.650 max 0.651*

*prm H1x 0.05840`_0.00605 min 0.058 max 0.0584*

*prm H1z 1.21290`_0.01172 min 1.2128 max 1.2129*

*prm H2ay 0.61680`_0.01112 min 0.6168 max 0.6169*

*prm Fe1beq 2.03690`_1.09329 min 0.1 max 5*

*prm Fe2beq 2.87588`_1.37744 min 0.1 max 5*

*prm N1beq 1.00000`_1.98487 min 1 max 2*

*prm N2beq 2.00000`_2.28288 min 1 max 2*

*prm C1beq 1.00000`_3.04254 min 1 max 2*

*prm C2beq 2.00000`_1.89394 min 1 max 2*

*prm C3beq 2.00000`_8.37352 min 1 max 2*

$R_{Bragg}$ *1.6689*

$R_{wp}$ *2.6856*

Table S1: Overview of the Fe-N bond lengths of $Fe(ta)_2$ derived from Rietveld refinements of the HPPXRD data.

| $p$ / GPa | $R_{wp}$ | *Fe1-N1*/Å | *Fe2-N2*/Å |
|---|---|---|---|
| ambient | 6.8140 | 1.97360 | 1.99082 |
| 0.0194 | 6.6503 | 1.97374 | 1.99096 |
| 0.0398 | 7.0890 | 1.97358 | 1.99080 |
| 0.0598 | 7.5883 | 1.97309 | 1.99030 |
| 0.0797 | 7.8771 | 1.97257 | 1.98978 |
| 0.0995 | 7.9865 | 1.97208 | 1.98928 |
| 0.1199 | 7.9965 | 1.97170 | 1.98890 |
| 0.1399 | 7.9905 | 1.97114 | 1.98834 |
| 0.1593 | 7.7592 | 1.97058 | 1.98777 |
| 0.1793 | 7.7794 | 1.97024 | 1.98743 |
| 0.1996 | 7.7105 | 1.96972 | 1.98691 |
| 0.2196 | 7.7578 | 1.96934 | 1.98653 |
| 0.2397 | 7.7167 | 1.96895 | 1.98613 |
| 0.2597 | 7.7362 | 1.96857 | 1.98575 |
| 0.2797 | 7.6352 | 1.96807 | 1.98524 |
| 0.2997 | 7.6308 | 1.96774 | 1.98491 |
| 0.3198 | 7.6966 | 1.96713 | 1.98429 |
| 0.3397 | 7.8345 | 1.96673 | 1.98389 |
| 0.3598 | 7.7522 | 1.96619 | 1.98335 |
| 0.3798 | 7.9929 | 1.96576 | 1.98291 |
| 0.3998 | 7.8943 | 1.96538 | 1.98253 |

Table S2: Overview of the Fe-N bond lengths of $Fe(cta)_2$ derived from Rietveld refinements of the HPPXRD data.

| $p$ / GPa | $R_{wp}$ | *Fe1-N1*/Å | *Fe2-N2*/Å |
|---|---|---|---|
| ambient | 2.6856 | 2.15631 | 2.09172 |
| 0.0194 | 1.5022 | 2.15648 | 2.09188 |
| 0.0398 | 1.2959 | 2.15550 | 2.09093 |
| 0.0598 | 1.4141 | 2.15423 | 2.08970 |
| 0.0793 | 2.7892 | 2.15388 | 2.08936 |
| 0.0995 | 1.5303 | 2.15377 | 2.08925 |
| 0.1198 | 1.3998 | 2.15350 | 2.08899 |
| 0.1399 | 2.2272 | 2.15303 | 2.08853 |
| 0.1594 | 1.4342 | 2.15227 | 2.08780 |
| 0.1794 | 1.4543 | 2.15200 | 2.08753 |
| 0.1996 | 1.7422 | 2.15113 | 2.08670 |
| 0.2196 | 1.6495 | 2.15073 | 2.08631 |
| 0.2397 | 1.7356 | 2.15035 | 2.08594 |
| 0.2597 | 1.4728 | 2.15003 | 2.08563 |
| 0.2798 | 1.4311 | 2.14961 | 2.08522 |
| 0.2998 | 1.5466 | 2.14906 | 2.08469 |
| 0.3198 | 1.6351 | 2.14867 | 2.08431 |
| 0.3397 | 1.8914 | 2.14822 | 2.08387 |
| 0.3598 | 2.1734 | 2.14777 | 2.08344 |
| 0.3798 | 1.9975 | 2.14735 | 2.08302 |
| 0.3998 | 1.8562 | 2.14708 | 2.08276 |

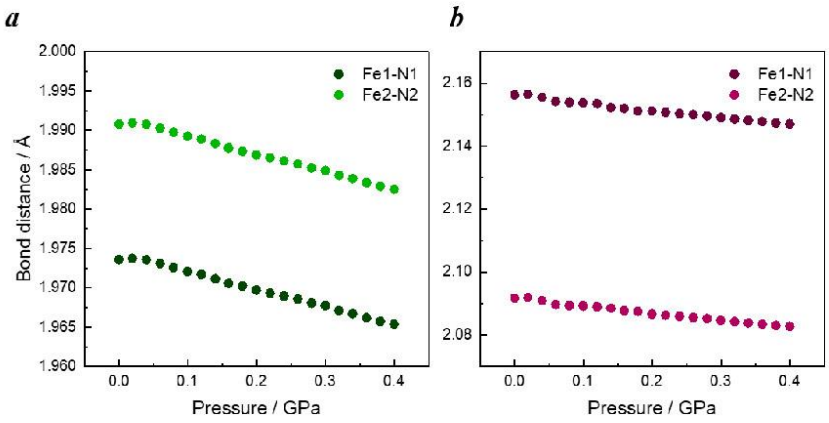


Figure S21: The evolution of the bond distances (Fe1-N1 and Fe2-N2) as a function of pressure up to 0.4 GPa of $Fe(ta)_2$ (a) shown in green and $Fe(cta)_2$ (b) in purple.

**Pawley profile fits**

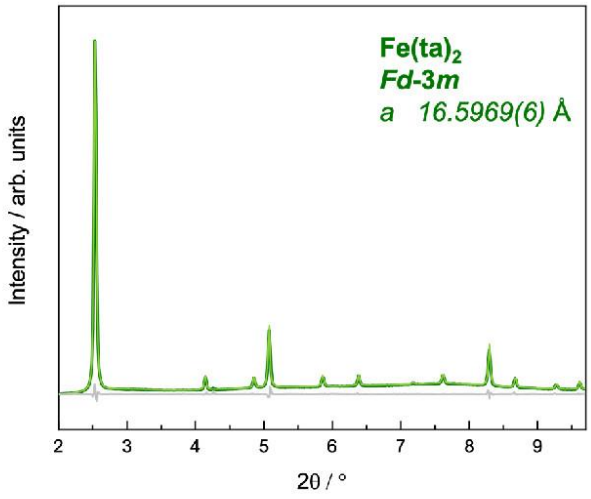


Figure S22: Pawley fit for $Fe(ta)_2$ at ambient pressure. Experimental data is shown as dark green line, Pawley fit as light green line, and the difference curve (fit – data) as grey line.

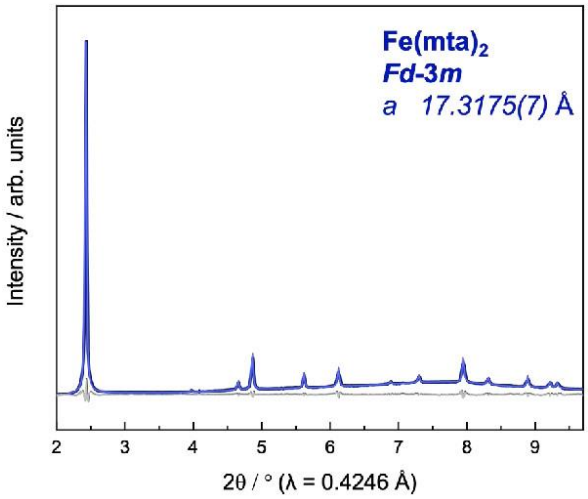


Figure S23: Pawley fit for $Fe(mta)_2$ at ambient pressure. Experimental data is shown as dark blue line, Pawley fit as light blue line, and the difference curve (fit – data) as grey line.

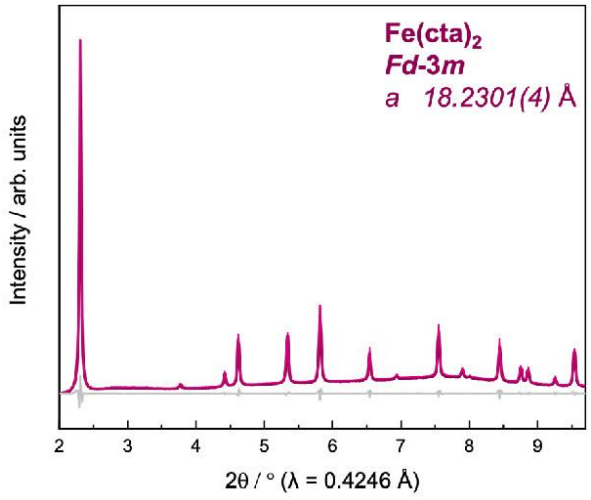


Figure S24: Pawley fit for $Fe(cta)_2$ at ambient pressure. Experimental data is shown as dark pink line, Pawley fit as light pink line, and the difference curve (fit – data) as grey line.

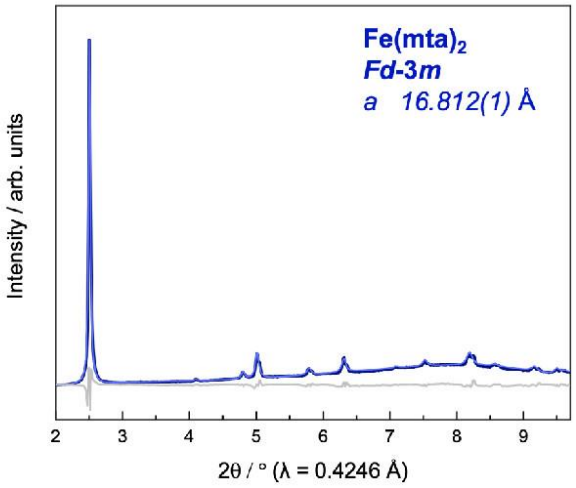


Figure S25: Pawley fit for $Fe(mta)_2$ at 0.4 GPa. Experimental data is shown as dark blue line, Pawley fit as light blue line, and the difference curve (fit – data) as grey line.

Table S3: Structural parameters (lattice parameter *a*, volume *V*, and space group *S.G.*) for all studied triazole-based Fe(II) MOFs obtained from Pawley refinement of the ambient pressure PXRD data.

| $Fe(x)_2$ | $Fe(ta)_2$ | $Fe(mta)_2$ | $Fe(cta)_2$ |
|---|---|---|---|
| ***a*** **/ Å** | *16.5969(6)* | *17.3175(7)* | *18.2301(4)* |
| ***V*** **/ Å³** | *4571.8(5)* | *5193.5(7)* | *6058.6(4)* |
| **S.G.** | *Fd-3m* | *Fd-3m* | *Fd-3m* |

Table S4: Overview of the unit cell parameters and volumes of $Fe(ta)_2$ derived from Pawley fits of the HPPXRD data.

| $p$ / GPa | $R_{wp}$ | $a$ / Å | $V$ / Å$^3$ |
|---|---|---|---|
| ambient | 2.73774 | 16.5969(6) | 4571.8(5) |
| 0.0194 | 2.73552 | 16.5969(6) | 4571.8(5) |
| 0.0398 | 2.45438 | 16.5955(6) | 4570.6(5) |
| 0.0598 | 2.58785 | 16.5914(6) | 4567.2(5) |
| 0.0797 | 2.75515 | 16.5870(6) | 4563.6(5) |
| 0.0995 | 2.81962 | 16.5829(6) | 4560.2(5) |
| 0.1199 | 2.83131 | 16.5797(6) | 4557.5(5) |
| 0.1399 | 2.82163 | 16.5750(6) | 4553.7(5) |
| 0.1593 | 2.81628 | 16.5703(6) | 4549.8(5) |
| 0.1793 | 2.78023 | 16.5674(7) | 4547.4(5) |
| 0.1996 | 2.77953 | 16.5631(7) | 4543.9(5) |
| 0.2196 | 2.71871 | 16.5599(6) | 4541.3(5) |
| 0.2397 | 2.68595 | 16.5566(6) | 4538.5(5) |
| 0.2597 | 2.70596 | 16.5534(6) | 4535.9(5) |
| 0.2797 | 2.73582 | 16.5492(7) | 4532.4(5) |
| 0.2997 | 2.76427 | 16.5464(7) | 4530.1(5) |
| 0.3198 | 2.78284 | 16.5413(7) | 4526.0(5) |
| 0.3397 | 2.81206 | 16.5379(7) | 4523.2(5) |
| 0.3598 | 3.10945 | 16.5334(7) | 4519.5(6) |
| 0.3798 | 2.86024 | 16.5298(7) | 4516.5(5) |
| 0.3998 | 2.87148 | 16.5266(7) | 4513.9(5) |

Table S5: Overview of the unit cell parameters and volumes of $Fe(cta)_2$ derived from Pawley fits of the HPPXRD data.

| $p$ / GPa | $R_{wp}$ | $a$ / Å | $V$ / Å$^3$ |
|---|---|---|---|
| ambient | 2.66004 | 18.2301(4) | 6058.6(4) |
| 0.0194 | 1.57839 | 18.2315(9) | 6060.0(9) |
| 0.0398 | 1.5153 | 18.2232(8) | 6051.7(8) |
| 0.0598 | 1.53717 | 18.2125(6) | 6041.1(6) |
| 0.0793 | 2.33418 | 18.2095(9) | 6038.1(9) |
| 0.0995 | 1.40499 | 18.2086(7) | 6037.2(7) |
| 0.1198 | 1.49129 | 18.2063(7) | 6034.9(7) |
| 0.1399 | 1.51052 | 18.2023(7) | 6030.9(7) |
| 0.1594 | 1.54993 | 18.1959(9) | 6024.5(8) |
| 0.1794 | 1.55415 | 18.1936(9) | 6022.3(9) |
| 0.1996 | 1.51402 | 18.1863(8) | 6015.1(8) |
| 0.2196 | 1.548 | 18.1829(8) | 6011.6(8) |
| 0.2397 | 1.54349 | 18.1797(7) | 6008.5(7) |
| 0.2597 | 1.56373 | 18.1770(7) | 6005.8(7) |
| 0.2798 | 1.57277 | 18.1734(7) | 6002.2(7) |
| 0.2998 | 1.56371 | 18.1688(8) | 5997.6(7) |
| 0.3198 | 1.57561 | 18.1655(7) | 5994.4(7) |
| 0.3397 | 1.55788 | 18.1617(7) | 5990.6(7) |
| 0.3598 | 1.59253 | 18.1579(8) | 5986.9(7) |
| 0.3798 | 1.56215 | 18.1543(7) | 5983.3(7) |
| 0.3998 | 1.61549 | 18.1520(7) | 5981.0(7) |

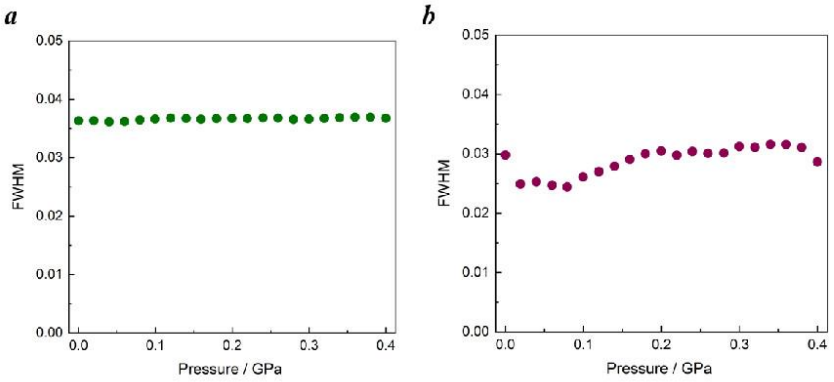


Figure S26: Fwhm extracted from Pawley profile fits for $Fe(ta)_2$ (a) and $Fe(cta)_2$ (b) as a function of increasing hydrostatic pressure up to 0.4 GPa.

## 10. Bulk moduli (EOSFit)

The unit cell volume changes obtained by HPPXRD data analysis were fitted to 2nd order Birch-Murnaghan (B-M) equation of state using EoSFitGui to estimate the bulk moduli of $Fe(ta)_2$ and $Fe(cta)_2$.[12] The standard deviations of the volumes extracted by Pawley profile fitting and a standard pressure error ($\sigma p$ = ± 0.003 GPa) were included in the B-M fitting routine. For both studied MOFs, variable pressure unit cell volumes across the $p$ range between ambient – 0.4 GPa were used for fitting. In addition, we present 2nd and 3rd order calculations of the bulk moduli for completeness (Table S6).

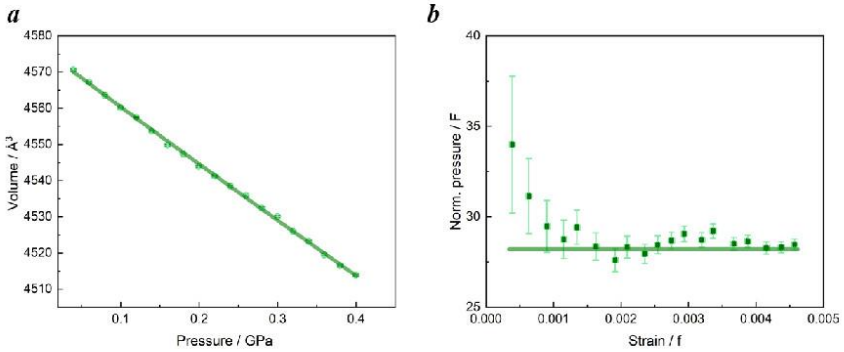


Figure S27: The evolution of the unit cell volume of $Fe(ta)_2$ is fitted using 2nd order B-M equation of state shown as green line in the $V(p)$-plot (a) and $F(f)$-plot (b), confirming the applicability of the 2nd order fit to calculate the bulk modulus.

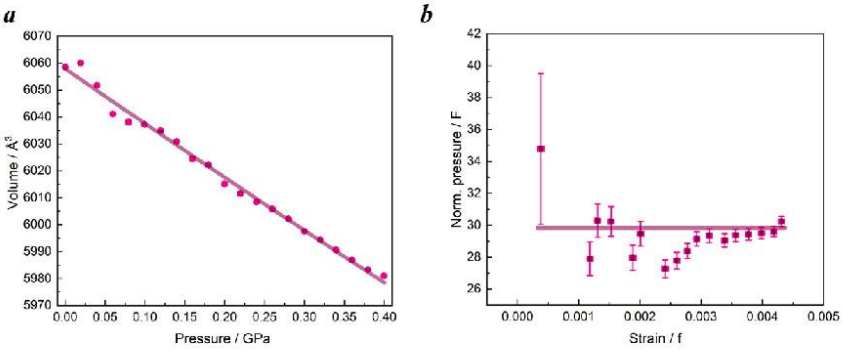


Figure S28: The evolution of the unit cell volume of $Fe(cta)_2$ is fitted using 2nd order B-M equation of state shown as pink line in the $V(p)$-plot (a) and $F(f)$-plot (b), confirming the applicability of the 2nd order fit to calculate the bulk modulus.

Table S6: Overview of bulk moduli ($B$) determined by using 2nd and 3rd order B-M equation of state calculations for the unit cell volume at ambient pressure ($V_0$ at zero pressure and temperature) with standard deviations.

| | **Fe(ta)$_2$** | **Fe(cta)$_2$** |
|---|---|---|
| $B$ (2nd) / GPa | 28.2 | 29.5 |
| $\sigma B$ (2nd) / GPa | 0.2 | 0.5 |
| $V_0$ (2nd) / Å$^3$ | 4576.5 | 6057.9 |
| $\sigma V_0$ (2nd) / Å$^3$ | 0.3 | 0.8 |
| $B$ (3rd) / GPa | 27.3 | 26.8 |
| $\sigma B$ (3rd) / GPa | 0.9 | 0.5 |
| $V_0$ (3rd) / Å$^3$ | 4576.9 | 6058.8 |
| $\sigma V_0$ (3rd) / Å$^3$ | 0.5 | 0.8 |

## 11. Standard material for high-pressure PXRD analysis

To validate the high-pressure cell setup, we used $Ni(dmgH)_2$ (Nickel dimethylglyoxime) as reference material with literature-known variable pressure behaviour.[13,14] The sample was prepared in a similar fashion as described above in the HPPXRD experimental details (Chapter 8). The HPPXRD data was collected in the pressure range (ambient pressure to 0.4 GPa) with a defined pressure step size (0.02 GPa). Pawley refinement of the PXRD data at ambient pressure reveals unit cell parameters $a$ = 16.5717(6) Å, $b$ = 10.4331(3) Å, $c$ = 6.4621(2) Å, and $V$ = 1117.28(6) Å$^3$ is in great accordance across variable pressure PXRD data with the reported structure.[15] The calculated bulk moduli, *i.e.* $B$ = 8.43 ± 0.15 GPa (derived from the B-M 3$^{rd}$ order equation of state fit) and $B$ = 9.57 ± 0.09 GPa (derived from the B-M 2$^{nd}$ order equation of state fit) are in line with literature data, confirming the applicability of the setup.[13]

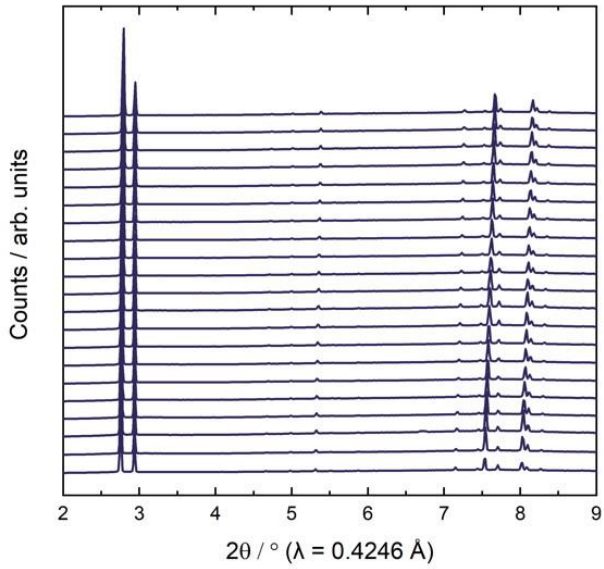


Figure S29: Normalised HPPXRD data of the standard material $Ni(dmgH)_2$ recorded in the pressure range from ambient pressure up to 0.4 GPa.

Table S7: Unit cell parameters and the corresponding $R_{wp}$ values for $Ni(dmgH)_2$ derived from Pawley profile fitting of the HPPXRD data.

| $p$ / GPa | $R_{wp}$ | $a$ / Å | $b$ / Å | $c$ / Å | $V$ / Å$^3$ |
|---|---|---|---|---|---|
| ambient | 2.95280 | 16.5717(6) | 10.4331(3) | 6.4621(2) | 1117.28(6) |
| 0.0197 | 3.58596 | 16.5718(9) | 10.4265(5) | 6.4539(4) | 1115.16(10) |
| 0.0398 | 2.99285 | 16.5677(7) | 10.4105(4) | 6.4483(3) | 1112.21(8) |
| 0.0598 | 2.96639 | 16.5690(8) | 10.4004(4) | 6.4412(3) | 1109.99(9) |
| 0.0793 | 2.97736 | 16.5615(9) | 10.3890(5) | 6.4345(3) | 1107.11(10) |
| 0.0999 | 2.87619 | 16.5635(8) | 10.3808(6) | 6.4283(3) | 1105.31(10) |
| 0.1199 | 2.95232 | 16.5562(6) | 10.3677(5) | 6.4217(4) | 1102.29(9) |
| 0.1399 | 2.49250 | 16.5566(6) | 10.3571(4) | 6.4157(3) | 1100.16(7) |
| 0.1594 | 3.03165 | 16.5552(8) | 10.3482(6) | 6.4108(2) | 1098.30(11) |
| 0.1795 | 2.52741 | 16.5501(6) | 10.3387(4) | 6.4045(2) | 1095.86(7) |
| 0.1996 | 3.04075 | 16.5497(8) | 10.3310(5) | 6.3991(4) | 1094.11(10) |
| 0.2196 | 2.55868 | 16.5480(6) | 10.3221(4) | 6.3934(2) | 1092.07(7) |
| 0.2397 | 2.66187 | 16.5446(6) | 10.3129(4) | 6.3890(3) | 1090.12(7) |
| 0.2597 | 2.66473 | 16.5418(8) | 10.3073(6) | 6.3828(3) | 1088.29(9) |
| 0.2798 | 2.61754 | 16.5367(7) | 10.2969(4) | 6.3774(3) | 1085.93(8) |
| 0.2997 | 2.37638 | 16.5330(7) | 10.2919(5) | 6.3722(3) | 1084.28(9) |
| 0.3198 | 2.96540 | 16.5287(7) | 10.2873(6) | 6.3673(3) | 1082.68(9) |
| 0.3397 | 2.72334 | 16.5242(9) | 10.2765(6) | 6.3609(4) | 1080.17(10) |
| 0.3598 | 2.86385 | 16.5198(7) | 10.2708(5) | 6.3565(3) | 1078.52(9) |
| 0.3798 | 2.57641 | 16.5161(6) | 10.2624(5) | 6.3514(3) | 1076.54(8) |
| 0.3998 | 2.58556 | 16.5147(6) | 10.2581(4) | 6.3463(2) | 1075.14(7) |

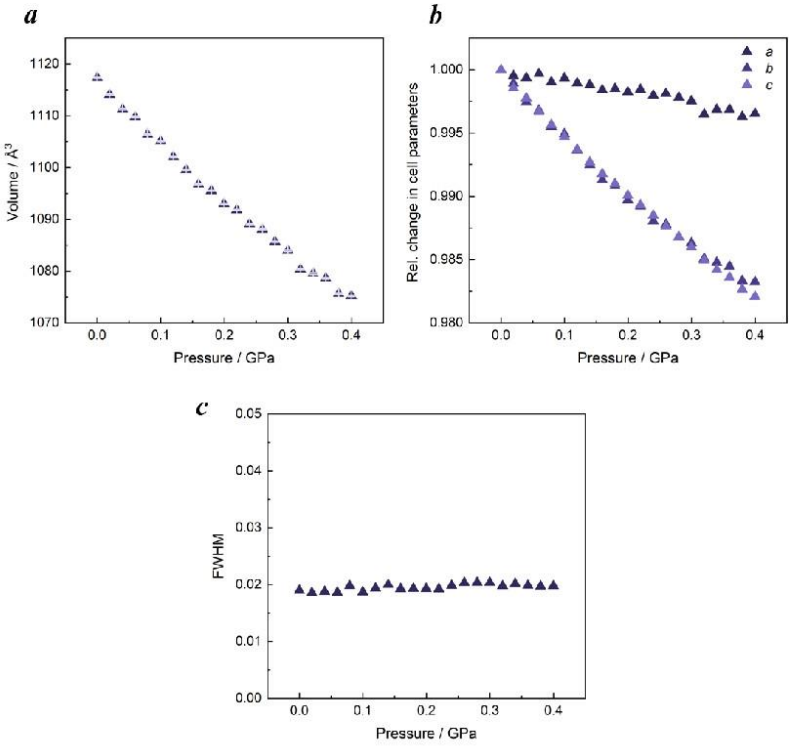


Figure S30: Change in volume (a), relative changes of the lattice parameters *a, b*, and *c* (b), and fwhm (c) for $Ni(dmgH)_2$ as a function of increasing hydrostatic pressure up to 0.4 GPa.

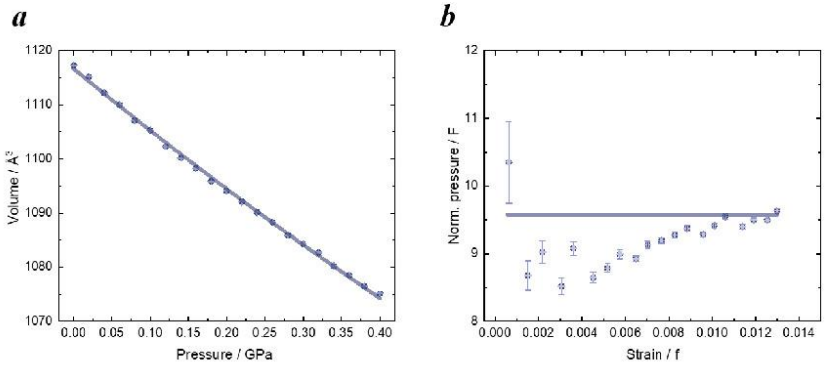


Figure S31: 2nd order -BM equation of state fit of $Ni(dmgH)_2$ shown as blue line in the *V*(*p*)-plot (a) and *F*(*f*)-plot (b), confirming the applicability of the 2nd order fit to derive the bulk modulus.

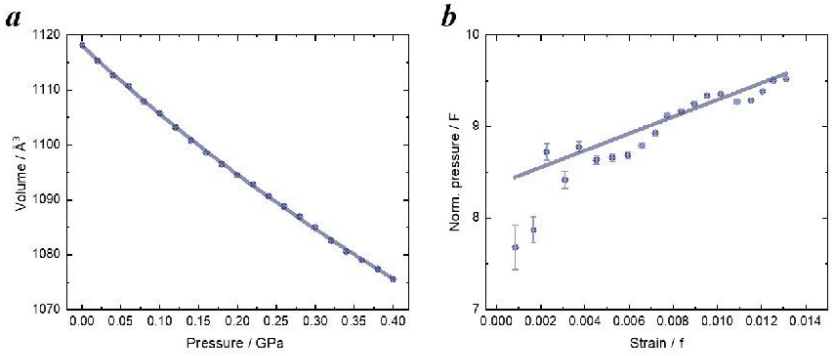


Figure S32: 3rd order B-M equation of state fit of $Ni(dmgH)_2$ shown as blue line in the *V*(*p*)-plot (a) and *F*(*f*)-plot (b), confirming the applicability of the 3rd order fit to derive the bulk modulus.

## 13. Scanning electron microscopy and energy-dispersive X-ray spectroscopy

Scanning electron microscopy (SEM) images were obtained with a *Zeiss Crossbeam 550* electron microscope, and subsequent energy-dispersive X-ray spectroscopy (EDX) of $Fe(mta)_2$ was performed using this device equipped with a *EDAX SiLi* detector. The EDX spectra of $Fe(cta)_2$ were collected using the *Philips XL 30 FEG* with an *EDAX SiLi* detector. The Fe:Cl ratios were determined as average from measurements on sample squares of at least 5 × 5 µm and applying an operating voltage of 20 kV.

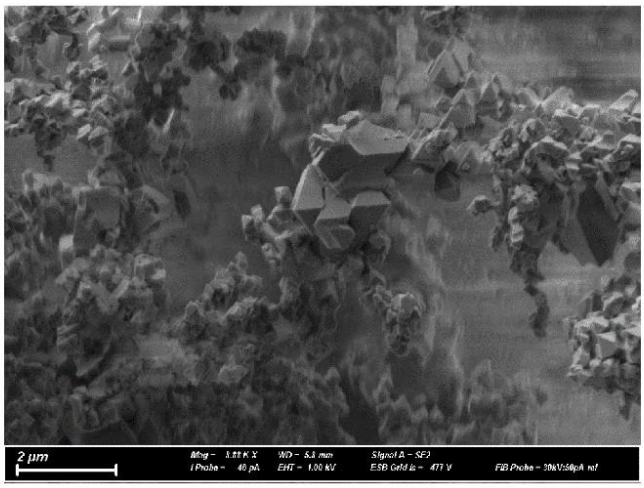


Figure S33: SEM micrograph of $Fe(mta)_2$.

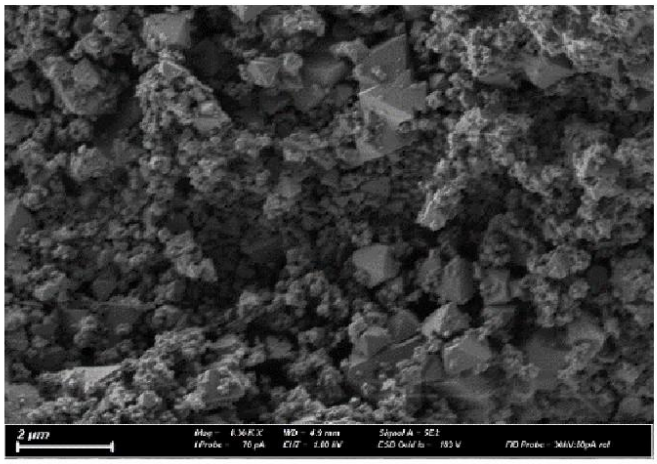


Figure S34: SEM micrographs of $Fe(cta)_2$.

## 14. 3D electron diffraction data

3D electron diffraction (3DED) data of $Fe(mta)_2$ and $Fe(cta)_2$ was collected using a Rigaku XtaLAB Synergy-ED system[17] equipped with a Rigaku HyPix-ED detector and $LaB_6$ electron source operating at 200 keV ($\lambda$ = 0.0251 Å) in a vacuum at different temperatures using Gatan's Elsa cryo-transfer holder. Data collection and processing, *i.e.* structure refinements, data reductions, and analysis were performed using the Rigaku Oxford Diffraction CrysAlis$^{Pro}$ program package.[18] The shutterless data was recorded in continuous crystal rotation mode at the 645 mm detector distance using the selected area configuration. The samples were placed on a standard amorphous carbon on a Cu grid and transferred to a holder at 233 K. The initial object search, electron beam sensitivity tests, selection and centering of crystal, and first measurements were performed at the transfer temperature. Next, the continuous grid was cooled down to 173 K, and the same crystal was located again and measured with the same scan conditions. In the last step, the grid was heated to 373 K, and measurements were repeated for the same crystals. Due to the high symmetry of the crystal structures, dataset merging was not required. The collected data was processed and finalised with frame scaling and empirical absorption correction up to 0.8 Å resolution. The structure was solved, and the space group *Fd*-3*m* was determined by the ShelXT 2018/2[19] structure solution program using Intrinsic Phasing and refined in the kinematic approximation model using atomic electron scattering factors[20] by Least Squares using ShelXL 2018/3.[21] An extinction parameter has been refined to mitigate the effect of dynamic intensity data. All non-hydrogen atoms were refined anisotropically. Hydrogen atom positions were calculated geometrically and refined using the riding model. Hydrogen atom positions were calculated geometrically and refined using the riding model. A static disorder of ligand molecules around the symmetry elements in both crystal structures can be observed and refined with constrained atom occupancies and RIGU/SIMU restrains.

Table S8: Crystal structure and refinements details for $Fe(mta)_2$.

| **Compound** **$Fe(mta)_2$** | data_M-173 | data_M-233 | data_M-293 | data_M-373 |
|---|---|---|---|---|
| Formula | | $C_{18}H_{18}Fe_3N_{18}$ | | |
| $D_{calc.}$ / g cm$^{-3}$ | 1.820 | 1.760 | 1.688 | 1.690 |
| Formula weight | 654.00 | 654.00 | 654.00 | 654.00 |
| **$T$ / K** | **173(1)** | **233(1)** | **293(2)** | **373(1)** |
| Crystal system | cubic | cubic | cubic | cubic |
| Space group | *Fd*-3*m* | *Fd*-3*m* | *Fd*-3*m* | *Fd*-3*m* |
| $a$ / Å | 16.84(8) | 17.0(4) | 17.26(9) | 17.26(8) |
| V / Å$^3$ | 4773(68) | 4936(316) | 5146(78) | 5140(74) |
| $Z$ | | 8 | | |
| $Z'$ | | 1/24 | | |
| Wavelength / Å | | 0.0251 | | |
| Radiation type | | electrons | | |
| $\Theta_{min}$ / ° | 0.074 | 0.073 | 0.072 | 0.072 |
| $\Theta_{max}$ / ° | 0.896 | 0.898 | 0.897 | 0.898 |
| Measured refl. | 4981 | 1808 | 5776 | 4510 |
| Independent refl. | 270 | 267 | 291 | 291 |
| Reflections with I > 2(I) | 188 | 134 | 208 | 251 |
| $R_{int}$ | 0.5094 | 0.2492 | 0.4135 | 0.2358 |
| Parameters | 31 | 30 | 30 | 31 |
| Restraints | 0 | 0 | 30 | 0 |
| Largest peak | 0.710 | 0.350 | 0.250 | 0.212 |
| Deepest hole | -0.230 | -0.098 | -0.177 | -0.274 |
| GoF | 1.310 | 1.117 | 1.268 | 1.285 |
| $wR_2$ (all data) | 0.3978 | 0.3815 | 0.3803 | 0.3491 |
| $wR_2$ | 0.3804 | 0.3236 | 0.3453 | 0.3406 |
| $R_1$ (all data) | 0.1904 | 0.1702 | 0.1420 | 0.1288 |
| $R_1$ | 0.1779 | 0.1198 | 0.1209 | 0.1218 |
| CCDC Deposition number | 2311804 | 2311805 | 2311806 | 2311807 |

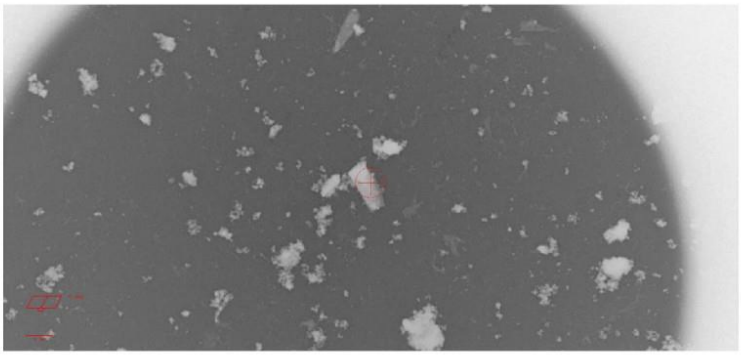

Figure S35: Image of $Fe(mta)_2$, showing suitable crystals used for ED.

***a*** **Fe(mta)$_2$ at 173 K**

| Atom | Atom | Length / Å |
|---|---|---|
| Fe1 | N3 | 2.083(14) |
| Fe1 | N3$^{1}$ | 2.083(14) |
| Fe1 | N3$^{2}$ | 2.083(14) |
| Fe1 | N3$^{3}$ | 2.083(14) |
| Fe1 | N3$^{4}$ | 2.083(14) |
| Fe1 | N3$^{5}$ | 2.083(14) |
| Fe2 | N4$^{6}$ | 2.048(14) |
| Fe2 | N4 | 2.048(14) |
| Fe2 | N4$^{7}$ | 2.048(14) |
| Fe2 | N4$^{8}$ | 2.048(14) |
| Fe2 | N4$^{9}$ | 2.048(14) |
| Fe2 | N4$^{10}$ | 2.048(14) |
| N3 | N4 | 1.303(12) |
| N3 | N4$^{11}$ | 1.303(12) |
| N4 | C5 | 1.322(16) |
| C5 | C5$^{11}$ | 1.39(3) |
| C5 | C6 | 1.44(3) |

$^{1}$-1/2+z,3/4-x,5/4-y; $^{2}$-1/2+z,1/2+x,+y; $^{3}$3/4-y,+z,3/4-x; $^{4}$1/4-x,5/4-y,+z; $^{5}$-1/2+y,+z,1/2+x; $^{6}$1-y,1/4+z,1/4+x; $^{7}$-1/4+z,1-x,-1/4+y; $^{8}$-1/2+y,5/4-z,3/4-x; $^{9}$1/2-x,3/2-y,1-z; $^{10}$3/4-z,1/2+x,5/4-y; $^{11}$x,5/4-y,5/4-z

***b*** **Fe(mta)$_2$ at 233 K**

| Atom | Atom | Length / Å |
|---|---|---|
| Fe2 | N4 | 2.08(5) |
| Fe2 | N4$^{1}$ | 2.08(5) |
| Fe2 | N4$^{2}$ | 2.08(5) |
| Fe2 | N4$^{3}$ | 2.08(5) |
| Fe2 | N4$^{4}$ | 2.08(5) |
| Fe2 | N4$^{5}$ | 2.08(5) |
| Fe1 | N3$^{6}$ | 2.15(5) |
| Fe1 | N3 | 2.15(5) |
| Fe1 | N3$^{7}$ | 2.15(5) |
| Fe1 | N3$^{4}$ | 2.15(5) |
| Fe1 | N3$^{8}$ | 2.15(5) |
| Fe1 | N3$^{7}$ | 2.15(5) |
| N3 | N4 | 1.29(3) |
| N3 | N4$^{9}$ | 1.29(3) |
| N4 | C5 | 1.33(3) |
| C5 | C5$^{9}$ | 1.33(4) |
| C5 | C6 | 1.54(5) |

$^{1}$1-z,1-x,1-y; $^{2}$+z,+x,-y; $^{3}$1-y,1-z,1-x; $^{4}$+y,+z,+x; $^{5}$1-x,1-y,1-z; $^{6}$3/4-y,+z,3/4-x; $^{7}$-z,3/4-x,3/4-y; $^{8}$3/4-x,3/4-y,+z; $^{9}$3/4-x,+y,3/4-z

***c*** **Fe(mta)$_2$ at RT**

| Atom | Atom | Length / Å |
|---|---|---|
| Fe1 | N1$^{1}$ | 2.198(15) |
| Fe1 | N1$^{2}$ | 2.198(15) |
| Fe1 | N1$^{3}$ | 2.198(15) |
| Fe1 | N1$^{4}$ | 2.198(15) |
| Fe1 | N1$^{5}$ | 2.198(15) |
| Fe1 | N1$^{6}$ | 2.198(15) |
| Fe2 | N2$^{2}$ | 2.117(14) |
| Fe2 | N2$^{5}$ | 2.117(14) |
| Fe2 | N2$^{7}$ | 2.117(14) |
| Fe2 | N2$^{8}$ | 2.117(14) |
| Fe2 | N2$^{9}$ | 2.117(14) |
| Fe2 | N2$^{10}$ | 2.117(14) |
| N1 | N2 | 1.302(11) |
| N1 | N2 | 1.302(11) |
| N2 | C1 | 1.369(15) |
| C1 | C1 | 1.338(19) |
| C1 | C3 | 1.43(3) |

$^{1}$+z,x+1/2,y+1/2; $^{2}$-y+3/4,-z+1/4,x+1/2; $^{3}$-z+3/4,-x+1/4,y+1/2; $^{4}$-x+3/4,z+1/2,-y+1/4; $^{5}$-y+3/4,x+1/2,-z+1/4; $^{6}$-x+3/4,-y+1/4,z+1/2; $^{7}$ y+1/4,-x+1/2,z+3/4; $^{8}$ –z+3/4,x+1/2,-y+1/4; $^{9}$ y−1/4,z−3/4,-x−1/2; $^{10}$ z−1/4,-x−1/2,y−3/4

***d*** **Fe(mta)$_2$ at 373 K**

| Atom | Atom | Length / Å |
|---|---|---|
| Fe1 | N3$^{1}$ | 2.198(13) |
| Fe1 | N3$^{2}$ | 2.198(13) |
| Fe1 | N3$^{3}$ | 2.198(13) |
| Fe1 | N3$^{4}$ | 2.198(13) |
| Fe1 | N3$^{5}$ | 2.198(13) |
| Fe1 | N3 | 2.198(13) |
| Fe2 | N4 | 2.129(13) |
| Fe2 | N4$^{6}$ | 2.129(13) |
| Fe2 | N4$^{7}$ | 2.129(13) |
| Fe2 | N4$^{8}$ | 2.129(13) |
| Fe2 | N4$^{4}$ | 2.129(13) |
| Fe2 | N4$^{3}$ | 2.129(13) |
| N3 | N4$^{9}$ | 1.285(10) |
| N3 | N4 | 1.285(10) |
| N4 | C5 | 1.331(14) |
| C5 | C5$^{9}$ | 1.39(2) |
| C5 | C6 | 1.38(3) |

$^{1}$+y,3/4-z,3/4-x; $^{2}$3/4-z,3/4-x,+y; $^{3}$+z,+x,+y; $^{4}$+y,+z,+x; $^{5}$3/4-x,-y,3/4-z; $^{6}$1-x,1-y,1-z; $^{7}$1-z,1-x,1-y; $^{8}$1-y,1-z,1-x; $^{9}$3/4-x,3/4-y,+z

Figure S36: Bond lengths for Fe(mta)$_2$ as determined at different temperatures (a-d).

Table S9: Crystal structure and refinements details for $Fe(cta)_2$.

| **Compound** **$Fe(cta)_2$** | data_C-173 | data_C-233 | data_C-293 | data_C-373 |
|---|---|---|---|---|
| Formula | $C_{30}H_{36}Fe_3N_{18}$ | | | |
| $D_{calc.}$ / g cm$^{-3}$ | 1.840 | 1.836 | 1.802 | 1.828 |
| Formula weight | 816.28 | 816.28 | 816.28 | 816.28 |
| ***T* / K** | **173(1)** | **233(1)** | **293(2)** | **373(1)** |
| Crystal system | cubic | cubic | cubic | cubic |
| Space group | *Fd*-3*m* | *Fd*-3*m* | *Fd*-3*m* | *Fd*-3*m* |
| *a* / Å | 18.06(7) | 18.08(16) | 18.19(10) | 18.10(10) |
| V / Å$^3$ | 5893(65) | 5907(158) | 6017(99) | 5932(99) |
| *Z* | 8 | | | |
| *Z'* | 1/24 | | | |
| Wavelength / Å | 0.0251 | | | |
| Radiation type | electrons | | | |
| $Q_{min}$ / ° | 0.069 | 0.069 | 0.068 | 0.069 |
| $Q_{max}$ / ° | 0.896 | 0.896 | 0.898 | 0.899 |
| Measured refl. | 6138 | 6134 | 4041 | 4241 |
| Independent refl. | 327 | 327 | 333 | 328 |
| Reflections with I > 2(I) | 310 | 306 | 306 | 250 |
| $R_{int}$ | 0.3114 | 0.2070 | 0.1988 | 0.4731 |
| Parameters | 39 | 42 | 31 | 39 |
| Restraints | 27 | 45 | 0 | 27 |
| Largest peak | 0.233 | 0.249 | 0.492 | 0.256 |
| Deepest hole | -0.157 | -0.164 | -0.319 | -0.155 |
| GoF | 1.255 | 1.352 | 1.844 | 1.238 |
| $wR_2$ (all data) | 0.3649 | 0.3568 | 0.4424 | 0.3659 |
| $wR_2$ | 0.3605 | 0.3535 | 0.4358 | 0.3380 |
| $R_1$ (all data) | 0.1530 | 0.1491 | 0.2025 | 0.1734 |
| $R_1$ | 0.1479 | 0.1434 | 0.1950 | 0.1434 |
| CCDC Deposition number | 2311808 | 2311809 | 2311810 | 2311811 |

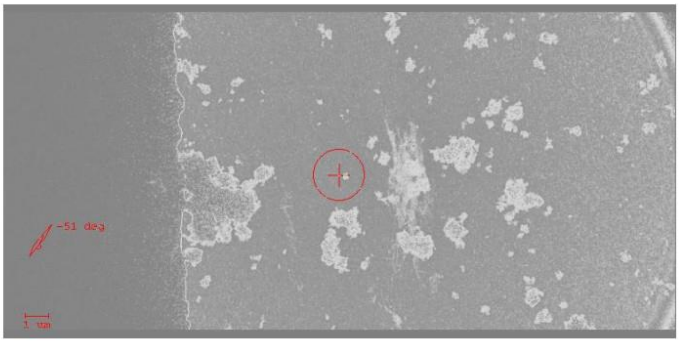


Figure S37: Image of $Fe(cta)_2$, showing suitable crystals used for ED.

## 15. Note to the structural chemistry of $Fe(mta)_2$

The crystal structure of $Fe(mta)_2$ was obtained by 3DED at four different temperatures (173 K, 233 K, RT and 373 K). In addition, a Rietveld-based structure refinement was performed based on the PXRD data at ambient pressure (s. S-20). Due to the aromaticity of triazolate linker, one would expect that $-CH_3$ groups of $(mta)^-$ are disordered between two sites (50% occupancy) and located within the plane of the trizolate ligand. During structure solution and refinement of 3DED and PXRD data, a significantly better structural model was obtained when moving the $-CH_3$ group out of the triazolate plane, leading to a 25% occupancy of carbon atoms. Since this leaves some open questions related to the final structure of $Fe(mta)_2$ and translates to ambiguities when analyzing the pressure-induced phase transition of $Fe(mta)_2$, we decided focus on the comparison of the high-pressure behaviour of $Fe(ta)_2$ and $Fe(cta)_2$ in this work and address the high-pressure behaviour of $Fe(mta)_2$ in a follow-up study.

## 16. References


1 J. Thomas, S. Jana, S. Liekens and W. Dehaen, *Chem. Commun.*, 2016, **52**, 9236–9239.
2 P. R. Clark, G. D. Williams, J. F. Hayes and N. C. O. Tomkinson, *Angew. Chem. Int. Ed. Engl.*, 2020, **59**, 6740–6744.
3 M. Grzywa, R. Röß-Ohlenroth, C. Muschielok, H. Oberhofer, A. Błachowski, J. Żukrowski, D. Vieweg, H.-A. K. von Nidda and D. Volkmer, *Inorg. Chem.*, 2020, **59**, 10501–10511.
4 A. B. Andreeva, K. N. Le, K. Kadota, S. Horike, C. H. Hendon and C. K. Brozek, *Chem. Mater.*, 2021, **33**, 8534–8545.
5 E. W. Müller, H. Spiering and P. Gütlich, *Chem. Phys. Lett.*, 1982, **93**, 567–571.
6 a) N. J. Brooks, B. L. L. E. Gauthe, N. J. Terrill, S. E. Rogers, R. H. Templer, O. Ces and J. M. Seddon, *Rev. Sci. Instrum.*, 2010, **81**, 64103; b) S. Dissegna, P. Vervoorts, C. L. Hobday, T. Düren, D. Daisenberger, A. J. Smith, R. A. Fischer and G. Kieslich, *J. Am. Chem. Soc*, 2018, **140**, 11581–11584;
7 J. Filik, A. W. Ashton, P. C. Y. Chang, P. A. Chater, S. J. Day, M. Drakopoulos, M. W. Gerring, M. L. Hart, O. V. Magdysyuk, S. Michalik, A. Smith, C. C. Tang, N. J. Terrill, M. T. Wharmby and H. Wilhelm, *J. Appl. Crystallogr.*, 2017, **50**, 959–966.
8 G. S. Pawley, *J. Appl. Crystallogr.*, 1981, **14**, 357–361.
9 A. A. Coelho, *J. Appl. Crystallogr.*, 2018, **51**, 210–218.
10 F. Gándara, F. J. Uribe-Romo, D. K. Britt, H. Furukawa, L. Lei, R. Cheng, X. Duan, M. O'Keeffe and O. M. Yaghi, *Chemistry-A European Journal*, 2012, **18**, 10595–10601.
11 T. Runčevski, *J. Appl. Crystallogr.*, 2019, **52**, 1238–1239.
12 J. Gonzalez-Platas, M. Alvaro, F. Nestola and R. Angel, *J. Appl. Crystallogr.*, 2016, **49**, 1377–1382.
13 K. Takeda, J. Hayashi, I. Shirotani, H. Fukuda and K. Yakushi, *Mol. Cryst. Liq.*, 2006, **460**, 131–144.
14 I. F. Bruce-Smith, B. A. Zakharov, J. Stare, E. V. Boldyreva and C. R. Pulham, *J. Phys. Chem. C*, 2014, **118**, 24705–24713.
15 D. E. Williams, G. Wohlauer and R. E. Rundle, *J. Am. Chem. Soc*, 1959, **81**, 755–756.
16 M. J. Cliffe and A. L. Goodwin, *J. Appl. Crystallogr.*, 2012, **45**, 1321–1329.
17 S. Ito, F. J. White, E. Okunishi, Y. Aoyama, A. Yamano, H. Sato, J. D. Ferrara, M. Jasnowski and M. Meyer, *CrystEngComm*, 2021, **23**, 8622–8630.
18 *Rigaku Oxford Diffraction CrysAlisPro Software System*, 2023, Rigaku Corporation: Wrocław, Poland.
19 G. M. Sheldrick, *Acta Crystallogr., A, Found. Crystallogr.*, 2015, **71**, 3–8.
20 A. Saha, S. S. Nia and J. A. Rodríguez, *Chem. Rev.*, 2022, **122**, 13883–13914.
21 G. M. Sheldrick, *Acta Crystallogr. C Struct. Chem.*, 2015, **71**, 3–8.

## 4.4. Supporting Information for Study IV

Electronic Supplementary Material (ESI) for Materials Advances.


# Supporting Information
# Tuning the Mechanical Properties of Molecular Perovskites by Controlling Framework Distortions *via* A-site Substitution

Silva M. Kronawitter,[a] Shinjoo Park,[a] Sebastian A. Hallweger,[a] Emily Myatt,[b] Jem Pitcairn,[b] Matthew J. Cliffe,[b] Dominik Daisenberger,[c] Markus Drees[a] and Gregor Kieslich*[a]

[a] Technical University of Munich, TUM Natural School of Sciences, Lichtenbergstr. 4, 85748, Garching, Germany.
[b] School of Chemistry, University of Nottingham, Nottingham NG7 2RD, United Kingdom.
[c] Diamond Light Source Ltd., Diamond House, Harwell Campus, Didcot OX11 ODE, United Kingdom.
*gregor.kieslich@tum.de

Contents:

**1. Material synthesis ..... 2**
Synthesis of the A-site precursor 1,1-diethylpiperidinium bromide – [DEP]Br: ..... 2
Synthesis of the A-site precursor 1-ethyl-1-propylpiperidinium bromide – [PEP]Br: ..... 2
Synthesis of the A-site precursor 1,1-diisopropylpiperidinium bromide – [DIP]Br: ..... 3
Synthesis of the A-site precursor 1,1-dipropylpiperidinium bromide – [DPP]Br: ..... 3
Synthesis of molecular perovskites $[A]Ni(C_2N_3)_3$: ..... 5
Elemental analysis: ..... 6
Synthesis of $[PEP]_{1-x}[DPP]_xNi(C_2N_3)_3$ solid solutions: ..... 6
**2. Single crystal X-ray diffraction (SCXRD) data ..... 7**
**3. NMR spectroscopy of the precursor A-site cations ..... 18**
**4. Thermogravimetric analysis and differential scanning calorimetry (TGA-DSC) ..... 24**
**5. Differential scanning calorimetry ..... 27**
**6. Powder X-ray diffraction (PXRD) data ..... 29**
**7. High-pressure powder X-ray diffraction (HPXRD) ..... 32**
**8. HPPXRD analysis ..... 38**
**9. Bulk modulus ..... 62**
**10. $Ni(dmgH)_2$ as reference material ..... 66**
**11. Tilt analysis of molecular perovskites ..... 69**
**12. DFT calculations ..... 73**
**13. PASCal calculations ..... 74**
**14. Data overview of $[A]Ni(C_2N_3)_3$ materials ..... 76**
**15. References ..... 77**

## 1. Material synthesis

All used chemicals for the A-site cation ($A^+$) precursor synthesis and molecular perovskite synthesis were purchased from Sigma Aldrich without further purification. Solvents and ultrapure (Millipore) water were in the quality of reagent grade.

**Synthesis of the A-site precursor 1,1-diethylpiperidinium bromide – [DEP]Br:**
12.30 mL (0.9 mol, 1 eq.) 1,5-dibromopentane was added in a three-necked flask setup to 20 ml acetonitrile under stirring. The solution was heated up to reflux, and 10.30 mL (1 mol, 1.1 eq.) diethylamine was added dropwise. After stirring overnight, 12 g of potassium carbonate was added, and the mixture was stirred overnight at reflux temperature. The mixture was filtered, and the excess solvent was removed *in vacuo*, yielding a white, crystalline precipitate recrystallised in isopropanol and dried *in vacuo*. 10.55 g (52.2% yield) of the product was obtained.

**$^1$H NMR:** (400 MHz, deuterated chloroform): $\delta$ / ppm = 3.65 (*t*, 4 H), 3.58 (*q*, 4 H), 1.88 (*q,* 4 H), 1.81 (*q,* 2 H), 1.33 (*t*, *J* = 7.3 Hz, 6 H).
**$^{13}$C NMR:**(100 MHz, deuterated chloroform): $\delta$ / ppm = 57.78, 52.82, 20.37, 19.42, 7.12.

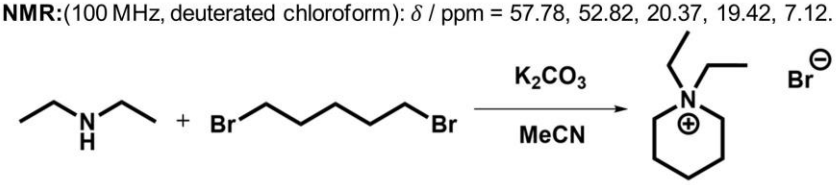


**Figure S1:** Nucleophilic substitution reaction scheme towards the synthesis of the A-site cation precursor salt [DEP]Br ([DEP]$^+$ = [$C_9H_{20}N$]$^+$).

**Synthesis of the A-site precursor 1-ethyl-1-propylpiperidinium bromide – [PEP]Br:**
In a three-necked flask, 9.11 mL (0.1 mol, 1 eq.) bromopropane was added dropwise to a stirring solution of 13.81 mL (0.1 mol, 1 eq.) ethylpiperidine in 40 mL acetonitrile. The mixture was heated to reflux overnight, and 14 g of potassium carbonate was added. The mixture was stirred at reflux temperature overnight. The solvent was removed *in vacuo*, and the crystalline product was washed using 70 mL ethyl acetate, yielding a pure product of 19.18 g (81.2%).

**$^1$H NMR:** (400 MHz, deuterium oxide): $\delta$ / ppm = 3.28 (*q*, 2 H), 3.22 (*m*, 4 H), 3.12 (*m*, 2 H), 1.77 (*m,* 4 H), 1.60 (*m,* 4 H), 1.18 (*t*, *J* = 1.8 Hz, 3 H), 0.88 (*t*, *J* = 7.3 Hz, 3 H).
**$^{13}$C NMR:** (100 MHz, deuterium oxide): $\delta$ / ppm = 59.01, 58.70, 53.78, 20.74, 19.06, 14.36, 9.91, 6.33.

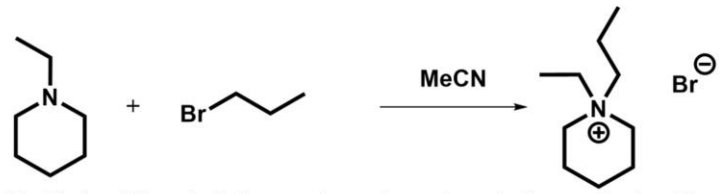


**Figure S2:** Nucleophilic substitution reaction scheme towards the synthesis of the A-site cation precursor salt [PEP]Br ($[PEP]^+ = [C_{10}H_{22}N]^+$).

**Synthesis of the A-site precursor 1,1-diisopropylpiperidinium bromide – [DIP]Br:**

12.30 mL (0.9 mol, 1 eq.) 1,5-dibromopentane was added in a three-necked flask to 40 ml methanol under stirring. The solution was heated to reflux, and 14.05 mL (1 mol, 1.1 eq.) di-isopropylamine was added dropwise. The mixture was stirred overnight. In the next step, 16 g potassium carbonate was added, and the mixture was stirred for 3 h at reflux temperature. After cooling down to room temperature, the base was filtered, forming a white, crystalline precipitate, which was recrystallised in isopropanol and dried *in vacuo*, yielding 3.77 g (16.5% yield).

**$^1$H NMR:** (400 MHz, deuterium oxide): $\delta$ / ppm = 3.98 (*p*, 2 H), 3.29 (*t*, 4 H), 1.79 (*m,* 4 H), 1.58 (*p,* 2 H), 1.35 (*dt*, *J* = 1.5 Hz, 12 H).

**$^{13}$C NMR:** (100 MHz, deuterium oxide): $\delta$ / ppm = 60.27, 53.47, 20.61, 19.46, 17.10.

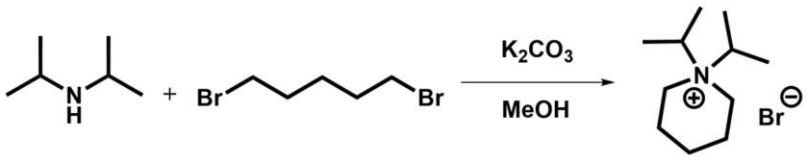


**Figure S3:** Nucleophilic substitution reaction scheme towards the synthesis of the A-site cation precursor salt [DIP]Br ($[DIP]^+ = [C_{11}H_{24}N]^+$).

**Synthesis of the A-site precursor 1,1-dipropylpiperidinium bromide – [DPP]Br:**

1,1-dipropylpiperidinium bromide was prepared in a two-step synthesis. First 1-propylpiperidinium bromide was synthesised starting from 4.10 mL (41.4 mmol, 1 eq.) piperidine and 4.15 mL (45.6 mmol, 1.1 eq.) bromopropane in 30 mL acetonitrile. Next, the solution was heated to reflux and stirred overnight. After cooling to room temperature, the solvent was removed *in vacuo*, followed by working up with 70 mL ethyl acetate to remove the solvent *via* decantation. The white crystalline product was recrystallised in 10 mL acetonitrile and washed with ethyl acetate, yielding 5.11 g (24.55% yield).

**$^1$H NMR:** (400 MHz, deuterium oxide): $\delta$ / ppm = 3.29 (d, 3*J* = 12.3 Hz, 2H), 3.00 (m, 2H), 2.87 (td, 3*J* = 12.6, 3.1 Hz, 2H), 1.91 (d, 3*J* = 14.7 Hz, 2H), 1.57 (m, 6H), 0.92 (t, *J* = 37.4 Hz, 3H).
**$^{13}$C NMR:** (100 MHz, deuterium oxide): $\delta$ / ppm = 58.42, 53.02, 22.76, 21.13, 17.04, 10.11.

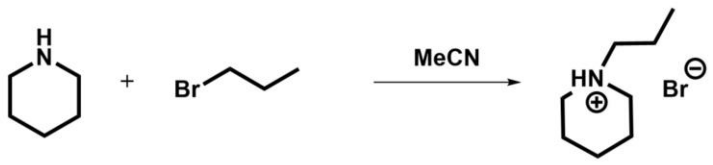


**Figure S4:** Synthesis of 1-propylpiperidinium bromide.

In a second step, 4.10 g (19.7 mmol, 1 eq.) 1-propylpiperidinium bromide was dissolved in 40 mL ethanol and 9 g potassium carbonate was added. Next, the solution was heated to reflux temperature and 3.85 mL (39.4 mmol, 2 eq.) bromopropane was added dropwise followed by stirring under reflux overnight. After cooling down, the base was removed *via* filtration. The remaining solvent was removed, and the crystalline product was recrystallised in 30 mL ethyl acetate, yielding 4.032 g (81.7% yield).

**$^1$H NMR:** (400 MHz, deuterium oxide): $\delta$ / ppm = 3.29 (t, 3*J* = 5.8 Hz, 4H), 3.19 (m, 4H), 1.82 (m, 4H), 1.65 (m, 6H), 0.92 (t, 3*J* = 7.3 Hz, 6H).
**$^{13}$C NMR:** (100 MHz, deuterium oxide): $\delta$ / ppm = 61.66, 59.17, 20.71, 19.08, 14.40, 9.82.

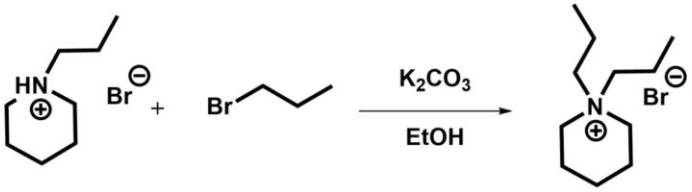


**Figure S5:** Synthesis towards 1,1-dipropylpiperidinium bromide used as A-site precursor salt [DPP]Br ($[DPP]^+ = [C_{11}H_{24}N]^+$).

**Synthesis of molecular perovskites $[A]Ni(C_2N_3)_3$:**

Single crystals of the family of molecular perovskites $[A]Ni(C_2N_3)_3$ ($A^+$ = $[DEP]^+$ = $[C_9H_{20}N]^+$, $[PEP]^+$ = $[C_{10}H_{22}N]^+$, $[DIP]^+$ = $[C_{11}H_{24}N]^+$ and $[DPP]^+$ = $[C_{11}H_{24}N]^+$) were synthesised following an established mild solution crystallisation method in aqueous solution from commercially available $Na(C_2N_3)$ (96 %, Sigma-Aldrich), $Ni(NO_3)_2{\cdot}6H_2O$ (98 %, Sigma-Aldrich) and ultrapure water.[1] In a typical crystallisation routine, 1 mL ultrapure water was placed in a glass vial, and the precursor solutions were layered on top in order of 0.5 mL of the respective aqueous [DIP]Br solution (0.2 M), 1.0 mL of an aqueous $Ni(NO_3)_2$ solution (0.4 M) and 0.3 mL of an aqueous sodium dicyanamide solution (2 M). After cooling in a refrigerator overnight, small, well-defined block single crystals with sizes between 2 and 4 mm were collected at ambient temperature, washed with ultrapure water, and dried (Fig. S6).

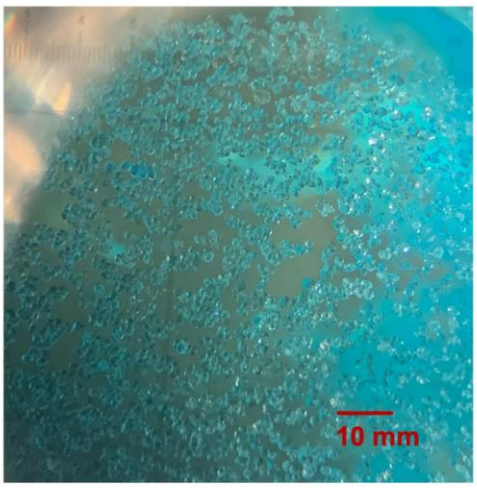


**Figure S6:** Microscopic image of the crystalline compound $[DIP]Ni(C_2N_3)_3$ showing small block-shaped blue crystals.

**Elemental analysis:**

The elemental analysis measurements and quantifications of the synthesised molecular perovskites $[A]Ni(C_2N_3)_3$ ($A^+$ = $[PEP]^+$ = $[C_{10}H_{22}N]^+$, $[DEP]^+$ = $[C_9H_{20}N]^+$, $[DIP]^+$ = $[C_{11}H_{24}N]^+$ and $[DPP]^+$ = $[C_{11}H_{24}N]^+$) were determined by the technical staff of the microanalytical laboratory at the Catalysis Research Center at the Technical University of Munich. The elemental composition (sample weight around 5 – 10 mg) was analysed using a *HEKAtech* Euro EA elemental analyser with flash combustion at 1800 °C and subsequent chromatographical separation and quantification with a thermal conductivity detector (TCD).

**$[DEP]Ni(C_2N_3)_3$:** calc. C 45.60 H 4.08 N 35.46 Ni 14.86, found C 45.63 H 4.09 N 35.02 Ni 14.71.

**$[PEP]Ni(C_2N_3)_3$:** calc. C 46.52 H 5.37 N 33.91 Ni 14.26, found C 46.23 H 5.32 N 33.23 Ni 14.20.

**$[DIP]Ni(C_2N_3)_3$:** calc. C 47.80 H 5.66 N 32.79 Ni 13.74, found C 46.82 H 5.51 N 32.41 Ni 13.42.

**$[DPP]Ni(C_2N_3)_3$:** calc. C 47.80 H 5.66 N 32.79 Ni 13.74, found C 47.56 H 5.48 N 32.73 Ni 13.89.

**Synthesis of $[PEP]_{1-x}[DPP]_xNi(C_2N_3)_3$ solid solutions:**

Similar to the described synthesis of the pure molecular perovskite compounds $[A]Ni(C_2N_3)_3$, the solid solutions were prepared *via* a mild solution route in aqueous solution using commercially available $Na(C_2N_3)$ (96 %, Sigma-Aldrich), $Ni(NO_3)_2{\cdot}6H_2O$ (98 %, Sigma-Aldrich) and ultrapure water. After adding 1 mL of ultrapure water to the bottom of a glass vial, a mixture of the A-site precursors [PEP]Br/[DPP]Br (0.5/0 mL, 0.4/0.1 mL, 0.25/0.25 mL, 0.15/0.35 mL, 0.05/0.45 mL and 0/0.5 mL) in varying ratios was added, followed by 1 mL of an aqueous $Ni(NO_3)_2$ solution (0.4 M) and 0.3 mL of an aqueous sodium dicyanamide solution (2 M). After cooling overnight, small single crystals were obtained, which were not suitable for SCXRD analysis.

## 2. Single crystal X-ray diffraction (SCXRD) data

The single crystal X-ray diffraction experiments of the molecular perovskites $[A]Ni(C_2N_3)_3$ ($A^+$ = $[DEP]^+$ = $[C_9H_{20}N]^+$, $[PEP]^+$ = $[C_{10}H_{22}N]^+$, $[DIP]^+$ = $[C_{11}H_{24}N]^+$ and $[DPP]^+$ = $[C_{11}H_{24}N]^+$) were performed using a *Bruker* APEX-II CCD diffractometer equipped with a fine focus tube with a Mo $K_a$ radiation source (λ = 0.71073 Å), a *Triumph* monochromator, a CMOS plate detector and an *Oxford Cryosystem* for temperature control. Suitable single crystals were selected and mounted onto a Kapton micro-sample loop in perfluorinated ether, fixed to the instrument goniometer and cooled to 100 K under a stream of cold nitrogen flow. A matrix scan for initial unit cell determination, data reduction and absorption correction (including odd and even ordered spherical harmonics was performed using SADABS[2]) was performed by using the APEX III software package.[3] Reflections were merged and corrected for Lorentz and polarisation effects, scan speed and background using SAINT.[4] The successful structure refinement and systematic absences were used as the basis for the respective space group assignments. The structure solution was performed by using SHELX[5,6] as integrated in Olex2.[7] Structures were solved by direct methods with the aid of successive difference Fourier maps and were refined against all data. The VESTA software package 3.4.0 was used to visualise the crystal structures (Fig. S7-S10).[8]

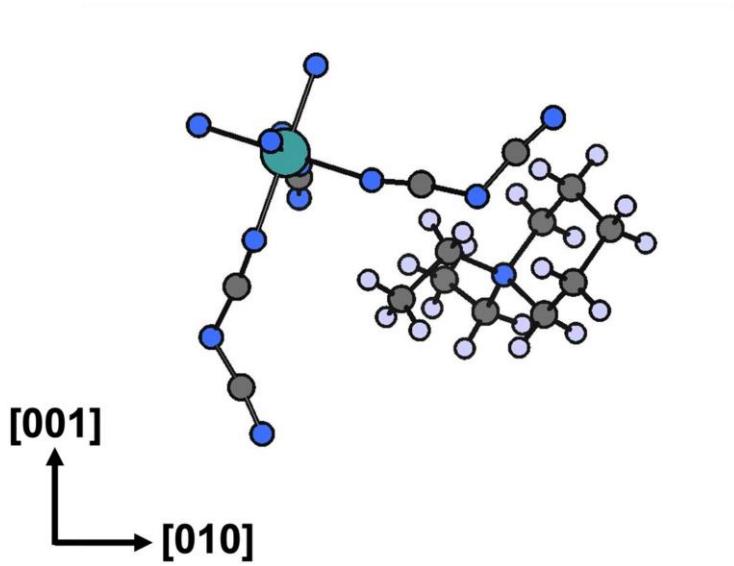


**Figure S7:** Structure of the asymmetric unit of [DEP]Ni($C_2N_3$)$_3$ when looking along the [100] axis with $(C_2N_3)^-$ ligands acting as bridges between the $Ni^{2+}$ cations while the $[DEP]^+$ cations occupy the void of the pseudo-cubic $ReO_3$ cavities. Colour code: Ni – green, N – blue, C – dark grey and H – light purple.

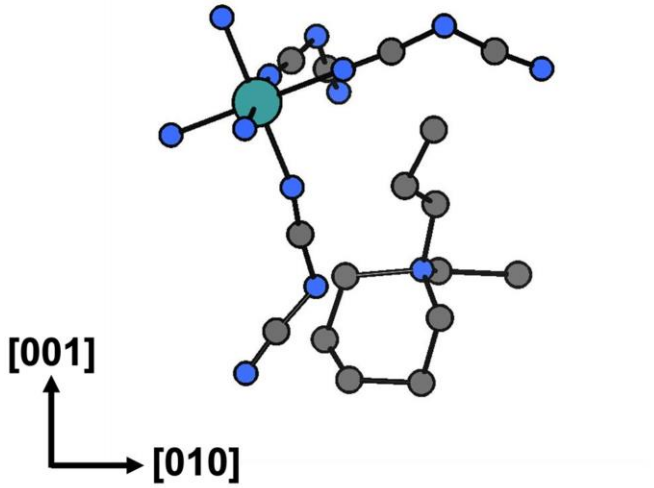


**Figure S8:** Structure of the asymmetric unit of [PEP]Ni($C_2N_3$)$_3$ when looking along the [100] axis with $(C_2N_3)^-$ ligands acting as bridges between the $Ni^{2+}$ cations while the $[PEP]^+$ cations occupy the void of the pseudo-cubic $ReO_3$ cavities. Colour code: Ni – green, N – blue, C – dark grey and H – atoms were neglected.

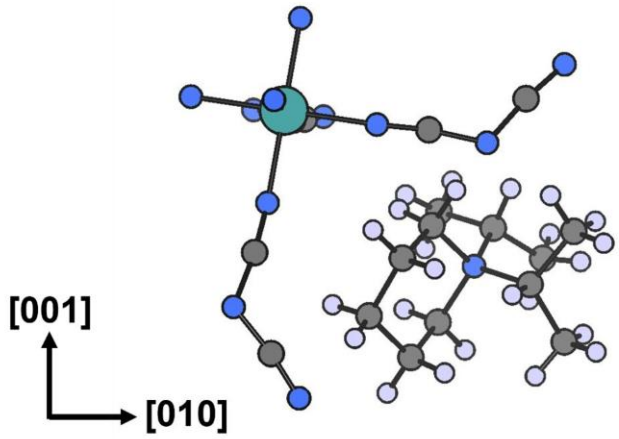


**Figure S9:** Structure of the asymmetric unit of [DIP]Ni($C_2N_3$)$_3$ when looking along the [100] axis with $(C_2N_3)^-$ ligands acting as bridges between the $Ni^{2+}$ cations while the $[DIP]^+$ cations occupy the void of the pseudo-cubic $ReO_3$ cavities, with the longer butyl group slightly extending into the neighbouring cavity. Colour code: Ni – green, N – blue, C – dark grey and H – light purple.

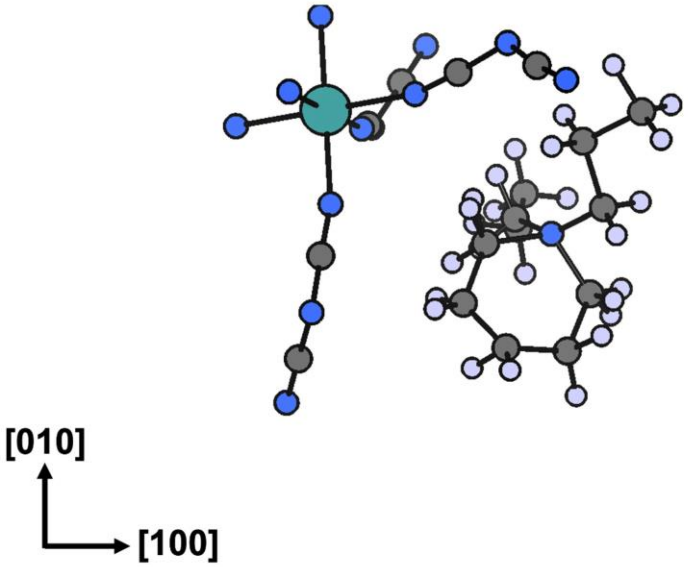


**Figure S10:** Structure of the asymmetric unit of [DPP]Ni($C_2N_3$)$_3$ when looking along the [001] axis with $(C_2N_3)^-$ ligands acting as bridges between the $Ni^{2+}$ cations while the $[DPP]^+$ cations occupy the void of the pseudo-cubic $ReO_3$ cavities, with the longer butyl group slightly extending into the neighbouring cavity. Colour code: Ni – green, N – blue, C – dark grey and H – light purple.

**Table S1:** Crystallographic data from SCXRD for the as-synthesised [DEP]Ni($C_2N_3$)$_3$ at 100 K.

| | |
|---|---|
| **Compound** | [DEP]Ni($C_2N_3$)$_3$ |
| **Chemical Formula** | $C_{15}H_{20}NiN_{10}$ |
| **Formula weight (g/mol)** | 399.12 |
| **Temperature (K)** | 100 |
| **Crystal system** | monoclinic |
| **Space group** | $P2_1/c$ |
| **a (Å)** | 16.3161(17) |
| **b (Å)** | 12.1389(13) |
| **c (Å)** | 10.1679(11) |
| **α (°)** | 90 |
| **β (°)** | 101.691(3) |
| **γ (°)** | 90 |
| **Volume (Å$^3$)** | 1972.1(4) |
| **Z** | 4 |
| **$\rho_{calc}$ (g/cm$^3$)** | 1.344 |
| **μ (mm$^{-1}$)** | 1.004 |
| **F (000)** | 832.0 |
| **Radiation** | Mo$K_\alpha$ (λ = 0.71073) |
| **2θ range for data collection (°)** | 2.65 to 26.47 |
| **Index ranges** | $-20 \le h \le 20$ |
| | $-15 \le k \le 15$ |
| | $-12 \le l \le 12$ |
| **Reflections collected** | 48266 |
| **Independent reflections** | 4029 [$R_{int}$ = 0.0267, $R_{sigma}$ = 0.0110] |
| **Data/restraints/parameters** | 4029/0/198 |
| **Goodness of fit on F$^2$** | 1.048 |
| **Final R indexes [I > 2σ (I)]** | $R_1$ = 0.0523, $wR_2$ = 0.1136 |
| **Final R indexes [all data]** | $R_1$ = 0.0555, $wR_2$ = 0.1159 |
| **Largest diff. peak/hole/ (Å$^{-3}$)** | 1.015/-0.709 |
| **Deposition number** | CCDC 2309035 |

**Table S2:** Crystallographic data from SCXRD for the as-synthesised [PEP]Ni($C_2N_3$)$_3$ at 100 K.

| | |
|---|---|
| **Compound** | [PEP]Ni($C_2N_3$)$_3$ |
| **Chemical Formula** | $C_{16}H_{22}NiN_{10}$ |
| **Formula weight (g/mol)** | 413.14 |
| **Temperature (K)** | 100 |
| **Crystal system** | monoclinic |
| **Space group** | $P2_1/c$ |
| **a (Å)** | 16.3743(14) |
| **b (Å)** | 11.9171(9) |
| **c (Å)** | 10.4761(8) |
| **α (°)** | 90 |
| **β (°)** | 105.903(4) |
| **γ (°)** | 90 |
| **Volume (Å$^3$)** | 1966.0(3) |
| **Z** | 4 |
| **$\rho_{calc}$ (g/cm$^3$)** | 1.396 |
| **μ (mm$^{-1}$)** | 1.010 |
| **F (000)** | 864.0 |
| **Radiation** | Mo$K_\alpha$ (λ = 0.71073) |
| **2θ range for data collection (°)** | 2.59 to 30.31 |
| **Index ranges** | $-22 \le h \le 23$ |
| | $-17 \le k \le 17$ |
| | $-14 \le l \le 15$ |
| **Reflections collected** | 32134 |
| **Independent reflections** | 6028 [$R_{int}$ = 0.0814, $R_{sigma}$ = 0.0650] |
| **Data/restraints/parameters** | 6028/0/239 |
| **Goodness of fit on F$^2$** | 1.054 |
| **Final R indexes [I > 2σ (I)]** | $R_1$ = 0.0685, $wR_2$ = 0.1592 |
| **Final R indexes [all data]** | $R_1$ = 0.1315, $wR_2$ = 0.1920 |
| **Largest diff. peak/hole/ (Å$^{-3}$)** | 1.096/-1.163 |
| **Deposition number** | CCDC 2309049 |

**Table S3:** Crystallographic data from SCXRD for the as-synthesised [DIP]Ni($C_2N_3$)$_3$ at 100 K.

| | |
|---|---|
| **Compound** | [DIP]Ni($C_2N_3$)$_3$ |
| **Chemical Formula** | $C_{17}H_{24}NiN_{10}$ |
| **Formula weight (g/mol)** | 427.15 |
| **Temperature (K)** | 100 |
| **Crystal system** | monoclinic |
| **Space group** | $P2_1/c$ |
| **a (Å)** | 16.1247(8) |
| **b (Å)** | 11.9812(5) |
| **c (Å)** | 10.8829(5) |
| **α (°)** | 90 |
| **β (°)** | 95.986(2) |
| **γ (°)** | 90 |
| **Volume (Å$^3$)** | 2091.04(17) |
| **Z** | 4 |
| **$\rho_{calc}$ (g/cm$^3$)** | 1.281 |
| **μ (mm$^{-1}$)** | 0.952 |
| **F (000)** | 896.0 |
| **Radiation** | Mo$K_\alpha$ (λ = 0.71073) |
| **2θ range for data collection (°)** | 2.122 to 28.312 |
| **Index ranges** | $-21 \le h \le 21$ |
| | $-15 \le k \le 15$ |
| | $-14 \le l \le 14$ |
| **Reflections collected** | 96894 |
| **Independent reflections** | 5203 [$R_{int}$ = 0.0211, $R_{sigma}$ = 0.0080] |
| **Data/restraints/parameters** | 5203/0/260 |
| **Goodness of fit on F$^2$** | 1.037 |
| **Final R indexes [I > 2σ (I)]** | $R_1$ = 0.0237, $wR_2$ = 0.0627 |
| **Final R indexes [all data]** | $R_1$ = 0.0258, $wR_2$ = 0.0644 |
| **Largest diff. peak/hole/ (Å$^{-3}$)** | 0.363/-0.247 |
| **Deposition number** | CCDC 2309038 |

**Table S4:** Crystallographic data from SCXRD for the as-synthesised [DPP]Ni($C_2N_3$)$_3$ at 100 K.

| | |
|---|---|
| **Compound** | [DPP]Ni($C_2N_3$)$_3$ |
| **Chemical Formula** | $C_{17}H_{24}NiN_{10}$ |
| **Formula weight (g/mol)** | 427.15 |
| **Temperature (K)** | 100 |
| **Crystal system** | monoclinic |
| **Space group** | *C2/c* |
| **a (Å)** | 17.1198(15) |
| **b (Å)** | 12.3344(10) |
| **c (Å)** | 10.2007(9) |
| **α (°)** | 90 |
| **β (°)** | 110.800(3) |
| **γ (°)** | 90 |
| **Volume (Å$^3$)** | 2013.6(3) |
| **Z** | 4 |
| **$\rho_{calc}$ (g/cm$^3$)** | 1.409 |
| **μ (mm$^{-1}$)** | 0.989 |
| **F (000)** | 896.0 |
| **Radiation** | MoK$_\alpha$ (λ = 0.71073) |
| **2θ range for data collection (°)** | 2.55 to 25.37 |
| **Index ranges** | $-20 \le h \le 20$ |
| | $-14 \le k \le 14$ |
| | $-12 \le l \le 12$ |
| **Reflections collected** | 22253 |
| **Independent reflections** | 1847 [$R_{int}$ = 0.0652, $R_{sigma}$ = 0.0257] |
| **Data/restraints/parameters** | 1847/0/153 |
| **Goodness of fit on F$^2$** | 1.074 |
| **Final R indexes [I > 2σ (I)]** | $R_1$ = 0.0473, $wR_2$ = 0.1184 |
| **Final R indexes [all data]** | $R_1$ = 0.0534, $wR_2$ = 0.1226 |
| **Largest diff. peak/hole/ (Å$^{-3}$)** | 0.875/-0.789 |
| **Deposition number** | CCDC 2309042 |

**Table S5:** Crystallographic data from SCXRD for the as-synthesised [DEP]Ni($C_2N_3$)$_3$ at 300 K.

| | |
|---|---|
| **Compound** | [DEP]Ni($C_2N_3$)$_3$ |
| **Chemical Formula** | $C_{15}H_{20}NiN_{10}$ |
| **Formula weight (g/mol)** | 399.12 |
| **Temperature (K)** | 300 |
| **Crystal system** | monoclinic |
| **Space group** | $P2_1/c$ |
| **a (Å)** | 16.3871(7) |
| **b (Å)** | 12.2076(5) |
| **c (Å)** | 10.2673(4) |
| **α (°)** | 90 |
| **β (°)** | 100.250(2) |
| **γ (°)** | 90 |
| **Volume (Å$^3$)** | 2021.16(14) |
| **Z** | 4 |
| **$\rho_{calc}$ (g/cm$^3$)** | 1.312 |
| **μ (mm$^{-1}$)** | 0.980 |
| **F (000)** | 832.0 |
| **Radiation** | Mo$K_\alpha$ (λ = 0.71073) |
| **2θ range for data collection (°)** | 2.092 to 31.032 |
| **Index ranges** | $-23 \le h \le 23$ |
| | $-17 \le k \le 17$ |
| | $-14 \le l \le 14$ |
| **Reflections collected** | 61583 |
| **Independent reflections** | 6371 [$R_{int}$ = 0.0957, $R_{sigma}$ = 0.0473] |
| **Data/restraints/parameters** | 6371/0/240 |
| **Goodness of fit on F$^2$** | 1.172 |
| **Final R indexes [I > 2σ (I)]** | $R_1$ = 0.0609, $wR_2$ = 0.1782 |
| **Final R indexes [all data]** | $R_1$ = 0.1254, $wR_2$ = 0.2452 |
| **Largest diff. peak/hole/ (Å$^{-3}$)** | 0.609/-0.593 |
| **Deposition number** | CCDC 2309036 |

**Table S6:** Crystallographic data from SCXRD for the as-synthesised [PEP]Ni($C_2N_3$)$_3$ at 300 K.

| | |
|---|---|
| **Compound** | [PEP]Ni($C_2N_3$)$_3$ |
| **Chemical Formula** | $C_{16}H_{22}NiN_{10}$ |
| **Formula weight (g/mol)** | 413.14 |
| **Temperature (K)** | 300 |
| **Crystal system** | monoclinic |
| **Space group** | $P2_1/c$ |
| **a (Å)** | 16.4756(7) |
| **b (Å)** | 11.9516(5) |
| **c (Å)** | 10.6587(4) |
| **α (°)** | 90 |
| **β (°)** | 104.9160(10) |
| **γ (°)** | 90 |
| **Volume (Å$^3$)** | 2028.08(14) |
| **Z** | 4 |
| **$\rho_{calc}$ (g/cm$^3$)** | 1.353 |
| **μ (mm$^{-1}$)** | 0.979 |
| **F (000)** | 864.0 |
| **Radiation** | Mo$K_\alpha$ (λ = 0.71073) |
| **2θ range for data collection (°)** | 2.56 to 24.09 |
| **Index ranges** | $-18 \le h \le 18$ |
| | $-13 \le k \le 13$ |
| | $-12 \le l \le 12$ |
| **Reflections collected** | 30600 |
| **Independent reflections** | 3184 [$R_{int}$ = 0.0737, $R_{sigma}$ = 0.0362] |
| **Data/restraints/parameters** | 3184/0/249 |
| **Goodness of fit on F$^2$** | 1.117 |
| **Final R indexes [I > 2σ (I)]** | $R_1$ = 0.0606, $wR_2$ = 0.1630 |
| **Final R indexes [all data]** | $R_1$ = 0.0943, $wR_2$ = 0.2082 |
| **Largest diff. peak/hole/ (Å$^{-3}$)** | 0.603/-0.481 |
| **Deposition number** | CCDC 2309050 |

**Table S7:** Crystallographic data from SCXRD for the as-synthesised [DIP]Ni($C_2N_3$)$_3$ at 300 K.

| | |
|---|---|
| **Compound** | [DIP]Ni($C_2N_3$)$_3$ |
| **Chemical Formula** | $C_{17}H_{24}NiN_{10}$ |
| **Formula weight (g/mol)** | 427.17 |
| **Temperature (K)** | 300 |
| **Crystal system** | monoclinic |
| **Space group** | $P2_1/c$ |
| **a (Å)** | 16.346(2) |
| **b (Å)** | 12.0065(16) |
| **c (Å)** | 11.0462(17) |
| **α (°)** | 90 |
| **β (°)** | 93.708(6) |
| **γ (°)** | 90 |
| **Volume (Å$^3$)** | 2163.4(5) |
| **Z** | 4 |
| **$\rho_{calc}$ (g/cm$^3$)** | 1.312 |
| **μ (mm$^{-1}$)** | 0.920 |
| **F (000)** | 896.0 |
| **Radiation** | Mo$K_\alpha$ (λ = 0.71073) |
| **2θ range for data collection (°)** | 2.50 to 26.25 |
| **Index ranges** | $-20 \le h \le 20$ |
| | $-15 \le k \le 15$ |
| | $-13 \le l \le 13$ |
| **Reflections collected** | 46500 |
| **Independent reflections** | 4227 [$R_{int}$ = 0.0445, $R_{sigma}$ = 0.0230] |
| **Data/restraints/parameters** | 4227/0/260 |
| **Goodness of fit on F$^2$** | 2.669 |
| **Final R indexes [I > 2σ (I)]** | $R_1$ = 0.1450, $wR_2$ = 0.5296 |
| **Final R indexes [all data]** | $R_1$ = 0.1558, $wR_2$ = 0.5445 |
| **Largest diff. peak/hole/ (Å$^{-3}$)** | 1.639/-0.765 |
| **Deposition number** | CCDC 2309039 |

**Table S8:** Crystallographic data from SCXRD for the as-synthesised [DPP]Ni($C_2N_3$)$_3$ at 300 K.

| | |
|---|---|
| **Compound** | [DPP]Ni($C_2N_3$)$_3$ |
| **Chemical Formula** | $C_{17}H_{24}NiN_{10}$ |
| **Formula weight (g/mol)** | 427.15 |
| **Temperature (K)** | 300 |
| **Crystal system** | monoclinic |
| **Space group** | C2/*c* |
| **a (Å)** | 17.3196(5) |
| **b (Å)** | 12.3357(3) |
| **c (Å)** | 10.4909(3) |
| **α (°)** | 90 |
| **β (°)** | 111.9170(10) |
| **γ (°)** | 90 |
| **Volume (Å$^3$)** | 2079.38(10) |
| **Z** | 4 |
| **$\rho_{calc}$ (g/cm$^3$)** | 1.365 |
| **μ (mm$^{-1}$)** | 0.957 |
| **F (000)** | 896.0 |
| **Radiation** | Mo$K_\alpha$ (λ = 0.71073) |
| **2θ range for data collection (°)** | 2.081 to 29.145 |
| **Index ranges** | $-23 \le h \le 23$ |
| | $-16 \le k \le 16$ |
| | $-14 \le l \le 14$ |
| **Reflections collected** | 52302 |
| **Independent reflections** | 2803 [$R_{int}$ = 0.0502, $R_{sigma}$ = 0.0194] |
| **Data/restraints/parameters** | 2803/0/131 |
| **Goodness of fit on F$^2$** | 1.180 |
| **Final R indexes [I > 2σ (I)]** | $R_1$ = 0.0592, $wR_2$ = 0.1756 |
| **Final R indexes [all data]** | $R_1$ = 0.0848, $wR_2$ = 0.2271 |
| **Largest diff. peak/hole/ (Å$^{-3}$)** | 0.736/-1.038 |
| **Deposition number** | CCDC 2309043 |

## 3. NMR spectroscopy of the precursor A-site cations

To confirm the chemical composition of the A-site precursor salts ([DEP]Br, [PEP]Br, [DIP]Br and [DPP]Br), we used a combination of $^{1}H$ and $^{13}C$ NMR measurements. All NMR spectra were recorded on a *Bruker* AVIII 400 US spectrometer at ambient temperature (298 K). Chemical shifts are expressed as parts per million ($\delta$/ ppm) and are corrected for the strongest residual solvent shift as an internal standard for $^{1}H$ NMR spectra. The following descriptions of signal multiplicity are used: *t* = triplet, *dt* = doublet of triplets, *p* = pentet, *q* = quartet and *m* = multiplet. NMR data are reported in the order of chemical shifts (multiplicity, coupling constant and integral). The coupling constants are absolute values and are expressed in Hertz (Hz).[9]

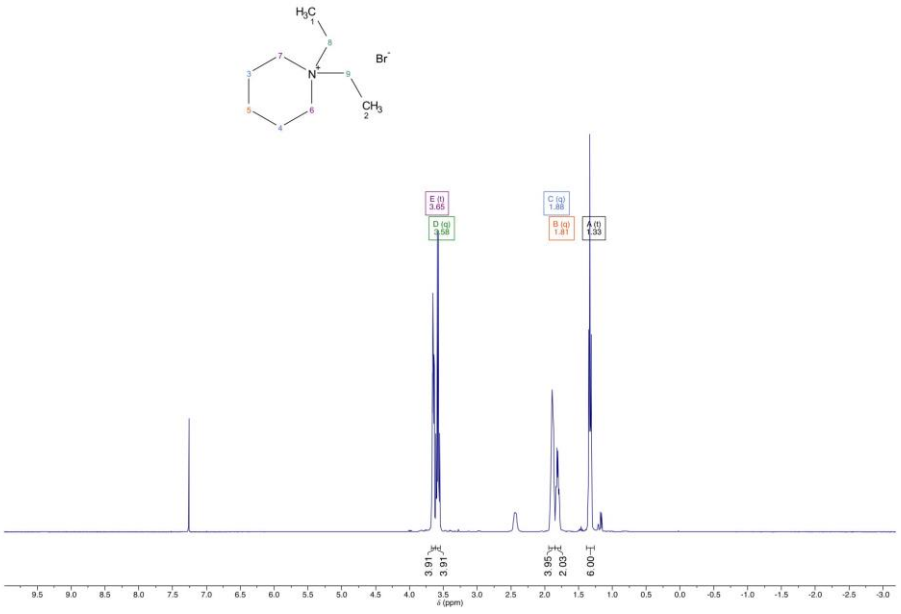


**Figure S11:** $^{1}H$ NMR spectrum of [DEP]Br in $CDCl_3$.

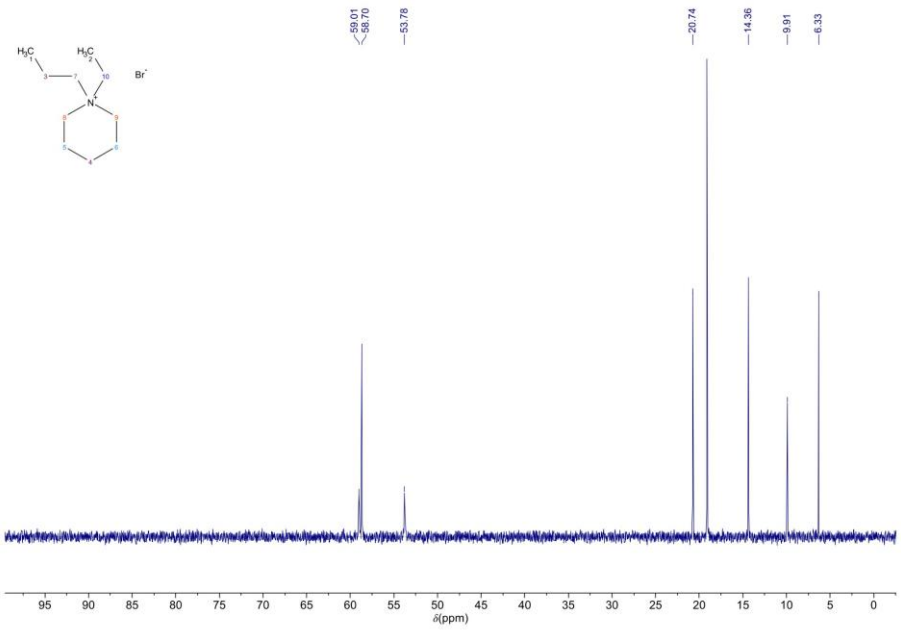


**Figure S14:** $^{13}C$ NMR spectrum of [PEP]Br in $D_2O$.

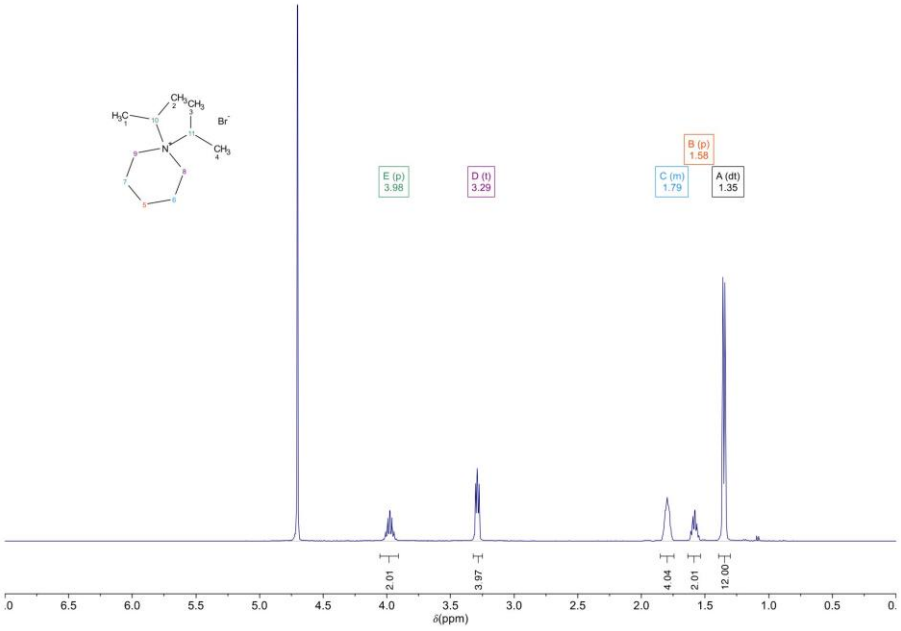


**Figure S15:** $^{1}H$ NMR spectrum of [DIP]Br in $D_2O$.

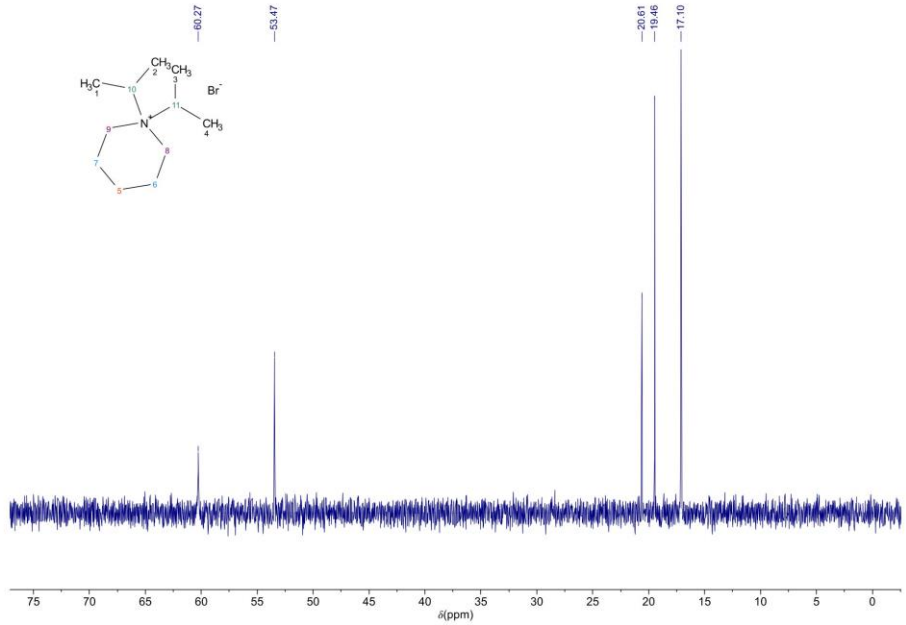


**Figure S16:** $^{13}C$ NMR spectrum of [DIP]Br in $D_2O$.

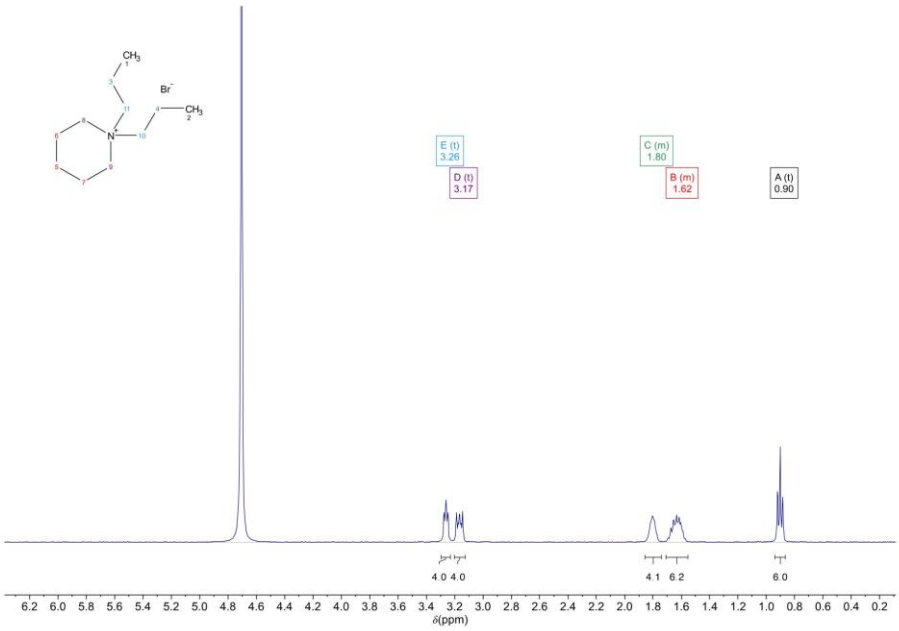


**Figure S17:** $^{1}H$ NMR spectrum of [DPP]Br in $D_2O$.

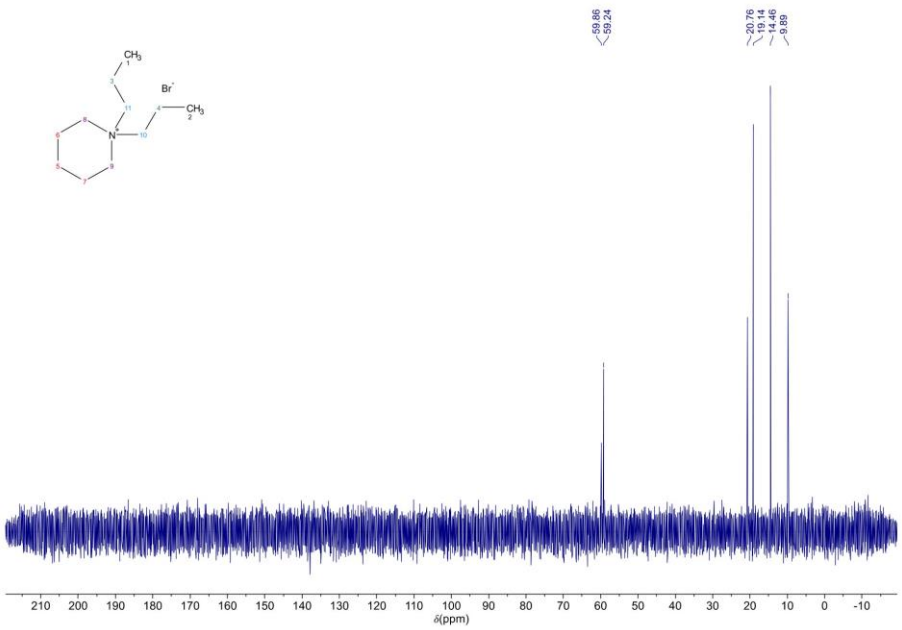


**Figure S18:** $^{13}C$ NMR spectrum of [DPP]Br in $D_2O$.

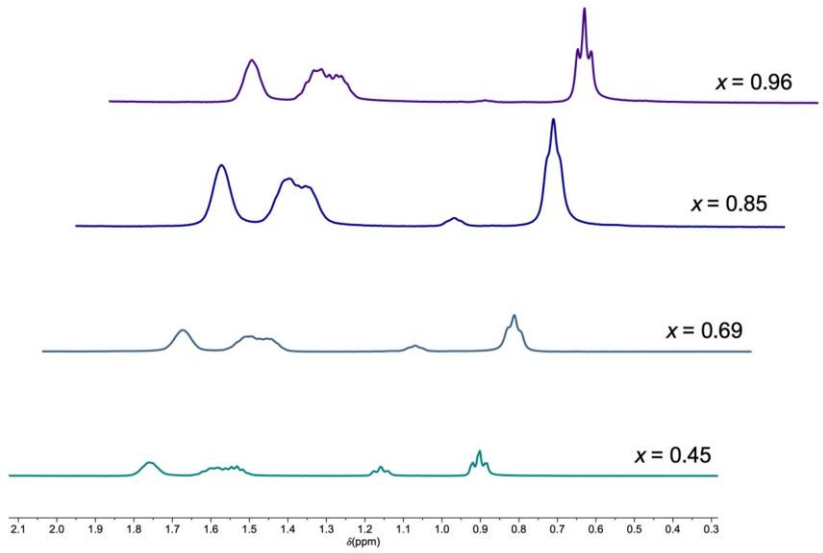


**Figure S19:** Stacked $^1H$ NMR spectra of the solid solutions $[PEP]_{1-x}[DPP^-]_xNi(C_2N_3)_3$ with $x$ = 0.45, 0.69, 0.85 and 0.96 in $D_2O$ including the chemical shift range (0.8 – 1.3 ppm) used for determination of $x$.

We performed $^1$H NMR spectroscopy to calculate the composition of the A-site cations present in the solid solutions $[PEP]_{1-x}[DPP^-]_xNi(C_2N_3)_3$ (Table S9). The terminal carbon atoms of the propyl groups of $[PEP]^+$ and $[DPP]^+$ are both visible in the spectra as a triplet at around 0.9 ppm. The terminal carbon atom of the ethyl group of $[PEP]^+$ is also visible as a triplet, but at a much higher chemical shift, around 1.2 ppm. The triplet resulting from the terminal carbon of ethyl and propyl groups of the $[PEP]^+$ should hypothetically have the same integral size. Consequently, the size of the ethyl integral was subtracted from the propyl integral to calculate *x*, resulting in a value that is directly related only to the $[DPP]^+$ propyl groups. Compared to other possible analytical methods, we used NMR spectroscopy to avoid contamination by residual X- or M-site precursor salts.

**Table S9:** Overview of determined composition *via* $^1$H NMR spectroscopy and the used stoichiometry during mild solution synthesis in the ratio of [PEP]Br/[DPP]Br.

| ***x* in $[PEP]_{1-x}[DPP^-]_xNi(C_2N_3)$** | ***x* ($^1$H NMR)** | ***x* (Synthesis)** |
|---|---|---|
| | 0.45 | 0.2 |
| | 0.69 | 0.5 |
| | 0.85 | 0.7 |
| | 0.96 | 0.9 |

## 4. Thermogravimetric analysis and differential scanning calorimetry (TGA-DSC)

Thermal analysis (TGA-DSC experiments) of the molecular perovskites $[A]Ni(C_2N_3)_3$ ($A^+$ = $[DEP]^+$ = $[C_9H_{20}N]^+$, $[PEP]^+$ = $[C_{10}H_{22}N]^+$, $[DIP]^+$ = $[C_{11}H_{24}N]^+$ and $[DPP]^+$ = $[C_{11}H_{24}N]^+$) was performed on a *Netzsch* STA449F5 Jupiter TGA-DSC device using aluminium oxide pans with a lid (70 µL) under flowing argon (20 mL $min^{-1}$). The temperature calibration of the oven cell was carried out based on the melting points of metals (In, Sn, Bi, Zn, Al, Au and Ag). The baseline was corrected by screening an empty sample pan with the respective temperature program from room temperature to 1073.15 K using a heating rate of 10 K $min^{-1}$. The respective sample masses ($m_0$) are given below in the captions (Fig. S20-S23). The onset of significant thermal decomposition ($T_d$) was determined by extrapolating the linear range of the relative mass loss observed with a heating rate of 10 K $min^{-1}$. We observe the following decomposition temperatures: $T_d$ of $[DEP]Ni(C_2N_3)_3$ = 595.15 K, $T_d$ of $[PEP]Ni(C_2N_3)_3$ = 598.35 K, $T_d$ of $[DIP]Ni(C_2N_3)_3$ = 568.95 K and $T_d$ of $[DPP]Ni(C_2N_3)_3$ = 598.05 K.

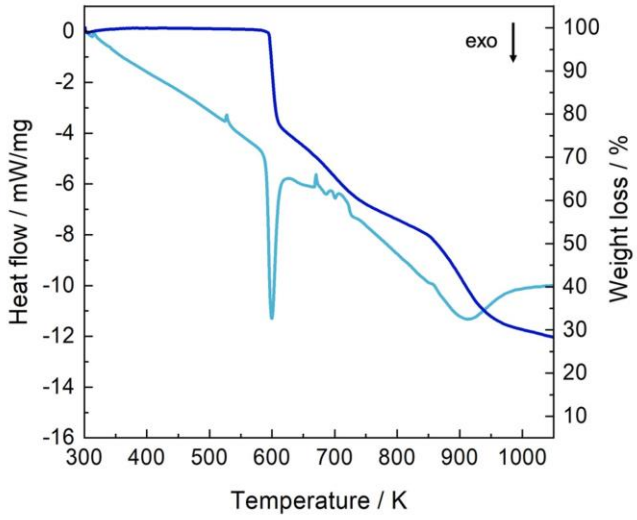


**Figure S20:** TGA-DSC of $[DEP]Ni(C_2N_3)_3$ with a sample mass of 5.0842 mg from room temperature to 1073.15 K with a heating rate of 10 K $min^{-1}$. TGA curve is shown in dark blue, indicating the thermal stability under constant argon flow before thermal decomposition, and the corresponding DSC curve is highlighted in light blue.

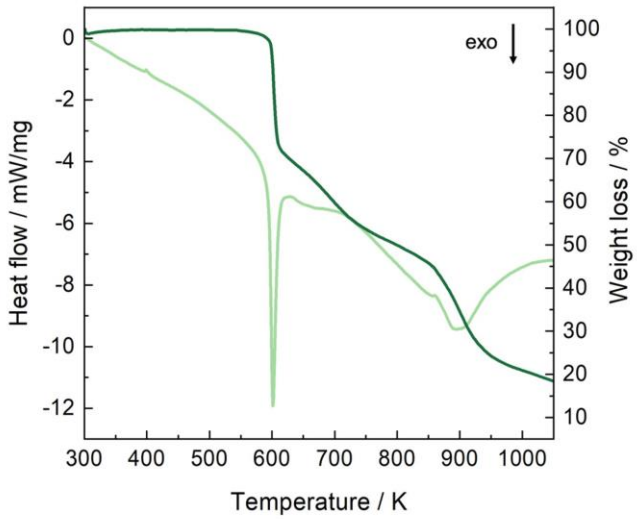


**Figure S21:** TGA-DSC of [PEP]Ni($C_2N_3$)$_3$ with a sample mass of 5.608 mg from room temperature to 1073.15 K with a heating rate of 10 K min$^{-1}$. TGA curve is shown in dark green, indicating the thermal stability under constant argon flow before thermal decomposition, and the corresponding DSC curve is highlighted in light green.

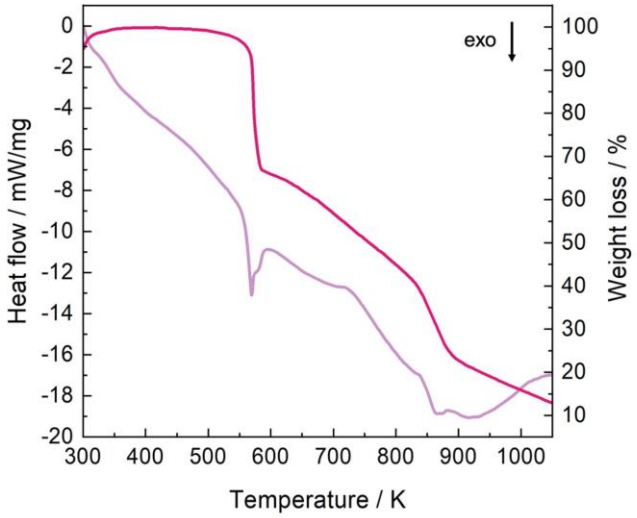


**Figure S22:** TGA-DSC of [DIP]Ni($C_2N_3$)$_3$ with a sample mass of 3.1921 mg from room temperature to 1073.15 K with a heating rate of 10 K min$^{-1}$. TGA curve is shown in dark pink, indicating the thermal stability under constant argon flow before thermal decomposition, and the corresponding DSC curve is highlighted in light pink.

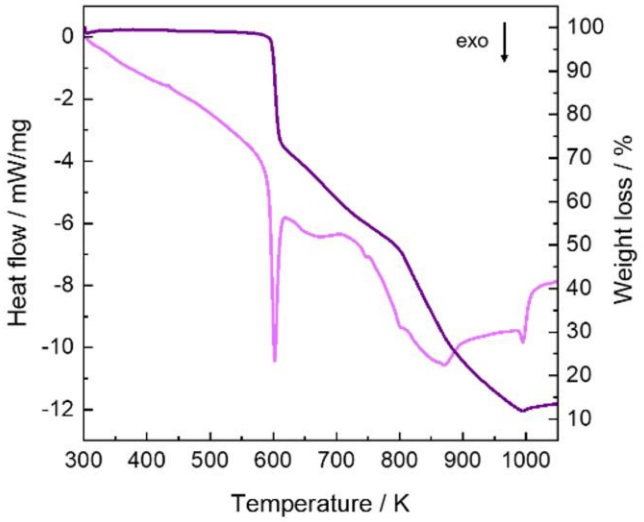


**Figure S23:** TGA-DSC of [DPP]Ni($C_2N_3$)$_3$ with a sample mass of 6.238 mg from room temperature to 1073.15 K with a heating rate of 10 K min$^{-1}$. TGA curve is shown in dark purple, indicating the thermal stability under constant argon flow before thermal decomposition, and the corresponding DSC curve is highlighted in light purple.

## 5. Differential scanning calorimetry

DSC experiments of powder samples [A]Ni($C_2N_3$)$_3$ (with $A^+$ = $[DEP]^+$ = $[C_9H_{20}N]^+$, $[PEP]^+$ = $[C_{10}H_{22}N]^+$, $[DIP]^+$ = $[C_{11}H_{24}N]^+$ and $[DPP]^+$ = $[C_{11}H_{24}N]^+$) were performed in a DSC (*TA Instruments* Q2000) under a constant He purging gas flow (25 mL min$^{-1}$) and a heating rate of 20 K min$^{-1}$ in the temperature range between 173 and 423 K by using liquid nitrogen for cooling.

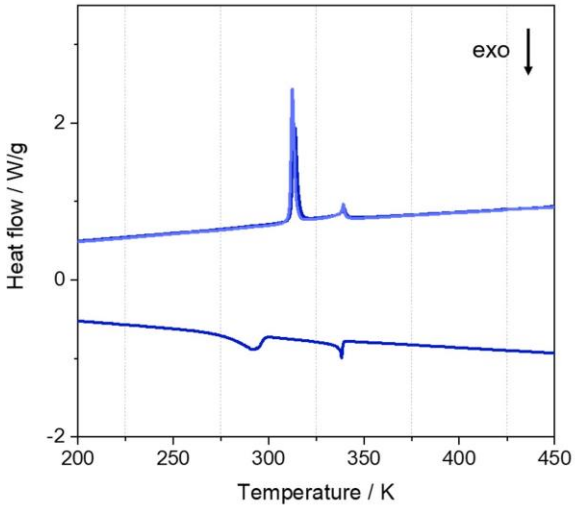


**Figure S24:** Reversible DSC measurement of [DEP]Ni($C_2N_3$)$_3$ with an initial heating run and subsequent cooling shown as dark blue line and the re-heating run in light blue.

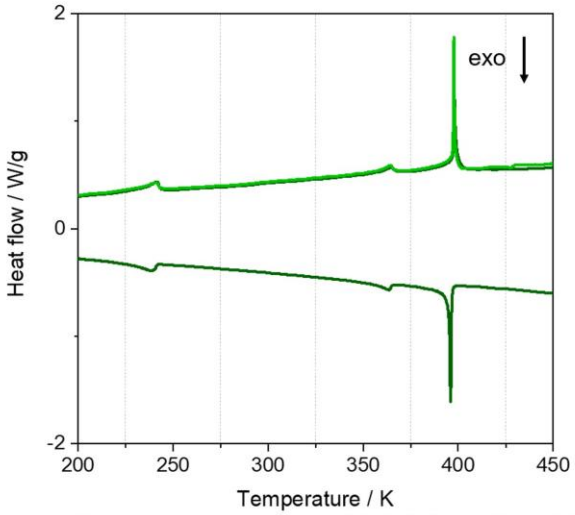


**Figure S25:** Reversible DSC measurement of [PEP]Ni($C_2N_3$)$_3$ with an initial heating run and subsequent cooling shown as dark green line and the re-heating run in light green.

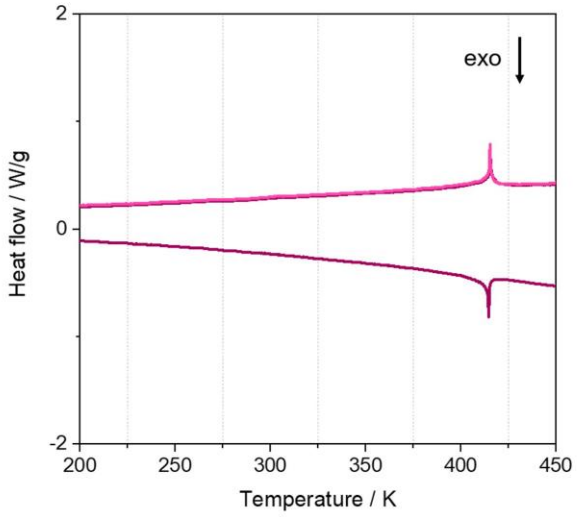


**Figure S26:** Reversible DSC measurement of [DIP]Ni($C_2N_3$)$_3$ with an initial heating run and subsequent cooling shown as dark pink line and the re-heating run in light pink.

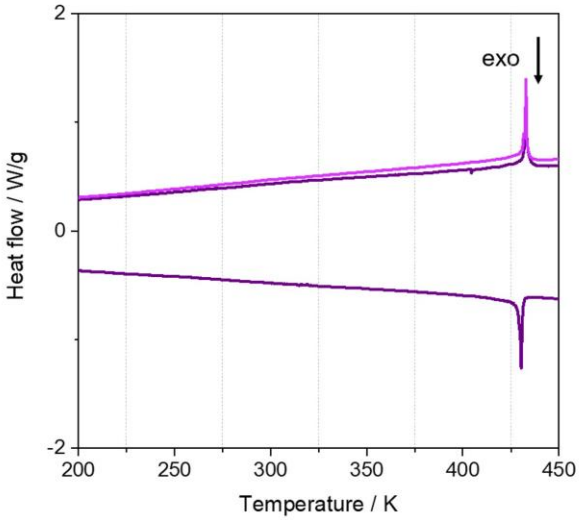


**Figure S27:** Reversible DSC measurement of [DPP]Ni($C_2N_3$)$_3$ with an initial heating run and subsequent cooling shown as dark purple line and the re-heating run in light purple.

## 6. Powder X-ray diffraction (PXRD) data

Laboratory PXRD measurements of the molecular perovskites $[A]Ni(C_2N_3)_3$ (with $A^+$ = $[DEP]^+$ = $[C_9H_{20}N]^+$, $[PEP]^+$ = $[C_{10}H_{22}N]^+$, $[DIP]^+$ = $[C_{11}H_{24}N]^+$ and $[DPP]^+$ = $[C_{11}H_{24}N]^+$) were performed at ambient temperature using *Debye-Scherrer* geometry with borosilicate glass capillaries (0.8 mm diameter) in a *STOE* Stadi P diffractometer with a *DECTRIS* MYTHEN 1K / *DECTRIS* Multi-MYTHEN detector, a curved Ge(111) monochromator and a Mo $K_\alpha$ source ($\lambda$ = 0.70926 Å). The measurement range was from 2° to 36.56° (2θ) with a step size of 0.015° (2θ). To verify the phase purity of the samples, we carried out a Pawley profile fit analysis of all PXRD patterns by using the TOPAS v6 software.[10] Standard deviations of all parameters were calculated, and "randomize_on_errors" was used to ensure that the refinement minimum was achieved.

Laboratory PXRD measurements of the series of solid solutions $[PEP]_{1-x}[DPP]_xNi(C_2N_3)_3$ with $x$ = 0, 0.45, 0.69, 0.85, 0.96 and 1, and a 1:1 mixture of $[PEP]Ni(C_2N_3)_3$ and $[DPP]Ni(C_2N_3)_3$ were collected at ambient temperature on a silicon wafer using *Bragg-Brentano* geometry in a *Rigaku* MiniFlex 600-C diffractometer with X-ray Cu $K_\alpha$ radiation ($\lambda_1$ - 1.5406 Å, $\lambda_2$ - 1.5444 Å, $I_2/I_1$ - 0.5, $K_\beta$ radiation was removed by a Ni-filter). The measurement range, unless stated otherwise, was from 2.0° to 50.0° (2θ) with a step size of 0.010° and a scan rate of 5° per min.

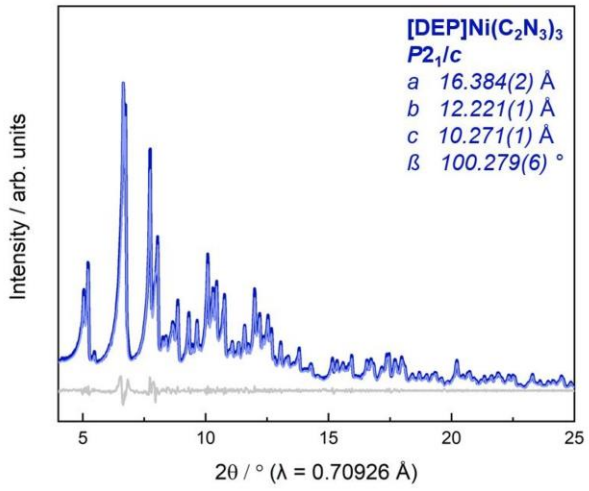


**Figure S28:** Powder X-ray diffraction data of $[DEP]Ni(C_2N_3)_3$ (dark blue) compared to the calculated data from Pawley profile fit analysis (light blue), with $R_{wp}$ = 2.334, $R_{exp}$ = 0.924 and GOF = 2.524. The grey difference curve (Pawley profile fit – experimental data) indicates phase purity.

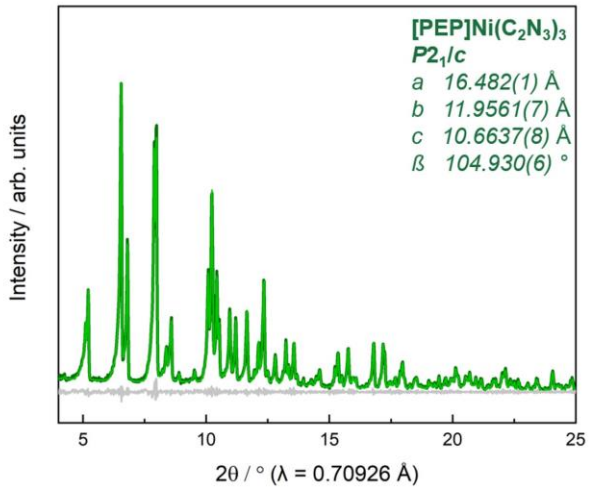


**Figure S29:** Powder X-ray diffraction data of [PEP]Ni($C_2N_3$)$_3$ (dark green) compared to the calculated data from Pawley profile fit analysis (light green), with $R_{wp}$ = 3.555, $R_{exp}$ = 3.244 and GOF = 1.095. The grey difference curve (Pawley profile fit – experimental data) indicates phase purity.

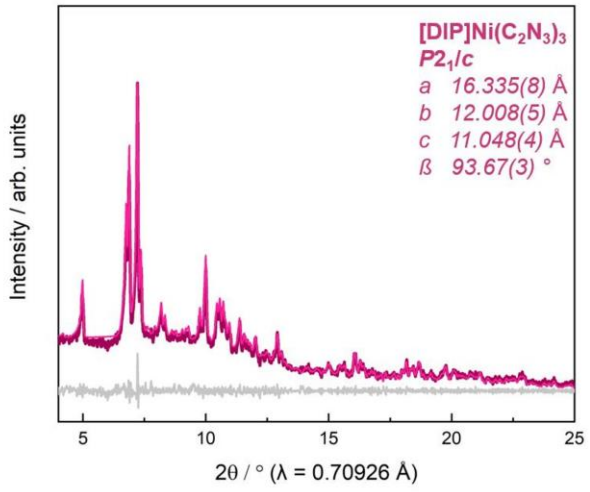


**Figure S30:** Powder X-ray diffraction data of [DIP]Ni($C_2N_3$)$_3$ (dark pink) compared to the calculated data from Pawley profile fit analysis (light pink), with $R_{wp}$ = 4.759, $R_{exp}$ = 3.959 and GOF = 1.202. The grey difference curve (Pawley profile fit – experimental data) indicates phase purity.

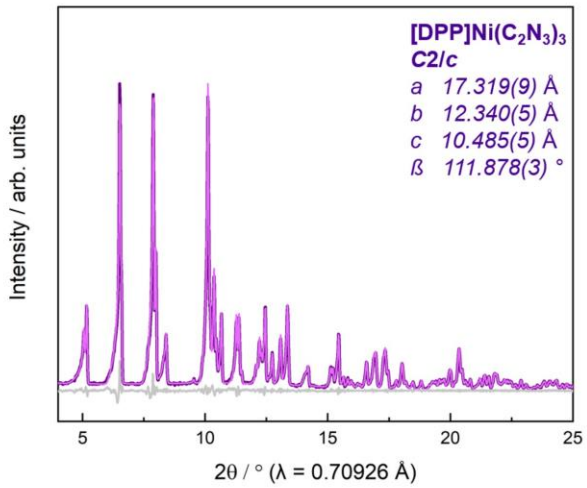


**Figure S31:** Powder X-ray diffraction data of $[DPP]Ni(C_2N_3)_3$ (dark purple) compared to the calculated data from Pawley profile fit analysis (light purple), with $R_{wp}$ = 3.635, $R_{exp}$ = 2.450 and GOF = 1.483. The grey difference curve (Pawley profile fit – experimental data) indicates phase purity.

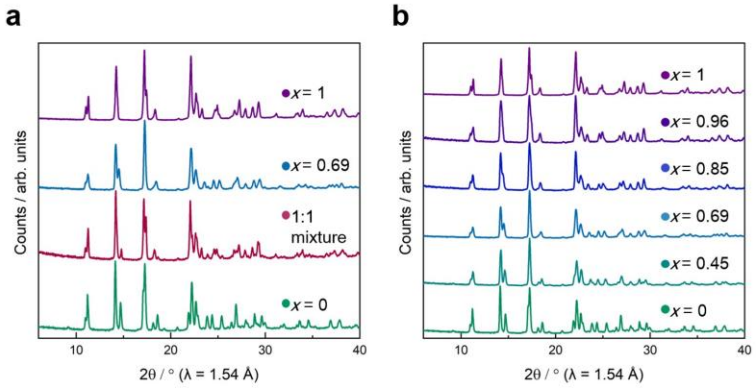


**Figure S32:** Collections of PXRD patterns of the pure perovskites $[PEP]Ni(C_2N_3)_3$, $[DPP]Ni(C_2N_3)_3$ and a 1:1 mixture compared to $[PEP]_{1-x}[DPP]_xNi(C_2N_3)_3$ (with $x$ = 0.69) (a) and stacked PXRD patterns of the solid solution series (b).

## 7. High-pressure powder X-ray diffraction (HPXRD)

High-pressure powder X-ray diffraction (HPPXRD) data was collected at beamline I15 (within beamtime CY30815-2) at the Diamond Light Source (UK) using a fixed operating photon energy of 29.2 keV ($\lambda$ = 0.4246 Å), equipped with a *Pilatus3 X CdTe 2M* area detector. Single crystals of the studied samples were ground to a fine powder and filled with Silicone oil AP100 as pressure transmitting medium into a plastic capillary (Makrolon, inside diameter 1.8 mm) and sealed with Araldyte-2014-1 by heating up to 60 °C for 20 min. Please note that Silicone oil AP100 has been previously applied in hydrostatic pressure experiments and is known to maintain hydrostatic conditions up to pressures of 0.9 GPa. We used an automated high-pressure setup with hydrostatic conditions, as described in detail in the literature.[11,12] To further validate the performance of the high-pressure setup, Nickel dimethylglyoxime ($Ni(dmgH)_2$) was used as a standard, see Chapter 10 of this supporting information. The samples were loaded into a chamber filled with water to transmit the pressure, and a hydraulic gauge pump was used to apply and release pressure. We collected HPPXRD data for all three samples through two diamond windows in the metal block (sample chamber) along beam direction in the range of $p$ = ambient – 0.4 GPa in small $p$ steps (0.02 GPa) with an estimated standard deviation of p = ± 0.003 GPa.

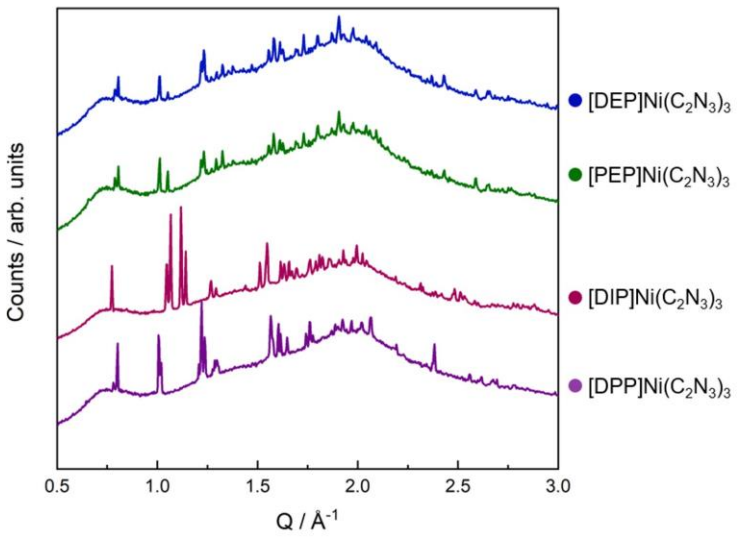


**Figure S33:** Collection of the normalised PXRD patterns recorded at ambient pressure of all studied $[A]Ni(C_2N_3)_3$ molecular perovskites.

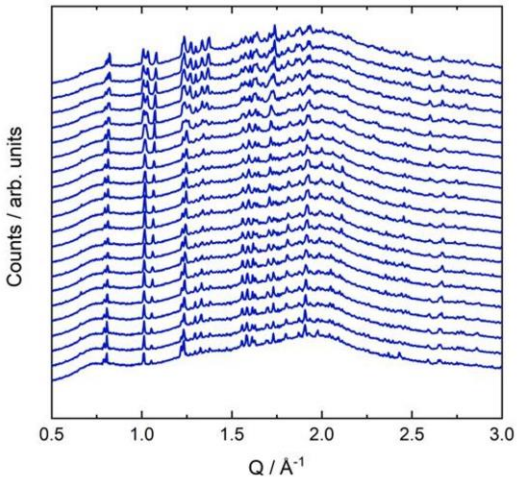


**Figure S34:** HPPXRD patterns for [DEP]Ni($C_2N_3$)$_3$ collected between the pressure range from ambient to 0.4 GPa.

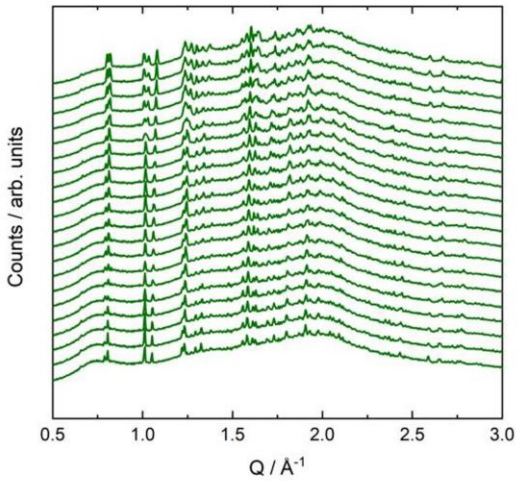


**Figure S35:** HPPXRD patterns for [PEP]Ni($C_2N_3$)$_3$ (within the solid solution solution [PEP]$_{1-x}$[DPP$^+$]$_x$Ni($C_2N_3$)$_3$, $x$ = 0) collected between the pressure range from ambient to 0.4 GPa.

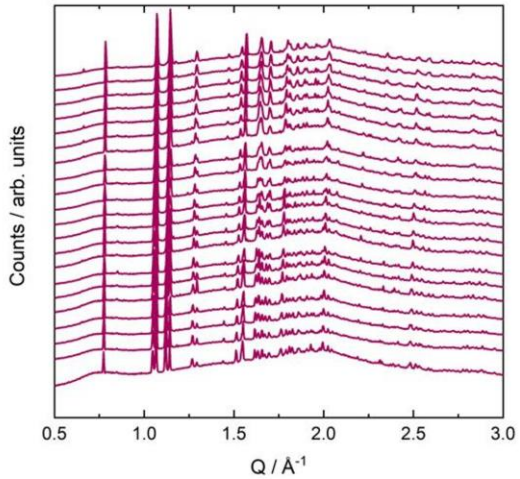


**Figure S36:** HPPXRD patterns for [DIP]Ni($C_2N_3$)$_3$ collected between the pressure range from ambient to 0.4 GPa.

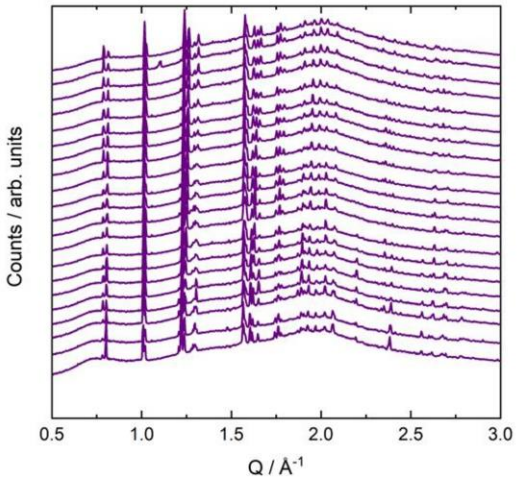


**Figure S37:** HPPXRD patterns for [DPP]Ni($C_2N_3$)$_3$ (within the solid solution [PEP]$_{1-x}$[DPP']$_x$Ni($C_2N_3$)$_3$, $x$ = 1) collected between the pressure range from ambient to 0.4 GPa.

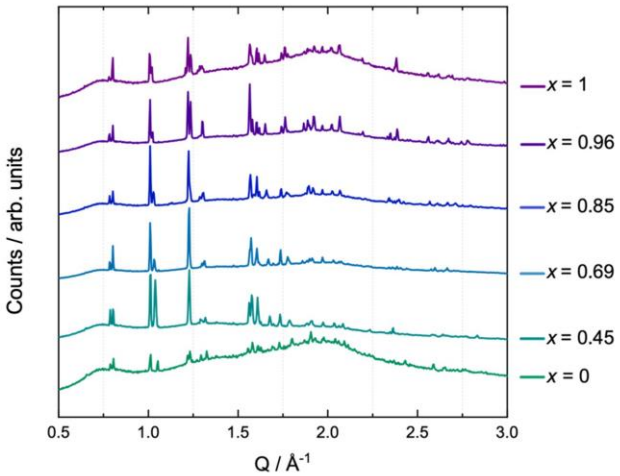


**Figure S38:** Collection of normalised PXRD patterns recorded at ambient pressure of the series of solid solutions $[PEP]_{1-x}[DPP]_xNi(C_2N_3)_3$ with $x$ = 0, 0.45, 0.69, 0.85, 0.96 and 1.

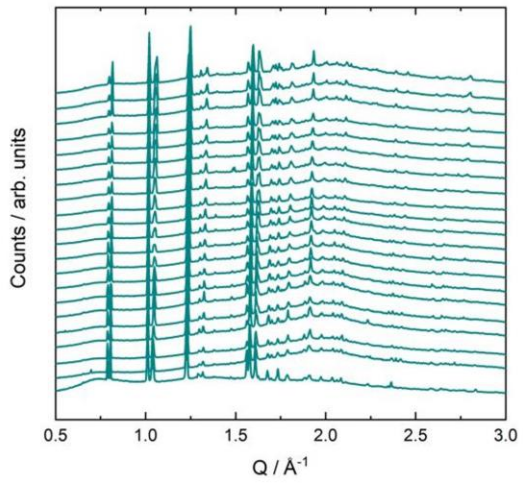


**Figure S39:** HPPXRD patterns for the solid solution $[PEP]_{1-x}[DPP]_xNi(C_2N_3)_3$ (with $x$ = 0.45) collected between the pressure range from ambient to 0.4 GPa.

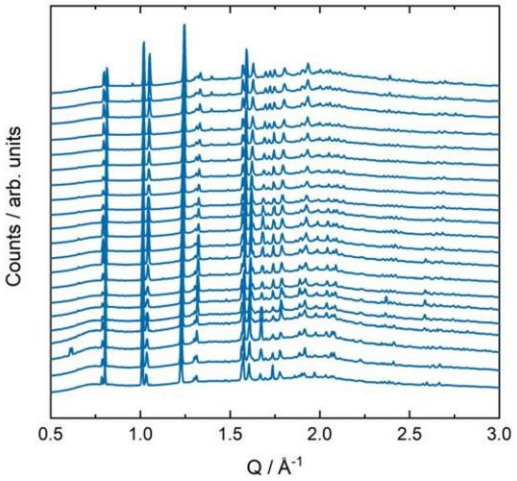


**Figure S40:** HPPXRD patterns for the solid solution $[PEP]_{1-x}[DPP]_xNi(C_2N_3)_3$ (with $x = 0.69$) collected between the pressure range from ambient to 0.4 GPa.

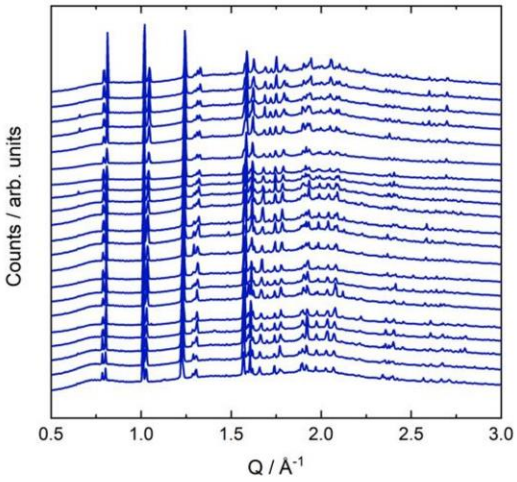


**Figure S41:** HPPXRD patterns for the solid solution $[PEP]_{1-x}[DPP]_xNi(C_2N_3)_3$ (with $x = 0.85$) collected between the pressure range from ambient to 0.4 GPa.

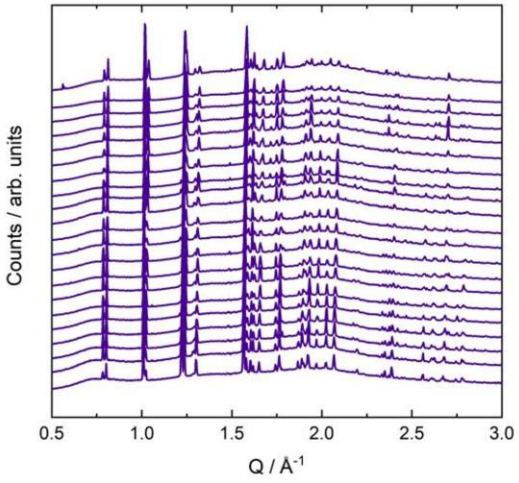


**Figure S42:** HPPXRD patterns for the solid solution $[PEP]_{1-x}[DPP]_xNi(C_2N_3)_3$ (with $x = 0.96$) collected between the pressure range from ambient to 0.4 GPa.

## 8. HPPXRD analysis

The collected HPPXRD detector images were calibrated and integrated using DAWN.[13] Subsequent analysis, *i.e.* Pawley refinements[14] on the HPPXRD data, was performed by sequential refinement of the multipattern datasets of each sample using TOPAS *v6*.[10] Representative Pawley profile fits of the ambient pressure PXRD data show a good fit to the monoclinic space groups as determined by SCXRD experiments at 300 K. We obtained pressure dependent cell parameters with standard deviations and full-width at half maximum (fwhm) using "pv_fwhm" of the average of peak profiles in the Pawley refinement of the diffraction data up to 0.28 GPa for [DIP]Ni($C_2N_3$)$_3$, 0.26 GPa for [PEP]Ni($C_2N_3$)$_3$ and 0.28 GPa for [DIP]Ni($C_2N_3$)$_3$ a pressure-induced phase transition ($p_{trs.}$) is observed and up to 0.4 GPa for [DPP]Ni($C_2N_3$)$_3$.

**Table S10:** Structural parameters (refined lattice parameter *a*, *b*, *c*, ß, volume *V* and space group *S.G.*) for all studied [A]Ni($C_2N_3$)$_3$ molecular perovskites obtained from Pawley refinement of the ambient pressure PXRD data.

| [A]Ni($C_2N_3$)$_3$ | [DIP]$^+$ | [PEP]$^+$ | [DEP]$^+$ | [DPP]$^+$ |
|---|---|---|---|---|
| S.G. | *P2$_1$/c* | *P2$_1$/c* | *P2$_1$/c* | *C2/c* |
| *a* / Å | 16.337(1) | 16.485(2) | 16.465(2) | 17.309(2) |
| *b* / Å | 12.005(8) | 11.949(1) | 11.950(2) | 12.330(1) |
| *c* / Å | 11.031(7) | 10.665(1) | 10.663(1) | 10.479(1) |
| ß / ° | 93.729(7) | 104.973(8) | 104.961(9) | 111.790(9) |
| *V* / Å$^3$ | 2159.1(3) | 2029.7(4) | 2027.2(5) | 2076.9(4) |

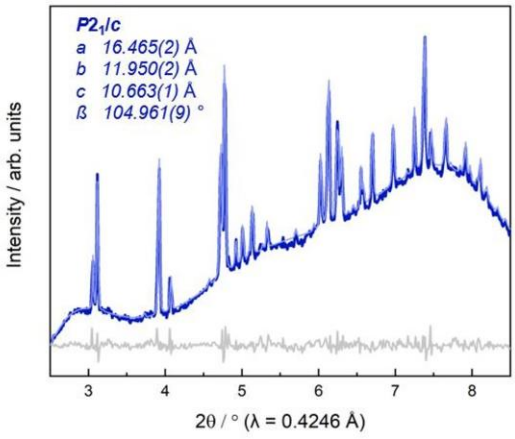


**Figure S43:** Pawley fit to synchrotron PXRD data at ambient pressure for [DEP]Ni($C_2N_3$)$_3$. Experimental data is shown as dark blue line, Pawley fit as light blue line, and the difference curve (fit – data) as grey line.

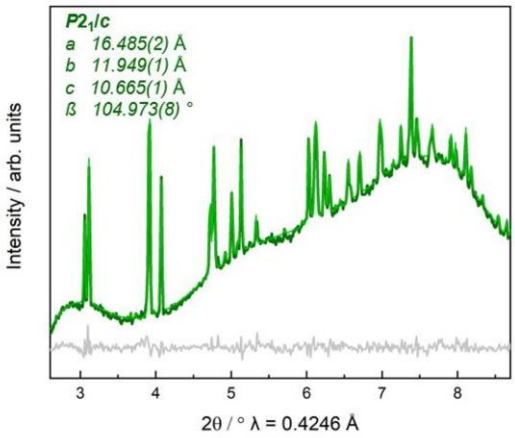


**Figure S44:** Pawley fit to synchrotron PXRD data at ambient pressure for [PEP]Ni($C_2N_3$)$_3$. Experimental data is shown as dark green line, Pawley fit as light green line, and the difference curve (fit – data) as grey line.

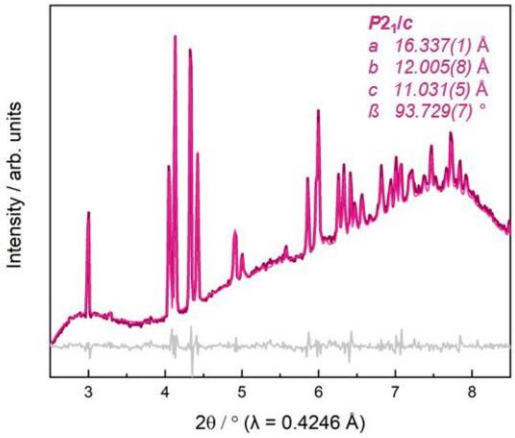


**Figure S45:** Pawley fit to synchrotron PXRD data at ambient pressure for [DIP]Ni($C_2N_3$)$_3$. Experimental data is shown as dark pink line, Pawley fit as light pink line, and the difference curve (fit – data) as grey line.

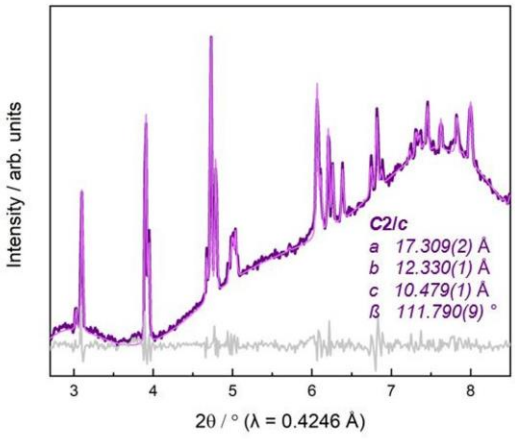


**Figure S46:** Pawley fit to synchrotron PXRD data at ambient pressure for [PEP]$_{1-x}$[DPP']$_x$Ni($C_2N_3$)$_3$ (with $x$ = 1). Experimental data is shown as dark purple line, Pawley fit as light purple line, and the difference curve (fit – data) as grey line.

**Table S11:** Overview of the unit cell parameters and volumes of [DEP]Ni($C_2N_3$)$_3$ obtained from Pawley fits of the HPPXRD data up to 0.28 GPa.

| *p* / GPa | $R_{wp}$ | *a* / Å | *b* / Å | *c* / Å | ß / ° | *V* / Å$^3$ |
|---|---|---|---|---|---|---|
| ambient | 1.66366 | 16.466(2) | 11.952(2) | 10.663(1) | 104.964(9) | 2027.4(5) |
| 0.0194 | 2.22259 | 16.456(3) | 11.921(3) | 10.659(3) | 104.88(2) | 2020.9(8) |
| 0.0398 | 1.46792 | 16.451(2) | 11.909(2) | 10.653(1) | 105.054(8) | 2015.6(4) |
| 0.0598 | 1.60712 | 16.442(2) | 11.906(2) | 10.648(1) | 105.067(8) | 2012.9(4) |
| 0.0794 | 1.75472 | 16.436(2) | 11.893(2) | 10.646(2) | 105.105(9) | 2009.3(5) |
| 0.0995 | 1.80946 | 16.428(3) | 11.871(2) | 10.636(2) | 105.19(1) | 2001.8(6) |
| 0.1199 | 1.69991 | 16.414(2) | 11.866(2) | 10.632(2) | 105.208(8) | 1998.2(6) |
| 0.1399 | 1.62644 | 16.412(2) | 11.846(2) | 10.632(2) | 105.20(1) | 1994.8(6) |
| 0.1594 | 1.59567 | 16.406(3) | 11.829(2) | 10.629(2) | 105.25(1) | 1990.3(6) |
| 0.1794 | 1.53563 | 16.387(2) | 11.822(2) | 10.623(2) | 105.316(8) | 1984.9(6) |
| 0.1996 | 1.77553 | 16.381(2) | 11.814(2) | 10.617(2) | 105.35(1) | 1981.4(6) |
| 0.2196 | 1.62587 | 16.378(2) | 11.799(2) | 10.624(2) | 105.38(1) | 1979.5(6) |
| 0.2397 | 1.69393 | 16.375(2) | 11.778(2) | 10.617(2) | 105.34(1) | 1974.6(6) |
| 0.2597 | 1.58818 | 16.357(3) | 11.771(2) | 10.623(2) | 105.51(1) | 1971.2(6) |
| 0.2798 | 1.60136 | 16.355(3) | 11.765(2) | 10.614(3) | 105.48(1) | 1968.1(8) |

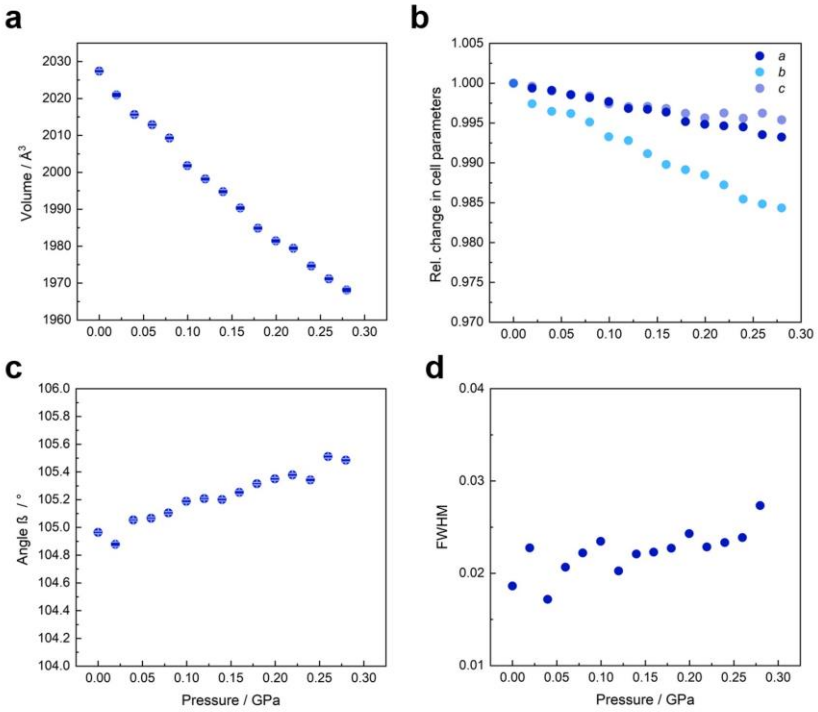


**Figure S47:** The evolution of unit cell volume (a), parameters (b), angle (c) and fwhm (d) as a function of hydrostatic compression until 0.28 GPa for [DEP]Ni($C_2N_3$)$_3$.

**Table S12:** Overview of the unit cell parameters and volumes of [PEP]Ni($C_2N_3$)$_3$ obtained from Pawley fits of the HPPXRD data up to 0.26 GPa.

| *p* / GPa | $R_{wp}$ | *a* / Å | *b* / Å | *c* / Å | ß / ° | *V* / Å$^3$ |
|---|---|---|---|---|---|---|
| ambient | 1.44525 | 16.486(2) | 11.949(1) | 10.667(1) | 104.981(8) | 2029.9(4) |
| 0.0198 | 1.53702 | 16.485(2) | 11.941(1) | 10.659(1) | 105.028(8) | 2026.6(4) |
| 0.0398 | 1.79636 | 16.478(4) | 11.926(1) | 10.656(3) | 105.03(2) | 2022.5(8) |
| 0.0598 | 1.70747 | 16.466(5) | 11.910(2) | 10.665(4) | 105.06(2) | 2019.7(9) |
| 0.0793 | 1.48532 | 16.447(3) | 11.889(1) | 10.643(3) | 105.08(1) | 2009.5(7) |
| 0.0999 | 1.43183 | 16.424(4) | 11.886(2) | 10.638(3) | 105.10(1) | 2004.9(8) |
| 0.1199 | 1.47878 | 16.417(3) | 11.883(2) | 10.631(2) | 105.23(1) | 2001.1(6) |
| 0.1393 | 1.51467 | 16.417(3) | 11.865(2) | 10.622(2) | 105.27(1) | 1996.1(7) |
| 0.1594 | 1.38044 | 16.414(3) | 11.851(2) | 10.622(3) | 105.335(9) | 1992.7(6) |
| 0.1793 | 1.72835 | 16.404(3) | 11.835(1) | 10.627(2) | 105.36(1) | 1989.5(6) |
| 0.1996 | 1.96211 | 16.403(3) | 11.822(1) | 10.619(3) | 105.39(1) | 1985.4(7) |
| 0.2195 | 1.80703 | 16.381(3) | 11.815(1) | 10.617(2) | 105.395(1) | 1981.0(6) |
| 0.2397 | 1.52922 | 16.383(2) | 11.796(1) | 10.612(1) | 105.417(9) | 1976.9(4) |
| 0.2597 | 1.84962 | 16.373(3) | 11.791(2) | 10.606(2) | 105.47(1) | 1973.5(6) |

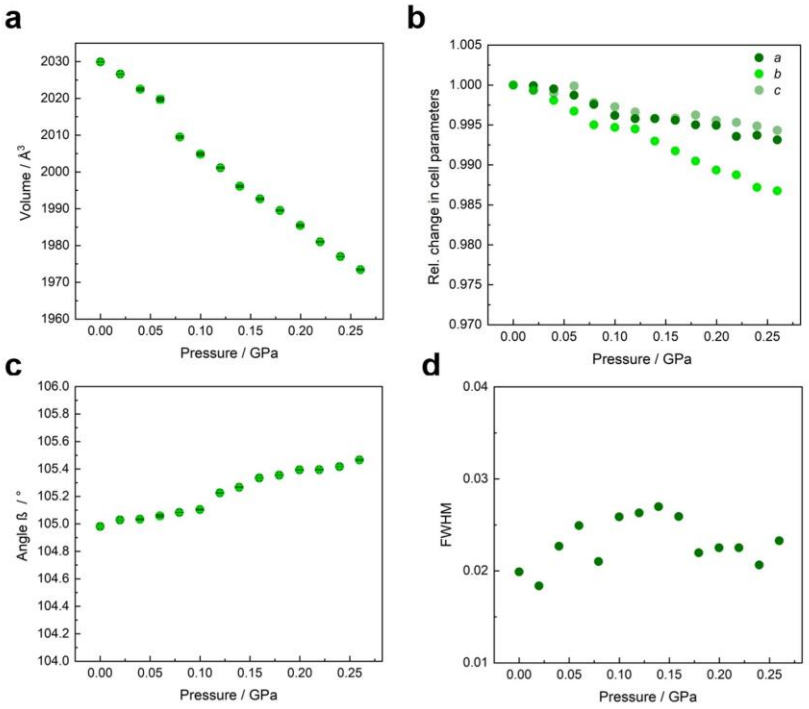


**Figure S48:** The evolution of unit cell volume (a), parameters (b), angle (c) and fwhm (d) as a function of hydrostatic compression until 0.26 GPa for [PEP]Ni($C_2N_3$)$_3$.

**Table S13:** Overview of the unit cell parameters and volumes of [DIP]Ni($C_2N_3$)$_3$ obtained from Pawley fits of the HPPXRD data up to 0.28 GPa.

| *p* / GPa | $R_{wp}$ | *a* / Å | *b* / Å | *c* / Å | ß / ° | *V* / Å$^3$ |
|---|---|---|---|---|---|---|
| ambient | 1.57572 | 16.337(1) | 12.006(1) | 11.031(1) | 93.727(7) | 2159.1(3) |
| 0.0196 | 1.54057 | 16.323(2) | 11.989(1) | 11.021(1) | 93.839(9) | 2152.1(3) |
| 0.0398 | 1.37845 | 16.307(1) | 11.975(1) | 11.014(1) | 93.883(4) | 2145.9(2) |
| 0.0598 | 1.69156 | 16.297(2) | 11.959(1) | 11.011(1) | 93.987(9) | 2140.9(3) |
| 0.0797 | 1.54961 | 16.276(1) | 11.957(1) | 11.005(1) | 94.102(5) | 2136.3(2) |
| 0.0993 | 1.56752 | 16.271(1) | 11.942(1) | 11.002(1) | 94.158(5) | 2132.1(3) |
| 0.1198 | 1.50498 | 16.251(1) | 11.920(1) | 11.001(1) | 94.229(5) | 2125.1(2) |
| 0.1399 | 1.33754 | 16.243(1) | 11.913(1) | 10.993(1) | 94.341(4) | 2121.2(2) |
| 0.1594 | 1.66066 | 16.223(2) | 11.904(1) | 10.993(1) | 94.437(7) | 2116.7(3) |
| 0.1794 | 1.62171 | 16.222(1) | 11.882(1) | 10.987(1) | 94.495(6) | 2111.3(3) |
| 0.1995 | 1.5133 | 16.206(1) | 11.872(1) | 10.986(1) | 94.549(5) | 2107.2(3) |
| 0.2195 | 1.37688 | 16.197(1) | 11.861(1) | 10.982(1) | 94.643(5) | 2102.9(3) |
| 0.2397 | 1.57011 | 16.191(1) | 11.846(2) | 10.982(1) | 94.711(6) | 2099.3(4) |
| 0.2597 | 1.31572 | 16.182(1) | 11.828(1) | 10.981(1) | 94.761(6) | 2094.5(3) |
| 0.2798 | 1.37773 | 16.164(2) | 11.821(1) | 10.979(1) | 94.872(8) | 2090.1(4) |

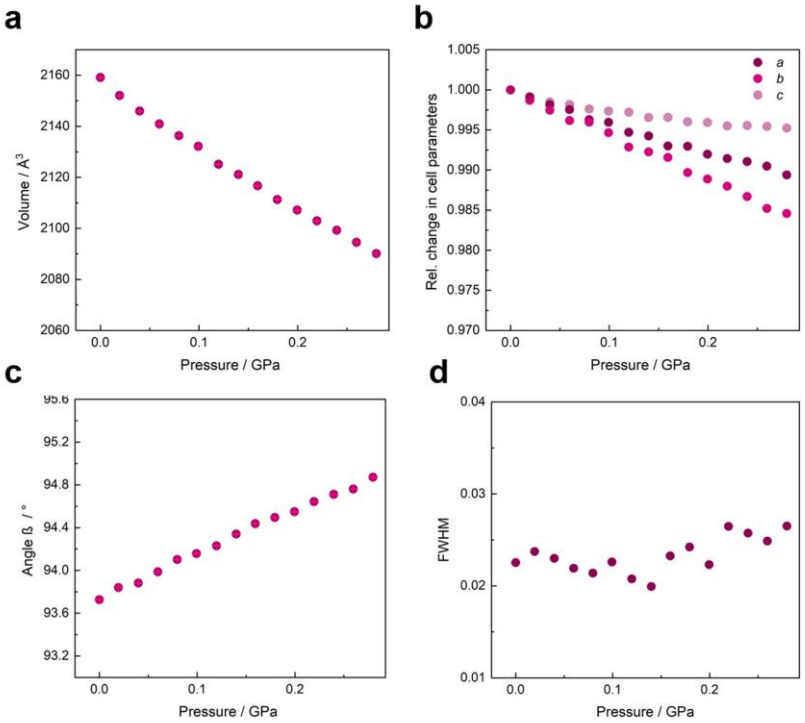


**Figure S49:** The evolution of unit cell volume (a), parameters (b), angle (c) and fwhm (d) as a function of hydrostatic compression until 0.28 GPa for [DIP]Ni($C_2N_3$)$_3$.

**Table S14:** Overview of the unit cell parameters and volumes of $[PEP]_{1-x}[DPP^{-}]_xNi(C_2N_3)_3$ (with $x$ = 1) obtained from Pawley fits of the HPPXRD data up to 0.4 GPa.

| $p$ / GPa | $R_{wp}$ | $a$ / Å | $b$ / Å | $c$ / Å | ß / ° | $V$ / Å$^3$ |
|---|---|---|---|---|---|---|
| ambient | 1.87831 | 17.306(2) | 12.330(2) | 10.482(1) | 111.801(9) | 2076.9(5) |
| 0.0197 | 1.55011 | 17.299(2) | 12.326(1) | 10.472(1) | 111.81(1) | 2073.3(4) |
| 0.0398 | 1.50488 | 17.266(1) | 12.318(1) | 10.453(1) | 111.825(5) | 2063.9(3) |
| 0.0598 | 1.55784 | 17.247(1) | 12.321(2) | 10.442(2) | 111.685(8) | 2061.9(5) |
| 0.0794 | 1.53154 | 17.241(1) | 12.311(1) | 10.429(1) | 111.694(6) | 2057.0(3) |
| 0.0999 | 1.64929 | 17.224(1) | 12.313(1) | 10.421(1) | 111.674(6) | 2053.8(3) |
| 0.1199 | 1.57977 | 17.219(1) | 12.302(1) | 10.412(1) | 111.616(5) | 2050.6(2) |
| 0.1399 | 1.8763 | 17.206(2) | 12.298(1) | 10.406(1) | 111.602(7) | 2047.2(4) |
| 0.1593 | 1.72529 | 17.196(2) | 12.289(1) | 10.393(1) | 111.543(7) | 2042.8(4) |
| 0.1793 | 2.08452 | 17.189(2) | 12.283(2) | 10.383(1) | 111.514(1) | 2039.6(4) |
| 0.1995 | 1.58205 | 17.179(1) | 12.277(1) | 10.365(1) | 111.409(7) | 2035.2(3) |
| 0.2196 | 1.85094 | 17.171(2) | 12.273(2) | 10.359(1) | 111.397(8) | 2032.5(4) |
| 0.2397 | 1.7263 | 17.158(2) | 12.272(2) | 10.345(1) | 111.320(7) | 2029.2(4) |
| 0.2597 | 1.58309 | 17.139(1) | 12.266(1) | 10.335(1) | 111.299(5) | 2024.4(3) |
| 0.2798 | 1.55227 | 17.131(1) | 12.263(1) | 10.328(1) | 111.264(5) | 2022.0(3) |
| 0.2997 | 1.59153 | 17.126(1) | 12.261(2) | 10.316(1) | 111.227(6) | 2019.2(4) |
| 0.3198 | 1.70593 | 17.108(1) | 12.260(2) | 10.308(1) | 111.171(7) | 2016.2(4) |
| 0.3397 | 1.42475 | 17.098(1) | 12.250(1) | 10.306(1) | 111.181(6) | 2012.9(3) |
| 0.3598 | 1.5862 | 17.089(2) | 12.235(2) | 10.297(1) | 111.209(8) | 2007.2(5) |
| 0.3798 | 1.82388 | 17.087(2) | 12.233(2) | 10.284(1) | 111.144(9) | 2005.0(5) |
| 0.3998 | 1.41571 | 17.082(1) | 12.231(2) | 10.272(1) | 111.112(7) | 2002.0(4) |

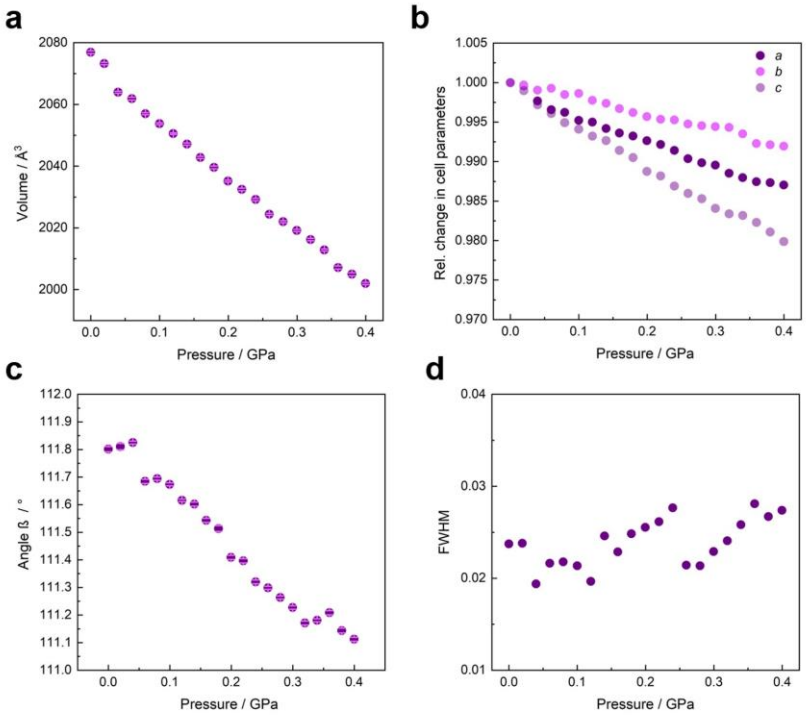


**Figure S50:** The evolution of unit cell volume (a), parameters (b), angle (c) and fwhm (d) as a function of hydrostatic compression until 0.4 GPa for $[PEP]_{1-x}[DPP]_xNi(C_2N_3)_3$ (with $x$ = 1).

We determined unit cell volumes, cell parameters, angles and fwhm of all solid solutions $[PEP]_{1-x}[DPP]_xNi(C_2N_3)_3$ (with $x$ = 0.45, 0.69, 0.85 and 0.96) with standard deviations up to 0.4 GPa.

**Table S15:** Volume ($V$), angle ($ß$) and space group ($S.G.$) for all studied solid solutions $[PEP]_{1-x}[DPP]_xNi(C_2N_3)_3$ (with $x$ = 0, 0.45, 0.69, 0.85, 0.96 and 1) obtained from Pawley fits of the ambient pressure PXRD data.

| ***x*** | **0** | **0.45** | **0.69** | **0.85** | **0.96** | **1** |
|---|---|---|---|---|---|---|
| S.G. | $P2_1/c$ | $P2_1/c$ | $P2_1/c$ | $P2_1/c$ | $P2_1/c$ | $C2/c$ |
| ß / ° | 104.973(8) | 104.59(1) | 104.446(9) | 104.295(6) | 104.17(1) | 111.790(9) |
| $V$ / Å$^3$ | 2029.7(4) | 2042.5(7) | 2054.3(4) | 2060.6(4) | 2072.6(5) | 2076.9(4) |

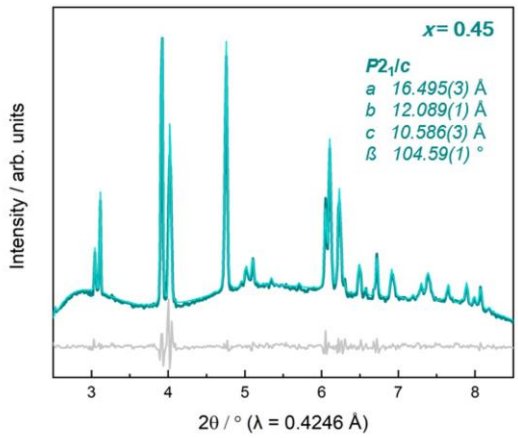


**Figure S51:** Pawley fit to synchrotron PXRD data at ambient pressure for $[PEP]_{1-x}[DPP]_xNi(C_2N_3)_3$ (with $x$ = 0.45). Experimental data is shown as dark turquoise line, Pawley fit as light turquoise line, and the difference curve (fit – data) as grey line.

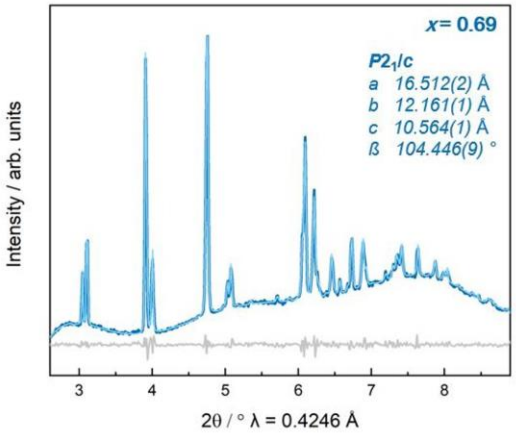


**Figure S52:** Pawley fit to synchrotron PXRD data at ambient pressure for $[PEP]_{1-x}[DPP]_xNi(C_2N_3)_3$ (with $x$ = 0.69). Experimental data is shown as dark blue line, Pawley fit as light blue line, and the difference curve (fit – data) as grey line.

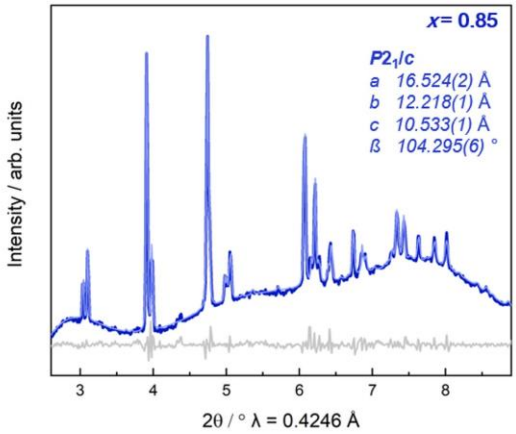


**Figure S53:** Pawley fit to synchrotron PXRD data at ambient pressure for $[PEP]_{1-x}[DPP]_xNi(C_2N_3)_3$ (with $x$ = 0.85). Experimental data is shown as dark blue line, Pawley fit as light blue line, and the difference curve (fit – data) as grey line.

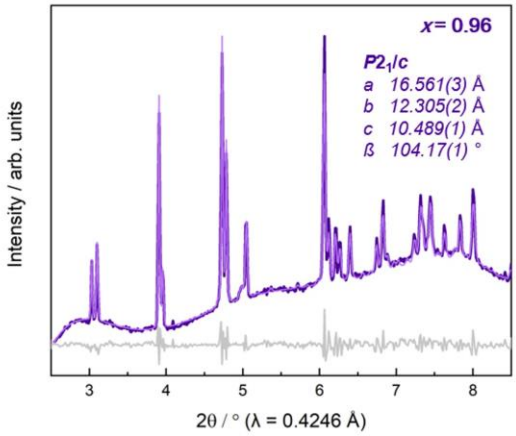


**Figure S54:** Pawley fit to synchrotron PXRD data at ambient pressure for $[PEP]_{1-x}[DPP]_xNi(C_2N_3)_3$ (with $x$ = 0.96). Experimental data is shown as dark purple line, Pawley fit as light purple line, and the difference curve (fit – data) as grey line.

**Table S16:** Overview of the unit cell parameters and volumes of $[PEP]_{1-x}[DPP]_xNi(C_2N_3)_3$ (with $x$ = 0.45) obtained from Pawley fits of the HPPXRD data up to 0.4 GPa.

| $p$ / GPa | $R_{wp}$ | $a$ / Å | $b$ / Å | $c$ / Å | ß / ° | $V$ / Å$^3$ |
|---|---|---|---|---|---|---|
| ambient | 3.41886 | 16.493(4) | 12.089(1) | 10.591(3) | 104.58(2) | 2043.6(9) |
| 0.0194 | 2.73906 | 16.479(3) | 12.070(2) | 10.601(3) | 104.59(1) | 2040.4(7) |
| 0.0398 | 2.53516 | 16.476(3) | 12.058(2) | 10.595(3) | 104.63(1) | 2036.6(7) |
| 0.0598 | 1.63417 | 16.481(2) | 12.040(1) | 10.581(2) | 104.757(9) | 2030.4(4) |
| 0.0795 | 2.13199 | 16.462(2) | 12.005(1) | 10.589(2) | 104.720(9) | 2024.0(5) |
| 0.0998 | 2.2139 | 16.455(1) | 11.998(1) | 10.582(2) | 104.778(9) | 2020.2(5) |
| 0.1199 | 2.30452 | 16.444(2) | 11.995(1) | 10.573(3) | 104.82(2) | 2016.1(7) |
| 0.1399 | 2.44387 | 16.434(2) | 11.980(2) | 10.574(2) | 104.886(9) | 2011.9(6) |
| 0.1593 | 2.35471 | 16.429(2) | 11.970(2) | 10.564(3) | 104.918(9) | 2007.5(7) |
| 0.1794 | 1.92737 | 16.423(2) | 11.959(1) | 10.554(2) | 105.006(7) | 2002.3(5) |
| 0.1996 | 2.103 | 16.413(2) | 11.950(2) | 10.551(2) | 105.007(8) | 1998.8(5) |
| 0.2196 | 2.26691 | 16.403(2) | 11.945(1) | 10.547(2) | 105.02(1) | 1995.9(5) |
| 0.2397 | 2.71957 | 16.385(3) | 11.945(2) | 10.543(3) | 105.04(1) | 1992.8(7) |
| 0.2597 | 2.61814 | 16.381(3) | 11.923(1) | 10.539(3) | 105.08(1) | 1987.5(6) |
| 0.2797 | 2.64843 | 16.378(2) | 11.916(1) | 10.528(3) | 105.09(1) | 1983.8(6) |
| 0.2997 | 2.95571 | 16.369(3) | 11.913(1) | 10.522(3) | 105.12(1) | 1980.7(6) |
| 0.3198 | 3.74298 | 16.355(4) | 11.904(2) | 10.518(3) | 105.15(2) | 1976.5(9) |
| 0.3397 | 2.7522 | 16.351(3) | 11.880(1) | 10.518(3) | 105.18(1) | 1971.8(7) |
| 0.3598 | 2.81426 | 16.341(3) | 11.874(1) | 10.515(3) | 105.17(1) | 1969.0(8) |
| 0.3798 | 2.94866 | 16.332(4) | 11.868(2) | 10.511(4) | 105.19(1) | 1965.9(9) |
| 0.3998 | 3.37968 | 16.323(4) | 11.866(2) | 10.504(2) | 105.22(2) | 1963.1(8) |

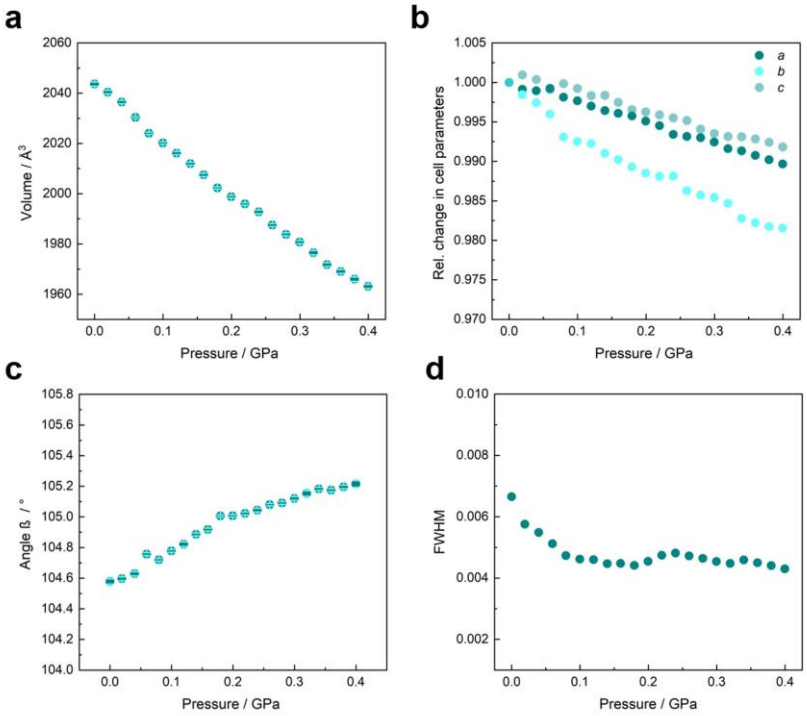


**Figure S55:** The evolution of unit cell volume (a), parameters (b), angle (c) and fwhm (d) as a function of hydrostatic compression until 0.4 GPa for $[PEP]_{1-x}[DPP]_xNi(C_2N_3)_3$ (with $x$ = 0.45).

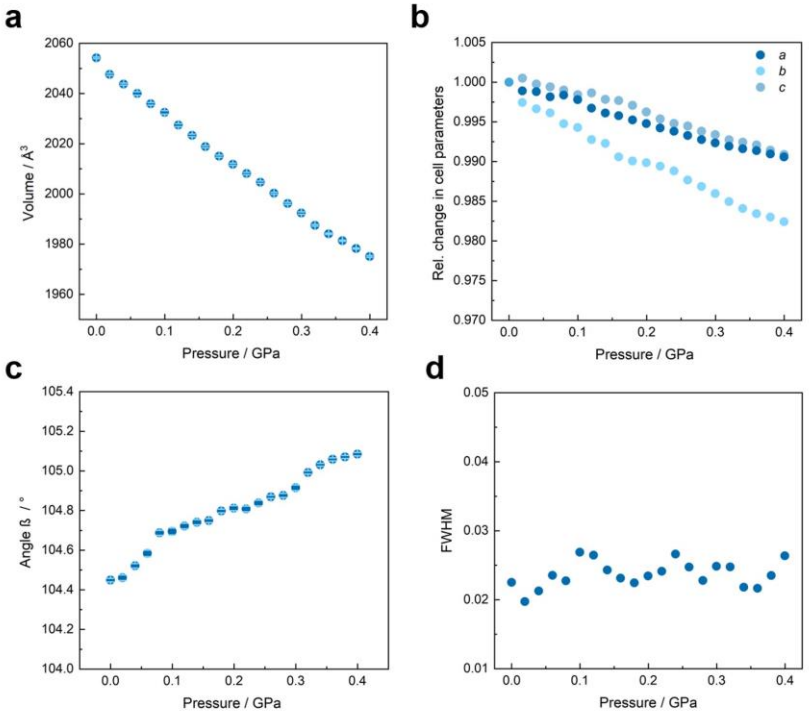


**Figure S56:** The evolution of unit cell volume (a), parameters (b), angle (c) and fwhm (d) as a function of hydrostatic compression until 0.4 GPa for $[PEP]_{1-x}[DPP]_xNi(C_2N_3)_3$ (with $x$ = 0.69).

**Table S18:** Overview of the unit cell parameters and volumes of $[PEP]_{1-x}[DPP]_xNi(C_2N_3)_3$ (with $x$ = 0.85) obtained from Pawley fits of the HPPXRD data up to 0.4 GPa (0.24 GPa was not used for further analysis of the $V(p)$ data due to the $R_{wp}$ value).

| $p$ / GPa | $R_{wp}$ | $a$ / Å | $b$ / Å | $c$ / Å | ß / ° | $V$ / Å$^3$ |
|---|---|---|---|---|---|---|
| ambient | 2.08697 | 16.527(2) | 12.221(1) | 10.526(1) | 104.298(6) | 2060.1(4) |
| 0.0194 | 2.00284 | 16.525(2) | 12.217(1) | 10.516(1) | 104.318(7) | 2057.1(4) |
| 0.0398 | 2.2769 | 16.509(1) | 12.213(1) | 10.512(1) | 104.356(6) | 2053.2(4) |
| 0.0598 | 2.20888 | 16.502(1) | 12.206(1) | 10.506(1) | 104.427(6) | 2049.3(4) |
| 0.0795 | 2.15894 | 16.491(2) | 12.197(1) | 10.499(1) | 104.485(7) | 2044.8(4) |
| 0.0998 | 2.01669 | 16.489(2) | 12.170(1) | 10.499(1) | 104.518(7) | 2039.8(3) |
| 0.1199 | 2.0015 | 16.469(1) | 12.161(1) | 10.497(1) | 104.521(9) | 2035.1(4) |
| 0.1399 | 2.65996 | 16.459(2) | 12.158(1) | 10.482(2) | 104.536(9) | 2031.1(5) |
| 0.1593 | 1.78337 | 16.459(2) | 12.131(1) | 10.491(1) | 104.54(1) | 2027.7(4) |
| 0.1794 | 2.20132 | 16.446(2) | 12.126(1) | 10.480(2) | 104.600(8) | 2022.5(4) |
| 0.1996 | 2.30149 | 16.439(2) | 12.122(1) | 10.473(1) | 104.611(7) | 2019.4(4) |
| 0.2196 | 2.08851 | 16.438(2) | 12.114(1) | 10.471(1) | 104.653(7) | 2017.4(4) |
| 0.2597 | 1.92212 | 16.418(1) | 12.079(1) | 10.472(1) | 104.714(8) | 2008.6(4) |
| 0.2797 | 2.21099 | 16.419(1) | 12.069(1) | 10.469(1) | 104.750(9) | 2006.1(4) |
| 0.2997 | 1.87295 | 16.409(2) | 12.051(1) | 10.475(1) | 104.77(1) | 2002.8(4) |
| 0.3198 | 1.97827 | 16.393(2) | 12.042(1) | 10.467(1) | 104.77(1) | 1997.9(4) |
| 0.3397 | 2.05381 | 16.386(2) | 12.039(1) | 10.453(1) | 104.73(1) | 1994.3(3) |
| 0.3598 | 2.26418 | 16.382(2) | 12.031(1) | 10.444(1) | 104.71(1) | 1991.1(4) |
| 0.3798 | 2.42483 | 16.379(2) | 12.025(1) | 10.438(1) | 104.807(9) | 1987.7(4) |
| 0.3998 | 1.96896 | 16.368(2) | 12.008(1) | 10.442(1) | 104.85(1) | 1983.8(4) |

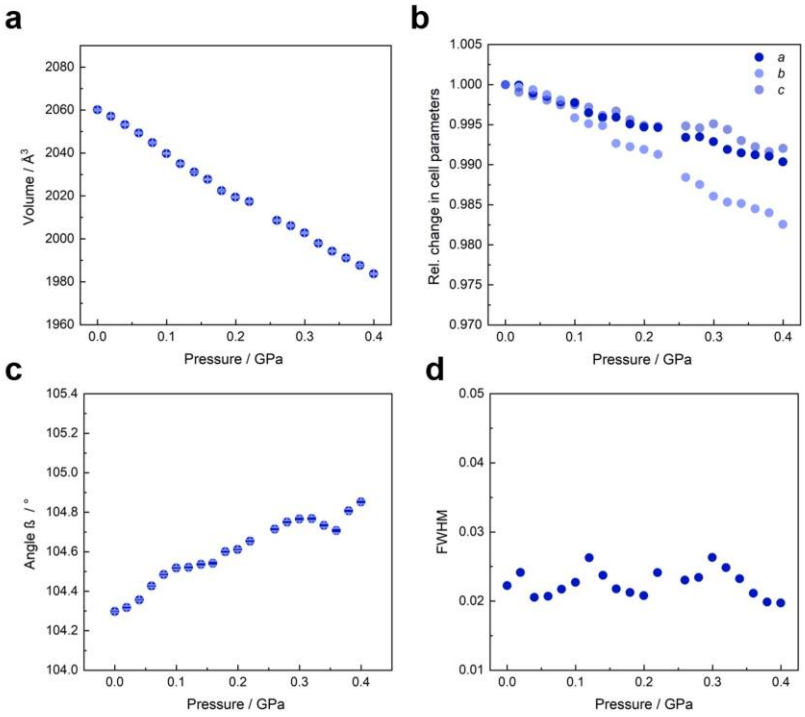


**Figure S57:** The evolution of unit cell volume (a), parameters (b), angle (c) and fwhm (d) as a function of hydrostatic compression until 0.4 GPa (without 0.24 GPa) for $[PEP]_{1-x}[DPP]_xNi(C_2N_3)_3$ (with $x$ = 0.85).

**Table S19:** Overview of the unit cell parameters and volumes of $[PEP]_{1-x}[DPP]_xNi(C_2N_3)_3$ (with $x$ = 0.96) obtained from Pawley fits of the HPPXRD data up to 0.4 GPa.

| $p$ / GPa | $R_{wp}$ | $a$ / Å | $b$ / Å | $c$ / Å | ß / ° | $V$ / Å$^3$ |
|---|---|---|---|---|---|---|
| ambient | 1.64612 | 16.559(1) | 12.307(1) | 10.488(1) | 104.158(5) | 2072.5(3) |
| 0.0194 | 1.69902 | 16.547(1) | 12.297(1) | 10.478(1) | 104.151(6) | 2067.3(3) |
| 0.0398 | 1.81976 | 16.535(1) | 12.295(1) | 10.469(1) | 104.172(5) | 2063.5(2) |
| 0.0598 | 1.88344 | 16.529(1) | 12.286(1) | 10.466(1) | 104.225(5) | 2060.2(2) |
| 0.0795 | 1.85947 | 16.524(1) | 12.279(1) | 10.455(1) | 104.275(6) | 2055.8(3) |
| 0.0998 | 1.9511 | 16.522(1) | 12.264(1) | 10.447(1) | 104.307(6) | 2051.2(3) |
| 0.1199 | 1.88938 | 16.516(1) | 12.259(1) | 10.438(1) | 104.346(6) | 2047.5(3) |
| 0.1399 | 2.20804 | 16.509(2) | 12.251(1) | 10.430(1) | 104.372(8) | 2043.4(3) |
| 0.1593 | 2.28441 | 16.506(2) | 12.247(1) | 10.423(1) | 104.436(8) | 2040.5(4) |
| 0.1794 | 1.76172 | 16.490(2) | 12.231(2) | 10.422(1) | 104.469(7) | 2035.3(4) |
| 0.1995 | 1.59709 | 16.486(1) | 12.220(1) | 10.418(1) | 104.489(6) | 2031.9(3) |
| 0.2195 | 1.94357 | 16.474(2) | 12.197(1) | 10.418(1) | 104.485(7) | 2026.9(4) |
| 0.2397 | 2.18806 | 16.459(2) | 12.197(2) | 10.408(1) | 104.506(7) | 2022.7(4) |
| 0.2596 | 2.00007 | 16.446(2) | 12.174(1) | 10.412(1) | 104.534(6) | 2017.7(3) |
| 0.2798 | 1.66219 | 16.445(1) | 12.163(1) | 10.408(1) | 104.559(6) | 2014.9(3) |
| 0.2998 | 1.8349 | 16.438(2) | 12.159(1) | 10.402(1) | 104.623(6) | 2012.1(3) |
| 0.3198 | 2.08299 | 16.422(1) | 12.154(1) | 10.403(1) | 104.631(6) | 2009.0(3) |
| 0.3397 | 1.78474 | 16.419(1) | 12.136(1) | 10.402(1) | 104.673(6) | 2005.1(3) |
| 0.3598 | 1.75927 | 16.416(1) | 12.128(1) | 10.401(1) | 104.682(5) | 2003.2(3) |
| 0.3798 | 1.85032 | 16.404(1) | 12.116(1) | 10.390(1) | 104.681(6) | 1997.7(3) |
| 0.3998 | 1.86516 | 16.397(1) | 12.096(1) | 10.389(1) | 104.692(5) | 1993.2(3) |

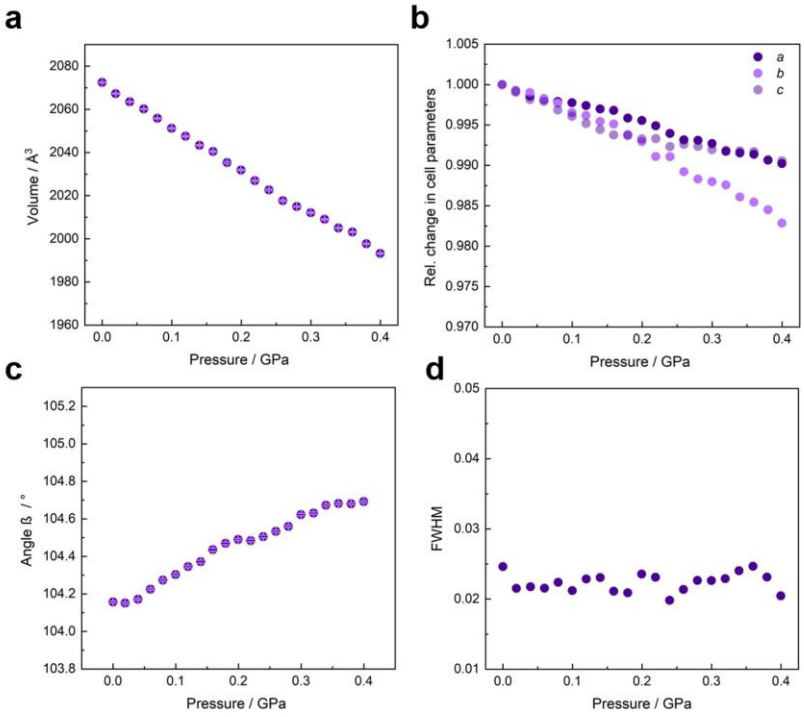


**Figure S58:** The evolution of unit cell volume (a), parameters (b), angle (c) and fwhm (d) as a function of hydrostatic compression until 0.4 GPa for $[PEP]_{1-x}[DPP]_xNi(C_2N_3)_3$ (with $x$ = 0.96).

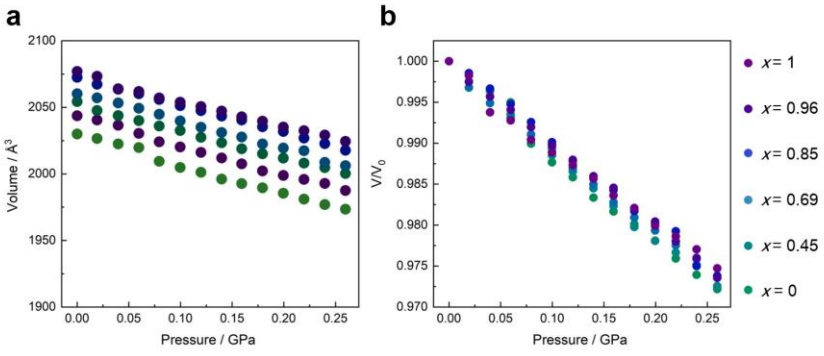


**Figure S59:** (a) The extracted unit cell volume including error bars as a function of pressure along the series of A-site solid solutions $[PEP]_{1-x}[DPP]_xNi(C_2N_3)_3$ with $x$ = 0, 0.45, 0.69, 0.85, 0.96 and 1 and (b) relative volumes ($V/V_0$) as a function of hydrostatic compression until 0.26 GPa.

**Rietveld refinements of solid solution samples.** We have performed Rietveld refinements of the PXRD patterns at $p$ = ambient with the goal of analysing tilt distortions across the solid solution $[PEP]_{1-x}[DPP]_xNi(C_2N_3)_3$ structures. This was done by using routines as implemented in TOPAS *v6* software.[10]

In detail, we have used the single crystal structure of $[PEP]Ni(C_2N_3)_3$ (monoclinic, $P2_1/c$) as a starting structural model. The unit cell parameters, as obtained from Pawley profile fits (Fig. S51-S54), were applied in the refinement (Rietveld method) and fixed. The structure models for $[PEP]_{1-x}[DPP]_xNi(C_2N_3)_3$ ($x$ = 0.45, 0.69, 0.85 and 0.96) were refined against ambient pressure PXRD data ($\lambda$ = 0.4246 Å) in the $2\theta$ range from 2.5° to 9.0°. The peak shapes were refined using "TCHZ_Peak_Type" (modified Thompson-Cox-Hastings pseudo-Voigt function with U, V, W and Y as refined parameters). Notably, the A-site cation has been refined as a rigid body. The A-site cation, *i.e.* $[PEP]_{1-x}[DPP]_{x}^{+}$, was modelled by starting from the structure of $[PEP]^+$ and adding one carbon atom at a chemically sensible position with a fixed occupancy. During the refinement, the A-site cation was allowed to move and rotate freely without conformational changes. Furthermore, distance and angle restraints were applied within the $(C_2N_3)^-$ units, and $NiN_6$ octahedra as a chemically informed guess for guiding the refinement.

We expect that this approach won't deliver an accurate model of the A-site cation but will enable us to analyse structural distortions of the $[Ni(C_2N_3)_3]^-$ network to an accuracy level that we can estimate $A_p$ and, overall, draw conclusions between $A_p$ and $B$; however, we would like to mention that a custom-built high-pressure diffraction setup was applied for data collection, where the background (water, plastic capillary and diamond windows) and a relatively large capillary diameter of (~ 1mm) decreased the quality of PXRD data for a quantitative structural analysis based on a Rietveld refinement. Furthermore, non-uniform Bragg rings were visible on the 2D detector with spots of high intensities. By applying intensities cut-off during data integration, we attempted to reduce these intensity inaccuracies to a minimum; however, these are certainly additional error sources for wrong intensities. Lastly, we would like to mention that we have tried several approaches (with and without restraints, with several different rigid bodies, etc.), where all structural refinements led to $A_p$ values between 2 – 4 for the solid solution series ($0 \leq x \leq 1$). Given the various sources for inaccuracies, however, we only provide structural models of the input for the ISODISTORT[15,16] analysis to avoid false interpretation, *i.e.* overinterpretation of the obtained structures.

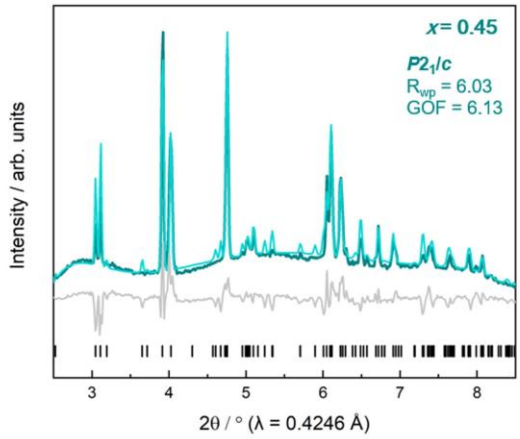


**Figure S60:** Rietveld fit of high-resolution PXRD data for $[PEP]_{1-x}[DPP]_xNi(C_2N_3)_3$ (with $x$ = 0.45). Experimental data is shown as dark turquoise line, Rietveld fit as light turquoise line, reflection positions as black vertical tick marks, and the difference curve (fit – data) as grey line.

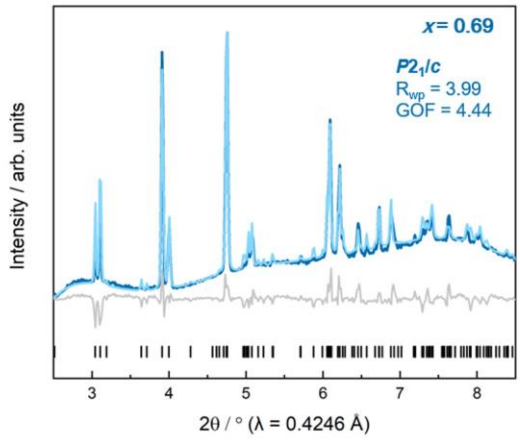


**Figure S61:** Rietveld fit of high-resolution PXRD data for $[PEP]_{1-x}[DPP]_xNi(C_2N_3)_3$ (with $x$ = 0.69). Experimental data is shown as dark blue line, Rietveld fit as light blue line, reflection positions as black vertical tick marks, and the difference curve (fit – data) as grey line.

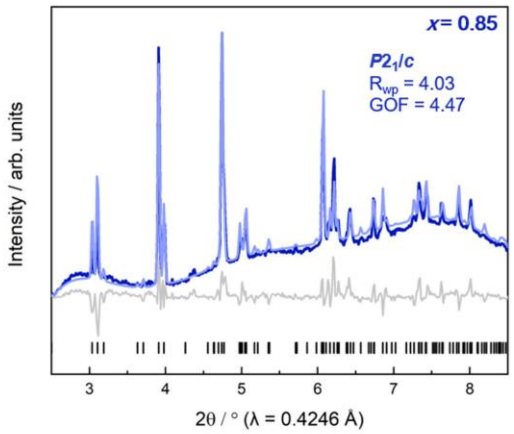


**Figure S62:** Rietveld fit of high-resolution PXRD data for $[PEP]_{1-x}[DPP]_xNi(C_2N_3)_3$ (with $x$ = 0.85). Experimental data is shown as dark purple line, Rietveld fit as light blue purple, reflection positions as black vertical tick marks, and the difference curve (fit – data) as grey line.

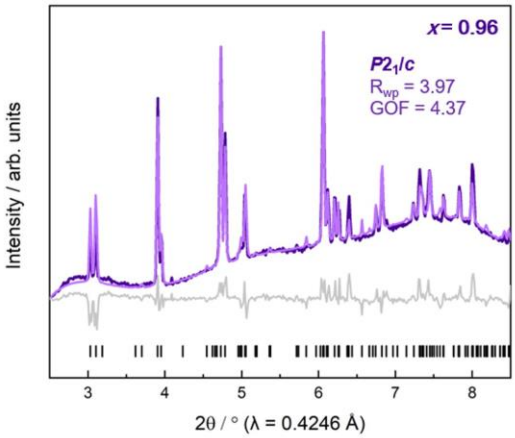


**Figure S63:** Rietveld fit of high-resolution PXRD data for $[PEP]_{1-x}[DPP]_xNi(C_2N_3)_3$ (with $x$ = 0.96). Experimental data is shown as dark purple line, Rietveld fit as light purple line, reflection positions as black vertical tick marks, and the difference curve (fit – data) as grey line.

## 9. Bulk modulus

The unit cell volume changes obtained by HPPXRD throughout the hydrostatic regime were fitted to a 2nd order Birch-Murnaghan (B-M) equation of states using the software EoSFit7-Gui to estimate each material's bulk modulus (*B*).[17] The standard deviations of the volumes extracted by Pawley fits and a standard pressure error ($p$ = ± 0.003 GPa) were included in the B-M fitting procedure. Additionally, 2nd and 3rd order calculations are given in Table S20 and Chapter 14 of this supporting information.

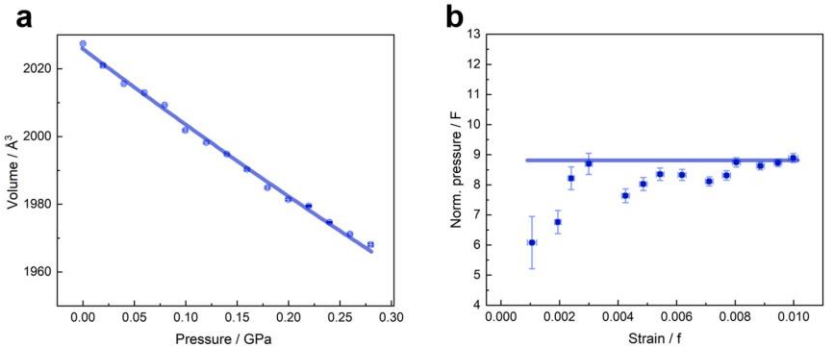


**Figure S64:** The change in unit cell volume of [DEP]Ni($C_2N_3$)$_3$ is fitted using 2nd order B-M equation of state shown as blue line in the *V*(*p*)-plot (a) and *F*(*f*)-plot (b), confirming the applicability of the 2nd order fit to calculate *B*.

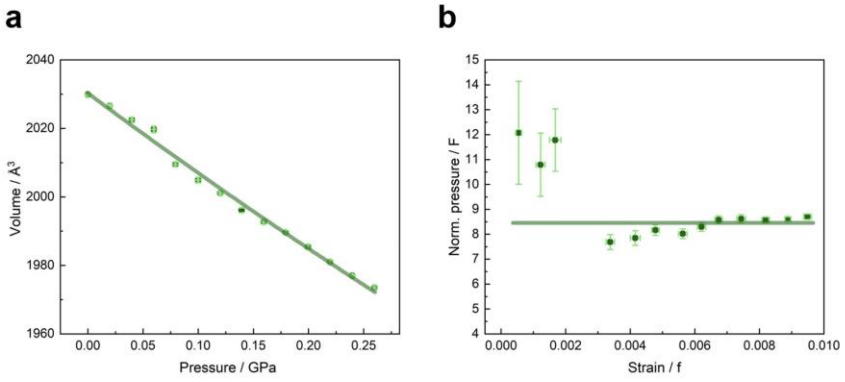


**Figure S65:** The change in unit cell volume of [PEP]Ni($C_2N_3$)$_3$ (within the solid solution $x$ = 0) is fitted using 2nd order B-M equation of state shown as green line in the *V*(*p*)-plot (a) and *F*(*f*)-plot (b), confirming the applicability of the 2nd order fit to calculate *B*.

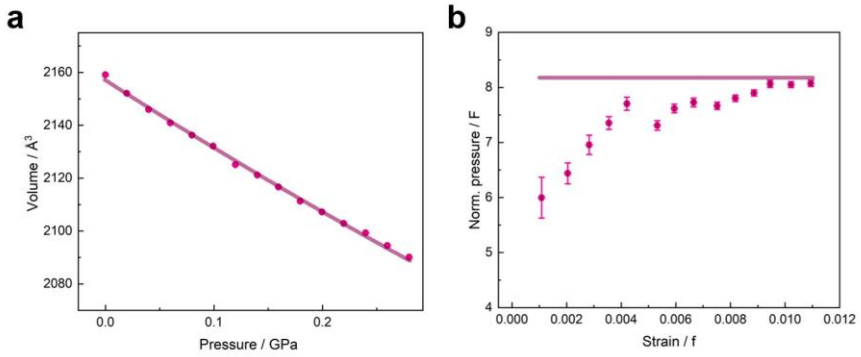


**Figure S66:** The change in unit cell volume of [DIP]Ni($C_2N_3$)$_3$ is fitted using 2$^{nd}$ order B-M equation of state shown as blue line in the *V*(*p*)-plot (a) and *F*(*f*)-plot (b), confirming the applicability of the 2$^{nd}$ order fit to calculate *B*.

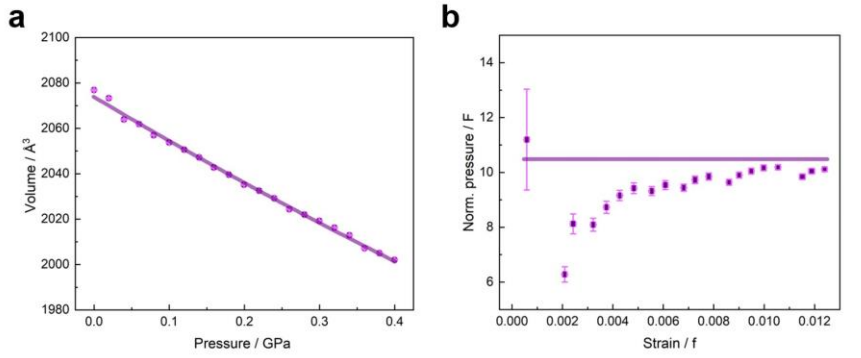


**Figure S67:** The change in unit cell volume of [DPP]Ni($C_2N_3$)$_3$ (within the solid solution *x* = 1) is fitted using 2$^{nd}$ order B-M equation of state shown as blue line in the *V*(*p*)-plot (a) and *F*(*f*)-plot (b), confirming the applicability of the 2$^{nd}$ order fit to calculate *B*.

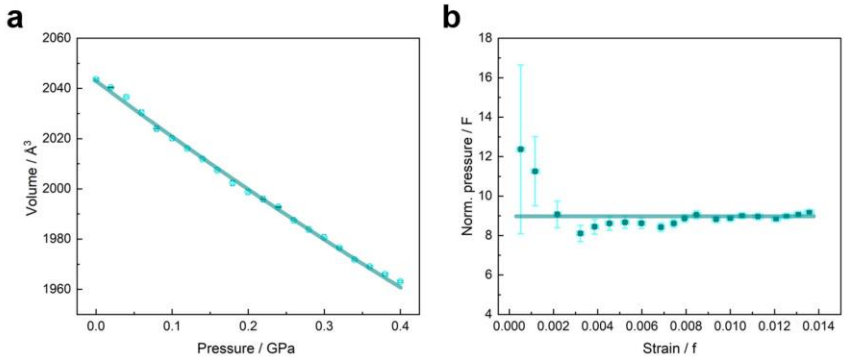


**Figure S68:** The change in unit cell volume of [PEP]$_{1-x}$[DPP]$_x$Ni($C_2N_3$)$_3$ (with *x* = 0.45) is fitted using 2$^{nd}$ order B-M equation of state shown as blue line in the *V*(*p*)-plot (a) and *F*(*f*)-plot (b), confirming the applicability of the 2$^{nd}$ order fit to calculate *B*.

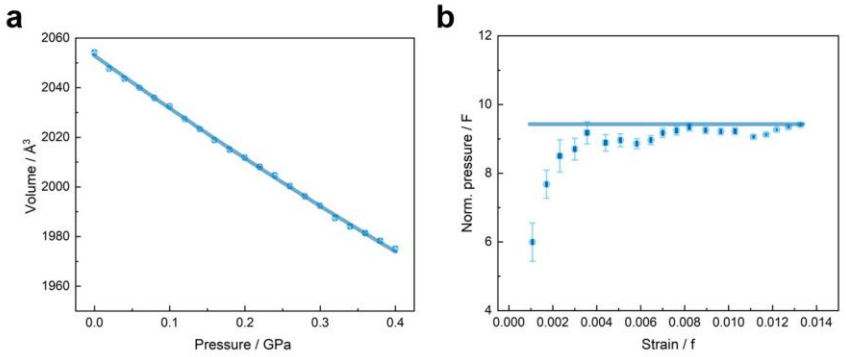


**Figure S69:** The change in unit cell volume of $[PEP]_{1-x}[DPP]_xNi(C_2N_3)_3$ (with $x = 0.69$) is fitted using 2nd order B-M equation of state shown as blue line in the $V(p)$-plot (a) and $F(f)$-plot (b), confirming the applicability of the 2nd order fit to calculate $B$.

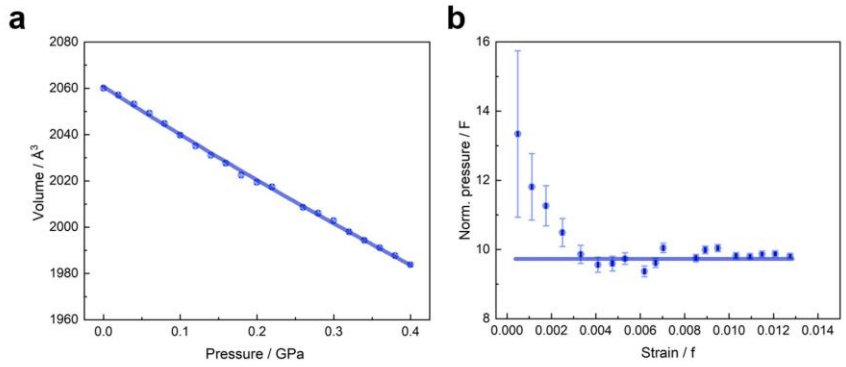


**Figure S70:** The change in unit cell volume of $[PEP]_{1-x}[DPP]_xNi(C_2N_3)_3$ (with $x = 0.85$) is fitted using 2nd order B-M equation of state shown as blue line in the $V(p)$-plot (a) and $F(f)$-plot (b), confirming the applicability of the 2nd order fit to calculate $B$.

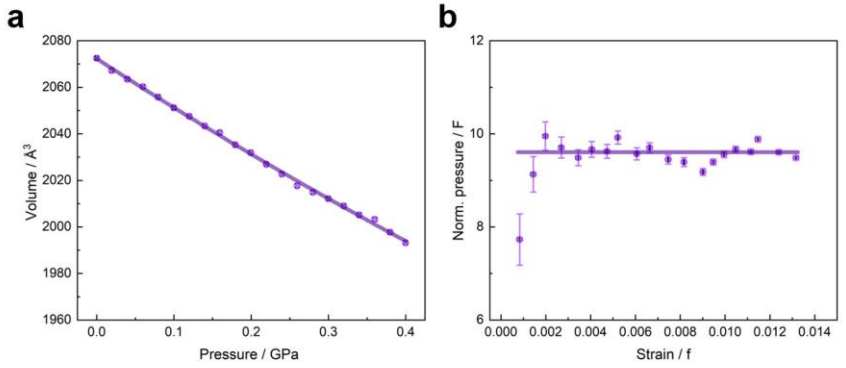


**Figure S71:** The change in unit cell volume of $[PEP]_{1-x}[DPP]_xNi(C_2N_3)_3$ (with $x = 0.96$) is fitted using 2nd order B-M equation of state shown as blue line in the $V(p)$-plot (a) and $F(f)$-plot (b), confirming the applicability of the 2nd order fit to calculate $B$.

**Table S20:** Bulk moduli ($B$) of $[PEP]_{1-x}[DPP]_xNi(C_2N_3)_3$ calculated from 2nd and 3rd order B-M equation of state fits to the HPPXRD data using EOSFit.

| ***x*** | **0.45** | **0.69** | **0.85** | **0.96** |
|---|---|---|---|---|
| $B$ (2nd) / GPa | 8.9 | 9.4 | 9.7 | 9.6 |
| $\sigma B$ (2nd) / GPa | 0.1 | 0.1 | 0.1 | 0.1 |
| $V_0$ (2nd) / Å$^3$ | 2042.9 | 2052.9 | 2060.7 | 2072.3 |
| $\sigma V_0$ (2nd) / Å$^3$ | 0.5 | 0.4 | 0.4 | 0.3 |
| $B$ (3rd) / GPa | 7.7 | 9.1 | 9.3 | 9.6 |
| $\sigma B$ (3rd) / GPa | 0.3 | 0.3 | 0.3 | 0.3 |
| $V_0$ (3rd) / Å$^3$ | 2045.1 | 2053.4 | 2061.3 | 2072.3 |
| $\sigma V_0$ (3rd) / Å$^3$ | 0.6 | 0.5 | 0.5 | 0.5 |

## 10. $Ni(dmgH)_2$ as reference material

We used $Ni(dmgH)_2$ (Nickel dimethylglyoxime) as reference material with well-known reported variable pressure behaviour to verify the applied pressure cell setup.[18,19] The sample was prepared similiarly as described above in Chapter 7, including HPPXRD experimental details. The HPPXRD data was collected in the same pressure regime (ambient pressure to 0.4 GPa) with the same pressure step size of 0.02 GPa (Fig. S72). Pawley refinement of the PXRD data at ambient pressure shows unit cell parameters $a$ = 16.5717(6) Å, $b$ = 10.4331(3) Å, $c$ = 6.4621(2) Å and $V$ = 1117.28(6) $Å^3$, which is in great accordance across variable pressure PXRD data with the reported structure.[20] The calculated bulk moduli, *i.e.* $B$ = 8.43±0.15 GPa (derived from the 3rd order B-M equation of state fit) and $B$ = 9.57±0.09 GPa (derived from the 2nd B-M order equation of state fit) are in line with reported data, confirming the applicability of the setup (Fig. S74).[21]

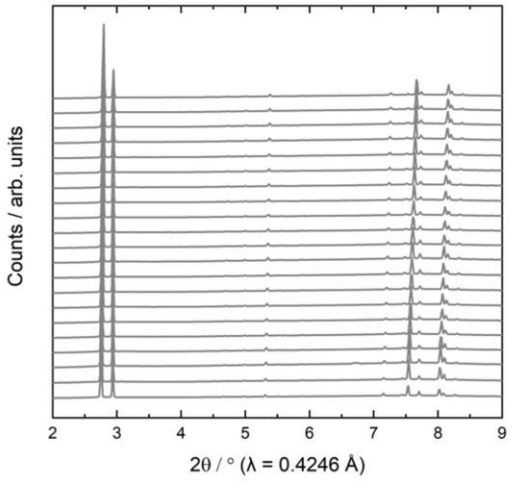


**Figure S72:** Collection of HPPXRD data of $Ni(dmgH)_2$ up to 0.4 GPa.

**Table S21:** Overview of the unit cell parameters and volumes $Ni(dmgH)_2$ obtained from Pawley fits of the HPPXRD data up to 0.4 GPa.

| *p*/bar | $R_{wp}$ | *a* / Å | *b* / Å | *c* / Å | *V* / Å$^3$ |
|---|---|---|---|---|---|
| ambient | 2.95280 | 16.5717(6) | 10.4331(3) | 6.4621(2) | 1117.28(6) |
| 0.0197 | 3.58596 | 16.5718(9) | 10.4265(5) | 6.4539(4) | 1115.16(10) |
| 0.0398 | 2.99285 | 16.5677(7) | 10.4105(4) | 6.4483(3) | 1112.21(8) |
| 0.0598 | 2.96639 | 16.5690(8) | 10.4004(4) | 6.4412(3) | 1109.99(9) |
| 0.0793 | 2.97736 | 16.5615(9) | 10.3890(5) | 6.4345(3) | 1107.11(10) |
| 0.0999 | 2.87619 | 16.5635(8) | 10.3808(6) | 6.4283(3) | 1105.31(10) |
| 0.1199 | 2.95232 | 16.5562(6) | 10.3677(5) | 6.4217(4) | 1102.29(9) |
| 0.1399 | 2.49250 | 16.5566(6) | 10.3571(4) | 6.4157(3) | 1100.16(7) |
| 0.1594 | 3.03165 | 16.5552(8) | 10.3482(6) | 6.4108(2) | 1098.30(11) |
| 0.1795 | 2.52741 | 16.5501(6) | 10.3387(4) | 6.4045(2) | 1095.86(7) |
| 0.1996 | 3.04075 | 16.5497(8) | 10.3310(5) | 6.3991(4) | 1094.11(10) |
| 0.2196 | 2.55868 | 16.5480(6) | 10.3221(4) | 6.3934(2) | 1092.07(7) |
| 0.2397 | 2.66187 | 16.5446(6) | 10.3129(4) | 6.3890(3) | 1090.12(7) |
| 0.2597 | 2.66473 | 16.5418(8) | 10.3073(6) | 6.3828(3) | 1088.29(9) |
| 0.2798 | 2.61754 | 16.5367(7) | 10.2969(4) | 6.3774(3) | 1085.93(8) |
| 0.2997 | 2.37638 | 16.5330(7) | 10.2919(5) | 6.3722(3) | 1084.28(9) |
| 0.3198 | 2.96540 | 16.5287(7) | 10.2873(6) | 6.3673(3) | 1082.68(9) |
| 0.3397 | 2.72334 | 16.5242(9) | 10.2765(6) | 6.3609(4) | 1080.17(10) |
| 0.3598 | 2.86385 | 16.5198(7) | 10.2708(5) | 6.3565(3) | 1078.52(9) |
| 0.3798 | 2.57641 | 16.5161(6) | 10.2624(5) | 6.3514(3) | 1076.54(8) |
| 0.3998 | 2.58556 | 16.5147(6) | 10.2581(4) | 6.3463(2) | 1075.14(7) |

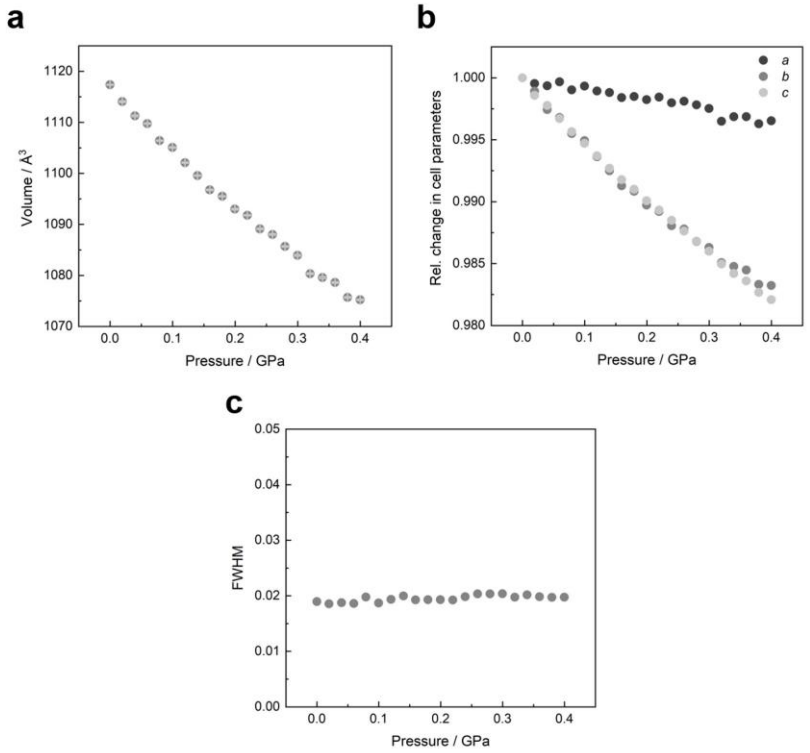


**Figure S73:** Change in volume (a), relative changes of the lattice parameters *a, b*, and *c* (b) and fwhm (c) for $Ni(dmgH)_2$ as a function of hydrostatic pressure.

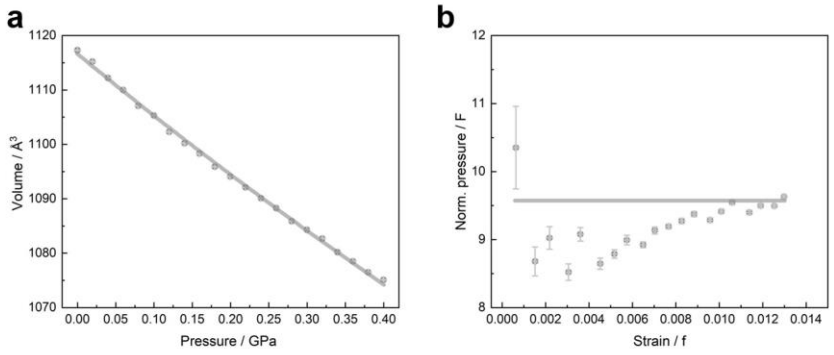


**Figure S74:** Variable pressure unit cell volume of $Ni(dmgH)_2$ is fitted using 2nd order B-M equation of state shown as grey line in the $V(p)$-plot (a) and $F(f)$-plot (b), confirming the applicability of the 3rd order fit to calculate $B$.

## 11. Tilt analysis of molecular perovskites

We used the web-based software tool ISODISTORT[15,16] to explore the active framework distortion modes of the $[Ni(C_2N_3)_3]^-$ framework. Herein, group theoretical analysis was applied to SCXRD data of 300 K to describe network distortions compared to a hypothetical cubic $[MX_3]^-$ network. In a first step, we created a hypothetical highly symmetric parent perovskite structure (aristotype) from two atom sites (***Ni*** *1.0 0.500000 0.50000 0.500000 Biso 1.000000 Ni* and ***N*** *1.0 0.250000 0.500000 0.500000 Biso 1.000000 N*) in *Pm*-3*m* cubic symmetry with unit cell parameters $a = b = c = 8$ Å and $\alpha = \beta = \gamma = 90$ °. This parent structure was used for all compounds and uploaded as a cif structure file to start the structural distortion mode analysis in ISODISTORT. After simplifying the low-symmetry crystal structure (hettotype) by removing the respective $A^+$ atom coordinates, resulting in the $[Ni(C_2N_3)_3]^-$ network structure composed of linear dicyanamide linkers, we subsequently uploaded all the distorted cif files to proceed with Method 4: "Mode decomposition of a distorted structure" implemented in ISODISTORT. Here, the mode decomposition of the distorted structure was analysed with respect to the cubic parent framework, identifying all active distortion modes corresponding to octahedral tilts and columnar shifts, as well as the overall distortion mode amplitude ($A_p$). These active distortions were assigned to a combination of irreducible representations (irreps) for conventional ($R_5^-$ and $M_2^+$), unconventional tilts ($\Gamma_4^+$, $X_5^-$ and $M_5^+$) and columnar shifts ($\Gamma_5^+$).

To showcase how $A_p$ can be calculated, we present the procedure on the example of $[DPP]Ni(C_2N_3)_3$ in the following. In a first step, we simplified the cif file by removing all atom coordinates of $[DPP]^+$ and atom coordinates of $(C_2N_3)^-$ despite the N atoms of the $NiN_6$ octahedra. This cif file contains the distorted octahedral network structure from four atom sites (***Ni1*** *1.0 0.250000 0.250000 0.500000 Uiso 0.034915 Ni,* ***N1*** *1.0 0.1264(2) 0.2917(4) 0.4062(4) Uiso 0.058012 N,* ***N2*** *1.0 0.2812(2) 0.4008(4) 0.4472(4) Uiso 0.056581 N* and ***N4*** *1.0 0.2540(2) 0.6843(4) 0.1851(4) Uiso 0.056376 N*) with space group symmetry *C*2/*c* ($a$ = 17.3196(5) Å, $b$ = 12.3357(3) Å, $c$ = 10.4909(3) Å and $\alpha = \gamma = 90$ ° $\beta = 111.917(1)$ °). Our next step was to start the analysis in the web-based software ISODISTORT and import our chosen high symmetry structure as a cif file. Important here, both cif files must contain the same types of atoms (*e.g.* ***Ni*** and ***N***). Then, we used Method 4: "Mode decomposition of a distorted structure", and uploaded our modified cif file of the distorted structure. Here, a specified sublattice basis must be provided, *i.e.* a set of basis vectors specified as a transformation matrix (a' (211) b' (01-1) and c' (011) for the crystallographic basis vectors of the modified cif file of $[DPP]Ni(C_2N_3)_3$). This basis is chosen with real-space lattice vectors of the distorted structure in relation to the lattice vectors of the undistorted structure. In this case, the "nearest-site method" to match each atom of the parent structure to the nearest atom in the distorted structure failed. Therefore, the "more robust but slower method: $d_{max}$ = 3 Å" is chosen, mapping an atom in the

parent structure to every atom in the distorted structure within the chosen distance, *e.g.* here, 3 Å. The distortion page then appears, giving complete mode details with displacive mode amplitudes for each active irrep and an overall amplitude ($A_p$) normalised to the parent cell.[15,16]

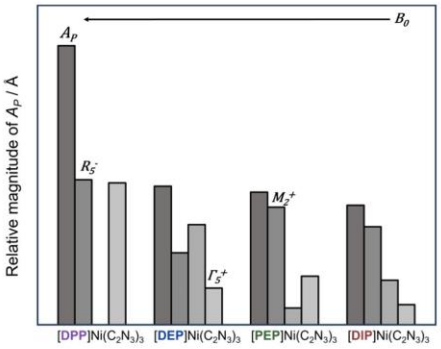


**Figure S75:** Relative magnitude of the overall parent-cell normalised amplitude ($A_p$) and the framework distortion modes with the largest amplitude associated with the irreducible representations (irreps) for conventional tilting ($R_5^-$ and $M_2^+$) and columnar shifts ($\Gamma_5^+$) derived from the mode decomposition analysis of the distorted [A]Ni($C_2N_3$)$_3$ structures along the series with varying $A^+$. The colour saturation corresponds to a higher magnitude within the respective primary order parameters.

**Table S22:** Group theoretical analysis of $AMX_3$ materials for the crystal structures obtained at 100 and 300 K, showing the strongest irreps from the left to right in order of decreasing relative magnitude and a possible set (not a unique set, one of several possible sets) of distortions accounting for the symmetry with the largest magnitude, giving the primary order parameters (POPs).

| Compounds | Temperature / K | Irreps | S.G. | *POPs* |
|---|---|---|---|---|
| [DIP]Ni($C_2N_3$)$_3$ | 100 | $R_5^- M_2^+ M_5^+ \Gamma_5^+ X_5^- \Gamma_4^+$ | $P2_1/c$ | $\Gamma_4^+ R_3^- X_2^-$ |
| [PEP]Ni($C_2N_3$)$_3$ | 100 | $R_5^- \Gamma_5^+ M_5^+ M_2^+ X_5^- \Gamma_4^+$ | $P2_1/c$ | $\Gamma_4^+ R_3^- X_2^-$ |
| [DEP]Ni($C_2N_3$)$_3$ | 100 | $M_2^+ R_5^- \Gamma_5^+ X_5^- M_5^+ \Gamma_4^+$ | $P2_1/c$ | $\Gamma_4^+ R_3^- X_2^-$ |
| [DPP]Ni($C_2N_3$)$_3$ | 100 | $\Gamma_4^+ R_5^- \Gamma_5^+$ | $C2/c$ | $\Gamma_4^+ R_3^-$ |
| [DIP]Ni($C_2N_3$)$_3$ | 300 | $R_5^- M_2^+ M_5^+ X_5^- \Gamma_5^+ \Gamma_4^+$ | $P2_1/c$ | $\Gamma_4^+ R_3^- X_2^-$ |
| [PEP]Ni($C_2N_3$)$_3$ | 300 | $R_5^- \Gamma_5^+ M_5^+ X_5^- M_2^+ \Gamma_4^+$ | $P2_1/c$ | $\Gamma_4^+ R_3^- X_2^-$ |
| [DEP]Ni($C_2N_3$)$_3$ | 300 | $M_2^+ R_5^- \Gamma_5^+ X_5^- M_5^+ \Gamma_4^+$ | $P2_1/c$ | $\Gamma_4^+ R_3^- X_2^-$ |
| [DPP]Ni($C_2N_3$)$_3$ | 300 | $\Gamma_4^+ R_5^- \Gamma_5^+$ | $C2/c$ | $\Gamma_4^+ R_3^-$ |

**Table S23:** Mode decomposition of the distorted [A]Ni($C_2N_3$)$_3$ structures (obtained from SCXRD of 100 K) with displacive mode amplitudes displaying the parent-cell normalised amplitude ($A_p$) for each active mode. Displacive modes are given in Angstrom units.

| | **[DIP]Ni($C_2N_3$)$_3$** | **[PEP]Ni($C_2N_3$)$_3$** | **[DEP]Ni($C_2N_3$)$_3$** | **[DPP]Ni($C_2N_3$)$_3$** |
|---|---|---|---|---|
| S.G. | *P2$_1$/c* | *P2$_1$/c* | *P2$_1$/c* | *C2/c* |
| $R_5^-$ | 1.67136 | 1.91172 | 1.17738 | 2.39294 |
| $M_2^+$ | 0.74040 | 0.33760 | 1.64960 | - |
| $\Gamma_4^+$ | 0.23561 | 0.12105 | 0.19103 | 2.86078 |
| $X_5^-$ | 0.37122 | 0.25950 | 0.56322 | - |
| $M_5^+$ | 0.69707 | 0.45264 | 0.44891 | - |
| $\Gamma_5^+$ | 0.42617 | 0.83306 | 0.60846 | 2.09049 |
| $A_p$ / Å | 2.08543 | 2.19858 | 2.27946 | 4.39524 |

**Table S24:** Mode decomposition of the distorted [A]Ni($C_2N_3$)$_3$ structures (obtained from SCXRD of 300 K) with displacive mode amplitudes displaying the parent-cell normalised amplitude ($A_p$) for each active mode. Displacive modes are given in Angstrom units.

| | **[DIP]Ni($C_2N_3$)$_3$** | **[PEP]Ni($C_2N_3$)$_3$** | **[DEP]Ni($C_2N_3$)$_3$** | **[DPP]Ni($C_2N_3$)$_3$** |
|---|---|---|---|---|
| S.G. | *P2$_1$/c* | *P2$_1$/c* | *P2$_1$/c* | *C2/c* |
| $R_5^-$ | 1.48752 | 1.78415 | 1.09421 | 2.20013 |
| $M_2^+$ | 0.67680 | 0.25480 | 1.51840 | - |
| $\Gamma_4^+$ | 0.10579 | 0.07128 | 0.14934 | 2.76733 |
| $X_5^-$ | 0.33173 | 0.29571 | 0.54472 | - |
| $M_5^+$ | 0.55209 | 0.31201 | 0.39960 | - |
| $\Gamma_5^+$ | 0.30552 | 0.73871 | 0.55841 | 2.15237 |
| $A_p$ / Å | 1.81201 | 2.01309 | 2.10231 | 4.23220 |

**Table S25:** Mode decomposition of the distorted $[Pr_3NMe]M(C_2N_3)_3$ structures with varying $M^{2+}$ (for SCXRD data of 300 K accessed from the CCDC) with displacive mode amplitudes displaying the parent-cell normalised amplitude ($A_p$) for each active mode. Displacive modes are given in Angstrom units.

| $[Pr_3NMe]M(C_2N_3)_3$ (reference[22]) | $Mn^{2+}$ | $Co^{2+}$ | $Ni^{2+}$ |
|---|---|---|---|
| CCDC number | 2068843 | 2068842 | 2068716 |
| S.G. | *Pnma* | *Pnma* | *Pnma* |
| $R_5^-$ | 1.68563 | 1.55756 | 1.50846 |
| $M_2^+$ | 1.02984 | 0.99776 | 0.97728 |
| $\Gamma_4^+$ | - | - | - |
| $X_5^-$ | 1.04105 | 0.90069 | 0.84449 |
| $M_5^+$ | - | - | - |
| $\Gamma_5^+$ | 0.65560 | 0.57760 | 0.54528 |
| *POP* | $R_5^-$ | $R_5^-$ | $R_5^-$ |
| $A_p$ / Å | 2.35863 | 2.16636 | 2.09184 |

**Table S26:** Mode decomposition of the distorted $[PEP]_{1-x}[DPP]_xNi(C_2N_3)_3$ structures (obtained from Rietveld refinement data at ambient pressure) with displacive mode amplitudes displaying the parent-cell normalised amplitude ($A_p$) for each active mode. Displacive modes are given in Angstrom units.

| ***x*** | **0.45** | **0.69** | **0.85** | **0.96** |
|---|---|---|---|---|
| S.G. | $P2_1/c$ | $P2_1/c$ | $P2_1/c$ | $P2_1/c$ |
| $R_5^-$ | 1.83227 | 1.97842 | 1.97021 | 2.70344 |
| $M_2^+$ | 0.40800 | 0.62800 | 0.04000 | 0.22400 |
| $\Gamma_4^+$ | 0.12445 | 0.16405 | 0.46386 | 0.09051 |
| $X_5^-$ | 0.64647 | 0.62405 | 0.57822 | 0.26242 |
| $M_5^+$ | 0.67090 | 0.68071 | 0.23786 | 0.51480 |
| $\Gamma_5^+$ | 0.92413 | 0.88532 | 1.25633 | 0.89385 |
| *POP* | $R_5^-$ | $R_5^-$ | $R_5^-$ | $R_5^-$ |
| $A_p$ / Å | 2.32350 | 2.46623 | 2.51368 | 2.93780 |

## 12. DFT calculations

All density functional theory (DFT) calculations were performed using the Gaussian16 software[23] at the B3LYP/6-311+G** level of theory to approximate the molecular geometry of $A^+$, *i.e.* molecular volumes ($V_{A+}$) and radius ($r_{A+}$), that were used in the model study of [A]Ni($C_2N_3$)$_3$ materials. Therefore, the polarisable continuum model (PCM) was used and we chose the simplified crystal structure data (of 300 K) of [A]Ni($C_2N_3$)$_3$ materials reduced to the atom coordinates of the organic $A^+$ molecules as a basis.

**Table S27:** DFT calculations using the PCM model based on SCXRD data from 300 K to describe the $A^+$ geometry and shape incorporated in the [A]Ni($C_2N_3$)$_3$ series, including the volume ($V^*_{A+}$), the surface ($S_{m,A+}$), the surface derived from the volume of sphere ($S_{sp,A+}$) and the globularity factor ($G' = S_{sp,A+}/S_{m,A+}$).

| $A^+$ | $[DIP]^+$ | $[PEP]^+$ | $[DEP]^+$ | $[DPP]^+$ |
|---|---|---|---|---|
| $V^*_{A+}$ / Å$^3$ | 270.986 | 242.984 | 235.791 | 271.266 |
| $S_{m,A+}$ / Å$^2$ | 241.078 | 234.653 | 219.225 | 259.426 |
| $S_{sp,A+}$ / Å$^2$ | 202.068 | 188.205 | 184.335 | 203.078 |
| $G'$ | 0.838 | 0.802 | 0.841 | 0.783 |

## 13. PASCal calculations

To verify the calculation of *B* as described in Chapter 9, we used the web-based tool PASCal to fit the HPPXRD data to a 2nd and 3rd order B-M equation of states.[24] The calculated *B* of $Ni(dmgH)_2$, *i.e.* *B* = 9.26±0.12 GPa (derived from 2nd order B-M equation of state fit) and *B* = 7.89±0.28 GPa (derived from 3rd order B-M equation of state fit) are in line with the obtained values as described in Chapter 10.

**Table S28:** Bulk moduli (*B*) calculated from 2nd and 3rd order B-M equation of state fits to the HPPXRD data using PASCal.

| | **[DIP]Ni($C_2N_3$)$_3$** | **[PEP]Ni($C_2N_3$)$_3$** | **[DEP]Ni($C_2N_3$)$_3$** | **[DPP]Ni($C_2N_3$)$_3$** |
|---|---|---|---|---|
| *B* (2nd) / GPa | 8.2 | 8.4 | 8.9 | 10.4 |
| *σB* (2nd) / GPa | 0.1 | 0.2 | 0.2 | 0.1 |
| $V_0$ (2nd) / Å$^3$ | 2156.9 | 2030.5 | 2025.5 | 2074.2 |
| $\sigma V_0$ (2nd) / Å$^3$ | 0.5 | 0.9 | 0.7 | 0.6 |
| *B* (3rd) / GPa | 7.8 | 6.7 | 7.4 | 9.3 |
| *σB* (3rd) / GPa | 0.3 | 0.8 | 0.5 | 0.5 |
| $V_0$ (3rd) / Å$^3$ | 2157.6 | 2032.6 | 2027.2 | 2075.5 |
| $\sigma V_0$ (3rd) / Å$^3$ | 0.7 | 1.5 | 0.9 | 0.8 |

**Table S29:** Bulk moduli ($B$) of the solid solutions calculated from 2nd and 3rd order B-M equation of state fits to the HPPXRD data using PASCal.

| ***x*** | **0.45** | **0.69** | **0.85** | **0.96** |
|---|---|---|---|---|
| $B$ ($2^{nd}$) / GPa | 9.0 | 9.4 | 9.7 | 9.6 |
| $\sigma B$ ($2^{nd}$) / GPa | 0.5 | 0.1 | 0.1 | 0.1 |
| $V_0$ ($2^{nd}$) / Å$^3$ | 2043.0 | 2052.8 | 2060.6 | 2072.4 |
| $\sigma V_0$ ($2^{nd}$) / Å$^3$ | 0.5 | 0.3 | 0.4 | 0.6 |
| $B$ ($3^{rd}$) / GPa | 7.9 | 9.2 | 9.0 | 9.5 |
| $\sigma B$ ($3^{rd}$) / GPa | 0.3 | 0.3 | 0.3 | 0.3 |
| $V_0$ ($3^{rd}$) / Å$^3$ | 2044.8 | 2053.1 | 2061.4 | 2072.4 |
| $\sigma V_0$ ($3^{rd}$) / Å$^3$ | 0.6 | 0.5 | 0.6 | 0.6 |

## 14. Data overview of $[A]Ni(C_2N_3)_3$ materials

**Table S30:** Crystallographic data of the $[A]Ni(C_2N_3)_3$ series at 100 and 300 K. Differences of the $A^+$ were captured by the volume ($V_{A+}$) enclosed by the "promolecule electron density isosurface" and the globularity factor ($G$) obtained by Crystal Explorer17 based on 300 K SCXRD data. Additionally, the volume ($V^*_{A+}$) and surface ($S_{m,A+}$) of all $A^+$ were determined using Gaussian16 based on 300 K SCXRD data. Here, the surface was derived from the spherical volume ($S_{sp,A+}$) to obtain a second globularity factor defined as ($G' = S_{sp,A+}/S_{m,A+}$) to provide a comprehensive data set of $A^+$'s size and shape. The overall parent-cell normalised amplitude ($A_p$), as determined from group theoretical analysis, is given based on 300 K SCXRD data. The calculated bulk moduli ($B$, calculated from 2nd and 3rd order B-M equation of state fits *via* EOSFit) and volumes ($V_0$ at zero pressure and temperature obtained from experimental HPPXRD) are given below.

| $[A]Ni(C_2N_3)_3$ | $A^+$ = $[DIP]^+$ | $[DEP]^+$ | $[PEP]^+$ | $[DPP]^+$ |
|---|---|---|---|---|
| $V_{A+}$ / Å$^3$ | 227.25 | 190.56 | 202.18 | 225.87 |
| $G$ | 0.872 | 0.879 | 0.831 | 0.807 |
| $V^*_{A+}$ / Å$^3$ | 270.986 | 235.791 | 242.984 | 271.266 |
| $S_{m,A+}$ / Å$^2$ | 241.078 | 219.225 | 234.653 | 259.426 |
| $S_{sp,A+}$ / Å$^2$ | 202.068 | 184.335 | 188.205 | 203.078 |
| $G'$ | 0.838 | 0.841 | 0.802 | 0.783 |
| T/ K | 100 | 100 | 100 | 100 |
| Space group | $P2_1/c$ | $P2_1/c$ | $P2_1/c$ | $C2/c$ |
| $a$ / Å | 16.1247(8) | 16.3161(17) | 16.3743(14) | 17.1198(15) |
| $b$ / Å | 11.9812(5) | 12.1389(13) | 11.9171(9) | 12.3344(10) |
| $c$ / Å | 10.8829(5) | 10.1679(11) | 10.4761(8) | 10.2007(9) |
| $\beta$ / ° | 95.986(2) | 101.691(3) | 105.903(4) | 110.800(3) |
| $V$ / Å$^3$ | 2091.04(17) | 1972.1(4) | 1966.0(3) | 2013.6(3) |
| $A_p$ / Å | 2.085 | 2.279 | 2.199 | 4.395 |
| T / K | 300 | 300 | 300 | 300 |
| Space group | $P2_1/c$ | $P2_1/c$ | $P2_1/c$ | $C2/c$ |
| $a$ / Å | 16.346(2) | 16.3871(7) | 16.4756(7) | 17.3196(5) |
| $b$ / Å | 12.0065(16) | 12.2076(5) | 11.9516(5) | 12.3357(3) |
| $c$ / Å | 11.0462(17) | 10.2673(4) | 10.6587(4) | 10.4909(3) |
| $\beta$ / ° | 93.708(6) | 100.250(2) | 104.9160(10) | 111.9170(10) |
| $V_{cell}$ / Å$^3$ | 2163.4(5) | 2021.16(14) | 2028.08(14) | 2079.38(10) |
| $A_p$ / Å | 1.812 | 2.102 | 2.013 | 4.232 |
| $B$ (2nd) / GPa | 8.2±0.1 | 8.8±0.2 | 8.5±0.1 | 10.5±0.2 |
| $V_0$ (2nd) / Å$^3$ | 2157.1±0.5 | 2025.9±0.2 | 2030.3±0.6 | 2073.8±0.6 |

| | | | | |
|---|---|---|---|---|
| $B$ ($3^{rd}$) / GPa | 7.1±0.2 | 7.5±0.5 | 7.3±0.6 | 9.0±0.5 |
| $V_0$ ($3^{rd}$) / Å$^3$ | 2158.5±0.5 | 2027.2±0.8 | 2031.1±0.7 | 2075.6±0.8 |

## 15. References


1 S. Burger, S. Kronawitter, H. L. B. Boström, J. K. Zaręba and G. Kieslich, *Dalton Trans.*, 2020, **49**, 10740–10744.
2 Bruker AXS Inc., Madison, Wisconsin, USA, *APEX suite of crystallographic software*, **2015**, SADABS, Version 2014/15.
3 Bruker AXS Inc., Madison, Wisconsin, USA, *APEX suite of crystallographic software*, 2015, APEX 3, Version 2015–5.2.
4 Bruker AXS Inc., Madison, Wisconsin, USA, *APEX suite of crystallographic software*, 2014, SAINT, Version 8.34A.
5 G. M. Sheldrick, *Acta Crystallogr. C Struct. Chem.*, 2015, **71**, 3–8.
6 G. M. Sheldrick, *Acta Cryst. A*, 2015, **71**, 3–8.
7 O. V. Dolomanov, L. J. Bourhis, R. J. Gildea, J. A. K. Howard and H. Puschmann, *J. Appl. Crystallogr.*, 2009, **42**, 339–341.
8 K. Momma and F. Izumi, *J. Appl. Crystallogr.*, 2011, **44**, 1272–1276.
9 G. R. Fulmer, A. J. M. Miller, N. H. Sherden, H. E. Gottlieb, A. Nudelman, B. M. Stoltz, J. E. Bercaw and K. I. Goldberg, *Organometallics*, 2010, **29**, 2176–2179.
10 A. A. Coelho, *J. Appl. Crystallogr.*, 2018, **51**, 210–218.
11 N. J. Brooks, B. L. L. E. Gauthe, N. J. Terrill, S. E. Rogers, R. H. Templer, O. Ces and J. M. Seddon, *Rev. Sci. Instrum.*, 2010, **81**, 64103.
12 S. Dissegna, P. Vervoorts, C. L. Hobday, T. Düren, D. Daisenberger, A. J. Smith, R. A. Fischer and G. Kieslich, *J. Am. Chem. Soc*, 2018, **140**, 11581–11584.
13 J. Filik, A. W. Ashton, P. C. Y. Chang, P. A. Chater, S. J. Day, M. Drakopoulos, M. W. Gerring, M. L. Hart, O. V. Magdysyuk, S. Michalik, A. Smith, C. C. Tang, N. J. Terrill, M. T. Wharmby and H. Wilhelm, *J. Appl. Crystallogr.*, 2017, **50**, 959–966.
14 G. S. Pawley, *J. Appl. Crystallogr.*, 1981, **14**, 357–361.
15 B. J. Campbell, H. T. Stokes, D. E. Tanner and D. M. Hatch, *J. Appl. Crystallogr.*, 2006, **39**, 607–614.
16 H. T. Stokes, D. M. Hatch, and B. J. Campbell, *ISODISTORT, ISOTROPY Software Suite, iso.byu.edu*.
17 J. Gonzalez-Platas, M. Alvaro, F. Nestola and R. Angel, *J. Appl. Crystallogr.*, 2016, **49**, 1377–1382.
18 I. F. Bruce-Smith, B. A. Zakharov, J. Stare, E. V. Boldyreva and C. R. Pulham, *J. Phys. Chem. C*, 2014, **118**, 24705–24713.
19 K. Takeda, J. Hayashi, I. Shirotani, H. Fukuda and K. Yakushi, *Mol. Cryst. Liq.*, 2006, **460**, 131–144.
20 D. E. Williams, G. Wohlauer and R. E. Rundle, *J. Am. Chem. Soc*, 1959, **81**, 755–756.
21 K. Takeda, T. Sasaki, J. Hayashi, S. Kagami, I. Shirotani and K. Yakushi, *J. Phys.: Conf. Ser.*, 2010, **215**, 12065.
22 S. Burger, S. Grover, K. T. Butler, H. L. B. Boström, R. Grau-Crespo and G. Kieslich, *Mater. Horiz.*, 2021, **8**, 2444–2450.
23 M. J. Frisch, G. W. Trucks and H. B. Schlegel, *Gaussian 16 Rev. B.01*, Wallingford, CT, 2016.
24 M. J. Cliffe and A. L. Goodwin, *J. Appl. Crystallogr.*, 2012, **45**, 1321–1329.

2 Bruker AXS Inc., Madison, Wisconsin, USA, *APEX suite of crystallographic software*, **2015**, SADABS, Version 2014/15.
3 Bruker AXS Inc., Madison, Wisconsin, USA, *APEX suite of crystallographic software*, 2015, APEX 3, Version 2015–5.2.
4 Bruker AXS Inc., Madison, Wisconsin, USA, *APEX suite of crystallographic software*, 2014, SAINT, Version 8.34A.
5 G. M. Sheldrick, *Acta Crystallogr. C Struct. Chem.*, 2015, **71**, 3–8.
6 G. M. Sheldrick, *Acta Cryst. A*, 2015, **71**, 3–8.
7 O. V. Dolomanov, L. J. Bourhis, R. J. Gildea, J. A. K. Howard and H. Puschmann, *J. Appl. Crystallogr.*, 2009, **42**, 339–341.
8 K. Momma and F. Izumi, *J. Appl. Crystallogr.*, 2011, **44**, 1272–1276.
9 G. R. Fulmer, A. J. M. Miller, N. H. Sherden, H. E. Gottlieb, A. Nudelman, B. M. Stoltz, J. E. Bercaw and K. I. Goldberg, *Organometallics*, 2010, **29**, 2176–2179.
10 A. A. Coelho, *J. Appl. Crystallogr.*, 2018, **51**, 210–218.
11 N. J. Brooks, B. L. L. E. Gauthe, N. J. Terrill, S. E. Rogers, R. H. Templer, O. Ces and J. M. Seddon, *Rev. Sci. Instrum.*, 2010, **81**, 64103.
12 S. Dissegna, P. Vervoorts, C. L. Hobday, T. Düren, D. Daisenberger, A. J. Smith, R. A. Fischer and G. Kieslich, *J. Am. Chem. Soc*, 2018, **140**, 11581–11584.
13 J. Filik, A. W. Ashton, P. C. Y. Chang, P. A. Chater, S. J. Day, M. Drakopoulos, M. W. Gerring, M. L. Hart, O. V. Magdysyuk, S. Michalik, A. Smith, C. C. Tang, N. J. Terrill, M. T. Wharmby and H. Wilhelm, *J. Appl. Crystallogr.*, 2017, **50**, 959–966.
14 G. S. Pawley, *J. Appl. Crystallogr.*, 1981, **14**, 357–361.
15 B. J. Campbell, H. T. Stokes, D. E. Tanner and D. M. Hatch, *J. Appl. Crystallogr.*, 2006, **39**, 607–614.
16 H. T. Stokes, D. M. Hatch, and B. J. Campbell, *ISODISTORT, ISOTROPY Software Suite, iso.byu.edu*.
17 J. Gonzalez-Platas, M. Alvaro, F. Nestola and R. Angel, *J. Appl. Crystallogr.*, 2016, **49**, 1377–1382.
18 I. F. Bruce-Smith, B. A. Zakharov, J. Stare, E. V. Boldyreva and C. R. Pulham, *J. Phys. Chem. C*, 2014, **118**, 24705–24713.
19 K. Takeda, J. Hayashi, I. Shirotani, H. Fukuda and K. Yakushi, *Mol. Cryst. Liq.*, 2006, **460**, 131–144.
20 D. E. Williams, G. Wohlauer and R. E. Rundle, *J. Am. Chem. Soc*, 1959, **81**, 755–756.
21 K. Takeda, T. Sasaki, J. Hayashi, S. Kagami, I. Shirotani and K. Yakushi, *J. Phys.: Conf. Ser.*, 2010, **215**, 12065.
22 S. Burger, S. Grover, K. T. Butler, H. L. B. Boström, R. Grau-Crespo and G. Kieslich, *Mater. Horiz.*, 2021, **8**, 2444–2450.
23 M. J. Frisch, G. W. Trucks and H. B. Schlegel, *Gaussian 16 Rev. B.01*, Wallingford, CT, 2016.
24 M. J. Cliffe and A. L. Goodwin, *J. Appl. Crystallogr.*, 2012, **45**, 1321–1329.

## 4.5. Source Data for Literature Survey of Molecular Perovskites

To place both studies (*Chapters 2.1* and *2.4*) on Molecular Perovskites into a broader context, this thesis aims to provide a comprehensive literature overview of various Molecular Perovskite structures reported to date. In the following, different Molecular Perovskite subclasses (grouped by the X-site linker) are presented and listed by the organic A-site cations. Additionally, the tables include the space group and year of publication of the structures corresponding to the given reference. Since the $[A]B(C_2N_3)_3$ subclass has been in the focus of this thesis, a more detailed survey is given below.

**Table columns (in order):** References, Year, $[A]B(C_2N_3)_3$ Materials, Organic $A^+$ Cation, Polar Space group? (Yes / No), Phase Transition? (Yes / No), Melting? (Yes / No), Special Feature.

| | | | | | | | |
|---|---|---|---|---|---|---|---|
| [46] | 2020 | $[ASU]Cd(C_2N_3)_3$ | azaspiroundecanium | Yes (*Pna*$2_1$ 100 K) | Yes (irrev. 328 K, rev. 293 K) | n. a. | SHG active |
| [47] | 2003 | $[BeTriBu]B(C_2N_3)_3$ (B = $Mn^{2+}$, $Co^{2+}$) | benzyltributylammonium | No (*Pnma* RT) | n. a. | n. a. | n. a. |
| [47] | 2003 | $[BeTriEt]B(C_2N_3)_3$ (B = $Mn^{2+}$, $Fe^{2+}$) | benzyltriethylammonium | No (*Pnma* RT) | n. a. | n. a. | n. a. |
| [48] | 2005 | $[Cp^*_2Co]B(C_2N_3)_3$ (B = $Mn^{2+}$, $Co^{2+}$, $Ni^{2+}$) | decamethylcobaltoceniu m | No (*Im*-3 123 K) | n. a. | n. a. | n. a. |
| [48] | 2005 | $[Cp^*_2Fe]B(C_2N_3)_3$ (B = $Mn^{2+}$, $Fe^{2+}$, $Co^{2+}$, $Ni^{2+}$, $Cd^{2+}$) | decamethylferrocenium | No (*Im*-3 123 K) | n. a. | n. a. | n. a. |
| [142] | 2024 | $[DEP]Ni(C_2N_3)_3$ | diethylpiperidinium | No ($P2_1/c$ RT) | Yes (rev. 313, 527 K) | n. a. | n. a. |
| [142] | 2024 | $[DIP]Ni(C_2N_3)_3$ | diisopropylpiperidinium | No ($P2_1/c$ RT) | Yes (rev. 434 K) | n. a. | n. a. |
| [142] | 2024 | $[DPP]Ni(C_2N_3)_3$ | dipropylpiperidinium | No ($C2/c$ RT) | Yes (rev. 433 K) | n. a. | n. a. |
| [196] | 2017 | $[Et_3(CH_2CHCH_2)P]Mn(C_2N_3)_3$ | allyltriethylphosphonium | No ($P2_1/c$ RT) | Yes (rev. 350 K) | n. a. | n. a. |
| [180] | 2018 | $[Et_3P(CH_2)_2Cl]Cd(C_2N_3)_3$ | triethyl-(2-chloro-ethyl)-phosphonium | No ($P2_12_12_1$ RT) | Yes (rev. 320, 374 K) | n. a. | switchable dielectric behaviour |
| [180] | 2018 | $[Et_3P(CH_2)_2F]Cd(C_2N_3)_3$ | triethyl-(2-fluoro-ethyl)-phosphonium | No ($C2/c$ RT) | Yes (rev. 357, 428 K) | n. a. | ferroelastic, switchable dielectric behaviour |
| [196] | 2017 | $[Et_3(CH_2OCH_3)P]Mn(C_2N_3)_3$ | triethylmethoxy-methylphosphonium | No ($P2_12_12_1$ RT) | Yes (rev. 265, 333 K) | n. a. | switchable NLO |
| [197] | 2017 | $[Et_3(n\text{-}Pr)P]Cd(C_2N_3)_3$ | propyltriethylphosphoniu m | No ($P2_12_12_1$ RT) | Yes (rev. 270, 386, | n. a. | switchable NLO, PL active |

| | | | | | | | |
|---|---|---|---|---|---|---|---|
| | | | | | 415 K) | | |
| [196] | 2017 | $[Et_3(n\text{-}Pr)P]Mn(C_2N_3)_3$ | propyltriethylphosphonium | No ($P2_12_12_1$ RT) | Yes (rev. 363 K) | n. a. | switchable NLO |
| [90] | 2021 | $[Et_4P]Mn(C_2N_3)_3$ | tetraethylphosphonium | No ($P2_12_12_1$ RT) | Yes (irrev. 313 K and rev. 407, 476, 486 K) | n. a. | two ferroelectric transitions |
| [178] | 2020 | $[Pr_3(CH_2CHOHCH_3)N]Mn(C_2N_3)_3$ | (2-hydroxy-propyl)-tripropyl-ammonium | Yes ($P$-$42_1c$ 143 K) | Yes (rev. 207 K) | n. a. | n. a. |
| [178] | 2020 | $[Pr_3(CH_3CHCH_2OH)N]Mn(C_2N_3)_3$ | (2-hydroxy-1-methyl–ethyl)-tripropyl-ammonium | Yes ($Pna2_1$ 193 K) No ($P2_12_12_1$ 282 K) | Yes (rev. 267, 287, 331 K) | n. a. | ferroelastic, two-step switchable NLO |
| [198] | 2004 | $[SPh_3]Mn(C_2N_3)_3$ | triphenylsulfonium | No ($P2_1/c$ RT) | n. a. | n. a. | spin canted antiferromagnet |
| [87] | 2019 | $[TriBuMeN]Co(C_2N_3)_3$ | tributylmethylammonium | No ($P2_1/n$ RT) | No | Yes 389 K | paramagnet |
| [87] | 2019 | $[TriBuMeN]Fe(C_2N_3)_3$ | tributylmethylammonium | No ($P2_1/n$ RT) | Yes (rev. 399 K) | Yes 409 K | paramagnet |
| [87] | 2019 | $[TriBuMeN]Mn(C_2N_3)_3$ | tributylmethylammonium | No ($P2_1/n$ RT) | Yes (irrev. 384 K) | Yes 404 K | paramagnet and orange emission |
| [87] | 2019 | $[TriBuMeN]Ni(C_2N_3)_3$ | tributylmethylammonium | No ($P2_1/n$ RT) | Yes (rev. 394 K) | Yes 434 K | paramagnet |
| [90] | 2021 | $[TriBuMeP]Mn(C_2N_3)_3$ | tributylmethylphosphonium | No ($P2_1/n$ RT) | Yes (irrev. 348 K and rev. 410 K) | n. a. | ferroelectric transition |
| [85] | 2021 | $[TriPrMeN]Co(C_2N_3)_3$ | tripropylmethylammonium | No (*Pnma* RT) | Yes (irrev. 359 K, rev. 301 K) | n. a. | polymorphism |
| [85] | 2021 | $[TriPrMeN]Mn(C_2N_3)_3$ | tripropylmethylammonium | No (*Pnma* RT) | Yes (irrev. 350 K, rev. 284 K) | n. a. | polymorphism |
| [85] | 2021 | $[TriPrMeN]Ni(C_2N_3)_3$ | tripropylmethylammonium | No (*Pnma* RT) | Yes (irrev. 365 K, rev. 312 K) | n. a. | polymorphism |
| [142] | 2024 | $[PEP]Ni(C_2N_3)_3$ | ethylpropylpiperidinium | No ($P2_1/c$ RT) | Yes (rev. | n. a. | n. a. |

| | | | | | | | |
|---|---|---|---|---|---|---|---|
| | | | | | 401 K) | | |
| [102] | 2023 | $[Pr_3NBu]Mn(C_2N_3)_3$ | tripropylbutylammonium | No (*Pbcn* RT) | Yes (irrev. 368 K) | *Yes 474 K | melting |
| [59] | 2018 | $[Pr_4N]Cd(C_2N_3)_3$ | tetrapropylammonium | Yes (*P*-42$_1$*c* RT) | Yes (rev. 242, 363, 387 K) | n. a. | barocaloric |
| [62] *[101] | 2016 | $[Pr_4N]Co(C_2N_3)_3$ | tetrapropylammonium | Yes (*P*-42$_1$*c* 200 K) | Yes (rev. 246, 301, 341 K) | *Yes 503 K | dielectric transition |
| [62] *[101] | 2016 | $[Pr_4N]Fe(C_2N_3)_3$ | tetrapropylammonium | Yes (*P*-42$_1$*c* 200 K) | Yes (rev. 286, 300, 331 K) | *Yes 536 K | dielectric transition |
| [36] *[101] **[41] | 2005 | $[Pr_4N]Mn(C_2N_3)_3$ | tetrapropylammonium | Yes (*P*-42$_1$*c* RT) | Yes (rev. 332 K) | *Yes 544 K | dielectric transition, **barocaloric |
| [36] *[62] | 2005 | $[Pr_4N]Ni(C_2N_3)_3$ | tetrapropylammonium | Yes (*P*-42$_1$*c* 160 K) | Yes (rev. 216, 302, 356 K) | n. a. | *dielectric transition |

**Table columns (in order):** References, Year, $[A]B(N_3)_3$ Materials, Organic $A^+$ Cation, Space group (***polar***).

| | | | | |
|---|---|---|---|---|
| [199] | 2017 | $[CPrN]Mn(N_3)_3$ | cyclopropylammonium | *Pbca* 296 K |
| [200] | 1986 | $[Et_4N]Ca(N_3)_3$ | tetraethylammonium | *P*2/*m* 293 K |
| [201] | 2013 | $[MeN]Mn(N_3)_3$ | methylammonium | *P*2$_1$/*c* 173 - 320 K |
| [202] | 2019 | $[Me_2EtN]Mn(N_3)_3$ | dimethylethylammonium | ***Cc*** 296 K |
| [203] | 2014 | $[Me_2N]Cd(N_3)_3$ | dimethylammonium | *P-1* 296 K *R*-3 203 - 273 K |
| [201] | 2013 | $[Me_2N]Mn(N_3)_3$ | dimethylammonium | ***P*2$_1$** 173 K *Cmca* 323 K |
| [204] | 2015 | $[Me_3N]Cd(N_3)_3$ | trimethylammonium | *P*2$_1$/*c* 283 K *C*2/*c* 348 K |
| [201] | 2013 | $[Me_3N]Mn(N_3)_3$ | trimethylammonium | *P*2$_1$/*c* 173 - 298 K *C*2/*c* 330 - 350 K *R*-3*m* 360 - 393 K |
| [205] | 1988 | $[Me_4N]Ca(N_3)_3$ | tetramethylammonium | *P*4/*nmm* RT |
| [35,206] | 2000 | $[Me_4N]Cd(N_3)_3$ | tetramethylammonium | *C*2/*c* 220 K *P*2$_1$/*m* 300 K *Pm*-3/*m* 350 K |
| [201] | 2013 | $[Me_4N]Mn(N_3)_3$ | tetramethylammonium | *P*2$_1$/*m* 173 K *Pm*-3*m* 333 K |

**Table columns (in order):** References, Year, $[A]B(BX_4)_3$ Materials with $BX_4$ = BH – borohydride or BF – tetrafluoroborate, Organic $A^+$ Cation, Space group.

| | | | | |
|---|---|---|---|---|
| [207] | 2019 | $[H_2dabco]Na(BF_4)_3$ | dabconium | *Pa*-3 293 K *Pm*-3*m* 408 K |
| [208] | 2017 | $[H_2dabco]K(BF_4)_3$ | dabconium | *Pa*-3 293 K |
| [208] | 2017 | $[H_2pz]Na(BF_4)_3$ | piperazinium | *P*4$_3$ 293 K |
| [208] | 2021 | $[MedabcoF]Rb(BF_4)_3$ | fluoromethyldabconium | *P*2$_1$/*c* 168 K *P*4$_2$/*mbc* 253 K *Fm*-3*c* 315 K *Pm*-3*m* 353 K |
| [209] | 2015 | $[NH_4]Ca(BH_4)_3$ | ammonium | *Pm*-3*m* RT |

**Table columns (in order):** References, Year, $[A]_2BB'(CN)_6$ Materials, Organic $A^+$ Cation, Space group (***polar***).

| | | | | |
|---|---|---|---|---|
| [210] | 2016 | $[Ac]_2KFe(CN)_6$ | acetamidinium | *C*2/*m* 150 K *R*-3*m* RT *Fm*-3*m* 395 K |
| [211] | 2016 | $[Az]_2KCo(CN)_6$ | azetidinium | *Fm*-3*m* 113 K |
| [210] | 2016 | $[Gua]_2KFe(CN)_6$ | guanidinium | *R*-3*c* RT *R*-3*m* 425 K *Fm*-3*m* 455 K |
| [212] | 2015 | $[Im]_2KCo(CN)_6$ | imidazolium | *R*-3*m* 293 K |
| [213] | 2010 | $[Im]_2KFe(CN)_6$ | imidazolium | *C*2/*c* 83 K *R*-3*m* 173, 293 K |
| [214] | 2013 | $[Me_2N]_2KCo(CN)_6$ | dimethylammonium | *P*4/*mnc* 113, 280, 293 K |
| [215] | 2015 | $[Me_2N]_2KFe(CN)_6$ | dimethylammonium | *P*4/*mnc* 165 K, RT |
| [216] | 2019 | $[Me_2N]_2KCr(CN)_6$ | dimethylammonium | *P*4/*mnc* 140, 230 K |
| [217] | 2016 | $[MeN]_2KCo(CN)_6$ | methylammonium | *C*2/*c* 293 K *Fm*-3*m* 463 K |
| [215] | 2016 | $[MeN]_2KFe(CN)_6$ | methylammonium | *C*2/*c* 193 K *Fm*-3*m* 443 K |
| [217] | 2016 | $[MeN]_2NaCo(CN)_6$ | methylammonium | *Fm*-3*m* 293 K |
| [218] | 1994 | $[MeN]_2NaFe(CN)_6$ | methylammonium | *Fm*-3*m* 295 K |
| [217] | 2016 | $[MeN]_2RbCo(CN)_6$ | methylammonium | *C*2/*c* 293 K |
| [219] | 2018 | $[Me_3N]_2KFe(CN)_6$ | trimethylammonium | *C*2/*c* 113 K *Fm*-3*m* 350 K |
| [220] | 2022 | $[Me_3FMeN]_2KFe(CN)_6$ | trimethylfluoromethylammonium | *C*2/*c* 243 K |
| [221] | 2020 | $[Me_3NOH]_2KCo(CN)_6$ | trimethylhydroxylammonium | ***Cc*** @ 100 K *Fm*-3*m* 440 K |
| [163] | 2017 | $[Me_3NOH]_2KFe(CN)_6$ | trimethylhydroxylammonium | ***Cc*** @ RT *Fm*-3*m* 408 K |
| [218] | 1994 | $[Me_4N]_2CsCo(CN)_6$ | tetramethylammonium | *I*2/*m* 295 K |
| [222] | 2000 | $[Me_4N]_2CsCr(CN)_6$ | tetramethylammonium | *C*2/*c* RT |
| [222] | 2000 | $[Me_4N]_2KCr(CN)_6$ | tetramethylammonium | *Fm*-3*m* RT |
| [215] | 2016 | $[Me_4N]_2KFe(CN)_6$ | tetramethylammonium | *I*4/*m* RT *Fm*-3*m* 373 K |
| [223] | 1997 | $[Me_4N]_2RbCr(CN)_6$ | tetramethylammonium | *R*-3*m* RT |
| [223] | 1997 | $[Me_4N]_2RbFe(CN)_6$ | tetramethylammonium | *R*-3*m* RT |
| [223] | 1997 | $[Me_4N]_2TlCr(CN)_6$ | tetramethylammonium | *R*-3*m* RT |
| [223] | 1997 | $[Me_4N]_2TlFe(CN)_6$ | tetramethylammonium | *C*2/*c* RT |

**Table columns (in order):** References, Year, $[A]B(M(CN)_2)_3$ with $M(CN)_2$ = Au – dicyanoaurates, Organic $A^+$ Cation, Space group.

| | | | | |
|---|---|---|---|---|
| [65] | 2016 | $[PPN]Cd(Au(CN)_2)_3$ | bistriphenlyphosphineiminium | *I*2/*a* 291 K |
| [224] | 2007 | $[PPN]Co(Au(CN)_2)_3$ | bistriphenlyphosphineiminium | *R*-3*c* RT |
| [65] | 2016 | $[PPN]Mn(Au(CN)_2)_3$ | bistriphenlyphosphineiminium | *I*2/*a* 150 K |
| [224] | 2007 | $[PPN]Ni(Au(CN)_2)_3$ | bistriphenlyphosphineiminium | *R*-3*c* RT |

**Table columns (in order):** References, Year, $[A]B(HCOO)_3$ Materials, Organic $A^+$ Cation, Space group (***polar***).

| | | | | |
|---|---|---|---|---|
| [225] | 2017 | $[Ac]Mn(HCOO)_3$ | acetamidinium | $P2_1/n$ 100 K *Imma* 320 K |
| [226] | 2011 | $[Az]Cu(HCOO)_3$ | azetidinium | $P2_1/c$ 123, 280, 243, 260 K *Pnma* 300, 333 K |
| [34] | 2004 | $[Az]Mn(HCOO)_3$ | azetidinium | $P2_1/c$ 180 K, *Pnma* 290 K |
| [227] | 2012 | $[Az]Zn(HCOO)_3$ | azetidinium | *Pnma* RT |
| [228] | 2011 | $[DMe_2N]Co(DCOO)_3$ | perdeuterodimethylammonium | ***Cc*** 93 K, *R*-3*c* 293, 373 K |
| [229] | 2015 | $[EtN]Cu(HCOO)_3$ | ethylammonium | $Pna2_1$ 93, 180, 291, 320, 340 K $P2_12_12_1$ 360 K |
| [230] | 2014 | $[EtN]Mg(HCOO)_3$ | ethylammonium | $Pna2_1$ 93, 280, 292, 363 K *R*-3 378 K *Imma* 430 K |
| [34] | 2004 | $[EtN]Mn(HCOO)_3$ | ethylammonium | $Pna2_1$ 180, 290 K |

| | | | | |
|---|---|---|---|---|
| [231] | 2016 | $[EtN]Na_{0.5}Al_{0.5}(HCOO)_3$ | ethylammonium | *Pn* 270 K $P2_1/n$ 375 K |
| [231] | 2016 | $[EtN]Na_{0.5}Al_{0.475}Cr_{0.025}(HCOO)_3$ | ethylammonium | *Pn* RT |
| [231] | 2016 | $[EtN]Na_{0.5}Cr_{0.5}(HCOO)_3$ | ethylammonium | *Pn* 297 K $P2_1/n$ 400 K |
| [232] | 2015 | $[EtN]Na_{0.5}Fe_{0.5}(HCOO)_3$ | ethylammonium | *Pn* 297 K $P2_1/n$ 377 K |
| [233] | 2015 | $[Fmd]Co(HCOO)_3$ | formamidinium | *Pnna* 295 K |
| [234] | 2017 | $[Fmd]Cu(HCOO)_3$ | formamidinium | *Pnna* 173 K |
| [233] | 2015 | $[Fmd]Fe(HCOO)_3$ | formamidinium | *Pnna* 294 K |
| [235] | 2012 | $[Fmd]Mg(HCOO)_3$ | formamidinium | *Pnna* 120 K |
| [236] | 2014 | $[Fmd]Mn(HCOO)_3$ | formamidinium | *C*2/*c* 110, 295 K *R*-3*c* 355 K |
| [237] | 1986 | $[Fmd]Zn(HCOO)_3$ | formamidinium | *Pnna* 295 K |
| [238] | 2009 | $[Gua]Co(HCOO)_3$ | guanidinium | *Pnna* 293 K |
| [238] | 2009 | $[Gua]Cu(HCOO)_3$ | guanidinium | ***Pna*2$_1$** 293 K |
| [239] | 2016 | $[Gua]Cd(HCOO)_3$ | guanidinium | *R*-3*c* 150, 250, 300, 450 K |
| [238] | 2009 | $[Gua]Fe(HCOO)_3$ | guanidinium | *Pnna* 293 K |
| [235] | 2012 | $[Gua]Mg(HCOO)_3$ | guanidinium | *Pnna* 298 K |
| [238] | 2009 | $[Gua]Mn(HCOO)_3$ | guanidinium | *Pnna* 293 K |
| [238] | 2009 | $[Gua]Ni(HCOO)_3$ | guanidinium | *Pnna* 293 K |
| [238] | 2009 | $[Gua]Zn(HCOO)_3$ | guanidinium | *Pnna* 293 K |
| [240] | 2016 | $[Im]Mg(HCOO)_3$ | imidazolium | $P2_1/n$ 296 K |
| [241] | 2013 | $[Im]Mn(HCOO)_3$ | imidazolium | $P2_1/n$ 293 K $P\text{-}42_1m$ 453 K |
| [242] | 2017 | $[Hym]Co(HCOO)_3$ | hydrazinium | ***Pna*2$_1$** 100, 298 K *Pnma* 353, 393 K |
| [243] | 2016 | $[Hym]Fe(HCOO)_3$ | hydrazinium | ***Pna*2$_1$** 290 K *Pnma* 360 K |
| [244] | 2014 | $[Hym]Mg(HCOO)_3$ | hydrazinium | $P2_12_12_1$ 110, 200, 292 K $P6_3$ 400 K |
| [244] | 2014 | $[Hym]Mn(HCOO)_3$ | hydrazinium | ***Pna*2$_1$** 110, 200, 290 K *Pnma* 400 K |
| [244] | 2014 | $[Hym]Zn(HCOO)_3$ | hydrazinium | ***Pna*2$_1$** 110, 200, 290 K *Pnma* 375 K |
| [245] | 2021 | $[Me_2Hym]Mn(HCOO)_3$ | dimethylhydrazinium | $P2_1/n$ 99.9, 299.9 K |
| [246] | 2017 | $[MeHym]Fe(HCOO)_3$ | methylhydrazinium | *R*-3*c* 200, 280, 330 K |
| [246] | 2017 | $[MeHym]Mg(HCOO)_3$ | methylhydrazinium | *R*-3*c* 240, 280, 345 K |
| [246] | 2017 | $[MeHym]Mn(HCOO)_3$ | methylhydrazinium | ***P*1** 100 K *R*-3*c* 230, 290, 330 K |
| [246] | 2017 | $[MeHym]Zn(HCOO)_3$ | methylhydrazinium | *R*-3*c* 180, 300, 350 K |
| [247] | 2010 | $[Me_2N]Cd(HCOO)_3$ | dimethylammonium | *R*-3*c* 293 K |
| [248] | 2004 | $[Me_2N]Co(HCOO)_3$ | dimethylammonium | *R*-3*c* 297 K |
| [249] | 1973 | $[Me_2N]Cu(HCOO)_3$ | dimethylammonium | *I*2/*c* 295 K |
| [49] | 2009 | $[Me_2N]Fe(HCOO)_3$ | dimethylammonium | *R*-3*c* 273 K |
| [250] | 2008 | $[Me_2N]Mg(HCOO)_3$ | dimethylammonium | *R*-3*c* 293 K |
| [34] | 2004 | $[Me_2N]Mn(HCOO)_3$ | dimethylammonium | *R*-3*c* 180, 290 K |
| [251] | 2015 | $[Me_2N]Na_{0.5}Cr_{0.5}(HCOO)_3$ | dimethylammonium | *R*-3 115, 302 K |
| [252] | 2014 | $[Me_2N]Na_{0.5}Fe_{0.5}(HCOO)_3$ | dimethylammonium | *R*-3 115, 293 K |
| [248] | 2004 | $[Me_2N]Ni(HCOO)_3$ | dimethylammonium | *P*-1 110 K *R*-3*c* 297 K |
| [44] | 2008 | $[Me_2N]Zn(HCOO)_3$ | dimethylammonium | *R*-3*c* 273 K |
| [245] | 2021 | $[Me_2Hym]Mn(HCOO)_3$ | dimethylhydrazinium | $P2_1/n$ 100, 300 K |
| [253] | 2016 | $[MeN]Co(HCOO)_3$ | methylammonium | *Pnma* 100 K |
| [239] | 2016 | $[MeN]Cd(HCOO)_3$ | methylammonium | *Pnma* RT |
| [239] | 2016 | $[MeN]Fe(HCOO)_3$ | methylammonium | *Pnma* RT |
| [239] | 2016 | $[MeN]Mg(HCOO)_3$ | methylammonium | *Pnma* RT |
| [34] | 2004 | $[MeN]Mn(HCOO)_3$ | methylammonium | *Pnma* 180, 290 K |

| | | | | |
|---|---|---|---|---|
| [239] | 2016 | [MeN]Zn(HCOO)$_3$ | methylammonium | *Pnma* RT |
| [254] | 2014 | [Me$_4$N]Mn(HCOO)$_3$ | tetramethylammonium | *Pnma* RT |
| [75,255] | 1983 | [NH$_4$]Cd(HCOO)$_3$ | ammonium | ***Pna2$_1$*** 100, 295, 350 K |
| [254] | 2014 | [NH$_4$]Mn(HCOO)$_3$ | ammonium | *Im-3* RT |

**Table columns (in order):** References, Year, [A]B(H$_2$POO)$_3$ Materials, Organic A$^+$ Cation, Space group (***polar***).

| | | | | |
|---|---|---|---|---|
| [88] | 2017 | [Fmd]Mn(H$_2$POO)$_3$ | formamidinium | *P*2$_1$/*c* 115 K *C*2/*c* RT |
| [256] | 2022 | [Gua]Cd(H$_2$POO)$_3$ | guanidinium | *R*-3*c* 293 K |
| [256] | 2022 | [Gua]Co(H$_2$POO)$_3$ | guanidinium | *I*2/*m* 293 K |
| [88] | 2017 | [Gua]Mn(H$_2$POO)$_3$ | guanidinium | *I*2/*m* 298 K *P*-1 302 K |
| [256] | 2022 | [Im]Cd(H$_2$POO)$_3$ | imidazolium | *P*2$_1$/*c* RT |
| [256] | 2022 | [Im]Co(H$_2$POO)$_3$ | imidazolium | *Pbca* 295 K |
| [88] | 2017 | [Im]Mn(H$_2$POO)$_3$ | imidazolium | *P*2$_1$/*c* RT |
| [257] | 2020 | [MeHym]Mn(HCOO)$_3$ | methylhydrazinium | *Pnma* 100, 295 K |
| [61] | 2018 | [Me$_2$N]Mn(H$_2$POO)$_3$ | dimethylammonium | *P*2$_1$/*c* RT |
| [256] | 2022 | [Pyr]Cd(H$_2$POO)$_3$ | pyrrolidinium | ***Aea2*** 295 K |
| [88] | 2017 | [Trz]Mn(H$_2$POO)$_3$ | triazolium | *P*2$_1$/*c* RT |

**Table columns (in order):** References, Year, [A]$_2$BB'(SCN)$_6$ / [A]B(SCN)$_3$ Materials, Organic A$^+$ Cation, Space group.

| | | | | |
|---|---|---|---|---|
| [258] | 2021 | [Me$_2$N]$_2$CdNi(SCN)$_6$ | dimethylammonium | *P*-1 293 K |
| [258] | 2021 | [Me$_2$N]$_2$CdMn(SCN)$_6$ | dimethylammonium | *P*-1 293 K |
| [258] | 2021 | [Me$_3$S]Cd(SCN)$_3$ | trimethylsulfonium | *Pa*-3 RT |
| [259] | 2016 | [NH$_4$]$_2$CdNi(SCN)$_6$ | ammonium | *P*2$_1$/*c* 90 K, RT |

**Table columns (in order):** References, Year, [A]B(ClO$_4$)$_3$ Materials, Organic A$^+$ Cation, Space group.

| | | | | |
|---|---|---|---|---|
| [208] | 2017 | [H$_2$dabco]K(ClO$_4$)$_3$ | dabconium | *Pa*-3 293 K |
| [208] | 2017 | [H$_2$dabco]Na(ClO$_4$)$_3$ | dabconium | *Pa*-3 293 K |
| [260] | 2018 | [H$_2$dabco]Rb(ClO$_4$)$_3$ | dabconium | *Pa*-3 293 K |
| [261] | 2018 | [H$_2$dabcoO]K(ClO$_4$)$_3$ | hydroxydabconium | *P*2$_1$/*c* 223 K *Fm*-3*c* RT |
| [262] | 2017 | [H$_2$hpz]K(ClO$_4$)$_3$ | homopiperazinium | *Pbca* RT |
| [208] | 2017 | [H$_2$pz]Na(ClO$_4$)$_3$ | piperazinium | *P*2$_1$/*c* RT, 378 K |

# 5. REFERENCES


1 C. L. Hobday and G. Kieslich, *Dalton Trans.*, 2021, **50**, 3759–3768.

2 A. K. Cheetham, C. N. R. Rao and R. K. Feller, *Chem. Commun.*, 2006, 4780–4795.

3 O. M. Yaghi, H. Li, C. Davis, D. Richardson and T. L. Groy, *Acc. Chem. Res.*, 1998, **31**, 474–484.

4 W. Li, Z. Wang, F. Deschler, S. Gao, R. H. Friend and A. K. Cheetham, *Nat. Rev. Mater.*, 2017, **2**, 16099.

5 B. F. Hoskins and R. Robson, *J. Am. Chem. Soc.*, 1989, **111**, 5962–5964.

6 S. R. Batten, N. R. Champness, X.-M. Chen, J. Garcia-Martinez, S. Kitagawa, L. Öhrström, M. O'Keeffe, M. Paik Suh and J. Reedijk, *Pure Appl. Chem.*, 2013, **85**, 1715–1724.

7 B. Park, B. Philippe, S. M. Jain, X. Zhang, T. Edvinsson, H. Rensmo, B. Zietz and G. Boschloo, *J. Mater. Chem. A*, 2015, **3**, 21760–21771.

8 D. W. Lewis, A. R. Ruiz-Salvador, A. Gómez, L. M. Rodriguez-Albelo, F.-X. Coudert, B. Slater, A. K. Cheetham and C. Mellot-Draznieks, *CrystEngComm*, 2009, **11**, 2272.

9 D. B. Mitzi, C. A. Feild, W. T. A. Harrison and A. M. Guloy, *Nature*, 1994, **369**, 467–469.

10 X. Gao, X. Zhang, W. Yin, H. Wang, Y. Hu, Q. Zhang, Z. Shi, V. L. Colvin, W. W. Yu and Y. Zhang, *Adv. Sci.*, 2019, **6**, 1900941.

11 G. Rose, *Ann. Phys.*, 1839, **124**, 551–573.

12 *DIE KRISTALLSTRUKTUR VON PEROWSKIT UND VERWANDTEN*, 1926.

13 St. v. Náray-Szabó, *Naturwissenschaften*, 1943, **31**, 202–203.

14 A. R. Chakhmouradian and P. M. Woodward, *Phys. Chem. Miner.*, 2014, **41**, 387–391.

15 A. von Hippel, *Rev. Mod. Phys.*, 1950, **22**, 221–237.

16 B. Jaffe, R. S. Roth and S. Marzullo, *J. Appl. Phys.*, 1954, **25**, 809–810.

17 G. A. Smolenskii and A. I. Agranovskaya, *Sov Phys Tech Phys.*, 1958, **Vol: 28**.

18 A. Callaghan, C. W. Moeller and R. Ward, *Inorg. Chem.*, 1966, **5**, 1572–1576.

19 T. Fukuda and Y. Uematsu, *Jpn. J. Appl. Phys.*, 1972, **11**, 163–169.

20 H. Yamaguchi, K. Katsumata, M. Hagiwara, M. Tokunaga, H. L. Liu, A. Zibold, D. B. Tanner and Y. J. Wang, *Phys. Rev. B*, 1999, **59**, 6021–6023.

21 M. Safa and B. K. Tanner, *Physica B+C*, 1977, **86-88**, 1347–1348.

22 A. Moreira dos Santos, S. Parashar, A. R. Raju, Y. S. Zhao, A. K. Cheetham and C. Rao, *Solid State Commun.*, 2002, **122**, 49–52.

23 M. K. Wu, Ashburn, JR, C. J. Torng, P. H. Hor, R. L. Meng, L. Gao, Z. J. Huang, Y. Q. Wang and C. W. Chu, *Phys. Rev. Lett.*, 1987, **58**, 908–910.

24 F. S. Galasso, *Perovskites and high Tc superconductors*, Gordon and Breach Science Publishers, New York, 1990.

25 D. Weber, *Z. Naturforsch. B*, 1978, **33**, 1443–1445.

26 D. Weber, *Z. Naturforsch. B*, 1978, **33**, 862–865.

27 W. Li, A. Stroppa, Z.-M. Wang and S. Gao, *Hybrid organic-inorganic perovskites*, Wiley-VCH, Weinheim, 2020.
28 A. Kojima, K. Teshima, Y. Shirai and T. Miyasaka, *J. Am. Chem. Soc.*, 2009, **131**, 6050–6051.
29 G. E. Eperon, S. D. Stranks, C. Menelaou, M. B. Johnston, L. M. Herz and H. J. Snaith, *Energy Environ. Sci.*, 2014, **7**, 982.
30 J.-W. Lee, D.-J. Seol, A.-N. Cho and N.-G. Park, *Adv. Mater.*, 2014, **26**, 4991–4998.
31 H. L. B. Boström and A. L. Goodwin, *Acc. Chem. Res.*, 2021, **54**, 1288–1297.
32 H. A. Evans, Y. Wu, R. Seshadri and A. K. Cheetham, *Nat. Rev. Mater.*, 2020, **5**, 196–213.
33 W.-J. Xu, Z.-Y. Du, W.-X. Zhang and X.-M. Chen, *CrystEngComm*, 2016, **18**, 7915–7928.
34 Z. Wang, B. Zhang, T. Otsuka, K. Inoue, H. Kobayashi and M. Kurmoo, *Dalton Trans.*, 2004, 2209–2216.
35 Z.-Y. Du, Y.-P. Zhao, W.-X. Zhang, H.-L. Zhou, C.-T. He, W. Xue, B.-Y. Wang and X.-M. Chen, *Chem. Commun.*, 2014, **50**, 1989–1991.
36 J. A. Schlueter, J. L. Manson and U. Geiser, *Inorg. Chem.*, 2005, **44**, 3194–3202.
37 I. E. Collings, M. Bykov, E. Bykova, M. Hanfland, S. van Smaalen, L. Dubrovinsky and N. Dubrovinskaia, *CrystEngComm*, 2018, **20**, 3512–3521.
38 M. Mączka, I. E. Collings, F. F. Leite and W. Paraguassu, *Dalton Trans.*, 2019, **48**, 9072–9078.
39 H. L. B. Boström, J. A. Hill and A. L. Goodwin, *Phys. Chem. Chem. Phys.*, 2016, **18**, 31881–31894.
40 H. L. B. Boström, *CrystEngComm*, 2020, **22**, 961–968.
41 J. M. Bermúdez-García, M. Sánchez-Andújar, S. Castro-García, J. López-Beceiro, R. Artiaga and M. A. Señarís-Rodríguez, *Nat. Commun.*, 2017, **8**, 15715.
42 H. L. B. Boström, M. S. Senn and A. L. Goodwin, *Nat. Commun.*, 2018, **9**, 2380.
43 E. Sletten and L. H. Jensen, *Acta Cryst. B*, 1973, **29**, 1752–1756.
44 P. Jain, N. S. Dalal, B. H. Toby, H. W. Kroto and A. K. Cheetham, *J. Am. Chem. Soc.*, 2008, **130**, 10450–10451.
45 H. F. Clausen, R. D. Poulsen, A. D. Bond, M.-A. S. Chevallier and B. B. Iversen, *J. Solid State Chem.*, 2005, **178**, 3342–3351.
46 S. Burger, S. Kronawitter, H. L. B. Boström, J. K. Zaręba and G. Kieslich, *Dalton Trans.*, 2020, **49**, 10740–10744.
47 M.-L. Tong, J. Ru, Y.-M. Wu, X.-M. Chen, H.-C. Chang, K. Mochizuki and S. Kitagawa, *New J. Chem.*, 2003, **27**, 779–782.
48 P. M. van der Werff, E. Martínez-Ferrero, S. R. Batten, P. Jensen, C. Ruiz-Pérez, M. Almeida, J. C. Waerenborgh, J. D. Cashion, B. Moubaraki, J. R. Galán-Mascarós, J. M. Martínez-Agudo, E. Coronado and K. S. Murray, *Dalton Trans.*, 2005, 285–290.
49 P. Jain, V. Ramachandran, R. J. Clark, H. D. Zhou, B. H. Toby, N. S. Dalal, H. W. Kroto and A. K. Cheetham, *J. Am. Chem. Soc.*, 2009, **131**, 13625–13627.
50 G. Kieslich, S. Sun and A. K. Cheetham, *Chem. Sci.*, 2015, **6**, 3430–3433.
51 W. B. Jensen, *J. Chem. Educ.*, 2010, **87**, 587–588.
52 V. M. Goldschmidt, *Naturwissenschaften*, 1926, **14**, 477–485.
53 G. Kieslich, S. Sun and A. K. Cheetham, *Chem. Sci.*, 2014, **5**, 4712–4715.

54 R. D. Shannon, *Acta Cryst. A*, 1976, **32**, 751–767.
55 M. Becker, T. Klüner and M. Wark, *Dalton Trans.*, 2017, **46**, 3500–3509.
56 C. J. Bartel, C. Sutton, B. R. Goldsmith, R. Ouyang, C. B. Musgrave, L. M. Ghiringhelli and M. Scheffler, *Sci. Adv.*, 2019, **5**, eaav0693.
57 Q. Sun and W.-J. Yin, *J. Am. Chem. Soc.*, 2017, **139**, 14905–14908.
58 X. Cai, Y. Zhang, Z. Shi, Y. Chen, Y. Xia, A. Yu, Y. Xu, F. Xie, H. Shao, H. Zhu, D. Fu, Y. Zhan and H. Zhang, *Adv. Sci.*, 2022, **9**, e2103648.
59 J. M. Bermúdez-García, S. Yáñez-Vilar, A. García-Fernández, M. Sánchez-Andújar, S. Castro-García, J. López-Beceiro, R. Artiaga, M. Dilshad, X. Moya and M. A. Señarís-Rodríguez, *J. Mater. Chem. C*, 2018, **6**, 9867–9874.
60 S. Burger, M. G. Ehrenreich and G. Kieslich, *J. Mater. Chem. A*, 2018, **6**, 21785–21793.
61 Y. Wu, T. Binford, J. A. Hill, S. Shaker, J. Wang and A. K. Cheetham, *Chem. Commun.*, 2018, **54**, 3751–3754.
62 J. M. Bermúdez-García, M. Sánchez-Andújar, S. Yáñez-Vilar, S. Castro-García, R. Artiaga, J. López-Beceiro, L. Botana, A. Alegría and M. A. Señarís-Rodríguez, *J. Mater. Chem. C*, 2016, **4**, 4889–4898.
63 J. García-Ben, A. García-Fernández, P. Dafonte-Rodríguez, I. Delgado-Ferreiro, U. B. Cappel, S. Castro-García, M. Sánchez-Andújar, J. M. Bermúdez-García and M. A. Señarís-Rodríguez, *J. Solid State Chem.*, 2022, **316**, 123635.
64 B. K. Shaw, C. Castillo-Blas, M. F. Thorne, M. L. Ríos Gómez, T. Forrest, M. D. Lopez, P. A. Chater, L. N. McHugh, D. A. Keen and T. D. Bennett, *Chem. Sci.*, 2022, **13**, 2033–2042.
65 J. A. Hill, A. L. Thompson and A. L. Goodwin, *J. Am. Chem. Soc.*, 2016, **138**, 5886–5896.
66 J. García-Ben, L. N. McHugh, T. D. Bennett and J. M. Bermúdez-García, *Coord. Chem. Rev.*, 2022, **455**, 214337.
67 P. R. Spackman, M. J. Turner, J. J. McKinnon, S. K. Wolff, D. J. Grimwood, D. Jayatilaka and M. A. Spackman, *J. Appl. Crystallogr.*, 2021, **54**, 1006–1011.
68 W. Travis, E. N. K. Glover, H. Bronstein, D. O. Scanlon and R. G. Palgrave, *Chem. Sci.*, 2016, **7**, 4548–4556.
69 A. M. Glazer, *Acta Cryst. B*, 1972, **28**, 3384–3392.
70 A. M. Glazer, *Phase Transit.*, 2011, **84**, 405–420.
71 P. M. Woodward, *Acta Cryst. B*, 1997, **53**, 32–43.
72 C. J. Howard and H. T. Stokes, *Acta Cryst. B*, 1998, **54**, 782–789.
73 A. Stroppa, P. Jain, P. Barone, M. Marsman, J. M. Perez-Mato, A. K. Cheetham, H. W. Kroto and S. Picozzi, *Angew. Chem. Int. Ed. Engl.*, 2011, **50**, 5847–5850.
74 M. J. Pitcher, P. Mandal, M. S. Dyer, J. Alaria, P. Borisov, H. Niu, J. B. Claridge and M. J. Rosseinsky, *Science*, 2015, **347**, 420–424.
75 L. C. Gómez-Aguirre, B. Pato-Doldán, A. Stroppa, S. Yáñez-Vilar, L. Bayarjargal, B. Winkler, S. Castro-García, J. Mira, M. Sánchez-Andújar and M. A. Señarís-Rodríguez, *Inorg. Chem.*, 2015, **54**, 2109–2116.
76 H. T. Stokes, D. M. Hatch, and B. J. Campbell, ISODISTORT, ISOTROPY Software Suite, iso.byu.edu.
77 B. J. Campbell, H. T. Stokes, D. E. Tanner and D. M. Hatch, *J. Appl. Crystallogr.*, 2006, **39**, 607–614.
78 K. SIMKISS, *Nature*, 1964, **201**, 492–493.
79 J.-P. Brog, C.-L. Chanez, A. Crochet and K. M. Fromm, *RSC Adv.*, 2013, **3**, 16905.

80 G. R. Desiraju, *Cryst. Growth Des.*, 2008, **8**, 3–5.
81 A. Alaei, A. Circelli, Y. Yuan, Y. Yang and S. S. Lee, *Mater. Adv.*, 2021, **2**, 47–63.
82 R. J. Sutton, M. R. Filip, A. A. Haghighirad, N. Sakai, B. Wenger, F. Giustino and H. J. Snaith, *ACS Energy Lett.*, 2018, **3**, 1787–1794.
83 H. Mizoguchi, P. M. Woodward, S.-H. Byeon and J. B. Parise, *J. Am. Chem. Soc.*, 2004, **126**, 3175–3184.
84 H. A. Evans, Z. Deng, I. E. Collings, Y. Wu, J. L. Andrews, K. Pilar, J. M. Tuffnell, G. Wu, J. Wang, S. E. Dutton, P. D. Bristowe, R. Seshadri and A. K. Cheetham, *Chem. Commun.*, 2019, **55**, 2964–2967.
85 S. Burger, S. Grover, K. T. Butler, H. L. B. Boström, R. Grau-Crespo and G. Kieslich, *Mater. Horiz.*, 2021, **8**, 2444–2450.
86 A. J. Cruz-Cabeza and J. Bernstein, *Chem. Rev.*, 2014, **114**, 2170–2191.
87 M. Mączka, A. Gągor, M. Ptak, D. Stefańska, L. Macalik, A. Pikul and A. Sieradzki, *Dalton Trans.*, 2019, **48**, 13006–13016.
88 Y. Wu, S. Shaker, F. Brivio, R. Murugavel, P. D. Bristowe and A. K. Cheetham, *J. Am. Chem. Soc.*, 2017, **139**, 16999–17002.
89 M. Mączka, A. Gągor, J. K. Zaręba, M. Trzebiatowska, D. Stefańska, E. Kucharska, J. Hanuza, N. Pałka, E. Czerwińska and A. Sieradzki, *Dalton Trans.*, 2021, **50**, 10580–10592.
90 Y.-Q. Wu, J.-Y. Zhang, X. He, Z.-X. Wang, H.-L. Cai and M.-X. Li, *Cryst. Growth Des.*, 2021, **21**, 6245–6253.
91 S. Krivovichev, *Acta Cryst. A*, 2012, **68**, 393–398.
92 S. V. Krivovichev, *Angew. Chem. Int. Ed. Engl.*, 2014, **53**, 654–661.
93 S. V. Krivovichev, *Acta Cryst. B*, 2016, **72**, 274–276.
94 W. Hornfeck, *Acta Cryst. A*, 2020, **76**, 534–548.
95 C. Kaußler and G. Kieslich, *J. Appl. Crystallogr.*, 2021, **54**, 306–316.
96 S. A. Hallweger, C. Kaußler and G. Kieslich, *Phys. Chem. Chem. Phys.*, 2022, **24**, 9196–9202.
97 S. Burger, K. Hemmer, D. C. Mayer, P. Vervoorts, D. Daisenberger, J. K. Zaręba and G. Kieslich, *Adv. Funct. Mater.*, 2022, **32**, 2205343.
98 A. L. Goodwin, M. Calleja, M. J. Conterio, M. T. Dove, J. S. O. Evans, D. A. Keen, L. Peters and M. G. Tucker, *Science*, 2008, **319**, 794–797.
99 A. B. Cairns, A. L. Thompson, M. G. Tucker, J. Haines and A. L. Goodwin, *J. Am. Chem. Soc.*, 2012, **134**, 4454–4456.
100 S. Henke, A. Schneemann and R. A. Fischer, *Adv. Funct. Mater.*, 2013, **23**, 5990–5996.
101 B. K. Shaw, A. R. Hughes, M. Ducamp, S. Moss, A. Debnath, A. F. Sapnik, M. F. Thorne, L. N. McHugh, A. Pugliese, D. S. Keeble, P. Chater, J. M. Bermudez-Garcia, X. Moya, S. K. Saha, D. A. Keen, F.-X. Coudert, F. Blanc and T. D. Bennett, *Nat. Chem.*, 2021, **13**, 778–785.
102 S. M. Kronawitter, S. A. Hallweger, J. Meyer, C. Pedri, S. Burger, A. Alhadid, S. Henke and G. Kieslich, *APL Mater.*, 2023, **11**, 31119.
103 M. Kim, H.-S. Lee, D.-H. Seo, S. J. Cho, E.-C. Jeon and H. R. Moon, *Nat. Commun.*, 2024, **15**, 1174.

104 W. Xu, N. Hanikel, K. A. Lomachenko, C. Atzori, A. Lund, H. Lyu, Z. Zhou, C. A. Angell and O. M. Yaghi, *Angew. Chem. Int. Ed. Engl.*, 2023, **62**, e202300003.

105 T. D. Bennett, J.-C. Tan, Y. Yue, E. Baxter, C. Ducati, N. J. Terrill, H. H.-M. Yeung, Z. Zhou, W. Chen, S. Henke, A. K. Cheetham and G. N. Greaves, *Nat. Commun.*, 2015, **6**, 8079.

106 L. Frentzel-Beyme, M. Kloß, P. Kolodzeiski, R. Pallach and S. Henke, *J. Am. Chem. Soc.*, 2019, **141**, 12362–12371.

107 S. Vaidya, O. Veselska, A. Zhadan, M. Diaz-Lopez, Y. Joly, P. Bordet, N. Guillou, C. Dujardin, G. Ledoux, F. Toche, R. Chiriac, A. Fateeva, S. Horike and A. Demessence, *Chem. Sci.*, 2020, **11**, 6815–6823.

108 D. Umeyama, N. P. Funnell, M. J. Cliffe, J. A. Hill, A. L. Goodwin, Y. Hijikata, T. Itakura, T. Okubo, S. Horike and S. Kitagawa, *Chem. Commun.*, 2015, **51**, 12728–12731.

109 D. Umeyama, S. Horike, M. Inukai, T. Itakura and S. Kitagawa, *J. Am. Chem. Soc.*, 2015, **137**, 864–870.

110 T. D. Bennett and S. Horike, *Nat. Rev. Mater.*, 2018, **3**, 431–440.

111 S. Horike, S. S. Nagarkar, T. Ogawa and S. Kitagawa, *Angew. Chem. Int. Ed. Engl.*, 2020, **59**, 6652–6664.

112 C. Healy, K. M. Patil, B. H. Wilson, L. Hermanspahn, N. C. Harvey-Reid, B. I. Howard, C. Kleinjan, J. Kolien, F. Payet, S. G. Telfer, P. E. Kruger and T. D. Bennett, *Coord. Chem. Rev.*, 2020, **419**, 213388.

113 N. Ma and S. Horike, *Chem. Rev.*, 2022, **122**, 4163–4203.

114 L. Feng, K.-Y. Wang, G. S. Day, M. R. Ryder and H.-C. Zhou, *Chem. Rev.*, 2020, **120**, 13087–13133.

115 D. R. MacFarlane, M. Forsyth, E. I. Izgorodina, A. P. Abbott, G. Annat and K. Fraser, *Phys. Chem. Chem. Phys.*, 2009, **11**, 4962–4967.

116 I. J. Lin and C. S. Vasam, *J. Organomet. Chem*, 2005, **690**, 3498–3512.

117 J. Dupont, *Acc. Chem. Res.*, 2011, **44**, 1223–1231.

118 C. Ye, L. N. McHugh, C. Chen, S. E. Dutton and T. D. Bennett, *Angew. Chem. Int. Ed. Engl.*, 2023, **62**, e202302406.

119 D. R. MacFarlane, S. A. Forsyth, J. Golding and G. B. Deacon, *Green Chem.*, 2002, **4**, 444–448.

120 J.-C. Tan, P. Jain and A. K. Cheetham, *Dalton Trans.*, 2012, **41**, 3949–3952.

121 G. Feng, Di Gui and W. Li, *Cryst. Growth Des.*, 2018, **18**, 4890–4895.

122 L.-J. Ji, S.-J. Sun, Y. Qin, K. Li and W. Li, *Coord. Chem. Rev.*, 2019, **391**, 15–29.

123 J. Lu, Z. Shan, J. Zhang, Y. Su, K. Yi, Y. Zhang and Q. Zheng, *J. Non-Cryst. Solids: X*, 2022, **16**, 100125.

124 X. Moya and N. D. Mathur, *Science*, 2020, **370**, 797–803.

125 A. Kitanovski, U. Plaznik, U. Tomc and A. Poredoš, *Int. J. Refrig*, 2015, **57**, 288–298.

126 A. Greco, C. Aprea, A. Maiorino and C. Masselli, *Int. J. Refrig*, 2019, **106**, 66–88.

127 J. Salgado-Beceiro, A. Nonato, R. X. Silva, A. García-Fernández, M. Sánchez-Andújar, S. Castro-García, E. Stern-Taulats, M. A. Señarís-Rodríguez, X. Moya and J. M. Bermúdez-García, *Mater. Adv.*, 2020, **1**, 3167–3170.

128 R. X. Da Silva, C. W. de Araujo Paschoal, C. Costa Dos Santos, A. García-Fernández, J. Salgado-Beceiro, M. A. Señarís-Rodríguez, M. Sanchez-Andujar and A. Nonato Almeida de Abreu Silva, *Molecules*, 2020, **25**.

129 P. Lloveras, A. Aznar, M. Barrio, P. Negrier, C. Popescu, A. Planes, L. Mañosa, E. Stern-Taulats, A. Avramenko, N. D. Mathur, X. Moya and J.-L. Tamarit, *Nat. Commun.*, 2019, **10**, 1803.

130 S. P. Vallone, A. N. Tantillo, A. M. Dos Santos, J. J. Molaison, R. Kulmaczewski, A. Chapoy, P. Ahmadi, M. A. HALCROW and K. G. Sandeman, *Adv. Mater.*, 2019, **31**, e1807334.

131 D. Boldrin, *Appl. Phys. Lett.*, 2021, **118**.

132 M. Szafrański, W.-J. Wei, Z.-M. Wang, W. Li and A. Katrusiak, *APL Mater.*, 2018, **6**.

133 A. Aznar, P. Lloveras, M. Barrio, P. Negrier, A. Planes, L. Mañosa, N. D. Mathur, X. Moya and J.-L. Tamarit, *J. Mater. Chem. A*, 2020, **8**, 639–647.

134 B. Li, Y. Kawakita, S. Ohira-Kawamura, T. Sugahara, H. Wang, J. Wang, Y. Chen, S. I. Kawaguchi, S. Kawaguchi, K. Ohara, K. Li, D. Yu, R. Mole, T. Hattori, T. Kikuchi, S.-I. Yano, Z. Zhang, Z. Zhang, W. Ren, S. Lin, O. Sakata, K. Nakajima and Z. Zhang, *Nature*, 2019, **567**, 506–510.

135 M. Masche, L. Ianniciello, J. Tušek and K. Engelbrecht, *Int. J. Refrig*, 2021, **121**, 302–312.

136 L. Zhu, Z. Dai, Y. Gao, D. Wu, C. Wang, D. Zhao, X. She, Y. Ding and X. Zhang, *J. Therm. Sci.*, 2023, **32**, 2115–2125.

137 T. Hess, L. M. Maier, N. Bachmann, P. Corhan, O. Schäfer-Welsen, J. Wöllenstein and K. Bartholomé, *J. Appl. Phys.*, 2020, **127**.

138 J. Lin, P. Tong, K. Zhang, K. Tao, W. Lu, X. Wang, X. Zhang, W. Song and Y. Sun, *Nat. Commun.*, 2022, **13**, 596.

139 C. M. Miliante, A. M. Christmann, R. P. Soares, J. R. Bocca, C. S. Alves, A. M. G. Carvalho and A. R. Muniz, *J. Mater. Chem. A*, 2022, **10**, 8344–8355.

140 J. Seo, R. D. McGillicuddy, A. H. Slavney, S. Zhang, R. Ukani, A. A. Yakovenko, S.-L. Zheng and J. A. Mason, *Nat. Commun.*, 2022, **13**, 2536.

141 S. Grover, S. Burger, K. T. Butler, K. Hemmer, P. Vervoorts, G. Kieslich and R. Grau-Crespo, *CrystEngComm*, 2023, **25**, 3439–3444.

142 S. M. Kronawitter, S. Park, S. A. Hallweger, E. Myatt, J. Pitcairn, M. J. Cliffe, D. Daisenberger, M. Drees and G. Kieslich, *Mater. Adv.*, 2024.

143 V. Wadhawan, *Introduction to Ferroic Materials*, CRC Press, 2000.

144 J. Dai, *Ferroic materials for smart systems. From fundamentals to device applications*, Wiley-VCH, Weinheim, Germany, 2020.

145 L. Jin, F. Li and S. Zhang, *J. Am. Ceram. Soc.*, 2014, **97**, 1–27.

146 J. H. Haeni, P. Irvin, W. Chang, R. Uecker, P. Reiche, Y. L. Li, S. Choudhury, W. Tian, M. E. Hawley, B. Craigo, A. K. Tagantsev, X. Q. Pan, S. K. Streiffer, L. Q. Chen, S. W. Kirchoefer, J. Levy and D. G. Schlom, *Nature*, 2004, **430**, 758–761.

147 I. Inbar and R. E. Cohen, *Ferroelectrics*, 1997, **194**, 83–95.

148 G. Shirane and A. Takeda, *J. Phys. Soc. Jpn.*, 1952, **7**, 5–11.

149 P.-P. Shi, Y.-Y. Tang, P.-F. Li, W.-Q. Liao, Z.-X. Wang, Q. Ye and R.-G. Xiong, *Chem. Soc. Rev.*, 2016, **45**, 3811–3827.

150 N. A. Benedek and T. Birol, *J. Mater. Chem. C*, 2016, **4**, 4000–4015.

151 Y. Rakita, O. Bar-Elli, E. Meirzadeh, H. Kaslasi, Y. Peleg, G. Hodes, I. Lubomirsky, D. Oron, D. Ehre and D. Cahen, *Proc. Natl. Acad. Sci. U.S.A*, 2017, **114**, E5504-E5512.

152 H.-Y. Zhang, X.-G. Chen, Z.-X. Zhang, X.-J. Song, T. Zhang, Q. Pan, Y. Zhang and R.-G. Xiong, *Adv. Mater.*, 2020, **32**, e2005213.

153 T. Zhang, K. Xu, J. Li, L. He, D.-W. Fu, Q. Ye and R.-G. Xiong, *Natl. Sci. Rev.*, 2023, **10**, nwac240.

154 M. Guo, H.-L. Cai and R.-G. Xiong, *Inorg. Chem. Commun.*, 2010, **13**, 1590–1598.

155 Q. Pan, Z.-B. Liu, Y.-Y. Tang, P.-F. Li, R.-W. Ma, R.-Y. Wei, Y. Zhang, Y.-M. You, H.-Y. Ye and R.-G. Xiong, *J. Am. Chem. Soc.*, 2017, **139**, 3954–3957.

156 W.-Q. Liao, D. Zhao, Y.-Y. Tang, Y. Zhang, P.-F. Li, P.-P. Shi, X.-G. Chen, Y.-M. You and R.-G. Xiong, *Science*, 2019, **363**, 1206–1210.

157 H.-Y. Liu, H.-Y. Zhang, X.-G. Chen and R.-G. Xiong, *J. Am. Chem. Soc.*, 2020, **142**, 15205–15218.

158 H.-Y. Ye, Y.-Y. Tang, P.-F. Li, W.-Q. Liao, J.-X. Gao, X.-N. Hua, H. Cai, P.-P. Shi, Y.-M. You and R.-G. Xiong, *Science*, 2018, **361**, 151–155.

159 Y.-M. You, W.-Q. Liao, D. Zhao, H.-Y. Ye, Y. Zhang, Q. Zhou, X. Niu, J. Wang, P.-F. Li, D.-W. Fu, Z. Wang, S. Gao, K. Yang, J.-M. Liu, J. Li, Y. Yan and R.-G. Xiong, *Science*, 2017, **357**, 306–309.

160 W.-Q. Liao, Y.-Y. Tang, P.-F. Li, Y.-M. You and R.-G. Xiong, *J. Am. Chem. Soc.*, 2017, **139**, 18071–18077.

161 K. Li, Z.-G. Li, J. Xu, Y. Qin, W. Li, A. Stroppa, K. T. Butler, C. J. Howard, M. T. Dove, A. K. Cheetham and X.-H. Bu, *J. Am. Chem. Soc.*, 2022, **144**, 816–823.

162 P. Jain, A. Stroppa, D. Nabok, A. Marino, A. Rubano, D. Paparo, M. Matsubara, H. Nakotte, M. Fiebig, S. Picozzi, E. S. Choi, A. K. Cheetham, C. Draxl, N. S. Dalal and V. S. Zapf, *npj Quantum Mater.*, 2016, **1**.

163 W.-J. Xu, P.-F. Li, Y.-Y. Tang, W.-X. Zhang, R.-G. Xiong and X.-M. Chen, *J. Am. Chem. Soc.*, 2017, **139**, 6369–6375.

164 C.-C. Fan, C.-D. Liu, B.-D. Liang, W. Wang, M.-L. Jin, C.-Y. Chai, C.-Q. Jing, T.-Y. Ju, X.-B. Han and W. Zhang, *Nat. Commun.*, 2024, **15**, 1464.

165 E. K. H. Salje, *Contemp. Phys.*, 2000, **41**, 79–91.

166 S. H. Baek, H. W. Jang, C. M. Folkman, Y. L. Li, B. Winchester, J. X. Zhang, Q. He, Y. H. Chu, C. T. Nelson, M. S. Rzchowski, X. Q. Pan, R. Ramesh, L. Q. Chen and C. B. Eom, *Nat. Mater.*, 2010, **9**, 309–314.

167 J. Mastin, M.-A. Einarsrud and T. Grande, *Chem. Mater.*, 2006, **18**, 1680–1687.

168 K. Aizu, *J. Phys. Soc. Jpn.*, 1969, **27**, 387–396.

169 K. Aizu, *Phys. Rev. B*, 1970, **2**, 754–772.

170 F. Meschke, A. Kolleck and G. A. Schneider, *J. Eur. Ceram. Soc.*, 1997, **17**, 1143–1149.

171 J. D. Bierlein and A. W. Sleight, *Solid State Commun.*, 1975, **16**, 69–70.

172 K. Aizu, A. Kumada, H. Yumoto and S. Ashida, *J. Phys. Soc. Jpn.*, 1969, **27**, 511.

173 S. Chen, D.-C. Han, Le Ye and W.-X. Zhang, *Inorg. Chem.*, 2024.

174 J. Li, Y. Zhu, P.-Z. Huang, D.-W. Fu, Q.-Q. Jia and H.-F. Lu, *Chem. Eur. J.*, 2022, **28**, e202201005.

175 W. Li, Z. Zhang, E. G. Bithell, A. S. Batsanov, P. T. Barton, P. J. Saines, P. Jain, C. J. Howard, M. A. Carpenter and A. K. Cheetham, *Acta Mater.*, 2013, **61**, 4928–4938.

176 X.-X. Chen, X.-Y. Zhang, D.-X. Liu, R.-K. Huang, S.-S. Wang, L.-Q. Xiong, W.-X. Zhang and X.-M. Chen, *Chem. Sci.*, 2021, **12**, 8713–8721.

177 X.-X. Chen, D.-X. Liu, Y.-P. Gong, S.-S. Wang, W.-X. Zhang and X.-M. Chen, *Inorg. Chem.*, 2022, **61**, 2219–2226.

178 Z.-B. Liu, L. He, P.-P. Shi, Q. Ye and D.-W. Fu, *J. Phys. Chem. Lett.*, 2020, **11**, 7960–7965.

179 Y.-J. Cao, L. Zhou, P.-P. Shi, Q. Ye and D.-W. Fu, *Chem. Commun.*, 2019, **55**, 8418–8421.

180 M.-M. Zhao, L. Zhou, P.-P. Shi, X. Zheng, X.-G. Chen, J.-X. Gao, F.-J. Geng, Q. Ye and D.-W. Fu, *Chem. Commun.*, 2018, **54**, 13275–13278.

181 M.-M. Zhao, L. Zhou, P.-P. Shi, X. Zheng, X.-G. Chen, J.-X. Gao, L. He, Q. Ye, C.-M. Liu and D.-W. Fu, *Chem. Eur. J.*, 2019, **25**, 6447–6454.

182 L. He, P.-P. Shi, M.-M. Zhao, C.-M. Liu, W. Zhang and Q. Ye, *Chem. Mater.*, 2021, **33**, 799–805.

183 M. G. Marino and K. D. Kreuer, *ChemSusChem*, 2015, **8**, 513–523.

184 G. S. Pawley, *J. Appl. Crystallogr.*, 1981, **14**, 357–361.

185 T. Runčevski, *J. Appl. Crystallogr.*, 2019, **52**, 1238–1239.

186 R. E. Dinnebier, M. Etter and T. Runcevski, in *Handbook of Solid State Chemistry*, ed. R. Dronskowski, S. Kikkawa and A. Stein, Wiley, 2017, pp. 29–75.

187 A.-C. Dippel, H.-P. Liermann, J. T. Delitz, P. Walter, H. Schulte-Schrepping, O. H. Seeck and H. Franz, *J. Synchrotron Rad.*, 2015, **22**, 675–687.

188 L. León-Alcaide, R. S. Christensen, D. A. Keen, J. L. Jordá, I. Brotons-Alcázar, A. Forment-Aliaga and G. Mínguez Espallargas, *J. Am. Chem. Soc.*, 2023, **145**, 11258–11264.

189 M. J. Cliffe and A. L. Goodwin, *J. Appl. Crystallogr.*, 2012, **45**, 1321–1329.

190 N. J. Brooks, B. L. L. E. Gauthe, N. J. Terrill, S. E. Rogers, R. H. Templer, O. Ces and J. M. Seddon, *Rev. Sci. Instrum.*, 2010, **81**, 64103.

191 K. W. Chapman, G. J. Halder and P. J. Chupas, *J. Am. Chem. Soc.*, 2008, **130**, 10524–10526.

192 A. J. Graham, D. R. Allan, A. Muszkiewicz, C. A. Morrison and S. A. Moggach, *Angew. Chem. Int. Ed. Engl.*, 2011, **50**, 11138–11141.

193 J. Song, R. Pallach, L. Frentzel-Beyme, P. Kolodzeiski, G. Kieslich, P. Vervoorts, C. L. Hobday and S. Henke, *Angew. Chem. Int. Ed. Engl.*, 2022, **61**, e202117565.

194 J. Gonzalez-Platas, M. Alvaro, F. Nestola and R. Angel, *J. Appl. Crystallogr.*, 2016, **49**, 1377–1382.

195 B. J. Campbell, H. T. Stokes, D. E. Tanner and D. M. Hatch, *J. Appl. Crystallogr.*, 2006, **39**, 607–614.

196 F.-J. Geng, L. Zhou, P.-P. Shi, X.-L. Wang, X. Zheng, Y. Zhang, D.-W. Fu and Q. Ye, *J. Mater. Chem. C*, 2017, **5**, 1529–1536.

197 L. Zhou, X. Zheng, P.-P. Shi, Z. Zafar, H.-Y. Ye, D.-W. Fu and Q. Ye, *Inorg. Chem.*, 2017, **56**, 3238–3244.
198 J. A. Schlueter, J. L. Manson, K. A. Hyzer and U. Geiser, *Inorg. Chem.*, 2004, **43**, 4100–4102.
199 K. Qian, Y. Xu, Z. Wang and J. Yang, *Z. Naturforsch. B*, 2017, **72**, 409–413.
200 F. A. Mautner and H. Krischner, *Z. Kristallogr. – Cryst. Mater.*, 1986, **175**, 105–110.
201 X.-H. Zhao, X.-C. Huang, S.-L. Zhang, D. Shao, H.-Y. Wei and X.-Y. Wang, *J. Am. Chem. Soc.*, 2013, **135**, 16006–16009.
202 J. Yang, Y. Huang, T. Fang, K. Qian, W.-B. Chen, X.-F. Yu, Y.-C. Ai, J.-L. Ye and X.-Y. Li, *Z. Naturforsch. B*, 2019, **74**, 335–339.
203 Z.-Y. Du, T.-T. Xu, B. Huang, Y.-J. Su, W. Xue, C.-T. He, W.-X. Zhang and X.-M. Chen, *Angew. Chem. Int. Ed. Engl.*, 2015, **127**, 928–932.
204 Z.-Y. Du, Y.-Z. Sun, S.-L. Chen, B. Huang, Y.-J. Su, T.-T. Xu, W.-X. Zhang and X.-M. Chen, *Chem. Commun.*, 2015, **51**, 15641–15644.
205 F. A. Mautner, H. Krischner and C. Kratky, *Monatsh. fur Chem.*, 1988, **119**, 1245–1249.
206 S. Hanna, F. A. Mautner, B. Koppelhuber-Bitschnau and M. Abu-Youssef, *MSF*, 2000, **321-324**, 1098–1101.
207 Le Ye, Z.-X. Gong, C. Shi, J.-J. Ma, H. Liang, F.-W. Qi, D.-Y. E, C.-F. Wang, Y. Zhang and H.-Y. Ye, *CrystEngComm*, 2019, **21**, 7043–7047.
208 Y.-L. Sun, X.-B. Han and W. Zhang, *Chem. Eur. J.*, 2017, **23**, 11126–11132.
209 P. Schouwink, F. Morelle, Y. Sadikin, Y. Filinchuk and R. Černý, *Energies*, 2015, **8**, 8286–8299.
210 W.-J. Xu, K.-P. Xie, Z.-F. Xiao, W.-X. Zhang and X.-M. Chen, *Cryst. Growth Des.*, 2016, **16**, 7212–7217.
211 K. Qian, F. Shao, Z. Yan, J. Pang, X. Chen and C. Yang, *CrystEngComm*, 2016, **18**, 7671–7674.
212 X. Zhang, X.-D. Shao, S.-C. Li, Y. Cai, Y.-F. Yao, R.-G. Xiong and W. Zhang, *Chem. Commun.*, 2015, **51**, 4568–4571.
213 W. Zhang, Y. Cai, R.-G. Xiong, H. Yoshikawa and K. Awaga, *Angew. Chem. Int. Ed. Engl.*, 2010, **49**, 6608–6610.
214 W. Zhang, H.-Y. Ye, R. Graf, H. W. Spiess, Y.-F. Yao, R.-Q. Zhu and R.-G. Xiong, *J. Am. Chem. Soc.*, 2013, **135**, 5230–5233.
215 W.-J. Xu, S.-L. Chen, Z.-T. Hu, R.-B. Lin, Y.-J. Su, W.-X. Zhang and X.-M. Chen, *Dalton Trans.*, 2016, **45**, 4224–4229.
216 M. Rok, G. Bator, B. Zarychta, B. Dziuk, J. Repeć, W. Medycki, M. Zamponi, G. Usevičius, M. Šimėnas and J. Banys, *Dalton Trans.*, 2019, **48**, 4190–4202.
217 C. Shi, C.-H. Yu and W. Zhang, *Angew. Chem. Int. Ed. Engl.*, 2016, **128**, 5892–5896.
218 S. Peschel and D. Babel, *Z. Naturforsch. B*, 1994, **49**, 1373–1380.
219 M. Rok, G. Bator, W. Medycki, M. Zamponi, S. Balčiūnas, M. Šimėnas and J. Banys, *Dalton Trans.*, 2018, **47**, 17329–17341.
220 X.-G. Chen, Z.-X. Zhang, Y.-L. Zeng, S.-Y. Tang and R.-G. Xiong, *Chem. Commun.*, 2022, **58**, 3059–3062.

221 M. Rok, A. Ciżman, B. Zarychta, J. K. Zaręba, M. Trzebiatowska, M. Mączka, A. Stroppa, S. Yuan, A. E. Phillips and G. Bator, *J. Mater. Chem. C*, 2020, **8**, 17491–17501.

222 M. Schwarten and D. Babel, *Z. anorg. allg. Chem.*, 2000, **626**, 1921–1928.

223 M. Schwarten, B. Ziegler, M. Witzei and D. Babel, *Z. Naturforsch. B*, 1997, **52**, 391–397.

224 J. Lefebvre, D. Chartrand and D. B. Leznoff, *Polyhedron*, 2007, **26**, 2189–2199.

225 M. Mączka, J. Janczak, M. Trzebiatowska, A. Sieradzki, S. Pawlus and A. Pikul, *Dalton Trans.*, 2017, **46**, 8476–8485.

226 B. Zhou, Y. Imai, A. Kobayashi, Z.-M. Wang and H. Kobayashi, *Angew. Chem. Int. Ed. Engl.*, 2011, **123**, 11643–11647.

227 T. Asaji, Y. Ito, J. Seliger, V. Zagar, A. Gradišek and T. Apih, *J. Phys. Chem. A*, 2012, **116**, 12422–12428.

228 D.-W. Fu, W. Zhang, H.-L. Cai, Y. Zhang, J.-Z. Ge, R.-G. Xiong, S. D. Huang and T. Nakamura, *Angew. Chem. Int. Ed. Engl.*, 2011, **50**, 11947–11951.

229 R. Shang, S. Chen, B.-W. Wang, Z.-M. Wang and S. Gao, *Angew. Chem. Int. Ed. Engl.*, 2016, **128**, 2137–2140.

230 R. Shang, G.-C. Xu, Z.-M. Wang and S. Gao, *Chem. Eur. J.*, 2014, **20**, 1146–1158.

231 M. Ptak, M. Mączka, A. Gągor, A. Sieradzki, B. Bondzior, P. Dereń and S. Pawlus, *Phys. Chem. Chem. Phys.*, 2016, **18**, 29629–29640.

232 M. Ptak, M. Mączka, A. Gągor, A. Sieradzki, A. Stroppa, D. Di Sante, J. M. Perez-Mato and L. Macalik, *Dalton Trans.*, 2016, **45**, 2574–2583.

233 A. Ciupa, M. Mączka, A. Gągor, A. Pikul, E. Kucharska, J. Hanuza and A. Sieradzki, *Polyhedron*, 2015, **85**, 137–143.

234 C. Luo, M. Fang, Q. Luo, H. Lin, Y. Zhang, F. Yue, P. Xiang and H. Peng, *Crystal Research and Technology*, 2017, **52**.

235 A. Rossin, M. R. Chierotti, G. Giambastiani, R. Gobetto and M. Peruzzini, *CrystEngComm*, 2012, **14**, 4454.

236 M. Mączka, A. Ciupa, A. Gągor, A. Sieradzki, A. Pikul, B. Macalik and M. Drozd, *Inorg. Chem.*, 2014, **53**, 5260–5268.

237 R. E. Marsh, *Acta Crystallogr., Sect. C: Struct. Chem.*, 1986, **42**, 1327–1328.

238 K.-L. Hu, M. Kurmoo, Z. Wang and S. Gao, *Chem. Eur. J.*, 2009, **15**, 12050–12064.

239 I. E. Collings, J. A. Hill, A. B. Cairns, R. I. Cooper, A. L. Thompson, J. E. Parker, C. C. Tang and A. L. Goodwin, *Dalton Trans.*, 2016, **45**, 4169–4178.

240 M. Mączka, N. L. Marinho Costa, A. Gągor, W. Paraguassu, A. Sieradzki and J. Hanuza, *Phys. Chem. Chem. Phys.*, 2016, **18**, 13993–14000.

241 B.-Q. Wang, H.-B. Yan, Z.-Q. Huang and Z. Zhang, *Acta Crystallogr., Sect. C: Struct. Chem.*, 2013, **69**, 616–619.

242 W. D. C. B. Gunatilleke, K. Wei, Z. Niu, L. Wojtas, G. Nolas and S. Ma, *Dalton Trans.*, 2017, **46**, 13342–13344.

243 M. Mączka, K. Pasińska, M. Ptak, W. Paraguassu, T. A. Da Silva, A. Sieradzki and A. Pikul, *Phys. Chem. Chem. Phys.*, 2016, **18**, 31653–31663.

244 S. Chen, R. Shang, K.-L. Hu, Z.-M. Wang and S. Gao, *Inorg. Chem. Front.*, 2014, **1**, 83–98.

245 J. A. Zienkiewicz, D. A. Kowalska, K. Fedoruk, M. Stefanski, A. Pikul and M. Ptak, *J. Mater. Chem. C*, 2021, **9**, 6841–6851.

246 M. Mączka, A. Gągor, M. Ptak, W. Paraguassu, T. A. Da Silva, A. Sieradzki and A. Pikul, *Chem. Mater.*, 2017, **29**, 2264–2275.

247 S. Gao and S. W. Ng, *Acta Crystallogr., Sect. E: Struct. Rep*, 2010, **66**, m1599.

248 X.-Y. Wang, L. Gan, S.-W. Zhang and S. Gao, *Inorg. Chem.*, 2004, **43**, 4615–4625.

249 E. Sletten and L. H. Jensen, *Acta. Crystallogr. B. Struct. Sci. Cryst.*, 1973, **29**, 1752–1756.

250 A. Rossin, A. Ienco, F. Costantino, T. Montini, B. Di Credico, M. Caporali, L. Gonsalvi, P. Fornasiero and M. Peruzzini, *Cryst. Growth Des.*, 2008, **8**, 3302–3308.

251 M. Mączka, B. Bondzior, P. Dereń, A. Sieradzki, J. Trzmiel, A. Pietraszko and J. Hanuza, *Dalton Trans.*, 2015, **44**, 6871–6879.

252 M. Mączka, A. Pietraszko, L. Macalik, A. Sieradzki, J. Trzmiel and A. Pikul, *Dalton Trans.*, 2014, **43**, 17075–17084.

253 L. C. Gómez-Aguirre, B. Pato-Doldán, J. Mira, S. Castro-García, M. A. Señarís-Rodríguez, M. Sánchez-Andújar, J. Singleton and V. S. Zapf, *J. Am. Chem. Soc.*, 2016, **138**, 1122–1125.

254 J.-Q. Liu, J. Wu, J. Wang, L. Lu, C. Daiguebonne, G. Calvez, O. Guillou, H. Sakiyama, N. S. Weng and M. Zeller, *RSC Adv.*, 2014, **4**, 20605.

255 Antsyshkina A. S., Porai-Koshits M. A., Ostrikova V. N., Sadikov G. G., *Sov. J. Coord. Chem*, 1983, **9**, 855–858.

256 M. Mączka, A. Gągor, D. Stefańska, J. K. Zaręba and A. Pikul, *Dalton Trans.*, 2022, **51**, 9094–9102.

257 M. Mączka, A. Gągor, A. Pikul and D. Stefańska, *RSC Adv.*, 2020, **10**, 19020–19026.

258 D.-X. Liu, K.-P. Xie, W.-X. Zhang, M.-H. Zeng and X.-M. Chen, *CrystEngComm*, 2021, **23**, 2208–2214.

259 K.-P. Xie, W.-J. Xu, C.-T. He, B. Huang, Z.-Y. Du, Y.-J. Su, W.-X. Zhang and X.-M. Chen, *CrystEngComm*, 2016, **18**, 4495–4498.

260 S.-L. Chen, Z.-R. Yang, B.-J. Wang, Y. Shang, L.-Y. Sun, C.-T. He, H.-L. Zhou, W.-X. Zhang and X.-M. Chen, *Sci. China Mater.*, 2018, **61**, 1123–1128.

261 S.-L. Chen, Y. Shang, C.-T. He, L.-Y. Sun, Z.-M. Ye, W.-X. Zhang and X.-M. Chen, *CrystEngComm*, 2018, **20**, 7458–7463.

262 Y.-L. Sun, C. Shi and W. Zhang, *Dalton Trans.*, 2017, **46**, 16774–16778.

# 6. APPENDIX

## 6.1. Complete List of Publications

### 6.1.1. First Author Publications

Peer Reviewed Journal Publications

(1) S. M. Kronawitter, S. A. Hallweger, J. Meyer, C. Pedri, S. Burger, A. Alhadid, S. Henke, G. Kieslich: $Li(C_2N_3)$ as Eutectic Forming Modifier in the Melting Process of the Molecular Perovskite $[(C_3H_7)_3N(C_4H_9)]Mn(C_2N_3)_3$, *APL Mater* **2023**, *11*, 31119

(2) K. Hemmer,† S. M. Kronawitter,† N. Grover, B. Twamley, M. Cokoja, R. A. Fischer, G. Kieslich, M. O. Senge: Understanding and Controlling Molecular Compositions and Properties in Mixed-Linker Porphyrin Metal-Organic Frameworks, *Inorg. Chem.* **2024**, *63*, 4, 2122-2130

(3) S. M. Kronawitter,† R. Röß-Ohlenroth,† S. A. Hallweger, M. Hirrle, H. Krug von Nidda, T. Luxenhofer, E. Myatt, J. Pitcairn, M. J. Cliffe, D. Daisenberger, J. Wojciechowski, D. Volkmer, G. Kieslich: Spin-state dependent pressure responsiveness of Fe(II)-based triazolate metal-organic frameworks, *J. Mater. Chem. C* **2024**, 12, 4954-4960

(4) S. M. Kronawitter, S. Park, S. A. Hallweger, E. Myatt, J. Pitcairn, M. J. Cliffe, D. Daisenberger, M. Drees, G. Kieslich: Tuning the mechanical properties of molecular perovskites by controlling framework Distortions *via* A-site substitution, *Mater. Adv.* **2024**, 10.1039/d4ma00587b

† Equal contribution

Conference Contributions

(1) S. M. Kronawitter, G. Kieslich: $ABX_3$ Molecular Perovskites as Barocalorics, *ACS Spring 2022*, San Diego (US), **20.03.2022**

(2) S. M. Kronawitter, G. Kieslich: $ABX_3$ Molecular Perovskites as Potential Barocalorics, *8th International Conference on Metal-Organic Frameworks and Open Framework Compounds ("MOF2022")*, Dresden (GER), **06.09.2022**

(3) S. M. Kronawitter, G. Kieslich: Structural Chemistry of $ABX_3$ Molecular Perovskites, *26th Congress and General Assembly of the International Union of Crystallography 2023 ("IUCr 2023")*, Melbourne (AUS), **27.08.2023**

(4) S. M. Kronawitter, G. Kieslich: Towards Design Principles of $ABX_3$ Molecular Perovskites, *Conference on Porous Materials in Energy Science ("PoreEnergy2024")*, Herrsching on Lake Ammersee (GER), **29.05.2024**

### 6.1.2. Contributions to Other Publications

Peer Reviewed Journal Publications

(1) S. Burger, S. Kronawitter, H. L. B. Boström, J. K. Zaręba, G. Kieslich: A new polar perovskite coordination network with azaspiroundecane as A-site cation, *Dalton Trans.* **2020**, *49*, 10740-10744

(2) L. Petters, S. Burger, S. Kronawitter, M. Drees, G. Kieslich: Linear negative thermal expansion in $Pd(acac)_2$, *CrystEngComm* **2021**, *23*, 5425-5429

(3) S. Liu, M. W. Heindl, N. Fehn, S. Caicedo-Dávila, L. Eyre, S. M. Kronawitter, J. Zerhoch, S. Bodnar, A. Shcherbakov, A. Stadlbauer, G. Kieslich, I. D. Sharp, D. A. Egger, A. Kartouzian, F. Deschler: Optically Induced Long-Lived Chirality Memory in the Color-Tunable Chiral Lead-Free Semiconductor (*R*)/(*S*)-$CHEA_4Bi_2Br_xI_{10-x}$ ($x$ = 0–10), *J. Am. Chem. Soc.* **2022**, *144*, 31, 14079-14089

(4) A. Alhadid, C. Jandl, S. Nasrallah, S. M. Kronawitter, L. Mokrushina, G. Kieslich, M. Minceva: Estimating the nonideality of eutectic systems containing thermally unstable substances, *J. Chem. Phys.* **2023**, *159*, 94503

(5) M. Geers, D. M. Jarvis, C. Liu, S. S. Saxena, J. Pitcairn, E. Myatt, S. A. Hallweger, S. M. Kronawitter, G. Kieslich, S. Ling, A. B. Cairns, D. Daisenberger, O. Fabelo, L. Cañadillas-Delgado, M. J. Cliffe: High-pressure behavior of the magnetic van der Waals molecular framework $Ni(NCS)_2$, *Phys. Rev. B* **2023**, *108*, 144439

(6) F. S. Hegner, A. Cohen, S. S. Rudel, S. M. Kronawitter, M. Grumet, X. Zhu, R. Korobko, L. Houben, C. Jiang, W. Schnick, G. Kieslich, O. Yaffe, I. D. Sharp, D. A. Egger: The Critical Role of Anharmonic Lattice Dynamics for Macroscopic Properties of the Visible Light Absorbing Nitride Semiconductor CuTaN2, Adv. Energy Mater. **2024**, 2303059

(7) A. Alhadid, L. Kefalianakis, A. Wendler, S. Nasrallah, C. Jandl, S. M. Kronawitter, G. Kieslich, M. Minceva: Thermodynamic Approach for Estimating the Melting Enthalpy of Cocrystals, *Cryst. Growth Des.* **2024**, *24*, 11, 4770-4780

## 6.2. Reprint Permissions

**Study I:** (retrieved on the 10th of October 2023)

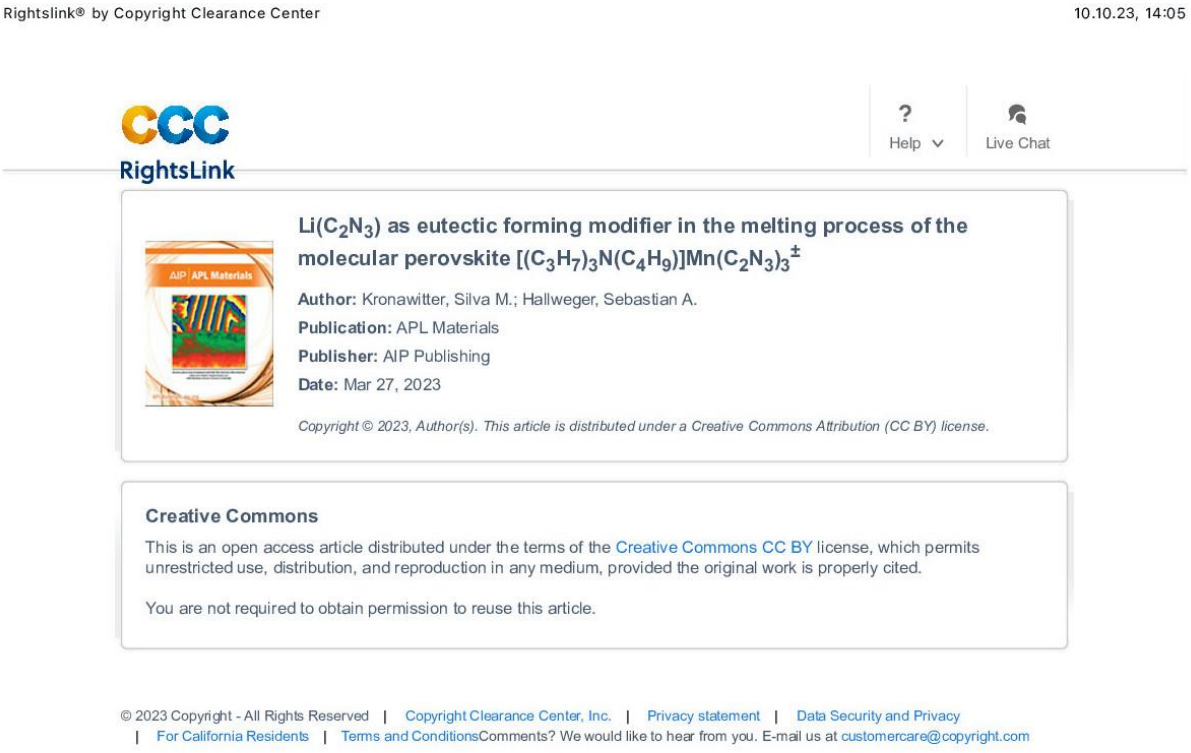

Rightslink® by Copyright Clearance Center 10.10.23, 14:05

RightsLink

Help Live Chat

$Li(C_2N_3)$ as eutectic forming modifier in the melting process of the molecular perovskite $[(C_3H_7)_3N(C_4H_9)]Mn(C_2N_3)_3^{\pm}$

**Author:** Kronawitter, Silva M.; Hallweger, Sebastian A.
**Publication:** APL Materials
**Publisher:** AIP Publishing
**Date:** Mar 27, 2023

*Copyright © 2023, Author(s). This article is distributed under a Creative Commons Attribution (CC BY) license.*

**Creative Commons**

This is an open access article distributed under the terms of the Creative Commons CC BY license, which permits unrestricted use, distribution, and reproduction in any medium, provided the original work is properly cited.

You are not required to obtain permission to reuse this article.



**Study II:** (retrieved on the 29th of January 2024)

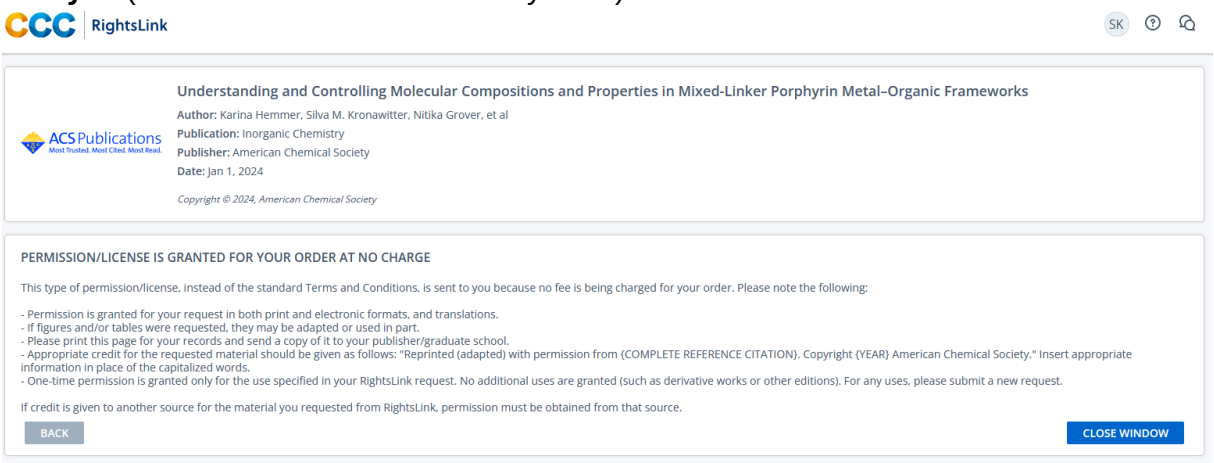

RightsLink

Understanding and Controlling Molecular Compositions and Properties in Mixed-Linker Porphyrin Metal–Organic Frameworks

**Author:** Karina Hemmer, Silva M. Kronawitter, Nitika Grover, et al
**Publication:** Inorganic Chemistry
**Publisher:** American Chemical Society
**Date:** Jan 1, 2024

*Copyright © 2024, American Chemical Society*

PERMISSION/LICENSE IS GRANTED FOR YOUR ORDER AT NO CHARGE

This type of permission/license, instead of the standard Terms and Conditions, is sent to you because no fee is being charged for your order. Please note the following:

- Permission is granted for your request in both print and electronic formats, and translations.
- If figures and/or tables were requested, they may be adapted or used in part.
- Please print this page for your records and send a copy of it to your publisher/graduate school.
- Appropriate credit for the requested material should be given as follows: "Reprinted (adapted) with permission from {COMPLETE REFERENCE CITATION}. Copyright {YEAR} American Chemical Society." Insert appropriate information in place of the capitalized words.
- One-time permission is granted only for the use specified in your RightsLink request. No additional uses are granted (such as derivative works or other editions). For any uses, please submit a new request.

If credit is given to another source for the material you requested from RightsLink, permission must be obtained from that source.

BACK CLOSE WINDOW

**Study III:** (retrieved on the 9th of April 2024)

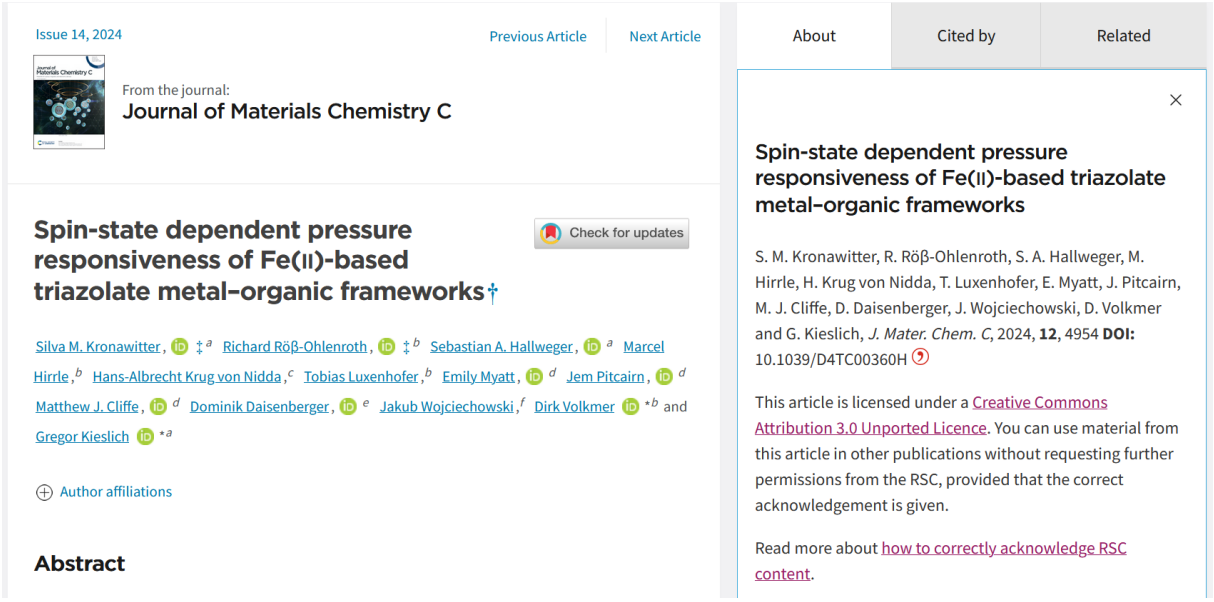

Issue 14, 2024 Previous Article Next Article

From the journal:
Journal of Materials Chemistry C

## Spin-state dependent pressure responsiveness of Fe(II)-based triazolate metal–organic frameworks†

Check for updates

Silva M. Kronawitter, ‡[a] Richard Röß-Ohlenroth, ‡[b] Sebastian A. Hallweger, [a] Marcel Hirrle,[b] Hans-Albrecht Krug von Nidda,[c] Tobias Luxenhofer,[b] Emily Myatt, [d] Jem Pitcairn, [d] Matthew J. Cliffe, [d] Dominik Daisenberger, [e] Jakub Wojciechowski,[f] Dirk Volkmer *[b] and Gregor Kieslich *[a]

Author affiliations

### Abstract

About | Cited by | Related

**Spin-state dependent pressure responsiveness of Fe(II)-based triazolate metal–organic frameworks**

S. M. Kronawitter, R. Röß-Ohlenroth, S. A. Hallweger, M. Hirrle, H. Krug von Nidda, T. Luxenhofer, E. Myatt, J. Pitcairn, M. J. Cliffe, D. Daisenberger, J. Wojciechowski, D. Volkmer and G. Kieslich, *J. Mater. Chem. C*, 2024, **12**, 4954 **DOI:** 10.1039/D4TC00360H



**Study IV:** (retrieved on the 30th of July 2024)

From the journal:
Materials Advances

## Tuning the mechanical properties of molecular perovskites by controlling framework distortions *via* A-site substitution†

Check for updates

Silva M. Kronawitter, [a] Shinjoo Park,[a] Sebastian A. Hallweger, [a] Emily Myatt, [b] Jem Pitcairn,[b] Matthew J. Cliffe, [b] Dominik Daisenberger, [c] Markus Drees[a] and Gregor Kieslich *[a]

Author affiliations

### Abstract

About | Cited by | Related

**Tuning the mechanical properties of molecular perovskites by controlling framework distortions *via* A-site substitution**

S. M. Kronawitter, S. Park, S. A. Hallweger, E. Myatt, J. Pitcairn, M. J. Cliffe, D. Daisenberger, M. Drees and G. Kieslich, *Mater. Adv.*, 2024, Advance Article , **DOI:** 10.1039/D4MA00587B